Porous Media Thermoacoustic Stacks: Measurements and Models

by

Syeda Humaira Tasnim

A thesis
presented to the University of Waterloo
in fulfilment of the
thesis requirement for the degree of
Doctor of Philosophy
in
Mechanical Engineering

Waterloo, Ontario, Canada, 2011

Author's Declaration

I hereby declare that I am the sole author of this thesis. This is a true copy of the thesis, including any required final revisions, as accepted by my examiners.

I understand that my thesis may be made electronically available to the public.

Abstract

The present research analyzes random porous thermoacoustic stack systems analytically, experimentally, and numerically with a primary objective to develop a comprehensive analytical porous media modeling for random porous (such as Reticulated Vitreous Carbon (RVC) foams) environment. Mathematical models are developed for flow, thermal, and energy fields within the random porous medium stack. Initially, the Darcy model is used for modeling the momentum equation and local thermal equilibrium assumption between the porous matrix and trapped fluid in the void space for energy equation. The expressions of temperature, energy flux density, and acoustic work absorbed or produced by a thermoacoustic device are compared with existing literature and observed good agreements. After obtaining the flow and thermal fields' information, the present study examines the entropy generation distribution within the stack. One important item revealed in this study is that entropy generation inside the porous medium completely follows the trend of the imaginary part of $\widetilde{f}_k$ profile. Another major contribution of this research is to identify the location of maximum entropy generation which is identical to the location of maximum thermoacoustic heat and work transport. The expression of Nusselt number for steady flow cannot be used in oscillatory random porous medium because of the phase difference between the temperature gradient at the wall and the temperature difference between the wall and the space averaged temperature.

The present study then extends the Darcy model by considering Brinkman-Forchheimer-extended Darcy model for the modeling of momentum equation. The reason for considering Brinkman-Forchheimer extended Darcy model is to consider the presence of high velocity and high porosity porous medium which are typical in thermoacoustic devices. Therefore, this model is applicable in practical thermoacoustic devices. Mathematical models are developed for flow, thermal, and energy fields within the random porous media. To verify the present study, the temperature difference obtained across the stack ends is compared with the experimental results. A very good agreement

is obtained between the modeling and the experimental results thus strengthening confidence in the newly developed model.

The present research experimentally examines novel stack configuration by considering "alternating conducting and insulating materials" as stack in thermoacoustic devices. The objective of considering such stack arrangement is to reduce the conduction heat transfer loss from the hot end of the stack to the cold end, thereby increasing the performance of the stack. Eight different heterogeneous (alternating conducting and insulating materials) stack arrangements are studied in this research. The performance (temperature difference generated across the stack ends at steady state and stack hot end temperature for a thermoacoustic heat pump) of the heterogeneous stack arrangement is compared with the typical homogeneous stacks. It is observed that heterogeneous stack arrangements of smaller length (0.02λ, where λ is the wavelength of the acoustic wave) show comparable performance to that of longer (0.04λ) homogeneous regular stack (Corning Celcor ceramic stack). This research shows that heterogeneous stacks can be used in thermoacoustic devices particularly in small (millimeter) scale thermoacoustic devices.

Numerically the present study investigates the influence of working fluid, geometric, and operating conditions on stack performance by solving the full Navier-Stokes, mass, energy equation, and equation of state. The drive ratio (DR) is varied from 1.7 to 10%, Prandtl number (Pr) is varied between 0.7 and 0.28, stack plate spacing (y_0) is varied from $3.33\,\delta_k$ to $1.0\,\delta_k$, and mean pressure (p_m) is varied from 10 kPa to 1000 kPa in these simulations. Results are presented in terms of velocity, temperature, cooling power, acoustic power, COP, and entropy generation contours. It is found that, lowering the Pr of the working fluid at a low mean pressure (for example, $p_m = 10\,\text{kPa}$), low DR (DR=1.7%), and at a stack plate spacing of $y_0 = 3.33\delta_k$ shows the best performance regarding the COP. An important finding of this study is that cooling power and acoustic power absorbed by a thermoacoustic refrigerator increase as the p_m and DR increase, but the increase of acoustic power is more significant than the cooling power at higher DR and p_m. Therefore, COP decreases at higher DR and p_m.

Acknowledgements

My sincere thank and appreciation goes to Professor R. A. Fraser, my research supervisor who gave me the freedom and the encouragement to pursue my own ideas and to manage my own research. His guidance, advice and assistance were invaluable during the course of this work. Words cannot express my gratitude of what you have done for me and once again, thank you very much. I look forward to future opportunities to interact on projects and papers.

For your invaluable assistance, personal involvement and encouragement, Prof. S. Mahmud, I wish to extend my profound gratitude. You did not only help me in my research work but also assisted me throughout my Ph.D. studies. Your immense patience and understanding help me to pursue my studies. Tanzim Mahmud, my sweet little son, I really appreciate your ever willingness to hug me with love and cheerfulness each day.

I would also like to express my indebtedness to Professor Kamran Siddiqui for his willingness to be my external examiner. Special thanks to my internal examiners, Dr. Richard Culham, Dr. Glenn Heppler, and Dr. Serhiy Yarusevych for your precious time to reviewing my thesis. To Dr. Amir Baserinia, for your valuable suggestions on my comprehensive report. My appreciation also goes to the staff in the engineering machine shop especially to John Bold for helping me with the fabrication of stack samples and resonators. Special thanks to Paul Thomson for fixing all my computer related problems while I was on campus.

Special thanks to Dr. S.L. Garrett (Penn State University, USA) for providing me with Corning Celcor stack materials, Dr. G. W. Swift (Los Alamos National Laboratory, USA) for giving me permission to use some of the figures from his book in my thesis and Dr. Tijani for providing me with a copy of his PhD thesis.

Financial support from the Natural Sciences and Engineering Research Council of Canada (NSERC), Alexander Graham Bell Graduate Scholarship, University of Waterloo President's Scholarship, Faculty of Engineering Graduate Scholarships and Department

of Mechanical and Mechatronics Engineering Scholarships and Research Award are acknowledged and sincerely appreciated.

Table of Contents

List of Figures

List of Tables

Nomenclature

a	adiabatic speed of sound, $\mathrm{m \cdot s^{-1}}$
A	total cross-sectional area, $\mathrm{m^2}$
A_f	cross-sectional area of fluid, $\mathrm{m^2}$
A_s	cross-sectional area of solid, $\mathrm{m^2}$
COP	coefficient of performance of refrigerator
$COPC$	Carnot coefficient of performance
$COPR$	relative coefficient of performance
C_c	specific heat of the channel wall at constant pressure, $\mathrm{J \cdot kg^{-1} \cdot K^{-1}}$
C_p	specific heat of the fluid at constant pressure, $\mathrm{J \cdot kg^{-1} \cdot K^{-1}}$
C_{sm}	specific heat of the solid matrix of the porous medium, $\mathrm{J \cdot kg^{-1} \cdot K^{-1}}$
Da	Darcy number, Eq.(5.6a)
DR	drive ratio, $= p_0/p_m$
$\dot{\mathrm{E}}_2$	second order energy flux density, $\mathrm{W \cdot m^{-2}}$
E_2	global energy flux, W
$\vec{E}$	energy flux density vector, $\mathrm{W \cdot m^{-2}}$
$\mathrm{E_y}$	energy flux density in the y-direction, $\mathrm{W \cdot m^{-2}}$
$\mathrm{E_x}$	energy flux density in the x-direction, $\mathrm{W \cdot m^{-2}}$
f	frequency of oscillation, Hz
f_ν	first Rott's or Swift's function of thermoacoustics, Eq.(5.19)
$\widetilde{f}_\nu$	complex conjugate of f_ν

f_k	second Rott's or Swift's function of thermoacoustics, Eq. (5.19)
$\widetilde{f}_k$	complex conjugate of f_k
f_s	third Rott's or Swift's function of thermoacoustics, Eq.(4.26)
$\widetilde{f}_s$	complex conjugate of f_s
h	enthalpy, $\mathrm{J \cdot kg^{-1}}$
i	complex number, $=\sqrt{-1}$
K	permeability of the porous medium, $\mathrm{m^2}$
k_c	thermal conductivity of the channel wall, $\mathrm{W \cdot m^{-1} \cdot K^{-1}}$
k_f	thermal conductivity of the fluid, $\mathrm{W \cdot m^{-1} \cdot K^{-1}}$
k	overall thermal conductivity of the porous medium, $\mathrm{W \cdot m^{-1} \cdot K^{-1}}$
k_{sm}	thermal conductivity of the solid matrix in the porous medium, $\mathrm{W \cdot m^{-1} \cdot K^{-1}}$
Lc_k	Lautrec number,$= y_0/\delta_k$
L_s	length of the stack, m
L_{sn}	non-dimensional stack length
l	half thickness of the channel wall/plate, m
Ma	Mach number, $=\lvert u_\mathrm{A}\rvert/c_m$
N_s	total entropy generation, $\mathrm{W \cdot m^{-3} \cdot K^{-1}}$
Nu	complex Nusselt number
p	pressure, Pa
p_m	mean pressure, Pa
p_1, p_0	fluctuating pressure amplitude, Pa

Pr	Prandtl number of the fluid, $=\delta_v^2 / \delta_k^2$
Q_2	global heat flux, W
Q_{hn}	non-dimensional heat flux
R	gas constant, $\mathrm{J \cdot kg^{-1} \cdot K^{-1}}$
Re_δ	Reynolds number $= \dfrac{\rho u_A \delta_v}{\omega} = \dfrac{\sqrt{2\rho}\, u_A}{\sqrt{\mu\omega}}$
r_h	hydraulic radius, m
S	entropy, $\mathrm{J \cdot K^{-1}}$
S_{gen}	volumetric entropy generation rate, $\mathrm{W \cdot m^{-3} \cdot K^{-1}}$
T	temperature, ºC
T_C	cold end temperature, ºC
T_H	hot end temperature, ºC
T_m	mean temperature, ºC
T_1	fluctuating fluid temperature amplitude, ºC
T_s	solid temperature, ºC
T_{s1}	fluctuating solid temperature amplitude, ºC
T_w	temperature fluctuation at the wall, ºC
t	time, s
U_1	volumetric velocity, $\mathrm{m^3 \cdot s^{-1}}$
$\widetilde{U}_1$	complex conjugate of U_1
u	axial velocity, $\mathrm{m \cdot s^{-1}}$
u_1	fluctuating velocity amplitude, $\mathrm{m \cdot s^{-1}}$

v	transverse velocity, $\mathrm{m \cdot s^{-1}}$
$\vec{V}$ **, v**	velocity vector, $\mathrm{m \cdot s^{-1}}$
W_2	total work flux, W
W_n	non-dimensional work flux
X	Exergy, $\mathrm{W \cdot m^{-3}}$
x_1	displacement amplitude, $= u_1/\omega$
x	axial distance, m
x_n	non-dimensional stack center position
y	transverse distance in fluid, m
y'	transverse distance in solid, m
y_0	half spacing of a stack/channel, m
Y	non-dimensional distance, $= y/y_0$

Greek Symbols

α_f	thermal diffusivity of the fluid, $\mathrm{m^2 \cdot s^{-1}}$
α_c	thermal diffusivity of the channel wall, $\mathrm{m^2 \cdot s^{-1}}$
β	thermal expansion coefficient, $\mathrm{K^{-1}}$
γ	isobaric to isochoric specific heat ratio, $=C_p/C_v$
Δ	change in any variable
Γ	ratio of ∇T_m to ∇T_{cr}
Γ_0	ratio of ∇T_{cr} to ∇T_m
δ_ν	viscous penetration depth, $=\sqrt{2\nu/\omega}$

δ_k thermal penetration depth, $=\sqrt{2\alpha_f / \omega}$

δ_s thermal penetration depth in the channel wall, $=\sqrt{2\alpha_c / \omega}$

ε_s heat capacity ratio, $= \sqrt{(k \rho_m C_p)/(k_s \rho_{ms} C_s)}$

∇p pressure gradient, $\mathrm{N \cdot m^{-3}}$

∇T temperature gradient, $\mathrm{K \cdot m^{-1}}$

∇T_m mean temperature gradient, $=\partial T_m / \partial x$

∇p_1 pressure gradient, $=\partial p_1 / \partial x$

∇T_{cr} critical temperature gradient, $\mathrm{K \cdot m^{-1}}$

μ dynamic viscosity of the fluid, $\mathrm{N \cdot m^{-2} \cdot s}$

ν kinematic viscosity, $\mathrm{m^2 \cdot s^{-1}}$

$\boldsymbol{\sigma}$ viscous stress tensor, $\mathrm{N \cdot m^{-2}}$

ω angular frequency, $\mathrm{rad \cdot s^{-1}}$

ρ density, $\mathrm{kg \cdot m^{-3}}$

ρ_{fm} mean fluid density, $\mathrm{kg\ m^{-3}}$

ρ_{sm} mean solid porous matrix density, $\mathrm{kg\ m^{-3}}$

ρ_c density of the channel wall, $\mathrm{kg \cdot m^{-3}}$

τ time period, $=2\pi/\omega$

λ wavelength, m

Π width of the plate, m

ϕ porosity of the porous medium, =void volume/total volume

Θ dimensionless temperature , Eq. (5.105)

Subscripts and Superscripts

0	reference value
1	first order variable
2	second order variable
b	boundary layer approximation (in Chapter 4)
cond	conduction heat transfer (in Chapter 4)
H	overall value (in Chapter 4)
av	average value
f	properties of the fluid
m	mean value
s	properties of the solid
sm	properties of the solid matrix in porous medium
w	value at wall

Symbols

^	over any variable represents both space and time dependency
$\Re$ [ ]	real part of an expression
$\Im$ [ ]	complex part of an expression
$\overline{\Gamma}$	time average of a complex expression $\Gamma, = \tau^{-1} \int_0^{\tau} \Gamma \, dt$
$\langle \Gamma \rangle$	space integration of a complex expression $\Gamma, = \lim_{Z \to \Pi} \int_0^{Z} \Gamma \, dt$
~	complex conjugate of a variable

Chapter 2

V	volume of the fluid, m^3
V_1	volume fluctuation, m^3
δ	change in a parameter
m	mass, kg, Eq. (2.6)
S_{gen}	entropy generation, $J \cdot K^{-1}$

Chapter 5

a_0	a parameter,$=(1+i)/\delta_\nu$
b_0	a parameter,$=(1+i)/\delta_k$
k_c	thermal conductivity of the channel wall, $W \cdot m^{-1} \cdot K^{-1}$
σ	porous medium heat capacity ratio, Eq. (5.11)
S_w	a dimensionless parameter,$= y_0/\delta_\nu$
Δx	length of the stack plate, m

Chapter 9

h_x	energy flux density in the x-direction, $W \cdot m^{-2}$
s	specific entropy, $J \cdot kg^{-1}$

Appendix C

Δx	grid spacing in the x-direction, m
Δy	grid spacing in the y-direction, m
Δt	time step size, s

Chapter 1

Introduction

In recent years, greenhouse emissions and climate changes are two critical issues being addressed by the scientists all over the world. As scientists and engineers are intensely working to invent advanced technologies to make peoples' life easier, climate changes and greenhouse emissions are becoming more critical issues. Consider the two greatest engineering achievements of the 20^{th} century: the automobile (and hence the internal combustion engine) and the refrigerator and air-conditioner. These two pillars of modern technology share another, less gratifying distinction: both have inadvertently damaged the environment by clouding skies with smog, discharging green house gases (CO_2, Chlorofluorocarbons) or leaking compounds that erode the earth's protective blanket of stratospheric ozone. The natural ozone levels in the atmosphere allow most harmful solar radiation to be absorbed before it can reach the earth's surface; ozone absorbs a significant portion of the ultraviolet light which has been linked to various types of skin cancer, cataracts and damage to the human immune system; it is also known to be harmful to some crops and some forms of marine life. Any changes in the amount of radiation that penetrates to the earth's surface as a result of the thinning of the ozone layer can have potentially serious implications for human health and ecological systems, and also for global climate (Khaligi et al. [2000]. Over the past two decades, investigators have worked to develop an entirely new class of engines and refrigerators that may help to reduce or eliminate such threats. A promising technology involves the thermoacoustic effect.

Thermoacoustics is the study of an elegant engineering field that involves both acoustics and thermodynamics - in other words, the study of fields that involve both acoustic waves and the conversion of one form of energy into another, such as heat into motion. Thermoacoustics thus describes energy conversion processes initiated by the interaction of the temperature oscillation accompanying by the pressure oscillation in a sound wave with solid boundaries. This interaction of sound and heat cannot be observed in ordinary

experience. Under suitable conditions it can be amplified to give rise to significant thermodynamic effects such as steep thermal gradients, convective heat fluxes, and strong sound fields. Thermoacoustic engines produce acoustic power using heat flow from a high temperature source to a low-temperature sink. In contrast, thermoacoustic heat pumps do the reverse; they use acoustic power to cause heat flow from a low-temperature source to a high temperature sink.

Advantages of thermoacoustic systems include environmental friendliness, potentially high reliability due to simple structure and minimum number of moving parts, and reasonable efficiency. These characteristics could lead to low manufacturing and maintenance costs.

The first quantitative analysis of the thermoacoustic effect published by the great thermoacoustician Nikolaus Rott [1980] almost three decade ago which was extended by Swift [1988] and provided a primary design tool based on the linearization of the equation of mass, momentum and energy conservation. This linear theory (Swift [1988]) is the basis for the design methodology of all the thermoacoustic devices built so far. So far, the limits of this theory are not firmly established. Therefore, the deviations between the theory and the measurements are difficult to explain. Generally the theoretical calculations overestimate the measured ones by 20%, 30%, 50%, and in some cases also by 300% (Kim et al. [1998]). From a practical point of view these deviations are deleterious because they are associated with a reduction in efficiency.

Also, practical applications are operated at drive ratio or high pressure amplitude where non-linear oscillations and non-linear effects can be excited and become important. Linear models do not accurately predict the performances of the device in such regimes. As a consequence and because of a general lack of a priori knowledge of the flow dynamics and heat transfer processes, the thermoacoustic devices designed and built so far achieve low performances. The most efficient engine built to date delivered acoustic power to the resonator with 18% efficiency (Los Alamos National Laboratories [2004]).

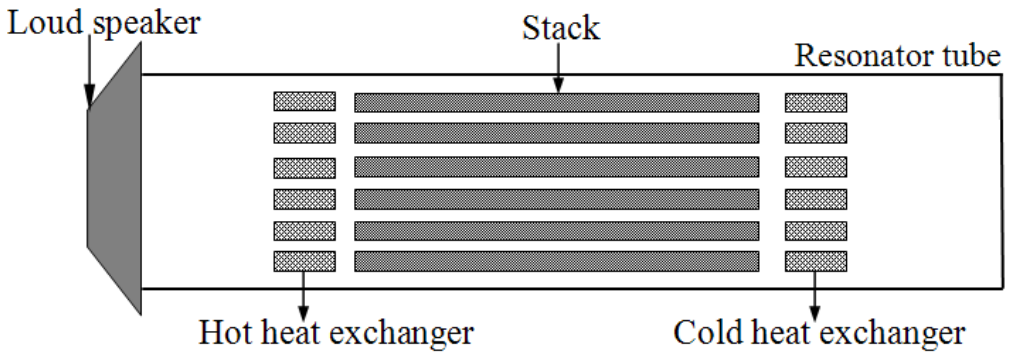

Figure 1.1: Schematic diagram of a typical thermoacoustic refrigerator.

Figure 1.1 shows a schematic of a simple thermoacoustic refrigerator. The functions of different parts of thermoacoustic engine and refrigerator are discussed in detail in Swift [2002]. Very briefly, a thermoacoustic heat pump, or refrigerator, consists of a resonator, two heat exchangers and a porous structure in between as shown in Fig.1.1. A driver, in most cases a loudspeaker, supplies the acoustic energy necessary to pump heat from the low temperature side to the high temperature side of the stack. This stack is usually made of thin parallel plates much longer than the particle displacement amplitude, whereas the heat exchanger's length is comparable to particle displacement amplitude. When a stack is properly placed inside an acoustically resonant tube, a thermal gradient rapidly develops across the stack plates because of heat flux along the stack in the direction of fluid oscillation. Installation of heat exchangers near the extremities of the stack provides an opportunity to supply the heat flux inside the resonator (through the cold heat exchanger) and extract the heat flux from the resonator (through the hot heat exchanger). Thus a thermoacoustic heat pump can be used to heat the other systems which are connected to the hot heat exchanger (for example, to the room as do the coils on the back of a conventional refrigerator) or a thermoacoustic refrigerator can be used to cool the other systems which are connected to the cold heat exchanger (for example, food in a refrigerator). A thermoacoustic engine reverses these works and thermal energy flows.

1.1 History

The earliest thermoacoustic engine was the Sondhauss tube (see Sondhauss [1850]), shown in Figure 1.2 (left). Over 100 years ago, glass blowers found that when a small hot

glass bulb was being blown on a cool glass tubular stem, the stem tip sometimes radiated sound. Rayleigh [1945] understood that the sound was generated by the oscillatory thermal expansion and compression of the air in the tube. The Sondhauss tube is a thermoacoustic prime mover, converting heat into mechanical work in the form of sound. It produces a standing acoustic wave, with the bulb and stem forming a resonator. But the reverse thermodynamic process of generating a temperature gradient by imposing acoustic oscillations is a more recent phenomenon. Although Rayleigh gave the correct qualitative description of the oscillating thermodynamics that is the core of standing – wave engines, an accurate theory was not developed until Rott [1980] derived the wave equation and energy equation for a single frequency sound propagating along a temperature gradient in a channel. These equations first received experimental verification (Yazaki et al. [1980]) in the context of Taconis oscillations, which can occur when a gas filled tube reaches from ambient temperature to cryogenics temperature. Rott's work forms the theoretical basis of most of modern standing-wave thermoacoustics. Gifford and Longsworth displayed a heat-pumping process along the inner surface of a closed tube, where pressure oscillations at low frequency were sustained (Gifford and Longsworth [1966]). Also Merkhli and Thomann [1975] published a paper describing their experimental finding that the oscillating flow generated in a gas-filled resonance tube can produce not only heating but also cooling of the tube wall. Merkhli and Thomann developed an analytical expression for heat flux in resonant tubes and tested its validity with laminar flow experiment. The oscillations were driven by a piston at one end of the tube and the other end is closed by a shiftable end and the walls of the resonance tube were kept at uniform temperature. They found both experimentally and theoretically that the wave motion is attended by time-averaged net heat flows. The longitudinal heat flux is transported from the velocity antinode to the adjacent pressure antinodes; and the transverse heat flux is rejected to the environment in a region near the pressure antinode or is absorbed from the environment in a region near the velocity antinode, if the Prandtl number of the ideal gas medium is smaller than unity. These two events formed the foundation of the work at Los Alamos National Laboratories (LANL) on thermoacoustic devices in the eighties, by Wheatley, Swift, and

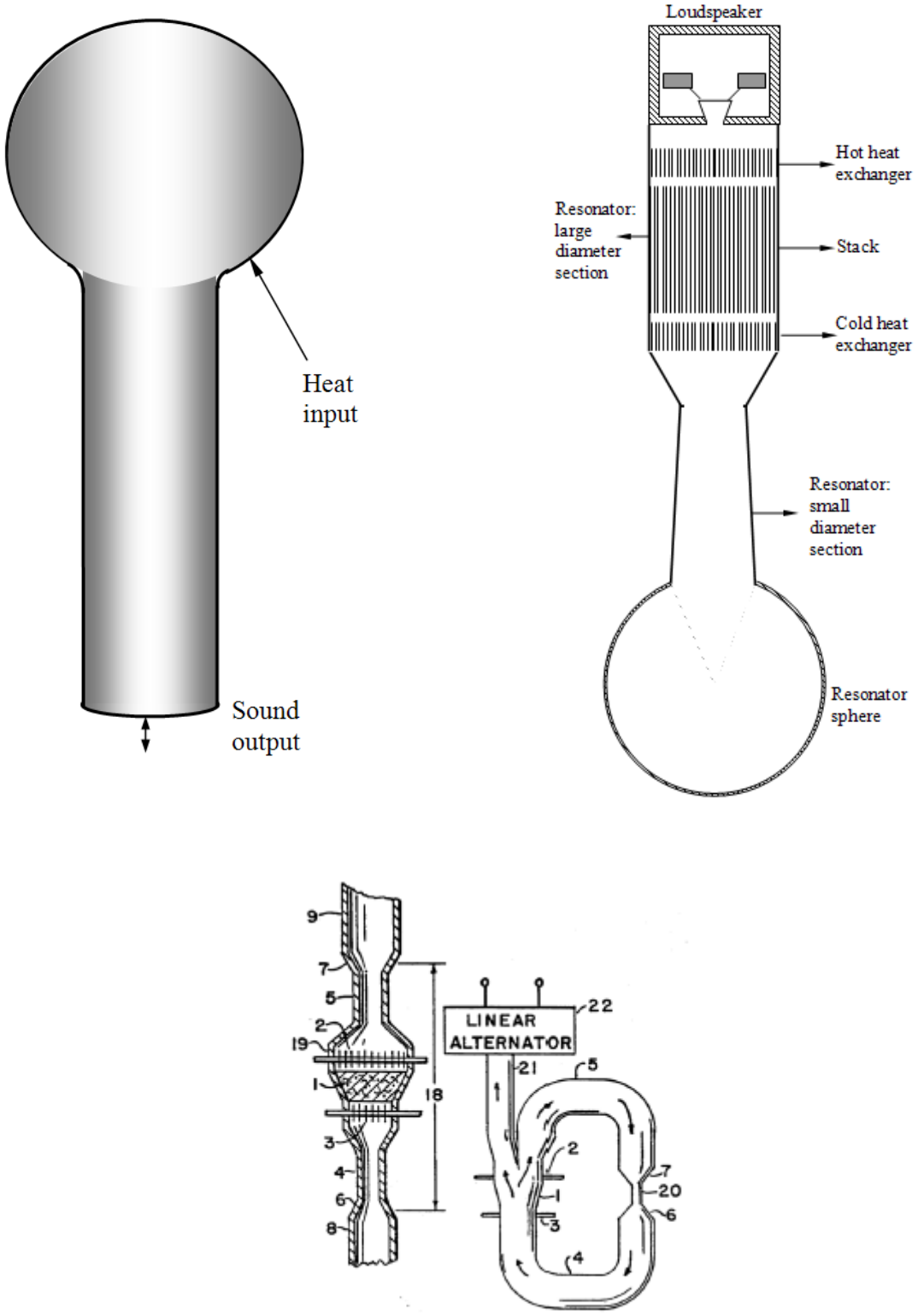

Figure 1.2: Examples of thermoacoustic engines: (left) the Sondhauss tube, (middle) Hofler's refrigerator, (right) the orifice pulse tube refrigerator, a traveling wave thermoacoustic heat pump (Swift [2002], presented with permission from Dr. G. Swift).

coworkers. The first thermoacoustic refrigerator, built at LANL, used a loudspeaker at one end of a closed tube, and a stack made of fiber glass plates positioned at the opposite end as shown in Fig. 1.2 (right). The stack of plates was used to improve the thermoacoustic effect. Since Feldman et al. [1970] examined that the performance of a Sondhauss tube could be improved by inclusion of a stack of small tubes. Using stack of small tubes has the effect of increasing the effective contact area between the gas and the solid over the cross section of the small tube, so that the whole gas contributes to the thermoacoustic heat transport process. Since then, several experimental set-ups have been built (Hofler [1986], Garrett et al. [1993], Garrett [1997]). Some examples will be given in **Section** 1.3. Ceperley's [1982] orifice pulse tube refrigerator Figure 1.2 (middle) is an example of a traveling wave thermoacoustic engine. Either a predominantly standing wave or a predominantly traveling wave can be used, although geometries for the two types of waves are substantially different.

1.2 Applications

First practical thermoacoustic apparatus was developed in the early eighties at LANL (Wheatly et al. [1983], Hofler [1986]). Since then thermoacoustic technology has received an increasing attention as a new research area of heat engines and heat pumps. After that many thermoacoustic systems have been built, mostly at LANL, Naval Postgraduate School (NPS) in Monterey (California), and at Pennsylvania State University. A detailed description of the application of thermoacoustic apparatus is available in Tijani [2001] and Mahmud [2005]. Therefore, only recent applications of thermoacoustic apparatus will be discussed in the current section.

Much of the attempts at LANL focused primarily on large thermoacoustic engines, using thermal energy (heat) to generate sound, which is used to generate electrical power or to drive coolers to liquefy natural gas. A recent example of such an engine (LANL [2004]), which produced acoustic powers up to 8.1 watts per kilogram and operated at efficiency as high as 18%. The generator is a thermoacoustic Sterling engine, where the sound waves from the engine drive a piston, which moves a coiled copper wire. As the wire moves through a magnetic field produced by a permanent magnet it produces electricity.

This thermoacoustic engine can generate electricity for space. Existing spaceship thermoelectric power converters are about seven percent efficient, and produce 5.2 watts per kilogram. Collaboration between LANL and Q-drive recently delivered a very special sterling cooler to pump heat out of drill tip electronics to a local environment well over 200 °C (LANL [2010]). This remarkable cooler fits into the restricted, narrow tubular space of a drill tip, using a set of five custom miniature STAR motors in coaxial concert, to drive an acoustic cold head. These motors include cobalt laminations, samarium magnets, and glass wire insulation, specially chosen to survive operation at over 250°C, plus the huge shock loads and vibration of rock drilling.

A ThermoAcoustically Driven ThermoAcoustic Refrigerator (TADTAR) has been built at NPS. This thermoacoustic refrigerator used a solar power driven prime mover instead of a loudspeaker to generate the sound necessary to drive the refrigerator. It has a cooling power capacity of 2.5 watt for a temperature span of 17.7 °C (Adeff and Hofler [2000]).

A prototype thermoacoustic chiller has been designed, constructed and tested at Pennsylvania State University to use in Benn and Jerry's ice cream (Poese et al. [2005]). The prototype machine, which is 10 inches (25.4 cm) in diameter and about 19 inches (48.3 cm) tall, has a cooling capacity of 119 W at a temperature of -24.6 ºC. The overall coefficient-of-performance (defined as the ratio of the cooling capacity to the electrical power consumption) of the chiller is measured to be 0.81 or 19% of the Carnot COP at the capacity and temperature listed above.

Noticeable research on thermoacoustic devices other than specified above are a thermoacoustic refrigerator designed, built, and tested by Tijani [2001] to produce a low temperature of -65 ºC with a cooling power of 4W, Junj et al.'s [2009] small scale prime mover which is 5.7 cm long, Tang et al. [2009]'s thermoacoustic engine with gas-liquid coupling oscillation, and Akhavanbazaz et al.'s [2007] thermoacoustic refrigerator that presents the effect of heat exchanger surface area on the performance of such kind of devices. Jin et al. [2003] built and tested a thermoacoustically driven pulse tube refrigerator. A cryogenic temperature lower than 120 K has been achieved from that system.

From the foregoing examples it can be seen that the potential of applications of thermoacoustic devices is substantial. Prime movers can be used to generate electricity, or to drive refrigerators. Thermoacoustic refrigerators that are highly reliable (because of no moving parts, no tight tolerances), environmentally safe (uses only inert gases, no CFC's), economical and compact are of considerable interest in space shuttles, warships, cooling of electronic instruments and situations where environmental concerns are critical. The reliability of a thermoacoustic refrigerator can be increased because of a lack of moving parts associated with an electrodynamic loudspeaker, if these loudspeakers as a source of the high intensity sound waves can be replaced. Significant progress has been made in the application of thermoacoustics, a technology capable of providing refrigeration using a variety of energy sources (e.g., solar energy, wind generated electricity, waste heat) in a device with 'no' internal moving parts! Such a device is being looked at for providing refrigeration or cooling needs in locations where refrigeration would usually be too expensive or simply unavailable. Being able to refrigerate would have the advantage of extending the shelf life of foods to either provide for a larger variety of foods at any given time of the year, or to reduce fluctuations in food supply in regions that experience food shortages. Thermoacoustic refrigerators powered by waste heat can be used in mobile refrigeration units for transportation of perishable goods and air conditioning units of passenger cars. The abundance of waste heat in vehicles renders mobile refrigeration and air conditioning a primary target market of thermoacoustic refrigerators powered by waste heat. The mobile air conditioning and refrigeration sectors contribute 40% of the total available Chlorofluorocarbons (CFC) in Canada in 1998 [2001]. Therefore, there is a strong motivation to switch to thermoacoustic refrigeration that can provide cooling without using any environmentally harmful substances, no internal moving parts, and using low grade of energy.

One drawback of standing- wave thermoacoustic devices is that they have a relatively low efficiency. However, thermoacoustic is still a young technology, the youngest of the heat engine cycles (Garrett [1993]). A new type of thermoacoustic engine based on traveling waves was developed and built and it delivered a thermal efficiency of 30%, corresponding to 41% of the Carnot efficiency (Backhaus et al. [2000]). The coefficient

of performance (COP) of today's automobile engine is 25-40%, vapor compression refrigeration systems with COP's about 50% of Carnot COP are common (Swift [2002]). Thermoacoustic refrigerators can also be made using this principle, and reach efficiencies comparable to vapor compression systems.

1.3 Existing Problems with Major Components of a Thermoacoustic Device

Figure 1.1 identifies the four major components of a thermoacoustic engine or refrigerator: the speaker, the resonant chamber, the stack, and the heat exchangers.

1.3.1 Resonant Speakers Needed

In thermoacoustic devices audio speakers are used to supply acoustic energy. There is a need to develop the speakers since to be efficient they must differ from the common audio speakers. The general audio speakers have efficiencies of 5% (Tijani [2001]) and produce a wide spectrum of frequencies that are not needed by a thermoacoustic device. Thermoacoustic dedicated speakers have been designed with an output to input energy efficiency in excess of 83% (Smith [1999]), as such the development of improved thermoacoustic speakers that resonant with low energy loss is more of a tuning problem, and hence is beyond the scope of this thesis.

1.3.2 Resonance Chamber Optimized for Stack Blockage Needed

The resonant chamber serves two purposes. It serves as housing for the stack and heat exchangers. Also the resonant chamber must reflect sound waves with little loss (due to heat transfer and viscous shear) in energy. Within the resonant chamber the standing sound waves will dissipate thus representing a source of inefficiency. Given that it is not possible to optimize the resonant chamber without first understanding how sound waves interact with the stack, heat exchanger, and wall of the chamber. Therefore, the interaction of the resonant chamber with the sound waves will be investigated in this thesis. The optimization of resonant chamber is beyond the scope of this thesis.

1.3.3 Tortuous and Non-Isotropic Stacks Should be Considered

The critical determinant element of thermoacoustic device efficiency is the stack. It is thus the structural heart of a thermoacoustic device which supports a longitudinal temperature gradient and is the element in which the desired interchange between thermal and acoustic energies takes place. They are finely subdivided into many parallel channels or pores in order to maintain moderate (standing-wave) thermal contact between the working gas and the stack across large cross-sectional areas. The surface of the stack material should be large enough so that most of the entrained gas lies within the thermal penetration depth and yet not significantly impede the oscillating sound wave. Therefore, the stack is no more than a means for increasing the total volume of gas in which heat pumping effects can occur. The qualitative understanding of the physical principle underlying the thermoacoustic effect within the stack is well established and has been discussed in many papers. But a quantitative experimental investigation of the effect of some important stack parameters on the behavior of the thermoacoustic devices is still lacking. Important parameters are the materials, geometry, dimension, and position of the stack as they determine the energy flow. Hence, the present research will quantitatively investigate the effect of these parameters on the performance of thermoacoustic devices. The explicit insertion of a stack into a thermoacoustic device offers a means to increase efficiency and power density. To operate, the stack must conduct thermal energy in a direction perpendicular to the sound wave direction, however, the stack inherently also experiences a finite temperature difference along its length resulting in heat transfer parallel to the sound waves from the hot to the cold heat exchangers. This inherent loss mechanism of the stack and its essential role in revealing a usable thermoacoustic effect makes it the central component of a thermoacoustic system that warrants further understanding of both its physics and its design considerations. For example, stacks have been considered to be made up of homogeneous, isotropic, materials. As a design consideration, and something that will be investigated in this work, there intuitively seems to be value in looking at a non-isotropic material stack design composed of alternating conductive and insulating material at regular intervals along the flow direction. This should reduce a stack's inherent finite temperature difference heat transfer losses.

There is evidence that use of tortuous porous materials as stacks or regenerators in thermoacoustic devices can raise the efficiency of thermoacoustic systems (Adeff et al. [1998]). To understand the oscillatory gas thermodynamics and heat transfer, and to implement thermoacoustic devices with high performance, fundamental research is required that addresses several problems important in thermoacoustic systems. These problems include thermoacoustic transport in tortuous porous media, acoustic and temperature fields in the system elements, and viscous and thermal losses within the stack element. The present research involves a (1) comprehensive analytical modeling and analysis of random porous media and (2) experimental investigation of random porous media under conditions specific to small scale systems.

1.3.4 Millimeter Scale Heat Transfer Improvements Needed

There is much work that needs to be done to enable high power, high efficiency heat transfer to and from the heat exchangers. With the smallest heat exchanger dimensions on the order of millimeters, the magnitude of convection heat transfer can be orders of magnitude greater than conduction heat transfer, but at the small millimeter scales of heat exchangers flow friction effects inhibit effective convection solutions. Much work needs to be done to understand these heat transfer processes and to optimize the heat transfer in heat exchanger. The optimization of heat transfer in heat exchangers is beyond the scope of this thesis.

1.4 Objectives

Despite recent progresses in thermoacoustic engines and refrigerators, many gaps in the understanding of the thermoacoustic phenomena remain. Major roadblocks to realizing high efficiency thermoacoustic devices as discussed in **Section** 1.3 falls largely into five categories: the speakers, the resonant chamber, the stack, the heat exchangers, and systems integration. The speaker problem, the resonator optimization problem, and heat exchanger design is outside the scope of this work.

The primary objective of the present research is:

To improve the efficiency of thermoacoustic devices by including stack design that incorporates porous media phenomena. Two different porous media modeling approaches are utilized by considering linear Darcy model and non-linear Brinkman Forchheimer extended Darcy model.

Specific sub-objectives are as follows:

- Perform experiments to verify porous media modeling;

- Quantify and compare the performance of regular stack to that of random porous stack in order to test the suitability of using random porous stack in thermoacoustic devices;

- Investigate the suitability of using non-isotropic stack material in thermoacoustic devices;

- Measure the performance of a thermoacoustically driven thermoacoustic refrigerator (TADTAR) and compare its performance to that of an acoustically driven thermoacoustic refrigerator (TAR); and

- Examine the influence of working fluid, geometric, and operating conditions on stack performance using numerical simulations.

1.5 Modeling Strategy

The flowchart below shows the modeling strategy that has been applied to achieve the objectives set in **Section** 1.4.

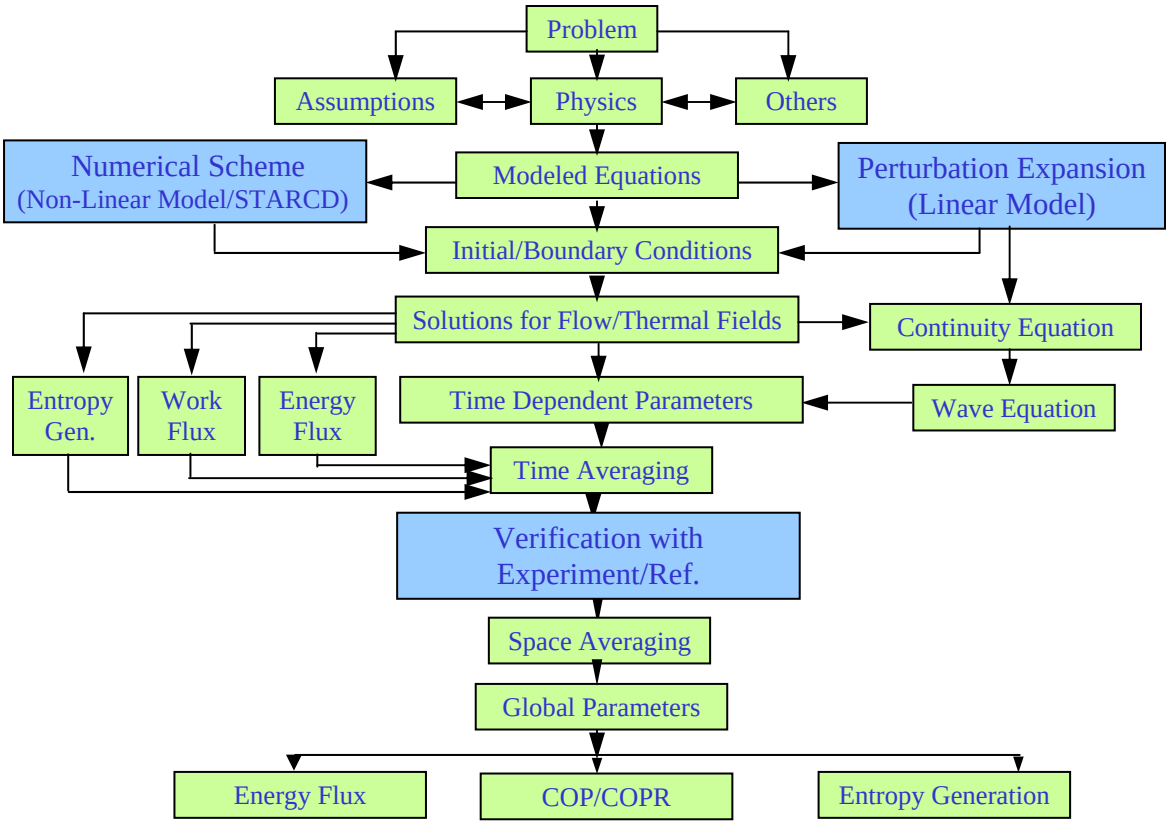

Figure 1.3: Flowchart of modeling strategy

1.6 Major Contributions of the Thesis

Figure 1.4 illustrates the major contributions of the present research. The current study predominantly focuses on the stack element of thermoacoustic devices. The primary objective of the present research is a comprehensive analytical porous media modeling using two different approaches. One approach is the Darcy model and the other one is the Brinkman Forchheimer extended Darcy model. The analytical modeling results are verified with experiments. Experiments in the present study are performed in two steps. In step 1, experiments on homogeneous stacks are performed. Homogeneous stacks again have two classifications: one is random porous media stack and the other one is regular

stack. Results on random porous media stacks are used for the verification of the analytical modeling. And results on regular stacks are used for the comparison of performance of random porous media stacks in order to test the suitability of using

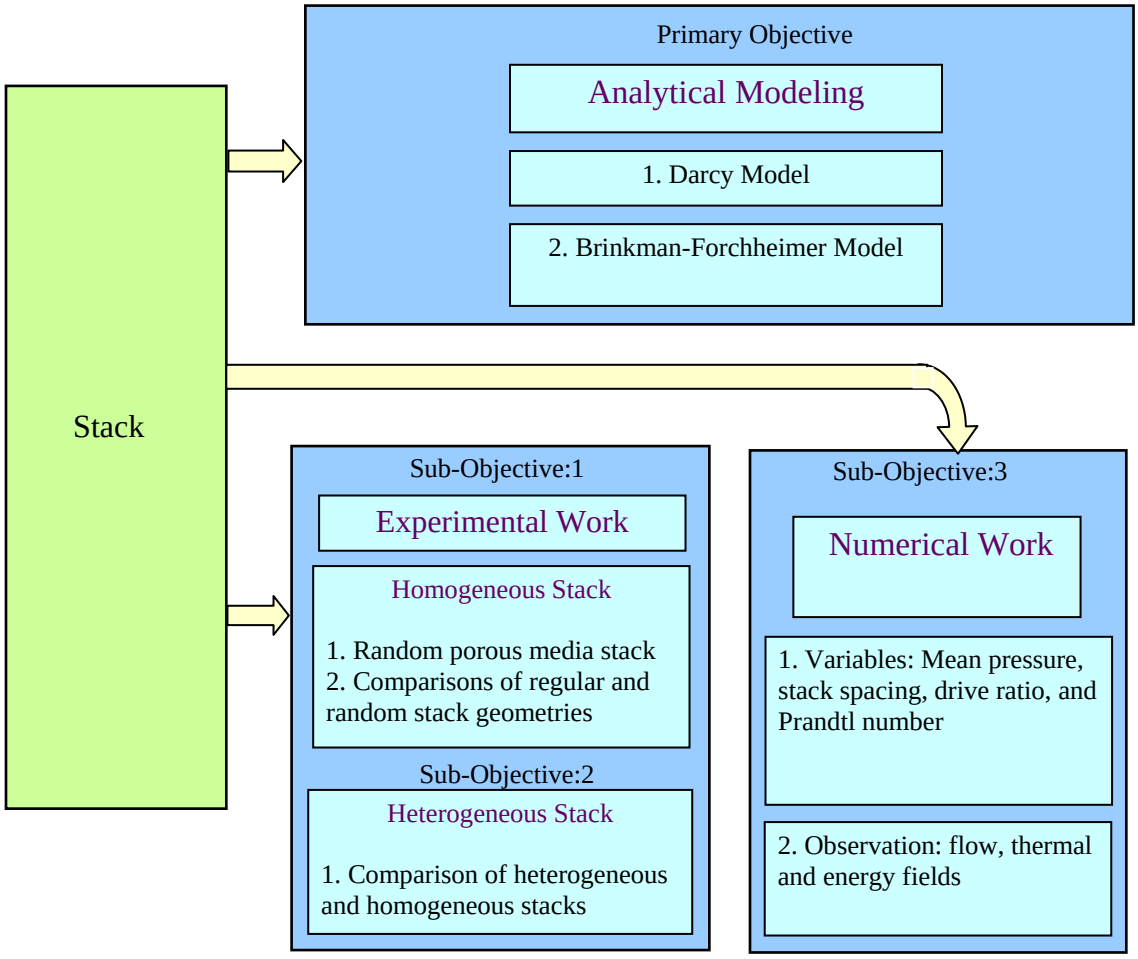

Figure 1.4: Pictorial representation of the major contributions of the present study. Numbered items identify major contribution trends.

random porous media stacks in thermoacoustic devices. In step 2 of the experiments, novel heterogeneous stack geometry is proposed and the performance of this heterogeneous stack geometry is compared to that of the homogeneous stacks in order to examine the suitability of using heterogeneous stacks in thermoacoustic devices. Now, experiments in thermoacoustics are time consuming, lengthy, and sometimes very complicated which motivates to perform the numerical simulations to investigate the influence of working fluid, geometric, and operating conditions on stack performance.

All the issues covered in **Section** 1.6 are absent in the current literature and therefore are the major contributions of the present research. The absence of the topics in **Section** 1.6 also provides the motivation for considering such research areas.

1.7 Outline of Thesis

The thesis consists of ten chapters and three appendices. In this chapter, after a brief description to the ideas, working principle, history, and applications of thermoacoustics, the objectives of the present research are proposed and scope of work is presented. In Chapter 2, first the thermoacoustic principles and thermoacoustic effects are reviewed. After that the literature are reviewed that justified the reasons for considering the objectives in **Section** 1.4. Chapter 3 is dedicated to the experimental set-up along with the measurements. Chapter 4 is devoted to the porous media modeling using Darcy Law (Bejan [1984]) by considering stacks as channels filled with porous medium. No such modeling exists in the literature except Mahmud [2005], who developed some preliminary porous media modeling. The assumption of Darcy model has obvious limitations (Darcy model is applicable to low Reynolds number flow), however this model is introduced to help more clearly describe the physical processes of thermoacoustic device while a porous medium is embedded in between the channel walls, and together the channel walls and the porous medium act as a stack. After obtaining the flow and thermal fields' expressions, entropy generation in a porous medium stack is analyzed and investigated. Mathematical models are developed in Chapter 5 using Brinkman Forchheimer extended Darcy model (Vafai and Kim [1989]) in order to overcome the limitations of Darcy model. As mentioned by Matveev and Jung [2010] that a theoretical understanding of tortuous stack environment is required to understand and increase the efficiency of thermoacoustic devices that uses tortuous stacks. Thus the system of equations developed in Chapter 4 and 5 is a helpful tool for thermal engineers and physicists to design porous stacks for thermoacoustic devices. A verification of the newly developed models with the experimental results of random porous stack is also reported. Chapter 6 focuses on the development of a thermoacoustically driven thermoacoustic refrigerator (TADTAR), measures the thermal performance, and compares the performance with a typical thermoacoustic refrigerator with an objective to

test the TADTAR's suitability. In chapter 7, the results of the experiments performed in homogenous stacks of different materials, geometries, dimensions, and positions are presented and discussed. A quantitative comparison of thermal field results is provided for regular and random porous media stacks (such as Reticulated Vitreous carbon foam). COP and COPR of regular stack geometry are compared to that of random porous media using the expressions provided in Appendix A. No such results exist in the literature that quantitatively evaluate and compare the thermal performance of regular and random porous media stacks of different porosities and dimensions. The outcome of this research has application to the search for efficient stack configurations for particular applications (especially for use in small scale thermoacoustic devices). Chapter 8 presents the results on novel heterogeneous stacks. The heterogeneous stack structure is assumed to reduce the conduction heat transfer loss from the hot to the cold end side of the stack and thus reduces the stack irreversibility. Thus the investigation on heterogeneous stack is crucial to understand the stack irreversibility. Chapter 9 deals with the numerical modeling of a thermoacoustic refrigerator to understand the nonlinear and low Prandtl number effects on flow, thermal, and energy fields. There is a need to understand the nonlinear phenomenon as linear theory (Swift [1988]) does not consider nonlinear effects and how nonlinear phenomenon effects the linear theory predictions. Tijani [2001] showed that lowering the Prandtl number for a particular stack increases the COP of a thermoacoustic device. Therefore, Chapter 9 numerically investigates the effect of lowering the Prandtl number on the COP of a thermoacoustic device for various stack plate spacing and operating conditions which are still unexplored in the existing literature. The results of these investigations will help to identify the appropriate geometry and operating conditions when a low Prandtl number fluid is utilized to increase the performance of a thermoacoustic device. Finally, conclusions and recommendations for future work are presented in Chapter 10.

Chapter 2

Physical Background

The basic principles of the thermoacoustic device are described in brief here in Chapter 2. For a detailed discussion of the topic see articles by Wheatley et al. [1983, 1986], Swift [1988], Tijani [2001] and Mahmud [2005]. The literature is reviewed following the introduction to the thermoacoustic effect, in order to clarify what has been done and what are the further investigations needed in the development of thermoacoustic engines and refrigerators.

2.1 Thermoacoustic Effect

Thermoacoustic devices mainly consist of an acoustic resonator filled with a gas. In the resonator, a stack consisting of a number of parallel plates, and two heat exchangers, are appropriately installed (Fig. (2.1)). The stack is the element that supports a longitudinal temperature gradient and in which the heat-pumping process takes place. It is sandwiched between heat exchangers which either supply or remove heat from the stack. The acoustic driver (e.g., loudspeaker) sustains an acoustic standing wave in the acoustic resonator. A simplified picture of the thermoacoustic effect will be given in the current section to explain how a temperature gradient and hence cooling develops across a stack. A heuristic derivation of the critical temperature gradient, the heat, and the work flows follow. The articles of Wheatley et al. [1983, 1986], Swift [1988], and Tijani [2001] form the basis for the discussion in this section.

Let's begin by discussing the thermodynamics of a small parcel of gas as it completes a thermoacoustic cycle. The parcel of gas is oscillating along a stack plate, being compressed and expanded by the sound wave. It is assumed that an average longitudinal temperature gradient ∇T_m exists along the stack plate. Additionally, it is supposed that the pressure antinode is to the right of the plate and a node to the left (as shown in Fig. (2.1)). The analysis performed in the current section presumes an inviscid ideal gas of

vanishing Prandtl number for simplicity, a complete theory that includes viscosity is briefly reviewed in Appendix A.

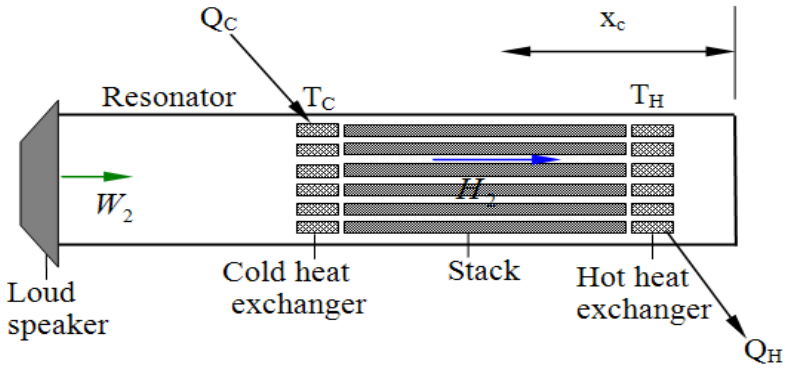

Figure 2.1: A quarter wave length standing wave thermoacoustic heat pump with different components along with acoustic power ($\dot{W}_2$) and energy flow ($\dot{H}_2$) directions.

Figure 2.2 shows the four steps of the thermoacoustic cycle. It is assumed that the initial temperature, pressure, and volume of the gas parcel at the start of the cycle are $T_m - x_1\nabla T_m$, $p_m - p_1$, and V. In step 1, the parcel of gas moves a distance x_1, where x_1 is the fluid displacement amplitude $(= u_1/\omega)$ and u_1 is the amplitude of the speed of motion of the gas caused by the sound wave. Near the pressure anti-node, the parcel of gas is compressed and increases in temperature by an amount $2T_1$. After the displacement and compression in step 1, the temperature, pressure, and volume becomes $T_m - x_1\nabla T_m + 2T_1$, $p_m + p_1$, and V-V_1. At this time, the temperature difference between the plate and the parcel of gas is (from Fig. 2.2)

$$\delta T = 2T_1 - 2x_1\nabla T_m = 2T_1\left(1 - \frac{\nabla T_m}{T_1/x_1}\right) \tag{2.1}$$

In Eq. (2.1), ∇T_m is the temperature gradient along the stack and $2x_1\nabla T_m$ is the temperature change of the stack plate. The value of ∇T_m that makes δT =0 is the critical temperature gradient, so

$$\nabla T_{crit} = \frac{T_1}{x_1}, \tag{2.2}$$

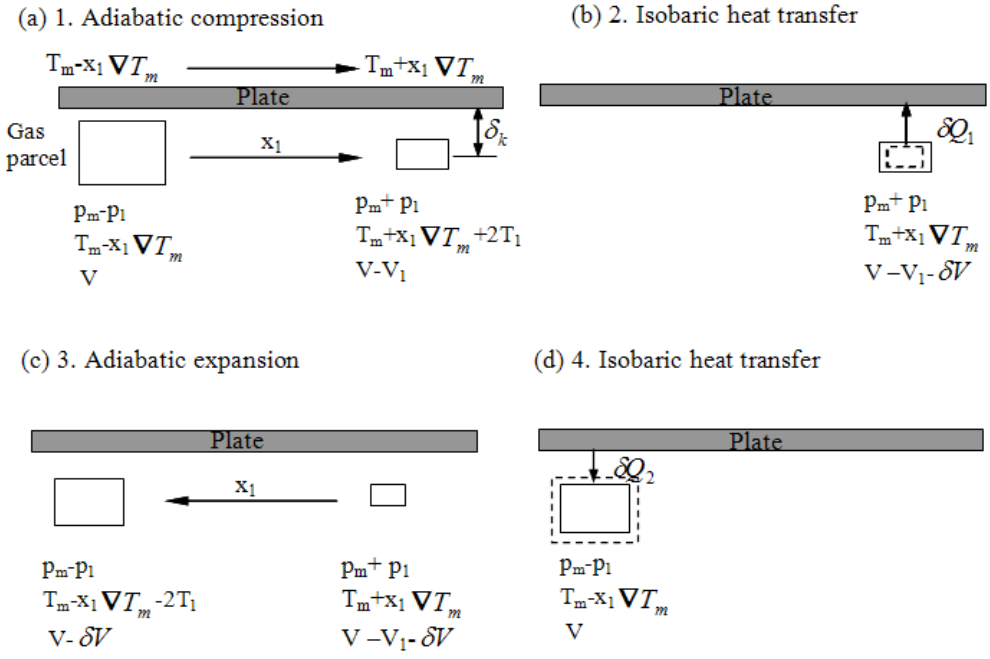

(a)

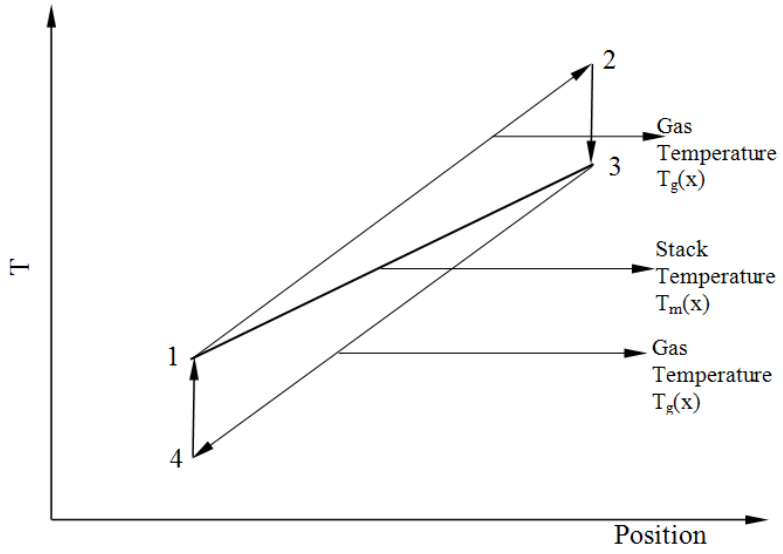

(b)

Figure 2.2 : A typical gas parcel in a thermoacoustic refrigerator passing through a four-step cycle with two adiabatic compression and expansion (step 1 and 3) and two constant-pressure heat transfer steps (steps 2 and 4) in (a) and (b).

can be written from Eq. (2.1). In Eq. (2.2), T_1 is the adiabatic temperature change. The temperature change T_1 accompanying the pressure change p_1 is obtained by assuming the temperature change of a fluid as a function of pressure and entropy change, so that one can write

$$dT = \left(\frac{\partial T}{\partial s}\right)_p ds + \left(\frac{\partial T}{\partial p}\right)_s dp \,. \tag{2.3}$$

The first term on the right hand side of Eq. (2.3) is zero due to the reversible adiabatic oscillation approximation ($ds \approx 0$). Using Maxwell's thermodynamic relation, Eq. (2.3) becomes

$$dT = \left(\frac{\partial T}{\partial p}\right)_s dp = -\frac{1}{\rho^2}\left(\frac{\partial \rho}{\partial s}\right)_p dp = -\frac{1}{\rho^2}\left(\frac{\partial \rho}{\partial T}\right)_p \left(\frac{\partial T}{\partial s}\right)_p dp \,. \tag{2.4}$$

Using thermodynamic relations, $-\left(\partial\rho/\partial T\right)_p / \rho_m = \beta$ and $T_m\left(\partial s/\partial T\right)_p = C_p$, and after integration, a relation between oscillating temperature (T_1) and pressure (p_1) can be obtained in the following form:

$$T_1 = \frac{p_1}{\rho_m C_p} \,. \tag{2.5}$$

Now, in step 2, for positive δT (the temperature difference between the plate and the parcel of gas) heat δQ flows from the gas parcel to the stack plate at constant pressure. Therefore, the heat that flows out of the parcel is given by

$$\delta Q = m C_p \delta T \,, \tag{2.6}$$

where m is the mass of the parcel of gas. A schematic pV-diagram of the cycle is shown in Fig. (2.3b). The work used in the cycle is equal to the area ABCD, and is given by

$$\delta W = \int_{ABCD} p dV \,, \tag{2.7}$$

times the rate at which that work occurs (the angular acoustic frequency ω). The volumetric change that will contribute to the net work is

$$\frac{\delta V}{V} = \beta \delta T \,, \tag{2.8}$$

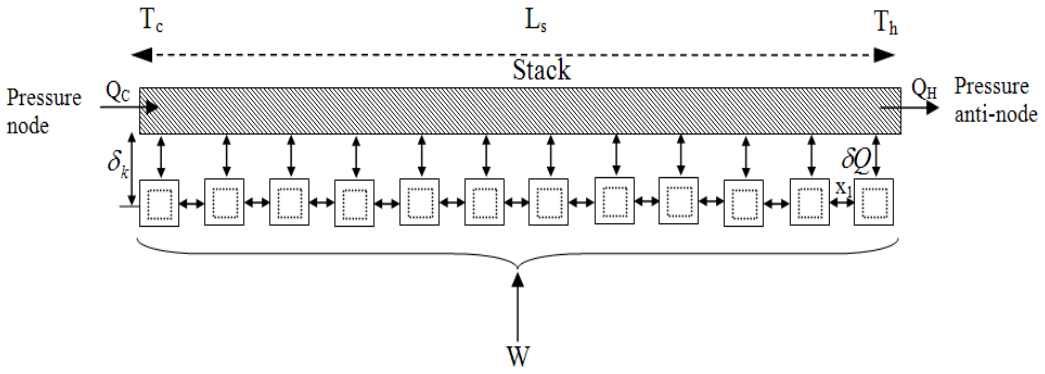

(a)

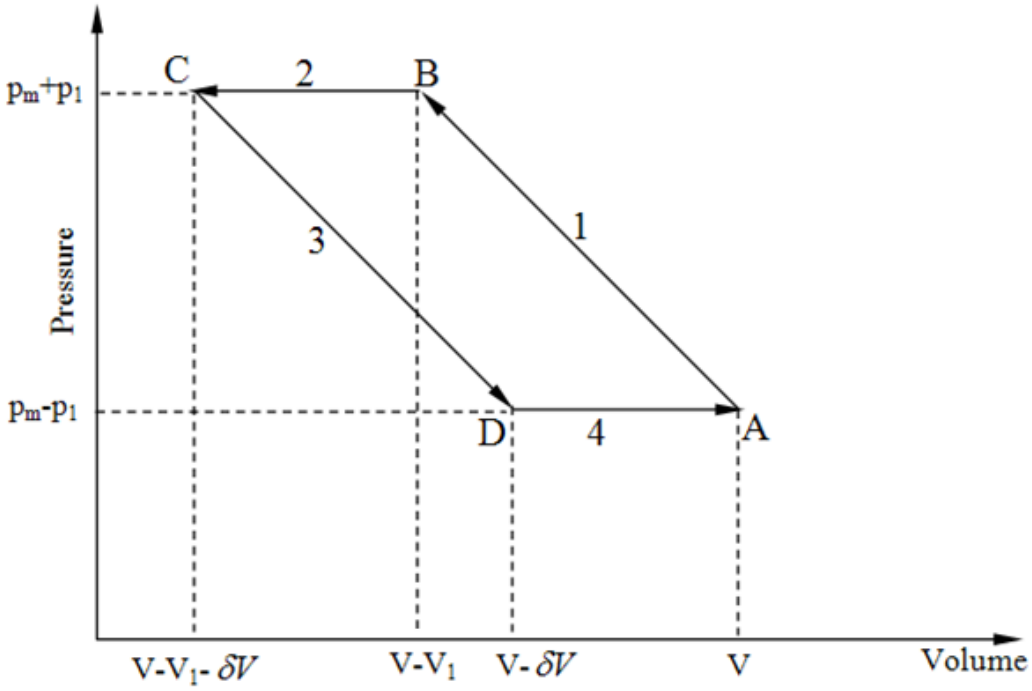

(b)

Figure 2.3: (a) An amount of heat is shuttled along the stack plate from one parcel of gas to the next; as a result heat Q is transported from the left end of the plate to the right end, using work W, (b) schematic pV -diagram of the thermoacoustic cycle of Fig. (2.3)(a). The four steps of the thermoacoustic cycle are illustrated: adiabatic compression (1), isobaric heat transfer (2), adiabatic expansion (3), and isobaric heat transfer (4). The area ABCD is the work used in the cycle which is also equal to the sum of the works used in the different steps.

again using thermodynamic relations, $-\left(\partial\rho/\partial T\right)_p/\rho_m=\beta$. In Eq. (2.8), δT is the temperature change of Eq. (2.1). V is the total volume of the gas that is thermodynamically active and is given by

$$V=\Pi\delta_k L_s\,, \tag{2.9}$$

where Π and L_s are the perimeter and the length of the stack plate, and δ_k is the thermal penetration depth, which is the lateral distance through which heat can diffuse during a characteristic time interval of $1/\left(\pi f\right)$, where *f* denotes the frequency of the acoustic wave.

In step 3, the parcel of gas moves back to its initial position, expands and cools. At this time, the parcel of gas is colder than the local stack surface, and heat δQ flows into the parcel (step 4) from the stack plate thereby raising its temperature back to its original value, $T_m-x_1\nabla T_m$. The net effect is that the system has completed a cycle which has returned to its original state and an amount of heat, δQ has been transported up a temperature gradient by work done in the form of sound. If we now consider the full length of the stack as shown in the upper portion of Fig. 2.1, the overall heat pumping process is analogous to a "bucket brigade" in which each set of gas parcels picks up heat from its neighbor to the left at a lower temperature and hands off the heat to its neighbor to the right at a higher temperature (as shown in Fig. 2.3(a)).

Now, the effective volume rate of flow of the gas is $\Pi\delta_k u_1$. The thermoacoustic heat flow rate along the stack plate from T_C to T_H (refrigerator mode) is obtained by replacing *m* in Eq. (2.6) by the effective mass flow $\Pi\delta_k u_1\rho_m$, i.e.

$$\delta Q=\Pi\delta_k u_1\rho_m C_p\delta T\,. \tag{2.10}$$

Using Eqs. (2.1), (2.2), and (2.5) in Eq. (2.10), the thermoacoustic heat flow rate along the stack plate can be written as

$$Q = -\Pi \delta_k \, p_1 u_1 (\Gamma - 1), \tag{2.11}$$

where the temperature gradient ratio parameter $\Gamma = \nabla T_m / \nabla T_{crit}$ is used. Again, using Eqs. (2.1), (2.2), (2.5) and (2.9), we can write down the work flow as

$$\begin{aligned} W &\approx -2 p_1 \delta V \omega \\ &\approx 2\Pi \delta_k \frac{T_m \beta^2}{\rho_m C_p} p_1^2 \omega L_s (\Gamma - 1) \end{aligned} . \tag{2.12}$$

The total heat flow and absorbed acoustic power in the stack can be obtained by using the total perimeter of the plate's Π_{tot} instead of the perimeter of one plate Π. Both Q and W are quadratic in the acoustic amplitude p_1 or u_1; both change sign as Γ passes through unity.

As shown in Fig. 2.3(a), the thermoacoustic effect occurs within the thermal penetration

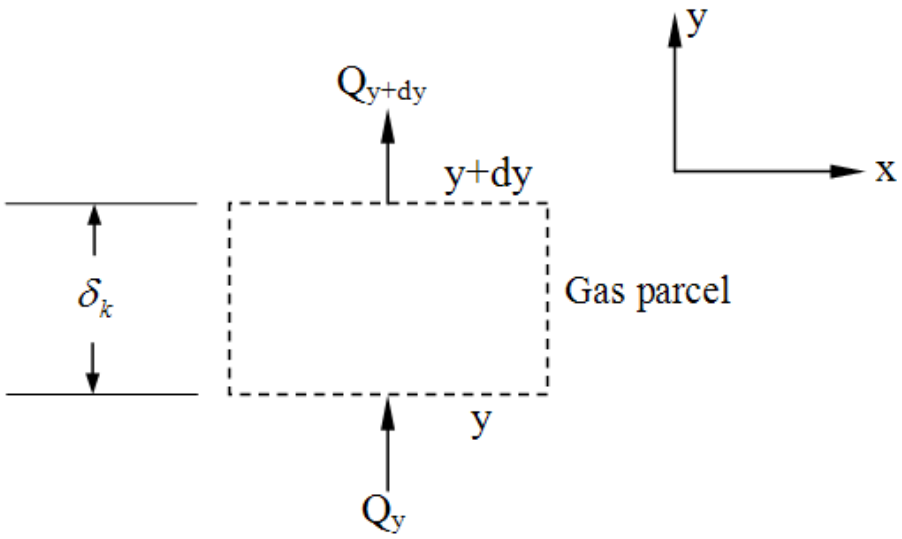

Figure 2.4: Illustration used in the derivation of the heat conduction equation.

depth δ_k. In Fig. 2.4, the 1-D heat conduction through a gas parcel of cross-section A is illustrated. Considering the energy balance for a small element dy of the gas parcel, we suppose that heat is the only form of energy that enters or leaves the gas parcel dy, at y and $y + dy$, and that no energy is generated inside the gas parcel element. Energy conservation yields

$$\rho_m C_p A \frac{\partial T}{\partial t} = -\frac{\partial Q}{\partial y} \text{ with } Q = -k_f A \frac{dT}{dy}, \tag{2.13}$$

where $\rho_m, C_p,$ and k_f are the density, isobaric specific heat, and thermal conductivity of the gas. Now, Eq. (2.13) can be written as

$$\frac{\rho_m C_p}{k_f} \frac{\partial T}{\partial t} = -\frac{\partial^2 T}{\partial y^2}. \tag{2.14}$$

If we substitute the characteristic dimensions $y' = y/\delta_k$ and $t' = \omega t/2$ into Eq. (2. 14) we get

$$\frac{\rho_m C_p \omega}{2k_f} \frac{\partial T}{\partial t'} = -\frac{\partial^2 T}{\delta_k^2 \partial y'^2}. \tag{2.15}$$

Therefore, we can write

$$\delta_k^2 = \frac{2k_f}{\rho_m C_p \omega}, \tag{2.16}$$

and hence

$$\delta_k = \sqrt{\frac{2\alpha_f}{\omega}}, \tag{2.17}$$

where α_f is the thermal diffusivity of the gas, $\alpha_f = k_f / \rho_m C_p$. Closely related to the thermal penetration depth is the viscous penetration depth in a gas δ_v. The viscous

penetration depth δ_ν indicates how far the momentum can diffuse laterally during a characteristic time interval ($=2/\omega$). The characteristic time interval is of the order of the period of oscillation ($\tau = 2\pi/\omega$), divided by π.

The viscous penetration depth is expressed by

$$\delta_\nu = \sqrt{\frac{2\nu}{\omega}}, \tag{2.18}$$

in Eq. (2.18), ν the kinematic viscosity of the gas.

2.2 Literature Review

The following sections focus on recent thermoacoustic application developments and related topics. Literature is reviewed based on work done on the components of a thermoacoustic device, starting from the stack, followed by heat exchanger, resonator, electroacoustic power transducer, working fluids, and on complete thermoacoustic systems. This review of recent application developments helped set the objectives of the present research.

2.2.1 Stack and Channel/Pore Topics

2.2.1.1 Analytical Work on Stack/Channel

The stack forms the heart of the refrigerator where the heat-pumping process takes place, and it is thus an important element which determines the performance of the refrigerator. The heat conductivity through the stack material and gas in the stack region has a negative effect on the performance of the thermoacoustic refrigerators. The stack material must have a low thermal conductivity and a heat capacity much larger than the heat capacity of the working gas in order that the temperature of the stack plates remains steady (Swift [2002]). In a typical thermoacoustic device a stack usually occupies less than 10% of the overall device volume (Swift [1992]). Stacks are finely subdivided into many parallel channels or pores in order to maintain moderate (standing-wave) or good

(traveling-wave) thermal contact between the working gas and the stack across large cross-sectional areas. Stacks are available in different sizes and shapes; honeycombs, spiral rolls, parallel plates, circular pores, and pin arrays are examples of stacks commonly used in thermoacoustic engines and refrigerators. Figure 2.5(a) to (d) show examples of stack used in thermoacoustic devices (Swift [2002]).

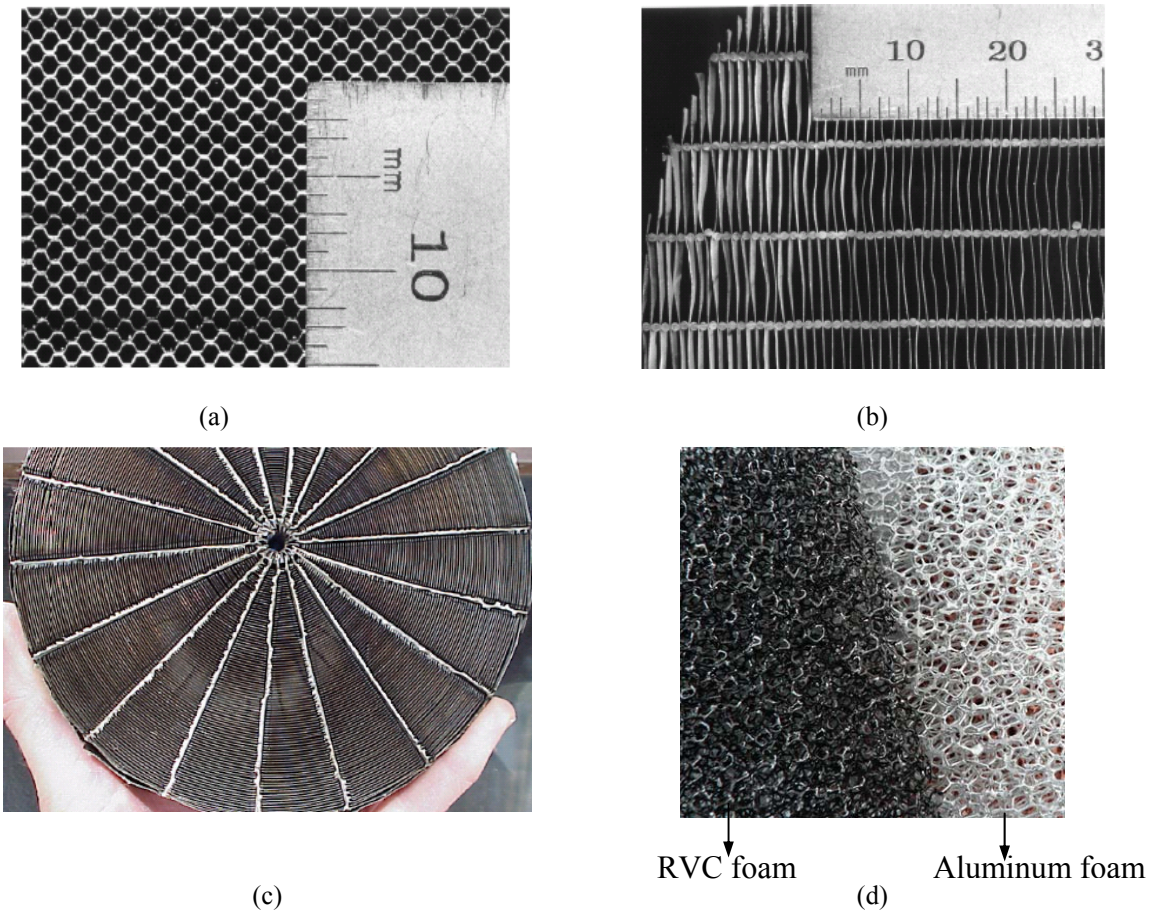

(a) (b)

(c) (d)

Figure 2.5: (a) stainless-steel metal honeycomb hexagonal stack [Swift, 2002], (b) parallel-plate stack made of stainless-steel sheet and stainless-steel spacer wires [Swift, 2002], (c) stainless-steel spiral stack [Swift, 2002], and (d) RVC and Aluminum foams [ERG, 2009]. Figures 2.5(a) to (c) are reprinted with permission from G. W. Swift and Acoustical Society of America, and Fig. 2.5(d) from KRReynolds Company.

Swift [1988] deduced expressions for temperature and heat flux for both inviscid and viscous fluid in a standing wave for both single and multiple plates. The behavior of the simplest class of thermoacoustic engines – a stack of short plates – is well explained by Wheatley [1983], Swift [1988] and Atchley et al. [1990]. In order to investigate the effects of pore geometry on heat and work flows, Arnott et al. [1991] have analytically investigated thermoacoustic effects in stacks having arbitrarily shaped pore cross sections. Heat and work flows expressions are developed for stacks having parallel, circular, rectangular, and equilateral triangular pore geometries and compared in the short stack approximation.

The short stack approximation (the stack is short enough that the empty tube standing wave is unaffected) is also used by Swift [1988] to get an interpretable analytical expression for energy flow. In the inviscid short stack approximation, heat and work flows are approximately 10% greater for the parallel plate geometry than for the circular, square, and equilateral triangular pore geometries.

Swift and Keolian [1993] have proposed a new geometry, the pin array stack and derived expressions for velocity and temperature in the pin array. They have shown that devices with this stack geometry can have significantly higher efficiency relative to the previous parallel-plate stack design. Construction of such stacks will be challenging since the crucial characteristic of the pin stack is the convexity of the gas-solid interface, on a length scale comparable to the penetration depths.

In order to test the suitability of using porous reticulated vitreous carbon (RVC) as a stack material and thereby increasing the number of choice of using stack materials, Adeff et al. [1998] have successfully used RVC in thermoacoustic devices. It is a rigid glassy carbon material, with a porous sponge like structure, has low thermal conductivity and reasonably high specific heat. Based on the measurements, the acoustic pressure amplitude and efficiency for the prime mover mode and temperature ratio and coefficient of performance for the refrigerator mode, RVC has a definite potential as a low cost, easy to fabricate material suitable for use in all types of thermoacoustic devices. The authors'

emphasis that further investigation is needed to determine exactly which combinations of stack and resonator dimensions and gas parameters would yield optimum performance. The only drawback of RVC is that it is extremely brittle and a loose fitting stack can vibrate against the heat exchangers enough to cause the filaments to break.

To improve the power density of thermoacoustic engines, Bösel et al. [1999] has proposed an alternative stack arrangement (see Fig. 2.6) consisting of parallel-plate segments which are only a fraction of the acoustic field displacement amplitude long and randomly oriented to each other. In a traditional thermoacoustic engine, the stack consists of parallel plates much longer than the acoustic displacement amplitude. The alternative stack arrangement proposed by Bösel et al. is expected to benefit from improved heat transfer characteristics since thermal boundary layers develop anew with large temperature gradients at the leading edges of the plates. This improves the efficiency of the heat transfer process at the solid/fluid interface. Since boundary layers do not completely develop (because the segments are ‘‘short’’) the thermal and viscous penetration depths become smaller, allowing the plates to be stacked closer together. The point contacts between consecutive sections of plates reduce the cross-sectional plate area

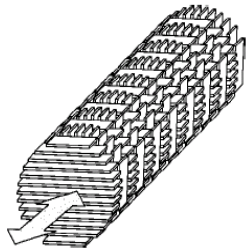

Figure 2.6: Alternative stack arrangement (Bösel et al. [1999]): each segment is aligned at a 90° angle to the neighbouring segment.

available for conduction. This yields a lower overall thermal conductivity in the direction of oscillating flow. Subsequent numerical calculations by Bösel et al. confirmed these expectations.

The main objectives of Mahmud’s work [2005] are to undertake an optimization of the inherently irreversible thermoacoustic stack, and to investigate the utility of magneto-

hydrodynamic and porous media stacks for improving stack efficiency. EG (entropy generation) and EGM (entropy generation minimization) are used as tools. Mahmud's [2005] work starts by investigating flow, thermal, entropy generation, and energy transfer features of thermoacoustic stack-like geometries in the steady state-limit. Wherever possible, entropy generation minimization (EGM) is applied to determine the optimum features (for example, geometric parameter, energy transfer, etc.) of these stack-like geometries. In connection to the energy transfer analysis, a novel concept of "energy streamfunction" is proposed and mathematically formulated. Mahmud's work includes one of the first attempts to develop analytical models for single-plate and multi-plate magnetohydrodynamic thermoacoustic systems (MHD thermoacoustics). Analytical expressions for velocity, temperature, Nusselt number, local and global heat and work fluxes, and local and global entropy generation rates are developed using perturbation expansions of governing equations. Finally, the original general thermoacoustic theory developed in the earlier part of the work is extended to include porous media where the fluid gap inside two consecutive stack plates is packed with porous material. The wall is considered of finite in thickness making this a conjugate heat transfer problem.

A thermoacoustic theory for a bulk porous medium has developed by Roh et al. [2007] from that for a single pore, parallel, capillary-tube-based theories. The authors have introduced the tortuosity, the viscous dynamic shape factor, and the thermal dynamic shape factor to extend thermoacoustic theory to a bulk porous medium. Comparisons of thermoacoustic properties (of RVC and aluminum foam developed by Roh et al. [2007]) have showed good agreement with experiment. This prediction has showed that random porous media stacks should perform as well as parallel pore stacks in high frequency prime movers. A more complete analysis is necessary for small refrigerators since enhanced viscosity may affect the performance.

The thermoacoustic properties of fibrous porous materials are studied by Jensen and Raspet [2010] using a computational fluid simulation as a test of proposed analytical models by Roh et al. [2007]. The simulations of several porous materials with an ambient

temperature gradient show that the models yield a reliable prediction of thermoacoustic performance from the shape factors and relaxation times.

A simplified model based on steady-flow correlations and Lagrangian approach has developed by Matveev [2010] for thermoacoustic analysis of short transverse-pin stacks with moderate temperature differences. This method provides fast estimations for thermoacoustic power conversion and the efficiency of this process. The model is subjected to several limitations, including a requirement of having a large acoustic displacement relative to a longitudinal spacing between pins. This theory can also be applied to tortuous stacks but requires knowledge of corresponding steady-flow heat transfer and flow resistance correlations.

Piccolo and Cannistrato [2002] have proposed a simple calculus procedure based on the linear thermoacoustic theory to investigate the origin of the deviations of the predictions of the linear theory from the measured performances of real devices. The temperature differences measured in steady states by the authors do not match the linear theory predictions even at low DR (DR=0.15%), and discrepancies up to 40% are measured. The calculus procedure proposed by the authors to calculate the convective heat flux in the early stage of transient regime indicates that the thermoacoustic heat flux carried by the stack as proposed by the linear theory is well predicted for that regime. Their results show that the reasons for the discrepancy regarding the steady state temperature difference might be the time average heat transfer processes not taken into account by the standard linear theory. Lotton et al. [2009] have presented an analytical modeling for predicting the transient temperature profile in thermoacoustic refrigerators. In their modeling, the authors have included the transverse heat conduction in the stack, heat leakages through the duct walls, heat generated by viscous losses in the stack, heat generated by vorticity at the ends of the stack, and heat transfer through both ends of the stack. The theoretical transient response of temperature of a thermoacoustic refrigerator is compared with experimental measurements. A good qualitative agreement is obtained between analytical and experimental results after fitting empirical coefficients.

Also there exist different explanations about temperature distribution along the stack in different literatures. Reid and Swift [2000] have showed both experimentally and theoretically that temperature oscillations within a stack are linear for low temperature difference between the two ends of the stack. Their theoretical prediction is based on inviscid boundary-layer, short-stack approximations, and neglecting the ordinary conduction of heat down the temperature gradient, as it is small compared to the hydrodynamic one. The experimental measurement provided by the authors is only for a single stack location within a standing wave thermoacoustic refrigerator. Gusev et al. [2001] have analytically showed that the temperature oscillations near the edge of the thermoacoustic stack are highly anharmonic even in the case of harmonic oscillations in the thermoacoustic engines. The authors have showed that hydrodynamic heat flow along the stack generates thermal wave harmonics even in the absence of the higher harmonics of the acoustic field. The authors have also emphasized that the existence of the high spatial temperature gradients should favor thermal wave harmonic generation.

Babaei and Siddiqui [2011] have proposed a modified theoretical model to predict the steady state temperature difference for thermoacoustic couples. The authors have performed experimental studies using 20PPI RVC stacks to validate the analytical modeling for drive ratio ranging from 0.48 % to 1.20%.

Therefore, the literature review on stack geometry shows that there is no comprehensive analytical modeling on random porous medium stack using porous media modeling. Only one analytical modeling (Mahmud [2005]) exists, which is a preliminary work and it does not consider the presence of high velocity (when Reynolds number based on pore size is greater than unity) and high porosity porous medium (such as RVC stack).

2.2.1.2 Numerical Work on Thermoacoustic Stack

The primary analysis of thermoacoustic devices has in large part relied on analytical solutions to oscillating 1-D flow within a slot (Rott [1980] and Swift [1988]). Briefly, very good agreement between theory and experiment is obtained when the drive-ratio is

small. When the drive-ratio is large, significant deviations between 1-D predictions and experimental data occur (Atchley [1990]). Potential causes behind these discrepancies are many; these include nonlinear acoustic waves and shocks, multi-dimensional effects, transition to turbulence, nonlinear flow-acoustics interactions, convective heat transfer, and heat losses. To overcome such situations numerical models and solutions to thermoacoustic problems have been pursued as discussed below.

Several numerical calculations have recently addressed the modeling of the flow field inside a thermoacoustic couple. Cao et al. [1996] are the first to simulate thermoacoustics over a 1-D isothermal plate, solving the full 2-D Navier–Stokes equations. Cao et al. have used the energy flux density, and energy streamlines in order to present the time averaged energy flow pattern inside two consecutive stack plates (stack plate length is 2.4% of acoustic wavelength).

The numerical calculations of Ishikawa and Mee [2002] are an extension of the work of Cao et al. [1996]. Ishikawa and Mee [2002] used both short and long (compared with fluid particle displacement length, ranging from 1 to 11 times particle displacement length) stacks to examine energy flux densities, particle paths, and entropy generation rates. Their simulation results showed that a heat-pumping effect can be seen not only on long plates, but also on the shortest plates tested, when plate spacings are greater than the thermal penetration depth.

Worlikar and Knio [1996] have developed a low Mach-number compressible flow model to simulate acoustically driven flows around a thermoacoustic stack (finite thickness) for a wide range of drive-ratios. Worlikar and Knio have found that a periodic vortex dominates the flow near the edges of the stacks. Worlikar et al. [1998] have extended the idea of Worlikar and Knio [1996] by using a numerical solver for the energy equations of the fluid and the stack plates, and by using a fast solver for the velocity potential. The modified model can handle unsteady thermally stratified flows in two-dimensional (2-D) thermoacoustic stacks. Worlikar and Knio [1999] have further extended their model by adding heat exchangers to the thermoacoustic stack assuming that the heat exchangers

(one hot and one cold) are isothermal and in perfect thermal contact with stack plates. Their results reveal optimum stack performance is achieved when the length of the heat exchanger is nearly equal to peak-to-peak fluid particle displacement. Besnion [2001] has further extended Worlikar and Knio's model [1999] by adding heat exchangers located at an adjustable distance from the thermoacoustic stack. Besnion [2001] has concluded that around the stack corners, flow and heat transfer processes are dominated by edge effects and multi dimensional phenomena. Besnion's numerical model is applicable to low Mach number limit.

In order to study the limitations of the linear theory, Marx and Blanc-Benon [2005] have considered a simple case of a stack plate placed in a stationary acoustic wave and numerically calculated the temperature difference between the extremities of the plate. The computed temperature difference is compared to the one predicted by the linear theory (Swift [1988]). Some discrepancies are found even at the low acoustic Mach numbers. The authors conclude that these discrepancies can not be attributed to non-linear effects; rather they exist because of thermal effects. In particular the mean temperature in the fluid and in the plate is not equal. Marx and Blanc-Benon [2004] have also observed the mean flow field in the vicinity of the stack plate. Therefore, there exists inconsistency in experimental/analytical (**Section** 2.2.1.1) and numerical temperature difference (**Section** 2.2.1.2) across the stack ends and the linear theory predictions.

2.2.1.3 Experimental Work on Stack

Several experimental works have been carried out that helped to improve our understanding of the thermoacoustic phenomena. Wheatley et al. [1983] have experimentally studied the thermoacoustic effects on thermoacoustic couples in resonant tubes, and reported the existence of acoustical heating, acoustical cooling, and heat pumping effects. Wheatley et al. [1986] have demonstrated an apparatus that showed the characteristics of acoustically stimulated entropy flow, of a thermally driven acoustic oscillator, and of an acoustically driven refrigerator. A brief description is also provided

by Wheatley et al. [1986] of the variables on which the behavior of thermoacoustic heat engines depend.

Wetzel and Herman [1999, 2000] have used holographic interferometry and high-speed cinematography to visualize the flow and temperature fields when a single plate (stack) interacts thermally with an acoustically driven working fluid. They have highlighted the presence of a vortex at the edge of a stack plate, but no precise description of the phenomenon was given.

Petculescu and Wilen [2001] have experimentally investigated nonlinear effects on thermoacoustic gain in a uniform cross-section single pore (stack) by creating a sharp temperature gradient in the pore. The objective of the investigation is to understand the effects of nonlinearities on thermoacoustic devices driven at high amplitudes. The effect of high displacement amplitudes relative to the stack length is isolated from other high amplitude effects by making measurements on a single pore at low acoustic Reynolds number (<50). The results (power flow) measured at displacement amplitudes ranging from 2.5% to 60% of the stack length are consistent with the prediction of the linear theory (Rott [1980]). The corresponding pressure amplitudes are approximately 0.1% to 2.5% of the equilibrium pressure. The authors conclude that other types of high-amplitude nonlinear effects must be responsible for some of the discrepancies commonly observed between experiment and theory.

Tijani [2001] has reported a quantitative experimental investigation into the effect of the pore dimensions on the performance of thermoacoustic devices. Parallel-plate stacks with plate spacings varying between 0.15 mm and 0.7 mm have been constructed and measured. Tijani has showed that plate spacing in the stack of 0.25 mm ($2.5\delta_k$) is optimum for the cooling power, and for the performance defined by the coefficient of performance ratio (COPR) it is about $3\delta_k$ (where COPR=COP/COPC, where COP is the coefficient of performance and COPC is the Carnot coefficient of performance). The behavior of the cooling power and COPR can be explained as follows: The cooling power is proportional to the product of the total perimeter of the stack and the thermal

penetration depth δ_k (Swift [1988]). An increase in the spacing (larger than about $2\delta_k$) means a decrease of the number of plates and hence a decrease of perimeter. This results in a decrease of cooling power. On the other hand, once the spacing becomes smaller than about $2.5\delta_k$, the thermoacoustic effect will be reduced, which will decrease the cooling power. Additionally, most of the gas layer between the plates contributes to the viscous shear and the small spacing induces higher velocities and extra viscous losses. This explains the rapid decrease of COPR for spacings smaller than about $3\delta_k$. The author has concluded that plate spacing in the stack of about three times the penetration depth should be optimal ($3\delta_k$) for thermoacoustic refrigeration. These results are also confirmed by DeltaEC (Design Environment for Low amplitude ThermoAcoustic Energy Conversion, [2007]) calculations.

Experimental studies of thermoacoustic systems mainly focus on performance measurements, such as in Poese and Garrett [2000] or Swift [1992] (will be discussed in **Section** 2.3). Little experimental work has been done, however, to visualize flow structures and measure the unsteady velocity fields. Berson et al. [2008] have used

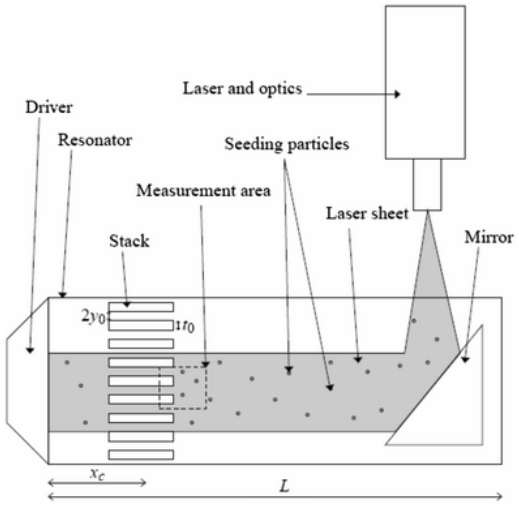

Figure 2.7: Schematic of the experimental setup (Berson et al. [2008]).

particle image velocimetry (PIV) to measure velocity field near the end of stack plates in a thermoacoustic refrigerator (see Fig. 2.7 for the schematic of their experimental setup). Velocity is measured inside the oscillating boundary layers between the plates of the

stack and compared to a linear model. At low acoustic pressure level (*DR*=0.5%), the authors observed the generation of symmetric pairs of counter rotating vortices at the end of the stack plates. As the acoustic pressure level increases (*DR*=2%), detachment of the vortices and symmetry breaking are observed. These experimental investigations contributed to key data against which the validity of numerical and analytical approaches can be tested.

The literature review on experimental stack element shows that there is no effort exists that considers the non-isotropic stack material in thermoacoustic devices. Also there is no major efforts in the literature that compare the performance of regular stack to that of the random porous stack using different dimensions and porosities in order to test the suitability of using random porous stack in thermoacoustic devices. Also there exist no major efforts to examine the influence of working fluid on different geometric and operating conditions on stack performance.

2.2.2 Heat Exchanger

Swift [1992] has performed an investigation on the performance of a large (13 cm diameter) thermoacoustic engine and showed that only 60% of the acoustic power produced in the stack is actually delivered to the load. 25% of the produced power is absorbed by the thermal and viscous losses in the heat exchangers, and the remaining 15% is absorbed by such processes on the surfaces of the resonator. This study shows that improved heat exchanger design can improve the performance of thermoacoustic systems significantly. The critical nature of heat exchangers presents a particular challenge in thermoacoustic systems because the useful length of a heat exchanger in a thermoacoustic system is roughly equal to the acoustic displacement amplitude, typically only 10^{-3} m to 10^{-2} m (Mozurkewich [2001]), and plate spacings at almost the thermal penetration depth. Therefore, improved understanding of thermoacoustic system heat exchangers is a key requirement for the practical development of thermoacoustic systems. Although heat exchangers are crucial parts to thermoacoustic engines, few investigations have focused on heat exchangers. Swift's experiment [1992] (see Fig. 2.8) using a large thermoacoustic

engine showed that reducing the length of the heat exchanger plates to half the fluid particle displacement length did not affect the performance of the heat exchanger.

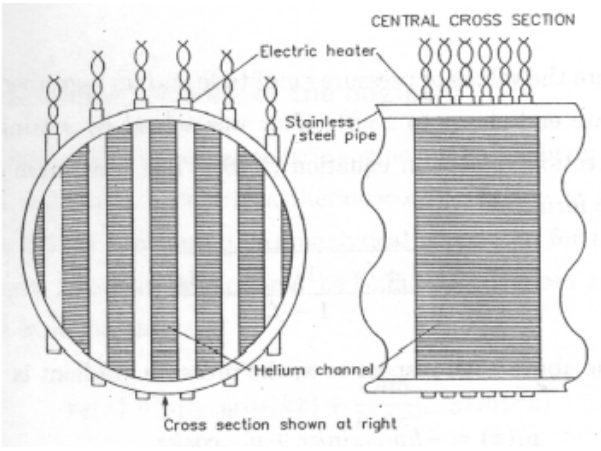

Figure 2.8: Schematic of a hot heat exchanger in a thermoacoustic engine (Swift [1992]).

Garrett [1997] has invented a high powered fin and tube heat exchanger while developing a high powered thermoacoustic refrigerator, capable of providing hundreds of watts of cooling power over wider temperature spans between hot and cold heat exchangers of 20°C to 70°C. The use of short fin length (0.1″ or less) and high fin density (fifty or more fins per inch) on the leading edge on a fluid filled tube gas to liquid heat exchange capable of transferring hundreds of watts of heat with only small temperature differences between the gas and the liquid. The fluid within the hot side tubing is water and on the cold side it is an alcohol with a low freezing temperature.

Mozurewich [2001] has experimentally showed that the time average steady flow equivalent (TASFE) approximation is useful for the analysis of heat exchangers consisting primarily of transversely oriented cylindrical elements in an acoustic standing wave. The TASFE approximation assumes that the heat transfer in an acoustic standing wave is equivalent to averaging the corresponding steady flow correlation (proposed by Zukauskas [1972]) over a sinusoidal distribution of gas speeds. Results for transverse tube heat exchangers agree quantitatively with the TASFE approximation for acoustic Reynolds number less than ≈ 1000 and qualitatively for larger Reynolds numbers.

In order to improve the efficiency of stack based thermoacoustic devices, Wakeland and Keolian [2002] have explored a different type of device that has no stack. These "no-stack" devices have heat exchangers placed close together in standing wave acoustic fields of sufficient amplitude to allow individual parcels of gas to enter both heat exchangers. The investigation shows that thermoacoustic device with no stack can have a very high inviscid efficiency, but has other problematic inefficiencies. Such as losses that occur on the walls of the enclosure due to increased acoustic pressure amplitude, which are only minor consideration in stack-based devices. In order to produce an efficient no stack device, the resonant enclosure must have a large ratio of exchanger area to sidewall area, short, non resonant enclosure is a possible alternative.

Paek et al. [2005] have developed experimental procedures and calculation methods to evaluate the oscillating flow heat transfer coefficients of heat exchangers (fin and tube) within a thermoacoustic cooler. Dimensionless heat transfer coefficients are estimated based on the oscillating-flow variables and compared with results from steady-flow measurements. The results are also compared with heat transfer coefficients predicted from a boundary-layer conduction model, and methods that utilize steady-flow correlations with Reynolds numbers that characterize oscillating flow conditions. Although the boundary layer model is commonly employed for thermoacoustic calculations, it does not accurately predict heat transfer coefficients and the influence of Reynolds number on heat transfer performance. However, accurate predictions are obtained using a steady-flow correlation and a modified Reynolds number that accounts for the oscillating flow field. Nevertheless, more experiments are needed for validation of the proposed modified model with other heat-exchanger geometries.

Poingnand et al. [2007] have investigated oscillatory heat transfer at the heat exchanger of a thermoacoustic refrigerator. The study has identified significant factors that influence this heat transfer. Based on the experimental results a new correlation has been developed in terms of Nusselt, Prandtl, and Reynolds numbers for heat transfer at the heat exchangers. Results show that using steady flow heat transfer correlation for analyses of

this system could result in significant errors. A relationship exists among the oscillatory heat transfer coefficient at the heat exchangers, the mean pressure and frequency of oscillation. Higher mean pressure results in greater heat transfer coefficient if the thermoacoustic refrigerator operates at the corresponding resonant frequency. However, a compromise has to be reached to accommodate construction of the stack since higher mean pressure or increase in operating frequency results in decreasing the thermal penetration depth and the stack spacing.

2.2.3 Resonator

A primary goal of a resonator design is to maintain a desired resonance frequency, while simultaneously minimizing the dissipation of acoustic power (Swift [2002]). The resonator can be fabricated out of metallic (stainless-steel, aluminum, copper) or non-metallic (Plexiglas, PVC) materials. For the lowest dissipation of acoustic power, the transitions between portions of the resonator, and all internal surfaces in the engine or refrigerator, should be smooth and streamlined. Steps, misalignments, and abrupt transitions generate turbulence unnecessarily (Swift [2002]). In the standing wave engine shown in Fig. 2.9, the internal angle of the gradual tapers joining the ambient heat exchangers and the central resonator was chosen to minimize minor losses and represents good streamlining. A resonator with a nonuniform area is often necessary in order to reduce losses associated with the generation of higher harmonics and shock waves.

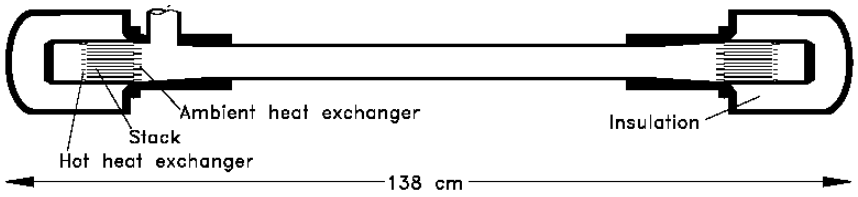

Figure 2.9: Scale drawing of the Tektronix resonator and its standing wave engines. The spacings in stacks and heat exchangers are not to scale. The upward branch near the left is connected to the two pulse tube refrigerators (Swift [2002]).

Thermal effects in a resonance tube depend on the state of the boundary layer, the transition Reynolds number is determined, and a critical Reynolds number (≈ 400) is

found by Merkhli and Thomann [1975]. The observations are made with hot wires and with flow visualization by means of smoke, and provide new details on turbulence in a Stokes layer. The authors have noticed that turbulence occurs in the form of periodic bursts which are followed by relaminarization in the same cycle and do not lead to turbulent flow during the whole cycle.

The linearized theory (Rott [1980], Swift [1988]) has been used in most of the early work on the study of the thermoacoustic transport phenomena in a resonant tube. In the pioneering work of Rott [1980], the governing equations for an axisymmetric viscous compressible flow are linearized for the case of high oscillating frequencies, with small oscillation amplitudes in a long tube with a prescribed axial temperature gradient. Rott's [1980] and Merkli and Thomann's works [1975] provided the foundation for understanding the thermoacoustic phenomena in a resonance tube.

Swift [1988] presented an extended review of thermoacoustic engines and extended Rott's [1980] thermoacoustic theory by considering the conjugate heat transfer problem in the fluid as well as in the solid.

Guoqiang and Ping [2000] have analyzed the transport phenomena for a viscous compressible oscillating flow in a tube subjected to a prescribed cycle-steady axial temperature gradient. The governing equations are linearized under the assumptions of high oscillating frequencies, small amplitudes in a tube with high length to radius ratio. Based on a linearized theory, analytical expressions for the local friction factor and Nusselt number on solid/fluid interface have been obtained.

A set of coupled equations for the time averaged pressure gradient, velocity, and temperature are obtained by expanding the equations of fluid dynamics and heat transfer to second order in Mach number by Waxler [2001]. The author has paid particular attention to the time averaged mass flux and pressure gradient. In the presence of an acoustic disturbance the linear relation between time averaged mass flux and pressure

gradient develops a nonzero constant term. The author interprets the constant term as the pressure drop for which the total mass flux is zero.

Rott [1974a] has extended his revolutionary thermoacoustic ideas by calculating acoustic streaming (acoustic streaming is the mean motion caused by acoustic waves) for thermoacoustic systems. The classic idea of acoustic streaming was first proposed by Lord Rayleigh in 1883. Rott [1974a] is to be credited for the extension of the phenomenon of 'acoustic streaming' to 'thermoacoustic streaming' by considering heat conduction, variable wall temperature, and temperature gradient along the axis of the tube. A further extension to 'thermoacoustic streaming' is performed by Rott [1974b] by including nonlinear oscillations. Rott [1974b] has calculated second-order effects of steady 'thermoacoustic streaming' using the boundary layer approximations. The results are applied to the calculation of the heat flux distribution in a resonance tube, in the case where weak shocks occur. Problems associated with the combined effects of shock heating and boundary layers heating are also discussed.

Hamilton et al. [2003] have derived an analytical solution for thermoacoustic streaming (see Fig. 2.10) generated by a standing wave in a viscous fluid that occupies a

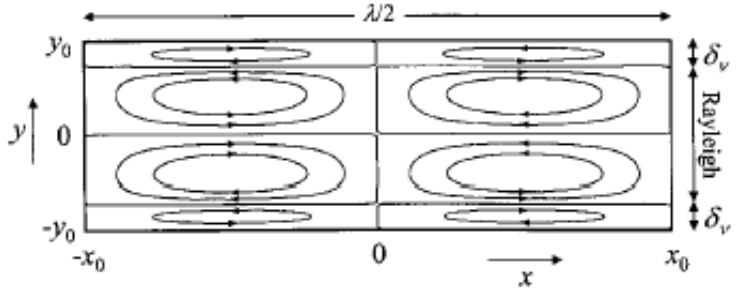

Figure 2.10: Acoustic streaming pattern in a resonator with rigid ends, excited in its lowest mode.

two-dimensional channel of arbitrary width. The authors consider a gas in which heat conduction and dependence of the viscosity on temperature are taken into account. The main restriction of their work is that the boundary layer thickness is a small fraction of the acoustic wavelength. The authors observed that, in channels having intermediate

widths, 10-20 times the viscous penetration depth, the effect of heat conduction can be substantial. Calculations are presented for typical working gases used in thermoacoustic engines at standard temperature and pressure.

Thompson and Atchley [2005] have used Laser Doppler anemometry (LDA) to study the acoustic streaming generated in a cylindrical standing-wave resonator filled with air. The axial component of fluid velocity is measured along the resonator axis, across the diameter, and as a function of acoustic amplitude. The observed Lagrangian streaming velocities are consistent with Rott's theory [1974] indicating that the dependence of viscosity on temperature is important. The onset of streaming is observed to occur within approximately 5 second after switching on the acoustic field. Acoustic streaming is also observed by Nabavi et al. [2007, 2008 (a), 2008 (b), 2008(c)] experimentally in a resonator.

2.2.4 Electroacoustic Power Transducer (or Speaker)

For simple thermoacoustic heat pump experiments, ordinary audio loudspeakers (see Figs. 2.11(a) and (b)) are used as a source of acoustic energy, with low cost, easy availability, and versatility (Swift [2002]). These loudspeakers use copper wires and permanent magnets (Swift [2002]). Electrical signals sent through the coil (see Fig. 2.11 (b)) cause it to act as an electromagnet which is alternately repelled by or attracted to the permanent magnet. This movement causes the cone diaphragm to vibrate, creating sound waves. Unfortunately, the power transduction efficiency of loud speakers is usually less than 5% (Tijani [2001]). The paper cones are weak and fragile and their strokes are limited. A few researchers have either built or modified the existing loudspeaker in order to pump large quantities of heat from low temperatures to high temperatures, to produce refrigeration. Moving magnet electrodynamic linear motor is another attractive power source in small electrically driven thermoacoustic refrigerator applications (Liu and Garrett [2005]). Pressure wave generators produced by Q-drive [2010] are extremely powerful audio speakers that produce high intensity acoustic power (2 kW). Pressure amplitudes up to 25% of mean pressure and mean pressure up to 30 bar are possible with

matched pressurized loads. Another product of Q-drive is the STAR acoustic driver (linear motor/alternator) coupled with piston/cylinder to deliver high efficiency acoustic power (4 kW) Q-drive [2010]. Figures 2.11(c) and (d) show a pressure wave generator and a STAR motor manufactured by Q-drive. These generators are costly for low budget researchers.

Garrett [1997] has designed and built an efficient and reliable loudspeaker in order to pump large quantities of heat from low temperatures to high temperatures, to produce refrigeration. The loudspeaker built is unlike the conventional electrodynamic loudspeaker, which is optimized for high efficiency operation over a much narrower range of frequencies.

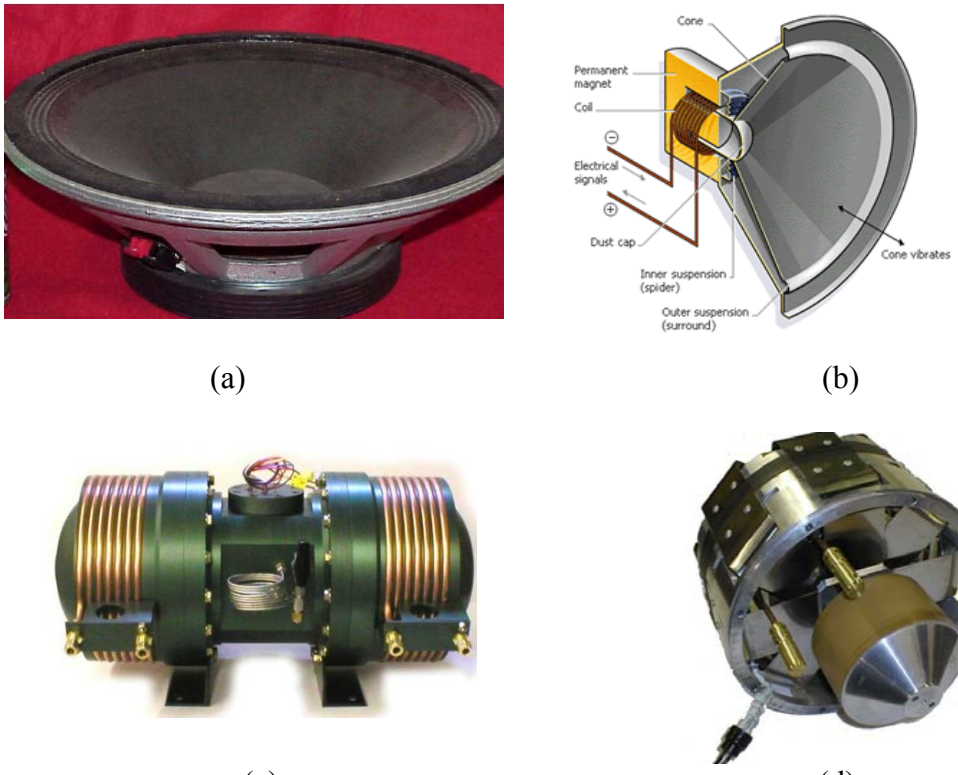

Figure 2.11: (a) An ordinary loudspeaker used to drive the standing-wave refrigerator (Swift [2002]),(b) Cut out of a loudspeaker, (c)A pressure wave generator and (d) a START motor manufactured by Q-drive (reprinted with permission from Q-drive).

Wakeland [1999] has examined some issues involved in matching electrodynamic drivers to thermoacoustic refrigerators using equivalent circuit model. The author has discussed how to select an appropriate driver for a particular thermoacoustic application, and how the requirements differ depending on whether the driver is in a location of high or low impedence.

A moving-magnet electrodynamic driver is described by Smith et al. [1999] which is intended to maintain an acoustic resonance within a thermoacoustic air conditioner containing an inert gas mixture of helium and argon at 30 bar. It is energized by a linear motor. An auxiliary spring system augments the magnetic stiffness (154 kN/m) to provide a driver mechanical resonance frequency near 60 Hz. Bellows form a flexure seal which provide an effective piston area that maximizes electroacoustic conversion efficiency by making the Joule heating losses in the coil equal to the mechanical dissipation in the magnetic suspension. The driver's electroacoustic conversion efficiency is predicted to be 83%.

2.2.5 Working Fluid

The selection of working fluid for a thermoacoustic device involves a trade-off among many issues, including power density, efficiency, and convenience. The ultimate choice depends on the specific goals of the apparatus. According to Swift [2002], the thermoacoustic power generally scales as $p_m a A$ (mean pressure × sound speed × cross-sectional area). Therefore, higher mean pressure and higher sound speed yield higher power per unit volume of hardware. The lightest gasses: "H_2", "He", and "Ne" have the highest sound speeds and hence can yield high powers. Light gases also have higher thermal conductivities, leading to higher thermal penetration depths (δ_k), enabling larger stack gaps, heat-exchanger gaps and easier stack and heat-exchanger fabrication. Sometimes, in practice, the efficiency of a thermoacoustic engine or refrigerator can be improved by adding a small amount of heavy gas to a light gas, thereby reducing the Prandtl number (a dimensionless parameter characterizing the ratio of kinematic viscosity to thermal diffusivity). Tijani [2001] has experimentally examined the influence of the Prandtl number on the performance of the refrigerator by using mixtures of helium and

other heavier noble gases; argon, krypton, and xenon. These combinations provided gas mixtures with Prandtl numbers varying between 0.2 and 0.67. The theoretical and experimental results show that the coefficient of performance improves as the Prandtl number decreases. The viscosity has a negative effect on the performance of thermoacoustic devices, so a reduction of the effect of viscosity (by lowering the Prandtl number) means an increase in efficiency. However when the mole fraction of the heavy noble gas component increases in the mixture, the cooling power decreases. This decrease of cooling power is a consequence of the increase of the density. The energy flux equation (Swift [1998]) shows that the cooling power is proportional to the inverse of the product of the density times the speed of sound squared if the length of the resonator is held constant. Therefore, the cooling power decreases as density increases. By using a mixture of helium and xenon containing 30% xenon, a maximum performance relative to Carnot of 17% is obtained. This is an improvement of 70% in comparison with pure helium. In the design of a thermoacoustic refrigerator this trade-off between the performance and the cooling power has to be considered. But Tijani [2001] has not considered the effects of variation of Prandtl number along with geometric and operating conditions on the performance of thermoacoustic devices.

2.3 Thermoacoustic Engines and Refrigerators

So far, research on thermoacoustic components and subsystems has been discussed. Research on complete thermoacoustic systems are discussed in the following sections.

2.3.1 Thermoacoustic Engines

Swift [1992] has designed and built a large thermoacoustic engine of 13-cm-diam. The resonator was built with a 4.32 m long stainless-steel pipe and 4.62 cm honeycomb stack made of stainless-steel foil. At its most powerful operating point, using 13.8-bar helium, the engine delivered 630 Watt to an external acoustic load, converting heat to delivered acoustic power with an efficiency of 9%.

Baillliet et al. [2000] and Biwa et al. [2001] have used laser Doppler anemometry (LDA) to measure the acoustic power flow in a thermoacoustic engine. J. Andrej [2003] has designed and built a simplified thermally driven sound oscillator for demonstration purpose. The simplified engine consists of three mechanically robust and easily separated parts: the acoustic resonator is a copper tube closed at one end, the internal structure is a piece of massive plastic that divides the copper tube into two parts, and thin copper disks pressed on each side of the plastic by stainless steel bolts with matching nuts. The engine starts to emit sound with a frequency of 200 Hz when the open end of the tube is cooled (by liquid nitrogen (77 K)) and the closed end is kept warm at room temperature (300 K) by the hand. The frequency of the sound increases as the cold end warms up.

With a hope to optimize the concept for thermal-to-electric energy conversion, Jung and Matveev [2010] have studied miniature thermoacoustic engines of lengths ranging from 57 mm to 124 mm using 80 PPI RVC stacks. The system is equipped with a pressure transducer measuring acoustic pressure inside the resonator and two thermocouples measuring temperatures at the stack ends. This engine-demonstrator generates sound at temperature difference about 200°C. The maximum sound amplitude reaches a value of 2 kPa. Jung and Matveev [2010] hope to reduce the temperature differences to 50 °C and to reach the overall efficiencies about 5-10%. Typical efficiencies of other types of centimeter-scale energy conversion systems are around 1 %.

2.3.2 Thermoacoustic Refrigerators

Hofler's [1986] thermoacoustic refrigerator has used 10-bar helium at pressure amplitudes up to 3% of mean pressure. The observed ratio of temperatures of the cold and hot heat exchangers differed from calculations based on Rott's theory [1980] by 2% to 9%. The agreement is best at low pressure amplitudes. Powers are presented in terms of COP, for which measurements differed from calculations by roughly 10%.

Poese and Garrett [2001] have measured performance on a thermoacoustic refrigerator driven at high amplitudes. Measurements are reported of a modified version of the Space

Thermo-Acoustic Refrigerator (STAR), driven at peak-to-mean pressure ratios up to 6%. This pressure ratio corresponds to 30 W of cooling power-five times as large as reported for STAR in 1993. The results of these measurements are compared to a DeltaEC computer model of the low-amplitude (linear) performance that matches experimental conditions on a point-by-point basis. It is found that there is a small but measurable deviation in heat pumping power from the power predicted with a linear acoustic computer model at moderate amplitudes. This deviation in heat pumping power at 6% pressure ratio is about 23%. A large disagreement in the acoustic power needed to attain a specific pressure ratio is found between measured data and DeltaEC results.

The solar powered refrigerator (Adeff and Hofler [2000]) is one of the latest applications which would render possible refrigeration in remote areas. For instance, it could be employed for storing ice or other medical supplies in the desert. A thermoacoustically driven thermoacoustic refrigerator powered by solar thermal energy has been successfully built and tested by Adeff and Hofler [2000]. A 0.457 m diameter Fresnel lens focuses sunlight onto the hot end of a 0.0254 m diameter reticulated vitreous carbon prime mover stack, heating it to 475°C, thereby eliminating the need for the most troublesome component in a heat driven prime mover, the hot heat exchanger. The high intensity sound waves produced by the prime mover drive a thermoacoustic refrigerator to produce 2.5 watts of cooling power at a cold temperature of 5°C and a temperature span of 18°C.

Reid and Swift [2000] have deliberately superimposed a steady flow parallel to the thermoacoustic oscillations in a stack to cool the steady flow as it passes through the stack. The refrigerator is driven by a loudspeaker to cool a flowing helium-argon mixture from 35 to 27°C and provides additional cooling power at a traditional cold heat exchanger. The measured temperature profile and cooling power along the stack are in agreement with the numerical results obtained by the DeltaEC software. The steady flow has a dramatic effect on the temperature profile. The temperature profile changes from linearly linear to exponential when such steady flow exists. The total refrigeration power rises as the steady flow rate increases. This increase in total cooling power illustrates the

increase in efficiency while the acoustic power needed to drive the device remains constant.

A design methodology for a loud speaker-driven thermoacoustic refrigerator is provided by Tijani [2001]. The targeted temperature of their refrigerator is -65°C, and can be achieved at a modest drive ratio *DR*=3%. Linear theory is the basis for the design methodology of their thermoacoustic refrigerator.

Holmberg et al. [2003] have designed and tested a heat-driven thermoacoustic refrigerator. They have presented and discussed a detailed thermal model of the device as a tool for performance analysis as well as for determining system heat losses and finding input heat flows required by DeltaEC code. A method of using the control volume balance equations (thermal model) is presented to find stack work and device efficiencies from experimental temperature and heat flow measurements. The accuracy of the thermal model depends on the accuracy of several factors such as (accurate device dimensions, contact resistances, thermal conductivity variation with temperature, internal and external convection and radiation, and consideration of nonuniform temperature profiles within system elements). Generally, considering all of these elements in the design phase can lead to a better design with more accurate measurements.

Jin et al. [2003] have designed, built, and tested a thermoacoustically driven pulse tube refrigerator utilizing sound from a thermoacoustic prime mover to drive a pulse tube refrigerator. A cryogenic temperature lower than 120 K has been achieved from the present system.

A summary of the literature reviewed so far on the components of thermoacoustic devices has been presented in the following flowchart (Fig. 2.12) below.

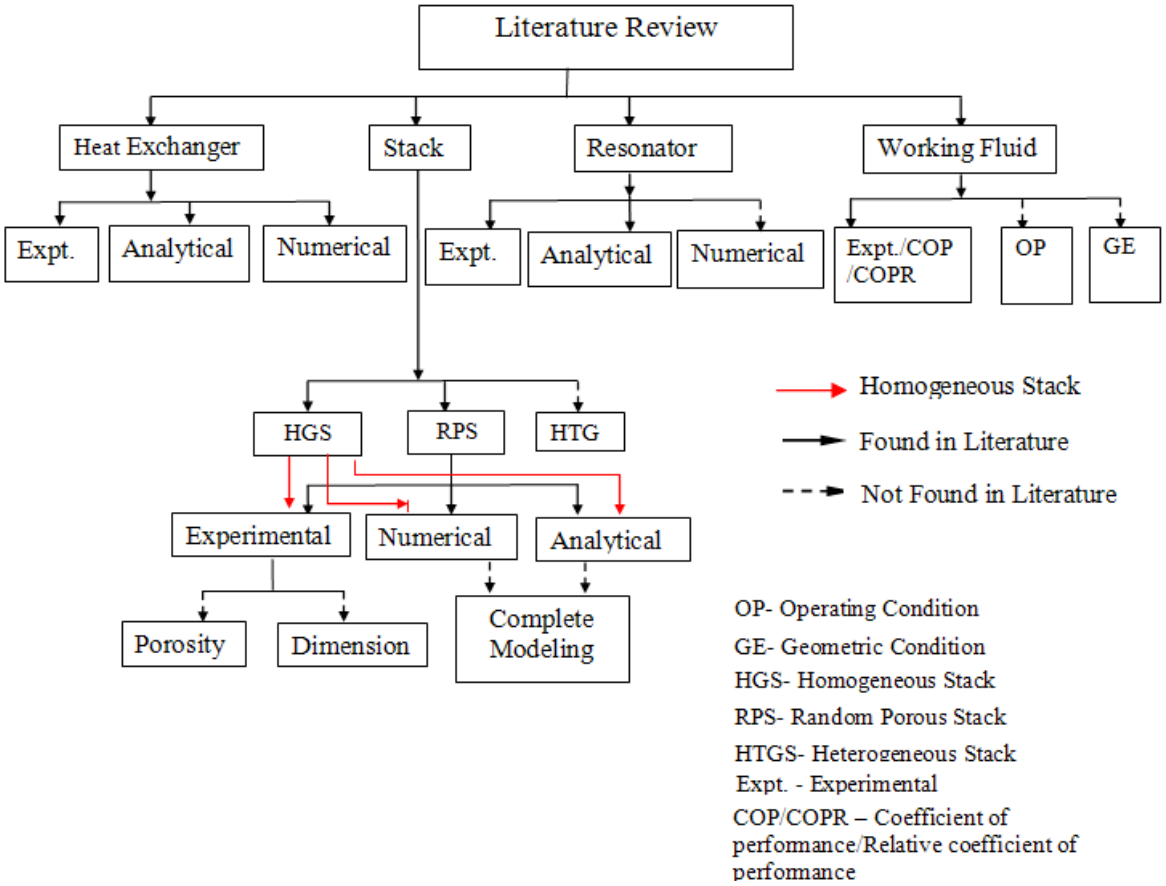

Figure 2.12: Flowchart of Literature Review

2.4 Summary

Each of those reported studies discussed above has its own advantages and disadvantages. Nevertheless, these studies serve as a basis for more advanced and sophisticated analyses of the thermoacoustic engines. In spite of the remarkable contributions by many researchers in developing thermoacoustic theories and improving thermoacoustic engine performance, industrial applications are still hindered by poor performance and by insufficient understanding of the flow field, heat transfer processes, and overall system component integration. Particularly lacking is a comprehensive research on random porous media stack. There is a strong need for the development of a comprehensive analytical modeling for random porous media stack in order to understand and increase the efficiency of thermoacoustic devices. No research effort exists

investigating the idea of using stacks having alternating conductive and insulative material at regular intervals along the flow direction, an idea that may improve the performance of thermoacoustic engines by reducing conduction loss within the stack material. There is no research effort that investigates the performance of a thermo acoustically driven thermoacoustic refrigerator (TADTAR) and compare the performance to an acoustically driven thermoacoustic refrigerator (TAR) in order to test the suitability of using TADTAR. Also lacking is research on the transport processes of fluid and energy inside thermoacoustic engines and refrigerators using different working fluids in different geometric and operating conditions numerically. Since experimental works on thermoacoustics are time consuming, lengthy, and complicated. This research is important for the enhancement of performance of thermoacoustic devices. These omissions from the literature provide the basis for some very nice research work into thermoacoustic engines.

Chapter 3

Experimental Scheme

3.1 Introduction

Some of the important roles of experiments in engineering are to provide the basis for scientific knowledge, to test theories, and to investigate novel techniques or materials or components for a specific application. The development of any analytical or numerical model is insignificant if it is not based on valid experimental evidence, criticism, and logical discussion. Therefore, a major objective of the comprehensive experimental scheme is to provide knowledge of thermoacoustic transport in stacks especially in the random porous media, temperature fields within the random and regular stack structures, thermal interaction between the stack and the acoustically driven working fluid in different regions, especially near the stack ends, and insight into the model developed in Chapter 4 and 5 and data for evaluating the ability of the models to accurately predict the thermal behavior of thermoacoustic stack under a range of design conditions. The second objective of the experiments is to develop a sustainable thermoacoustically driven thermoacoustic refrigerator that produces a measurable refrigeration effect and to compare its performance with a typical thermoacoustic refrigerator to test its applicability. Finally, the experimental scheme will be utilized to test a novel stack geometry.

Position of the stack in a resonator tube relative to the standing wave is an important factor in the design of the standing wave thermoacoustic devices. Also, important are the geometry and material of the stack as they affect the acoustic work produced or absorbed and cooling power of thermoacoustic devices. Equations (A.16) and (A.17) show that (thermoacoustic effect) work flux and energy flux depend on the gas and stack material cross-sectional areas. Increasing the gas area and lowering the stack material area (width$\times$thickness) result in an increase in the performance of thermoacoustic devices. However, lowering the stack material area can be realized by reducing the thickness of the stack plate material, and increasing the gas area that is effective in transporting heat

can be obtained by placing the stack plates closely together, therefore, increasing the volume of the gas residing in between the stack plates.

3.2 Experimental Objectives

The main objectives of this experimental scheme are to obtain the following characteristics of the stack:

- Measurements of temperature difference (ΔT) obtained across the stack ends at steady state under variable conditions; for example, different geometries (regular and random porous media (homogeneous stacks) and heterogeneous stacks of different combinations), materials (Celcor Ceramic, Kapton plastic, RVC, and Aluminum foams), dimensions (lengths of the stacks varying from 1.0 cm to 6.5 cm for Celocr ceramic and for RVC stacks from 1 to 4 cm), and positions of the stack (the hot end of the stack varies from 0.5 cm to 8 cm from the pressure anti-node) in the resonator.

- Measurements of temperature fields at different locations in the stack and in the working fluid (air in the present study) residing near the stack under variable conditions; for example, different geometries, materials, dimensions, and positions of the stack in the resonator.

The stack-end temperature difference, ΔT, will be used to analyse the temperature gradient developed along the stack at steady state. There are some inconsistencies in the existing literature regarding ΔT (will be discussed in Chapter 7). ΔT will also be used to evaluate and compare the performances of stacks of different geometries and materials using Eq. (A.16) for work flux, Eq. (A.17) for energy flux density or cooling power, and COP (using Eq. (A.18)). Measurement of temperature fields at different locations on the stack and of the working fluid provide us thermal field information within the stack and also provide information regarding the nature of heat flow at different locations of the stack which is still unexplored in the existing literature.

3.3 Experimental Facility

A thermoacoustic heat pump has been constructed to measure ΔT across the stack ends at steady state, temperature of the working fluid and stack at different locations on the stack, and the amplitude of the pressure (p_0) at the pressure anti-node of the resonator. The experimental facility has the following subsections:

- Experimental Setup
- Sensors
- Data Acquisition and Recording
- Sensor Installation
- Test Procedure

3.3.1 Experimental Setup

An experimental setup (heat pump) for measuring the thermal field characteristics of a stack has been designed and assembled. The setup (heat pump) has the following components:

1. A resonator
2. A stack
3. Heat Exchangers

Resonator

The resonator is an acrylic (thermal conductivity 0.20 W/m K at 23°C) tube of length 25 cm and inner diameter 2.1 cm, as illustrated in Fig. 3.1. The resonator is filled with air at atmospheric pressure. The position of the stack can be adjusted at any location on the resonator. One end of the tube is closed by a movable piston (reflector) of the resonator. At the other end a commercially available mid-range loudspeaker (Model NWX-516-8SQ) constituting the acoustic power source (driver). The loudspeaker has a frequency range of 70-7000 Hz and 10 W acoustic power output with RMS 70 W peak. This driver is mounted in a PVC-housing to which the resonator is connected. A function generator (GFG-8020H) and a 40 W power amplifier (NexxTech) have been used to drive the

system at the operation frequency and with the selected power. The accuracy of the frequency and the amplitude of the output signal are 1 μ Hz and 0.1 mV, respectively.

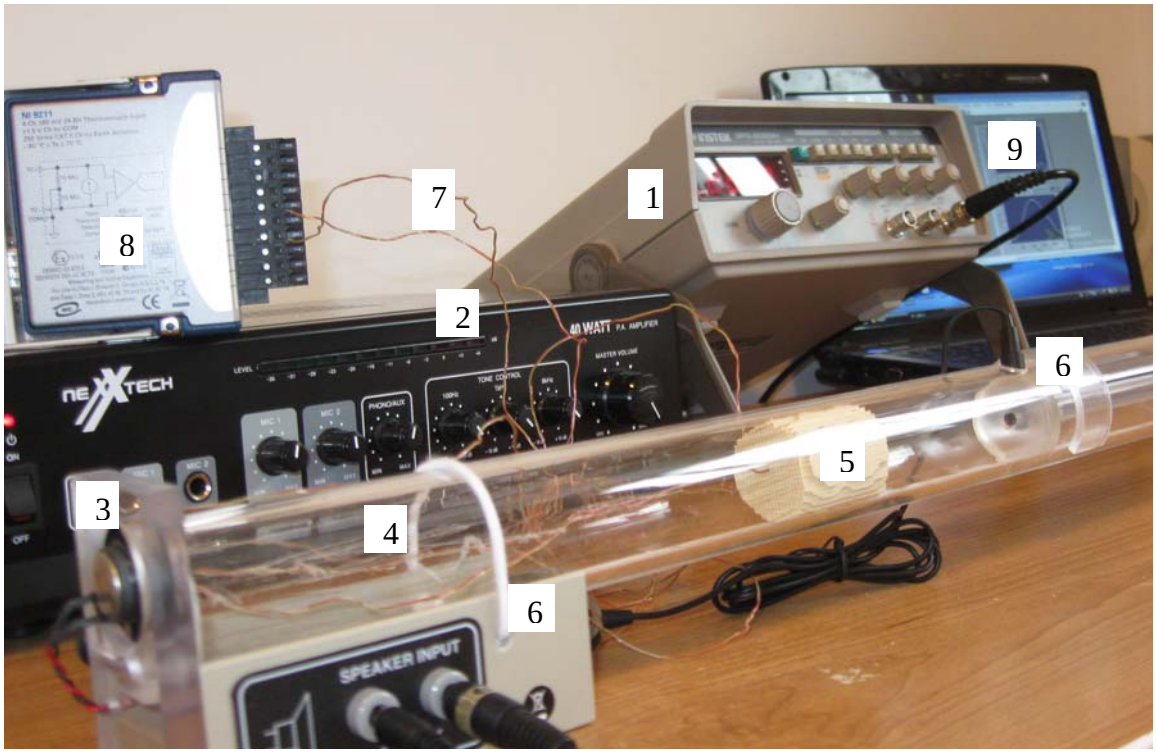

Figure 3.1: A thermoacoustic heat pump and the measuring systems.

1	Function generator	6	Microphone
2	Amplifier	7	Thermocouples
3	Speaker	8	NI Data Acquisition System
4	Resonant chamber	9	Lab VIEW Interface
5	Stack		

Stack

The stacks studied in the measurement set-up are the prefabricated stack made of 400-cpsi (cells per square inch) Corning Celcor ceramic material manufactured by Corning Inc. (Corning [2010]), Reticulated Vitreous Carbon (RVC) of different pore sizes ranged from 20-100 PPI (pore per linear inch) manufactured by Energy Research and Generation Inc. (ERG [2009]), and fabricated Kapton plastic (Swift [1988]), respectively. The Corning Celcor material is selected based on its strength, low thermal conductivity, high surface area for conversion efficiency, high temperature capability (up to 1400°C), and availability. RVC foam is an open pore foam material composed solely of vitreous

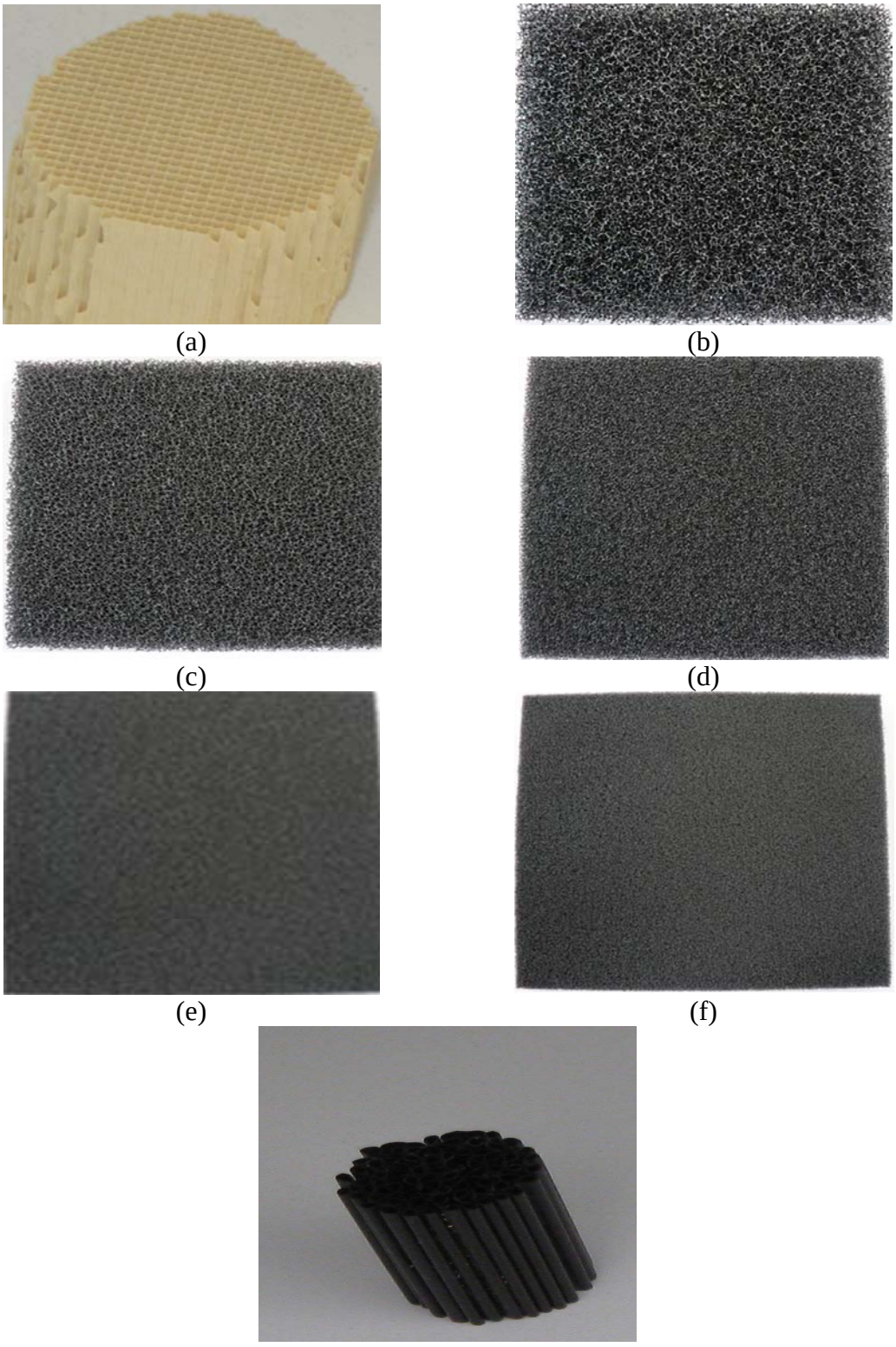

Figure 3.2:Stack samples used in the experiments, (a) Corning Celcor, (b) 20 PPI, (c) 30 PPI, (d) 45 PPI, (e) 80 PPI, (f) 100 PPI RVC stacks, and (g) Kapton plastic stack.

carbon, has a large surface area, low thermal conductivity, low resistance to fluid flow, and can withstand very high temperatures (315°C in air). The reason for selecting those stack materials and geometries is to compare their performance (for example, temperature difference across the stack ends, and the maximum temperature at the hot side of the heat pump stack). Figures 3.2(a) to (g) show the cross sections of the stack used in the present study. Corning Celcor stack (400-cpsi) with a square cross section (as shown in Fig. 3.2(a)) and six different lengths 1 cm, 2 cm, 2.5 cm, 4 cm, 5 cm, and 6.5 cm are considered. Celcor properties and channel dimensions are available in Tables 3.1(a) and (b) along with RVC and Kapton plastic stacks. The RVC foams are identified by the manufacturer according to pore density with values of 20 pores per inch (PPI), 30 PPI, 45 PPI, 80 PPI, and 100 PPI. The bulk density and specific heat of all RVC foam samples are 49.5 kg/m^3 and 1260 J/kg. K (ERG [2009]). Five different lengths, 1 cm, 1.5 cm, 2 cm, 2.5 cm, and 4 cm of RVC foam samples are studied along with circular plastic stack of 4 cm length and 1 mm pore diameter. The reason for selecting 1 mm pore diameter circular plastic stack is to compare the performance of the circular plastic stack to that of Celcor stack. It should be noted that all of the stacks have the identical outer diameter and is equal to the inner diameter of the resonator. Measurements are taken for six different Corning Celcor stack lengths and 20 PPI porosity, five different porosities and five different lengths of RVC stack, and a 1 mm pore diameter and 4 cm long plastic stack at eight different locations of the stack center from the pressure anti-node.

In Table 3.1(a), r_h is the hydraulic radius, which can be obtained as follows (Swift [2002]):

$$r_h = \frac{\text{Cross sectional area } (A)}{\text{Perimeter}}. \tag{3.1}$$

The hydraulic radius r_h can also be thought of as the ratio of gas volume to gas-solid contact area, or as the distance from a typical parcel of gas to the nearest solid surface. The hydraulic radius of a circular stack is half of the circle's actual radius, and of a square cross section stack is quarter of the spacing (if the spacing is $2\,y_0$, hydraulic radius

will be $y_0/2$). According to Tijani [2001], plate spacing in the parallel plate stack of $2.5\delta_k$ is for optimum for the cooling power of a thermoacoustic refrigerator and a

Table 3.1(a): Properties and Dimensions of Stack Materials (Corning [2010])

	Materials	
	Celcor Ceramic	Kapton plastic (Swift [1988])
Length (cm)	1, 2, 2.5, 4, 5 and 6.5	4
Hydraulic Radius(mm)	0.3175	0.25
Thickness (mm)	0.05	0.03
$\frac{r_h}{\delta_k}$	2.3	1.78
Blockage Ratio	0.74	0.89
Specific Heat (J/kg K)	1000	1100
Thermal Conductivity (W/m K)	1.46	0.16
Density (Kg/m^3)	2500	1400

Table 3.1(b): Properties and Dimensions of RVC Stack Materials (ERG [2009])

	Material(RVC)				
	20 PPI	30PPI	45PPI	80PPI	100PPI
Length (cm)	1,1.5, 2, 2.5, and 4	1,1.5, 2, 2.5, and 4	1,1.5, 2,2.5, and 4	1,1.5, 2,2.5, and 4	1,1.5, 2,2.5, and 4
Radius(mm)	0.635	0.424	0.282	0.16	0.127
$\frac{r_h}{\delta_k}$	2.27	1.52	1	0.57	0.45
Thermal Conductivity (W/m. K)	0.033	0.035	0.04	0.048	0.055

spacing of $4\delta_k$ leads to the lowest temperature. In the present study our objective is not to optimize a thermoacoustic refrigerator, but the plate spacing that are employed will

produce reasonably good performance regarding the cooling power or the temperature at the hot side of the stack.

RVC pores are assumed as circular pores; therefore for example 30 pores per linear inch (PPI) give the average pore size of about 0.03 inch or 0.85 mm ($r_h = r/2 = 0.212\,\text{mm}$).

RVC foam density - The actual density of a piece of foam is simply the bulk density of the base material of the struts or ligaments multiplied by the relative density.

Actual foam density = solid strut density × foam relative density

The relative density of the RVC foam is 3% as specified by the manufacturer (ERG [2009]). Density of solid vitreous carbon is 1650 kg/m^3, which results in an actual foam density of 49.5 kg/m^3.

Heat Exchangers

Two heat exchangers are required for the thermoacoustic heat pump, one for supplying heat to the cold side of the stack and another to extract heat from the hot side of the stack. The cold (ambient) heat exchanger used in the present study is a winding of Ni-Cr heater wire at the cold side of the stack. Shallow grooves are cut to the cold side of the stack to accommodate the Ni-Cr heater wire. This electrical heater wire provides an easily controlled and measured amount of heat for the heat pump to pump. The cold side of the heat pump is insulated form the room using standard Corning Pink fiberglass insulation (R value 1.8 m^2 K/W). At the hot side of the stack, two loops of 1/8 in. copper refrigeration tubing are wrapped around the perimeter of the resonator to allow water to be circulated. A Hedland flow meter (IR-OPFlow Model 502-101) is used to pump water through the loop. Heat exchangers are not shown in Fig. 3.1.

3.3.2 Sensors

In order to perform the measurements, several pieces of equipment are utilized. Thermal response is measured using thermocouples, and pressure measurements are made with sound level meter, while a data acquisition system records the measurements (as shown in Fig. 3.1).

Temperature Measurement

A common method for recording temperature is through the use of a thermocouple. The chosen thermocouple for this work is a K-type thermocouple composed of chromega and alomega from Omega Engineering, Inc., model GG-K-40-72 (Omega [2009]). Based on Omega [2009], these exposed junction type thermocouples which feature Glass Braid (melting point 600°C) insulation allow a temperature range of 0°C to 600°C. The accuracy of the thermocouples is ± 0.1°C (Omega [2009b]).

Pressure Measurement

The acoustic pressure measurements are made by a sound level meter (OMEGA HHSL1). The sound level meter, placed near the driver end, measures the dynamic pressure (p_0) and is used for determining the resonance frequency. Also the dynamic pressure measurement is used to evaluate the drive ratio (DR). The accuracy of the sound level meter as indicated by (Omega Engineering [2009]) is ±1.5 dB. To convert the sound level meter data from decibel (dB) to pascal (Pa), the following expression is used

$$L_p = 10\log_{10}(\frac{P^2}{P^2{}_{ref}}) = 20\log_{10}(\frac{P}{P_{ref}})dB\,. \qquad (3.2)$$

Where L_p = sound pressure level in dB

P =root mean square sound pressure $= p_0/\sqrt{2}$

$P_{ref} = 20\times10^{-6}\,Pa \quad or\ 20\mu Pa = reference\ pressure$

Accuracy of Instruments

Instrument	Accuracy
K-Thermocouple	± 0.1°C
Sound level meter	±1.5 dB
Function generator	10 μ Hz
Amplifier	1mV

3.3.3 Data Acquisition and Logging

Data acquisition (DAQ) hardware is required to read the analog signals generated by the sensors (as shown in Fig. 3.1). Once these signals are interpreted by the DAQ, a digital signal is sent to a computer for processing or recording and analyzing. There are

numerous solutions to acquiring and processing analog data. LabVIEW 8.5 (NI [2010]) is chosen as the environment for data visualization and processing and with LabVIEW came National Instruments (NI) DAQ hardware (NI USB-9211A, NI [2009]). In order to ensure flawless integration when necessary, it is decided that thermal data acquisition would also be made using NI hardware and LabVIEW.

3.3.4 Thermocouple and Sound Level Meter Data Acquisition

For thermocouple measurement, National Instruments' NI USB-9211A portable USB-based DAQ is chosen. As stated in National Instruments [2009], the module is compatible with J, K, R, S, T, N, E, and B type thermocouples, offers 24-bit resolution allowing for temperatures of 0 to 750°C to be read from any thermocouple type. It includes antialiasing filters and cold-junction compensation for high accuracy thermocouple measurements. It has four channels. The sampling rate is 14 samples per second per channel. The sound level meter is a portable 4 digit, compact sized, digital display sound level meter designed for long term measurements. Operating environment is -10 to 70°C. This sound level meter is connected to the NI DAQ hardware to compute the Fast-Fourier Transformation (FFT) for analyzing and measuring the signals from DAQ devices. FFT's are computed for the average frequency content of a signal over the entire time that the signal was acquired as shown in Fig. 6.3.

3.3.5 Sensor Installation

To understand the thermoacoustic effects and measure the stack performance, several thermocouples are employed. Based on the available data acquisition hardware, one USB-9211A [NI, 2009] module, the maximum number of simultaneous measurements is 4. Therefore, two DAQ hardwares are used for the maximum temperature measurements at 8 different locations.

3.3.5.1 Methods of Attachment

In order to attach the thermocouples to the stack plate surfaces, a thermal paste (a silicon grease, type OT-201-2) from Omega Engineering Inc., is employed. This paste offers a high thermal conductivity of 2.3 W/m K and is formulated for temporary bonds at

temperatures between 0° C and 400°C. The sound level meter passes through a cork that is fixed in a hole on the closed end of the resonator in order to keep acoustic losses low.

3.3.6 Test Procedure

Experiments are performed using the samples provided in Tables 3.1(a) and (b). The effect of material, geometry, dimensions, and position of the stack in the resonator are examined during the experiment. For each test (for a particular stack material or geometry), the position of the stack is varied between 0.5 to 8 cm from the pressure anti-node. Each test is allowed to reach steady state over a certain period of time (about 60 to 90 seconds) that is confirmed by LabVIEW graphics for the temperature measurements for the stack and the surrounding working gas.

The thermocouples are read with NI USB-9211A module, for which National Instruments [2009] present a graph to quantify the error associated with K-type thermocouples. The maximum temperature error in the range of interest, 10°C to 65°C is 2.2°C, and the minimum is 1.0°C. This error is stated to be associated with "gain errors, offset errors, mechanical disturbances, noise errors, and isothermal errors", and it is noted that this error is independent of any error associated with the thermocouple itself. The measurements positions are accurate to about ± 0.5 mm.

The uncertainty analysis of the measurements is discussed in Appendix A. The measurements related to the experimental setup discussed in Chapter 3 are presented in Chapters 7 and 8. For the thermoacoustically driven thermoacoustic refrigerator (TADTAR) presented in Chapter 6 the descriptions of the experimental setup are provided in that chapter (Chapter 6).

3.4 Summary

This chapter presents the details of the experimental procedure and data for various stack geometries, materials, and dimensions. One of the objectives of this experiment is to provide insight of the thermoacoustic effect and to eliminate the inconsistencies exist in the literature regarding the thermal field (will be discussed in Chapter 7). Experimental results are presented in Chapters 7 and 8

Chapter 4

Porous Media Thermoacoustic System: Darcy Model

4.1 Introduction

This chapter describes the extension of linear thermoacoustic theory for a random porous medium stack using Darcy model. Detail explanation for considering a random porous medium stack is also provided.

4.2 Understanding the Productive and Dissipative Effects in Thermoacoustics

The stacks in typical thermoacoustic devices are subdivided into many parallel channels or pores in order to maintain moderate (standing-wave) thermal contact between the working gas and the stack across large cross-sectional areas. The surface of the stack material should be large enough so that most of the entrained gas lies within the thermal penetration depth, and yet not significantly impede the oscillating sound wave.

In order to understand the productive and dissipative processes within a stack, consider two different stack geometries; parallel plates (Fig. A.2 in Appendix A.1) and pin array stacks (Fig. 4.1). The reason for better performance of pin array stack compared to the parallel plate stack (as showed by Swift and Keolian [1993]) is apparent when we consider the productive and dissipative processes in a stack. As shown in Fig. 4.2, the productive process (thermoacoustic effect) is maximum at a vertical distance of δ_k from the stack surface. While the dissipative process (dissipation of acoustic power) mostly occurs at the solid fluid interface (Swift and Keolian [1993]). Therefore, the thermoacoustic effect and the viscous losses occur at different distances from the stack surface, and so changing the curvature of the stack surface from planar to convex can

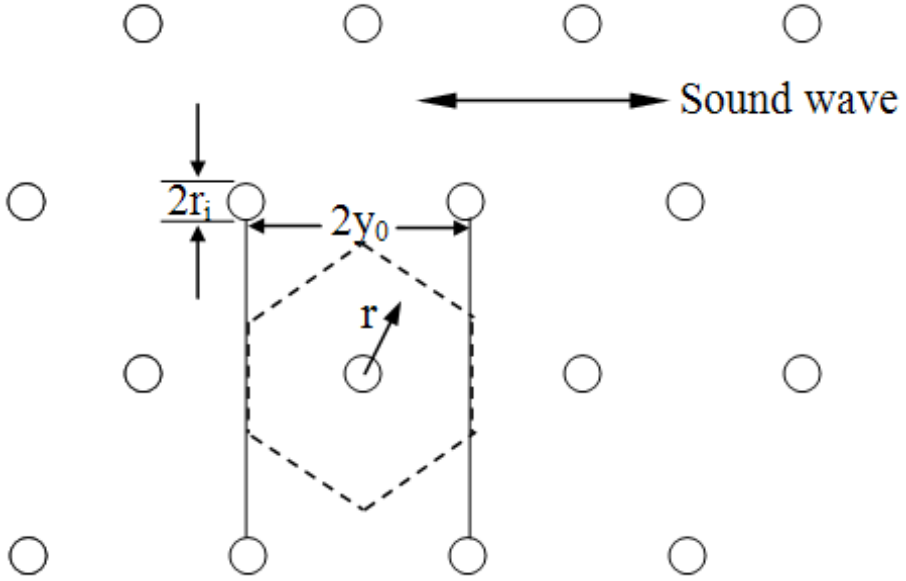

Figure 4.1: Geometry of pin array stack in a sound wave used by Swift and Keolian [1993].

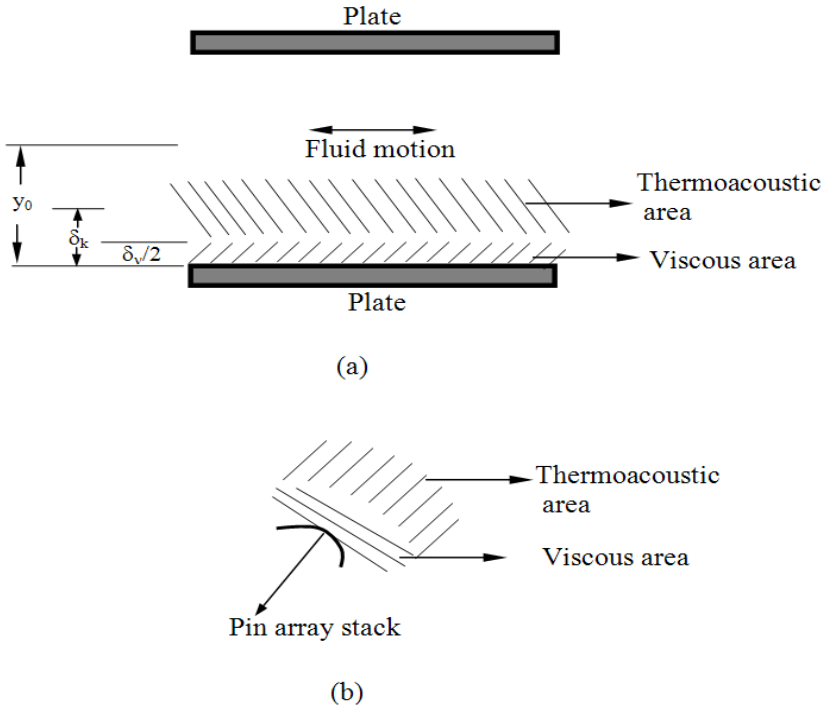

Figure 4.2: A schematic diagram for understanding the thermoacoustic effect vs. viscous effect.

change the ratio of thermoacoustic to dissipative effects. Swift and Keolian [1993] showed using a heuristic picture that a convex radius of curvature of the order of δ_k or δ_ν increases the ratio of thermoacoustic area to viscous area significantly than for the flat surface. In the next sections the linear thermoacoustic theory (Swift [1988]) will be extended using porous media approach and the thermoacoustic effects will be investigated.

4.3 Reasons for Considering the Specific Stack Geometry

Thermoacoustic theories developed by Rott [1980] and Swift [1988] considered the overall stack as a porous medium composed of multiple individual channels, these pores or channels are of circular, rectangular, hexagonal, etc., cross-section, and is filled with clear working fluid (such as air, helium or other inert gases). The primary goal of this chapter is to incorporate into the fundamental thermoacoustics theory of Swift [1988] and Rott [1980] a modification that treats the fluid-gaps within a stack of a thermoacoustic engine/refrigerator as porous media, not simply a multi-channel stack as pursued by Swift [1988, 2002]. The reason for inserting porous media in between the stack plates is to increase the thermoacoustic surface area (Fig. 4.2). The porous structures are capable of increasing the heat exchange surface area while producing a secondary flow path that breaks up the thermal boundary layer and enhances the heat transfer coefficient. However, the pressure drop across the porous media might be amplified, as a result, and increased pumping power. Therefore, COP of a thermoacoustic device using porous media stack will be compared to that of non porous media stacks in **Section** 4.4 after the systems of equations are developed using porous media approach.

Use of Porous Media in Heat Transfer Applications

Convection through porous media is of interest in a variety of heat transfer applications such as electronic cooling. The increase of execution speed and circuit density per chip of present computers leads to high heat dissipation. Presently, an average desktop and mobile processor peak power consumptions are about 100W and 30W (Gochman et al. [2009]), respectively. In conventional (natural or forced convection) cooling techniques,

the most common method to remove the increased heat is to increase the air flow rate and solid-air contact surface area. These methods, though, will increase the volume of heat sink and at the same time will increase the acoustic noise. The porous medium has emerged as a useful method of heat transfer augmentation, due to its large surface area to volume ratio and intense mixing of fluid flow. Leong et al. [2005] conducted an experimental study on the heat transfer of oscillating flow through a channel filled with aluminum foam (40 PPI) subjected to a constant wall heat flux. The results revealed that the heat transfer in oscillating flow (with a frequency range of 4.4 to 8.2 Hz) is significantly enhanced by employing porous media in a plate channel compared to the steady flow case. Leong and Jin [2004] and Fu et al. [2001] reported the results for heat transfer in porous channels in oscillating flow with RVC and metal foam materials. They reported that the length-averaged Nusselt number for oscillating flow is higher than that for steady flow.

Another application of porous medium is found in the applications of heat exchangers (condenser and evaporator) in cryogenic, power, refrigeration, and air conditioning industries. Although these industries have been using air flow heat exchangers for many years, new challenges appear and opportunities for performance enhancement continue. Enhancement of performance is achieved by increasing the heat transfer surface area in contact with the flowing air or by increasing the heat transfer coefficient. Another approach of performance enhancement is to use a louvered fin that acts to break up the thermal boundary layer and improve net heat transfer with an increase in both surface area and heat transfer coefficient (Chang et al. [1997]). While this arrangement will greatly enhance heat transfer, the increased pressure drop can make such a configuration undesirable due to increased pumping power. In general, there is an optimum spacing that represents a tradeoff between enhanced heat transfer and increased pumping power requirements. Another approach to enhancing the air side heat transfer rate is to replace the fins with a high thermal conductivity porous structure (such as aluminum, copper, or carbon foams). These structures are capable of increasing the heat exchange surface area while breaking up the thermal boundary layer and augment the heat transfer coefficient. However, the pressure drop across the porous media might be amplified, as a result, and

increased pumping power. More recently, performance of aluminum and carbon foams for air side heat transfer augmentation has been evaluated by Garrity et al. [2010]. The foam samples were placed in a forced convection arrangement (air velocity ranging from 1 to 6 m/s) using a foil heater as the heat source and ambient air as the sink. The steady volume-averaged momentum equation and a two equation non equilibrium heat transfer model are employed to extract the volumetric heat transfer coefficients. The performance of each sample is evaluated based on a coefficient of performance (COP, defined as the ratio of the total heat removed to the electrical input of the blower), compactness factor (CF, defined as the total heat removed per unit volume), and power density (PD, defined as the total heat removed per unit mass). Results show the carbon foam samples provide significant improvement in CF but the COP and PD are considerably lower than that for comparable multilouvered fin heat exchangers.

Another potential application of convection processes in porous media is found in the stack of thermoacoustic prime movers/engines and heat pumps/refrigerators [Swift, 2002]. In order to develop the theories of thermoacoustics for porous media, Mahmud and Fraser [2009] considered a simplification of Vafai and Tien's porous medium model [1981] for the modeling of momentum equation and local thermal equilibrium assumption between the porous matrix and the working fluid for the energy equation. Mahmud and Frasers' work [2009] showed that if a porous medium is used in between the thin parallel plates, much more efficient thermoacoustic engine designs are possible in the Da ($=K/\delta_\nu^2$, where K is the permeability of the porous medium and δ_ν is the viscous penetration depth) range 0.1-1.0 and for S_w (non-dimensional stack plate spacing) ≥ 2.

Overview of Modeling Approaches

The present study revises Mahmud and Frasers' work [2009] and considers Darcy flow model (Bejan [1984]) for the modeling of momentum equation followed by Brinkman Forchheimer extended Darcy model (Vafai and Kim [1989]) in the next chapter. The objective of porous media modeling of thermoacoustic stack is to provide a theoretical understanding of tortuous stack environment that is required to understand and increase

the efficiency of thermoacoustic devices that uses tortuous stacks. The assumption of Darcy model has obvious limitations however this model has introduced to help more clearly describe the concept of thermoacoustic engine while a random porous medium is embedded in between the channel walls, and together the channel walls and the porous medium act as a stack. In this study no effort will be taken to compare the present result to that of Mahmud and Frasers' result [2009], since their conclusion is for *Da* range of 0.1 to 1.0, whereas the present study deals with the zero *Da* limit. In the present study, the thickness of the stacks/channel walls is considered to be nonzero, and the entire problem is treated as a conjugate heat transfer problem The unique characteristic of this research is the complete heat transfer modeling by considering this conjugate heat transfer. For the modeling of energy equation, local thermal equilibrium assumption between the porous matrix and trapped fluid in the void space is considered in the present work. After the simplified governing differential equations are solved by the *Complex Exponential Method* (Temkin [1981]), the spatial distribution of the fluctuating temperature, Nusselt number, and energy flux density are presented. The real parts of these complex expressions represent the actual, physical solutions.

4.3.1 Analysis

Figure 4.3 depicts the schematic diagram of the problem that is being examined. The length (along the *x*-direction) and width (perpendicular to the paper) of the porous medium

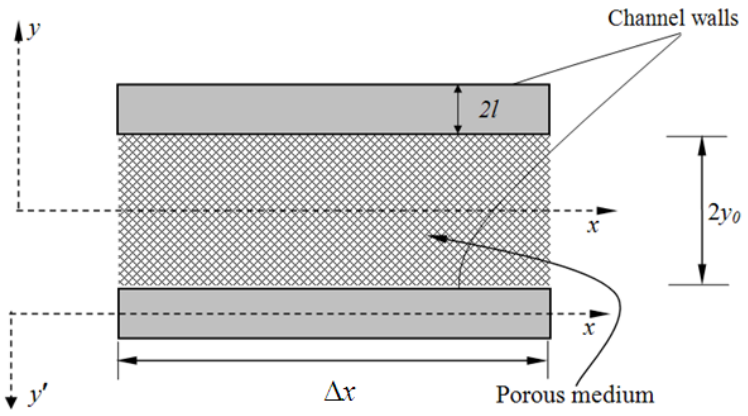

Figure 4.3: Co-ordinate system and dimensions of analytical domain in the porous medium.

are Δx and $\Pi/2$ (not shown in the figure), respectively. The x-axis represents the longitudinal direction (also the direction of fluid oscillation), whereas the y and y' axes represent the transverse (normal to the wall) directions in the porous medium and in the channel wall, respectively. The spacing between two consecutive walls is $2y_0$, and $2l$ is the thickness of the channel wall. The whole stack is a combination of multiple channels and porous medium in between the channel walls (see Fig. 4.3). The location $y=0$ is chosen to be the midpoint between the two adjacent walls and $x=0$ is chosen to be the beginning of the resonator to the right as shown in Fig. 2.1. An acoustic driver (such as a loudspeaker) initiates the fluid oscillation inside the resonator. The oscillating compressible fluids interact hydrodynamically and thermally with the porous medium and the solid wall and produce thermoacoustic effects. The following sections are devoted to calculating the fluctuating velocity in the porous medium, temperature in the porous medium and in the channel wall, complex Nusselt number, energy flux density, and the fluctuating pressure. Every time efforts will be taken to compare the present results to that of Swift [1988].

4.3.2 Velocity and Temperature Modeling

The modeling of the momentum equation is performed using the Darcy flow model (Bejan [1984]). The Darcy flow model constructs a relationship between the flow velocity in a certain direction to the pressure gradient in that direction, that is,

$$\mathbf{v} = -\frac{K}{\mu}\nabla p \tag{4.1}$$

in vector form where $\mathbf{v}$, K, μ, and p are the velocity vector, permeability, viscosity, and pressure, respectively. The effect of gravity is neglected in Eq. (4.1) and the permeability K (m^2) is an empirical constant. The Darcy flow model is valid in circumstances where the order of magnitude of the local pore Reynolds number, based on the local volume averaged speed ($|\mathbf{v}|^{1/2}$) and length scale $K^{1/2}$, is smaller than 1 (Bejan [1984]). In the present study, the thermophysical properties are chosen in such that the local pore Reynolds number is smaller than unity. The assumptions and linearization technique as employed by Swift [1988] and Rott [1980] (discussed in **Section** A.1 of Appendix A) are

also followed in the present investigation to obtain the required parameters. In such a case, the momentum equation reduces to

$$u_1 = -\frac{K}{\mu}\frac{dp_1}{dx}. \tag{4.2}$$

In Eq. (4.2), u_1 and $\frac{dp_1}{dx}$ are the average (incorporating both solid and fluid material) fluctuating velocity and pressure gradient, respectively. The porous medium in the present study is saturated with a single phase Newtonian fluid and is assumed to be in local thermal equilibrium with the working fluid. The governing energy equation, for such a case, can be obtained by integrating the solid's energy equation over the area occupied by the solid matrix and integrating the fluid's energy equation over the area occupied by the fluid (in the pores) followed by a subsequent addition of two area averaged equations and simplifications (Bejan [1984], Burmeister [1992]). If the thermal conductivity of the porous medium is high or in the presence of a very high fluid velocity, local thermal equilibrium assumption is not valid, separate energy equations need to be solved for the porous solid matrix and the fluid parts (Bejan [1984]).

According to Bejan [1984], for the current problem and assumptions, the energy equation inside the porous medium is

$$\rho_f C_{pf}\left[\sigma\frac{\partial T}{\partial t} + u\frac{\partial T}{\partial x} + v\frac{\partial T}{\partial y}\right] = k\left[\frac{\partial^2 T}{\partial x^2} + \frac{\partial^2 T}{\partial y^2}\right] + \beta T\left[\phi\frac{\partial p}{\partial t} + u\frac{\partial p}{\partial x} + v\frac{\partial p}{\partial y}\right], \tag{4.3}$$

where σ, k, C_p, ρ_f, and β are the porous medium heat capacity ratio, thermal conductivity, specific heat of fluid, density of fluid, and thermal expansion coefficient, respectively. In Eq. (4.3), u and v are average (incorporating both solid and fluid material) velocity in the x and y directions, and p is the average pressure. Viscous dissipation term is neglected in Eq. (4.3). The parameters σ (porous medium heat capacity ratio) and k (overall thermal conductivity) can be defined, according to Bejan [1984], as

$$\sigma = \phi + (1-\phi)(\rho C)_{sm} / (\rho_f C_{pf}) \tag{4.4a}$$

$$k = \phi k_f + (1-\phi) k_{sm}. \tag{4.4b}$$

Where ϕ is the porosity (=void volume/total volume) of the porous medium. In Eq. (4.4a) to Eq. (4.4b) the subscripts 'sm' and 'f' represent the properties correspond to the solid matrix and fluid, respectively. Several definitions regarding the overall thermal conductivity are available in the existing literatures. In general, the overall thermal conductivity of a porous medium depends on the geometry of the medium (Nield and Bejan [2006]). The definition (Eq. (4.4b)) used in this chapter corresponds to a parallel conduction model. If the heat conduction in the solid and fluid phases occurs in parallel, then the overall conductivity k is the weighted arithmetic mean of the conductivities k_s and k_f (Eq. 4.4(b)). Generally k must be measured experimentally, as the thermal conductivity of the porous matrix filled with fluid. On the other hand, if the structure and orientation of the porous medium is such that the heat conduction takes place in series, with all of the heat flux passing through both solid and fluid, then the overall conductivity k_H is the weighted harmonic mean of k_s and k_f (Nield and Bejan [2006]):

$$\frac{1}{k_H} = \frac{1-\phi}{k_s} + \frac{\phi}{k_f}. \tag{4.4c}$$

Generally, $k_H \le k$ with equality if and only if $k_s = k_f$. For practical purposes, a rough and easy estimate for overall thermal conductivity is provided by $k_s^{1-\phi} k_f^{\phi}$, as long as k_s and k_f are not too different from each other (Nield and Bejan [2006])). For the present study, the values of k_s and k_f are very similar. Using any of the above definitions will produce very similar results. Thus it is decided to use Eq. (4.4b) to define the overall thermal conductivity.

After linearization, and keeping only first order terms, and neglecting $\frac{\partial^2 T_l}{\partial x^2}$ compared to $\frac{\partial^2 T_l}{\partial y^2}$, Eq. (4.3) becomes

$$k\frac{\partial^2 T_1}{\partial y^2} - i\sigma\omega C_{pf}\rho_f T_1 = C_{pf}\rho_f u_1 \frac{dT_m}{dx} - i\omega\phi\beta T_m p_1 . \qquad (4.5)$$

Note that for the expansion of Eq. (4.1) and Eq. (4.5), it is assumed that the mean velocity component (u_m) is zero, since the fluid oscillation begins from a motionless state. A detailed description of the transformation of energy equation from Eq. (4.3) to Eq. (4.5) is discussed in Appendix B.

The general solution to Eq. (4.5) is

$$T_1 = C_1 \sinh\left(\frac{1+i}{\delta_k}\sqrt{\sigma}\, y\right) + C_2 \cosh\left(\frac{1+i}{\delta_k}\sqrt{\sigma}\, y\right) + \left[\frac{\phi T_m \beta\, p_1}{\sigma \rho_{f\,m} C_{p\,f}} - \frac{u_1}{i\sigma\omega}\frac{dT_m}{dx}\right], \qquad (4.6)$$

where C_1 and C_2 are the two constants of integration, and δ_k is the thermal penetration depth, respectively. The following boundary conditions will be applied: (a) at $y = 0, \quad \partial T_1 / \partial y = 0$ and (b) at $y = y_0, \quad T_1 = T_w$ to Eq. (4.6). For the first thermal boundary condition (a), at the center of the stack inside the porous medium, fluctuating temperature gradient at the transverse direction is zero, and for the second thermal boundary condition (b), it is assumed that at the wall and porous medium interface, the temperature fluctuation is equal to T_w (wall temperature). Since the channel wall does not have sufficient heat capacity per unit surface area to impose a zero fluctuation thermal boundary condition (i.e., $T_1 = 0$) at the wall and porous medium interface. After the first boundary condition is applied, C_1=0 in Eq. (4.6). And the application of the second boundary condition gives

$$T_w = C_2 \cosh\left(\frac{1+i}{\delta_k}\sqrt{\sigma}\, y\right) + \left[\frac{\phi T_m \beta\, p_1}{\sigma \rho_f C_{pf}} - \frac{u_1}{i\sigma\omega}\frac{dT_m}{dx}\right]. \qquad (4.7)$$

In order to evaluate C_2, it is necessary to solve the energy equation inside the channel wall

$$(\rho C)_c \frac{\partial T_s}{\partial t} = k_c \frac{\partial^2 T_s}{\partial y'^2}, \tag{4.8}$$

where ρ_c, C_c, and k_c are the mean density, specific heat, and the thermal conductivity of the channel wall, and y' represents the transverse coordinate in the solid region. After linearizing and keeping the first order term only, Eq. (4.8) reduces to

$$i\omega(\rho C)_c T_{s1} = k_c \frac{\partial^2 T_{s1}}{\partial y'^2}, \tag{4.9}$$

the general solution to Eq. (4.9) is

$$T_{s1} = C_3 \exp\left(\sqrt{\frac{i\omega(\rho C)_c}{k_c}}\, y'\right) + C_4 \exp\left(-\sqrt{\frac{i\omega(\rho C)_c}{k_c}}\, y'\right). \tag{4.10}$$

With the following boundary conditions: (c) at $y' = 0$, $\partial T_{s1}/\partial y' = 0$ and (d) at $y' = l$, $T_{s1} = T_w$, the final expression for temperature fluctuation inside the solid region becomes

$$T_{s1} = T_w \frac{\cosh\left(\sqrt{\frac{i\omega(\rho C)_c}{k_c}}\, y'\right)}{\cosh\left(\sqrt{\frac{i\omega(\rho C)_c}{k_c}}\, l\right)}. \tag{4.11}$$

In Eq. (4.11), T_w is unknown. To evaluate C_2 in Eq. (4.7) and therefore T_w (in Eq. (4.11)), an additional boundary condition is required, which is given by

$$k \left.\frac{\partial T_1}{\partial y}\right|_{y=y_0} = -k_c \left.\frac{\partial T_{s1}}{\partial y'}\right|_{y'=l}. \tag{4.12}$$

C_2 is evaluated if Eqs. (4.7) and (4.11) are substituted into Eq. (4.12). The final expression for T_1 then becomes

$$T_1 = \left[\frac{\phi T_m \beta\, p_1}{\sigma\left(\rho C_p\right)_f} - \frac{u_1}{i\sigma\omega}\frac{dT_m}{dx}\right]\left[1 - \frac{\cosh\left\{\frac{(1+i)}{\delta_k}\sqrt{\sigma}\,y\right\}}{\cosh\left\{\frac{(1+i)}{\delta_k}\sqrt{\sigma}\,y_0\right\}\left(1+\varepsilon_s\sqrt{\sigma}\right)}\right], \tag{4.13}$$

where the parameter ε_s (heat capacity ratio between the porous media and the wall) can be expressed as

$$\varepsilon_s = \sqrt{\frac{k\left(\rho C_p\right)_f}{k_c\left(\rho C\right)_c}}\,\frac{\tanh\left\{\frac{(1+i)y_0}{\delta_k}\right\}}{\tanh\left\{\frac{(1+i)l}{\delta_s}\right\}}, \tag{4.14}$$

and $\delta_s\left(=\sqrt{2\alpha_c/\omega}\right)$ is the thermal penetration depth inside the channel wall and dT_m/dx is the mean axial temperature gradient, respectively. Now the temperature at the wall (substituting C_2 in Eq. (4.7b)) becomes

$$T_w = \left[\frac{\phi T_m \beta\, p_1}{\sigma\left(\rho C_p\right)_f} - \frac{u_1}{i\sigma\omega}\frac{dT_m}{dx}\right]\left[1 - \frac{1}{\left(1+\varepsilon_s\sqrt{\sigma}\right)}\right]. \tag{4.15}$$

Detail discussions on the thermal field with graphical interpretation are left for the results and discussions section.

4.3.3 Heat Transfer between the Channel Wall and the Porous Medium

In the present study, the complex Nusselt number (Nu) is calculated in two different ways to evaluate dimensionless heat transfer between the channel wall and the porous media. First, using the definition available in Mahmud and Fraser [2005b], the complex Nu for current problem becomes

$$Nu = \left(\frac{y_0}{T_w - \langle T_1 \rangle}\right)\left.\frac{\partial T_1}{\partial y}\right|_{y=y_0}, \tag{4.16}$$

where

T_w = temperature at the wall

$< T_1 >$ = spatial averaged gas temperature

$y_0 = r_h =$ hydraulic radius=cross-sectional area/perimeter (as defined by Liu and Garrett [2006]).

After taking the spatial average, $1/A\int[\,]dA$, the solution for $< T_1 >$ becomes

$$< T_1 >= \left[\frac{\phi\beta T_m P_1}{\sigma(\rho C_p)_f} - \frac{u_1}{i\sigma\omega}\frac{dT_m}{dx}\right]\left(1 - \frac{f_k}{1+\varepsilon_s\sqrt{\sigma}}\right), \tag{4.17}$$

where the parameter f_k can be expressed as

$$f_k = \frac{\tanh\left(\frac{(1+i)}{\delta_k}\sqrt{\sigma}y_0\right)}{\left(\frac{(1+i)}{\delta_k}\sqrt{\sigma}y_0\right)}. \tag{4.18}$$

Here δ_k is the thermal penetration depth in the porous medium. The function f_k is the so called Rott's function and it is geometry dependent. The f_k functions for other stack geometries are given in the literature (Swift [2002]).

$$\left.\frac{\partial T_1}{\partial y}\right|_{y=y_0} = -\left[\frac{\phi\beta T_m P_1}{\sigma(\rho C_p)_f} - \frac{u_1}{i\sigma\omega}\frac{dT_m}{dx}\right]\left(\frac{1+i}{\delta_k}\sqrt{\sigma}\right)^2 y_0\left(\frac{f_k}{1+\varepsilon_s\sqrt{\sigma}}\right). \tag{4.19}$$

If Eq. (4.19) for $(\partial T_1/\partial y)_{y=y_0}$, Eq. (4.17) for $< T_1 >$, and Eq. (4.15) for T_w are substituted into Eq. (4.16)

$$Nu = y_o^2\left(\frac{(1+i)}{\delta_k}\sqrt{\sigma}\right)^2\frac{f_k}{1-f_k}. \tag{4.20}$$

Therefore,

$$Nu = 2i\sigma\frac{y_0^2}{\delta_k^2}\frac{f_k}{1-f_k} = 2i\sigma(Lc_k)^2\frac{f_k}{1-f_k}, \tag{4.21}$$

the parameter Lc_k (Lautrec number, Liu and Garrett [2006]) can be expressed as

$$Lc_k = \frac{y_0}{\delta_k}, \tag{4.22}$$

finally Nu can be written as

$$Nu = 2i\sigma\left(Lc_k\right)^2 \frac{f_k}{1-f_k}. \tag{4.23}$$

Equation (4.23) is a similar equation derived for complex *Nu* (Eq. (31)) by Liu and Garrett [2006].

Now the second definition, using the definition available in Guoqiang and Ping [2000], the complex Nu for current problem becomes

$$Nu = \left(\frac{y_0}{< T_{s1} > - < T_1 >}\right) \left.\frac{\partial T_1}{\partial y}\right|_{y=y_0}, \tag{4.24}$$

where

$< T_{s1} >$ = spatial averaged solid temperature inside the solid wall.

After taking the spatial average, $1/A\int[\,]dA,$ of Eq. (4.11), the solution for $< T_{s1} >$ becomes

$$< T_{s1} >= \left[\frac{\phi\beta T_m P_1}{\sigma\left(\rho C_p\right)_f} - \frac{u_1}{i\sigma\omega}\frac{dT_m}{dx}\right]\left(1 - \frac{1}{1+\varepsilon_s\sqrt{\sigma}}\right) f_s, \tag{4.25}$$

where the parameter f_s can be expressed as

$$f_s = \frac{\tanh\left(\frac{(1+i)}{\delta_s} l\right)}{\left(\frac{(1+i)}{\delta_s} l\right)}. \tag{4.26}$$

Substituting Eq. (4.25) for $< T_{s1} >$, Eq. (4.17) for $< T_1 >$, and Eq. (4.19) for $(\partial T_1 / \partial y)_{y=y_0}$ in Eq. (4.24) results in

$$Nu = \frac{2i\sigma\left(Lc_k\right)^2 f_k}{\left(1-f_s\right)\left(1+\varepsilon_s\sqrt{\sigma}\right)+\left(f_s-f_k\right)}. \tag{4.27}$$

Detail discussions of the complex *Nu* with graphical interpretation are left for the results and discussions section.

4.3.4 Energy Flux Density

The enthalpy is the correct energy for moving gases or liquids. In order to obtain the rate of change of the energy of the fluid in some given volume, energy flux density ($\dot{\mathbf{E}}$), according to Landau and Lifshitz [1982] can be used. The general equation for energy flux density ($\dot{\mathbf{E}}$), according to Landau and Lifshitz [1982], is

$$\dot{\mathbf{E}} = \rho \mathbf{V}\left(\frac{1}{2}\left|\mathbf{V}\right|^2 + h\right) - \mathbf{V}.\boldsymbol{\sigma} - k\,\mathbf{grad}\left(T\right), \tag{4.28}$$

where h, $\mathbf{V}$, $\boldsymbol{\sigma}$, and k are the enthalpy, velocity vector, viscous stress tensor, and thermal conductivity, respectively. The left hand side of Eq. (4.28) is the rate of change of the energy of the fluid in some given volume. The right hand side is therefore the amount of energy flowing out of this volume in unit time. From Eq. (4.28), energy flux density term consists of four terms, due to kinetic energy, enthalpy, viscous dissipation, and heat conduction. Therefore, Eq. (4.28) can be approximated to the total power flow or total energy flow through a thermoacoustic stack. If the amplitude of acoustic wave is small, the kinetic and viscous contributions are neglected since they are third order in velocity (Cao et al. [1996]). By considering all of these assumptions, the right hand side of Eq. (4.28) reduces to $\rho u h - k\,\partial T/\partial x$. The functional relationship of the enthalpy with the entropy and pressure (Bejan [1984] and Swift [2002]) leads to the following:

$$h = C_p dT + \left(1-T\beta\right)dp/\rho \ . \tag{4.29}$$

By integrating Eq. (4.29) and then using a linear thermoacoustic expansion, $\dot{\mathbf{E}}_2$ (in W/m^2) can be simplified to

$$\dot{\mathbf{E}}_2 \approx \left(\rho\, C_p\right)_f \left(T_1 u_1\right) + \left(1 - T_m \beta\right)\left(p_1 u_1\right) - \left(k + k_c\right)\, \frac{dT_m}{dx}. \tag{4.30}$$

In Eq. (4.30), the thermodynamic relation $s_1 = \left(C_p \,/ T_m\right) T_1 - \left(\beta/\rho\right) p_1$ is used. After time and space averaging, the total energy flux ($\mathbf{E}_2$ (in W)) becomes

$$\mathbf{E}_2 = \Pi\left(\rho C_p\right)_f \int_0^{y_0} \overline{T_1 u_1} dy + \Pi\left(1 - \beta T_m\right) \int_0^{y_0} \overline{p_1 u_1} dy - \left(y_0 \Pi k \; + l \Pi k_c\right) \frac{dT_m}{dx}. \tag{4.31}$$

If Eq. (4.13) for the fluctuating temperature is substituted into Eq. (4.31), and the integrations are performed

$$\mathbf{E}_2 = \frac{y_0 \Pi}{2} \Re\left[p_1 \tilde{u}_1 \left\{ 1 + \phi \frac{\beta T_m}{\sigma} \left(1 - \frac{f_k}{1 + \varepsilon_s \sqrt{\sigma}} \right) - \beta T_m \right\} \right] - \frac{y_0 \Pi}{2} \Re\left[\frac{u_1 \tilde{u}_1 \left(\rho \; C_p\right)_f}{i\omega\sigma} \frac{dT_m}{dx} \left(1 - \frac{f_k}{1 + \varepsilon_s \sqrt{\sigma}} \right) \right]$$
$$- \left(y_0 \Pi k \; + l \Pi k_c\right) \frac{dT_m}{dx}, \tag{4.32}$$

where $\Re[\;]$ signifies the real part and tilde (~) denotes the complex conjugation. Equation (4.32) is compared with Eq. (A-30) of Swift [1988] at the inviscid flow limit. The two expressions agree with each other for the limiting case of non-porous medium ($\sigma = 1$) and using the following velocity and temperature fluctuation expressions according to Swift [1988]

$$u_1 = \frac{i}{\omega \rho_m} \frac{dp_1}{dx}, \tag{4.33}$$

and

$$T_1 = \left[\frac{T_m \beta \, p_1}{\left(\rho \, C_p\right)_f} - \frac{1}{\rho_m \omega^2} \frac{dT_m}{dx} \frac{dp_1}{dx} \right] \left[1 - \frac{\cosh\left\{ \frac{(1+i)}{\delta_k} y \right\}}{\cosh\left\{ \frac{(1+i)}{\delta_k} y_0 \right\} (1 + \varepsilon_s)} \right]. \tag{4.34}$$

If Eq. (4.2) for fluctuating velocity is substituted into Eq. (4.32), the energy flux ($\mathbf{E}_2$) for the present study becomes

$$\mathbf{E}_2 = \frac{y_0 \Pi K}{2\mu} \Re\left[p_1 \frac{d\tilde{p}_1}{dx} \left\{ 1 + \phi \frac{\beta T_m}{\sigma} \left(1 - \frac{f_k}{1+\varepsilon_s \sqrt{\sigma}} \right) - \beta T_m \right\} \right] - \Re\left[\frac{y_0 \Pi K^2}{2\mu^2} \frac{(\rho C_p)_f}{i\omega\sigma} \frac{dp_1}{dx} \frac{d\tilde{p}_1}{dx} \frac{dT_m}{dx} \left(1 - \frac{f_k}{1+\varepsilon_s \sqrt{\sigma}} \right) \right]$$
$$- \left(y_0 \Pi k + l \Pi k_c \right) \frac{dT_m}{dx}. \tag{4.35}$$

By using Γ_0 ($=\nabla T_{cr} / \nabla T_m$, will be discussed later in **Section** 4.4.1), the non-dimensional global energy flux equation can finally be expressed as

$$\frac{\mathrm{E}_2}{\mathrm{E}_0} = -\frac{\sigma \Gamma_0}{\phi} \Re\left[-\frac{\phi \beta T_m}{\sigma} \left(1 - \frac{f_k}{1+\varepsilon_s \sqrt{\sigma}} \right) - \left(1 - \beta T_m \right) \right] + \Re\left[f_k \right] - 1 - \Gamma_{cond}, \tag{4.36}$$

where E_0 is a reference global energy flux and is given by

$$\mathrm{E}_0 = \frac{y_0 \Pi K^2 \rho_f C_p f}{2i\mu^2 \omega\sigma} \nabla T_m \Re\left(\nabla \mathrm{p}_1 \nabla \tilde{p}_1 \right) \text{ and } \Gamma_{cond} = \frac{\left(y_0 \Pi k + l \Pi k_c \right) \frac{dT_m}{dx}}{E_0}. \tag{4.37}$$

4.3.5 Wave Equation

For the current problem, it is assumed that the stack is short enough that it does not perturb a standing wave like pressure fluctuation appreciably so that

$$p_1 = p_0 \sin\left(\frac{2\pi x}{\lambda} \right), \tag{4.38}$$

where λ and p_0 are the wavelength and fluctuating pressure amplitude, respectively. Using Eqs. (4.2) and (4.38), the fluctuating velocity expression becomes

$$u_1 = -\frac{2\pi K p_0}{\mu \lambda} \cos\left(\frac{2\pi x}{\lambda} \right). \tag{4.39}$$

Thermoacoustic literatures (Swift [1988], Arnott et al. [1991], and Roh et al. [2007]) use the linear momentum equation to obtain the velocity expression using the standing wave pressure fluctuation.

The continuity equation (Burmeister [1992]) for this problem is

$$\frac{\partial(\phi\rho)}{\partial t}+\frac{\partial(\rho u)}{\partial x}+\frac{\partial(\rho v)}{\partial y}=0\,. \tag{4.40}$$

Using the linearized first order form of Eq. (4.40) gives

$$i\phi\omega\rho_{f1}+\frac{\partial\left(\rho_{fm}u_1\right)}{\partial x}+\frac{\partial\left(\rho_{fm}v_1\right)}{\partial y}=0\,. \tag{4.41}$$

If Eq. (4.2) is differentiated with respect to *x* and combined with Eq. (4.41)

$$i\phi\omega\rho_{f1}-\frac{K}{\mu}\rho_{fm}\frac{d^2p_1}{dx^2}+\frac{\partial\left(\rho_{fm}v_1\right)}{\partial y}=0\,. \tag{4.42}$$

With the thermodynamic relation $\rho_1=-\rho_m\beta T_1+(\gamma/a^2)p_1$, ρ_{f1} can be eliminated from Eq. (4.42) to obtain

$$-i\phi\omega\rho_{fm}\beta T_1+\left(\gamma/a^2\right)p_1-\frac{K}{\mu}\rho_{fm}\frac{d^2p_1}{dx^2}+\frac{\partial\left(\rho_{\ fm}v_1\right)}{\partial y}=0\,. \tag{4.43}$$

Equation (4.43) may be integrated between 0 to y_0 to eliminate v_1, at $y=y_0, v_1=0$ and at $y=0, v_1=0$. By using Eq. (4.13) for fluctuating temperature and following thermodynamic relations: (i) $a^2=\gamma RT_m$ and (ii) $C_p=\gamma R/(\gamma-1)$, the final form of the wave equation for current problem becomes

$$\frac{d^2p_1}{dx^2}+\frac{\phi}{\sigma}\left(\frac{1}{T_m}\frac{dT_m}{dx}\right)\left(1-f_k\right)\frac{dp_1}{dx}+\phi\left(\frac{\omega'}{a}\right)^2\left[\gamma-\frac{(\gamma-1)}{\sigma}\left(1-\frac{f_k}{1+\varepsilon_s\sqrt{\sigma}}\right)\right]p_1=0, \tag{4.44}$$

where ω' $(=\sqrt{\omega/(iK\rho_{fm}/\mu)})$. For a non-porous media $\phi = 1$, and $\sigma \to 1$, for no-stack situation $\nabla T_m \to 0$, and $f_k \to 0$. Substituting these values in Eq. (4.43) results in

$$\frac{d^2 p_1}{dx^2} + \left(\frac{\omega'}{a}\right)^2 p_1 = 0, \tag{4.45}$$

which is a well known Helmholtz equation (Kinsler et al. [2000]). Equation (4.44) is an ordinary differential equation for the complex acoustic pressure amplitude $p_1(x)$ in terms of the distribution of the mean temperature $T_m(x)$ and temperature dependent thermophysical properties and geometry of the fluid and solid. Once p_1 is obtained, the other first order quantities (u_1 and T_1) can be obtained from Eqs. (4.2) and (4.13).

An alternate pressure equation other than standing wave (Eq. (4.38)) can be derived by combining the linearized continuity and the Darcy momentum equations and after subsequent integration and simplifications. Appendix B shows the derivation of this alternate pressure equation along with the modified equations (for energy flux and heat flux) due to the change of this pressure equation.

4.4 Results and Discussion

In this section, graphical results are presented in order to understand the influence of different parameters; for example, Lc_k, ε_s, and σ, on T_1, Nu, and E_2. Calculations are performed at the middle of the stack using the properties from Table 1 of Swift [1988]. Although dimensionless forms of the fluctuating temperature (T_1/T_{c1}), Nu, and global energy flux (E_2/E_0) are plotted in this section, the properties of helium at 1,010 kPa ($= p_m$), 255 K ($= T_m$), and a frequency of 500 *Hz* are used where it is necessary using Table 1 of Swift [1988]. All the data are taken from Table 1 of Swift [1988] (such as stack length, stack plate spacing, stack plate thickness, stack material, position of the stack, working fluid, frequency of oscillation, mean pressure, and temperature) in order to

compare the present result to that of Swift [1988]. Different foam samples (such as RVC and aluminum foams) manufactured by Energy Research and Generation Inc. (ERG [2009]) are assumed embedded in between the channel walls in this study.

4.4.1 Oscillatory Velocity and Temperature Fields

The expression of velocity, given in Eq. (4.2), is independent of the transverse distance *y*. Therefore, the fluctuating velocity profiles inside the porous medium are similar to that seen in the 'slip flow' situation (Bejan [1984]). The magnitude of the velocity changes with the changes in working fluid properties, permeability of the porous medium, and the pressure gradient along the flow direction. The velocity boundary layer thickness is not encountered in the vicinity of the wall because of the consideration of negligible pore Reynolds number in Darcy model. The wall friction effect is not felt beyond a few pore lengths $\sqrt{K}$ in the *y* direction. In other words, the hydrodynamic boundary layer thickness is so small that one can neglect it and consider the flow situation as inviscid. In such a case, the *u*-velocity profile is a vertical line and its magnitude is given by Eq. (4.2).

General Discussion on Oscillatory Temperature for Channel Wall Heat Capacity Ratio, $\varepsilon_s = 0$

In the present study, T_1 is normalized by T_{c1}, which is a complex constant at a given *x* and can be expressed as

$$T_{c1} = \frac{\phi T_m \beta\, p_1}{\sigma\left(\rho C_p\right)_f} - \frac{u_1}{i\sigma\omega}\frac{dT_m}{dx}. \tag{4.46}$$

From Eq. (4.46), a critical temperature gradient (∇T_{cr}) can be proposed as explained in Swift [1988] and can be expressed as

$$\nabla T_{\mathrm{cr}} = \left(\frac{\phi T_m \beta\omega\mu}{iK\left(\rho C_p\right)_f}\right)\frac{p_1}{\nabla p_1} = \frac{\phi T_m \beta\mu a}{K\left(\rho C_p\right)_f}. \tag{4.47}$$

The dimensionless critical temperature gradient ratio can be expressed as $\Gamma_0 = \nabla T_{cr} / \nabla T_m$; detail about critical temperature gradient (∇T_{cr}) is discussed in Swift [1988]. Figure 4.4 shows the normalized porous medium temperature (T_1 / T_{c1}) ratio as expressed in Eq. (4.48)

$$\frac{T_1}{T_{c1}} = \left[1 - \frac{\cosh\left\{ \frac{(1+i)}{\delta_k} \sqrt{\sigma}\, y \right\}}{\cosh\left\{ \frac{(1+i)}{\delta_k} \sqrt{\sigma}\, y_0 \right\} \left(1 + \varepsilon_s \sqrt{\sigma}\right)} \right], \tag{4.48}$$

as a function of non dimensional transverse distance (y / y_0). Although in Figs. 4.4(a) and (b), both $\varepsilon_s = 0$ and $\varepsilon_s = 0.07$ cases are considered, in the current section (**Section** 4.4.1), only $\varepsilon_s = 0$ case is considered. Non-zero ε_s is discussed in **Section** 4.4.2.

Figures 4.4(a) and (b) present non-dimensional temperature fluctuations for non-porous medium and Fig. 4.4(c) is for porous medium i.e., when a porous medium is inserted in between the channel walls. For a limiting case of a non-porous medium the porosity of the porous medium (ϕ) approaches to unity and so does the porous medium heat capacity ratio (σ, Eq. 4.4(a)). The fluctuating temperature is zero at the wall $(y = y_0)$ in Figs. 4.4(a) and (b) when $\varepsilon_s = 0$. The fluctuating temperature decreases monotonously from a maximum at the centre to zero at the wall for all the Lc_k (in Figs. 4.4(a) and (b)). The hyperbolic cosine term in Eq. (4.48) is a function of y, σ, ε_s, and Lc_k. So, increasing the transverse distance (y/y_0) in Eq. (4.48) will reduce the influence of the channel wall on the fluctuating temperature at high Lc_k and σ when $\varepsilon_s = 0$. For example, a large portion of the temperature profile shows a negligible transverse temperature gradient at $Lc_k = 10$ in Fig. 4.4(b). One interesting feature of these fluctuating temperature profiles is that at $Lc_k = 2, 5,$ and 10 in Figs. 4.4(a) and (b) at $\sigma = 1$, and at $\sigma = 11.47$ in Fig. 4.4(c), they show a region in which T_1 is larger than T_{c1}. Richardson and Tyler [1929]

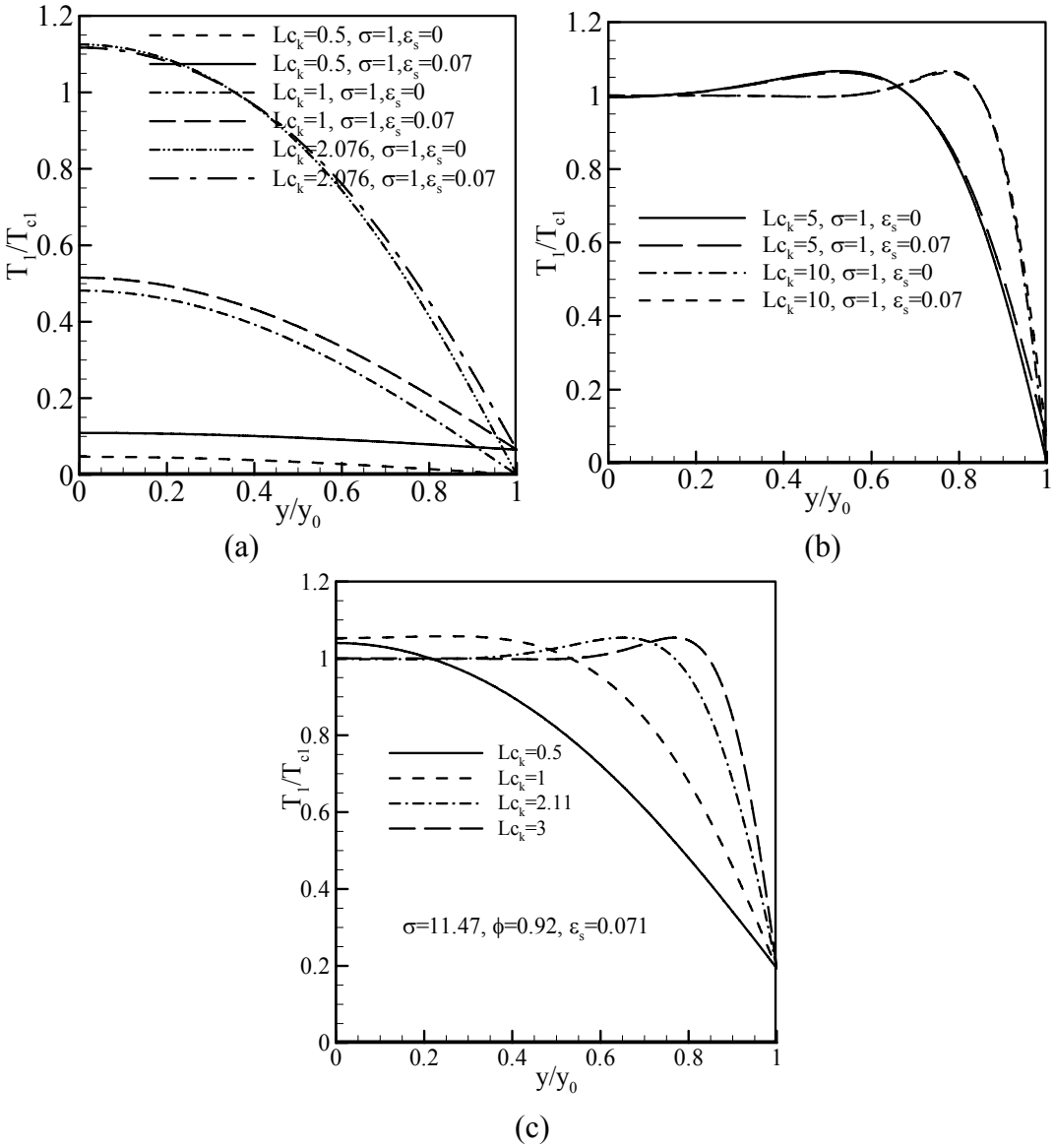

Figure 4.4: Normalized porous medium temperature as a function of non-dimensional transverse distance at (a) $\phi = 1$ and $Lc_k = 0.5$ to 2.076, (b) $\phi = 1$ and $Lc_k = 5$ to 10, and (c) $\phi = 0.92$ and Lc_k =0.5 to 3. Note that in Figs. (a), (b), and (c), the location of the thermal penetration depth changes as Lc_k changes.

confirmed similar behavior of the velocity profile in an oscillating laminar duct flow. The effect can be understood recognizing that Eq. (4.13) is, in effect, the superposition of a transverse oscillation and a uniform longitudinal oscillation. The transverse wave has, at $y = y_0$, a fluid temperature that is consistently equal and opposite to that of the uniform oscillation. For $y < y_0$, however, the fluid temperature in the transverse wave can exceed

its value at $y = y_0$ and combine with the uniform temperature to produce, a temperature that is larger for some values of *y* than the value of the centerline (T_{c1}) temperature. The Richardson effect is absent in Fig. 4.4(a) at $Lc_k < 2$.

Now, the nonzero wall thickness (conjugate effect), that influences the porous medium temperature (T_1) by the heat capacity ratio (ε_s) term (Eq. (4.18)) will be discussed. For the present study, the boundary layer approximation will be used to interpret heat capacity ratio (ε_s in Eq. (4.14)) and f_k (in Eq. (4.18)) by assuming that $y_0 >> \delta_k$ and $l >> \delta_s$. The purpose to make this approximation is to set the hyperbolic tangents (in Eq. (4.14) and (4.18)) equal to unity (Swift [1988]). In Figs. 4.5(a) and (b), real and imaginary parts of $\tanh\left((1+i)\sqrt{\sigma}\, y_0 / \delta_k\right)$ and $\tanh\left((1+i) l / \delta_s\right)$ are plotted. Note that in Fig. 4.5(a), the real part of the function is unity and the imaginary part is zero at $y_0 = 0.2\delta_k$ and $\sigma = 11.47$ (using Eq. 4.4(a), corresponding to $\phi = 0.92$). In Fig. 4.5(b), at $l = 2\delta_s$, the real part of the function is within a few percent of unity. Practical engines always have $\delta_k \le y_0 \le 2\delta_k$ (and similar for l and δ_s) (Swift [1988]), so in practical situations the boundary layer approximation is quite good. Using the boundary layer approximation heat capacity ratio can be expressed by the following equation:

$$\varepsilon_s = \sqrt{\frac{k\left(\rho C_p\right)_f}{k_c\left(\rho C\right)_c}} \quad . \tag{4.49}$$

4.4.2 Effect of the Channel Wall Spacing (Lc_k) and Porous Medium to the Channel Wall Heat Capacity Ratio (ε_s) on the Oscillatory Temperature (at $\phi = 1$)

Figure 4.4(a) shows the normalized porous medium temperature (T_1 / T_{c1}) ratio as a function of non dimensional transverse distance (y / y_0) at $\sigma = 1$, $\varepsilon_s = 0$, and 0.07 and at

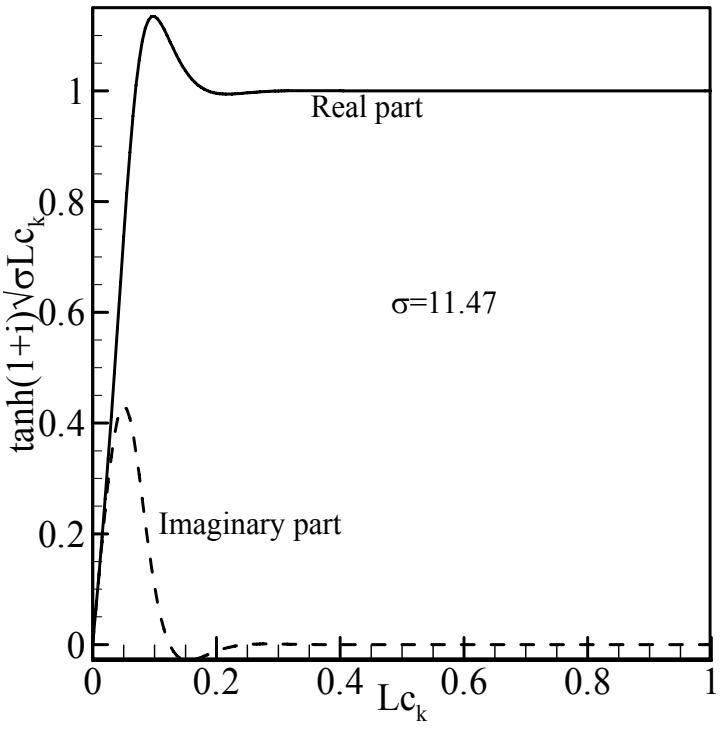

(a)

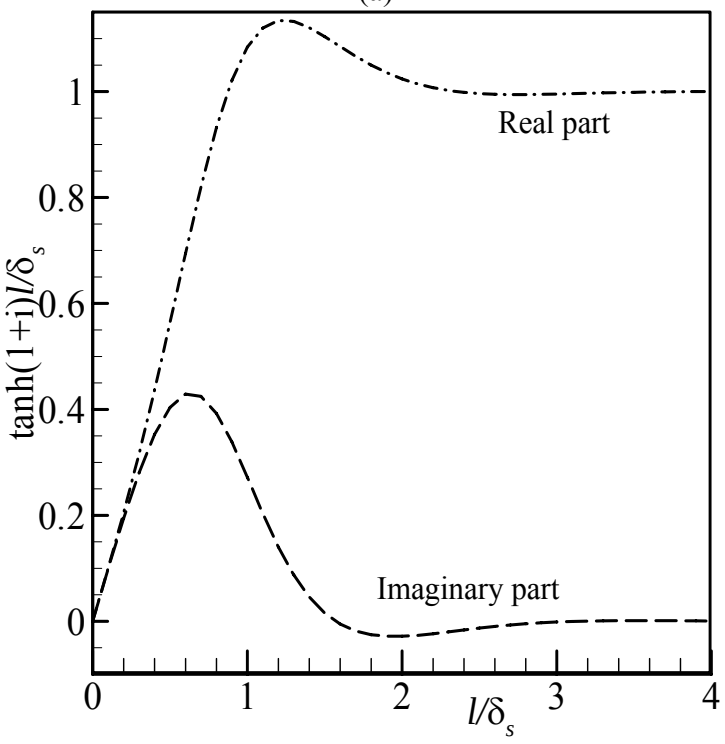

(b)

Figure 4.5: (a) The real and imaginary parts of $\tanh\left((1+i)\sqrt{\sigma}y_0/\delta_k\right)$ for the porous medium, (b) The real and imaginary parts of $\tanh\left((1+i)l/\delta_s\right)$ for the solid region.

$Lc_k = 0.5, 1,$ and 2.076. The values of $\varepsilon_s = 0.07$ and $Lc_k = 2.076$ were used by Swift [1988], the other values of Lc_k are used only for the sake of comparison. The normalized temperature in Eq. (4.48) depends on ε_s, ϕ, σ, Lc_k, and y. At $\sigma = 1$ and $\varepsilon_s = 0.07$, the non dimensional fluctuating temperature ratio for all Lc_k is no longer zero at the wall ($y = y_0$) in Fig. 4.4(a); rather it is T_w / T_{c1} (Eq. (4.15)) due to the imposed boundary condition (boundary condition (b) in **Section** 4.3.2). The T_w / T_{c1} term (Eq. (4.15)) depends only on ε_s and σ; hence, an increase in ε_s increases the T_w / T_{c1} term at $\sigma = 1$. One important feature of this condition ($\sigma = 1$, $\varepsilon_s = 0.07$ and $Lc_k = 2.076$) is that the dash-dot line ($\varepsilon_s = 0.07$) continues to stay slightly higher than the long dashed line ($\varepsilon_s = 0$) up to $y / y_0 = 0.46$, and then slightly lower than the long dashed line up to $y / y_0 = 0$. Mathematically, it can be shown that as the factor of $1/(1+\varepsilon_s)$ is considered, the second term in Eq. (4.48) drops compared to the $\varepsilon_s = 0$ case, thereby increasing the values of T_1 / T_{c1} in Eq. (4.48) (for $\varepsilon_s = 0.07$) up to $y / y_0 = 0.46$. The second term in Eq. (4.48) is zero at $y / y_0 = 0.356$, becomes negative as y / y_0 decreases from 0.357 to further down. Now these negative values are smaller compared to the $\varepsilon_s = 0$ cases, thereby slightly decreasing the T_1 / T_{c1} ratio compared to the long dashed line ($\varepsilon_s = 0$) up to the center of the channel. The effect of the transverse distance (y/y_0) in the T_1 / T_{c1} ratio is maximum at the wall (the second term in Eq. (4.48) is 1 at the wall at $\varepsilon_s = 0$), thereby making $T_1 / T_{c1} = 0$ at the wall. Whereas at $\varepsilon_s = 0.07$, the second term in Eq. (4.48) is $1/(1+\varepsilon_s) = 0.935$, thereby making a non-zero T_1 / T_{c1} ratio at the wall. A very small variation of T_1 / T_{c1} ratio in the transverse direction is observed at σ=1, $Lc_k = 0.5$ and for $\varepsilon_s = 0$ and 0.07. The second term in Eq. (4.48) in these conditions remains extremely close to 1 making the T_1 / T_{c1} ratio small in the transverse direction. Because of the $1/(1+\varepsilon_s)$ factor, the dashed line at $\varepsilon_s = 0.07$ shows higher values than the solid line ($\varepsilon_s = 0$) at $Lc_k = 0.5$ along the transverse direction. One interesting feature of Fig. 4.4(a) is that the effect of ε_s is more pronounced at lower Lc_k (=0.5, and 1), i.e., as long as the y

dependent part in Eq. (4.48) is large. In Fig. 4.4(a), the Richardson and Tyler effect, as explained in Richardson and Tyler [1929], is observed at $Lc_k = 2.076$ near the centre of the stack. The Richardson and Tyler effect is not observed at lower Lc_k (= 0.5, and 1), i.e., in situations when the second term in Eq. (4.48) is close to 1.

4.4.3 Effect of Porosity (ϕ) on the Oscillatory Temperature

Figure 4.4(c) shows the normalized porous medium temperature (T_1 / T_{c1}) ratio as expressed in Eq. (4.48) as a function of non dimensional transverse distance (y / y_0) at $\sigma = 11.47$, $\phi = 0.92$, $\varepsilon_s = 0.071$, and at different Lc_k ranging from 0.5 to 3. The reason for selecting a $Lc_k = 2.11$ in Fig. 4.4(c) is that $y_0 = 0.19$ mm according to Swift [1988] which gives $Lc_k = 2.11$. Lc_k is changed from 2.076 to 2.11 when RVC foam of $\phi = 0.92$ is introduced in between the channel walls, because of the change of *k* (in Eq. (4.4b)). ε_s is calculated according to Eq. (4.46) using RVC foam as a porous medium. Figure 4.4(c) follows the similar trend to that of Fig. 4.4(a) at $Lc_k = 2.076$. The difference between Fig. 4.4(a) at $Lc_k = 2.076$ and Fig. 4.4(c) is that the effect of the transverse distance (*y*) is negligible (T_1 / T_{c1} ratio is 1) after $y / y_0 = 0.338$ in Fig. 4.4(c). The Richardson and Tyler effect as explained in [1929] is observed for all of the cases in Fig. 4.4(c). At lower Lc_k i.e., $Lc_k < 2$ the Richardson and Tyler effect is observed near the centerline, as opposed to higher Lc_k, i.e., $Lc_k > 2$, where the Richardson effect is observed near the porous medium and the channel wall interface. Hence, Fig. 4.4(c) at lower Lc_k i.e., $Lc_k < 2$ shows similar behavior to that of Fig. 4.4(a) at $Lc_k = 2.076$. At higher Lc_k, i.e., $Lc_k > 2$, Fig. 4.4(c) shows similar behavior to that of Fig. 4.4(b). Therefore, comparing Figs. 4.4(a) to (c) for the identical plate spacing; the effect of the transverse distance (y/y_0) is significantly reduced for the stack composed of porous medium compared to the non-porous medium stack. Observing Figs. 4.4(a) to (c) for dimensionless temperature fluctuations as a function of non-dimensional transverse distance, three different cases based on σ and Lc_k are identified. These are as follows:

Case 1: $\sigma = 1$, $Lc_k = 0.5 - 1.5$ ($\varepsilon_s = 0 - 0.07$) in Fig. 4.4(a)

Case 2: $\sigma = 1$, $Lc_k = 1.6 - 4$ ($\varepsilon_s = 0 - 0.07$) in Figs. 4.4(a) and (b), at $\sigma = 11.47$ and $Lc_k = 0.5 - 1$ in Fig. 4.4 (c)

Case 3: $\sigma = 1$, $Lc_k = 5 - 10$, in Fig. 4.4(b), $\sigma = 11.47$ ($\varepsilon_s = 0 - 0.071$), and $Lc_k > 1.5$ in Fig. 4.4(c)

Case 1: $\sigma = 1$, $Lc_k = 0.5 - 1.5$, and $\varepsilon_s = 0 - 0.07$

As the gas oscillates along the stack, it experiences changes in temperature. Much of the gas' temperature change comes from adiabatic compression and expansion of the gas by the acoustic pressure and also velocity along the temperature gradient (which is denoted by T_{c1} in the present study, Eq. (4.46)), and the rest is a consequence of heat transfer with the channel wall. The present study shows that gas' temperature change is also affected by the heat pumping effect for some of the above mentioned cases.

Let us consider a magnified view of a gas particle within a channel in a region near the channel wall as it completes an acoustic cycle (considering the pressure anti-node is to the right of the stack). At the rightmost position (state 2) of the parcel of gas shown in Fig. 4.6(a) during the first half of the cycle, it rejects heat to the channel wall, because its temperature is raised above the local wall temperature by isothermal compression. At this range of wall spacing, gas elements are too close to the wall, have a good thermal contact, and are compressed isothermally. This is the reason why the temperature fluctuations (in Fig. 4.4(a)) at $Lc_k = 0.5$ and 1 are small compared to the center line fluctuation (T_{c1}). Up to $Lc_k = 1.5$ (not shown in the figure), fluctuating temperature values are less than T_{c1} because of the isothermal compression of the gas. At these ranges of Lc_k, very low heat pumping effect (Q_c) is observed, which does not have any significant influence on the fluctuating temperature.

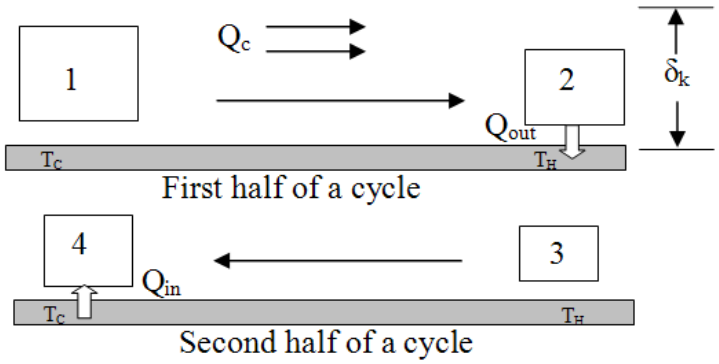

(a)

Case 2: $\sigma = 1$, $Lc_k = 1.6 - 4$, and $\varepsilon_s = 0 - 0.07$ and $\sigma = 1$, $Lc_k = 0.5 - 1$

Figure 4.6(b) shows a magnified view of a gas particle within a channel in a region near the wall as it completes an acoustic cycle. At state 2 near the wall in Fig. 4.6(b), gas elements that are too close to the wall, have a good thermal contact, and are compressed isothermally, so the gas' temperature fluctuations will be less than the complex fluctuation values (T_{c1}) as shown in Fig. 4.6(b). Then as we move vertically up away from the channel wall, gas' temperature fluctuations will gradually increase, since the

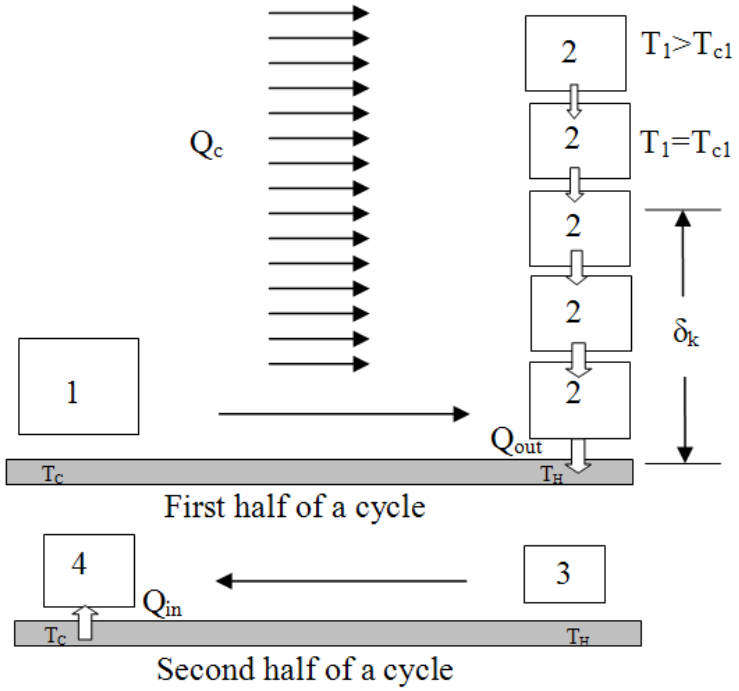

(b)

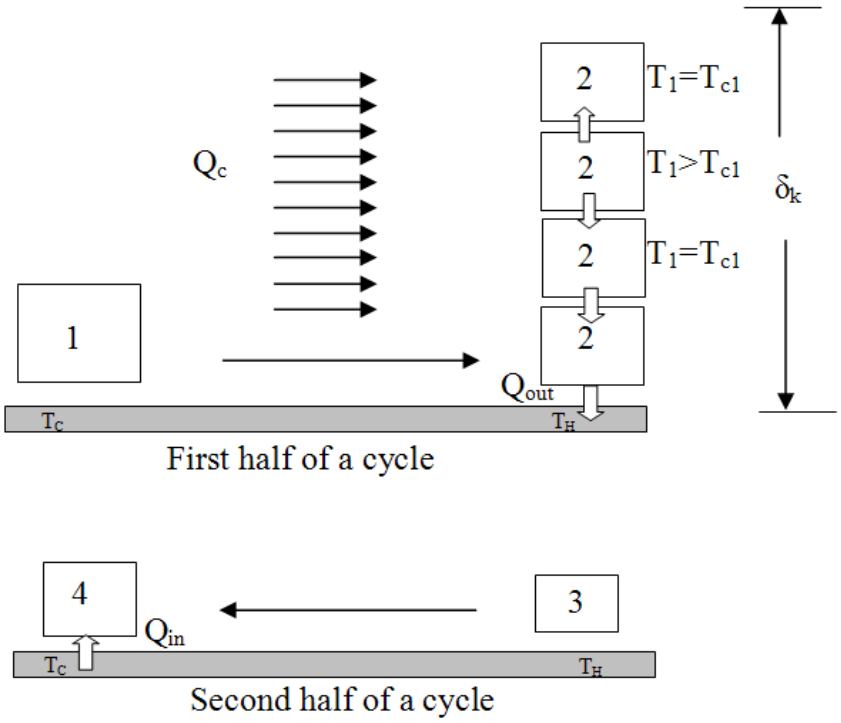

(c)

Figure 4.6: Magnified view of a gas parcel as it completes an acoustic cycle, (a) case1, (b) case 2, and (c) case 3.

elements of gas far away from the wall have little thermal contact with the wall. At a certain vertical distance from the wall, temperature fluctuation will be equal to the complex fluctuation value (T_{c1}), i.e., the gas' temperature change comes from adiabatic compression and expansion of the gas by the acoustic pressure and also by the velocity along the temperature gradient, and then increases further due to heat pumping effect. A heat pumping effect from low temperature source (T_C) to high temperature (T_H) sink (refrigeration effect) is observed in Fig. 4.6(b). The reason for the heat pumping effect is described later in Fig. 4.12 at $\sigma = 1$, which shows that the heat pumping effect is maximum away from the channel wall at a characteristic distance almost equal to the thermal penetration depth. The temperature fluctuations will be higher than the complex fluctuation values (T_{c1}) near the plate centre line because of the heat pumping effect at Lc_k between 1.6 to 4 and near the channel wall and gas interface at Lc_k >5.

Case 3: $\sigma = 1$, $Lc_k = 5 - 10$, and $\sigma = 11.47$ $(\varepsilon_s = 0 - 0.071)$, and $Lc_k > 1.5$

Figure 4.6(c) shows a magnified view of a gas particle within a channel in a region near the wall as it completes an acoustic cycle. At these ranges of Lc_k, very close to the wall, temperature fluctuation will be equal to the complex fluctuation value (T_{c1}), and then increases due to heat pumping effect. The temperature fluctuations will readily become equal to the complex fluctuation value as heat pumping effect is not observed after certain vertical distance from the plate. Figures 4.7(a) and (b) show the heat pumping effect as a function of non-dimensional transverse distance at $Lc_k = 2.11$ and 5 and at $\sigma = 11.47$ and 1, respectively. *Figure 4.7(a) shows that heat pumping effect is maximum at a certain distance very close to the channel wall (far less than δ_k) when a porous medium is introduced. Note that, when a porous medium is introduced in between the channel walls, the actual thermal penetration depth becomes $\delta_k/\sigma^{1/2}$ (Eq. (4.13)) instead of δ_k. The $\delta_k/\sigma^{1/2}$ term is a modified thermal penetration depth for porous medium.*

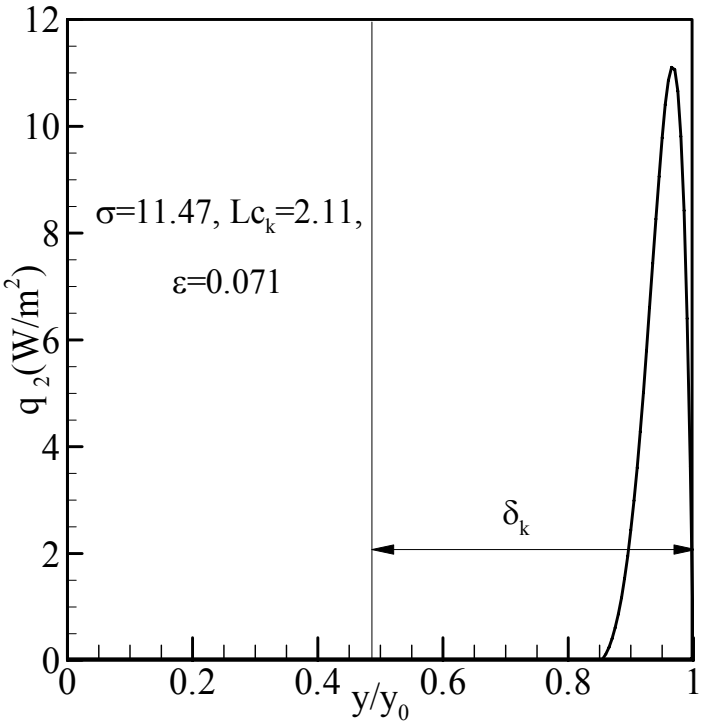

(a)

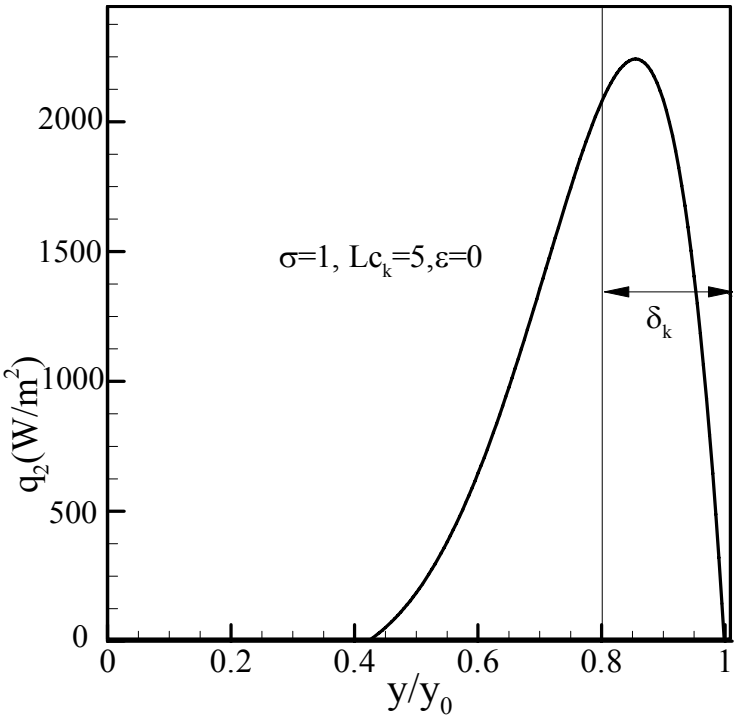

(b)

Figure 4.7: Heat flux density as a function of y/y_0 at (a) $\sigma = 11.47$, $\varepsilon_s = 0.07$ ε_s=0.07, $Lc_k = 2.11$, and (b) $\sigma = 1$, $\varepsilon_s = 0$, and $Lc_k = 5$.

Therefore, the thermal penetration depth decreases when a porous medium is introduced in between the channel walls. Thus the thermoacoustic effects are confined near the channel walls in Fig.4.4(c) at Lc_k *=2.11 and 3 while a porous medium is embedded in between the plates in contrary to Fig. 4.4(b) at* Lc_k *=5 and 10 for bare plates . Because of this lower thermal penetration depth, in Fig.4.4(c), at* Lc_k *=0.5 and 1, the magnitudes of fluctuating temperatures are high compared to Fig. 4.4(a) at* Lc_k *=0.5 and 1 for bare plates. In the absence of the porous medium (*$\sigma = 1$*), this modified thermal penetration depth approaches to the conventional thermal penetration depth.* Figure 4.7(b) shows the heat pumping effect for a non-porous medium ($\sigma = 1$) and large Lc_k (=5). This figure also demonstrates that heat pumping effect is maximum at a certain distance close to the channel wall (almost equal to the thermal penetration depth), therefore, shifting the peak temperature fluctuation near the channel wall (in Fig. 4.7(b)).

4.4.4 Effect of the Porous Medium to the Channel Wall Heat Capacity Ratio (ε_s) and Porous Medium Heat Capacity Ratio (σ) on the Oscillatory Solid Wall Temperature

Figure 4.8 depicts the normalized solid temperature ratio (T_{s1}/T_{c1}) as a function of non dimensional transverse distance (y'/l) at different values of ε_s (0, 0.07 and 0.071), and σ (1 and 11.47) and at $l/\delta_s = 4.92$, since the channel wall thickness used by Swift [1988] is $2l = 0.04$ mm. T_{s1}/T_{c1} (in Eqs. (4.11) and (4.15)) are functions of ε_s, σ, y' and plate half thickness, l, respectively. There is no temperature variation along the channel wall at $\sigma = 1$, and $\varepsilon_s = 0.0$ (solid line) in Fig. 4.8, since at this condition the heat capacity per unit area of the channel wall material is sufficiently large than that of the working fluid. Therefore, the channel wall will transfer heat without changing its temperature. As ε_s is increased from 0.0 to 0.07, the solid wall's temperature ratio at the wall and porous medium interface increases from 0 to 0.065 (the dashed line in Fig. 4.8). Since at the wall at $\sigma = 1$, and $\varepsilon_s = 0.0$, the $1 - 1/\left(1 + \varepsilon_s\sqrt{\sigma}\right)$ term in Eq. (4.15) becomes

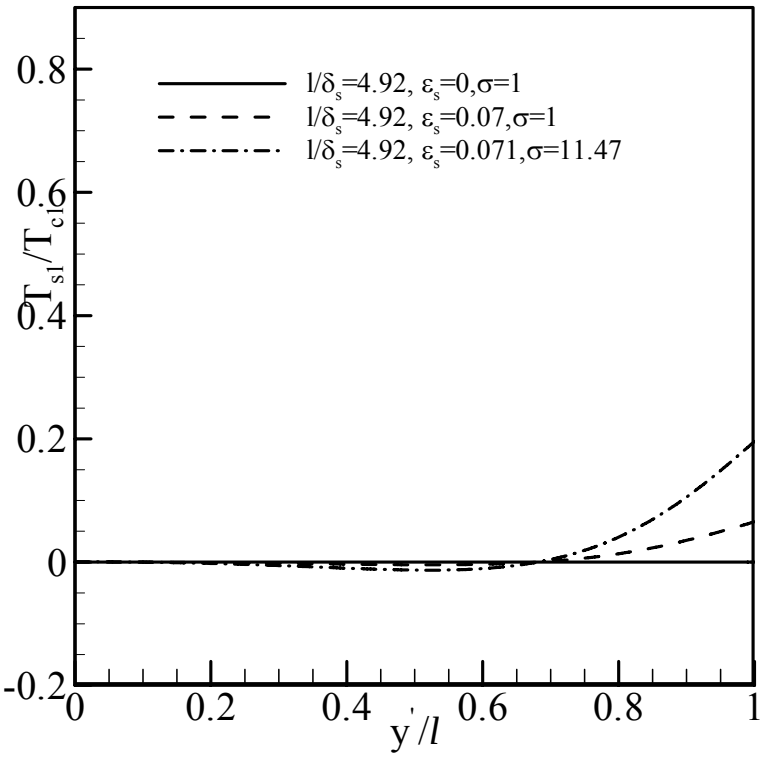

Figure 4.8: Normalized solid temperature inside the stack as a function of normalized transverse distance.

zero, while at $\sigma = 1$ and $\varepsilon_s = 0.07$, the $1 - 1/\left(1 + \varepsilon_s \sqrt{\sigma}\right)$ term becomes 0.065. Therefore, there is temperature variation along the channel wall at $\sigma = 1$ and $\varepsilon_s = 0.07$ in Fig. 4.8 (the dashed line). The dimensionless fluctuating temperature is maximum at the wall and porous medium interface, since the hyperbolic cosine function in Eq. (4.11) is maximum at $y' = l$. The hyperbolic cosine term is a function of y' and l/δ_s. For a fixed l/δ_s (which we have considered in the present study), as one moves away from the solid porous medium interface through the channel wall, the hyperbolic cosine term and so does the dimensionless fluctuating temperature gradually decreases. It becomes zero at $y'/l = 0.65$, negative after that, and becomes zero near the middle of the stack. This is the reason why the dimensionless fluctuating temperature at $\sigma = 1$ and 11.47 and $\varepsilon_s = 0.07$ and 0.071 (the dashed and dash dot lines) show slightly negative values in Fig. 4.8.

4.4.5 Complex Nusselt Number (*Nu*)

The first definition of complex Nu (Eq. (4.23)) matches quantitatively with the expression derived by Liu and Garrett [2006] for infinitely large pores i.e., at $\sigma = 1$. Liu and Garrett [2006] obtained the *Nu* expression for an inviscid ideal gas and disregarding the presence of steady flow or a static temperature gradient in the linearized energy equation. Although the modeling approach and assumptions are different, the result of *Nu* obtained from the current study matches with the non-porous medium expression derived by Liu and Garrett [2006]. Therefore, comparison of Eq. (4.23) with the expression derived by Liu and Garrett [2006] give us confidence that the systems of equations developed for T_1, T_{s1}, and Nu are free from errors. Figure 4.9(a) shows the complex *Nu* distribution as a function of Lc_k at $\sigma = 1$. The increasing pattern of *Nu* distribution with Lc_k in Fig. 4.9(a) is supported by Eq. (4.23). The real part of the *Nu* is much larger than the imaginary part at low Lc_k. This means that the spatial averaged temperature is in phase with the temperature gradient at the wall at low Lc_k. Figure 4.11 supports this finding (will be discussed later in this section). Mathematically, it can be shown that f_k (in Eq. (4.23) also shown graphically in Fig. 4.10(a)) is responsible for the phase shift of

the spatial averaged temperature and the temperature gradient at the stack plate surface in time. No phase shift is observed in Fig. 4.9(a) at $f_k \approx 1$, when $\sigma = 1$ and $Lc_k = 0.1$. This means that the real part of the *Nu* is much larger than the imaginary part at $\sigma = 1$ and $Lc_k = 0.1$ in Fig. 4.9(a).

The second definition of complex *Nu* expressed in Eq. (4.27) is a function of σ, Lc_k, ε_s, f_k, and f_s and is shown in Fig. 4.9(b). To indicate the effect of σ, Lc_k, ε_s, and f_k on *Nu*, Fig. 4.9(b) shows the real part of the complex *Nu* distribution as a function of Lc_k at different values of σ (1 and 11.47), ε_s (0, 0.07, and 0.071), and at a fixed value of f_s (since the channel wall thickness is constant in the present study and is equal to Swift [1988]). At $\sigma = 1$, $\varepsilon_s = 0.07$ and for all Lc_k (dashed line), *Nu* is decreased by a factor of $(1+\varepsilon_s)$ than $\sigma = 1$, and $\varepsilon_s = 0$ (solid line). Therefore, *Nu* distribution is decreased by a factor of $(1+\varepsilon_s)$ when finite heat capacity channel wall is considered. This is the reason for the lower *Nu* distribution at $\varepsilon_s = 0.07$ (dashed line) than $\varepsilon_s = 0$ case (solid line).

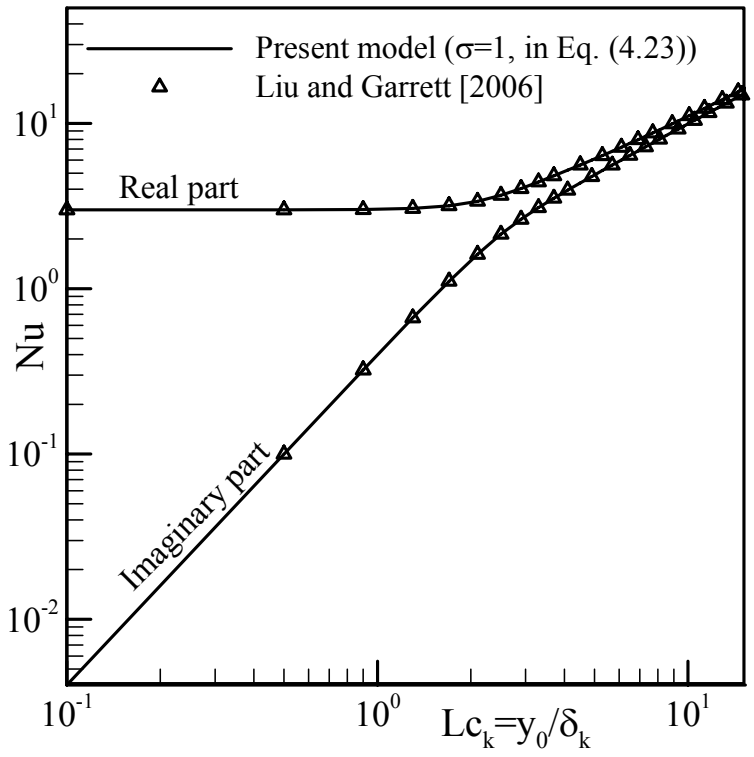

(a)

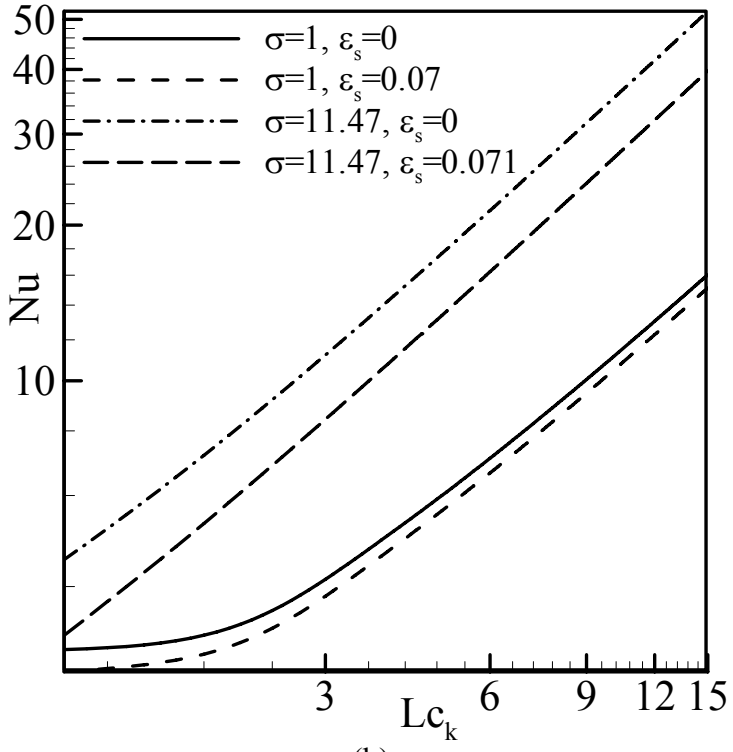

(b)

Figure 4.9: (a) Comparison of complex Nu to the existing literature vs. Lc_k at $\sigma = 1$, (b) Real part of complex Nu vs. Lc_k at different values of ε_s and σ.

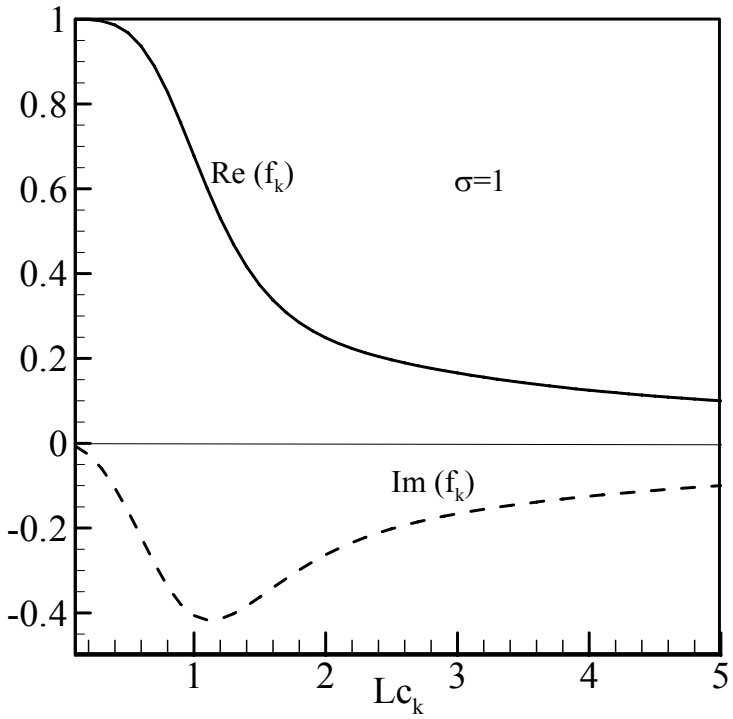

(a)

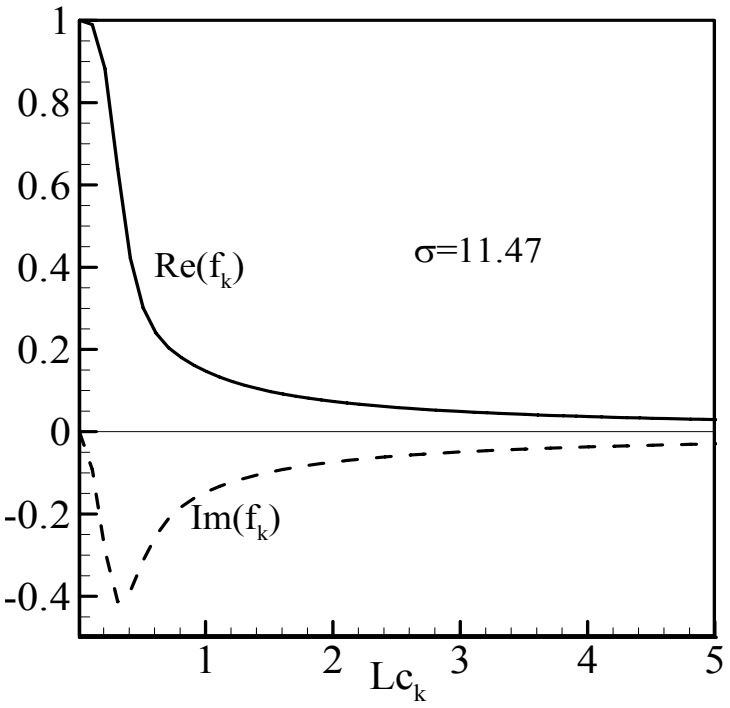

(b)

Figure 4.10: Imaginary and real parts of f_k as a function of Lc_k in the porous medium at (a) $\sigma = 1$ and (b) $\sigma = 11.47$.

Similarly at $\sigma = 11.47$, $\varepsilon_s = 0.071$ and for all Lc_k (long dashed line), *Nu* is decreased by a factor of $(1 + \varepsilon_s \sqrt{\sigma})$ than $\sigma = 11.47$ and $\varepsilon_s = 0$ (dash dot line). Since *Nu* is a complex number, it is dependent on real and imaginary parts of f_k and f_s. Figures 4.10(a) and (b) show the real and imaginary parts of f_k as a function of Lc_k at $\sigma = 1$ and 11.47 (f_s profiles are not shown but will follow the similar trend to that of f_k at $\sigma = 1$). Observing the f_k profile in Fig. 4.10(a), it is apparent that the *Nu* distribution (Fig. 4.9(b)) at $\sigma = 1$ (for both $\varepsilon_s = 0$ and 0.07) becomes almost constant until $Lc_k \leq 2$ because of the asymmetric nature of real and imaginary parts of f_k at these Lc_k values. At $Lc_k > 2$, *Nu* distribution (Fig. 4.9(b)) at $\sigma = 1$ (for both $\varepsilon_s = 0$ and 0.07) increases with an increase in Lc_k because of the symmetric nature of real and imaginary parts of f_k at these Lc_k values. Similarly, observing the f_k profile in Fig. 4.10(b), it is apparent that *Nu* distribution (Fig. 4.9(b)) at $\sigma = 11.47$ (for both $\varepsilon_s = 0$ and 0.071) increases with an

increase in the Lc_k values because of the symmetric nature of real and imaginary parts of f_k at $Lc_k \geq 1$. Figure 4.9(b) shows that convection heat transfer dominates as Lc_k increases (for both $\sigma = 1$ and 11.47). One interesting feature of Fig. 4.9(a) at lower Lc_k values is that a large difference between the real and imaginary parts of complex *Nu* is observed which is absent in Fig. 4.9(b) at $\sigma = 11.47$ (not shown in Fig. 4.9(b)). This means that the spatial averaged temperature is not in phase with the temperature gradient at the wall at low Lc_k and at $\sigma = 11.47$. To give physical insight to the problem, temperature gradient normal to the stack plate surface and the spatial averaged gas temperature with respect to time are presented in Fig. 4.11 at $\sigma = 1$, and 11.47 and $Lc_k = 0.1,\ 1,$ and 10, respectively. Over the period of an acoustic cycle, the *Nu* is zero, because of the symmetric nature of the profiles with respect to time at $Lc_k = 0.1$ and $\sigma = 1$ in Fig. 4.11(a). As Lc_k increases from 0.1 to 10, this symmetric nature disappears. There is a phase shift between temperature gradient at the wall and the spatial averaged gas temperature in Figs. 4.11(c) and (e) at $Lc_k = 1$ and 10, while $\sigma = 1$. This phase shift is absent in Fig. 4.11(a). Therefore, Figs. 4.11(a), (c), and (e) support Fig. 4.9(a). At $\sigma = 11.47,$ phase shift between the temperature gradient at the wall surface and the spatial averaged gas temperature appears at $Lc_k = 0.1, 1,$ and 10 in Figs. 4.11(b), (d), and (f). This is the reason the real and imaginary parts of *Nu* values are closer at $\sigma = 11.47,$ and $Lc_k = 0.1,$ and identical at higher Lc_k (not shown in Fig. 4.9(b)). Overall, temperature gradient at the stack plate surface and the spatial averaged gas temperature change with the frequency of oscillations, mean temperature gradient, pressure amplitude, permeability, porosity of the porous medium and Lc_k.

4.4.6 Energy Flux Density

The energy flux equation, Eq. (4. 32) is an important result, since it gives the total energy flux along *x* in terms of $T_m(x),\ p_1(x),$ material properties, and geometry. In Fig. 4.12, heat

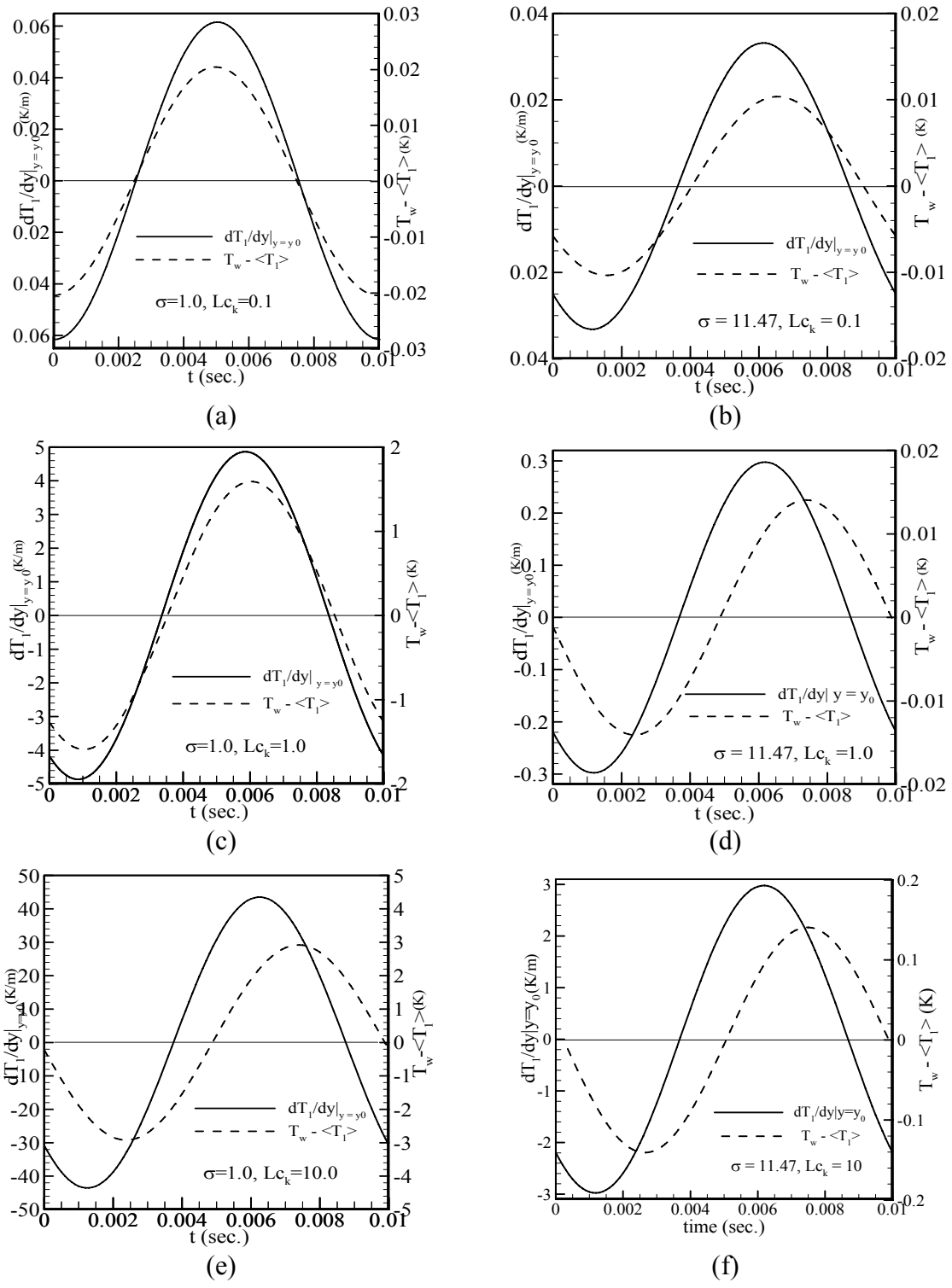

Figure 4.11: Temperature gradient at the stack plate surface and the temperature difference between the stack plate surface and the spatial averaged gas vs. time at different values of Lc_k (0.1, 1.0, and 10.0) and σ (1 and 11.47).

flux density (heat flux per unit area, q_2 (right hand side of Eq. (4.30) except $\Pi \int_0^{y_0} \overline{p_1 u_1} dy$ term and without the spatial averaging) is shown schematically as a function of non-dimensional transverse distance (y/y_0) at $\sigma = 1$, $Lc_k = 4$, and $\varepsilon_s = 0$. Figure 4.12

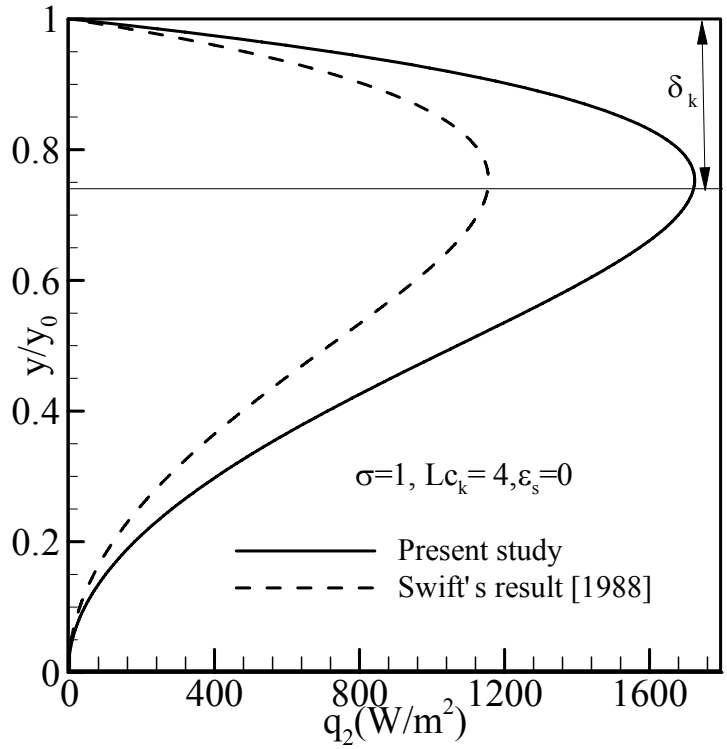

Figure 4.12: Heat flux density as a function of y/y_0.

compares the heat flux density profile with the result of Swift [1988]. In order to compare, Swift's equation (Eq. A.29) is used without spatial averaging, the equation is further simplified using non-conjugate heat transfer, and inviscid flow assumptions. The difference between the two results (present model assumes higher heat flux values which is also expected) is due to the modeling of the velocity profile. In the present study velocity profile is modeled using (Eq. (4.2)), and Swift's velocity profile is derived from inviscid momentum equation. The heat flux is largest at a distance almost δ_k from the plate surface, and falls to zero both at the plate surface and at the middle of the channel. For an ideal gas $T_m \beta = 1$ (Eq. (4.30)), the heat flux is zero at the wall because $\varepsilon_s = 0$). The phase shift in temperature of the standing wave at about $y \approx \delta_k$, due to the thermal

presence of the stack plate is responsible for this time averaged heat flux. The absence of the phase shift in temperature results in zero heat flux at $y >> \delta_k$. If suitable heat exchangers are installed at the ends of the stack plates, this heat flux carries heat from one heat exchanger to the other.

4.4.7 Work Flux

The wave equation, Eq. (4.44) is modified (followed by Swift [1988]) to give an expression for acoustic power. We begin by noticing that, in the geometry of Fig. 4.3, the net acoustic power cannot escape in the transverse (*y*) direction. Thus, the acoustic power generated or absorbed must show up in as a difference in average acoustic intensity $p_1 u_1$ between the two ends of the channel wall

$$W_2 = \Pi y_0 \left[\left(\overline{p_1 u_1} \right)_{left} - \left(\overline{p_1 u_1} \right)_{right} \right] = \Pi y_0 \Delta x \frac{d}{dx} \left(\overline{p_1 u_1} \right), \tag{4.50}$$

proportional to the total volume $\Pi y_0 \Delta x$ of fluid in the stack region. The overbar in Eq. (4.50) represents time averaging and will be discussed in **Section** 4.6. Equation (4.50) can be written as

$$\frac{W_2}{\Pi y_0 \Delta x} = \frac{d}{dx} \left(\overline{p_1 u_1} \right) = \frac{1}{2} \mathrm{Re} \left[p_1 \frac{d\tilde{u}_1}{dx} + \tilde{u}_1 \frac{dp_1}{dx} \right]. \tag{4.51}$$

Using Eq. (4.2) for dp_1/dx, the wave equation can be rewritten as

$$\frac{d\tilde{u}_1}{dx} = -\frac{\phi}{\rho_f} \frac{i\omega p_1}{a^2} \left[\gamma - \frac{(\gamma - 1)}{\sigma} \left(1 - \frac{f_k}{1 + \varepsilon_s \sqrt{\sigma}} \right) + \frac{(\gamma - 1)(1 - f_k)}{\sigma \Gamma_0} \right], \tag{4.52}$$

and substitute this into Eq. (4.51) to find

$$W_2 = \frac{1}{2} \Pi y_0 \Delta x \frac{(\gamma - 1)\omega \phi}{\rho_f a^2 \sigma} p_1^2 f_k \left(\frac{1}{\Gamma_0} - \frac{1}{1 + \varepsilon_s \sqrt{\sigma}} \right) - \frac{1}{2} \Pi y_0 \Delta x \frac{\mu}{K} u_1^2 . \tag{4.53}$$

Equation (4.53) is a complete result for total work flux in a thermoacoustic engine for the present study. Thus, we see that the inclusion of finite heat capacity of the plate adds considerable complication to the acoustic energy in a thermoacoustic engine in the short stack approximation. However, we will make boundary layer approximation to keep the results of this section intuitively understandable.

Using boundary layer approximation, the final expression for acoustic power of thermoacoustic engine becomes

$$W_{2b} = \frac{1}{4}\Pi\delta_k \Delta x \frac{(\gamma-1)\omega\phi}{\rho_f a^2 \sigma^{2/3}\left(1+\varepsilon_s\sqrt{\sigma}\right)} p_1^2\left(\frac{1}{\Gamma_0}-1\right) - \frac{1}{2}\Pi y_0 \Delta x \frac{\mu}{K} u_1^2 . \qquad (4.54)$$

This equation is similar to Eq. (82) of Swift [1988] at $\phi = 1$, $\sigma = 1$, and except the second term, which is different in the present study because of the difference in the modeling of the momentum equation. The effect of finite specific heat of the channel wall is observed in the first term of Eq. (4.54). The finite specific heat of the wall material decreases the acoustic power by the factor $1/\left(1+\varepsilon_s\sqrt{\sigma}\right)$. Numerical calculations show that the second part of Eq. (4.54) is much larger than the first part; therefore the effect of heat capacity ratio is insignificant for the generation or absorption of the acoustic power. Acoustic power is dominated by the amplitude of the velocity fluctuation and the viscosity of the working fluid.

4.4.8 Energy Flux

Non-dimensional global energy flux (E_2/E_0) in Eq. (4.36) is a function of ε_s, σ, Γ_0, and f_k (which is also a function of Lc_k). E_2/E_0 is plotted as a function of Lc_k at different values of ε_s (0, 0.07, and 0.071) and σ (1 and 11.47), and at a constant value of $\Gamma_0 = 1.33$ (used by Swift [1988]) in Fig. 4.14 in order to understand the effect of ε_s and σ on E_2/E_0. Γ_{cond} (the last term in Eq. (4.36)) is the ratio of axial conduction to E_0 is assumed negligible in Fig. 4.14. In order to understand the effect of ε_s on E_2/E_0; at $Lc_k \le 0.5$ and $\varepsilon_s \neq 0$, E_2/E_0 values are much more than $\varepsilon_s = 0$, for both $\sigma = 1$ and

11.47. The reason for this increased E_2/E_0 values is the $\left(1-\frac{f_k}{1+\varepsilon_s\sqrt{\sigma}}\right)$ term in Eq. (4.36), which increases dramatically as ε_s increases from zero to other values, since the imaginary part of f_k at $Lc_k \le 0.5$ is close to zero in Figs. 4.10(a) and (b). The effect of ε_s is more pronounced at higher σ, i.e., at $\varepsilon_s = 0.071$ and $\sigma = 11.47$, showing higher E_2/E_0 values at this condition. The effect of ε_s almost diminishes as Lc_k increases beyond 4. For a fixed value of ε_s and σ, E_2/E_0 will be dominated by the f_k profile as shown in Fig. 4.10(a) and (b). E_2/E_0 in Fig. 4.13 is nearly zero at $Lc_k \le 0.5$, $\varepsilon_s = 0$, and $\sigma = 1$ and 11.47. For $Lc_k \le 0.5$, $\varepsilon_s = 0$, and $\sigma = 1$ and 11.47, the real part of f_k is nearly unity and the imaginary part is nearly zero in Figs. 4.10(a) and 4.11(b),

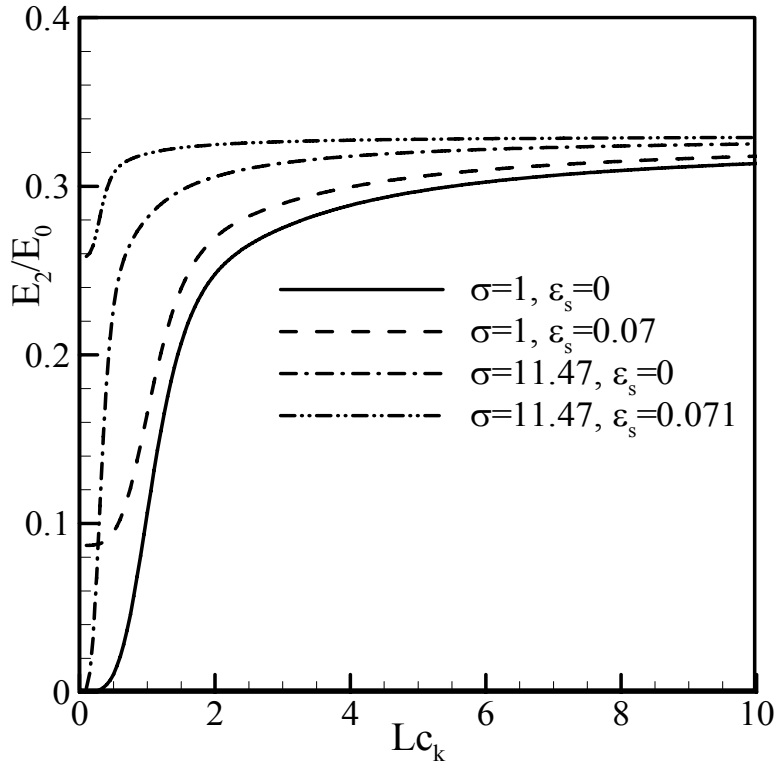

Figure 4.13: Distribution of normalized E_2 as a function of Lc_k.

therefore reducing the E_2/E_0 values near zero. E_2/E_0 will gradually increase with Lc_k for $\varepsilon_s = 0$, and $\sigma = 1$, and becomes constant after $Lc_k \ge 3$, as the imaginary part of f_k in Fig. 4.10(a) gradually increases from zero as Lc_k increases, becomes maximum at Lc_k

around one, and finally becomes constant at $Lc_k \geq 3$. The difference between $\sigma = 1$ and 11.47 at $\varepsilon_s = 0$ and at $Lc_k \leq 0.5$ is the quick increase of E_2/E_0 values with Lc_k at $\sigma = 11.47$, since the imaginary part of f_k profile in Fig. 4.10(b) increases very rapidly at $Lc_k \leq 0.5$. E_2/E_0 values (at $\sigma = 11.47$ and $\varepsilon_s = 0$) become constant as Lc_k increases, since the imaginary part of f_k profile in Fig. 4.10(b) becomes constant at $Lc_k \geq 2$. At $\sigma = 11.47$ and $\varepsilon_s = 0.071$, maximum E_2/E_0 is observed at $Lc_k \leq 0.5$. Figure 4.13 is very insightful as it indicates that using porous medium in between the parallel plates show significantly better performance while $Lc_k \leq 2$. Also, Fig. 4.13 emphasis the importance of f_k function on non-dimensional global energy flux (E_2/E_0).

Now, Fig. 4.14 shows the mesh-contour plot of the dimensionless energy flux density distribution (E_2/E_0) corresponds to the dimensionless temperature gradient ratio Γ ($\Gamma = \nabla T_m / \nabla T_{cr}$) and dimensionless stack spacing (Lc_k) for RVC foam embedded in between the channel walls. The mesh plots are helpful for understanding the pattern of variation in E_2/E_0 with Lc_k and Γ, while the contour plots may be used as performance plots describing dimensionless stack spacing at the maximum E_2/E_0. In Fig. 4.14, Γ is varied to cover both the prime mover and refrigerator mode of operation of a thermoacoustic device. For lower Lc_k, $Lc_k < 1$, E_2/E_0 values change significantly with the change of Γ, whereas at higher Lc_k, the change of Γ on E_2/E_0 is insignificant. At a constant Lc_k, E_2/E_0 values change linearly with Γ, with a higher slope at larger Lc_k values, and lower slope at lower Lc_k values.

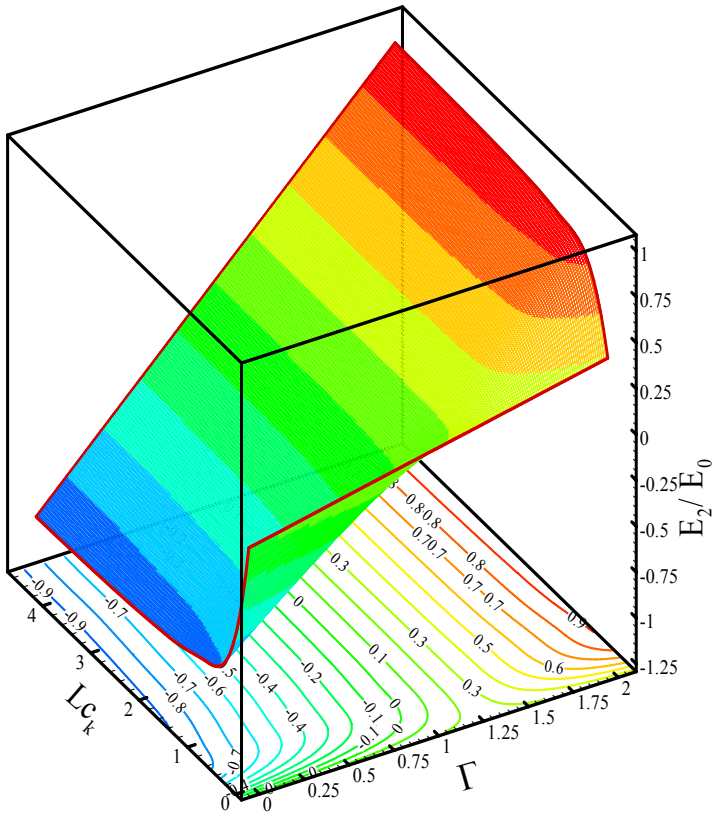

Figure 4.14: Mesh-contour plot showing the dimensionless energy flux density distribution (E_2/E_0) corresponds to the dimensionless temperature gradient ratio (Γ) and dimensionless stack spacing (Lc_k) for RVC foam embedded in between the channel wall.

4.4.9 Energy Flux using Boundary Layer Assumption

By using boundary layer approximation and ideal standing wave assumption, the following expressions can be written:

$$\begin{aligned} p_1 &= p_0 \sin(k_1 x) = p_1^s, \\ u_1 &= ip_0 / \rho_m a \cos(k_1 x) = iu_1^s, \\ f_k &= 1/(1+i)\sqrt{\sigma}\, Lc_k, \end{aligned} \tag{4.55}$$

where the superscript "*s*" stands for standing wave, and p_0 is the fluctuating pressure amplitude at the pressure antinode. Using Eq. (4.55), the total energy flux equation, Eq. (4.32) can be written as

$$\mathrm{E}_{2b}=\frac{y_0\Pi}{2}\Re\left[-ip_1^s u_1^s\left\{1+\frac{\phi\beta T_m}{\sigma}\left(1-\frac{\delta_k}{\left(1+\varepsilon_s\sqrt{\sigma}\right)\left(1+i\right)\sqrt{\sigma}y_0}\right)-\beta T_m\right\}\right]-$$

$$\frac{y_0\Pi}{2}\Re\left[-\frac{\phi\beta T_m\, i}{\sigma\Gamma_0}\,p_1^s u_1^s\left(1-\frac{\delta_k}{\left(1+\varepsilon_s\sqrt{\sigma}\right)\left(1+i\right)\sqrt{\sigma}y_0}\right)\right] \tag{4.56}$$

$$-\left(y_0\Pi k\ +l\,\Pi k_c\right)\frac{dT_m}{dx}.$$

Only considering the real parts, Eq. (4.56) becomes

$$\mathrm{E}_{2b}=-\frac{\Pi\delta_k}{4\sigma^{3/2}}\frac{\phi\beta T_m}{\left(1+\varepsilon_s\sqrt{\sigma}\right)}\,p_1^s u_1^s\left(\frac{1}{\Gamma_0-1}\right)-\Pi\left(y_0 k+l k_c\right)\frac{dT_m}{dx}. \tag{4.57}$$

Equation (4.57) at $\sigma=1$ is similar to Eq. (81) of Swift [1988] for $\mathrm{Pr}\approx 0$, where $\mathrm{Pr}=\mu C_p/k$ is the Prandtl number.

Equation (4.57) shows that the finite specific heat of the wall material decreases the total energy by the factor $1/\left(1+\varepsilon_s\sqrt{\sigma}\right)$. Therefore, this factor decreases both the efficiency of thermoacoustic prime movers and the coefficient of performance (COP) of thermoacoustic refrigerators. The comparisons of Eq. (4.23) for Nu with Jin and Garrett [2006], Eq. (4.54) for work flux, and Eq. (4.57) for energy flux density with Swift [1988]'s work gives us confidence that the systems of equations developed in the present modeling are free from errors.

For accurate calculations, the energy flux results presented in **Section** 4.3.4 or Appendix B.2 for total energy and **Section** 4.4.7 (Eq. (4.53)) for total work flux must be used; but for rough estimates, the results of **Sections** 4.4.7(Eq. (4.54)) and 4.4.9 (Eq.(4.57)) are good approximations, and are much simpler to interpret. Table 4.1 shows the values of energy flux density, E_2, calculated using Eq. (B.12) and work flux density, W_2, calculated using Eq. (4.53) along with the coefficient of performance (COP) for a thermoacoustic device in which a porous medium is embedded in between the parallel plates. Data for Table 4.1 are collected as before from Table 1 of Swift [1988]. 45 PPI RVC foam and 40

PPI aluminum foam are considered to be embedded in between the parallel plates. Properties of RVC and aluminum foams (such as porosity, ϕ and permeability, K) are collected from Fu et al. [2001]. The first row of Table 4.1 shows the experimental values. Table 4.1 shows that using 45 PPI RVC foam in between the parallel plate stacks results in a COP value of 6.6 in the present study, which is almost seven times higher than that obtained by Swift [1988] using only parallel plate stack. Using 40 PPI aluminum foam increases COP almost three times than the experimental value. Therefore, COP of a thermoacoustic device increases when a porous medium is introduced in between the parallel plates. Although, acoustic work absorbed by the porous medium increases compared to the non-porous medium case, the energy flux density also increases significantly. Energy flux density values are extremely sensitive on the properties (such as porosity, density, specific heat, and thermal conductivity) of the porous materials. This result indicates that better refrigeration performance is achievable using RVC foam ($\phi = 0.92$, $K = 2.09 \times 10^{-8}\,\mathrm{m}^2$) or aluminum foam ($\phi = 0.9$, $K = 3.36 \times 10^{-8}\,\mathrm{m}^2$) as porous media instead of bare parallel plates. This study also supports the observation of Adeff et al. [1998].

Table 4.1: Values of energy flux density, E_2, work flux density, W_2, and COP of a stack

Material in between the plates	ϕ	K (m^2)	E_2 (W)	W_2 (W)	$COP = E_2/W_2$
No material	1	∞	6	6	1
45 PPI RVC	0.92	2.09×10^{-8}	232.16	35.24	6.6
40 PPI AL	0.9	3.36×10^{-8}	146.12	55.11	2.7

4.5 Irreversibility Analysis of Porous Thermoacoustic Stack Systems

The objective of this section (**Section** 4.5) is to apply irreversibility analysis in porous stacks of thermoacoustic systems. Entropy generation rate is used as a measure of irreversibilities associated with viscous and heat transfer effects in the stack region. Thermoacoustic stacks are modelled in this section as before as parallel channel walls filled with porous medium with finite wall thickness. Velocity and temperature results obtained from **Section** 4.3.2 are used for subsequent entropy generation analysis. For the specific thermoacoustic situation considered in this section a time-averaged entropy generation rate followed by local and global entropy generation rates are calculated and graphically presented for further analysis. The entropy generation distribution in the stack thus enables the designers to find and modify the parameters producing high energy losses characterized by large entropy production rates.

Recently, a few of the articles that consider irreversibility through entropy generation analysis in a thermoacoustic couple are Ishikawa and Mee [2002] and Zontjens et al. [2009]. Ishikawa and Mee [2002] studied the flow, energy fields, and entropy generation of a zero thickness thermoacoustic couple. The focus of their study was flow and energy fields while varying the drive ratio and the plate spacing. Only a little attention was provided on entropy generation analysis. The authors found that entropy generation in a thermoacoustic couple increased quadratically with the drive ratio. Zoontjens et al. [2009] numerically studied the flow, energy fields, and entropy generation in a thermoacoustic couple of non-zero thickness. Again, the main focus was on flow and energy fields. For a single plate non-porous thermoacoustic system, Mahmud and Fraser [2005a] derived an analytical expression for entropy generation rate as a function of stack plate geometry, fluid and solid stack properties, amplitude of fluctuation, and temperature gradient ratio Γ ($\Gamma = \nabla T_m / \nabla T_{cr}$). For a multi-plate non porous thermoacoustic system Mahmud and Fraser [2005b] derived expression for entropy generation rate. The normalized entropy generation rate in Mahmud and Fraser s' study [2005b] is a function of Rott's functions (f_k and f_ν), amplitude of oscillation, fluid properties, frequency of oscillation, and mean

temperature of the fluid. Ishikawa and Hobson [1996] presented an analytical analysis for the time averaged entropy generation rate due to both flow and heat transfer losses in the heat exchangers of thermoacoustic devices. An expression for the optimum dimensionless heat exchanger area corresponding to minimum entropy generation had been determined in terms of other dimensionless parameters. It was concluded from the analysis that for a thermoacoustics prime mover the hot heat exchanger area at the hot end of the stack should be smaller than the cold heat exchanger's. Mahmud and Fraser [2006] presented an analytical investigation on the thermagoustic (thermo-magneto-acoustic) irreversibility for a single-plate thermoacoustic system. The authors derived a general equation for entropy generation from first principles that accounted for the transverse magnetic force present in a magnetohydrodynamic system. This entropy generation equation was then simplified in order to model the specific thermoacoustic situations. Finally, a time-averaged entropy generation rate followed by a global entropy generation rate were calculated and graphically presented for further analysis.

The objective of this study is to examine the nature of irreversibility found in multi- plate thermoacoustic stack system in the presence of a porous medium. Entropy generation rate is used as the measure of irreversibility.

4.6 Entropy Generation Equation

For a two dimensional system in Cartesian coordinates, the entropy generation rate per unit volume of homogeneous porous medium using Darcy Law can be written as (Bejan [1984])

$$S_{gen} = \frac{k}{T^2}\left[\left(\frac{\partial T_1}{\partial y}\right)^2\right] + \frac{k_c}{T^2}\left[\left(\frac{\partial T_{s1}}{\partial y'}\right)^2\right] + \frac{\mu}{KT}u_1^2, \tag{4.58}$$

where T is the mean temperature of the small control volume, T_1 is the temperature fluctuations inside the porous medium, T_{s1} is the temperature fluctuations inside the channel wall, k is the overall thermal conductivity of the porous medium, k_c is the thermal conductivity of the channel wall, and u_1 is the velocity fluctuation, respectively. In linear theory (Swift [1988]), it is assumed that the stack length is short enough that the standing

wave pressure and velocity fluctuations may be regarded as independent of *x*- direction. Similar assumption is also used in the present study; therefore temperature fluctuation in the *x*-direction is independent or negligible compared to the *y*-direction. T is a characteristic (reference) absolute temperature. Instead of defining a new reference temperature, one may set $T = T_m$ (mean temperature) in order to keep analysis manageable. Equation (4.58) is a function of both time and space with a unit of W m^{-3} K^1. The first square bracketed term represents entropy generation due to heat transfer inside the porous medium, the second one is due to heat transfer through the channel wall, and the third term represents the fluid friction entropy generation rate inside the porous medium. Therefore, the first two terms of Eq. (4.58) represent entropy generation due to heat transfer contribution. The main intention in the present study is to obtain a time-averaged and then a total entropy generation rate in order to reduce the dependency of entropy generation rate on multiple parameters. Both time-averaged and total entropy generation rates have more physical meanings and applications. The time averaging technique (Temkin [1981]) of the product of two complex quantities (for example, $\Phi_1\Psi_1$) can be expressed as

$$\overline{\Phi_1 \Psi_1} = \frac{1}{\tau}\int_0^{\tau} \Re\left[\Phi_1\right]\Re\left[\Psi_1\right] dt = \frac{1}{2}\Re\left[\Phi_1\widetilde{\Psi}_1\right] = \frac{1}{2}\Re\left[\widetilde{\Phi}_1\Psi_1\right], \tag{4.59}$$

where '$\Re$[ ]' signifies the real part of a complex quantity and tilde (~) denotes the complex conjugate. In Eq. (4.59), τ (=$2\pi/\omega$) is the period of oscillation. In this thesis, an over bar (¯) is used to specify the time-averaged of certain quantity/quantities. When $\Phi_1 = \Psi_1$, Eq. (4.59) reduces to a special form and is given by

$$\overline{\Phi_1\Phi_1} = \frac{1}{\tau}\int_0^{\tau} \left(\Phi_1\Phi_1\right) dt = \frac{1}{2}\Re\left[\Phi_1\widetilde{\Phi}_1\right] = \frac{1}{2}\left|\Phi_1\right|^2, \tag{4.60}$$

where '| |' denotes the absolute value of a complex quantity. Equations (4.59) and (4.60) are applied to obtain the time-average heat transfer entropy generation rate from Eq. (4.58) (using Eq. (4.2) for velocity fluctuation and Eq. (4.13) for temperature fluctuation) as

$$\bar{S}_{gen} = \frac{k}{T_m^2}\frac{T_{c1}^2}{b_0^2}\frac{1}{\delta_k^2}\frac{\sinh(a_0 y)\sinh(\tilde{a}_0 y)}{\cosh(a_0 y_0)\cosh(\tilde{a}_0 y_0)} + \frac{k_s}{T_m^2}\frac{T_{c1}^2}{b_1^2}\frac{1}{\delta_c^2}\frac{\sinh(c_0 y')\sinh(\tilde{c}_0 y')}{\cosh(c_0 l)\cosh(\tilde{c}_0 l)}, \tag{4.61}$$

where

$$T_{c1} = \left[\frac{\phi T_m \beta\, p_1}{\sigma \rho_{f_m} C_{p_f}} - \frac{iK}{\sigma \omega \mu}\frac{dT_m}{dx}\frac{dp_1}{dx}\right], \tag{4.62}$$

and

$$b_0 = \frac{1}{\left(1+\varepsilon_s\sqrt{\sigma}\right)},\ a_0 = \frac{1+i}{\delta_k}, \text{ and } \tilde{a}_0 = \frac{1-i}{\delta_k}, \tag{4.63a}$$

also

$$b_1 = 1 - \frac{1}{\left(1+\varepsilon_s\sqrt{\sigma}\right)},\ c_0 = \frac{1+i}{\delta_s}, \text{ and } \tilde{c}_0 = \frac{1-i}{\delta_s}. \tag{4.63b}$$

The time averaged fluid friction entropy generation becomes

$$\bar{S}_{gen} = 2\pi^2 \frac{K}{\mu T_m}\frac{p_0^2}{\lambda^2}. \tag{4.64}$$

Note that the unit of time averaged entropy generation rate (in Eq. (4.61) and Eq. (4.64)) remains to W m^{-3} K^{-1}. The time averaged fluid friction entropy generation rate given in Eq. (4.64), does not have any *y*-dependency because of the Darcy momentum modeling for the flow field. Therefore, at any axial position, the magnitude of Eq. (4.64) is identical at any transverse location inside the porous medium. Equation (4.64) is proportional to

the square of the fluctuating pressure amplitude. Therefore, the contribution of Eq. (4.64) to the overall irreversibility becomes significant at higher DR. Equation (4.64) is inversely proportional to the square of the wavelength (λ). Therefore, a significant contribution of Eq. (4.64) to overall irreversibility is expected in case where the frequency of the sound wave is moderate to high.

Equation (4.61) is a measure of time averaged heat transfer entropy generation rate in a porous channel in the presence of a standing wave. Now, the space averaged heat transfer entropy generation rate ($S_{gen,av}$) is calculated by using the following:

$$S_{gen,av} = \frac{1}{\forall}\int_{\forall}\left(\overline{S}_{gen}\right)d\forall = S_{gen,1} + S_{gen,2}\,, \tag{4.65}$$

$$S_{gen,av} = \frac{k}{{\delta_k}^2}\frac{\sigma}{2}\left(\frac{\phi\beta\, p_1}{\sigma\rho_f C_{pf}}\right)^2 \frac{(1-\Gamma)^2}{\left(1+\varepsilon_s\sqrt{\sigma}\right)^2}\Re\left[i\left(f_k - \tilde{f}_k\right)\right] + \frac{k_c}{{\delta_s}^2}\left(\frac{\phi\beta\, p_1}{\sigma\rho_f C_{pf}}\right)^2\left(1-\frac{1}{1+\varepsilon_s\sqrt{\sigma}}\right)^2(1-\Gamma)^2\Re\left[i\left(f_s - \tilde{f}_s\right)\right]\,, \tag{4.66}$$

$$S_{gen,1} = \frac{k}{{\delta_k}^2}\frac{\sigma}{2}\left(\frac{\phi\beta\, p_1}{\sigma\rho_f C_{pf}}\right)^2 \frac{(1-\Gamma)^2}{\left(1+\varepsilon_s\sqrt{\sigma}\right)^2}\Re\left[i\left(f_k - \tilde{f}_k\right)\right], \tag{4.67a}$$

and

$$S_{gen,2} = \frac{k_c}{{\delta_s}^2}\left(\frac{\phi\beta\, p_1}{\sigma\rho_f C_{pf}}\right)^2\left(1-\frac{1}{1+\varepsilon_s\sqrt{\sigma}}\right)^2(1-\Gamma)^2\Re\left[i\left(f_s - \tilde{f}_s\right)\right]. \tag{4.67b}$$

In Eq. (4.65) $\forall$ is the volume of the channel. In Eq. (4.67a) $S_{gen,1}$ is the total entropy generation inside the porous medium, and in Eq. (4.67b), $S_{gen,2}$ is the total entropy generation inside the solid channel wall. Note that the unit of time and space averaged entropy generation rate (in Eq. (4.66)) remains the same to W m^{-3} K^{-1}.

4.6.1 Relation between Performance and Entropy Generation

The performance of a thermoacoustic system can be expressed in different ways. For example, global heat flow, total work flow, total energy flow, COP, second law efficiency (COPR), exergy recovered, etc. (Swift [1988], Swift [2002]). One of the best ways to define performance by considering the second law efficiency, because indirectly it includes all components of a system's (components to assembly levels) irreversibilities associated with its design imperfection. By definition, a second law efficiency for a heat pump system can be expressed according to Ishikawa [1999] as

$$COPR = \frac{COP}{COPC} = \frac{1}{1 + \dfrac{T_H T_C}{T_H - T_C} \dfrac{\sum_i S_{gen,i}}{Q_C}} . \tag{4.68}$$

In Eq. (4.68), COPC is the Carnot coefficient of performance, T_H and T_C are the hot and cold end temperatures of the stack or heat exchanger, Q_c is the heat flow from the cold side of the stack or heat exchanger, and $S_{gen,i}$ is the entropy generation in each element of a thermoacoustic device. Equation (4.68) clearly relates the performance of a thermoacoustic heat pump system to its entropy generation rate. According to Eq. (4.68) COPR is inversely proportional to entropy generation. Therefore, a higher entropy generation reduces COP, i.e., system's performance. In another way, a smaller entropy generation rate corresponds to a higher heat-to-work conversion efficiency. Entropy generation can be described from another point of view. Every system possesses certain work potential for a given conditions of the system and its nearby environment. The work potential of the energy contained in a system at a specified state is simply the maximum useful work that can be obtained from the system. The rest of the energy is eventually discarded as waste energy and is not useful for practical purpose. According to the second law of thermodynamics, systems imperfection is related to its exergy destruction which is an undesirable quantity from a design point of view. Exergy destruction can be related to systems entropy generation using the following equation (Çengel [2008])

$$X_{destroyed} = T_0 S_{gen} , \tag{4.69}$$

here X represents exergy and T_0 is the thermodynamic temperature of the environment. In order to reduce exergy destruction, system's design parameters should be tuned in such a way those minimize entropy generation to maximize its performance.

4.7 Results and Discussion

4.7.1 Comparison of Modeling with Experimental Results

The experiments conducted in Chapter 3 are used here to compare the experimental results to that of the critical temperature gradient obtained analytically. RVC foam of 45 PPI and 4 cm length is considered for the comparison. Figure 4.15 shows the measured temperature difference generated across the stack ends at steady state and at different locations of the stack from the pressure anti-node. Figure 4.15 also shows the analytically calculated critical temperature difference across the stack ends. The critical temperature difference across the stack ends is calculated using Eq. (4.62). In Eq. (4.62), K is the permeability of the porous medium ($=2.09\times10^{-8}$ m^2, obtained from Fu et al. [2001]), a is the adiabatic speed of sound, and L_s is the length of the stack (which is 4 cm for the present experimental condition). Figure 4.15 also qualitatively verifies the analytical modeling that has been proposed in the present study. If the temperature gradient generated across the stack ends is lower than the critical temperature gradient then the thermoacoustic device will work as a heat pump. In the present experiment, we are measuring temperature difference across the stack ends in a thermoacoustic heat pump; therefore, temperature difference generated across the stack ends should be lower than the critical temperature gradient. The critical temperature gradient is important because it is the boundary between the heat pump and the prime mover functions of thermoacoustic engines (Swift [1988]). A location of the stack that produces maximum temperature difference across the stack ends at steady state is considered to analyze the entropy generation rate (in **Sections** 4.7.2 and 4.7.3). From Fig. 4.15, this location is 2 cm

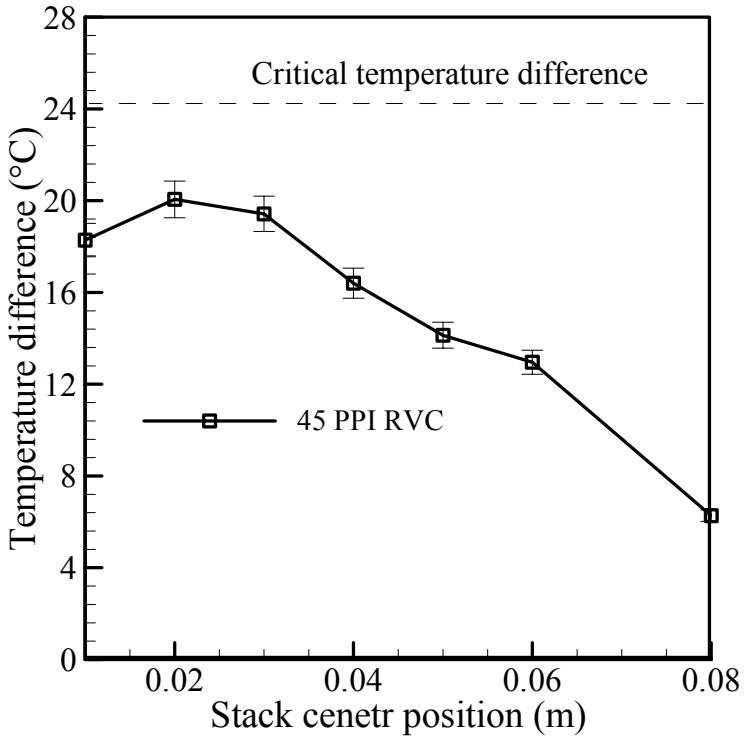

Figure 4.15: Measured temperature difference at different locations of the stack from the pressure anti-node, also comparison with analytical expression is shown.

on the horizontal axis. At this location a temperature difference (ΔT_m) of 20.7 °C is obtained across the stack ends at steady state in Fig. 4.15. This temperature gradient along with the critical temperature gradient gives the value of Γ=0.78. This value of Γ is used to analyze the entropy generation inside the porous RVC stack in **Sections** 4.7.2 and 4.7.3 (except Fig. 4.23 in **Section** 4.7.3) along with all the operating conditions used in the experiment in **Section** 4.7.1 if necessary. Detailed descriptions of the experimental conditions and discussions on thermal field are available on Chapter 7.

4.7.2 Total Entropy Generation

Table 4.2 shows the properties of different porous materials using helium and air as the working fluid at an average pressure and temperature of 100 kPa and 300K, respectively. Table 4.2 is used for part of the calculations in **Section**s 4.7.2 and 4.7.3.

The results of total entropy generation rate are presented only for a single location of the stack plate in the resonator where maximum temperature difference across the stack ends

Table 4. 2: Properties of Porous Materials (ERG [2009])

	Materials		
	Copper foam (45 PPI)	Aluminum foam (45 PPI)	RVC foam (45 PPI)
Specific Heat (J/kg. K)	385	895	1260
Thermal Conductivity (W/m. K)	10.1	5.8	0.040
Density (Kg/m^3)	715	216	49.5
ε_s (Eq.(4.14))	0.056 (helium) 0.0198 (air)	0.044(helium) 0.0152(air)	0.02(helium) 0.0035 (air)
σ (Eq.(4.4a), with $\phi = 0.92$)	27.33(helium) 19.54 (air)	16.47(helium) 13.51(air)	6.9(helium) 5.13(air)

is observed. In order to make an easier interpretation, the total entropy generation rate ($S_{gen,av}$ in Eq. (4.66)) is subdivided into two parts: total entropy generation due to (a) heat transfer in the porous medium ($S_{gen,1}$ in Eq.(4.67a)) and (b) heat transfer in channel wall ($S_{gen,2}$ in Eq.(4.67b)), respectively. $S_{gen,1}$ (in Eq.(4.67a)) is a linear superposition of the imaginary parts of f_k and $\tilde{f}_k$ multiplied by the modified adiabatic temperature oscillations due to the presence of the porous media along with fluid, porous media properties, and operating conditions. Now, the variation in $S_{gen,1}$ will be observed considering its dependency on the above mentioned parameters. For three selected range of frequencies, $S_{gen,1}$ (total entropy generation rate inside the porous medium) is plotted in Fig. 4.16(a) as a function of Lc_k. Figure 4.16(a) shows that maximum $S_{gen,1}$ is observed for all the selected frequencies with the lowest magnitude for the lowest frequency. As the values of Lc_k increase beyond 2, $S_{gen,1}$ becomes almost negligible. In Fig. 4.16(a), imaginary parts of f_k and $\tilde{f}_k$ are also shown as a function of Lc_k. *It is observed that $S_{gen,1}$ profiles follow the similar trend to that of the imaginary part of $\tilde{f}_k$ profile Therefore, in oscillatory flow porous media, the behavior of total entropy generation inside the porous media can be completely described by the imaginary part of*

the $\tilde{f}_k$ *profile.* Arnott et al. [1991] showed that thermoacoustic heat transport and work are proportional to $\Im(f_k)$ in the standing wave, inviscid limit. *One unique finding of this research is that maximum amount of entropy is generated where maximum thermoacoustic heat transport and work are produced/absorbed.* Therefore, a compromise has to be made when designing a stack considering maximum heat or work transport and entropy generation rates. The lowest selected frequency always shows the lowest $S_{gen,1}$ for all the Lc_k values in Fig. 4.16(a). As shown in Eq. (4.67a), $S_{gen,1}$ is inversely proportional to the square root of δ_k. An increase in frequency reduces δ_k and hence increases $S_{gen,1}$. Figure 4.16(b) also supports the findings of Fig. 4.16(a) that shows $S_{gen,1}$ as a function of operating frequency at different Lc_k. $S_{gen,1}$ is plotted as a function of drive ratio ($DR = p_0/p_m$) for a selected range of Lc_k in Fig. 4.17(a). For a given Lc_k, $S_{gen,1}$ increases with the increase of DR. Equation (4.67a) shows that $S_{gen,1}$ is proportional to the square of p_0, and p_0 increases as DR increases. Therefore, an increase in DR increases $S_{gen,1}$. However, $S_{gen,1}$ decreases with increasing Lc_k when DR is fixed. The reason for this behavior is already described earlier. Now, $S_{gen,1}$ is presented in Fig. 4.17(b) as a function of Lc_k for the selected mean pressures and for the RVC foam. At a higher mean pressure $S_{gen,1}$ increases considerably with a peak value near Lc_k=0.5, after that $S_{gen,1}$ decreases as Lc_k increases. The reason for this behavior is clearly understood from Eq. (4.67a) which shows that $S_{gen,1}$ is inversely proportional to the square root of δ_k. An increase in mean pressure reduces δ_k and hence increases $S_{gen,1}$. The position of the peak $S_{gen,1}$ depends on the value of the mean pressure. Note that the imaginary part of f_k profile with mean pressure remains almost unchanged. $S_{gen,1}$ as a function of ϕ in Fig. 4.18 (a) shows a rapid increasing trend with the increase of ϕ when $\phi > 0.9$ at Lc_k =1 and for all the foam materials selected for the present investigation. Maximum $S_{gen,1}$ is observed at $\phi = 1$, i.e., when no porous medium is

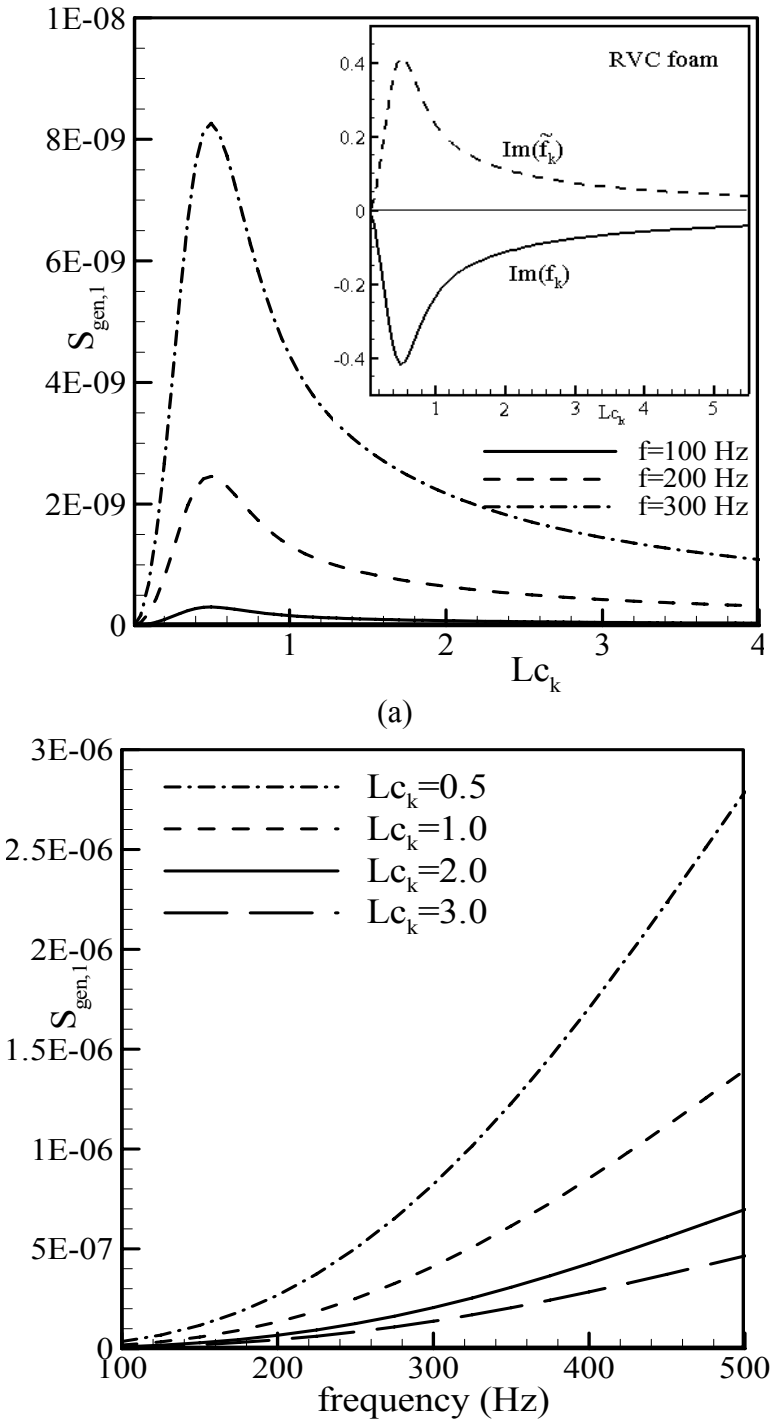

Figure 4.16: Time averaged entropy generation rate inside the porous medium (RVC foam) (a) as a function of Lc_k at selected frequencies, and (b) as a function of frequency at selected Lc_k values. In Fig. 4.16, $p_m = 100\text{kPa}$, $T_m = 300\text{K}$, and $\phi = 0.92$.

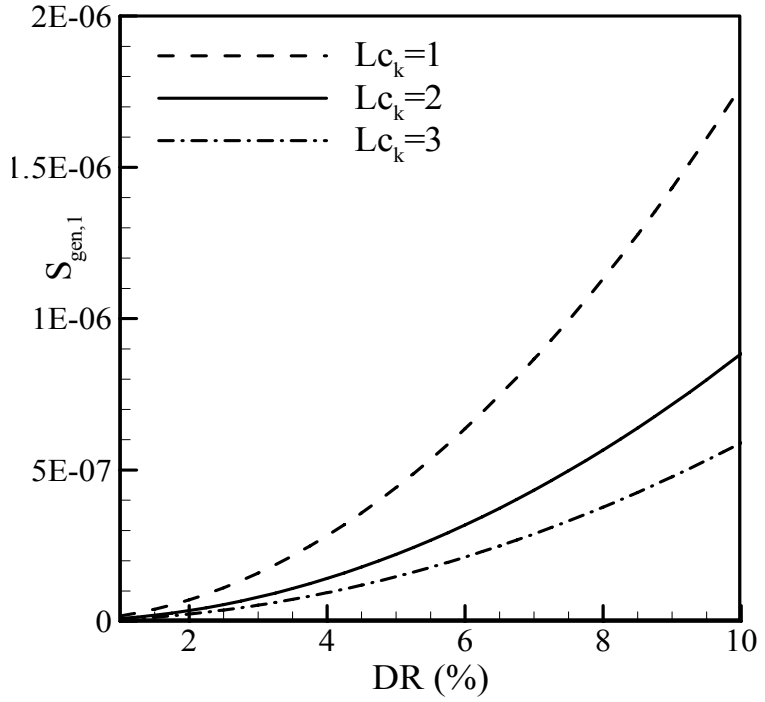

(a)

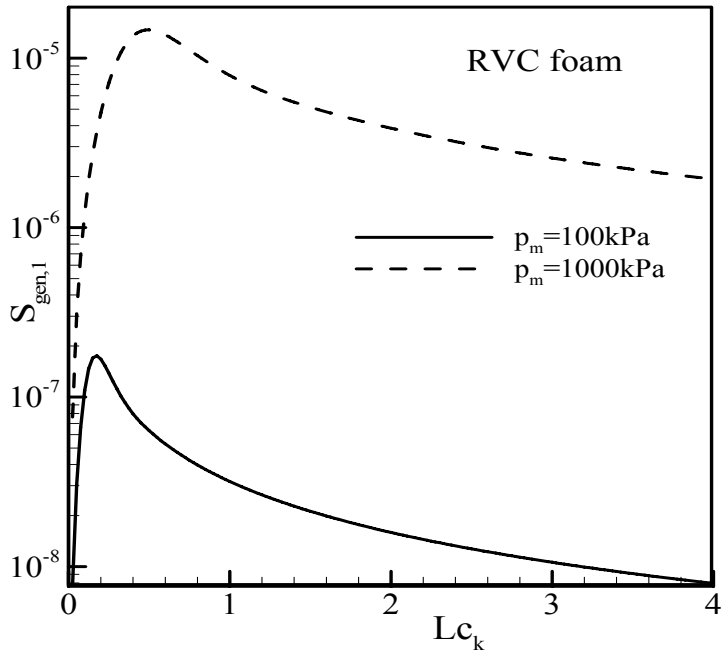

(b)

Figure 4.17: Time averaged entropy generation rate inside the porous medium (RVC foam) (a) as a function of DR at a selected Lc_k, and (b) as a function of Lc_k. In Fig. 4.17(a), $p_m = 100\text{kPa}$, $T_m = 300\text{K}$, f = 350 Hz and $\phi = 0.92$. In Fig. 4.17(b), $T_m = 300\text{K}$ f = 350 Hz and $\phi = 0.92$.

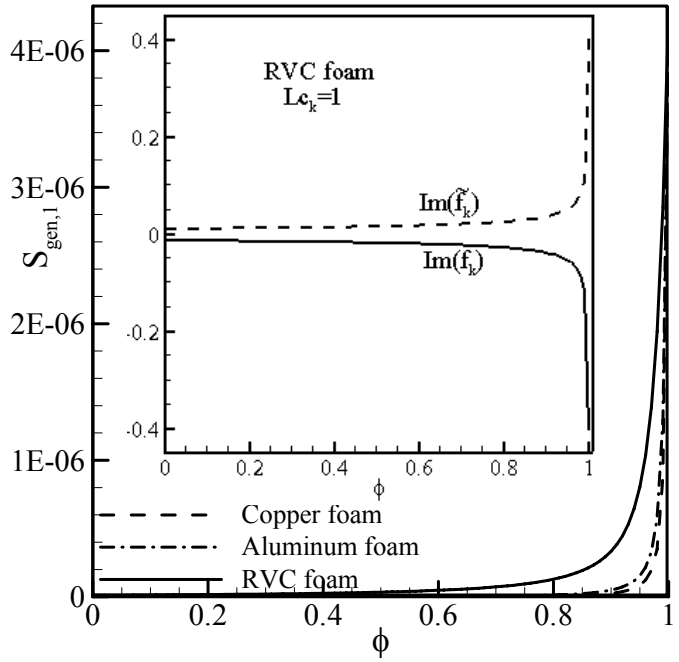

(a)

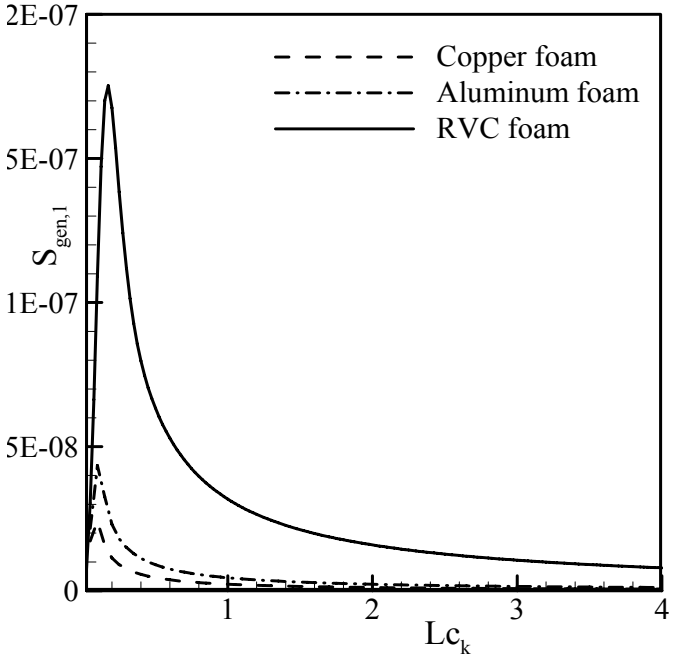

(b)

Figure 4.18: Time averaged entropy generation inside the porous medium (a) as a function of porosity (ϕ) of the porous medium at $p_m = 100\text{kPa}$, $T_m = 300\text{K}$, and $\text{f} = 350$ Hz, and (b) as a function of Lc_k for the selected foam materials at $p_m = 100\text{kPa}$, $T_m = 300\text{K}$, $\text{f} = 350$ Hz, and $\phi = 0.92$.

inserted in between the channel walls. To understand the influence of ϕ on $S_{gen,1}$, imaginary parts of f_k and $\tilde{f}_k$ profiles are also shown in the inset of Fig. 4.18(a) as a function of ϕ. $S_{gen,1}$ as a function of ϕ in Fig. 4.18(a) follows the similar trend to that of the imaginary part of $\tilde{f}_k$. At $\phi = 1$, imaginary part of $\tilde{f}_k$ is maximum, therefore experiencing maximum $S_{gen,1}$ at that ϕ value. As ϕ decreases from 1 to other lower values, imaginary part of $\tilde{f}_k$ reduces and so does $S_{gen,1}$, and becomes almost constant at a ϕ value of 0.5. For the three selected foam materials, $S_{gen,1}$ is shown as a function of Lc_k in Fig. 4.18(b). It is observed from the figure that for the selected foam materials peak values of $S_{gen,1}$ occur below $Lc_k = 1$. After that $S_{gen,1}$ values decrease with increasing Lc_k. This behavior of $S_{gen,1}$ with Lc_k is also observed in Figs. 4.16(a) and (b) and follows the similar trend to that of the imaginary part of $\tilde{f}_k$ profile. RVC foam shows the maximum values for all the Lc_k considered. $S_{gen,1}$ in Eq. (4.67a) is inversely proportional to σ, and RVC has the lowest value of σ when considering both of the working fluids compared to the other foam materials. Thus RVC foam shows the maximum $S_{gen,1}$ for all the Lc_k considered. Therefore, Fig. 4.16 to Fig. 4.18 demonstrate that $S_{gen,1}$ increases with the increase of frequency, drive ratio, and mean pressure, and follows the similar trend to that of the imaginary part of $\tilde{f}_k$ profile. Note that, $\tilde{f}_k$ values depend on the porous medium's material, porosity, and channel wall spacing. Thus changing any of these variables will change the $\tilde{f}_k$ profile and so does $S_{gen,1}$. $\tilde{f}_k$ values are weakly dependent on frequency, and independent on working gas, mean pressure and DR.

$S_{gen,2}$ (time averaged entropy generation rate inside the channel wall) in Eq.(4.67b) is a linear superposition of the imaginary parts of f_s and $\tilde{f}_s$, multiplied by the modified adiabatic temperature oscillations due to the presence of the porous media, along with channel wall, porous media properties, and operating conditions. $S_{gen,2}$ is plotted in Fig. 4.19 as a function of non-dimensional channel wall thickness (l/δ_s) for the selected

foam materials. Copper foam shows the maximum $S_{gen,2}$ near $l/\delta_s = 1$ followed by Aluminum and RVC foam. The pattern of Fig. 4.19 is dependent on the imaginary part of $\widetilde{f}_s$ profile also shown in the inset of Fig. 4.19. Although $S_{gen,2}$ pattern is dominated by

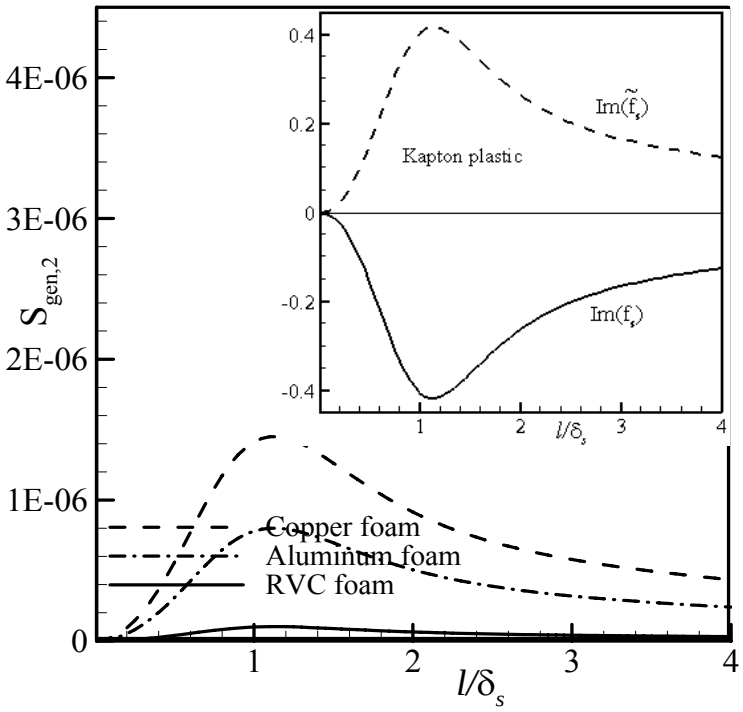

Figure 4.19: Time averaged entropy generation rate inside the channel wall as a function of non-dimensional channel wall thickness for the selected foam materials. In Fig. 4.19, $p_m = 100\text{kPa}$, $T_m = 300\text{K}$, and $f = 350$ Hz.

the imaginary parts of f_s and $\widetilde{f}_s$ profiles, the magnitudes are dominated by the porous medium properties (for example σ and k_{sm}) . $S_{gen,2}$ (in Eq. (4.67b)) is proportional to $k_{sm}(1-1/(1+\varepsilon_s\sqrt{\sigma}))^2/\sigma^2$, therefore an increase in σ and k_{sm} (for copper foam) causes an increase in magnitude of $S_{gen,2}$. In Fig. 4.19, $S_{gen,2}$ becomes independent after $l/\delta_s = 3$, since imaginary parts of f_s and $\widetilde{f}_s$ become independent at that l/δ_s value. Therefore, increasing the thickness of the channel wall does not affect $S_{gen,2}$. From the design point of view, it is evident from Fig. 4.19 that maintaining $l/\delta_s < 1$ will keep the channel wall heat transfer irreversibility as small as possible. Note that in Fig. 4.16 to Fig. 4.19,

different foam materials and operating conditions (other than experimental conditions indicated in **Section** 4.7.1) are considered only for the sake of comparisons.

4.7.3 Effect of Blockage Ratio

One of the most important design parameters of thermoacoustic devices is the geometric blockage ratio (*B*) (Rott [1980], Swift [1988], Zoontjens et al. [2009]). For a particular multichannel thermoacoustic stack system, *B* is defined as the ratio of gas cross sectional area to the total (gas and wall) cross sectional area. In the thin wall limit, *B* is one. However, in a typical thick wall thermoacoustic stack system, *B* is less than one but greater than zero. The value of *B* lower than one typically constricts the fluid flow movement and increases fluid friction irreversibility. In contrast, a lower *B* may increase/decrease heat transfer irreversibility depending on the wall spacing. In order to understand the effect of *B* on the overall performance of a typical thermoacoustic system, one of the methodologies is to observe its influence on the system's global entropy generation characteristics. However, the entropy generation expression, given in Eq. (4.66), does not have *B* in it. Therefore, in order to include *B* in the entropy generation expression, Eq. (4.66) is normalized with a characteristic entropy generation rate $k/(\delta_k l)$ (Mahmud and Fraser [2005b]). The equation of entropy generation, after normalization, can be expressed as

$$N_s = \frac{S_{gen,av}}{k/(\delta_k l)} = \frac{\sigma}{2} Lc_k \left(\frac{1}{B}-1\right)\left(\frac{\phi\beta p_1}{\sigma\rho_f C_{pf}}\right)^2 \frac{(1-\Gamma)^2}{\left(1+\varepsilon_s\sqrt{\sigma}\right)^2} \Re\left[i\left(f_k-\tilde{f}_k\right)\right] + \frac{(\rho C)_c}{(\rho C_p)_f} Lc_k \left(\frac{1}{B}-1\right)\left(\frac{\phi\beta p_1}{\sigma\rho_f C_{pf}}\right)^2 \left(1-\frac{1}{1+\varepsilon_s\sqrt{\sigma}}\right)^2 (1-\Gamma)^2 \Re\left[i\left(f_s-\tilde{f}_s\right)\right], \quad (4.70)$$

where $(\rho C)_c$ is the heat capacity of the channel wall, blockage ratio B $(= y_0/(y_0+l))$, non-dimensional stack spacing, $Lc_k = y_0/\delta_k$, and l is the half thickness of the channel wall, respectively. Total non-dimensional entropy generation rates given in Eq. (4.70) depend on working fluid properties, porous medium heat capacity ratio and porosity, plate spacing, plate thickness, heat capacity ratio between the porous medium and the

channel wall, drive ratio, frequency, blockage ratio, and the ratio of mean temperature gradient along the channel wall, the critical temperature gradient ratio, i.e., on the operating mode of the thermoacoustic device, and on the thermoviscous "f" functions.

Now, the total non-dimensional entropy generation rate (N_s) (Eq. (4.70)) is plotted in Fig. 4.20(a) as a function of *B* for the selected foam materials at $Lc_k \approx 1$. In Fig. 4.20(a) $Lc_k \approx 1$ is used instead of $Lc_k = 1$ (only for RVC foam $Lc_k = 1$), since overall thermal conductivity of different foam materials is different, and thus giving Lc_k close to unity. *Figure 4.20(a) shows N_s inside the channel wall*. The magnitude of N_s is controlled by *B*. The minimum value of N_s is obtained while *B* is unity, i.e., when the thickness of the channel wall is zero. The N_s profile with *B* is clearly understood if we compare Fig 4.20(a) with Fig. 4.20(b). Figure 4.20(b) shows $(1/B-1)\times \mathrm{Im}\left(f_s - \widetilde{f}_s\right)$ as a function of *B* along with $\mathrm{Im}\left(f_s - \widetilde{f}_s\right)$. Since, for a particular fluid, porous, and channel wall material and with constant operating conditions, N_s inside the channel wall are dominated by a linear superposition of imaginary parts of f_s and $\widetilde{f}_s$ times $(1/B-1)$. f_s and $\widetilde{f}_s$ are functions of *B* only. Imaginary parts of $\left(f_s - \widetilde{f}_s\right)$ are modified while multiplied by $(1/B-1)$ in Fig. 4.20(b). N_s inside the channel wall as a function of *B* follows the trend of $(1/B-1)\times \mathrm{Im}\left(f_s - \widetilde{f}_s\right)$ profile, since the rest of the parameters in Eq. (4.70) are constant. *Figure 4.20(c) shows N_s inside the porous medium*. The N_s pattern inside the porous medium is dominated by $(1/B-1)\times \mathrm{Im}\left(f_k - \widetilde{f}_k\right)$ profile, since the rest of the parameters in Eq. (4.70) are constant. f_k and $\widetilde{f}_k$ are functions of porous medium properties and stack plate spacing. Therefore, for a constant stack plate spacing, N_s profiles show different magnitudes for different porous materials. Comparing Fig. 4.20(a) and Fig. 4.20(c), a completely opposite scenario is observed, as N_s shows higher values near *B*=0 in Fig. 4.20(c) as opposed to *B*=1 in Fig. 4.20(a). In practical

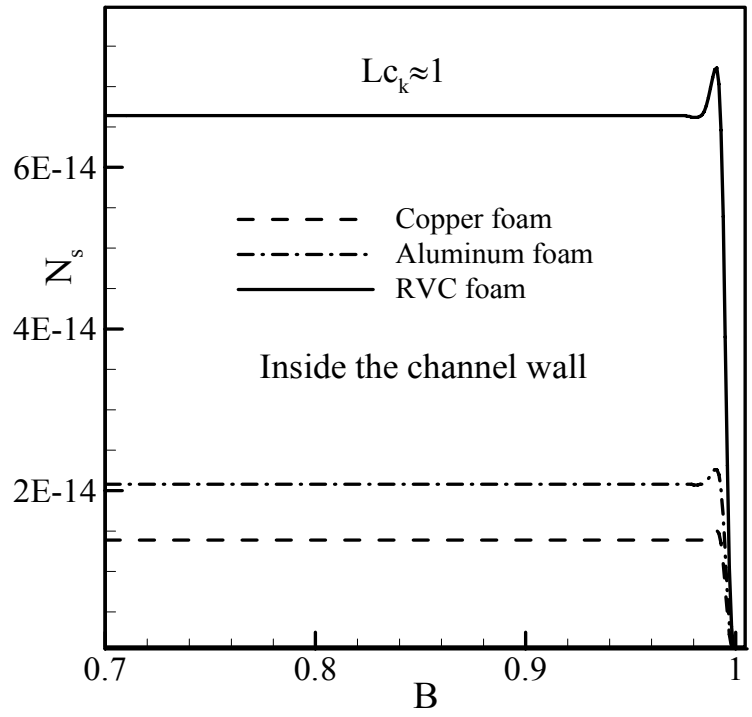
Lc_k≈1
6E-14
4E-14
2E-14
N_s
Copper foam
Aluminum foam
RVC foam
Inside the channel wall
0.7
0.8
0.9
1
B

(a)

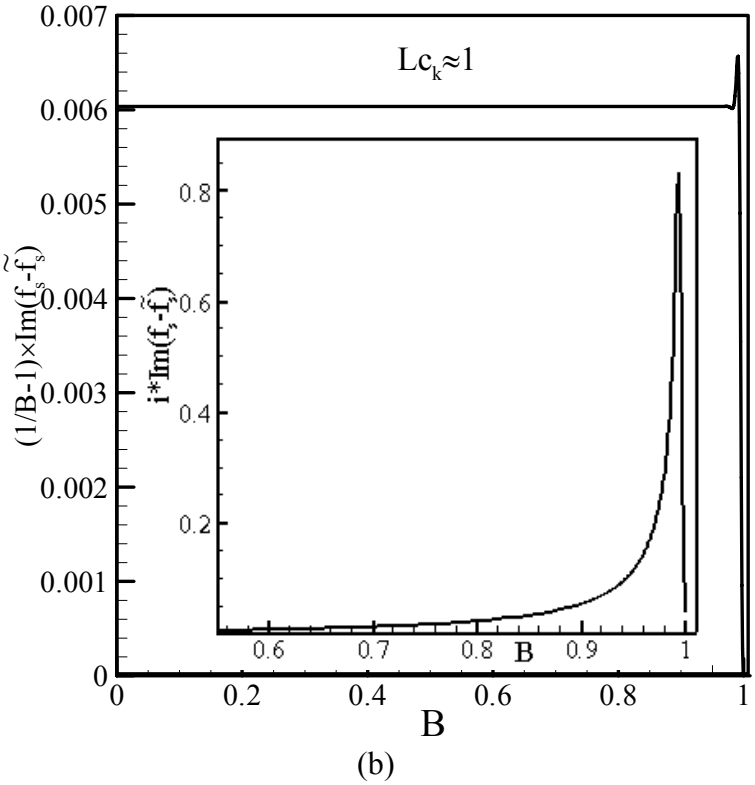
Lc_k≈1
0.007
0.006
0.005
0.004
0.003
0.002
0.001
0
(1/B-1)×Im(f_s-f_s)
i*Im(f_s-f_s)
0.8
0.6
0.4
0.2
0.6
0.7
0.8
B
0.9
1
0
0.2
0.4
0.6
0.8
1
B

(b)

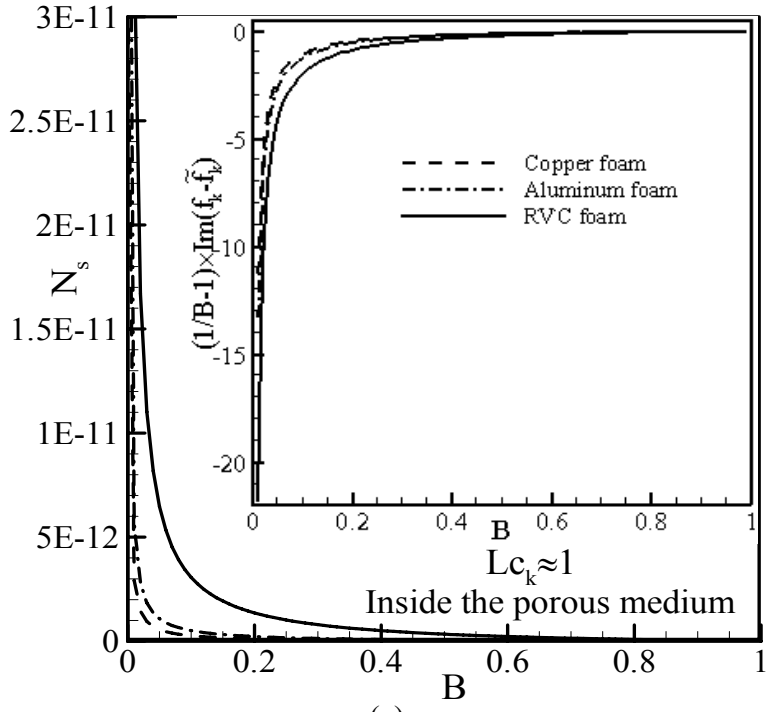

(c)

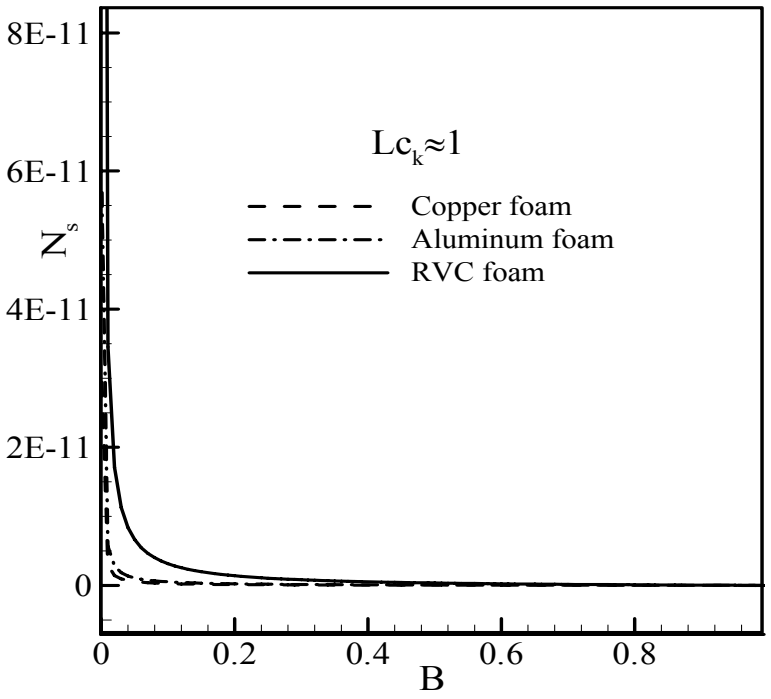

(d)

Figure 4.20: (a) N_s as a function of B inside the channel wall, (b) $(1/B-1)\times \mathrm{Im}\left(f_s - \tilde{f}_s\right)$ as a function of B, (c) N_s as a function of B inside the porous medium, and (d) total N_s for the three selected foam materials ($p_m = 100\text{kPa}$, $T_m = 300\text{K}$, $\phi = 0.92$, and f = 350 Hz).

thermoacoustic engines, *B* ranges from 0.65 to 85 (Swift [1988]). In this range of *B*, N_s values are independent of *B*. Observing Fig. 4.20(a) and (c), N_s is dominated by entropy generation inside the porous medium rather than inside the channel wall. This is expected, since thermoacoustic phenomenon occurs within the channel wall spacing occupied by the porous medium rather than inside the channel wall. Figure 4.20(d) shows total N_s, i.e., entropy generation inside the porous medium and channel wall.

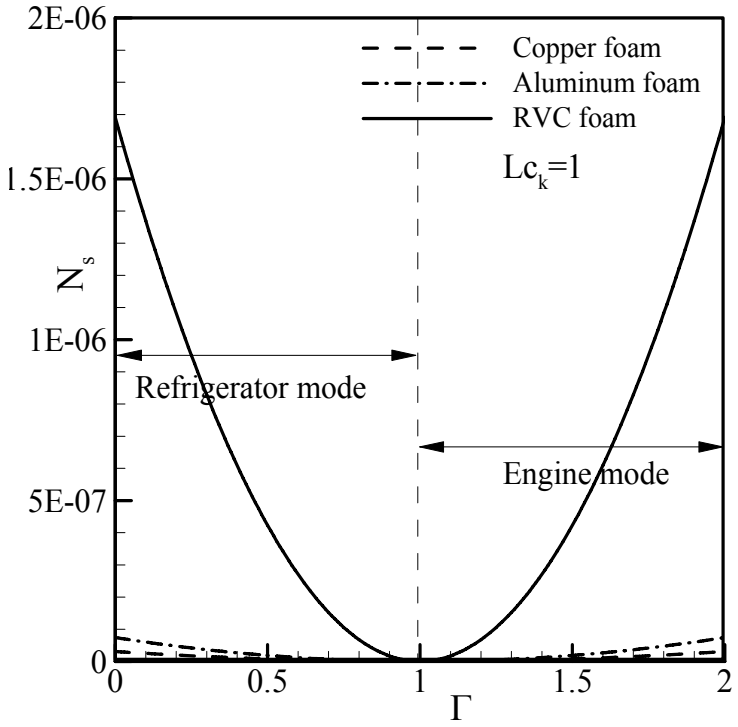

Figure 4.21: Total non-dimensional entropy generation rate N_s as a function of Γ for the selected porous medium materials.

Figure 4.21 depicts N_s as a function of Γ ($=\nabla T_m/\nabla T_{cr}$) for the selected foam materials, with the lowest value at Γ=1 for all the materials. The values of N_s for RVC foam are much larger than the other foams. Minimum N_s is observed at Γ=1. Therefore, Γ should be close to one along with using Copper foam to minimize irreversibility in a thermoacoustic stack. The N_s profile is symmetric about Γ=1. N_s is lower near Γ=1, then increases as ∇T_m is lower or higher than ∇T_{cr}. Depending on the value of Γ, a thermoacoustic device will work as a refrigerator (Γ<1) or a heat engine (Γ >1). In order to minimize N_s, a thermoacoustic device should be operated near the critical temperature

gradient generated along the stack for the selected operating conditions. Because of the losses associated in a real thermoacoustic device, ∇T_m is lower than ∇T_{cr} in a thermoacoustic refrigerator, and higher than ∇T_{cr} in a thermoacoustic engine. All the results in **Sections** 4.7.2 and 4.7.3 consider air as the working fluid. Using helium instead of air would increase the entropy generation rate (not shown in this paper) also indicated by the non-dimensional temperature distributions in Figs. 4.4(a) to (c). Up to Fig. 4.21, the plots correspond to a single position of the stack centre from the pressure anti-node. Figure 4.22 thus show the mesh-contour plots of total non-dimensional entropy generation rate (N_s) as a function of Γ and non-dimensional stack centre position ($k_1 x$,

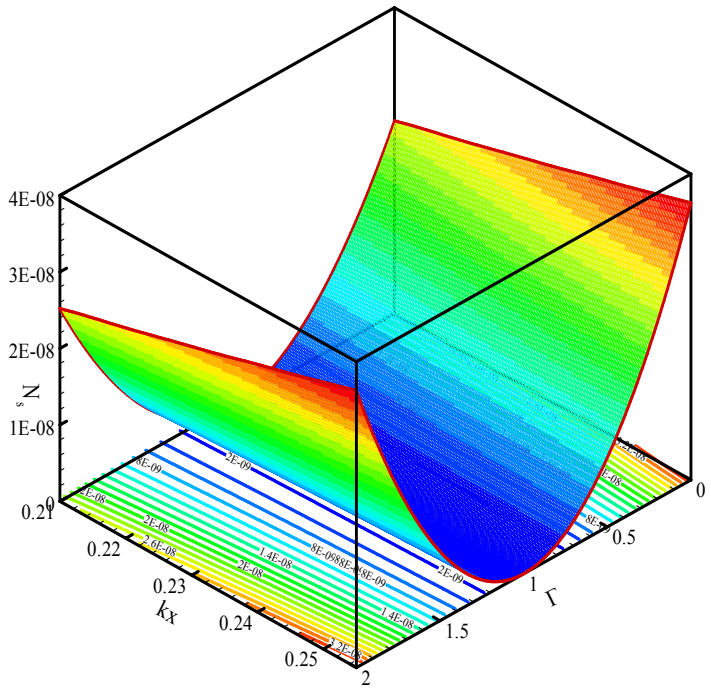

Figure 4.22: Mesh-contour plot showing the dimensionless temperature gradient ratio (Γ) distribution corresponds to the time averaged entropy generation rate (N_s) and dimensionless stack centre position (*kx*) from the pressure anti-node for copper foam. In Fig. 4.22, Lc_k=1, $p_m = 1000\text{kPa}$, $T_m = 300\text{K}$,and $f = 350\,\text{Hz}$.

where $k_1 = 2\pi/\lambda$) from the nearest pressure anti-node for copper foam. The mesh plots are helpful for understanding the pattern of variation in N_s with *kx* and Γ, while the contour plots may be used as performance plots describing stack-centre position at the minimum entropy generation rate. Figure 4.22 shows that N_s values are lower at a

position of the stack center closest to the pressure anti-node (or velocity node). Being closer to a velocity node (therefore leading to a lower magnitude of oscillating velocity) leads less viscous losses and therefore less entropy generation. Therefore, to minimize N_s, stack center should be closer to the pressure anti-node along with Γ close to unity.

4.8 Conclusions

The general thermoacoustic theories available in the existing literature are modified to consider the stack's fluid-gaps filled with a porous medium. A porous medium filled stack has a large heat transfer area in comparison to a conventional gas-filled stack. Therefore, it is worth trying to develop mathematical models for such stacks in order to test the suitability of using them in thermoacoustic devices to enhance their performance. The velocity field for such of kind of stack is modeled by a Darcy flow model, whereas the thermal field is modeled considering local thermal equilibrium between the porous matrix and trapped fluid in the void space. The thickness of the channel walls are considered as non-zero and the entire problem is treated as a conjugate heat transfer problem. Analytical expressions for oscillating velocity, temperature in the porous layer and in the solid matrix, complex Nu, and energy flux density are obtained after simplifying and solving the governing differential equations with reasonable approximations (such as long wave, short stack, small amplitude oscillation, etc). From the analysis the following conclusions are drawn:

- For a porous medium filled stack, δ_k is modified resulting in decrease in values. Modified δ_k for a porous medium becomes $\delta_k/\sqrt{\sigma}$.

- Nu is a function of $\Im(f_k)$ and $\Im(f_s)$, and increases as a porous medium is introduced in between the channel walls. Temperature gradient at the wall and the temperature difference between the wall and the space averaged temperature show a phase difference and because of this phase difference Nusselt number expression for steady flow cannot be used in for oscillatory flow.

- The analysis shows that refrigeration performance is achievable using RVC foam ($\phi = 0.92$, $K = 2.09 \times 10^{-8}\,\mathrm{m}^2$) or aluminum foam ($\phi = 0.9$, $K = 3.36 \times 10^{-8}\,\mathrm{m}^2$) as porous media instead of bare parallel plates. Non-dimensional global energy flux (E_2/E_0) values indicate that using porous medium in between the parallel plates show significantly better performance while $Lc_k \leq 2$.

In **Section** 4.5, the problem of irreversibility in a porous channel representative of the stack in a thermoacoustic engine is modeled and analyzed. Entropy generation rate is used as a measure of irreversibilities associated with viscous and heat transfer effects in the stack region. The expressions of fluctuating velocity, and temperature distributions obtained in **Section** 4.3.2 are used in subsequent entropy generation analysis. The following conclusions are drawn from the entropy generation analysis:

- Increasing frequency, drive ratio, and mean pressure increases the time averaged total entropy generation ($S_{gen,1}$) inside the porous medium. Maximum $S_{gen,1}$ is observed at $Lc_k < 1$, and $S_{gen,2}$ at $l/\delta_s = 1$.

- One important item revealed in this study is that entropy generation inside the porous medium completely follows the trend of the imaginary part of $\tilde{f}_k$ profile.

- Another major contribution of this research is to identify the location of maximum $S_{gen,1}$ which is identical to the location of maximum thermoacoustic heat and work transport. Therefore, a compromise has to be made to design a thermoacoustic device considering maximum entropy generation and heat or work transport.

- The ratio of temperature gradient along the stack and the critical temperature gradient (Γ) greatly influence the total non-dimensional entropy generation (N_s) of the stack showing minimum value near one which means temperature gradient

along the stack equals the critical temperature gradient along with using copper foam, air as the working fluid, $Lc_k > 1$, and stack center position close to the pressure anti-node.

- For the practical operation range of thermoacoustic engines, *B* does not influence N_s. Thus second law analysis applied to the stacks gives a good indication of geometries and operating conditions of thermoacoustic devices.

The minimum amount of entropy generation determines the optimum design parameters of stacks leading to highest heat removal rate in a thermoacoustic refrigerator and highest conversion of heat energy to acoustic energy in a thermoacoustic heat engine.

Chapter 5

Porous Media Thermoacoustic System: Brinkman-Forchheimer Model

5.1 Introduction

In this chapter the previous (in Chapter 4) porous media modeling is extended by considering the Brinkman-Forchheimer extended Darcy model for the modeling of the momentum equation. No such modeling for the porous stack exists in the published literature, thus providing the primary motivation for the work reported in this chapter. One of the limitations of Darcy's Law is that it does not consider inertia term in the momentum equation, which is important for high velocity (Reynolds number based on pore size is higher than unity) and high porosity porous medium (for example RVC stack). Therefore, Brinkman-Forchheimer extended Darcy model is used for the modeling of momentum equation in this chapter to account for the high velocity, high porosity porous medium bounded by impermeable walls which are typical in practical thermoacoustic devices. The modeling remains within the framework of the classical linear theory (Swift [1988])). Thus the addition of Forchheimer term which includes nonlinearity in the momentum equation makes it impossible to obtain a closed form analytical solution for the velocity. Taylor series expansion technique is utilized to transform this non-linear term to a linear form. The system of equations developed in this chapter is a helpful tool for thermal engineers and physicists to design porous stacks for thermoacoustic devices.

5.2 Analysis

Current analysis is carried out for an unsteady-state, compressible, two-dimensional flow within a parallel-plate channel filled with a homogeneous and isotropic porous medium. The geometry of the problem under consideration is shown in Fig. 5.1, which is a channel bounded by two parallel plates and is filled with an isotropic porous medium. In the present study, a rigid foam or wire-mesh material is considered such that porosity and permeability are assumed to be constant, even close to the walls. The *x*-axis represents the longitudinal direction (also the direction of fluid

oscillation), whereas the y axis represents the transverse (normal to the wall) direction in the porous medium, respectively. The calculations are performed in a pair of walls as depicted in

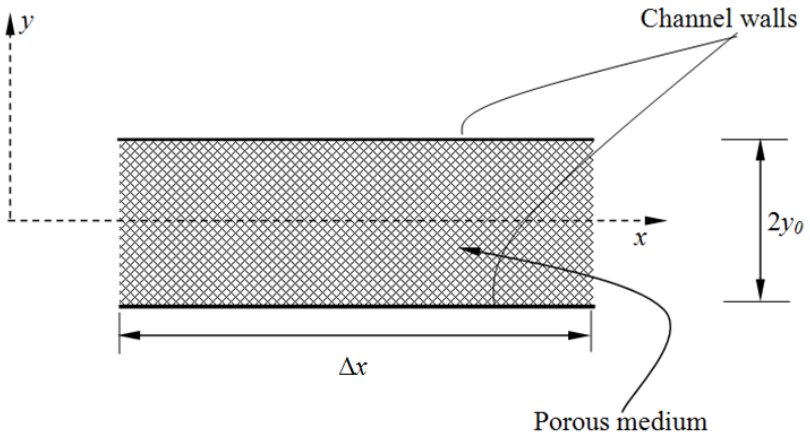

Figure 5.1: Co-ordinate system and dimensions of analytical domain of the porous stack.

Fig. 5.1, and together the channel walls and the embedded porous medium form the stack. The location $y = 0$ is chosen to be the midpoint between the two adjacent walls and $x = 0$ is chosen to be the closed end of the resonator. The thermophysical properties of the solid matrix and of the fluid (except the density of fluid) are assumed to be constant. The following sections are devoted to calculating the fluctuating velocity, temperature, and energy flux density in the porous medium. Every time efforts will be taken to compare the present results to the results obtained by Swift [1988].

5.3 Velocity Modeling

The equation for mass continuity, according to Nield and Bejan [2006], for a porous medium is

$$\frac{\partial(\phi\rho)}{\partial t} + \nabla.(\rho \mathbf{v}) = 0, \tag{5.1}$$

where ϕ, ρ, and $\mathbf{v}$ are the porosity of the porous medium, density of the fluid, and the volume averaged pore velocity vector, respectively. The modeling of the momentum equation is performed using the Brinkman-Forchheimer-extended Darcy model (Vafai and Kim [1989]). The modeling of momentum equation in a porous media depends on the flow situations. Darcy's Law

states that in flow through a porous medium the pressure drop caused by the friction force is directly proportional to velocity. Darcy's Law is applicable when the Reynolds number based on the pore size is less than unity in an unbounded porous medium. In most thermoacoustic applications the Reynolds number based on the pore size is greater than unity and there is an impermeable wall that makes Darcy's Law inapplicable. At higher velocities and high porosities porous media (such as RVC foams) inertia effects become important (Vafai and Tien [1981]). Experimental observations indicate that the pressure drop in a bulk porous medium is proportional to a linear combination of flow velocity and square of the flow velocity. This square term of flow velocity is caused by the inertial effects offered by the solid matrix. The presence of an impermeable wall is accounted by Brinkman [1947] by adding a viscous term to the Darcy's Law. Therefore, a Brinkman-Forchheimer-extended Darcy model proposed by Vafai and Kim [1989] is used in the present investigation. Since the present research considers a high porosity porous medium as a thermoacoustic stack, a relatively high drive ratio, and the stack is housed in a resonator; therefore, the governing equations that account for all these effects is the Brinkman-Forchheimer-extended Darcy model. The semi empirical model proposed by Vafai and Kim [1989] is

$$\rho \frac{\mathbf{D}\mathbf{v}}{\mathbf{D}t} + \frac{F\,\rho\phi}{\sqrt{K}} \left| \mathbf{v} \right| \mathbf{v} = -\nabla p - \phi \frac{\mu_{\mathrm{d}}}{K} \mathbf{v} + \mu_{\mathrm{e}} \nabla^2 \mathbf{v} \,. \tag{5.2}$$

The second term on the left and right hand sides of Eq. (5.2) are measure of the flow resistance offered by the porous medium. The pressure gradient (first term on the right hand side) can also be interpreted as a measure of the same resistance to flow in the bulk of the porous medium. The first two terms on the right hand side of Eq. (5.2) are the Darcy model and K is the permeability of the porous medium. The third term on the right hand side is the boundary viscous term that accounts the presence of a solid boundary (together the first three terms construct the Darcy Brinkman modeling). The effects of a solid boundary in a porous medium originate from vorticity diffusion caused by the boundary frictional resistance (Vafai and Tien [1981]). This resistance is additional to the bulk frictional force caused by the solid matrix as characterized by Darcy's Law. The second term on the left hand side of Eq. (5.2) is the inertia term; F is the Forchheimer's coefficient which is a function of porosity, pore structure, and Reynolds number and is usually determined from laboratory measurements (Kaviany [1995]). μ_{e} is the effective

viscosity and μ_d is the dynamic viscosity of the fluid. Note that the ratio of μ_e to μ_d is termed as the viscosity ratio (M) (Haji Sheikh et al. [2006]). In this work M is considered to be unity which means $\mu_e = \mu_d = \mu$, and it will increase monotonically with decreasing porosity (Nield and Bejan [2006]). The *x*-momentum equation for the current problem can be obtained from Eq. (5.2) as

$$\left(\rho\frac{\partial u}{\partial t}+\rho u\frac{\partial u}{\partial x}+\rho v\frac{\partial u}{\partial y}\right)+\frac{F\rho\phi}{\sqrt{K}}u^2=-\frac{\partial p}{\partial x}-\phi\frac{\mu}{K}u+\mu\left(\frac{\partial^2 u}{\partial x^2}+\frac{\partial^2 u}{\partial y^2}\right). \tag{5.3}$$

Now, Eq. (5.3) will be linearized according to the assumptions and approximations stated in **Section** A.1 of Appendix A.

5.3.1 Approximation of the Forchheimer Term

The Forchheimer term (i.e., the parameter with the velocity squared) in the momentum equation (Eq. (5.3)) is caused by the inertial effects offered through the porous medium (Vafai and Tien [1981]). Inertial effects are important for high porosity porous medium as is the case of RVC and open metal foam. If the linearized approximations (given in Eqs. (A.1) to (A.5) in **Section** A.1 of Appendix A), are applied to the momentum equation (Eq. (5.3)), the Forchheimer term disappears due to the presence of the velocity squared term in it. Therefore, a minimum second order expansion is required to observe the effect of the Forchheimer term in the momentum equation. Such a second order approximation will essentially introduce a high nonlinearity in the momentum equation which, in turn, makes it impossible to obtain any closed form of analytical solution for the fluctuating velocity u_1. Before perturbation expansion, one could, however, approximate the non-linear term in the general differential equation by simplifying it to a linear form as is done in the available literature (Mahmud and Fraser [2003], Arpaci et al. [2000]) without losing too much of physical meaning in the modeling.

Expressing u^2 as a Taylor series about u_0 (a reference velocity) yields

$$u^2=\sum_{n=0}^{\infty}\frac{(u-u_0)^n}{n!}\left[\frac{d^n}{du^n}f(u)\right]_{u=u_0}=u_0^2+2(u-u_0)u_0+(u-u_0)^2. \tag{5.4a}$$

Truncating the above series after the second term, Eq. (5.4a) gives

$$u^2 \approx u_0\left(2u - u_0\right) \quad . \tag{5.4b}$$

By substituting variable expansions (as presented in Eqs. (A.1) to (A.5) in Appendix A) into the axial momentum equation, after considering all of the assumptions stated in Appendix A, and using Eq. (5.4b), Eq. (5.3) can be further simplified to

$$i\omega\rho_m u_1 + \frac{F\phi\rho_m}{\sqrt{K}} u_0\left(2u_1 - u_0\right) = -\frac{\partial p_1}{\partial x} - \phi\frac{\mu}{K}u_1 + \mu\frac{\partial^2 u_1}{\partial y^2}\,. \tag{5.5}$$

After the following boundary conditions (a) at $y = 0,\ \partial u_1 / \partial y = 0$ and (b) at $y = y_0,\ u_1 = 0$ are applied, the solution to Eq. (5.5) becomes

$$u_1 = \frac{1}{1+\phi/(2iDa)}\left\{\frac{i}{\omega\rho_m}\frac{\partial p_1}{\partial x} - \frac{2F\phi}{i\omega\sqrt{K}}u_0^2\right\}\left\{1 - \frac{\cosh\left[(1+i)\sqrt{1+\phi/(2iDa)}\,y/\delta_\nu\right]}{\cosh\left[(1+i)\sqrt{1+\phi/(2iDa)}\,y_0/\delta_\nu\right]}\right\}\ , \tag{5.6}$$

with

$$Da = \frac{K}{\delta_\nu^2}\,. \tag{5.6a}$$

In Eq. (5.6a), δ_ν and Da are the viscous penetration depth (Swift [1988]) and Darcy number (Vafai and Kim [1989]), respectively. For the simplicity and convenience of presentation, the $(1+i)\sqrt{1+\phi/(2iDa)}\,/\,\delta_\nu$ term in Eq. (5.6) is expressed as a_0 in several locations in this thesis. In Eq. (5.6), a dimensionless transverse distance $Y\left(= y/y_0\right)$ and a non-dimensional Swift number $S_w\left(= y_0/\delta_\nu\right)$ as proposed by Mahmud and Fraser [2009] are introduced. Using the proposed parameter S_w and Y, Eq. (5.6) can be modified to

$$u_1 = \frac{1}{1+\phi/(2iDa)}\left\{\frac{i}{\omega\rho_m}\frac{\partial p_1}{\partial x} - \frac{2F\phi}{i\omega\sqrt{K}}u_0^2\right\}\left\{1 - \frac{\cosh\left[(1+i)\sqrt{1+\phi/(2iDa)}\ S_w Y\right]}{\cosh\left[(1+i)\sqrt{1+\phi/(2iDa)}\ S_w\right]}\right\}\ . \tag{5.7}$$

The fluctuating velocity expression obtained from Eq. (5.7) is compared with Eq. (A4) of Swift [1988] for the limiting cases. Equation (A4) is shown here as Eq. (5.8). The two expressions agree with each other for the limiting cases of non-porous media ($K \to \infty$ and $\sigma = 1$) and Forchheimer's coefficient $F = 0$.

$$u_1 = \frac{i}{\omega \rho_m} \frac{dp_1}{dx} \left\{ 1 - \frac{\cosh\left[(1+i)\, S_w Y\right]}{\cosh\left[(1+i) S_w\right]} \right\}. \tag{5.8}$$

By using the integration, $(y_0)^{-1} \int_0^{y_0} u_1 dy$ the average velocity ($u_{1,av}$) can be calculated from Eq. (5.7) as

$$u_{1,av} = \frac{1}{1+\phi/(2iDa)} \left\{ \frac{i}{\omega \rho_m} \frac{\partial p_1}{\partial x} - \frac{2F\phi}{i\omega\sqrt{K}} u_0^2 \right\} \left\{ 1 - \frac{\tanh\left[(1+i)\sqrt{1+\phi/(2iDa)}\; S_w\right]}{(1+i)\sqrt{1+\phi/(2iDa)}\; S_w} \right\} . \tag{5.9}$$

Detail discussions on the flow field with graphical interpretation are left for the results and discussions section.

5.4 Thermal Field Modeling

The porous medium studied in this chapter is considered to be saturated with a single phase Newtonian fluid and is assumed to be in local thermal equilibrium with the working fluid. In the present work, the working fluid and the porous medium both have similar thermal conductivity, therefore, making the local thermal equilibrium assumption valid.

For the current problem and considered assumptions, the following general form of the energy equation according to Nield and Bejan [2006] results

$$\rho C_p \left[\sigma \frac{\partial T}{\partial t} + (\mathbf{v}.\nabla) T \right] = \nabla.(k \nabla T) + \beta T \phi \frac{\mathbf{D}p}{\mathbf{D}t} + \left(\frac{\mu}{K} + \frac{\rho F}{K^{1/2}} |\mathbf{v}| \right) \mathbf{v}.\mathbf{v}\,, \tag{5.10}$$

for modeling the temperature inside a porous medium. Where σ, k, C_p, and β are the porous medium heat capacity ratio, overall thermal conductivity, specific heat of the fluid, and thermal expansion coefficient, respectively. The last term inside the bracket on the right hand side of Eq. (5.10) is the viscous dissipation term for the present problem. The parameters, porous medium heat capacity ratio (σ) and overall thermal conductivity (k) can be defined, according to Bejan [1984], as

$$\sigma = \phi + (1-\phi)(\rho_{sm} C_{sm})/(\rho C_p) \tag{5.11}$$

$$k = (1-\phi)\, k_{sm} + \phi\, k_f \tag{5.12}$$

,

where ρ_{sm}, C_{sm}, and k_{sm} are, respectively, the density, the specific heat, and the thermal conductivity of the solid matrix material of the porous medium. Following similar scaling arguments as performed in the previous section, and applying Rott's thermoacoustic linearization (Rott [1980]), the energy equation in the porous medium can be simplified to

$$i\omega\rho_m C_p \sigma T_1 + C_p \rho_m u_1 \frac{\partial T_m}{\partial x} = k \frac{\partial^2 T_1}{\partial y^2} + i\phi\omega\beta T_m p_1 . \tag{5.13}$$

In Eq. (5.13) the subscript 'm' represents the mean properties of the porous medium. The general solution to Eq. (5.13) yields

$$\begin{aligned} T_1 = {} & C_1 \cosh\left(\frac{1+i}{\delta_k}\sqrt{\sigma}\, y\right) + C_2 \sinh\left(\frac{1+i}{\delta_k}\sqrt{\sigma}\, y\right) + \frac{\Pr\sigma}{\sigma\Pr - \left[1+\phi/(2iDa)\right]} \frac{\nabla T_m \nabla p_1}{\omega^2 \rho_m \left[1+\phi/(2iDa)\right]} \\ & \times \frac{\cosh(a_0 y)}{\cosh(a_0 y_0)} - \frac{\nabla T_m \nabla p_1}{\omega^2 \rho_m \sigma \left[1+\phi/(2iDa)\right]} + \frac{\phi\beta T_m p_1}{\rho_m C_p \sigma} - \frac{\nabla T_m}{\omega\sigma\left[1+\phi/(2iDa)\right]} \left(\frac{2F\phi u_0^2}{i\omega\sqrt{K}}\right). \end{aligned} \tag{5.14}$$

In the above equation $\Pr$ and δ_k represent the effective Prandtl number ($\Pr = \mu Cp/k$) and thermal penetration depth, respectively. In Eq. (5.14), two gradients, $\partial T_m/\partial x$ and $\partial p_1/\partial x$, are expressed as ∇T_m and ∇p_1, respectively, by using the convention of the available thermoacoustic literature (Swift [1988]). For simplicity and convenience of presentation in this chapter, the $(1+i)\sqrt{\sigma}/\delta_k$ term in Eq. (5.14) is expressed later as b_0.

Applying the symmetry boundary condition, i.e., $\partial T_1/\partial y = 0$ at $y = 0$, results in $C_2 = 0$ in Eq. (5.14). However, in order to evaluate C_1, it is necessary to apply an appropriate boundary condition at the wall. One possible approximation is to assume a zero fluctuating temperature at the wall, i.e., $T_1 = 0$ at $y = y_0$ (assuming sufficient high heat capacity of the channel wall, Swift [1988]). Finally, the fluctuating temperature inside the porous medium (T_1) becomes

$$T_1 = \theta_1 - \theta_2 \left\{ 1 - \mathrm{Pr}' \frac{\cosh\left[(1+i)\sqrt{1+\phi/(2iDa)}\, S_w Y\right]}{\cosh\left[(1+i)\sqrt{1+\phi/(2iDa)}\, S_w\right]} \right\} - \left\{\theta_1 - \theta_2 + \mathrm{Pr}'\theta_2\right\} \frac{\cosh\left[(1+i)\sqrt{\sigma\,\mathrm{Pr}}\, S_w Y\right]}{\cosh\left[(1+i)\sqrt{\sigma\,\mathrm{Pr}}\, S_w\right]} \quad (5.15)$$

where

$$\theta_1 = \frac{\phi\beta T_m P_1}{\sigma \rho_m C_p}, \theta_2 = \frac{\nabla T_m}{i\omega\sigma} \frac{1}{1+\phi/(2iDa)} \left(\frac{i}{\omega\rho_m} \frac{\partial p_1}{\partial x} - \frac{2F\phi}{i\omega\sqrt{K}} u_0^2 \right), \mathrm{Pr}' = \frac{\sigma\,\mathrm{Pr}}{\sigma\,\mathrm{Pr} - \left[1+\phi/(2iDa)\right]}. \quad (5.16)$$

Equation (5.15) is compared with Eq. (A10) of Swift [1988] for the limiting cases. Equation (A10) is shown here as Eq. (5.17). The two expressions agree with each other for the limiting cases of non-porous media ($K \to \infty, \sigma = 1$) and Forchheimer's coefficient $F = 0$.

$$T_1 = \left[\frac{T_m \beta\, p_1}{\left(\rho\, C_p\right)_f} - \frac{1}{\rho_m \omega^2} \frac{dT_m}{dx} \frac{dp_1}{dx} \right] \left[1 - \frac{\cosh\left\{ \frac{(1+i)}{\delta_k} y \right\}}{\cosh\left\{ \frac{(1+i)}{\delta_k} y_0 \right\} (1+\varepsilon_s)} \right]. \quad (5.17)$$

By using the integration, $(y_0)^{-1} \int_0^{y_0} T_1 dy$, a space averaged temperature ($T_{1,av}$) can be calculated from Eq. (5.15) as

$$T_{1,av} = \frac{\phi\beta T_m p_1}{\rho_m C_p \sigma} (1 - f_k) - \frac{1}{\left[1+\phi/(2iDa)\right]} \left(\frac{\nabla T_m \nabla p_1}{\omega^2 \rho_m \sigma} + \frac{i\nabla T_m}{\omega\sigma} \frac{2F\phi}{i\omega\sqrt{K}} u_0^2 \right) \times \left\{ \frac{\left[\mathrm{Pr}\,\sigma - \phi/(2iDa) - 1\right] - \mathrm{Pr}\,\sigma\, f_\nu + f_k \left[1+\phi/(2iDa)\right]}{\left[\mathrm{Pr}\,\sigma - \phi/(2iDa) - 1\right]\left[1+\phi/(2iDa)\right]} \right\}. \quad (5.18)$$

The definitions of f_ν and f_k are given by the following equations:

$$f_\nu = \frac{\tanh\left[(1+i)\sqrt{1+\phi/(2iDa)}\, S_w\right]}{(1+i)\sqrt{1+\phi/(2iDa)}\, S_w} \text{ and } f_k = \frac{\tanh\left[(1+i)\sqrt{\sigma\,\mathrm{Pr}}\, S_w\right]}{(1+i)\sqrt{\sigma\,\mathrm{Pr}}\, S_w}. \quad (5.19)$$

Detail discussions on the thermal field with graphical interpretation are left for the results and discussions section.

5.5 Energy Flux Density

Equation (4.28) is used to evaluate the energy flux density ($\dot{\mathbf{E}}$) or total energy flow along the stack. In steady-state, for a thermoacoustic engine/refrigerator without heat flows to the

surroundings, the time-averaged energy flux ($<\dot{\mathbf{E}}>$) along the x direction is independent of x (Swift [2002]). The magnitude of $\dot{\mathbf{E}}$ is the amount of energy passing, in unit time, through a unit area perpendicular to the direction of the fluid velocity (Landau and Lifshitz [1982]). For the present problem, the $\mathbf{v}\cdot\boldsymbol{\sigma}$ (work done by viscous shear) term can be neglected by considering the long-wave approximation (Swift [2002]). The flow of kinetic energy can also be neglected since it is proportional to the cube of the velocity. By considering these assumptions along with other assumptions already mentioned in Appendix A, Eq. (4.28) reduces to

$$\dot{\mathbf{E}} \approx \rho u h - k\frac{\partial T}{\partial x}. \tag{5.20}$$

The unit of $\dot{E}$ in Eq. (5.20) is W/m^2. The functional relationship of the enthalpy with the entropy and pressure, i.e., $h = f(s, p)$ (Bejan [1984] and Swift [2002]), leads to the following:

$$h = C_p dT + (1 - T\beta)\frac{dp}{\rho}. \tag{5.21}$$

Integrating Eq. (5.21) results in an expression for h in terms of s and p. Using a linear thermoacoustic expansion, $\dot{E}$ in Eq. (5.20) can be simplified further to

$$\dot{\mathrm{E}}_2 \approx \rho_m C_p (T_1 u_1) + (1 - T_m\beta)(p_1 u_1) - k\frac{\partial T_m}{\partial x}. \tag{5.22}$$

Subscript "2" is used in Eq. (5.22) to indicate that energy flux density is a product of two first order quantities. The thermodynamic relation $s_1 = (C_p / T_m)T_1 - (\beta / \rho_m)p_1$ is used to obtain Eq. (5.22). After time and space averaging, the energy flux (E_2, in W) along x becomes

$$\mathrm{E}_2 = \Pi\rho_m C_p \int_0^{y_0} \overline{T_1 u_1} dy + \Pi(1 - \beta T_m)\int_0^{y_0} \overline{p_1 u_1} dy - y_0 \Pi k \nabla T_m. \tag{5.23}$$

In Eq. (5.23), an overbar ($-$) over a quantity represents time averaging. If Eq. (5.7) for u_1 and Eq. (5.15) for T_1 are substituted into Eq. (5.23), and the integrations are performed,

$$
\mathrm{E}_2 = \frac{y_0\Pi}{2}\Re\left[\begin{array}{l}
-\dfrac{ip_1\nabla\tilde{p}_1}{\omega\rho_m}\Lambda_1\left[1+\phi/(2iDa)\right]\left\{\Lambda_2+\dfrac{\phi\beta T_m}{\sigma}\Lambda_3\right\}+\dfrac{i\nabla T_m C_p}{\omega^3\rho_m\sigma}\nabla p_1\nabla\tilde{p}_1\Lambda_1\left\{\Lambda_2-\Lambda_4-\Lambda_5\right\} \\
+\dfrac{i\Lambda_6}{\omega\rho_m}p_1\nabla\tilde{p}_1\Lambda_1\left[1+\phi/(2iDa)\right]\Lambda_2+\dfrac{2F u_0^2\phi p_1\Lambda_1\left[1+\phi/(2iDa)\right]}{i\omega\sqrt{K}}\left\{\Lambda_2\left(1-\Lambda_6\right)+\dfrac{\phi\beta T_m}{\sigma}\Lambda_3\right\} \\
+\dfrac{u_0 C_p\nabla T_m\Lambda_1}{\omega^2\sigma}\dfrac{2F u_0\phi}{i\omega\sqrt{K}}\left(\Lambda_4-\Lambda_2\right)\left(\nabla\tilde{p}_1+\nabla p_1\right)-\dfrac{u_0^2\rho_m C_p}{\omega\sigma}\left(\dfrac{2F u_0\phi}{i\omega\sqrt{K}}\right)^2\nabla T_m\Lambda_1\left(\Lambda_2-\Lambda_4\right)+ \\
\dfrac{\nabla T_m}{\omega^2\sigma}\dfrac{\Lambda_3\Lambda_1\left[1+\phi/(2iDa)\right]}{\left[\sigma\,\mathrm{Pr}-\phi/(2iDa)-1\right]}\left\{\dfrac{2F u_0\phi}{i\omega\sqrt{K}}\nabla\tilde{p}_1+\dfrac{2F u_0\phi}{i\omega\sqrt{K}}\nabla p_1+i\omega\left(\dfrac{2F u_0\phi}{i\omega\sqrt{K}}\right)^2 u_0\rho_m C_p\right\}
\end{array}\right], \quad (5.24)
$$

$$
-y_0\Pi k\frac{\partial T_m}{\partial x}
$$

with

$$
\Lambda_1 = \frac{1}{\left[1+\phi/(2iDa)\right]\left[1-\phi/(2iDa)\right]}, \quad (5.24a)
$$

$$
\Lambda_2 = 1-\tilde{f}_\nu, \quad (5.24b)
$$

$$
\Lambda_3 = \frac{\left[1-\phi/(2iDa)\right]}{\sigma\,\mathrm{Pr}-\phi/(2iDa)+1}\left(\tilde{f}_\nu - f_k\right), \quad (5.24c)
$$

$$
\Lambda_4 = \frac{\sigma\,\mathrm{Pr}}{\sigma\,\mathrm{Pr}-\phi/(2iDa)-1}\frac{\left(f_\nu-\tilde{f}_\nu\right)-\phi/(2iDa)\,f_\nu+\phi/(2iDa)\,\tilde{f}_\nu}{2}, \quad (5.24d)
$$

$$
\Lambda_5 = \frac{\left[1-\phi/(2iDa)\right]\left[1+\phi/(2iDa)\right]}{\left[\sigma\,\mathrm{Pr}-\phi/(2iDa)+1\right]\left[\sigma\,\mathrm{Pr}-\phi/(2iDa)-1\right]}\left(\tilde{f}_\nu - f_k\right), \quad (5.24e)
$$

$$
\Lambda_6 = \beta\phi\frac{T_m(\sigma-1)}{\sigma}. \quad (5.24f)
$$

Where $\Re$ [ ] signifies the real part and tilde (~) denotes the complex conjugation. Equation (5.24) is compared with Eq. (A30) of Swift [1988] for the limiting cases. The two expressions agree with each other for the limiting cases of non-porous media ($K\to\infty$, $\sigma=1$) and Forchheimer's coefficient $F=0$. Equation (5.24g) presents Eq. (A 30) of Swift [1988]. These comparisons of fluctuating velocity, temperature, and energy flux density expressions to that of Swift [1988]'s

equations verify that the systems of equations developed in the present investigations are free from errors.

$$\mathrm{E}_2 = \frac{y_0\Pi}{2\omega\rho_m}\Im\left[p_1\frac{d\tilde{p}_1}{dx}\left\{1-\tilde{f}_\nu-\beta T_m\frac{f_k-\tilde{f}_\nu}{1+\mathrm{Pr}}\right\}\right]+\frac{y_0\Pi C_p}{2\omega^3\rho_m(1-\mathrm{Pr})}\frac{dp_1}{dx}\frac{d\tilde{p}_1}{dx}\frac{dT_m}{dx}\times \Im\left[\tilde{f}_\nu+\frac{f_k-\tilde{f}_\nu}{\mathrm{Pr}+1}\right]-k\,y_0\Pi\frac{dT_m}{dx} \quad . \tag{5.24g}$$

The global work flux (W_2) alone is estimated by integrating the time-averaged product of the fluctuating velocity and pressure with respect to *y* (Swift [1988]) from the channel centerline to the wall. The resulting equation is

$$\mathrm{W}_2 = \Pi\int_0^{y_0}\overline{p_1u_1}dy = \frac{y_0\Pi}{2}\Re\left[\left\{-\frac{1}{\omega\rho_m}\frac{ip_1\nabla\tilde{p}_1}{1-\phi/(2iDa)}+\frac{p_1}{1-\phi/(2iDa)}\frac{2F\phi}{i\omega\sqrt{K}}u_0^2\right\}\left(1-\tilde{f}_\nu\right)\right]. \tag{5.25}$$

The ratio of Eq. (5.24) to Eq. (5.25) gives the COP of a thermoacoustic heat pump (Swift [2002]) assuming that the energy flow from the cold side of the stack is removed at the hot side of the stack.

5.6 Results and Discussions

The expressions for several thermoacoustic parameters (e.g., the fluctuating velocity, temperature, and energy flux density) are derived in the previous sections. In this section, graphical results are presented along with interpretations of the derived expressions and experimental measurements. The geometric properties of the 45 PPI RVC stack obtained from Fu et al. [2001] are $\phi = 0.92$, $K = 2.09\times10^{-8}\,m^2$, and F=0.08 in Eq. (5.7), physical properties of RVC stack are collected from ERG [2009], and the length and the outer diameter of the stack are 4 cm and 2 cm, respectively. The value of u_0 in Eq. (5.7) is a reference velocity which is assumed to be the velocity amplitude at the velocity anti-node and equals 0.875 m/s for the present experimental conditions. The Reynolds number (Re) based on the velocity at the velocity anti-node for the present experimental condition is 50, where $\mathrm{Re} = \rho_m u_1 d/\mu$. At this Reynolds

number, the flow is dominated by inertia effects (Kaviany [1995]), therefore using Brinkman-Forchheimer-extended Darcy model in the present study is justified.

5.6.1 Discussion on the Flow Field

The expression of the fluctuating velocity (u_1), given in Eq. (5.7) is a function of stack geometry, porosity, permeability, viscous penetration depth (δ_v), Forchheimer coefficient (F), Swift number (S_w), and transverse distance (Y). Figure 5.2 shows the distribution of non-dimensional velocity (U), the expression of which can be obtained after dividing Eq. (5.7) by Eq. (5.9) and is given by

$$U = \left\{ \frac{(1+i)\sqrt{1+\phi/(2iDa)}\, S_w}{(1+i)\sqrt{1+\phi/(2iDa)}\, S_w - \tanh\left[(1+i)\sqrt{1+\phi/(2iDa)}\, S_w\right]} \right\} \left\{ 1 - \frac{\cosh\left[(1+i)\sqrt{1+\phi/(2iDa)}\, S_w Y\right]}{\cosh\left[(1+i)1+\phi/(2iDa) S_w\right]} \right\} \tag{5.26}$$

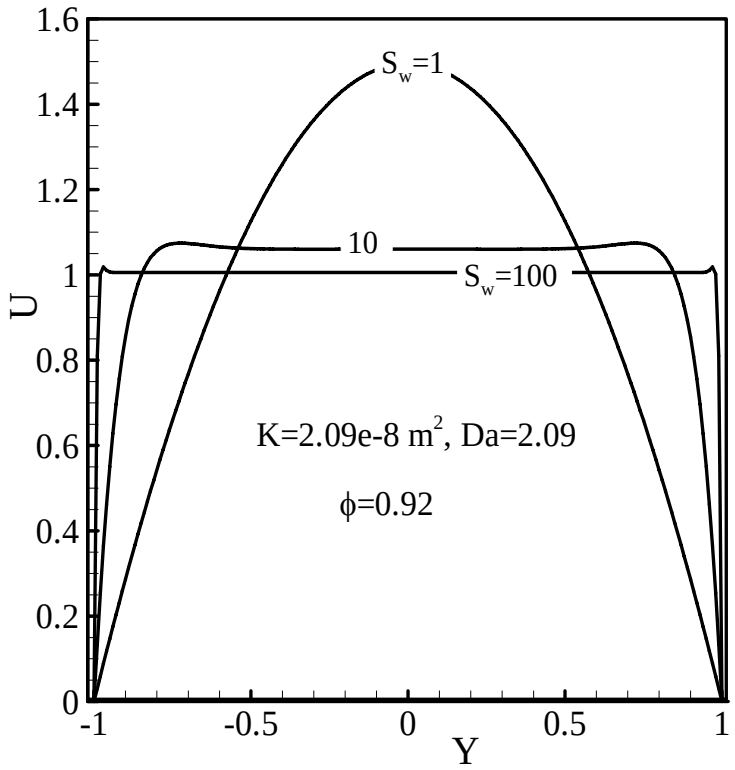

Figure 5.2: Dimensionless velocity as functions of S_w at Da=2.09.

Similar to the fluctuating velocity (u_1), the non-dimensional velocity (U) also has two terms, one is Y dependent (the hyperbolic cosine function in the numerator) and the other one is Y

independent. Figure 5.2 shows the non-dimensional velocity (U) as a function of non-dimensional transverse distance (Y) at different values of S_w. A relatively large S_w results in a thin shear layer adjacent to the boundary wall within a few viscous penetration depths. A large portion of the fluid away from the wall is unaffected by the viscous effect imposed by the boundary walls during a time period of oscillation at large S_w. As S_w approaches to a very large value ($S_w = 100$, experimental conditions considered in Chapter 7), the velocity profile becomes almost *y*-independent. In contrast to larger S_w, as S_w decreases and approaches relatively small values ($S_w = 1$), the velocity profile approaches to a shape similar to that seen in the plane Poiseuille flow (Landau and Lifshitz [1982]). At relatively lower S_w (S_w=1 or 10), the momentum boundary layer effect starts to increase, thereby increasing the velocity above the average velocity near the center line. At larger S_w (S_w=100), the effect of momentum boundary

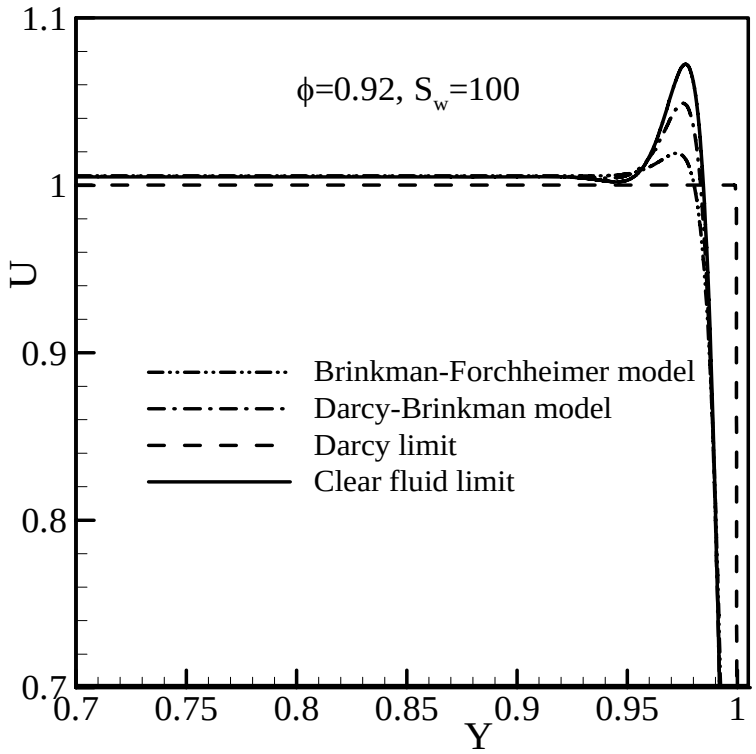

Figure 5.3: Dimensionless velocity as functions of different modeling approximations.

layer is negligible and flow near the center line is the average velocity of the channel. The values of S_w other than the experimental condition are shown to indicate the effect of the channel distance on the non-dimensional velocity. Figure 5.3 shows the non-dimensional velocity (U) as

a function of non-dimensional transverse distance (Y) for different modeling approximations of the momentum equation for the experimental conditions used in Chapter 7. Variation of U with respect to Y is observed only within the momentum boundary layer. The thickness of the momentum boundary layer is negligible for the Darcy limit. The effects of different modeling approximations of the momentum equation in the free stream region except the Darcy limit are almost negligible. The boundary and inertia effects are concentrated near the wall, and therefore, neglecting inertia effect (dash-dot line), or both inertia and viscous effects (dashed line, Darcy limit) change the peak non-dimensional velocity value near the wall only. To describe the shape of the non-dimensional velocity: at the wall, at $Y = 1$, the hyperbolic cosine term in Eq. (5.26) is unity, therefore resulting a non-dimensional zero velocity mathematically. As one moves away from the wall, the hyperbolic cosine term in Eq. (5.26) rapidly decreases from unity (showing lower non-dimensional magnitudes than the wall), becomes negative, therefore, showing values above the averaged velocity near the wall. As one continues to move farther away from the wall, the hyperbolic cosine term in Eq. (5.26) decreases gradually and becomes zero, therefore, showing negligible effect of the wall near the center of the channel at higher $S_w\,(=100)$. At lower $S_w\,(=1)$, the hyperbolic cosine term in Eq. (5.26) gradually decreases from 1 and thus showing lower non-dimensional magnitudes than the wall. As we continue to move farther away from the wall, this term becomes negative and shows values above the averaged velocity near the center of the channel. The hyperbolic tangent term in Eq. (5.26) is constant in the vertical direction, and hence does not affect the non-dimensional velocity profile.

5.6.2 Discussion on the Thermal Field

Similar to the fluctuating velocity (u_1) (Eq. (5.7)), the expression of the fluctuating temperature T_1, given in Eq. (5.15), is a superposition of a *y* independent temperature component represented by the terms before the first curly bracket and *y*-dependent components represented by the terms with the hyperbolic cosine functions. Figure 5.4 shows the non-dimensional temperature (Θ), the expression of which can be obtained after dividing Eq. (5.15) by Eq. (5.18) and is given by

$$\Theta = \frac{\theta_1 - \theta_2\left\{1 - \Pr' \dfrac{\cosh\left[(1+i)\sqrt{1+\phi/(2iDa)}S_w Y\right]}{\cosh\left[(1+i)\sqrt{1+\phi/(2iDa)}S_w\right]}\right\} - \left\{\theta_1 - \theta_2 + \Pr'\theta_2\right\}\dfrac{\cosh\left[(1+i)\sqrt{\sigma\,\Pr}\,S_w Y\right]}{\cosh\left[(1+i)\sqrt{\sigma\,\Pr}\,S_w\right]}}{\theta_1(1-f_k) - \theta_2\left\{\dfrac{\left[\Pr\sigma - \phi/(2iDa) - 1\right] - \Pr\sigma\, f_\nu + f_k\left[1+\phi/(2iDa)\right]}{\left[\Pr\sigma - \phi/(2iDa) - 1\right]\left[1+\phi/(2iDa)\right]}\right\}}. \quad (5.27)$$

In Fig. 5.4 the non-dimensional temperature (Θ) is plotted as a function of non-dimensional transverse distance (Y) at different values of S_w. At a lower S_w (e.g., $S_w = 1$), the non-

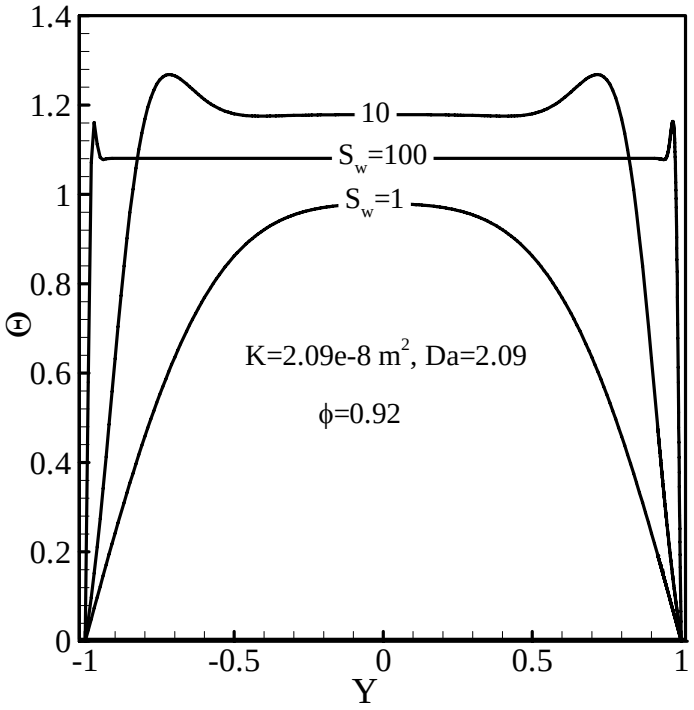

Figure 5.4: Dimensionless temperature as functions of S_w at Da=2.09.

dimensional temperature profile follows the similar trend to that of non-dimensional velocity as shown in Fig. 5.2. At higher S_w (e.g., $S_w = 10$), a high near wall temperature gradient and flat temperature distribution around the channel centerline characterize the non-dimensional temperature distribution. At $S_w = 100$, which is the experimental condition in the present investigation, the non-dimensional temperature distribution is flat through out the channel height except near the wall. The reason for the variation of the non-dimensional temperature (Θ) as a function of non-dimensional transverse distance (Y) at a particular S_w is the change of the

hyperbolic cosine term at the numerator of Eq. (5.27). Because only this term depends on the non-dimensional transverse distance (Y) at a particular S_w, while the remaining terms are independent of Y. One interesting feature observed in Fig. 5.4 is the variation of center line non-dimensional temperature along the non-dimensional transverse distance. At larger S_w (e.g., $S_w = 100$), the less mixing of the fluid suppresses the longitudinal convection. In contrast, the transverse conduction process is enhanced. These combined effects result in a minor variation in the non-dimensional temperature profiles for a given time period of oscillation. At lower S_w (e.g., $S_w = 10$), the rigorous mixing of the fluid causes a balance between longitudinal convection and the transverse conduction, and thus results in a more uniform non-dimensional temperature profile. At much less S_w (e.g., $S_w = 1$), longitudinal convection dominates the transverse conduction, and thus results in a parabolic non-dimensional temperature profile.

From discussion in **Section** 5.6.1, it is clear that in the limit of a very large S_w, the terms with the hyperbolic cosine functions in Eq. (5.15) become zero which results in the *y*-independent temperature component only, i.e.,

$$\lim_{S_w \to \infty}(T_1) = \frac{\phi \beta T_m p_1}{\rho_m C_p \sigma} - \frac{1}{1+\phi/(2iDa)}\left[\frac{\nabla T_m \nabla p_1}{\omega^2 \rho_m \sigma} + \frac{i \nabla T_m}{\omega \sigma}\left(\frac{2F u_0^2 \phi}{i\omega\sqrt{K}}\right)\right], \tag{5.28a}$$

$$\text{alternatively, } \lim_{s_W \to \infty}(T_1) = \frac{\phi T_{ad}}{\sigma} - \frac{T_{sw}}{\sigma\left[1+\phi/(2iDa)\right]} = T_0 . \tag{5.28b}$$

In Eq. (5.28a) and Eq. (5.28b), the appearance of ϕ, σ and $\left[1+\phi/(2iDa)\right]$ terms in the expression of T_0 signify the influence of the porous medium. T_{ad} $(= \beta T_m p_1 / \rho_m C_p)$ is the fluctuating temperature due to an adiabatic compression and expansion of the fluid in the absence of a porous medium (Swift [1988]) and $T_{sw} = \left[\nabla T_m \nabla p_1/(\omega^2 \rho_m) + 2F\,\nabla T_m u_0^2 \phi/(\omega^2\sqrt{K})\right]$ represents a modified standing wave temperature amplitude with momentum inertia influence in it. As the fluid oscillates along the *x* direction with an equivalent displacement amplitude u_0/ω (where $u_0 = \nabla p_1/\omega\rho_m$) the temperature at a

given point in space oscillates by an amount $\left[1+2F\,u_0\phi/(\omega\sqrt{K})\right](\nabla T_m u_0/\omega)$ $(=T_{sw})$. In Eq. (5.28a), the fluid properties, flow properties, porous medium properties, temperature gradient, and geometry can be set in such a way that both the terms on the right hand side of Eq. (5.28a) become equal, resulting in $T_0 = 0$. For such a unique case, the resulting temperature gradient is proposed to be a critical temperature gradient (∇T_{cr}) and is given by

$$\nabla T_{cr} = \frac{\sqrt{K}\,p_1}{\sqrt{K}\nabla p_1 + 2\rho_m F\,u_0^2\phi}\frac{\beta T_m\omega^2}{C_p}\left[1+\phi/(2iDa)\right] . \tag{5.29}$$

The critical temperature gradient determines the transition between the heat pump and prime mover functions of thermoacoustic devices (Swift [1988]). Typically, $\nabla T_m > \nabla T_{cr}$ signifies a heat engine mode of operation and $\nabla T_m < \nabla T_{cr}$ signifies a heat pump/refrigerator mode of operation for thermoacoustic devices. The ratio of ∇T_{cr} to ∇T_m can be termed the *temperature gradient ratio* (Γ_0) as proposed by Mahmud and Fraser [2009]. For the current problem Γ_0 can be expressed as:

$$\Gamma_0 = \frac{T_{ad}}{T_{sw}}\left[1+\phi/(2iDa)\right] . \tag{5.30}$$

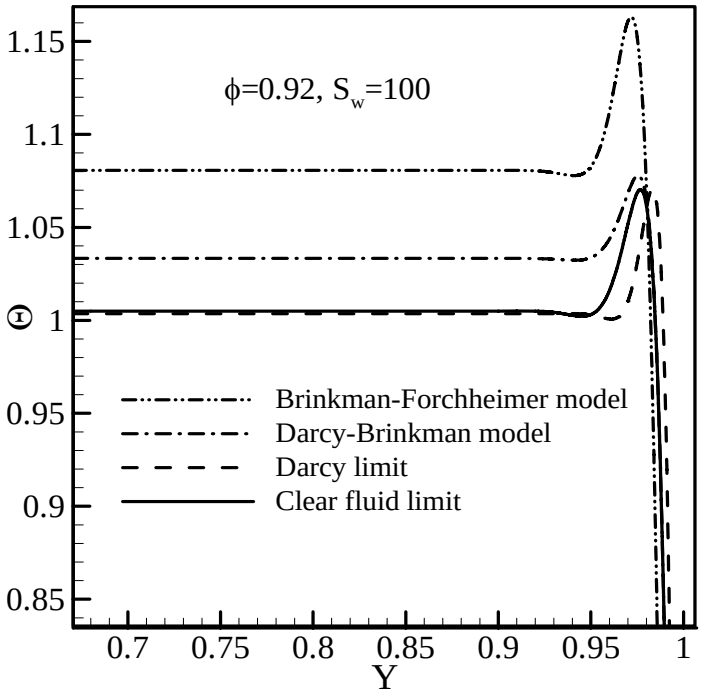

Figure 5.5: Dimensionless temperature as functions of different modeling approximations.

Figure 5.5 shows the non-dimensional temperature (Θ) as a function of non-dimensional transverse distance (Y) for different modeling approximations of the momentum equation for the experimental conditions used in Chapter 7. At $S_w = 100$, the variation of Θ is observed only near the wall in the vertical direction. Since, thermoacoustic effect is concentrated near the wall around a thermal penetration depth distance. Therefore, variation of Θ is observed only near the wall where thermoacoustic effect is present. The rest of the vertical distance shows no variation of Θ because of the absent of thermoacoustic effect. The values of Θ are higher throughout the transverse direction for the Brinkman–Forchheimer–extended Darcy model compared to the Darcy–Brinkman model. The reason for higher Θ for the Brinkman–Forchheimer–extended Darcy model may be the inertia term compared to the Darcy– Brinkman model. Figure 5.5 shows that neglecting inertia and solid boundary effects may lead to appreciable errors in thermal field and heat transfer computations.

5.6.3 Discussion on Heat Flux Density

As stated before, the energy flux density expression (E_2), presented in Eq. (5.23) or Eq. (5.24), has three terms in it. For an ideal gas with negligible longitudinal conduction the second and third terms of E_2 disappears (see Eq. (5.23) for better understanding). In such a case, the energy flux density equation is simplified to the hydrodynamic heat flux density equation (Q_2). The hydrodynamic heat flux density alone can be calculated using the following equation: Q_2 ($Q_2 = \Pi \rho_m C_p / 2\Re \int_0^{y_0} T_1 \tilde{u}_1 dy$). In this section, Q_2 is investigated in order to understand how heat flux changes with changes in the different thermoacoustic parameters (e.g., Da, S_w, etc.). Using Eq. (5.7) for fluctuating velocity and Eq. (5.15) for fluctuating temperature, the hydrodynamic heat flux density becomes

$$Q_2 = \frac{y_0 \Pi}{2} \Re \left[\begin{array}{l} \left\{ -\dfrac{i\phi\beta T_m p_1 \nabla \tilde{p}_1}{\omega\sigma\rho_m\left[1-\phi/(2iDa)\right]} - \dfrac{\phi\beta T_m p_1}{\sigma} \dfrac{\tilde{F}_u u_0}{\left[1-\phi/(2iDa)\right]} \right\} \left\{ 1 - \dfrac{\left[1-\phi/(2iDa)\right]\ f_k + \Pr\sigma \tilde{f}_\nu}{\sigma\Pr+1-\phi/(2iDa)} \right\} + \\ \left\{ \dfrac{-i\nabla T_m \nabla \tilde{p}_1 \nabla p_1 C_p}{\omega^3 \sigma \rho_m \left|1+\phi/(2iDa)\right|^2} + \dfrac{\nabla T_m C_p}{\sigma\omega^2} \left(\dfrac{2Fu_0\phi}{i\omega\sqrt{K}} \right)^2 \dfrac{\nabla p_1}{\left|1+\phi/(2iDa)\right|^2} u_0^2 (\nabla p_1 + \nabla \tilde{p}_1) - \right. \\ \left. \quad + \dfrac{i\nabla T_m C_p \rho_m}{\sigma\omega} \left(\dfrac{2Fu_0\phi}{i\omega\sqrt{K}} \right)^2 \dfrac{u_0^2}{\left|1+\phi/(2iDa)\right|^2} \right\} \times \\ \left\{ \dfrac{\sigma\Pr\ f_\nu}{\sigma\Pr-1-\phi/(2iDa)} - \dfrac{f_k\left[1+\phi/(2iDa)\right]}{\sigma\Pr-1-\phi/(2iDa)} - \left(1-\tilde{f}_\nu\right) - \dfrac{\sigma\Pr}{\sigma\Pr-1-\phi/(2iDa)} \right. \\ \left. \times \dfrac{f_\nu\left[1+\phi/(2iDa)\right] + \tilde{f}_\nu\left[1-\phi/(2iDa)\right]}{2} + \dfrac{\left[1+\phi/(2iDa)\right]}{\sigma\Pr-1-\phi/(2iDa)} \dfrac{\sigma\Pr\ f_k + \tilde{f}_\nu\left[1-\phi/(2iDa)\right]}{\sigma\Pr+1-\phi/(2iDa)} \right\} \end{array} \right] \tag{5.31}$$

Figure 5.6 shows the variation in Q_2 as a function of S_w at different Da. Note that for the present experimental conditions Da is equal to 2. Since, working fluid and operating conditions are unchanged in the present experimental condition, the viscous penetration depth (δ_ν) is constant. Therefore, Da is only changed while different porosities (ϕ) RVC stack is used.

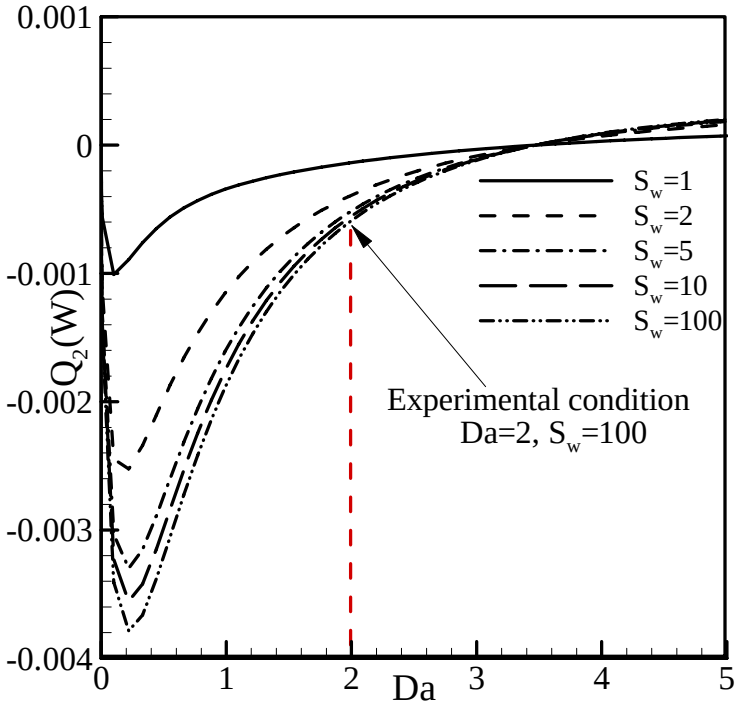

Figure 5.6: Heat flux as a function of S_w.

Permeability (K) of RVC stack will increase from 2.09×10^{-8} m^2 if less porous stacks are used, and decrease if high porosities stacks are used. For the selected range of Da in Fig. 5.6(a), Q_2 is negative which reveals that the heat is absorbed by the considered thermoacoustic system. An increasing Da from $Da = 0.1$ exhibits an increase in the magnitude of Q_2 and shows its maximum when $Da \approx 0.25$. Further increase in the Da decreases the magnitude of Q_2. Therefore, to increase the hydrodynamic heat flux along the stack (which is the power density of a thermoacoustic device), Da should be less than 1. Using higher porosity stack will result in high Q_2. For a constant Da, the magnitude of Q_2 shows increasing trend with increasing S_w. Figures 5.6 also supports Mahmud and Fraser's finding [2009], who showed that if a porous medium is used in between the thin parallel plates, much more efficient thermoacoustic engine designs are possible in the Da range 0.1-1.0 and $S_w > 2$. Using higher porosity stack will result in high Q_2 which is also supported by the experimental results in Chapter 7. Increasing S_w further is insignificant on Q_2. Figure 5.7 shows the mesh contour plot of Q_2 corresponding to Da and Forchheimer coefficient, F. Maximum Q_2 is obtained at Da less than 1 and F between 0.075-0.085, i.e., at higher F values.

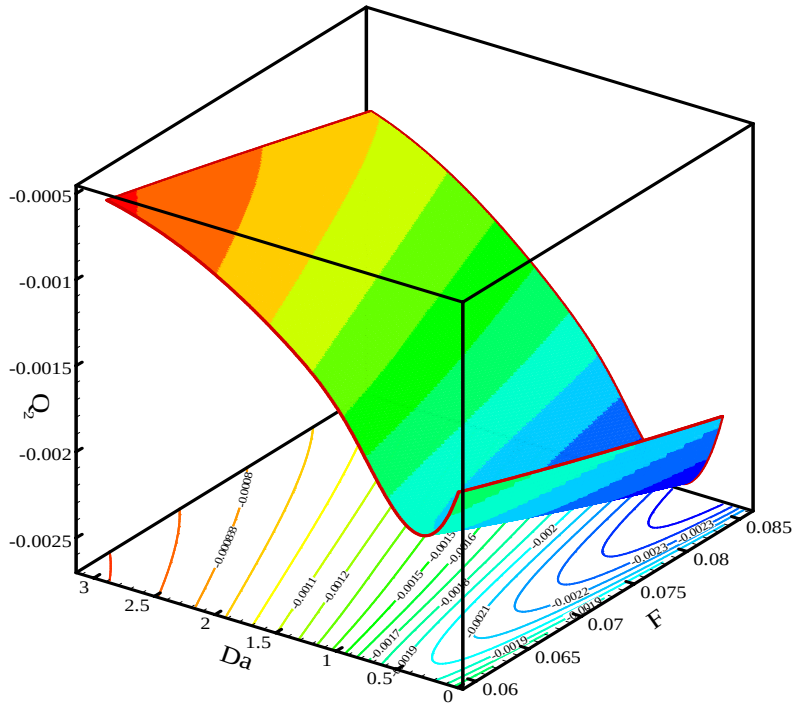

Figure 5.7: Mesh contour plot of heat flux (Q_2) as a function of Da and F.

5.6.4 Validation of the Modeling and Comparison with Other Works

Now, the temperature difference generated across the stack ends (ΔT) is derived from Eq. (5.23) neglecting the third term. This approach was followed by Atchley et al. [1990]). In steady state, at each point along the stack (according to Atchely et al. [1990]) it can be assumed that

$$E_2 - kA\frac{dT_m}{dx} = 0, \tag{5.32}$$

where kA is the product of diffusive thermal conductivity and cross sectional area of the stack. This assumes that hydrodynamic energy flow in the gas is balanced by the returned diffusive heat transfer through the porous medium. Inserting Eq. (5.23) (neglecting the third term as mentioned before) into (5.32), solving for dT_m/dx, and then integrating with respect to x over the length of the stack $\Delta x = L_s$ gives, for $\Delta T = T_H - T_C$ and for a short enough stack that we can replace spatially averaged values by their values at the center (x) of the stack,

$$\Delta T = \frac{\text{Numerator}}{\text{Denominator}_1 \text{ - Denominator}_2} L_s . \tag{5.33}$$

$$\text{Numerator} = \frac{y_0\Pi}{2}\Re\left[\begin{array}{l}\dfrac{ip_1\nabla\tilde{p}_1}{\omega\rho_m}\Lambda_1\left[1+\phi/(2iDa)\right]\left\{\Lambda_2+\dfrac{\phi\beta T_m}{\sigma}\Lambda_3\right\}-\dfrac{ip_1\nabla\tilde{p}_1\Lambda_1\Lambda_2\Lambda_6\left[1+\phi/(2iDa)\right]}{\omega\rho_m} \\ -\dfrac{2F\,u_0^2\phi}{i\omega\sqrt{K}}P_1\,\Lambda_1\left[1+\phi/(2iDa)\right]\left\{\Lambda_2(1-\Lambda_6)+\dfrac{\beta T_m}{\sigma}\Lambda_3\right\}\end{array}\right], \tag{5.34}$$

$$\text{Denominator}_1 = \frac{y_0\Pi}{2}\Re\left[\begin{array}{l}\dfrac{iC_p}{\omega^3\rho_m\sigma}\nabla p_1\nabla\tilde{p}_1\Lambda_1\{\Lambda_2-\Lambda_4-\Lambda_5\}+\dfrac{u_0C_p}{\omega^2\sigma}\Lambda_1(\Lambda_4-\Lambda_2)\left(\dfrac{2F\,u_0\phi}{i\omega\sqrt{K}}\right)(\nabla\tilde{p}_1+\nabla p_1) \\ +\dfrac{iu_0^2\rho_mC_p}{\omega\sigma}\Lambda_1(\Lambda_4-\Lambda_2)\left(\dfrac{2F\,u_0\phi}{i\omega\sqrt{K}}\right)^2+\dfrac{\Lambda_3\Lambda_1}{\omega^2\sigma}\dfrac{\left[1+\phi/(2iDa)\right]}{\left[\sigma\,\mathrm{Pr}-\phi/(2iDa)-1\right]} \\ \times\left(\dfrac{2F\,u_0\phi}{i\omega\sqrt{K}}\right)\left[\nabla\tilde{p}_1+\nabla p_1+i\omega\left(\dfrac{2F\,u_0\phi}{i\omega\sqrt{K}}\right)u_0\,\rho_mC_p\right]\end{array}\right], \tag{5.35}$$

and

$$\text{Denominator}_2 = ky_0\Pi . \tag{5.36}$$

The expression derived in Eq. (5.33) is compared with the existing solution available in the existing literature (Swift [2002]) and also with the experimental results in Chapter 7.

The goal of this section is to test the validity of Eq. (5.33) under a wide range of conditions. One way of testing the validity of Eq. (5.33) is to compare it with experimental results performed in Chapter 7. Another way is to find an expression of temperature difference (ΔT) for the linear theory and compare it with Eq. (5.33). To obtain an expression of steady state temperature difference across the stack ends for linear theory (Swift [1988]), Eq. (5.26) of Swift [2002] is utilized to predict the longitudinal energy flow along the stack, and using Eq. (5.32) that balances the energy flow along the stack. The expression for ΔT then becomes,

$$\Delta T = \frac{1}{2}\Re\left[p_1\tilde{U}_1\left(1-\frac{f_k-\tilde{f}_\nu}{(1+\mathrm{Pr})(1-\tilde{f}_\nu)}\right)\right]\left[kA-\frac{\rho_m C_p |U_1|^2}{2A\omega(1-\mathrm{Pr}^2)|1-f_\nu|^2}\Im\left(f_k+\mathrm{Pr}\,\tilde{f}_\nu\right)\right]^{-1} L_s . \qquad (5.37)$$

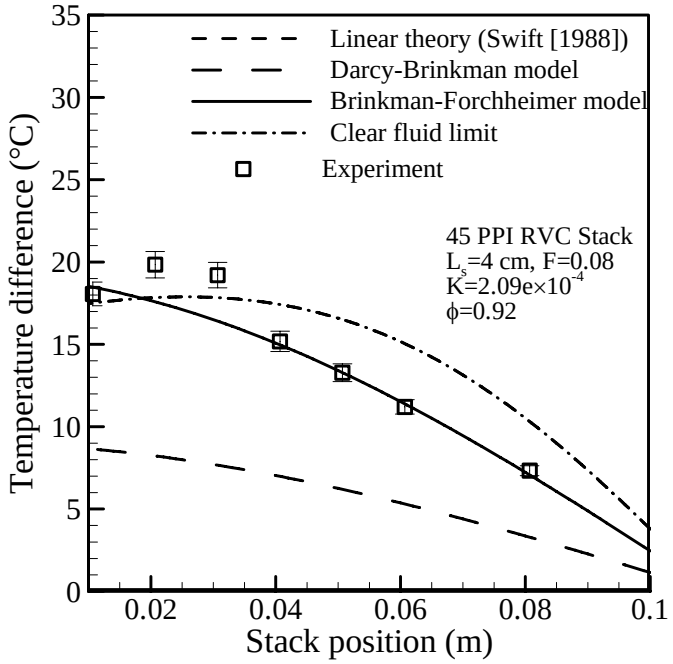

Figure 5.8: Validation of the present modeling.

Figure 5.8 shows the comparison of the present modeling results along with the experimental results plotted as a function of stack position from the pressure anti-node. The error bars in the experimental results indicate the uncertainty of the measurements. A very good agreement is

obtained between the modeling and the experimental results. The modeling prediction is almost within the uncertainty limit of the measurements. *It is observed that maximum difference between the experimental results and the present modeling predictions is 14%.* The reason for the discrepancy between the modeling and the measurements is the assumption used to derive Eq. (5.32). In practical thermoacoustic devices, this assumption is not appropriate, because there is heat transfer by conduction and convection from the stack ends to the surrounding fluid, there is heat leakage through the resonator walls containing the stack section, and there is heat generated by vortices near the stack ends. Because of low operating DR (0.03%) in the experiments, these heat transfer effects have less influence on the total energy flow and the predictions can quite accurately reproduce the experimental results. Figure 5.8 further shows the comparison of the present modeling results with the linear theory prediction of Swift [2002]. Linear theory predictions of Swift [2002]'s thermoacoustic theory are widely used for the design and analysis of thermoacoustic devices. Therefore, it is instructive to compare the present modeling results to that of Swift [2002]'s result. Swift [2002] did not derive any equation to predict the temperature difference across the stack ends at steady state. Therefore, to obtain an expression of steady state temperature difference across the stack ends (Eq. (5.37)), Eq. (5.26) of Swift [2002] is utilized to predict the longitudinal energy flow along the stack, and is combined with Eq. (5.32). To evaluate numerical values from Eq. (5.37), y_0 (half width of the channel) is substituted by RVC foam diameter (according to Wilen [2001]). Since, in linear theory, y_0 is the half width of the stack plate spacing. In order to calculate steady state temperature difference across the stack ends (ΔT), from Eq. (5.37), f_k and f_ν functions as indicated in Eq. (5.37) are evaluated according to Wilen [2001] as

$$f_{k,\nu} = \frac{\tanh\left(\sqrt{i}\,\lambda'_{k,\nu}/2\right)}{\sqrt{i}\,\lambda'_{k,\nu}/2}, \tag{5.38}$$

where

$$\lambda'_{k,\nu} = \frac{\sqrt{2}\times 1.15 R_p}{\delta_{k,\nu}}, \tag{5.39}$$

with

$$\lambda_{k,\nu} = \frac{\sqrt{2}\,y_0}{\delta_{k,\nu}}. \tag{5.40}$$

Equation (5.40) is used to calculate f_k and f_ν functions using Eq. (5.38) for parallel plate stacks and y_0 is the spacing of parallel plate stacks. It is suggested by Wilen [2001] that an RVC stack performs similar to a parallel plate stack whose spacing y_0 is 15 percent larger than the RVC pore size R_p (Eq. (5.39)) specified by the RVC manufacturer. *The maximum difference between the experimental results and the linear theory predictions (Swift [2002]) is 25%. Therefore, the overall agreement between the experimental results and the Brinkman-Forchheimer-extended Darcy model is better than between the experimental results and the linear theory*. Figure 5.8 also presents the temperature difference obtained using different approximations in the modeling of momentum equation. While inertia term is neglected ($F = 0$)

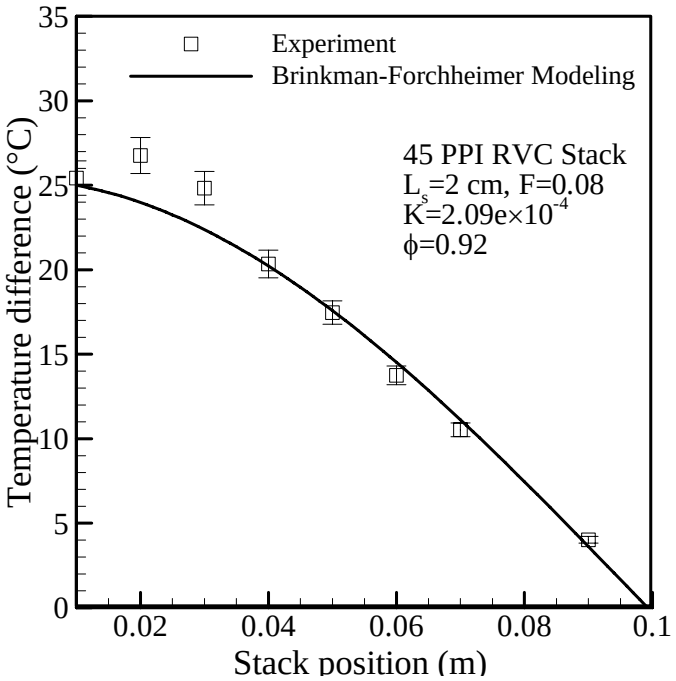

Figure 5.9: Validation of the present modeling.

from Brinkman-Forchheimer-extended Darcy model, the model is Darcy-Brinkman, and Darcy-Brinkman model under predicts the temperature difference obtained across the stack ends. In the clear fluid limit ($K \to \infty, \sigma = 1, F = 0$), the present approximation exactly matches with the linear theory prediction of Swift [1988].

5.7 Conclusions

The primary objective of the present study is to develop an analytical modeling while a porous medium (such as RVC foam) is embedded in between a pair of plates representing stack of thermoacoustic devices. This is accomplished by first formulating the flow in the porous medium by the Brinkman-Forchheimer-extended Darcy model. By using the linear perturbation analysis, the governing momentum and energy equations are linearized and solved in order to obtain the fluctuating velocity, temperature, and energy flux inside the porous medium in terms of several dimensionless parameters; e.g., Da, S_w, and Γ_0. To verify the present study, the temperature difference obtained across the stack ends is compared with the experimental results. A very good agreement is obtained between the modeling and the experimental results. The expression of temperature difference across the stack ends obtained in the present study is also compared with the existing thermoacoustic literature. The proposed expression surpasses the existing expression. The present modeling will help to understand the thermoacoustic effect in random porous media stacks and also to quantify the heat and work flow and thus the performance of such stacks. Random porous medium stacks (such as RVC foams) are very attractive for use in small (millimeter) scale thermoacoustic devices, which can be used as an alternatives to low energy density batteries, sensor networks, micro-electro-mechanical-systems, and other devices.

Chapter 6

Thermally Driven Sustainable Porous Medium Thermoacoustic System

6.1 Introduction

Thermoacoustic heat pumps and refrigerators can be classified according to the source of acoustic energy input. If acoustic energy is supplied by a thermoacoustic engine, the refrigerator is called thermoacoustically-driven thermoacoustic refrigerator (TADTAR) (Babaei and Siddiqui [2008]). In contrast, if the acoustic energy is supplied by an acoustic driver (such as a loudspeaker, pressure wave generator, and a linear motor/alternator coupled to piston/cylinder) (Q-drive [2010]), the device is termed as acoustically-driven thermoacoustic refrigerator (TAR) (Babaei and Siddiqui [2008]). Thermoacoustics is an emerging technology which has intense potential towards the development of sustainable and renewable energy systems by utilizing renewable energy sources. The TADTAR is more attractive from an environmental point of view. The present chapter deals with a TADTAR and the research related to a TAR is left for Chapter 7 and 8.

Recent research efforts in thermoacoustic refrigeration have moved from the use of electrodynamic loudspeakers as a source of the high intensity sound waves required to power these devices (Adeff and Hofler [2000], Holmberg et al. [2003], and Jin et al. [2003]). Thermoacoustic refrigerators can be powered by solar energy, wind generated electricity, and waste heat. Therefore, there is a strong motivation to switch to thermoacoustic refrigeration that can provide cooling without using any environmentally harmful substances, no internal moving parts, and using low grade of energy (for example solar energy). Thermoacoustic refrigerators powered by industrial or vehicles' waste heat will increase the overall performance of the entire system since the amount of total heat rejected to the environment will be reduced. In a typical vehicle system, the

percent of fuel energy lost to coolant and exhaust can be up to 68%. Thus, a complete thermoacoustic refrigeration system in which the heat engine powered by waste heat drives a refrigerator and the entire system has no harmful affects on the environment can be termed as a sustainable refrigeration system.

In the present chapter a thermally driven thermoacoustic heat pump is designed and constructed as set in the objectives. The heat pump is easy to make, uses no moving parts, and has proved to be an impressive illustration of simplicity, an inherent attribute of thermoacoustic engines. At the same time it can be used as working demonstration of a thermoacoustic heat pump.

In this thesis the author has been successful in building a thermoacoustically driven thermoacoustic heat pump which is powered by electric heater cartridges delivering 36 watts of energy directly to the hot heat exchanger of the prime mover section while producing a hot end temperature of 31°C, and a temperature difference of 10°C across the heat pump stack.

The primary objective of this chapter is to design and build a thermoacoustically driven thermoacoustic heat pump that produces a measurable temperature difference. The secondary objective is to identify the location of the prime mover stack that produces enough net acoustic power to overcome the acoustic power losses in the resonator section and to produce maximum temperature difference across the heat pump stack ends. To verify the present results the thermal field measurements are compared with DeltaEC predictions.

This chapter reports the thermal field results along with COP and COPR of the TADTAR calculated using linear theory predictions (using Eqs. (A.16) and (A.17)). Then, a comparison of performance between a TADTAR and a TAR is presented. The next step is to design and build a thermoacoustically driven thermoacoustic refrigerator possibly powered by waste heat.

A simplified thermally driven thermoacoustic heat pump is designed and built which is a combination of a thermoacoustic engine and a heat pump. Figure 6.1(a) shows a schematic diagram of a complete thermoacoustically driven thermoacoustic heat pump (TADTAR). This is a heat driven heat pump which consists of prime mover and heat pump stacks, and four heat exchangers, in a sealed resonator. When thermal energy is applied to the hot heat exchanger, some of the thermal energy is used to generate and sustain an acoustic wave at the prime mover stack ($\dot{W}_2$ is the acoustic energy produced by the stack) and the rest of the thermal energy is dumped to the room temperature

6.2 Experimental Setup

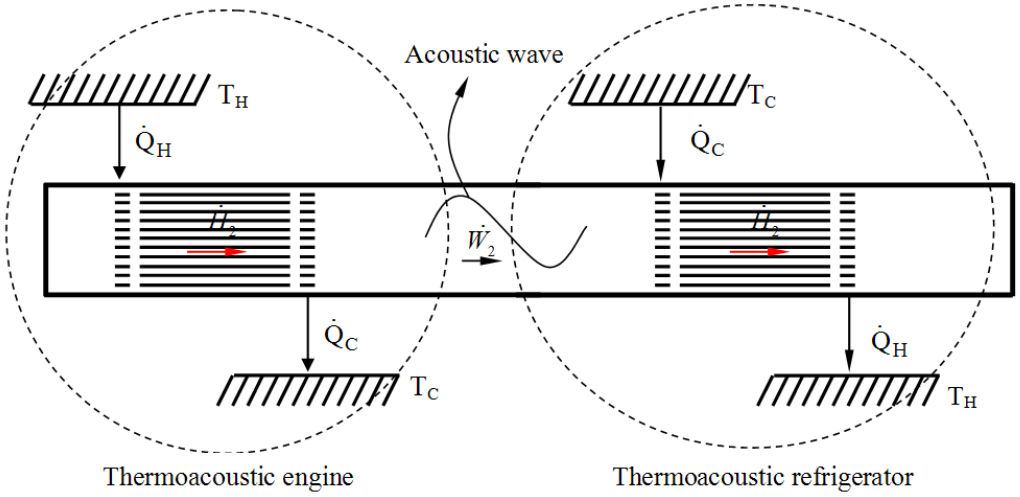

(a)

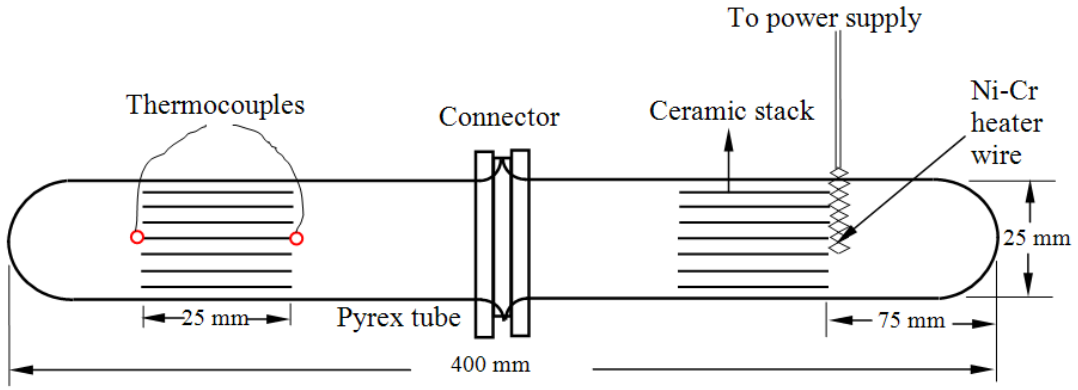

(b)

Figure 6.1: (a) A thermoacoustically driven thermoacoustic heat pump, and (b) A schematic diagram of a thermoacoustically driven thermoacoustic heat pump.

heat exchanger. Then, at the heat pump stack, the acoustic wave works to carry energy ($\dot{H}_2 = \dot{Q}_2 + \dot{W}_2$, is the energy flow through the stack) from the cold heat exchanger to the room temperature heat exchanger. The arrows show the different energy flows into or out of the system except the conductive heat flow which is neglected for ease of representation (in Fig. 6.1(a)).

Figure 6.1(b) shows a schematic diagram of a TADTAR that is built for the present investigation. The objective of this thesis is not to optimize the design of the heat pump, rather to build a TADTAR that produces a measurable amount of temperature difference. The resonator tube is 40 cm in length and has stacks of diameter 2.2 cm, and a length of 2.5 cm. Figure 6.2(a) shows a half wave-length resonant tube with pressure anti-nodes at the closed ends, followed by the temperature distribution along the stacks in Fig. 6.2(b).The TADTAR operates with air at atmospheric pressure and temperature. Figure 6.2(c) shows the energy flow diagram in a TADTAR with detailed descriptions of the terms used in the figure.

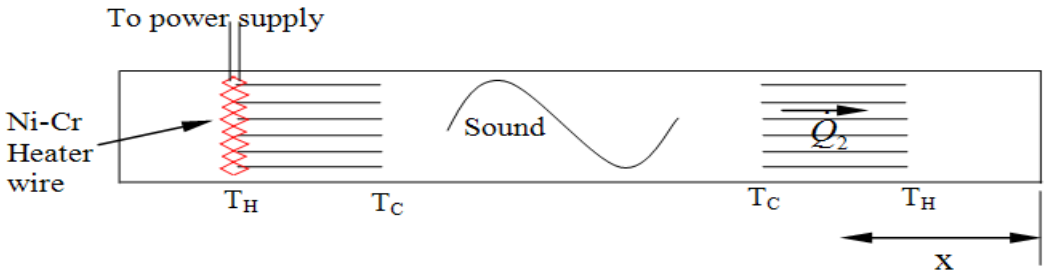

(a) A half wave-length TADTAR with pressure anti-nodes at the closed ends.

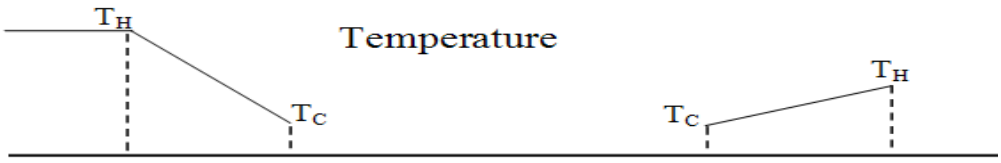

(b) Temperature distribution along the stacks in a TADTAR.

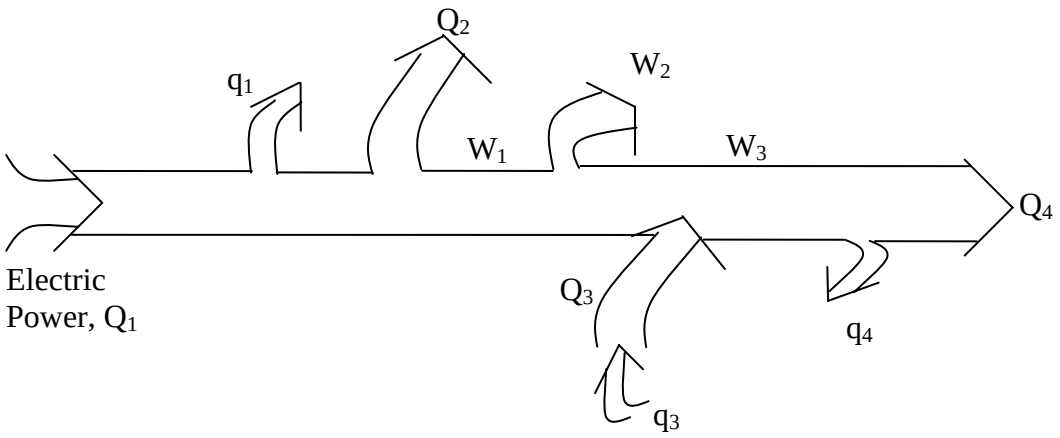

Q_1	(W)	Electric power supplied at high temperature, T_1
Q_2	(W)	Heat removed at ambient heat exchanger (in this setup, no ambient heat exchanger is connected)
Q_3	(W)	Heat supplied at the cold heat exchanger (in this setup, no cold heat exchanger is connected)
Q_4	(W)	Heat removal at ambient heat exchanger (in this setup, no ambient heat exchanger is connected)
q_1	(W)	Conduction, convection and radiation heat loss
q_3	(W)	Conduction and convection heat loss, and pressure amplitude related term
q_4	(W)	Conduction and convection heat loss, and pressure amplitude related term
W_1	(W)	Acoustic power output of the engine
W_2	(W)	Acoustic power loss in resonator
W_3	(W)	Acoustic power uses to drive the thermoacoustic heat pump

(c) Energy flow diagram in a TADTAR.

Figure 6.2: (a) Schematic diagram of a thermoacoustically driven thermoacoustic heat pump, (b) temperature distribution along the stacks, and (c) Energy flow diagram in a TADTAR.

6.3 Experimental Measurements

A thermoacoustic engine usually consists of an acoustic resonator with an internal structure. In the present study, the acoustic resonator is a Pyrex tube closed at one end (20 cm long, 2.2 cm inner diameter), and the internal structure is a piece of Corning ceramic stack (20 pores per linear inch (PPI), a length of 2.5 cm, and a pore wall thickness of 0.3 mm) as shown in Fig. 6.1(b). On one side of the stack winding of electric wire is used as a heat source and the other side is cooled naturally.

The engine starts to emit sound when one side of the stack near the closed end of the tube is heated and the open end of the tube is kept at room temperature. Electric energy of 36

watts is supplied to the hot side of the stack (that is 7.5 cm away from the nearest pressure anti-node). After approximately 10 seconds, a large temperature gradient, parallel to the engine axis builds up in the ceramic stack with the hot end temperature of 200°C and the engine starts to emit sound with a frequency of around 444 Hz as shown in the frequency spectrum of Figs. 6.3(a) and (b). Figures 6.3(a) to (b) show the frequency spectrums obtain from the pressure measurements at the open end of the resonator for two different positions of the prime mover stack. These positions are 5 and 7.5 cm from

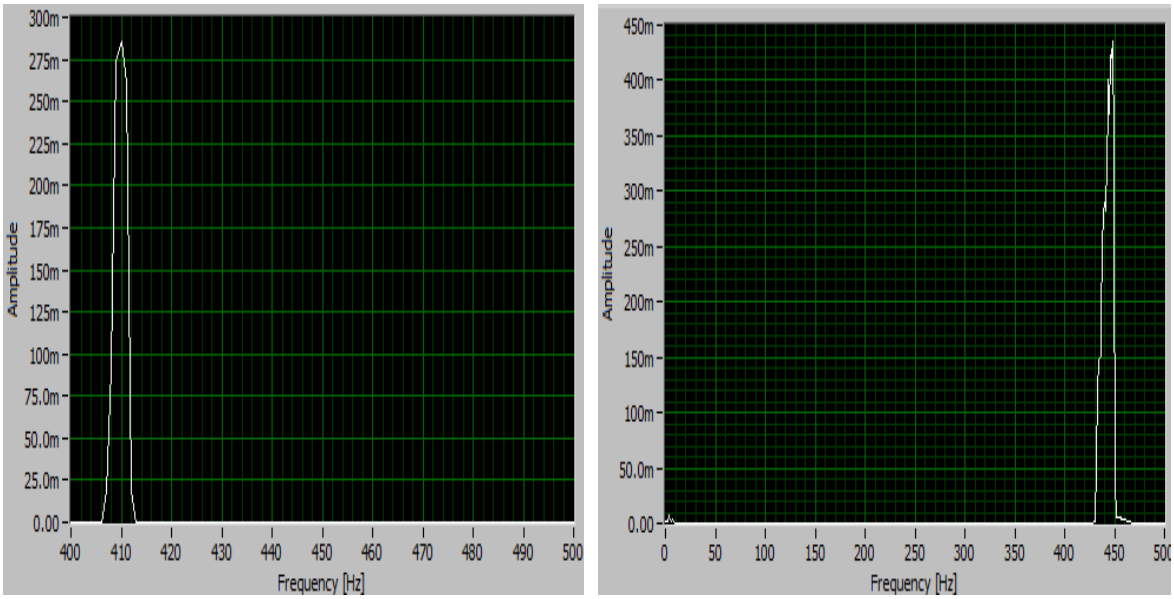

(a) (b)

Figure 6.3: Frequency spectrum of the emitted sound. Disregard the vertical scale. Prime mover stack is (a) 5 cm and (b) 7.5 cm from the nearest pressure anti-node.

the nearest pressure anti-node, respectively. It is observed in Figs. 6.3(a) and (b) that the peak frequency changes as the position of the prime mover stack changes, thereby changing the wavelength of the acoustic standing wave. The intensity of the sound also changes from 125 dB for 5 cm to 127 dB for the 7.5 cm stack position. These information are absent in the existing literature. The reasons for these behaviors are unknown at this stage and need further investigation. Figure 6.4 shows the plot of pressure amplitude and phase vs. frequency at the closed end of the tube. The phase changes smoothly through resonance with the largest rate-of-change of phase as a function of frequency occurring at the resonance frequency. This pressure and phase vs.

frequency plot is drawn using the DeltaEC software when prime mover stack is located 7.5 cm from the pressure anti-node.

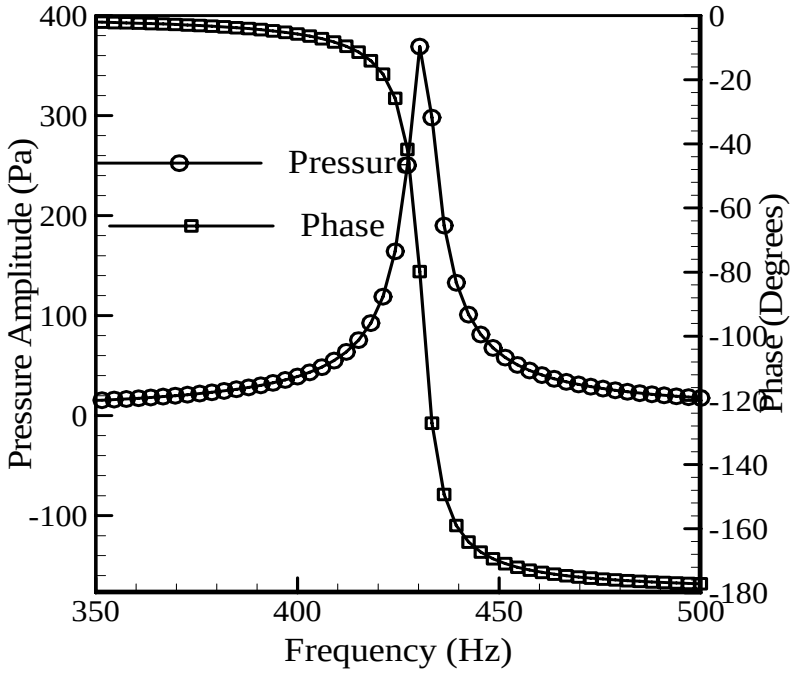

Figure 6.4: Plot of pressure magnitude and phase vs. frequency.

6.4 Performance Measurements

6.4.1 Temperature Difference across the Heat pump Stack Ends

The heat pump section consists of an acoustic resonator with an internal structure. Similar to the thermoacoustic prime mover, the acoustic resonator is a Pyrex tube closed at one end (20 cm long, 2.2 cm inner diameter), and the internal structure is a piece of Corning ceramic stack (20 pores per linear inch (PPI), and a length of 2.5 cm). The open end of the thermoacoustic prime mover is connected to the open end of the thermoacoustic heat pump. Therefore, the resonator is now a half wave-length resonant tube (40 cm long) with pressure anti-nodes at the closed ends as shown in Fig. 6.2(a). Electric energy of 36 watt is supplied to the hot end of the prime mover stack end, while the heater wire resistance is 1.5 ohm. Figure 6.5 shows the measured temperature difference across the heat pump stack as a function of x_n rather than x, where $x_n = k_1 x$, and $k_1 = 2\pi / \lambda$, in order to observe the effect of the position of the heat pump stack in the standing

wave. Figure 6.5 also presents the predictions of DeltaEC ([2007]). Symbols are experimental results and dashed line is the prediction. DeltaEC is a 1-D executable code that solves the wave equation (Eq. A19 of Swift [1988]) based on the low-amplitude

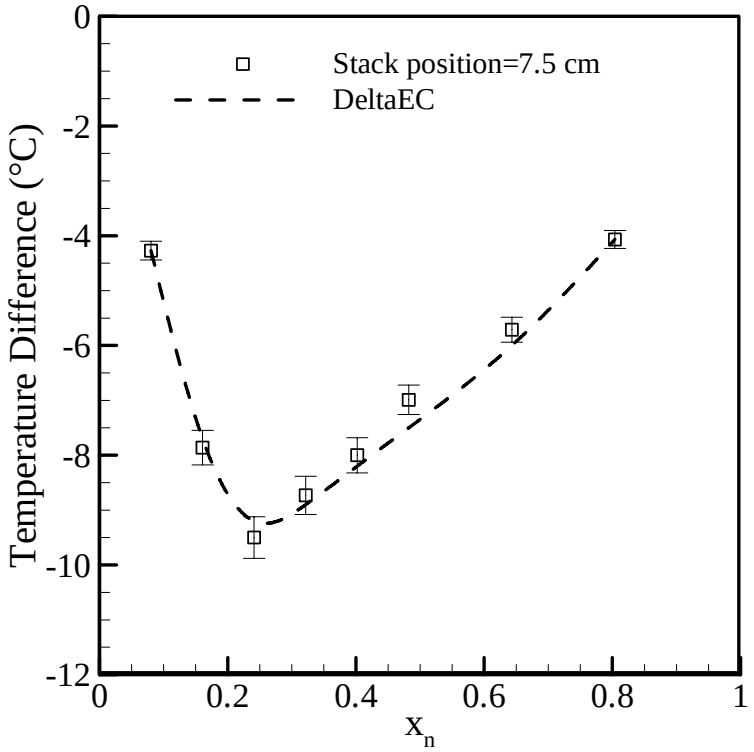

Figure 6.5: Measured temperature difference as a function of x_n when the prime mover stack is located 7.5 cm from the nearest pressure anti-node. Symbols are experimental results, and dashed line is the prediction of DeltaEC.

acoustic approximation. It solves the wave equation in a gas or in a geometry provided by the user as a sequence of segments. A solution to the appropriate 1-D wave equation is found for each segment, with pressure and volume flow rates matched at the junctions between segments. In stacks, the wave equation is solved simultaneously along with the energy flow equation (Eq. A30 of Swift [1988]) in order to find the temperature profile. In the present study very good agreement is obtained between the experimental results and the 1-D numerical predictions. The error bar indicates uncertainties in the experimental measurements and is discussed in Appendix A. The position of the heat pump stack in the standing wave is varied from the nearest pressure antinode i.e., $x = 1$ to $x = 10$ cm. Temperature difference vs. x_n curve shows that temperature difference across the stack is not a sinusoidal function of its position in the standing wave. Temperature

difference becomes zero almost half way between pressure antinode and node of the acoustic standing wave, and the maximum temperature difference shift towards the pressure antinode (which is also observed by Tijani [2001] for an acoustically driven thermoacoustic heat pump). The measured drive ratios for the 5 cm and 7.5 cm prime mover stack positions are 0.05% and 0.06%, respectively.

6.4.2 Comparisons of the time evolutions of temperatures and the temperature difference across the heat pump stack

Comparisons of the time evolution of heat pump stack temperature distributions as a function of time are shown in Figs. 6.6(a) to (d) for two different positions of the prime mover stack. These positions are 5 and 7.5 cm from the nearest pressure anti-node, respectively. Figures 6.6(a) to (d) clearly indicate a time shift of the heat pump stack temperature evolutions for the two different prime mover positions. The temperature evolutions are leading for all the heat pump stack positions when the prime mover stack is 7.5 cm from the nearest pressure anti-node compared to the other position which is 5 cm from the nearest pressure anti-node. That is refrigeration starts earlier when the prime mover stack is located further from the pressure anti-node. Figure 6.7 shows the comparison of temperature difference as a function of the location of heat pump stack from the nearest pressure anti-node for two different prime mover stack positions. Figure 6.7 shows that the location of the peak temperature difference changes as the position of the prime mover stack changes. Between the two profiles, the peak temperature difference occurs when the prime mover stack is 5 cm away from the nearest pressure anti-node, and the corresponding heat pump stack position is 4 cm. At this location of the heat pump stack, the cold end temperature is 20°C. Temperature difference sharply drops to zero when the prime mover stack is 5 cm away from the nearest pressure anti-node, compared to the other case. Therefore, observing Fig. 6.7, the maximum performance regarding temperature difference across the stack is 10°C, and the cold end temperature is 20°C, where the prime mover stack is 5 cm from the nearest pressure anti- node and the corresponding heat pump stack position is 4 cm $(\approx \lambda/20)$ from the nearest pressure anti-node.

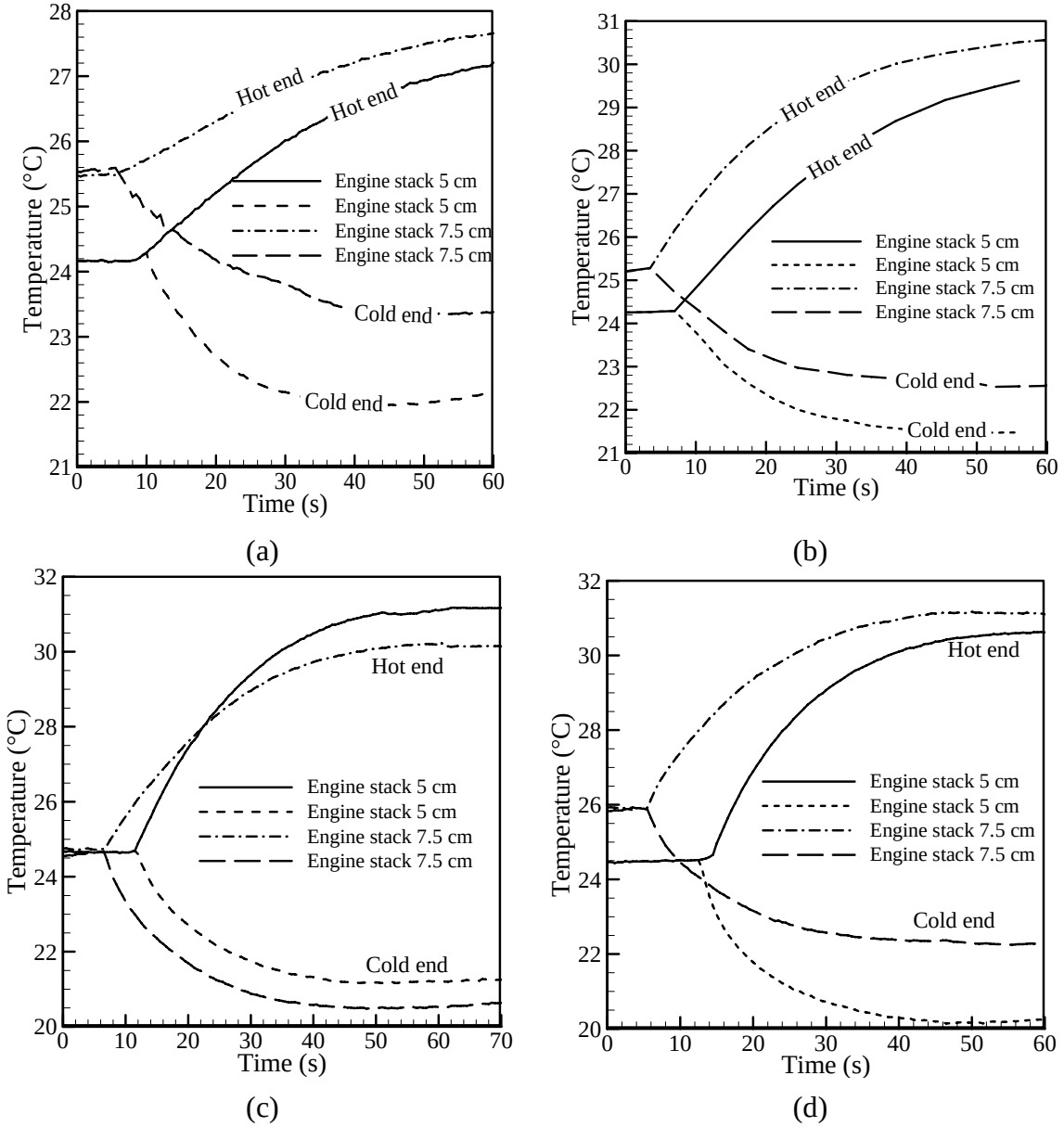

Figure 6.6: Comparison of the time evolution of temperature distributions for different positions of the prime mover stack when the heat pump stack is (a) 1 cm away (b) 2cm, (c) 3 cm, and (d) 4 cm from the nearest pressure antinode.

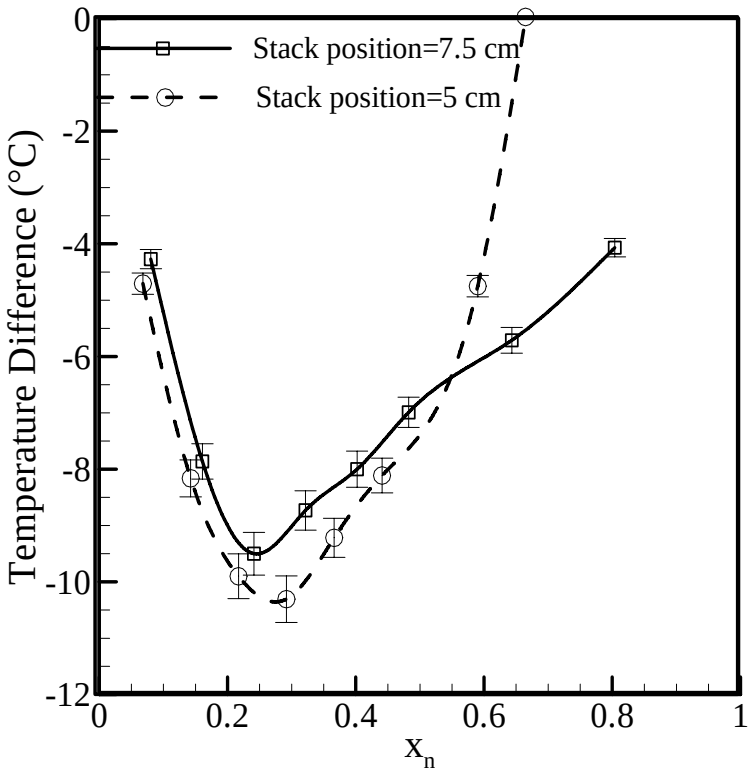

Figure 6.7: Temperature difference as a function of position of the heat pump stack in the standing wave for two different prime mover stack positions.

Now, a PVC (Polyvinyl Chloride) tube of 4.4 cm inner diameter and 40 cm length is considered to produce thermoacoustic effects. For this case, the diameter of the PVC tube is twice than the previous tube, and the heater wire resistance is 6 ohm, which is 4 times larger than the previous case. Therefore, 144 W of electrical power is supplied to the hot side of the prime mover stack, which is 4 times larger than the previous case. The length of the two stacks (used for the prime mover and the heat pump) is 3.8 cm. During the experiment, the PVC tube near the prime mover hot end of the stack starts to melt when the hot end temperature starts to increase, reaching near 200°C. Therefore, the experiment could not be finished. The cooling effect is observed in Fig. 6.8 before the stack hot end melts. The cold side of the heat pump stack reaches to 18°C with a temperature difference of 6.6 ° C, while the hot side of the stack remains constant to the ambient temperature. This trend reflects the fact that the heat flow from the cold to the hot end of the stack is dissipated near the hot end of the stack and the diffusive heat flux is not prominent during the elapsed time. The objective of considering larger diameter tube is to observe the cooling effect, with a hope that cooling effect might increase

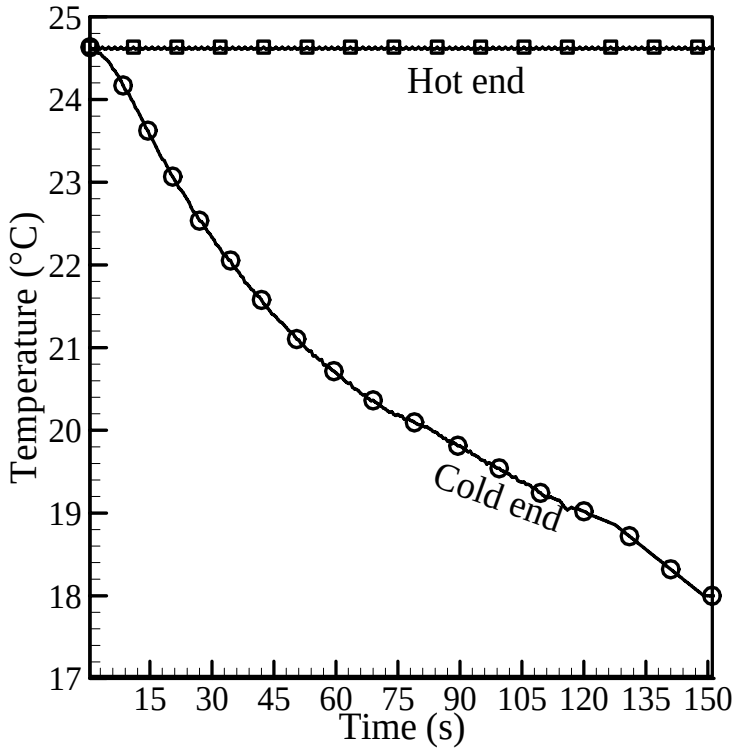

Figure 6.8: Temperature vs. time when the heat pump stack is 4cm away from the pressure antinode.

linearly with the increase of tube diameter. This case is left for future investigation. The PVC tube is chosen in this experiment because of its availability. Thin walled stainless steel tube might be used for the prime mover section to limit conduction heat transfer along the resonator wall, while still providing enough strength to withstand temperatures up to 400°C without the danger of rupturing. Also Pyrex tube can be used as an alternate to steel tube.

6.4.3 Estimation of COP and COPR

Figure 6.9(a) shows the non-dimensional acoustic work vs. non-dimensional stack center position form the pressure anti-node as a function of prime mover stack position. The non-dimensionalisation of acoustic work and enthalpy flow are obtained by dividing the acoustic work and enthalpy flow with the product of $p_m a A$ (according to Swift [1988]), where p_m is the mean pressure, a is the adiabatic speed of sound, and A is the cross

sectional area of the resonator. The acoustic work is calculated using Eq. (A.16). Figure 6.9(a) shows that acoustic work flow along the stack increases linearly with the increase of stack center position form the pressure anti-node. The reason for this behavior will be explained in Chapter 7. Figure 6.9(b) shows the enthalpy flow or cooling power as a function of the heat pump stack location from the nearest pressure anti-node. The cooling power is calculated using Eq. (A.17). Figure 6.9(c) shows the COP as a function of the normalized heat pump stack location (x_n) from the nearest pressure anti-node for both of the thermoacoustic prime mover stack positions. COP is estimated using Eq. (A.18). The COP shows a parabolic behavior with a maximum for all the stack positions, but the magnitude of the peak changes as the thermoacoustic prime mover stack position changes as shown in Fig. 6.9(c). The normalized heat pump stack location $x_n = 0$, corresponds to the pressure antinode. Initially COP increases as x_n increases. As the normalized heat pump stack location increases further, the COP decreases. This behavior is to be understood in the following way: A decrease of the position of the stack means that the stack is placed closed to the pressure antinode. This position is a velocity node, and

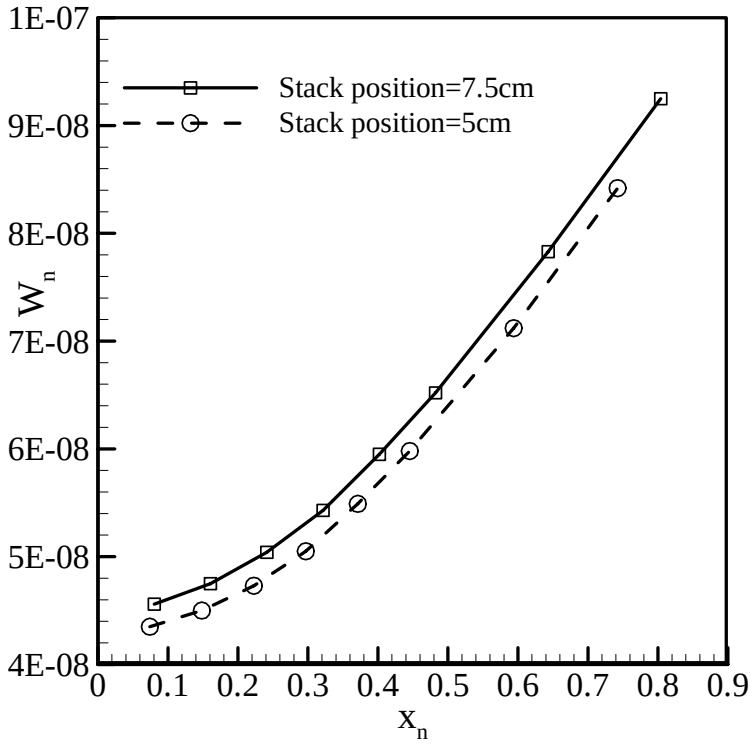

(a) Non-dimensionalized acoustic work as a function of the position of the heat pump stack in the standing wave.

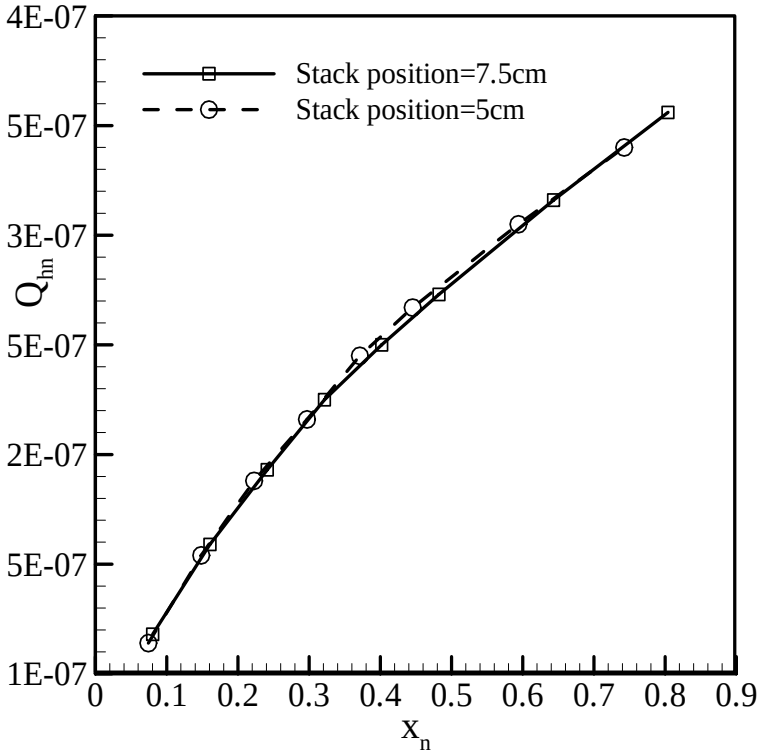

(b) Non-dimensionalized enthalpy flow as a function of the position of the heat pump stack in the standing wave.

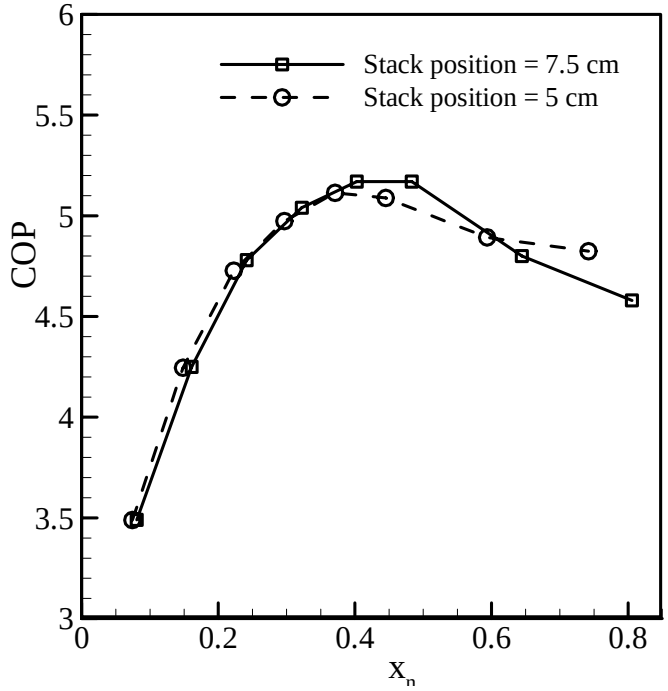

(c) COP as a function of the position of the heat pump stack in the standing wave.

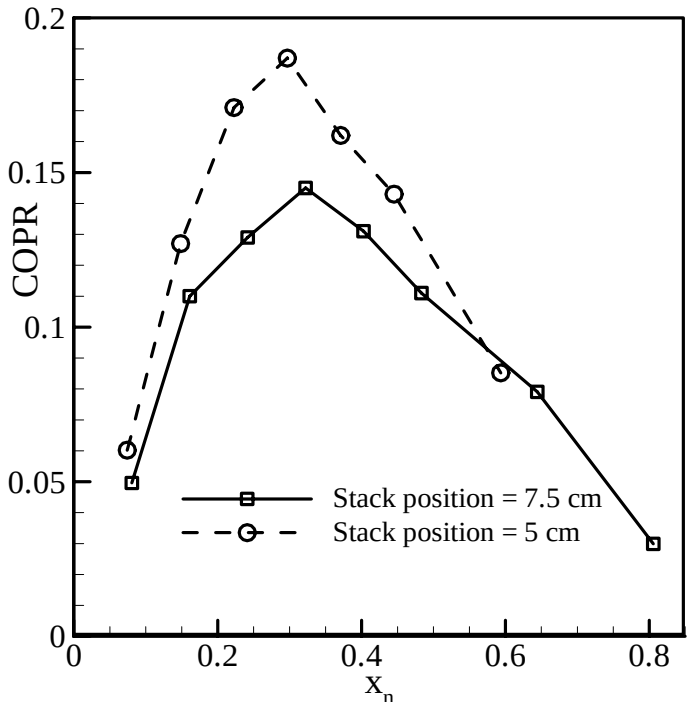

(d) COPR as a function of position of the heat pump stack in the standing wave.

Figure 6.9: (a) The acoustic power as a function of the heat pump stack location from the nearest pressure anti-node. (b) The cooling power as a function of the heat pump stack location from the nearest pressure anti-node. (c) The COP as a function of the normalized heat pump stack location from the nearest pressure anti-node. (d) The COPR as a function of the normalized heat pump stack location from the nearest pressure anti-node.

Eq. (A.16) shows that the viscous losses (first term on the right of Eq. (A.16)) are proportional to the square of the acoustic velocity. Thus decreasing the velocity results in a decrease of the losses and hence increases of COP. The power density of the TADTAR is independent of the prime mover position, but the acoustic work is not. A lower value of acoustic work is observed while the prime mover stack is located 5 cm pressure anti-node. Therefore less acoustic work is absorbed by a heat pump stack when the prime mover stack is located closest to the pressure anti-node and thus an increase in COP value at that location. The COPR also shows a parabolic behavior with a maximum for both stack positions, but the magnitude of the peak changes as the thermoacoustic prime mover stack position changes as shown in Fig. 6.9(d). Maximum COPR value is observed where maximum temperature difference is observed for both positions of the prime mover stack. Since COPC is minimum where temperature difference is maximum,

therefore showing higher COPR value at this location. Therefore, to obtain maximum performance the prime mover stack should be located close to (less than $\lambda/16$) the pressure anti-node. Maximum COP in Fig. 6.9(c), maximum COPR in Fig. 6.9(d), and maximum temperature difference along the stack in Fig, 6.7 all three are obtained while the heat pump stack is located 4 cm $(\approx \lambda/20)$ from the pressure anti-node. Swift [2002] suggested that to optimize the performance of a thermoacoustic device the stack should be located $\approx \lambda/20$ from the pressure anti-node. Therefore, to optimize the performance of a TADTAR, the prime mover and the heat pump stack should be located $\approx \lambda/20$ from the pressure anti-node.

6.4.4 Comparison of Thermal Field when Different Sound Sources are Utilized

Figures 6.10(a) and (b) show the time evolution of temperature profiles of two thermoacoustic heat pumps when different sound energy sources are utilized for the identical operating conditions ($p_m = 101\ kPa, T_m = 300K$). For the two cases, DR is also almost identical (0.03% (for TAR) and 0.05% (for a TADTAR)). Only difference is the frequency of operation (350 Hz for TAR and 410 for TADTAR), which should not alter the physical processes involved in thermoacoustics. There is no qualitative difference between the two temperature profiles; only difference is that for the TADTAR in Fig. 6.10(a), the thermoacoustic effect starts later (approximately 6 to 7 seconds) compared to the acoustic counterpart (Fig. 6.10(b)). This is the time which is required by the thermoacoustic engine to become self excited and to generate the sound upon achieving a critical temperature difference across the prime mover stack. The critical temperature difference across the prime mover stack for the conditions mentioned in Fig. 6.10(a) is 109°C. The quantitative difference between the two profiles is that, for a TADTAR, less temperature difference is generated across the refrigerator stack ends. The stack length is 2.5 cm for both of the cases.

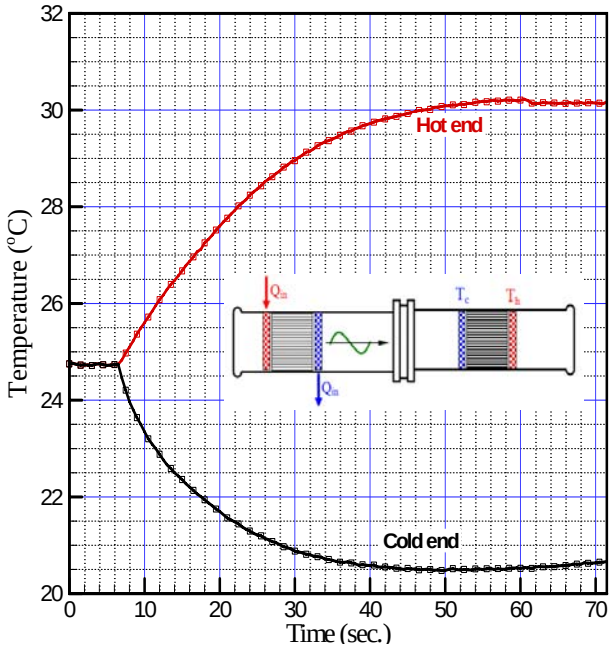

(a)

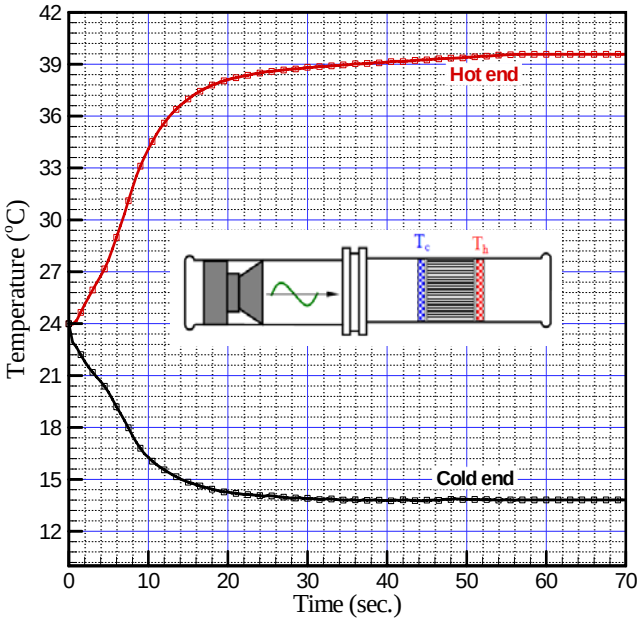

(b)

Figure 6.10: Experimental investigation on time evolution of temperature profiles (a) of a TADTAR when the prime mover stack is located 7.5 cm from the closed end, (b) of a TAR cooling system. For both of the system, the heat pump stack is located 3 cm from the closed end.

Now, the energy flow at the hot side of the heat pump stack is compared for these two different cases in Fig. 6.11(a). The magnitude of the TAR is higher also with the higher

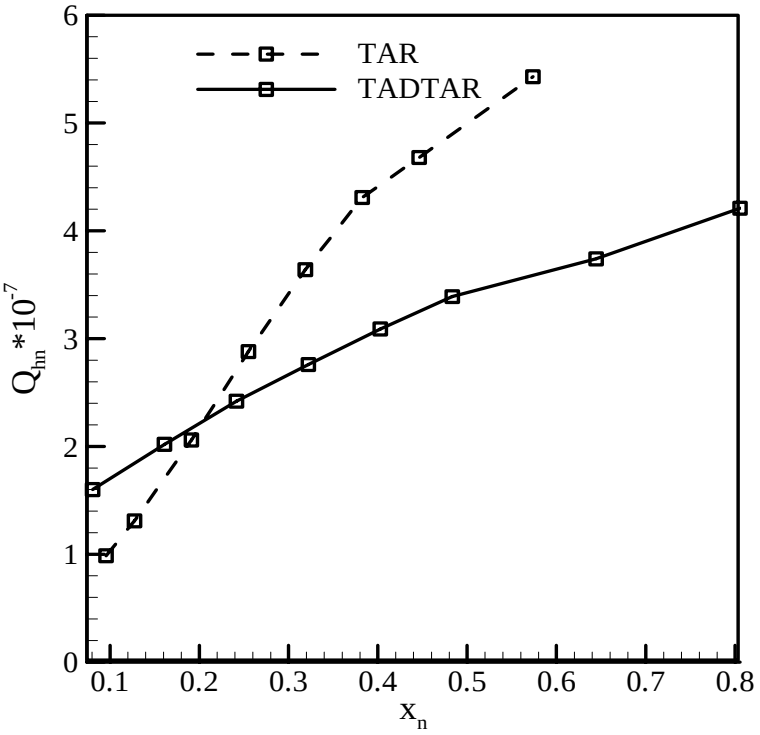

(a) Non-dimensionalized enthalpy flow as a function of the position of the heat pump stack in the standing wave.

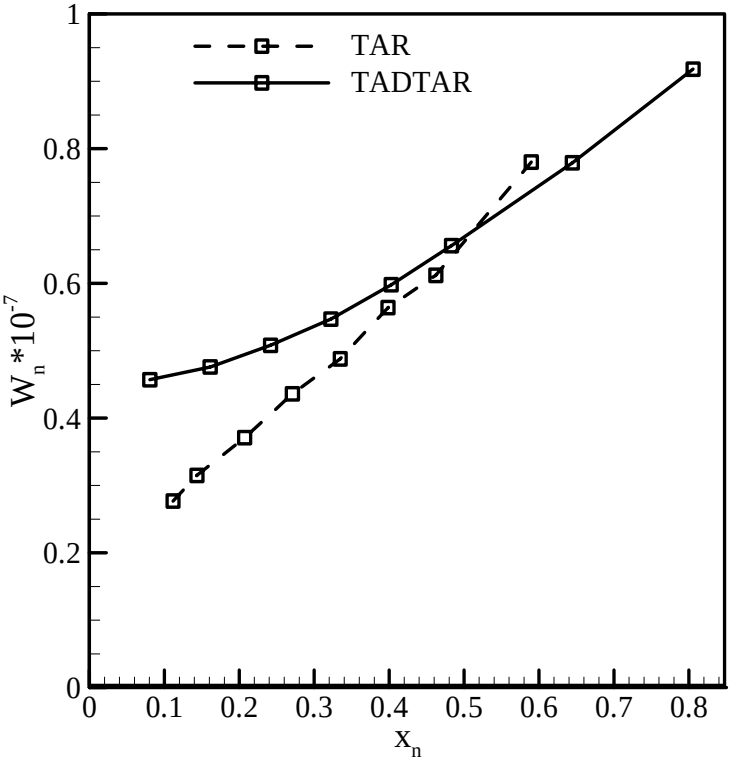

(b) Non-dimensionalized acoustic work as a function of the position of the heat pump stack in the standing wave.

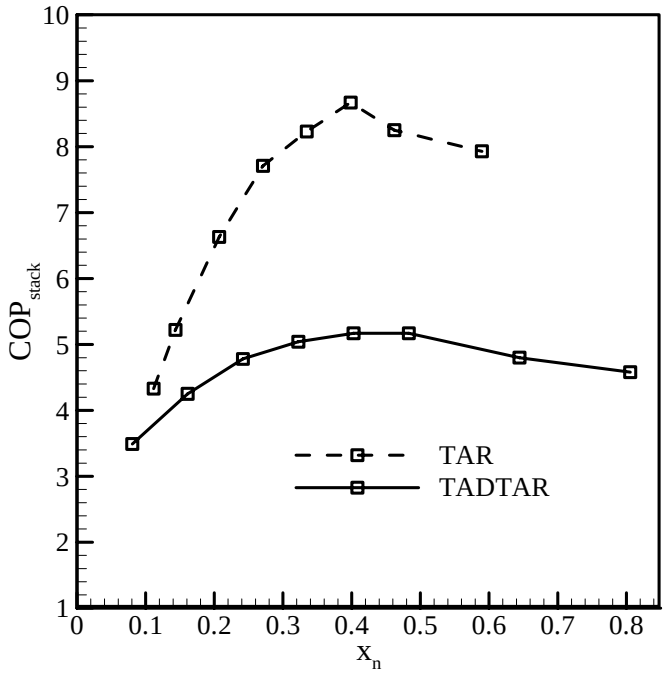

(c) COP as a function of the position of the heat pump stack in the standing wave.

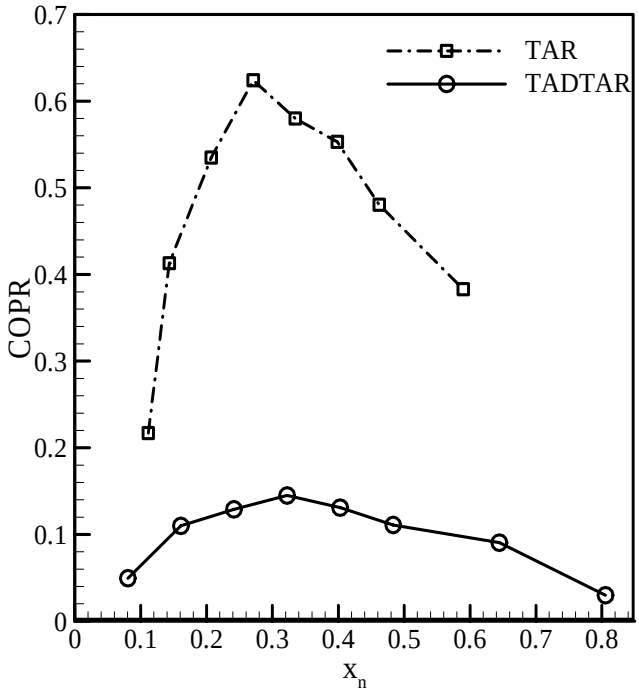

(d) COPR as a function of position of the heat pump stack in the standing wave.

Figure 6.11: (a) Energy flow at the hot side of the stack, (b) Acoustic work, (c) COP of the heat pump stack, and (d) COPR versus non-dimensional stack center position from the pressure anti-node as a function of non-dimensional stack position. The lines are visual guide.

slope than the TADTAR along with the distance from the closed resonator end. The reason might be the increased volume of the resonator for a TADTAR (according to Eq. (66) of Swift [1988]) that reduces the power density. Also the acoustic power from the prime mover stack in the TADTAR that is absorbed by the resonator walls would add an extra thermal load to the ambient end of the stack, thereby reducing the ability of the heat pump stack to pump heat. The acoustic power (Fig. 6.11(b)) absorbed by the TAR is lower when compared with the TADTAR. Acoustic power absorbed by a stack is proportional to ω (Eq. (82) of Swift [1988]), and since TADTAR operates at higher frequency than the TAR, therefore showing higher absorbed acoustic power. Also the operating frequency of the TADTAR is higher than the TAR; therefore δ_k is lower for the former case which makes the stack inefficient in thermal heat pumping and acoustic power absorption. Thus the COP (Fig. 6.11(c)) and COPR (Fig. 6.11(d)) of a TAR is higher than the TADTAR for the selected operating conditions tested.

6.5 Conclusions

Square cell Celcor ceramic stacks used for the prime mover and the heat pump sections enhance the thermal exchange area, leading to an increased amount of heat flux and thus an increased overall efficiency of the device. Some important information is revealed in the present study that is not available in the existing literature.

- First, the present study shows that refrigeration starts earlier in a TADTAR when the prime mover stack is located further from the pressure anti-node.

- Second, temperature difference generated in a TADTAR depends on the position of the prime mover stack. The maximum temperature difference and the maximum hot end temperature also depend on the position of the prime mover stack. The maximum temperature difference across the heat pump stack ends and the maximum hot end temperature are obtained when the prime mover stack is located close to the pressure anti-node. Therefore at that location, the prime mover stack has managed to produce enough net acoustic power to overcome the

acoustic power losses in the resonator section and to produce maximum temperature difference at the heat pump stack ends.

- Third, the position of the prime mover stack has no control on the cooling power of the heat pump.

- Maximum COP, maximum COPR and maximum temperature difference along the stack all three are obtained while the heat pump stack is located 4 cm $(\approx \lambda/20)$ from the pressure anti-node. Therefore, to optimize the performance of a TADTAR, the prime mover and the heat pump stack should be located $\approx \lambda/20$ from the pressure anti-node.

- A comparison between TAR and the TADTAR for the identical operating conditions shows improved heat flow from the hot side of the stack, low acoustic work absorption, higher COP and COPR for the TAR for the tested operating conditions. Much work needs to be done to understand the performance of these two devices by operating the prime mover stack at different positions from the pressure anti-node of the TADTAR and then compare the results with the TAR.

Chapter 7

Experimental Results on Regular and Random Porous Media

7.1 Introduction

In this chapter the experimental results are presented, analyzed, discussed, and compared to results obtained from the thermoacoustic system simulation program DeltaEC [2007]. There is evidence (Adeff et al. [1998] and Chapter 2) that use of random porous materials as stacks or regenerators in thermoacoustic devices can raise the efficiency of thermoacoustic systems. To understand the oscillatory gas thermodynamics and heat transfer, and to realize thermoacoustic devices with high performance, fundamental research is required that addresses several important problems in thermoacoustic systems. These problems include thermoacoustic transport in random porous media, temperature fields in the system elements, and evaluating COP to illustrate the viscous and thermal losses within the random porous media stacks.

To evaluate the thermal performance, the temperature difference across the stack ends and the hot stack end temperature are the main focus of the present work. Eventually the performance of the stack using first and second laws of thermodynamics is evaluated. Also studied in this chapter are the thermal field and heat transfer mechanisms at different locations of regular stack geometry. Therefore, the present work is a contribution to the study of temperature fields inside and at the edges of the stacks and at the neighboring working fluid, with an objective to improve the understanding of the physics underlying the thermoacoustic effect (longitudinal heat flux along the stack). Also, the objective of this chapter is to identify the limits of linear thermoacoustic theory (Swift [1988]), since this theory is the basis of the design methodologies of all thermoacoustic devices built so far (Tijani [2001], Swift [1988]). Finally, the experiments

performed in this chapter provide data to validate the analytical models developed in Chapter 4 and Chapter 5.

Several authors (Atchley et al. [1990], Worlikar et al. [1998], and Marx et al. [2005]) made a study of temperature difference at the stack extremities either experimentally or numerically and made comparisons with the linear theory predictions (Swift [1988]). But, there exists inconsistency in experimental and numerical temperature difference across the stack ends and the linear theory predictions. Therefore, the present investigation targets to study the temperature fields inside and at the edges of stacks and the surrounding working fluid with an objective to improve the understanding of the physics underlying the thermoacoustic effect and to eliminate the inconsistency exists in the available literature.

This chapter begins with the thermal field measurements of the RVC stack, followed by regular Corning Celocr ceramic stack. Temperature measurements are performed on different locations of the stack plate surface and of the working fluid, followed by the effect of different parameters on the performance of the stack, heat transfer mechanisms at the stack extremities, and finally evaluating the COPs' for different stack geometries.

Literature review of thermoacoustics show that no study exists in the literatures that examines

- Thermoacoustic transport in random porous media.
- The steady state temperature difference generated across the stack ends for a thermoacoustic heat pump for different dimensions and porosities and
- Compare them with conventional stack, and evaluate their performance by calculating their COP.

The outcome of this research has application to the search for efficient stack configurations for particular applications (especially for use in small scale thermoacoustic devices).

7.2 Thermal field within the Porous RVC Stack Structure

In the present investigation, a detail study has been performed in order to evaluate the temperature field within the porous stacks of porosity ranging from 20 PPI to 100 PPI. For each experimental condition, ten experimental runs are conducted for the consistency in the measured data. Figures 7.1(a) to (e) show the steady state temperature distribution along the stack length for 20, 30, 45, 80, and 100 PPI stacks at a DR of 0.03%. Temperatures at different locations on a stack are measured and the measurement points are equally distributed along the stack. Symbols in Figs. 7.1(a) to (e) represent the experimental values and solid lines are the linear fit through the data points. During the measurements the stack hot end is moved from 0.5 cm to 8 cm from the nearest pressure anti-node (to organize, all the positions of the stack are not shown in Figs. 7.1(a) to (e)). A constant stack length of 4 cm (0.04λ) is considered for the study in these figures. In all these figures, generally the lowest and highest temperatures are observed when the stack is located closer to the pressure anti-node. The lowest temperature increases and the highest temperature decreases as the distance of the stack from the pressure anti-node increases. This is a consequence of the decrease of critical temperature gradient as will be discussed in **Section** 7.4.2. Figures 7.1(f) to (h) show the steady state temperature distribution along the stack length for 80 and 100 PPI grades for stack lengths of 1.5 cm (0.015λ) and 2 cm (0.02λ), respectively. For shorter stack lengths temperature distributions along the stack are linear as shown in Figs. 7.1(f) to (h). As the stack length increases as shown in Figs. 7.1(a) to (e), temperature distributions show a small deviation from linear behavior. As the stack length increases, acoustic dissipation within the stack increases (as will be seen in Fig. 7.19), and temperature distribution started to deviate from linear behavior. The almost linear temperature distribution along the stack indicates that acoustic dissipation within the stack is almost negligible. An increase in the DR may cause a raise in acoustic dissipation within the stack, and deviation from linear temperature distribution might occur. The acoustic dissipation acts as a heat source inside the stack and results in non uniform temperature distribution along the stack. Therefore, it can be concluded from the present investigation that for the operating DR temperature distribution within the stack is linear and small stack length is preferable, as for larger

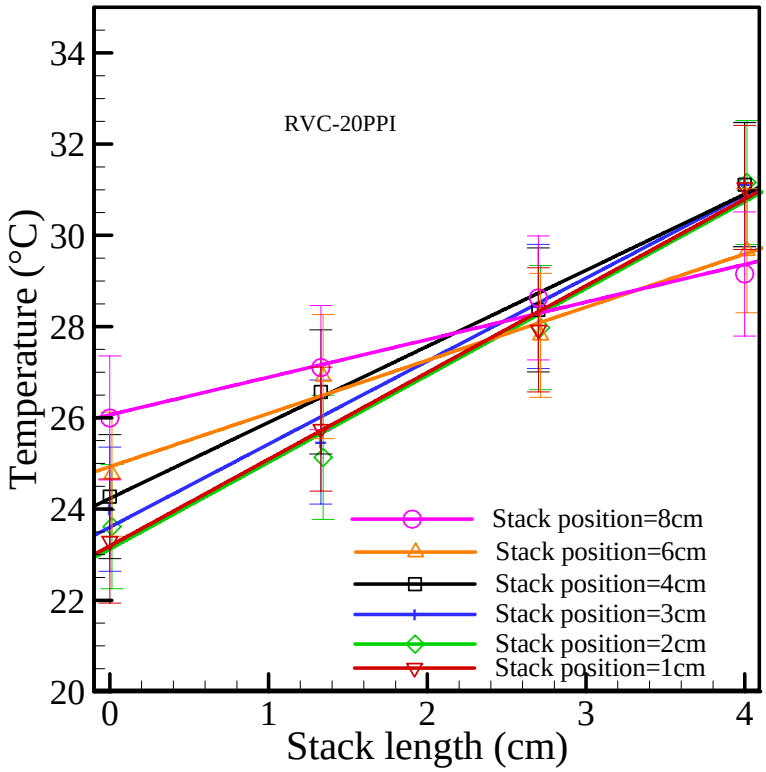

(a) Temperature distribution along the 4 cm long 20 PPI RVC stack

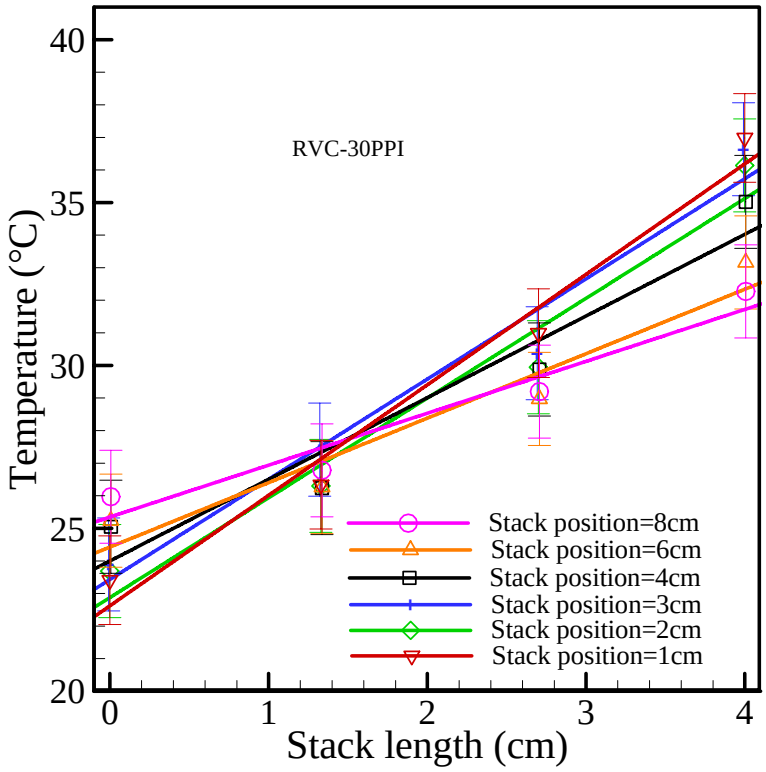

(b) Temperature distribution along the 4 cm long 30PPI RVC stack

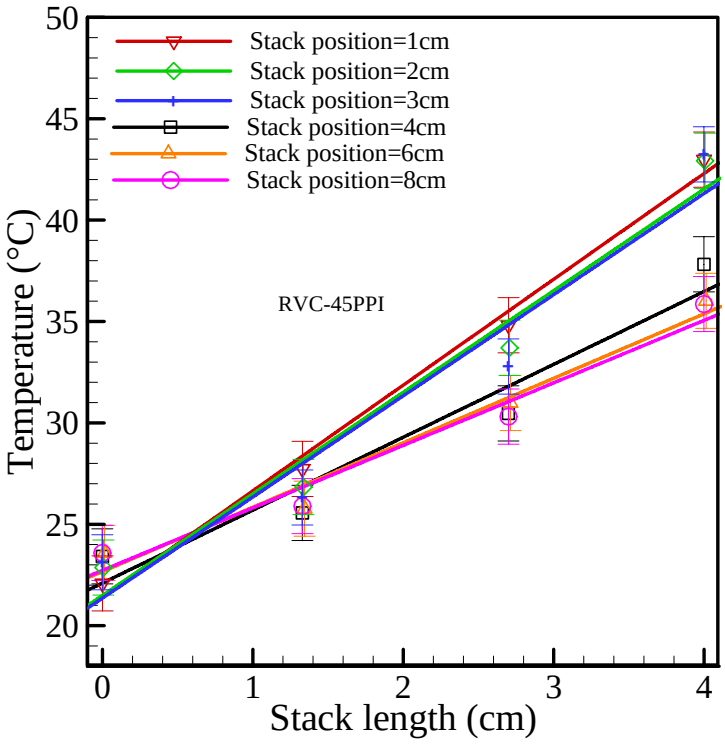

(c) Temperature distribution along the 4 cm long 45 PPI RVC stack

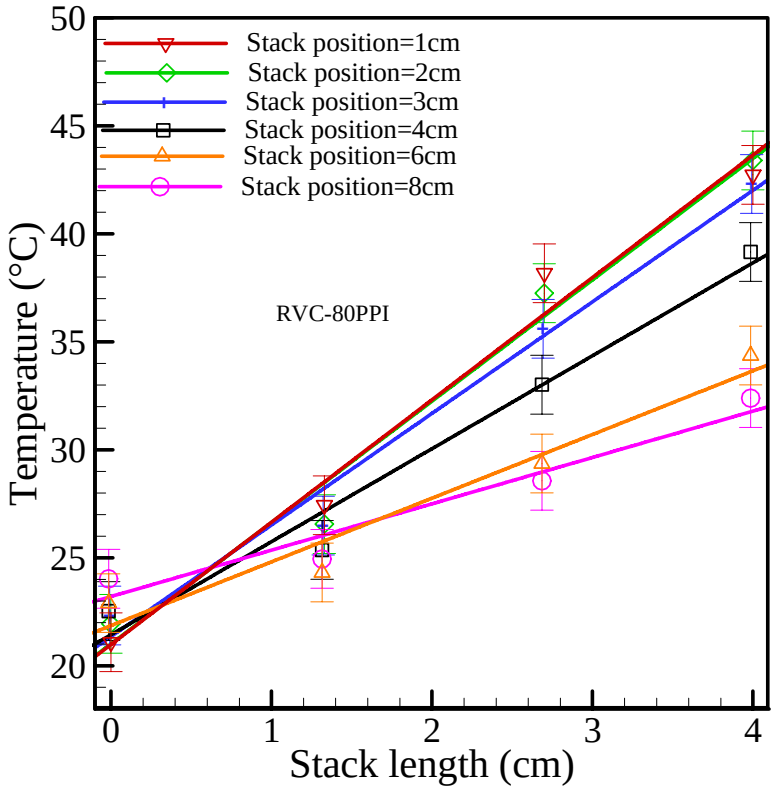

(d) Temperature distribution along the 4 cm long 80 PPI RVC stack

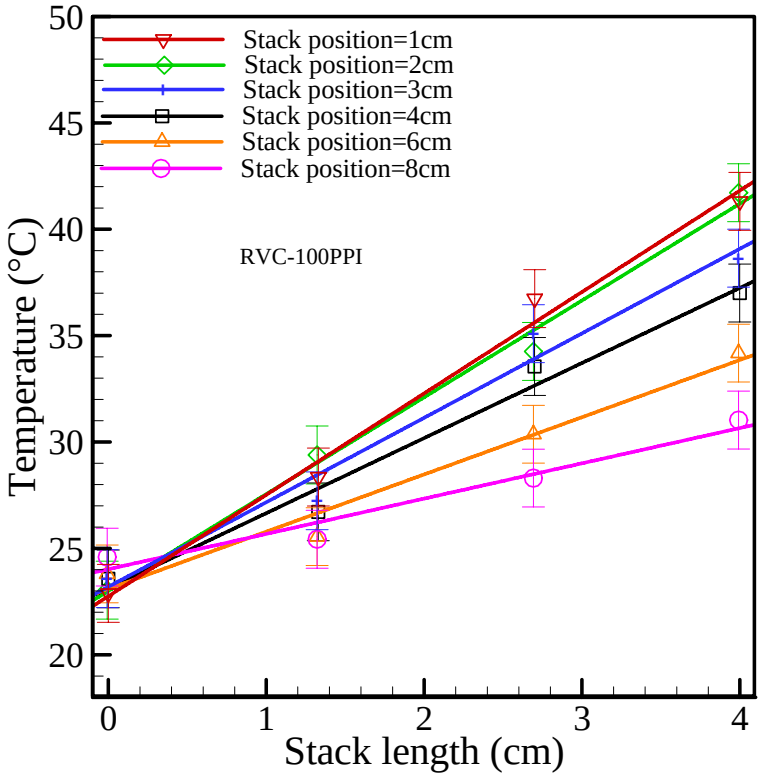

(e) Temperature distribution along the 4 cm long 100 PPI RVC stack

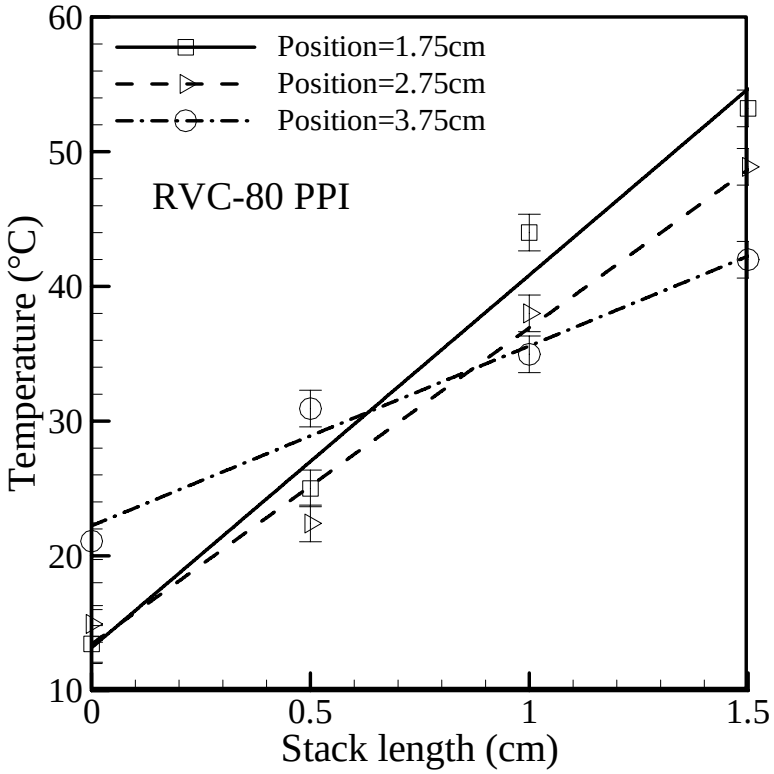

(f) Temperature distribution along the 1.5 cm long 80 PPI RVC stack

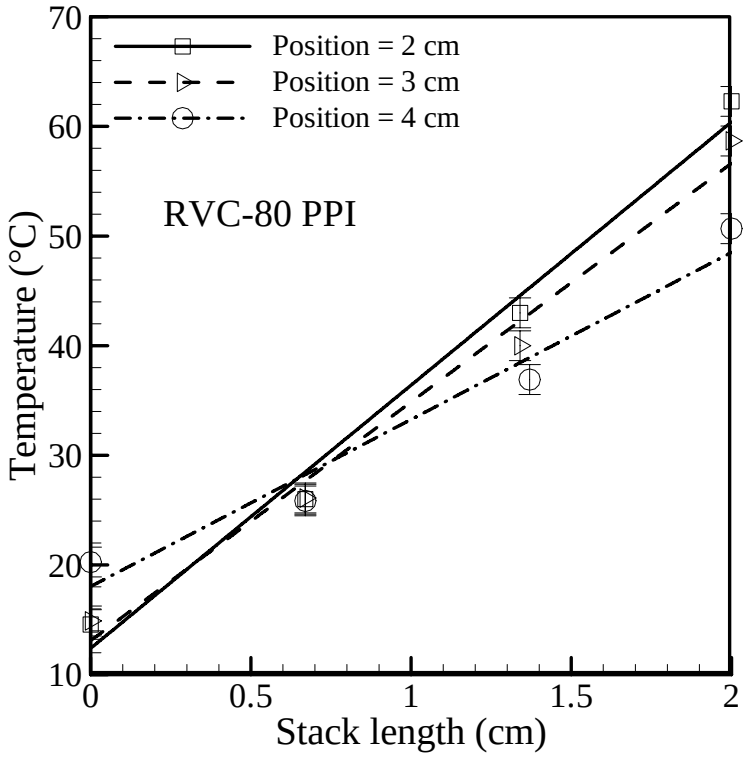

(g) Temperature distribution along the 2 cm long 80 PPI RVC stack

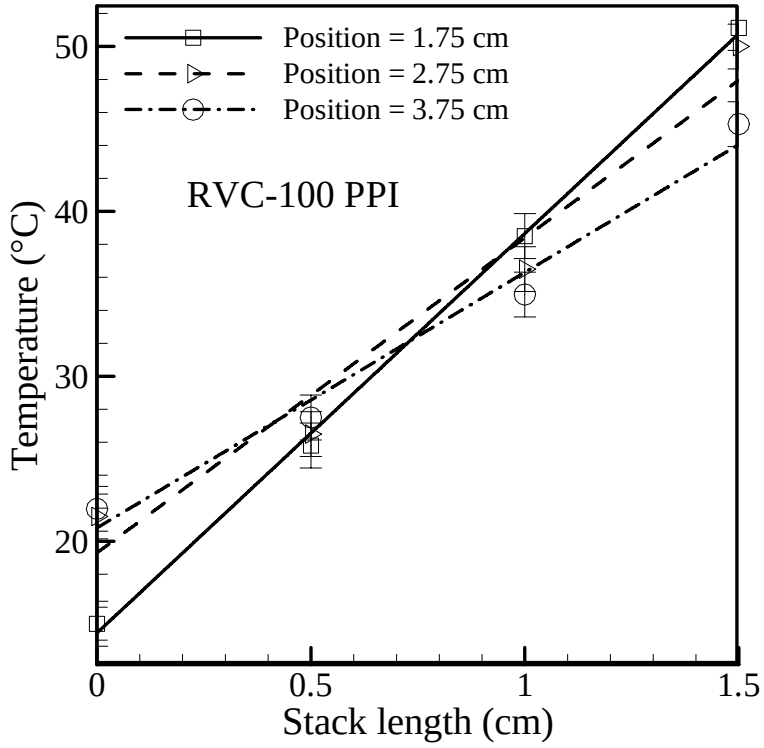

(h) Temperature distribution along the 1.5 cm long 100 PPI RVC stack

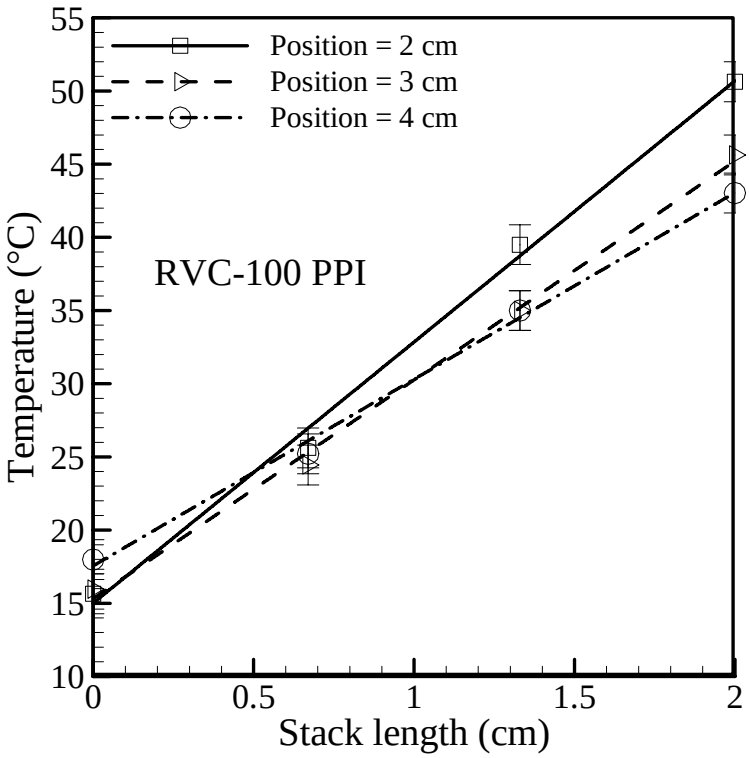

(i) Temperature distribution along the 2 cm long 100 PPI RVC stack

Figure 7.1: (a) to (e) Steady state temperature distributions for 20 to 100 PPI RVC stacks vs. stack length. A constant stack length of 4 cm is considered. (f) to (i) 80 to 100 PPI RVC stacks for stack lengths of 1.5 cm and 2 cm, respectively.

stack lengths acoustic dissipation may cause non uniform temperature distribution along the stack, and invalidating the use of linear theory. The error bars in Fig. 7.1 and all the figures in Chapter 7 indicate uncertainty in temperature measurements and is discussed in Appendix A.

7.3 Steady State Temperature Difference across the Stack Ends

Figure 7.2 shows the temperature difference generated across the RVC stack versus stack position for five different stack porosities (from 20 to 100 PPI) and at eight different stack positions (from 1 cm to 8 cm from the closed end of the resonator). Therefore, Fig.7.2 reveals the effect of stack porosities and position of the stack on the temperature difference generated across the stack ends. The length of the RVC stack is constant at 4 cm (0.04λ) in Fig. 7.2. Regarding the temperature difference generated across the stack

ends, 80 PPI RVC stack shows the best performance followed by 45 PPI and 100 PPI pores. 20 PPI RVC stack corresponds to the Corning Celcor stack (as will be shown in **Section** 7.4.1). Considering 20 PPI RVC stack, this stack spacing is too large for the moderate thermal contact between the stack and the gas and thus ineffective in transporting heat and therefore showing the least temperature difference. 45 and 80 PPI

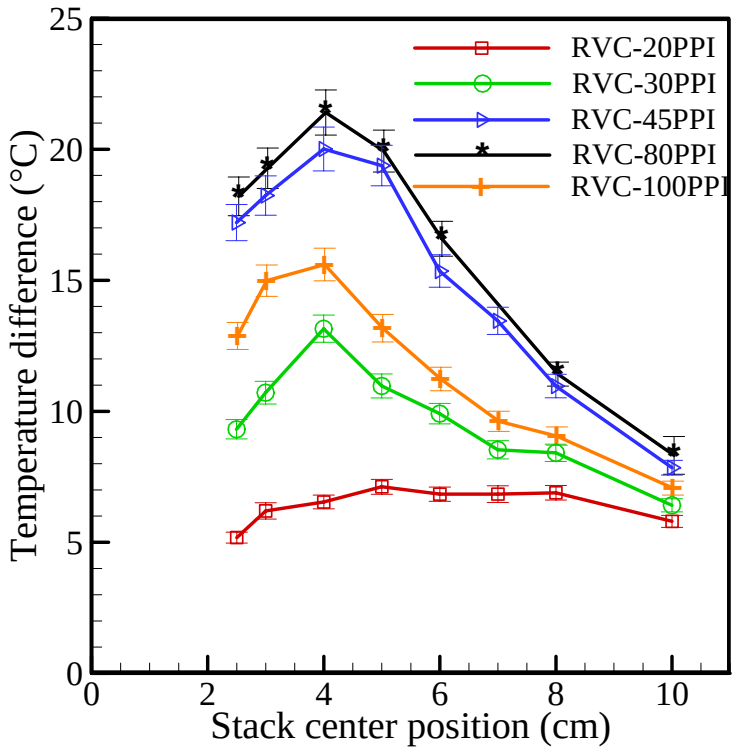

Figure 7.2: Temperature difference generated across the stack vs. stack position for different porosities RVC stacks. The length of the stack is 4 cm.

pores are adequate for moderate thermal contact, and thus producing almost identical temperature difference, whereas 100 PPI spacing is too small for effective heat transport (also shown in Fig. 7.16) and thus showing less temperature difference. Figure 7.3(a) to (c) show the steady state temperature difference generated across the stack ends as a function of stack length. Results of 45, 80, and 100 PPI grades are presented as they produce significant temperature difference across the stack ends at steady state compared to 20 and 30 PPI grades. In Figs. 7.3(a) and (b), five different lengths of RVC stacks are considered ranging from 1 cm to 4 cm. As the length of the stack increases from 1 cm to further, the temperature difference across the stack ends increases. It then decreases

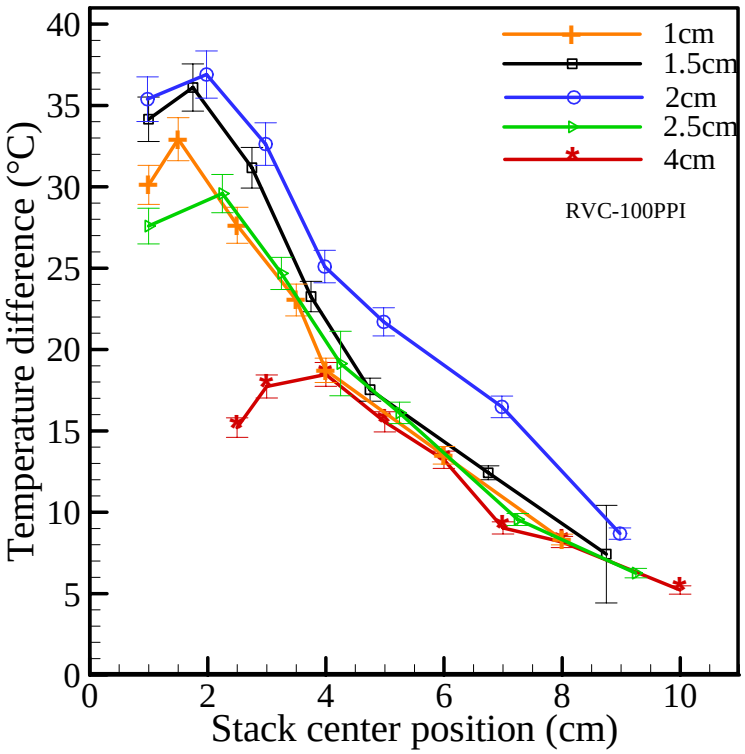

(a) 100 PPI grade, length varies from 1 to 4 cm

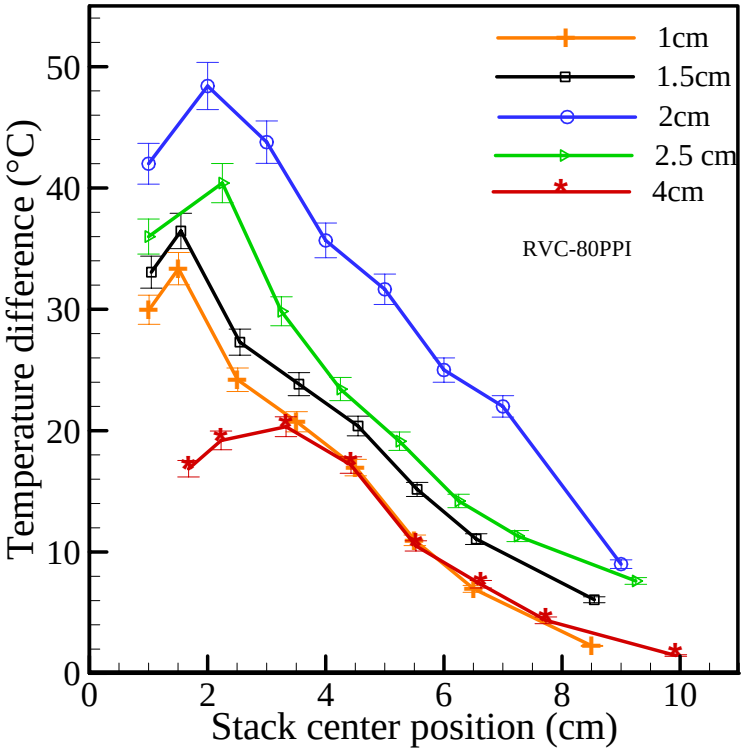

(b) 80 PPI grade, length varies from 1 to 4 cm

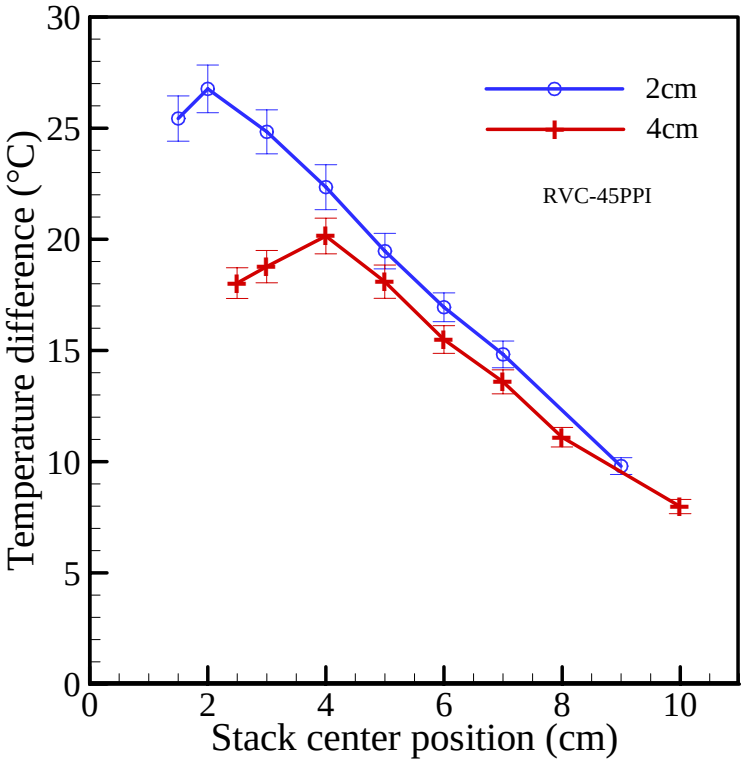

(c) 45 PPI grade and lengths are 2 and 4 cm, respectively

Figure 7.3: (a) to (c) Temperature difference generated across the stack vs. stack position for RVC stacks of different lengths and porosities.

as the stack length continues to increase. Among the five different stack lengths, 2 cm long stack produces the maximum temperature difference for all the RVC stack grades. 2 cm long 80 PPI RVC stack shows the maximum steady state temperature difference (48°C) generated across the stack ends while the stack is located 2 cm from the pressure anti-node. At this location maximum temperature at the hot end of the stack is observed which is 62°C. One interesting feature observed in Figs. 7.3(a) to (c) is that as the length of the stack increases beyond 2.5 cm, the peak temperature difference shifts to the right (will be discussed in **Section** 7.4.2). Figures 7.2 and 7.3 show the effect of porosity and dimension of the stack on the performance of a device using RVC stack.

7.4 A Detailed Study of Corning Ceramic Stacks

7.4.1 Thermal field within the Corning Ceramic Stack Structure

In the present investigation, a detail study has been performed in order to evaluate the temperature fields within the ceramic stack. Figures 7.4(a) to (d) show the temperature distributions along the stack versus stack position from the pressure anti-node as a function of stack length. Four different stack lengths of 1, 2, 2.5, and 4 cm are considered in Figs. 7.4(a) to (d). Temperatures are measured at four different locations on the stack which are equally distributed along the stack. Figures 7.4(a) to (d) show the temperature distribution along the stack plate at four different positions of the stack from the pressure anti-node. Temperatures along the stack at four different locations indicate almost linear profile along the stack in Figs. 7.4(a) to (d). The solid lines are linear fit through the data points. Gusev et al. [2001] in their analytical investigation indicated a non-linear behavior of temperature along the axial position near the extreme ends. This variation of

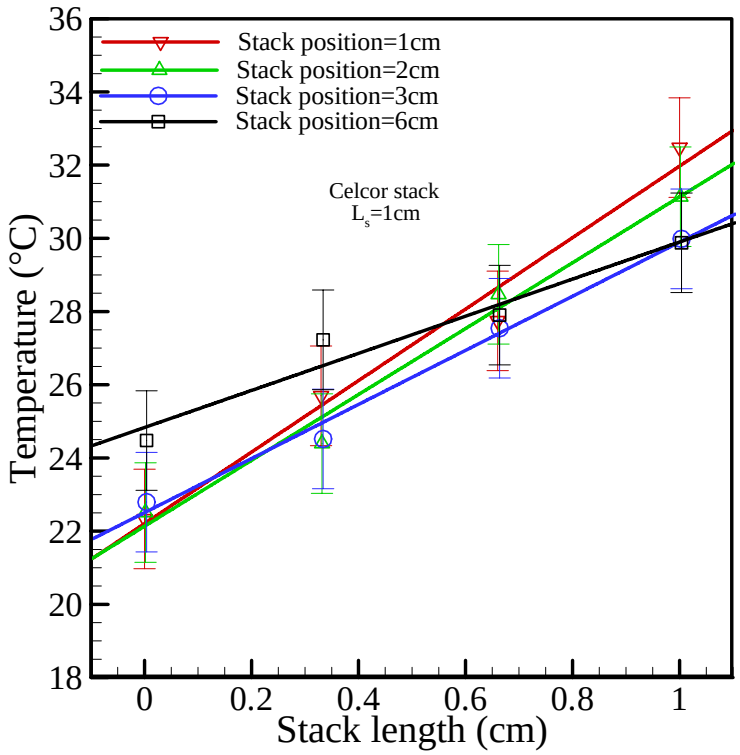

(a) Temperature distribution along the 1 cm long Ceramic stack.

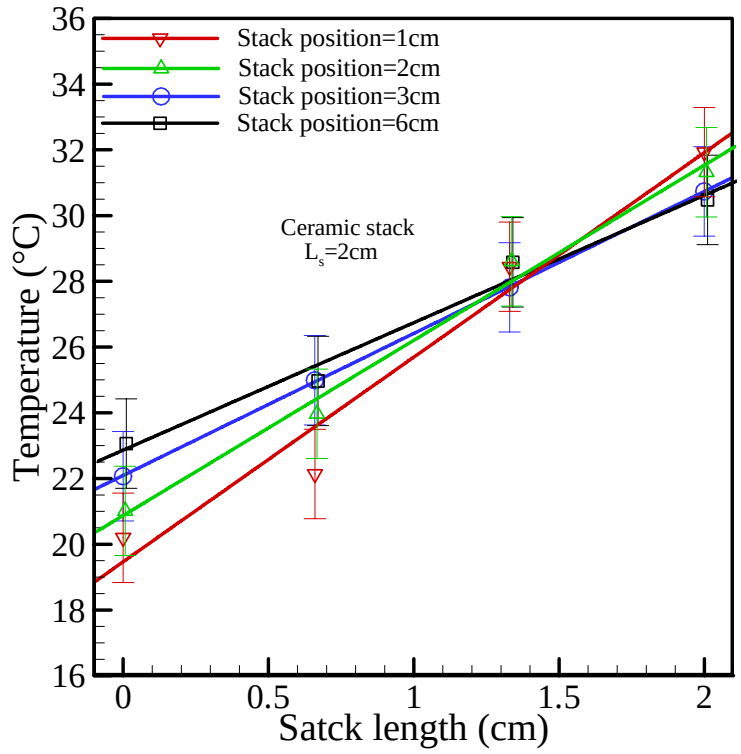

(b) Temperature distribution along the 2 cm long Ceramic stack.

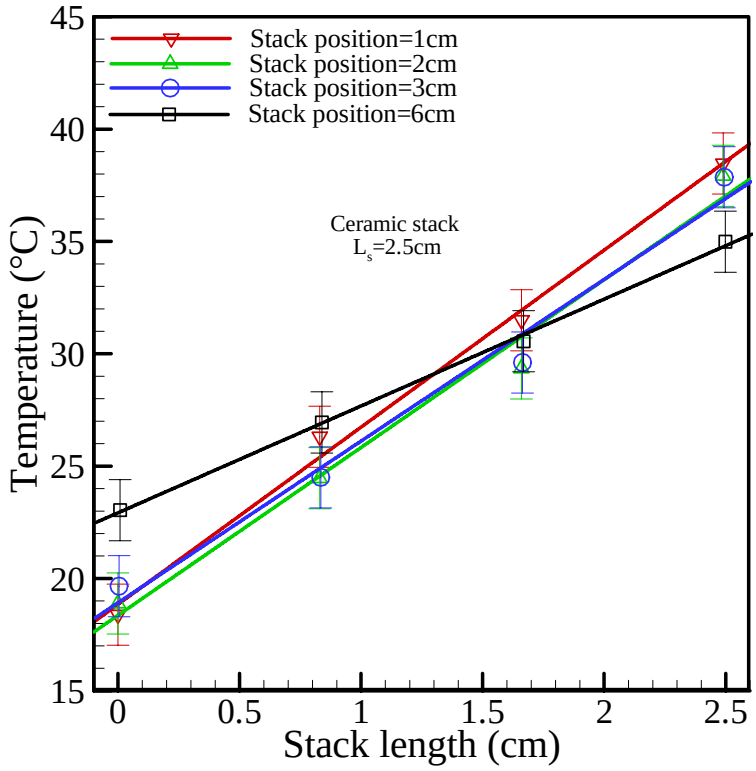

(c) Temperature distribution along the 2.5 cm long Ceramic stack.

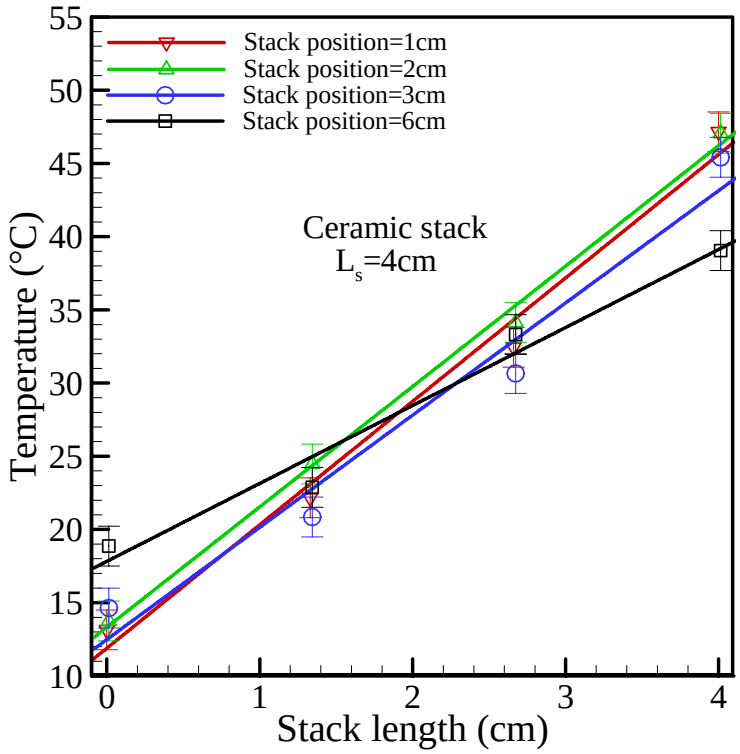

(d) Temperature distribution along the 4 cm long Ceramic stack.

Figure 7.4: Temperature distribution along the stack length at steady state. Symbols are experimental values and solid lines are the linear fit through the data points. Steady state data for (a) 1 cm, (b) 2cm, (c) 2.5 cm, and (d) 4 cm long stack, respectively.

temperature at the ends is not observed for the present experimental conditions due to the experimental uncertainties. During this measurement the stack hot end is moved from 0.5 cm to 8 cm from the nearest pressure anti-node (to organize, all the positions of the stack are not shown in Fig. 7.4(a) to (d)). An important information reveals from this figure is that as the stack is moved from the pressure anti-node (after 5 cm), temperature slope along the stack becomes flatter showing less temperature difference along the stack.

7.4.2 Steady State Temperature Difference across the Stack Ends

Steady state temperature difference generated across the stack versus stack position for six different Celcor stack lengths at eight different stack positions are shown in Fig. 7.5. In this figure, variable parameters are length and position of the stack from the nearest

pressure anti-node. Stack material and geometry are left unchanged. Figure 7.5 shows that the shortest stack length shows the lowest temperature difference for all the selected positions. The temperature difference gradually increases as the stack length increases and then gradually decreases if the stack length is further increased. Maximum temperature difference is obtained close to the pressure anti-node for all the stack lengths considered, which is also observed by Tijani [2001] and Atchley et al. [1990]. Figure 7.5 shows that as the stack length changes, the position of the maximum temperature

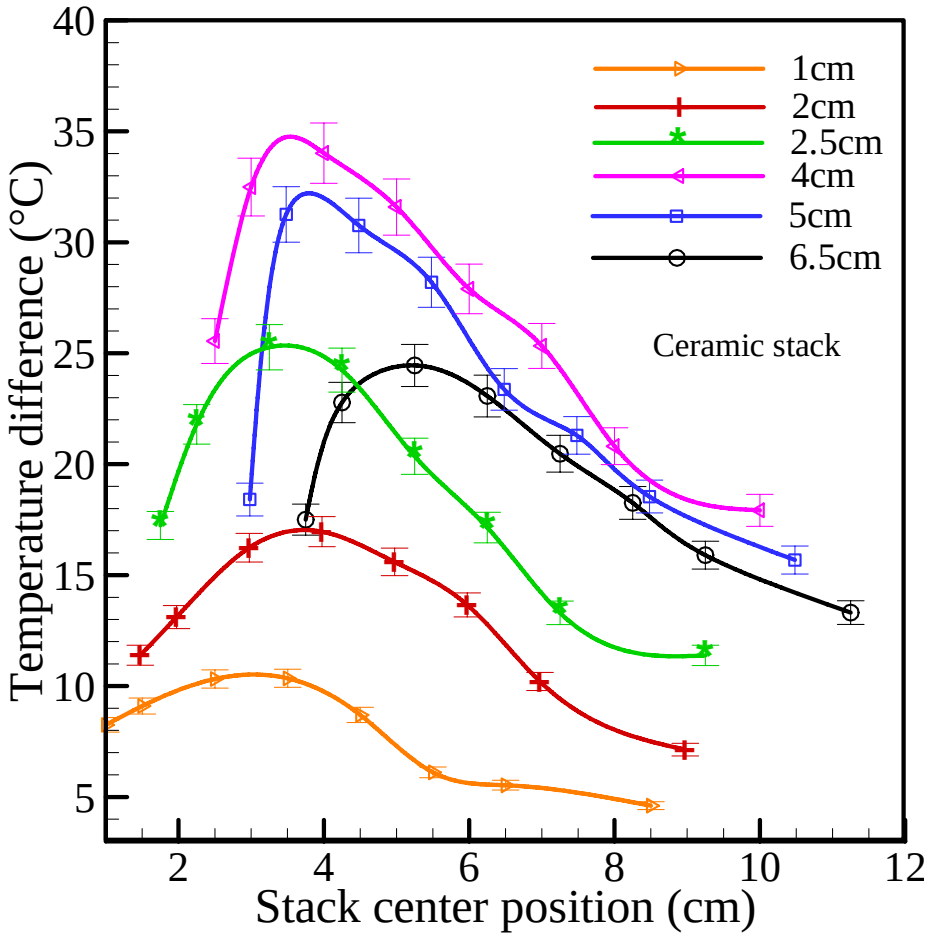

Figure 7.5 Temperature difference generated across the stack vs. stack position for different Celcor stack length stacks.

difference for a particular stack length changes, but the maximum temperature difference for all the stack lengths varies from 1 to 3 cm from the pressure anti-node. Maximum temperature difference is obtained when 4 cm (0.04λ) long stack hot end is located 2 cm from the pressure anti-node that is when 4 cm long stack center is located 4 cm from the

pressure anti-node. For a thermoacoustic device, a stack close to the pressure anti-node develops steep temperature gradient. In such a region the acoustic pressure change in a parcel of gas is large and thus the rise in temperature from compression is large. This region is very close to a velocity node, so displacement of the gas parcel is small. Large temperature changes over small displacements result in large temperature gradients. Further from the pressure anti-node, pressure and temperature change become smaller whereas displacements become larger, so the maximum temperature gradients that can be developed are smaller (Wheatley et al. [1986]). The temperature difference curves shift to the right as the length of the stack increases. Because as the length of the stack increases the distance of the stack center from the pressure anti-node increases, thereby shifting the curves to the right. Figure 7.5 shows the effect of variables such as length and position of the stack from the nearest pressure anti-node on the thermal performance of a thermoacoustic device. Figures 7.6(a) to (d) support the findings of Fig. 7.5 by presenting the time evolution of temperature at the two extreme stack ends at different

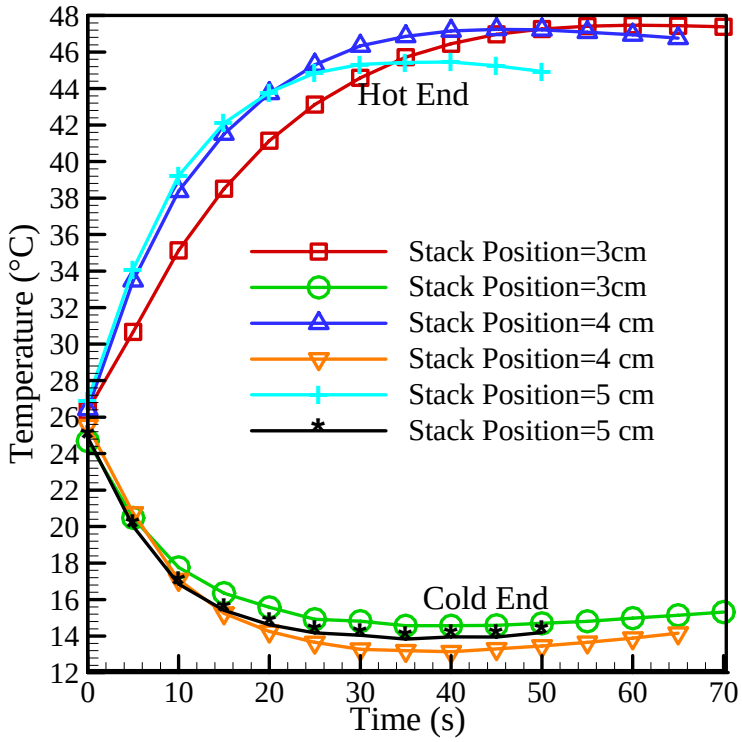

(a) Temperatures at two extreme ends of the stack when 4 cm long stack center is placed at different distances from the nearest pressure anti-node.

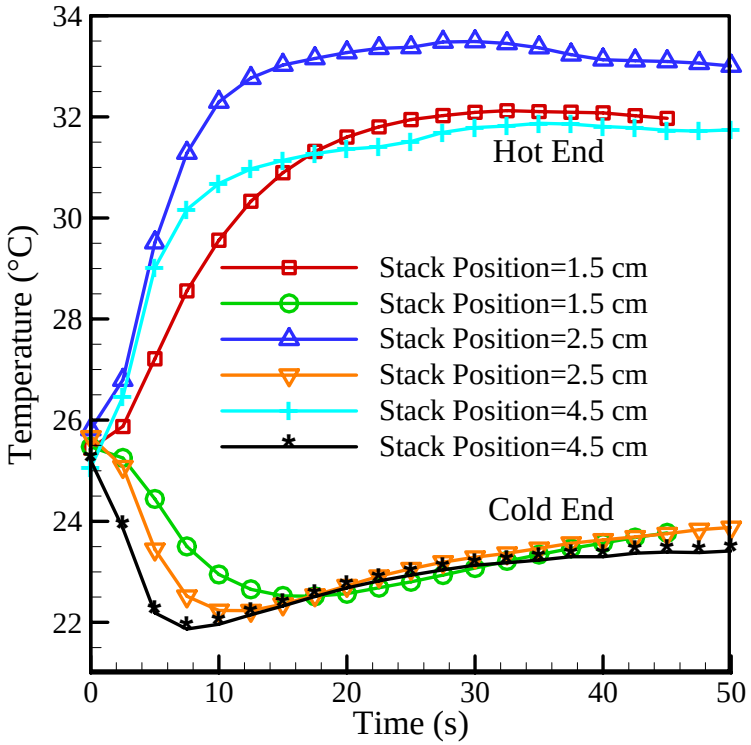

(b) Temperatures at two extreme ends of the stack when 1 cm long stack center is placed at different distances from the nearest pressure anti-node.

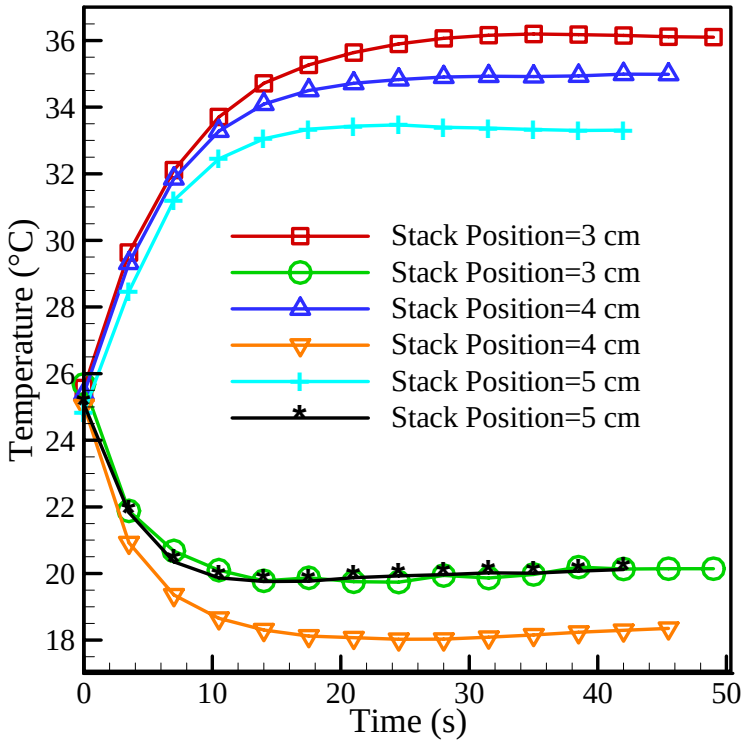

(c) Temperatures at two extreme ends of the stack when 2 cm long stack center is placed at different distances from the nearest pressure anti-node.

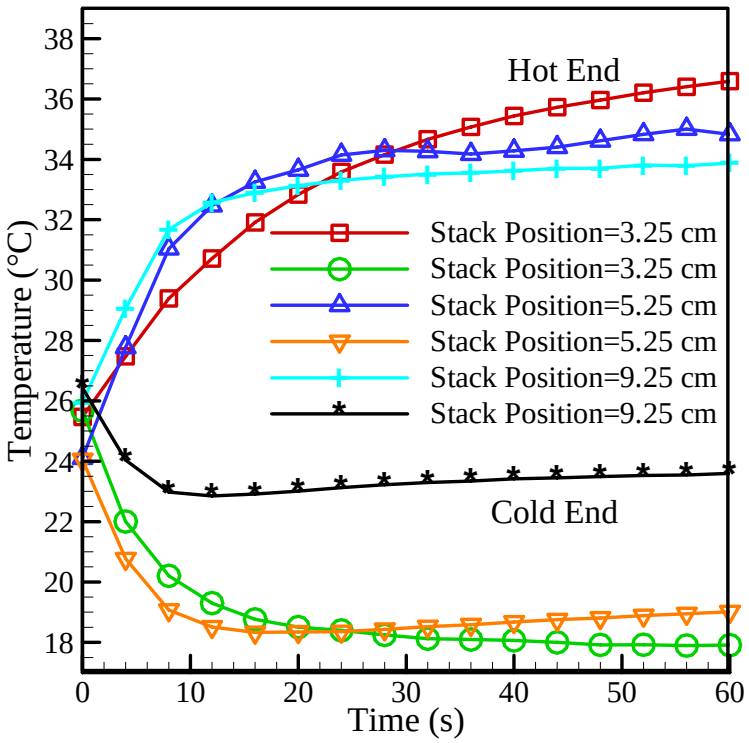

(d) Temperatures at two extreme ends of the stack when 2.5 cm long stack center is placed at different distances from the nearest pressure anti-node.

Figure 7.6: Time evolution of the measured temperatures at two extreme ends of the stack when (a) 4 cm, (b) 1 cm, (c) 2 cm, and (d) 2.5 cm stack centers are placed at different distances from the nearest pressure anti-node.

positions of the stack from the pressure anti-node. The effect of the position of the stack center from the nearest pressure anti-node is shown in Fig. 7.6(a) for the 4 cm (0.04λ) long Corning Celcor stack. The influence of stack position is almost negligible on the measured temperatures at two extreme ends of the stack for the selected positions (3, 4, and 5 cm, respectively). The hot end temperatures slopes' are almost identical for all the positions considered. Almost identical temperature slopes are observed for the cold end too. Maximum temperature (47.2°C) at the hot side and minimum at the cold side (13.1°C) of the stack is observed when 4 cm long stack center is located 4 cm form the nearest pressure anti-node. Figure 7.5 supports the findings of Fig. 7.6(a) showing almost negligible temperature difference at these positions. But temperature measurements at other positions show lower slopes because of less temperature difference across the stack (not shown in Fig. 7.6(a)). Figures 7.6(b) - (d) are for Celcor stack length of 1 cm

(0.01λ), 2 cm (0.02λ), and 2.5 cm (0.025λ), respectively. Figures 7.6(a) to (d) show that the effect of the stack hot end position (1, 2 and 3 cm, respectively) from the pressure anti-node has less influence on the time evolution of temperature at the stack extremities for the stack length of 1 to 4 cm (0.01λ to 0.04λ).

Figures 7.6(a) to (d) thus show the time evolution of the measured temperatures at the two extreme ends of stacks of different lengths that are placed at different distances from the nearest pressure anti-node. Application of acoustic power to the resonant tube immediately produces large temperature changes at the two extremities where thermodynamic symmetry is broken geometrically. The bucket brigade action of thermodynamic heat flow is discontinued at the stack extremities, thereby changing the temperatures there. Much smaller changes of temperatures occur at the middle and other locations of the stack (as shown in Figs. 7.8(a) to (f)) that are consequences of weak dynamic symmetry breaking due to viscosity and nonuniformity of the acoustic pressure and velocity fields (Wheatly et al. [1986]). For 1 cm long stack (Fig. 7.6(b)), the effect of return diffusive heat transfer is most prominent.

7.4.3 Comparisons of Temperature Difference for Stacks of Different Geometries, Materials, Dimensions and Positions on the Standing Wave

Figure 7.7 shows the comparisons of peak temperature difference generated across the stack vs. stack center position and therefore demonstrate the effect of stack material, geometry and position on the temperature difference generated across the stack ends. Figure 7.7 shows that temperature difference generated across the stack vs. stack center position is qualitatively similar for various geometries and materials at the identical operating conditions. In Fig. 7.7, the length of the stack is constant at 4 cm. Among all of the measurements, square cross- section Corning Celcor stack of 4 cm length shows the maximum temperature difference followed by the circular Kapton plastic stack and 80PPI RVC stack, respectively. But comparison of Fig. 7.7 with Figs 7.3(a) and (b) show that maximum temperature difference is obtained for 2 cm long 80 PPI RVC stack followed by 2 cm long 100 PPI RVC stack, and 4 cm long Corning Celcor stack. Therefore, the

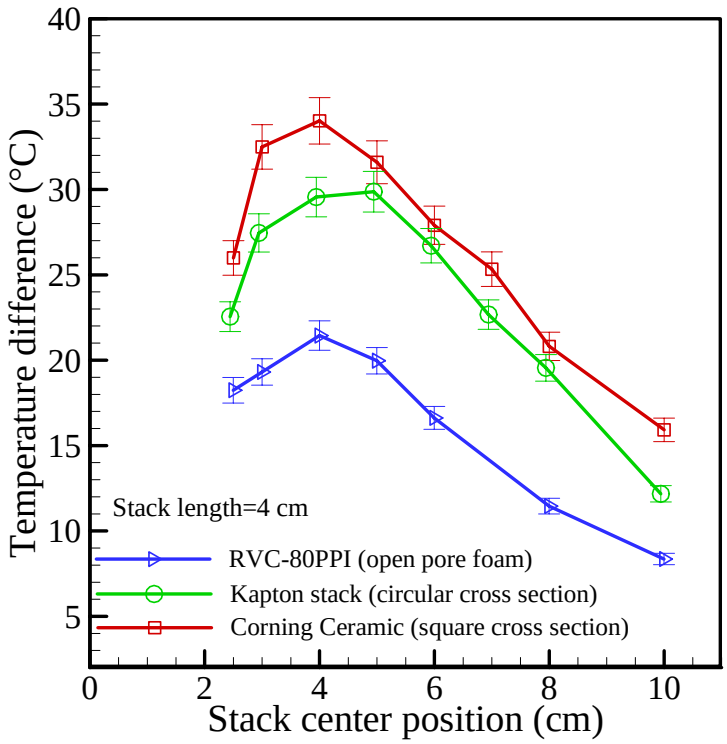

Figure 7:7: Comparison of peak temperature difference generated across the stack vs. stack position for different stack materials.

magnitude of maximum temperature difference generated at the stack ends, and maximum hot end temperature depend on the stack geometry, material, dimension, and position of the stack. The temperature profile along the stack is linear for the operating drive ratio. There is no qualitative disparity in temperature difference developed across the stack ends in Fig. 7.7 among the different geometries and materials. To better understand the effect of geometry and material on thermal field, time evolution of temperature profiles are presented in Figs. 7.8(a) to (f). Figures 7.8 (a) and (b) show identical time evolution of the temperatures measured on four different locations of the Kapton and Corning Celcor stack which are 4 cm long and the center of the stacks are located 3 cm from the nearest pressure anti-node. The slopes of temperatures at different locations on the stack except at the ends indicate less heat transfer between the fluid and the plate compared to the two extreme ends (in Figs. 7.8(a) and (b)).

Figures 7.8(c) to (f) show the effect of stack porosities on the time evolution of the measured temperatures at different locations on the stack when different porosities RVC

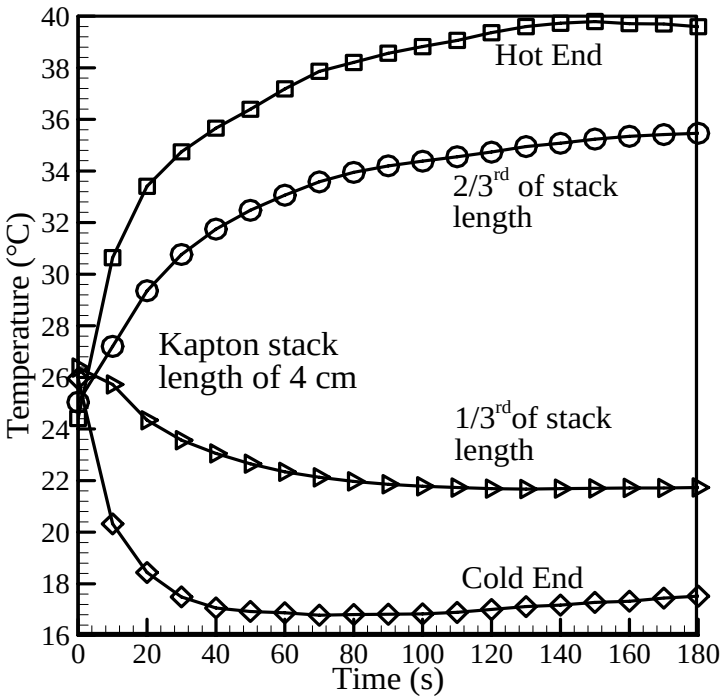

(a) Stack material: Kapton

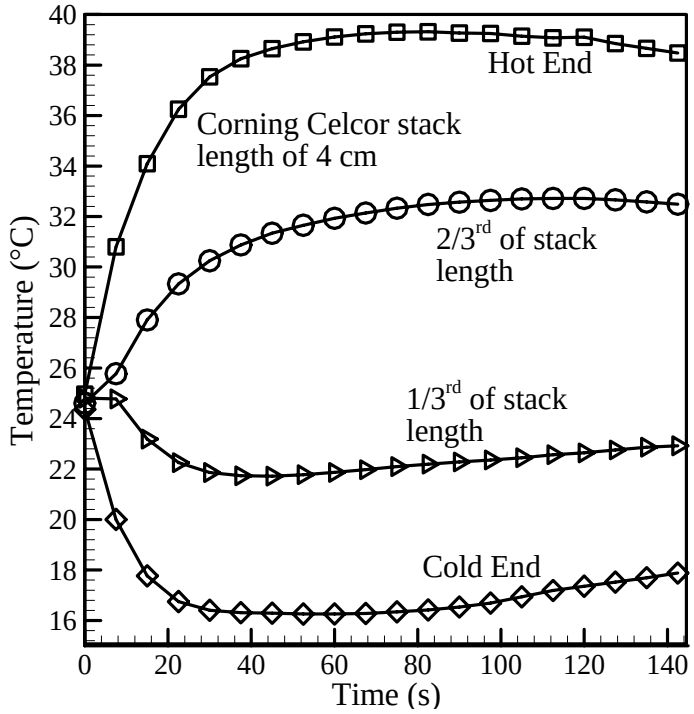

(b) Stack material: Corning Celcor

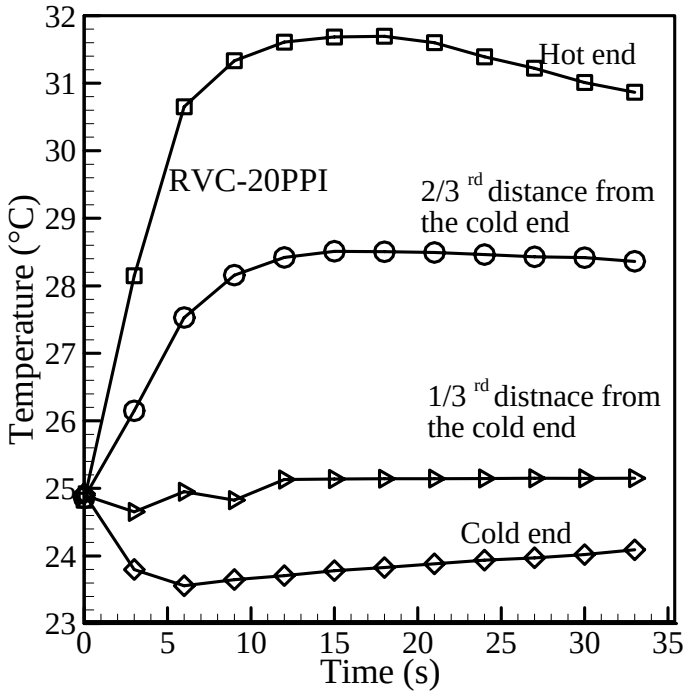

(c) Stack material: 20 PPI RVC

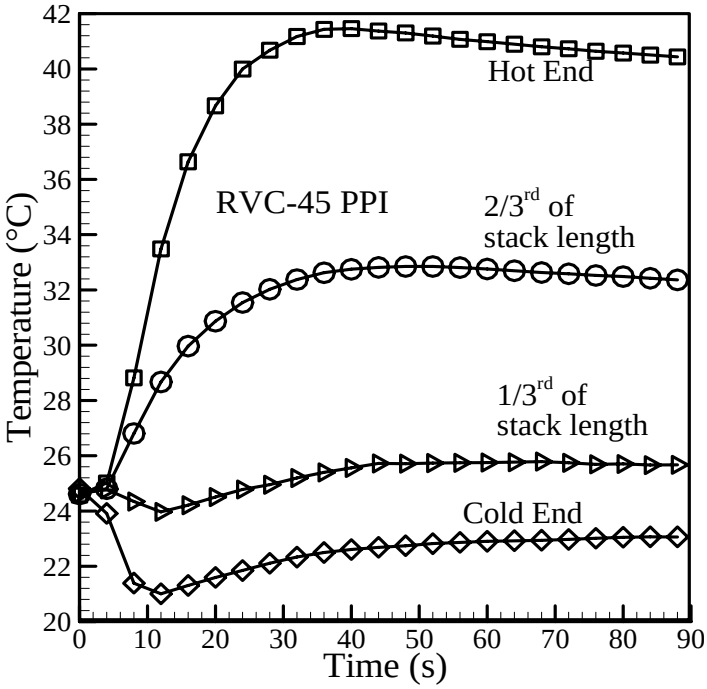

(d) Stack material: 45 PPI RVC

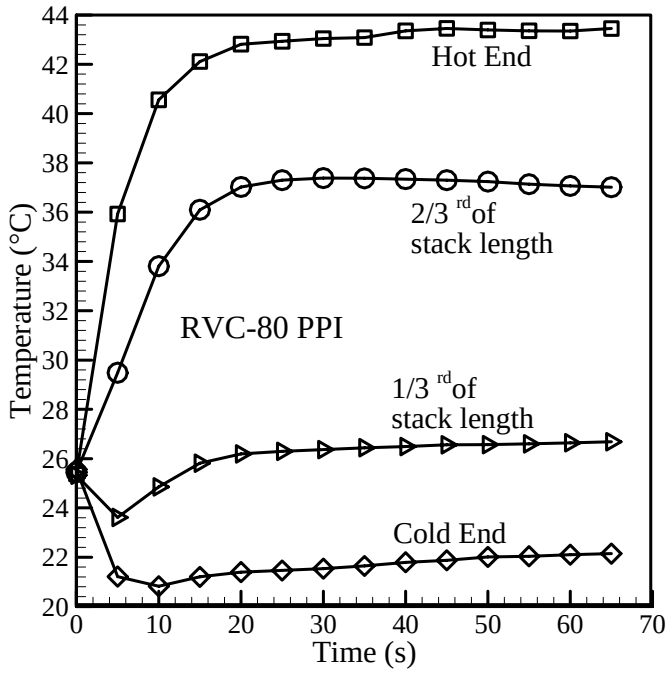

(e) Stack material: 80 PPI RVC

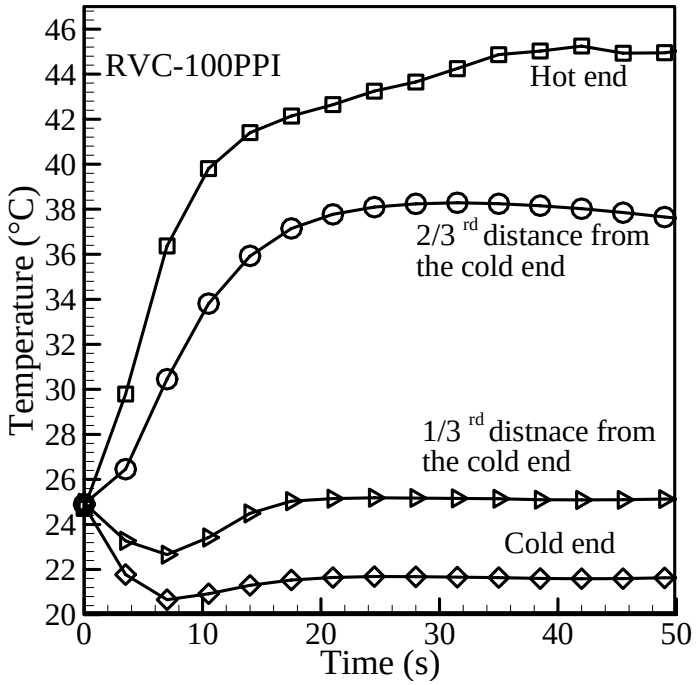

(f) Stack material: 100 PPI RVC

Figure 7.8: Time evolution of measured temperatures at different locations on the stack when (a) the Kapton, (b) Corning Celcor, (c) 20 PPI, (d) 45 PPI, (e) 80 PPI, and (f) 100 PPI RVC stacks are placed 3 cm from the closed end. In Fig. 7.8, the length of the stack is 4 cm.

stacks centers are placed 3 cm from the nearest pressure antinode. An attractive feature of Figs. 7.8(a) and (b) compared to Figs. 7.8(c) to (f) is that, thermoacoustic effect starts earlier in the latter case. The thermoacoustic effect starts right after the thermoacoustic heat pump has turned on; thereby instantly changing the temperatures on the RVC stacks, in order to obtain a steady state temperature difference across the ends of the stack. Temperatures at the hot end make high porosity RVC stack a suitable candidate for use in thermoacoustic heat pump. An interesting feature of Fig. 7.8(c) for 20 PPI RVC stack is that no cooling effect is observed at a location of the stack that is $1/3^{rd}$ of the stack length from the cold end (temperature at that location remains almost constant through all the time). The temperatures at and near the cold end then gradually increase (Fig. 7.8(c)) with a decrease in temperatures at and near the hot end. Identical behavior is observed for the 30 PPI grade (not shown here). The reason for this behavior might be the return diffusive heat transfer from the hot end towards the cold one, which is less obvious for the other cases in Figs. 7.8(d) to (f). At steady state no cooling effect is also observed at a location on the stack (in Figs. 7.8(d) to (f)) that is $1/3^{rd}$ of the stack length location from the cold end, for the 45 to 100 PPI stacks. A cooling effect is only observed at that location in the very early stage of operation. A dip in cold end temperature shows its minimum around 5 seconds after the device has started. After that, temperature at that location starts to increase with time, indicating heating effect at that location. Although temperature profiles are presented only at a single position of the stack in the resonator, other positions also show identical behavior for the respective pore sizes. The conclusion from Figs. 7.8(a) to (f) is that the time evolutions of temperature profiles of RVC stacks differ from the regular circular and square cross section stacks. For RVC stacks, the return diffusion heat transfer effect or viscous dissipation of acoustic power is significant compared to other regular stack geometry considered in the present study. At steady state, RVC stacks show cooling effect only at the cold end of the stack, different from the circular or square cross section stacks. The differences in hot and cold end temperature profiles with respect to the center of the stack show that much more acoustic work is absorbed by the stack to transport heat from the cold to the hot side of the stack compared to the circular or square cross section stacks.

7.4.4 Comparison of Experimental Works with Numerical Predictions

The experimental temperature difference is compared with a 1-D computer program, DeltaEC (Design Environment for low Amplitude ThermoAcoustic Energy Conversion, [2007]) that can calculate details of how thermoacoustic devices perform, or can help the user to design thermoacoustic devices to achieve desired performance. Results produced using DeltaEC are presented in Figs. 7.9(a) to (d). Figure 7.9(a) shows the acoustic power flow along the resonator with a sharp decrease along the stack. Since, acoustic power is absorbed by the gas parcels near the stack that are at a distance of about thermal penetration depth from the stack surface, a decrease in acoustic power is observed. Real and imaginary parts of pressure and velocity amplitudes along the resonator are shown in Figs. 7.9(b) and (c), along with the temperature difference results for the 2.5 cm long Corning Celcor stack in Fig. 7.9(d). Excellent agreement is observed between the experimental results and the numerical predictions. Therefore, the present experiment

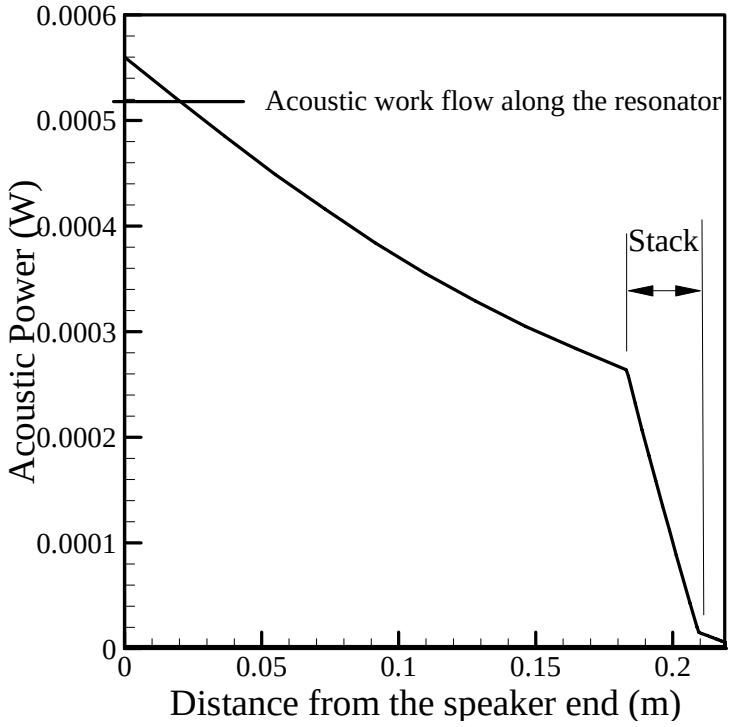

(a) Acoustic power flow along the resonator for a 2.5 cm long stack when the stack center is located 2.25 from the pressure anti-node.

shows that (DR=0.03%, thermal conductivity of the stack material, $k = 1.46\,\mathrm{W/m\,K}$), the temperature difference generated across the stack ends agrees quantitatively with the

linear theory predictions at low DR. Because the experiments are lengthy and time consuming, heat exchangers are not used every time the stack is moved from the pressure

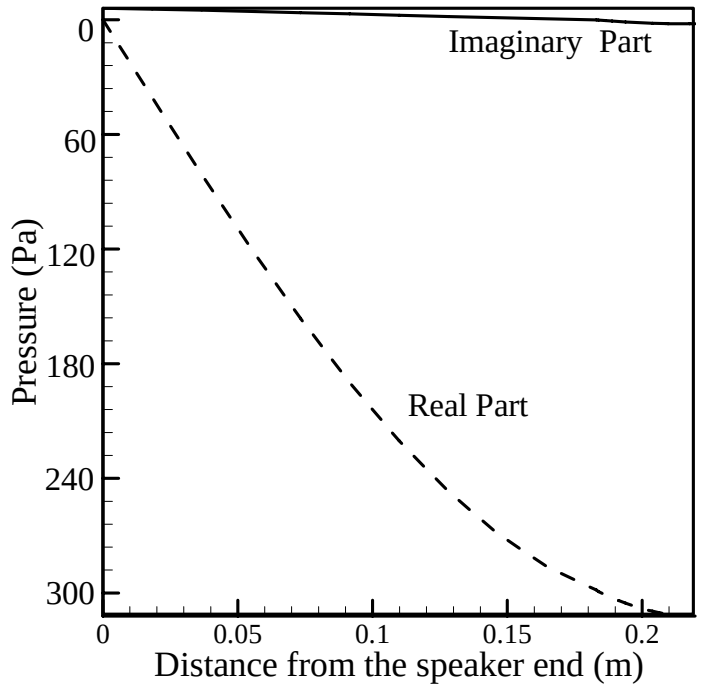

(b) Pressure amplitude along the resonator

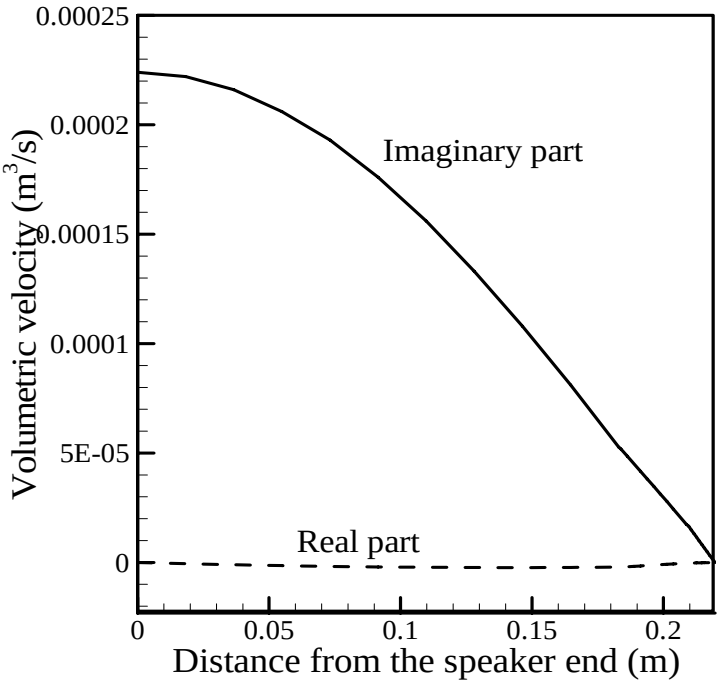

(c) Velocity amplitude along the resonator

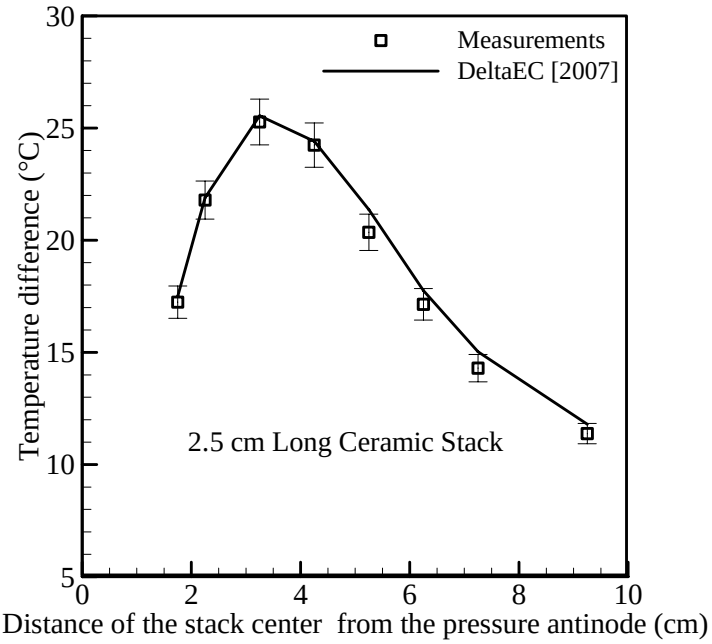

(d) Comparison of temperature difference between the measurements and the DeltaEC results.

Figure 7.9: (a) to (c) DeltaEC results of acoustic power, pressure, and velocity along the resonator. (d) Comparison of DeltaEC temperature predictions along the stack and the experimental measurements.

anti-node. Also, one of the objectives of the experiments is to provide data to validate the analytical modeling and the analytical analyses do not consider the presence of heat exchangers. For each stack length heat exchangers are installed at the cold and hot side of the stack for particular stack location, measurements are taken, and then the heat exchangers are removed for the rest of the stack positions.

7.5 Thermal Transport Processes between the Stack Plate and the Working Fluid

7.5.1 Temperature Distributions along the Stack Plate Surface and the Air

Figure 7.10 presents the time evolution of the stack and the corresponding gas parcels temperatures at four different locations on the Corning celcor stack. The gas temperatures are measured at a distance of 0.2 mm from the stack at each location. Note that for the measured operating frequency, pressure, and fluid properties, the

thermal penetration depth calculated for the present study is 0.14 mm. Location"1" indicates cold end of the stack, where the corresponding gas temperature is lower than the stack temperature, indicating heat transfer from the cold stack end to the gas. A similar heat transfer phenomenon occurs at location "2". Location "4" is the hot end of the gas, where gas temperature is higher than that of the stack, indicating heat transfer from the

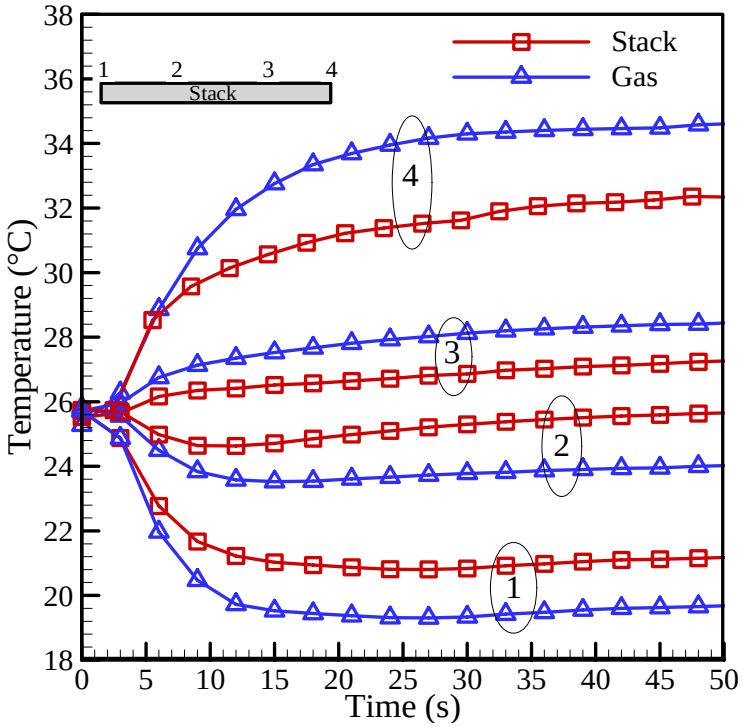

Figure 7.10: Time evolution of temperature measurements at four different locations in the 2cm stack and in the gas. "1" and "4" indicate cold and hot side of the stack, "2" and "3" are 0.67 cm and 1.33 cm from the cold end, respectively.

hot gas to the stack. Similarly at location "3", heat transfer occurs from the hot gas to the stack. This result shows the thermoacoustic heat transfer phenomena that are not available in the existing literature. The corresponding steady state temperatures are shown in Fig. 7.11(a), where heat flow direction is reversed for the two halves of the stack. Figure 7.11(a) is very insightful as it provides steady state heat transfer information between the stack and the nearby gas both at the edges and at other locations. This information is not available in the existing literature. A higher temperature difference between the stack and the corresponding gas indicates a higher convective heat transfer at the hot end compared to the cold end of the stack. A high temperature difference between the stack and the gas at the edges disappears at other locations on the stack. This high

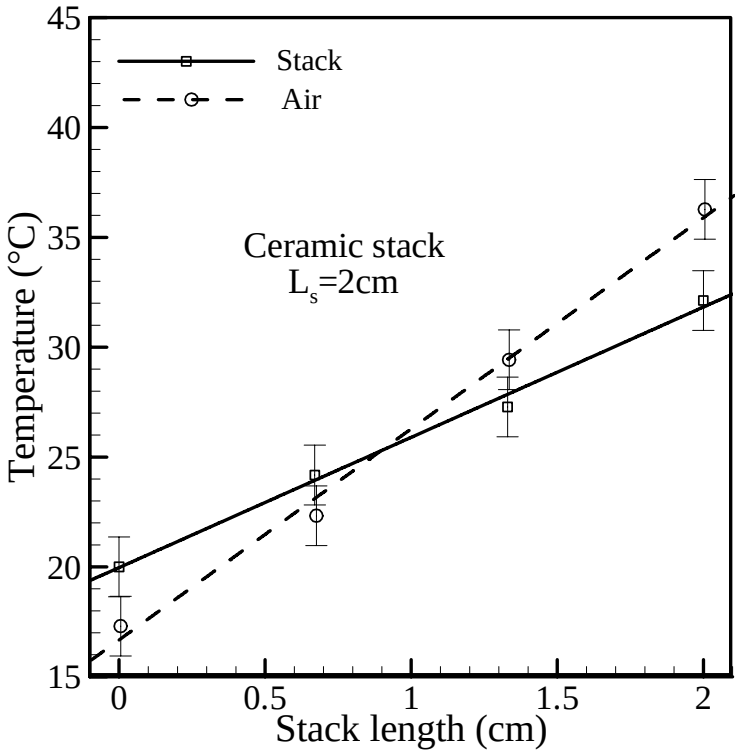

(a) Temperature along the 2 cm long stack and the gas residing near the stack when the stack center is located 3 cm from the pressure anti-node.

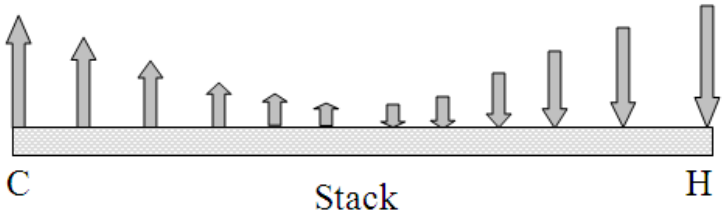

(b) Vertical heat flux along the stack based on the measurements.

Figure 7.11: (a) Steady state temperature along the stack and the gas; stack length 0 cm indicates starting of the stack and 2 cm the end of the stack. “0” indicates the cold end and “2” the hot end of the stack. In Fig.(a) the stack center is located 3 from the nearest pressure anti-node, respectively. The solid and dashed lines are linear fit through the data points. (b) Schematic diagram of the directions of the vertical heat flux along the stack based on the measurements. “C” and “H” are cold and hot sides of the stack, respectively.

temperature difference between the stack and the gas indicates high convective heat transfer at the edges that gradually decreases as one moves away from the edge, becomes zero right at the middle of the stack, and then changes its direction for the other half

section of the stack. Therefore, there is non-uniformity of the thermoacoustic process along the stack. Figure 7.11(a) supports Fig. 11(a) of Swift [1988] that describes the gas parcel model of thermoacoustics. The right part of the temperature profile from the center of the stack in Fig. 7.11(a) corresponds to the second step, and the left part of Fig. 7.11(a) corresponds to the fourth step of Fig. 11(a) of Swift [1988]. A higher temperature slope is observed for the gas parcels than the stack, and this phenomenon is due to thermoacoustic effect. Therefore, the prediction of linear thermoacoustic theory for calculating enthalpy flow along the stack or evaluating the temperature difference across the stack using similar temperature gradient along the stack plate and the nearby working gas is not perfect. A higher temperature gradient along the gas should be considered than along the stack. This information is not available in the existing literature. The lines through the data points are linear fit that indicate linear temperature profile along the gas and the stack. Figure 7.11(b) shows the time averaged transverse heat flow due to the thermoacoustic effect along the stack based on the temperature measurements in Fig. 7.10 and Fig. 7.11(a). The heat flow between the surface of the stack and the oscillating fluid is maximum at the edges, changes its direction at the middle of the stack plate due to the temperature distributions along the stack plate surface and the oscillating fluid. Because of this transverse heat flow, energy flow in the oscillating flow direction (longitudinal) is impossible to keep constant (the assumption of constant energy flow in the longitudinal direction is assumed in the linear theory Swift [1988]).

Figure 7.12(a) shows the time evolution of temperatures at two extreme ends of the stack and the corresponding gas that are 0.4 mm from both ends. The particle displacement amplitude at the hot end of stack is 0.4 mm. Figure 7.12(a) is very perceptive, location “2” is the cold and “3” is the hot end of the stack. Near the cold end gas temperature is higher than the stack end temperature. Therefore, heat will flow from the cold gas to the cold stack end. On the other hand, near the hot stack end, gas temperature is lower than the stack end temperature. Therefore, heat will flow from the hot stack end to the gas. The temperature measurements at the stack extremities and the neighboring gas show

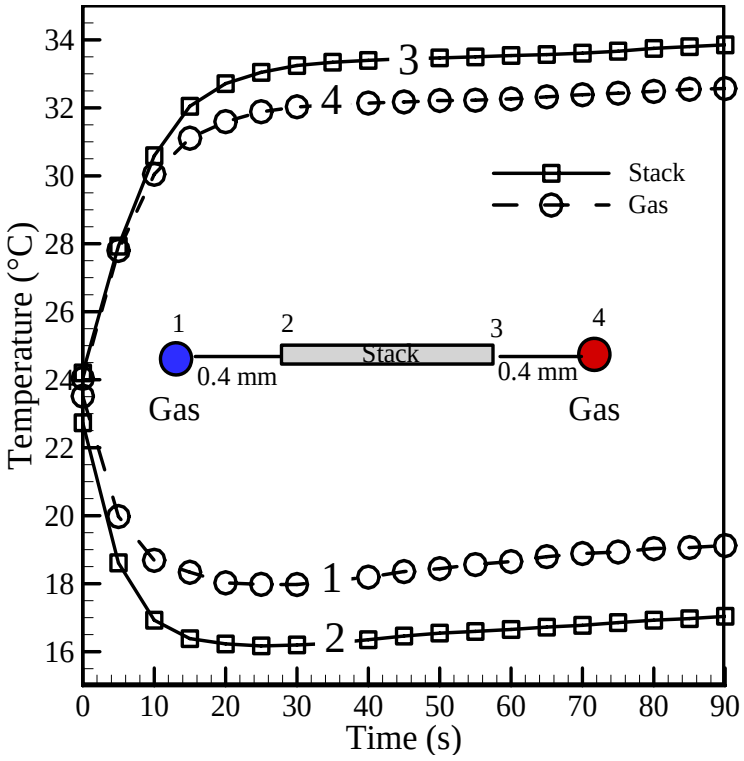

(a)

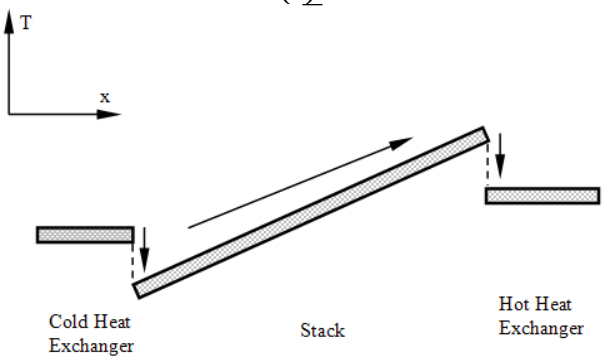

(b)

Figure 7.12: (a) Time evolution of temperature measurements at the extremities of 2 cm long stack. Gas temperatures are measured at 0.4 mm from both stack ends. "2" is the cold and "3" is the hot end of the stack. The stack center is placed 4 cm from the pressure anti-node. The lines are visual guide. (b) A schematic diagram illustrating the temperature distribution in a thermoacoustic heat pump. The arrows indicate thermoacoustic heat flow between the elements.

axial heat transfer at the stack extremities. This information is a clear challenge to the hypothesis of a perfectly isolated stack used in the linear thermoacoustic theory. According to linear thermoacoustic theory, the stack edges are perfectly isolated, i.e., no

heat is allowed to enter or leave either axially or transversally through the ends. This figure also supports the thermoacoustic heat pump process between the gas that resides near the edges of the stack and the heat exchangers. A schematic diagram illustrating the temperature distribution in a thermoacoustic heat pump is presented in Fig. 7.12(b). The arrows indicate thermoacoustic heat flow between the elements.

7.6 COP Calculation for Corning Celcor Stacks

COP of a thermoacoustic device indicates how effective the device is in converting sound energy to heat energy. Therefore, COP of the thermoacoustic heat pump is calculated using Eq. (A.18) given in Appendix A. Energy flux density or cooling power and work flux of a thermoacoustic heat pump are evaluated by utilizing Eqs. (A.17) and (A.16). Figure 7.13 presents the COP of a thermoacoustic heat pump using Corning ceramic stack of various lengths 1, 2, 2.5, 4, 5, and 6.5 cm, respectively. The plate spacing of the stack plate is constant. Stack center position and lengths are non-dimensionalized in Fig. 7.13 using $x_n = k_1 x_c$, where k_1 is the wave number and x_c is the

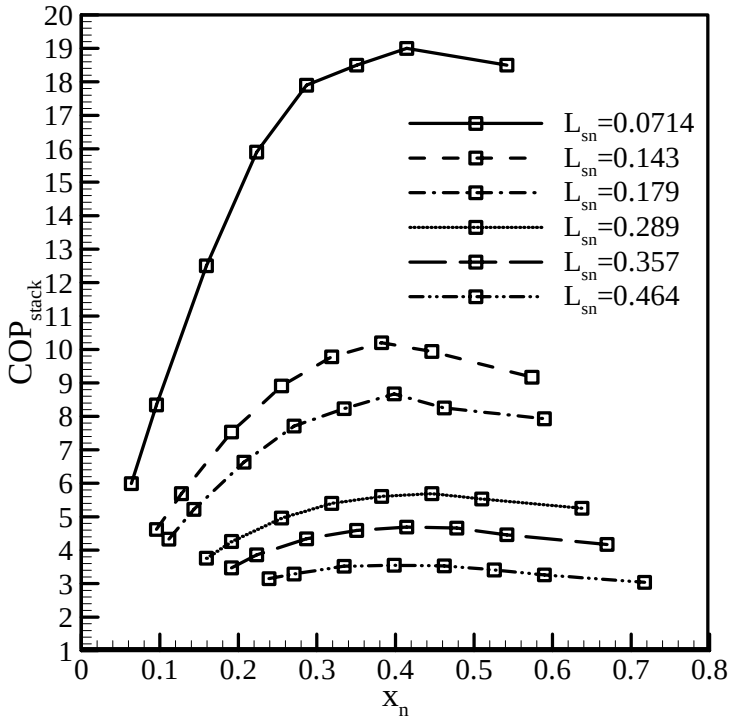

Figure 7.13: COP of the heat pump stack versus non-dimensional stack center position from the pressure anti-node as a function of non-dimensional stack length. The lines are visual guide.

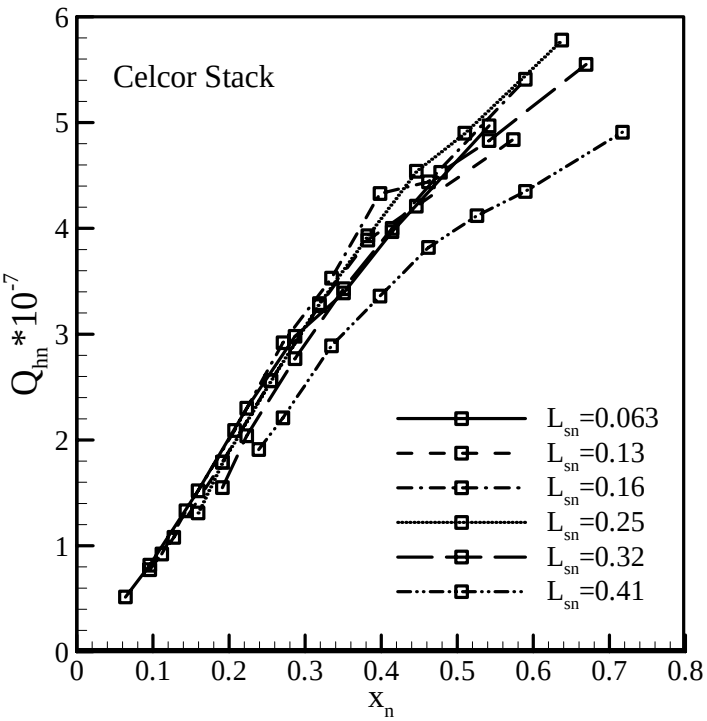

Figure 7.14: Energy flow at the hot side of the stack versus non-dimensional stack center position from the pressure anti-node as a function of non-dimensional stack length. The lines are visual guide.

stack center distance from the pressure anti-node, and $L_{sn} = k_1 L_s$, L_s is the length of the stack. For all the stack lengths considered, the values of COP in Fig. 7.13 are the least near the pressure anti-node gradually increases as the distance of the stack center increases from the pressure anti-node, shows maximum and then gradually decreases. Figure 7.13 shows that the values of COP changes as the stack length changes. The shortest stack length shows the maximum COP for all the selected positions of the Corning Celcor stack. The COP gradually decreases as the stack length increases. This behavior can be understood using Fig. 7.14 and Fig. 7.15. Figures 7.14 and 7.15 present the non-dimensional energy flux density and work flux density as a function of non-dimensional stack position for different stack lengths. Energy flux density and work flux density are non-dimensionalized by dividing them by a product of $p_m a A$ (Swift [1988]), where p_m is the mean pressure, a is the adiabatic speed of sound, and A is the cross sectional area of the resonator. The absolute value of the energy flux is directly proportional to the power density of the thermoacoustic devices. Therefore, energy flux

may serve as a power density. In evaluating the energy flux density at the hot end of the stack, the acoustic power absorbed by the stack is added to the energy flux density at the

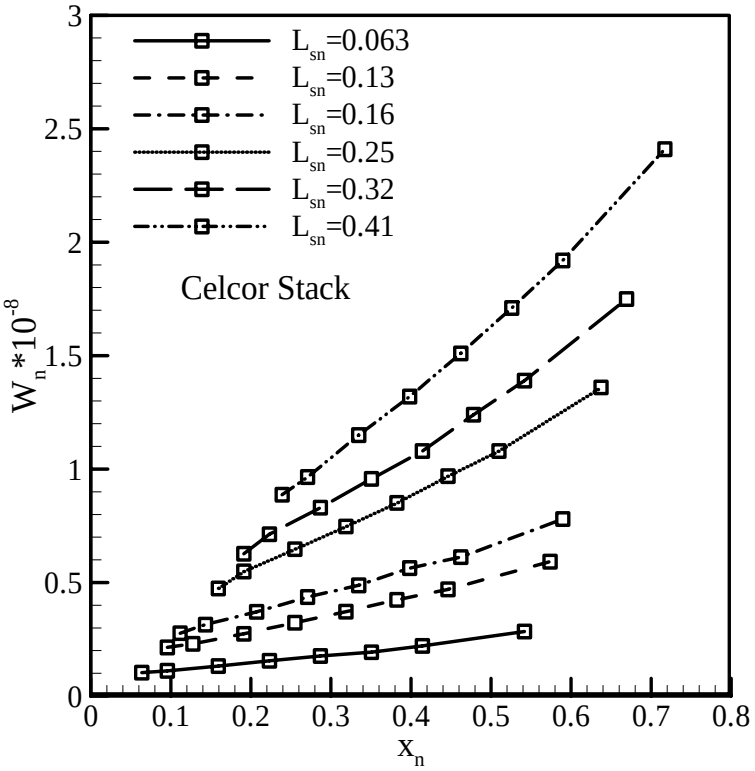

Figure 7.15: Acoustic work versus non-dimensional stack center position from the pressure anti-node as a function of non-dimensional stack length. The lines are visual guide.

cold end of the stack. It is observed that energy flux density is minimum near the pressure anti-node and increases linearly with distance from the pressure anti-node. Energy flux density is proportional to the product of $p_1 u_1$ (Eq. (76) of Swift [1988]). $p_1 u_1$ is minimum near the pressure anti-node and increases linearly as the stack distance from the pressure anti-node increases. It is concluded that the maximum energy flux may be expected at a position roughly halfway between the pressure anti-node and pressure node (Swift [1988]) which is also observed in Fig. 7.14. The power density or energy flow at the hot side of the stack is almost independent on the length of the stack in Fig. 7.14, which is also supported by Ishikawa and Mee [2002]. Equation (76) of Swift [1988] supports this finding which showed that energy flux density is proportional to the cross section area of fluid in the stack. Again, acoustic power absorbed by the gas near the stack plate depends

on the stack length and stack center position in Fig. 7.15. Equation (80) of Swift [1988] supports this finding which showed that acoustic power is proportional to the length the stack. An increase in the stack length and stack center position from the pressure anti-node increases the acoustic power absorbed by the gas. Since, acoustic power is proportional to the length of the stack, and the viscous loss is increased as the velocity amplitude increases. Therefore, a shorter stack length absorbs less acoustic power and shows higher COP in Fig. 7.13. The COPR shows a parabolic behavior in Fig. 7.16 with a maximum for all stacks, but the magnitude and the position of the peak changes as the stack length changes. The COPR is evaluated by dividing the COP to the Carnot Coefficient of performance (COPC). The COPR shows a maximum at a stack length of 2.5 cm (0.025λ) and a position of 4.25 cm which is almost $\approx \lambda/20$ as suggested by

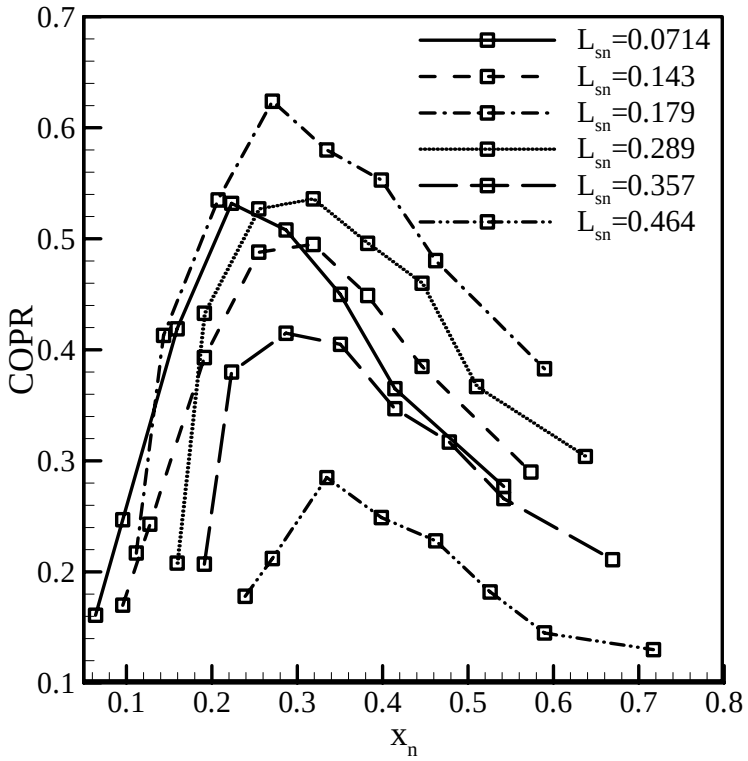

Figure 7.16: COPR versus x_n as a function of $L_{sn.}$ The lines are visual guide.

Swift [2002]. At this maximum location, COP is roughly 60% of Carnot's COP. Therefore, when thermoacoustic devices are used as heat pumps, a compromise has to be made between the COP and the maximum temperature at the hot side or the maximum temperature difference between the extremities of the stack ends. The maximum COPR

of a thermoacoustic refrigerator designed and tested by Hofler is 0.12 as indicated by Swift [1988]. The COPR indicated in the literature by Swift [1988] is for the complete thermoacoustic refrigerator as opposed to only stack in the present study. While considering the efficiency of a loudspeaker, and losses (viscous and thermal) along the stack, heat exchangers, and the resonator, heat leaks through the stack and the resonator, the COPR of a complete thermoacoustic heat pump will be lower than the COPR of a stack as presented in the presented study.

7.7 COP Calculation of RVC Stacks

Figures 7.17 and 7.18 show the energy flux density and work flux versus non-dimensional stack center position (x_n) from the pressure anti-node as a function of stack porosity. Energy flux density and work flux are evaluated by utilizing Eqs. (A.17) and (A.16), along with the modifications proposed by Wilen [2001] and provided in Chapter 5. The different porosities of the stack that are considered in this section are 20, 30, 45,

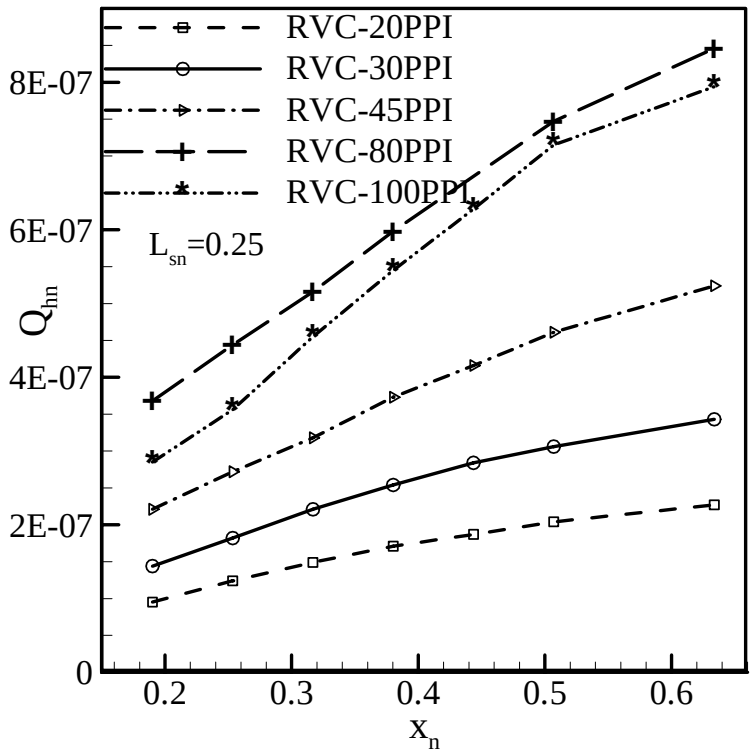

Figure 7.17: Energy flow at the hot side of the stack versus non-dimensional stack center position from the pressure anti-node as a function of stack porosity. The lines are visual guide. The stack is constant at 4 cm.

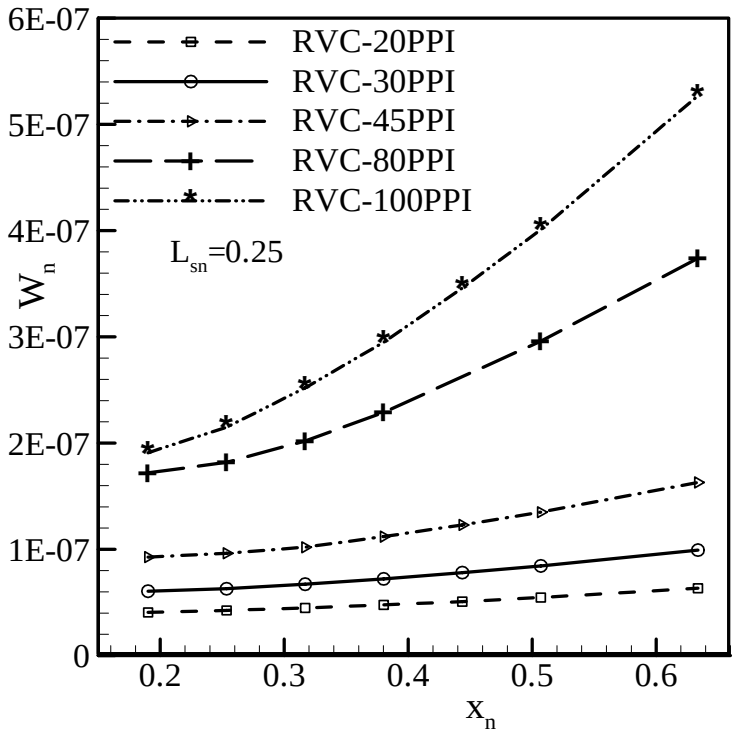

Figure 7.18: Acoustic work versus non-dimensional stack center position from the pressure anti-node as a function of stack porosity. The lines are visual guide. The stack is constant at 4 cm.

80, and 100 PPI, respectively. The length of the stack is constant at 4 cm (0.04λ). Figure 7.17 shows that power density varies as the porosity of the stack changes and the variation of power density is linear with the distance from the pressure anti-node. 80 PPI grade stack shows the maximum power density in Figure 7.18 followed by 100 and 45 PPI grades. 20 PPI grade shows the minimum cooling power extracted by the stack. The reason for minimum power density extracted by 20 PPI grade is already described in **Section** 7.4. Comparing Fig. 7.14 and 7.17 for non-dimensional power density of different geometries, 80 PPI RVC stack shows the maximum value, followed by 100 PPI RVC stack. 100 PPI grade shows the maximum acoustic power absorbed by the stack followed by the 80 and 45 PPI grade in Fig. 7.18. For 100 PPI grade, the pore size is too small, therefore contributing maximum for the dissipation of acoustic energy. For the small pore sizes for example 20, 30, and 45 PPI grades, acoustic work absorbed by the stack increases linearly as the stack center moves away from the pressure anti-node. But for 80 and 100 PPI grades, acoustic work absorbed by the stack increases exponentially with the distance. Figures 7.19 and 7.20 present the change of power density versus non-

dimensional stack center position (x_n) from the pressure antinode as a function of stack length for 45 and 80 PPI grades. Figure 7.20 shows that power density increases as the stack length increases from 1.5 cm to 4 cm. The increase of stack length with the stack position from the pressure anti-node is linear with a steep slope for longer stacks. The effect of stack length is more pronounced for RVC stacks compared to the Corning Celcor stack (in Figs. 7.19, 7.20, and 7.14). Figure 7.21 shows the variation of acoustic work versus non-dimensional stack center position from the pressure anti-node as a function of stack length for 45 PPI grade. Acoustic work increases as the stack length increases. Figure 7.22 presents the COP of the heat pump stack versus non-dimensional stack center position from the pressure anti-node as a function of stack porosity for a constant stack length of 4 cm. 100 PPI grade shows the lowest COP of the stack and maximum COP is obtained for 20 PPI grades which are expected. Since 100 PPI grade absorbs the maximum acoustic work which is significantly higher than the 20 PPI grade, thereby showing minimum COP values. Maximum COPR is obtained by the 45 PPI grade.

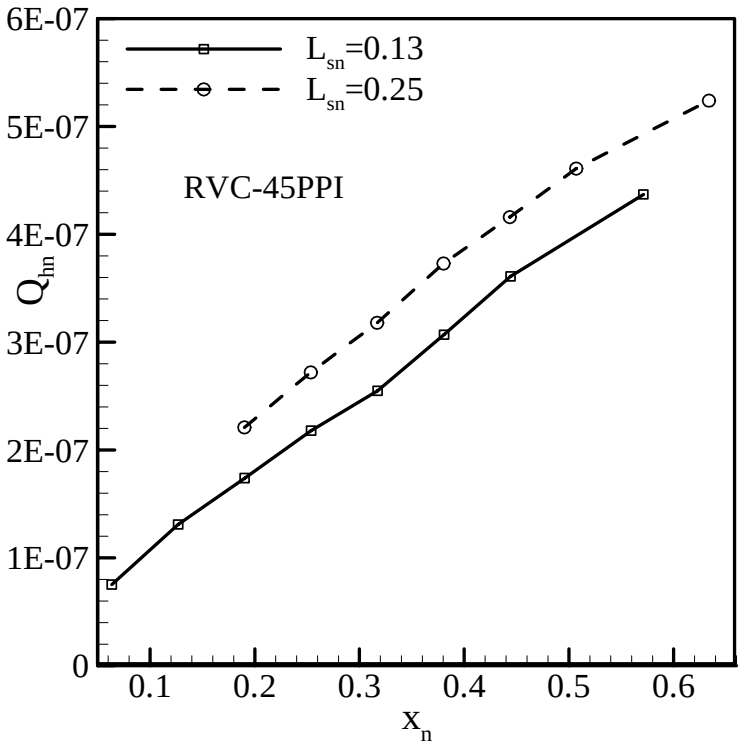

Figure 7.19: Energy flow at the hot side of the stack versus non-dimensional stack center position from the pressure anti-node as a function of stack length. The lines are visual guide.

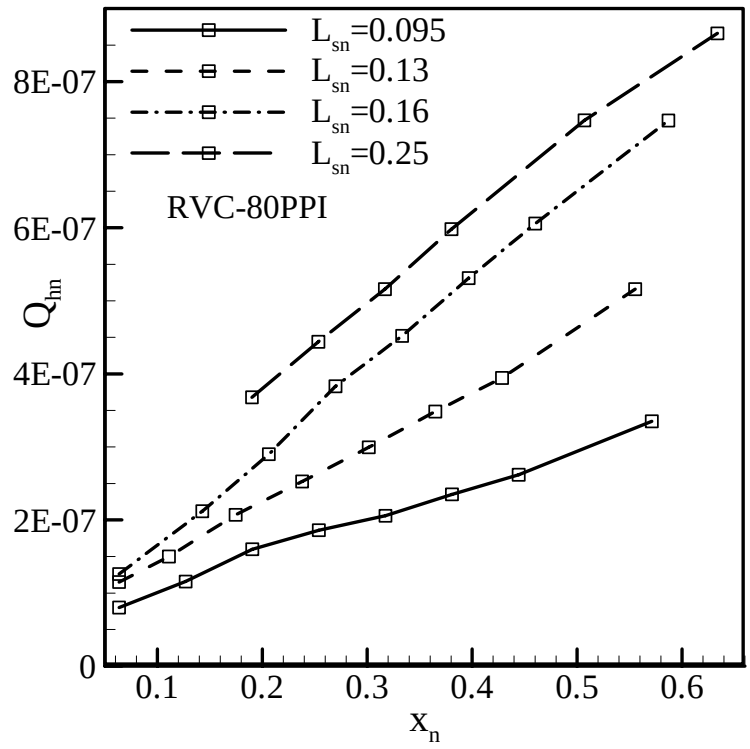

Figure 7.20: Energy flow at the hot side of the stack versus non-dimensional stack center position from the pressure anti-node as a function of stack length. The lines are visual guide.

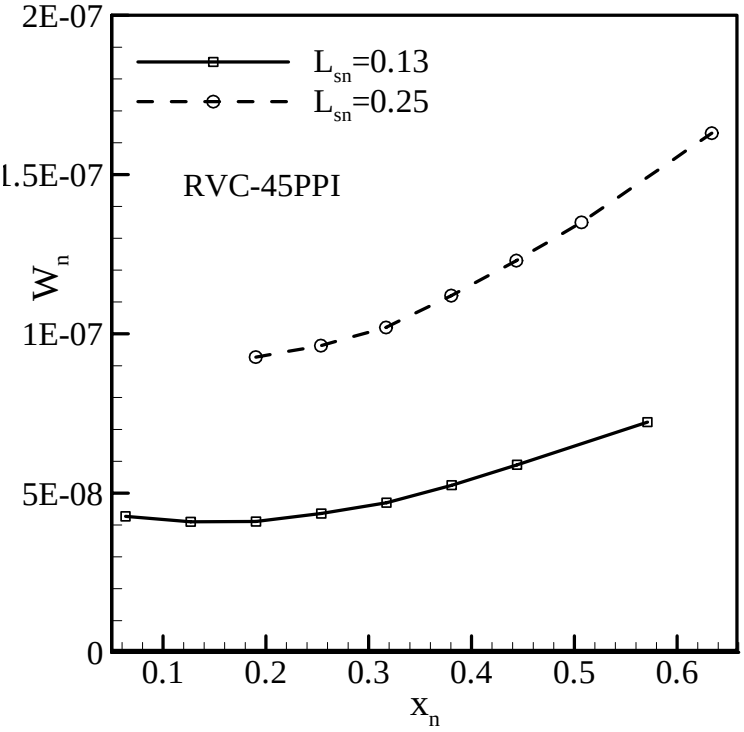

Figure 7.21: Acoustic work versus non-dimensional stack center position from the pressure anti-node as a function of stack length. The lines are exponential fit through the data points.

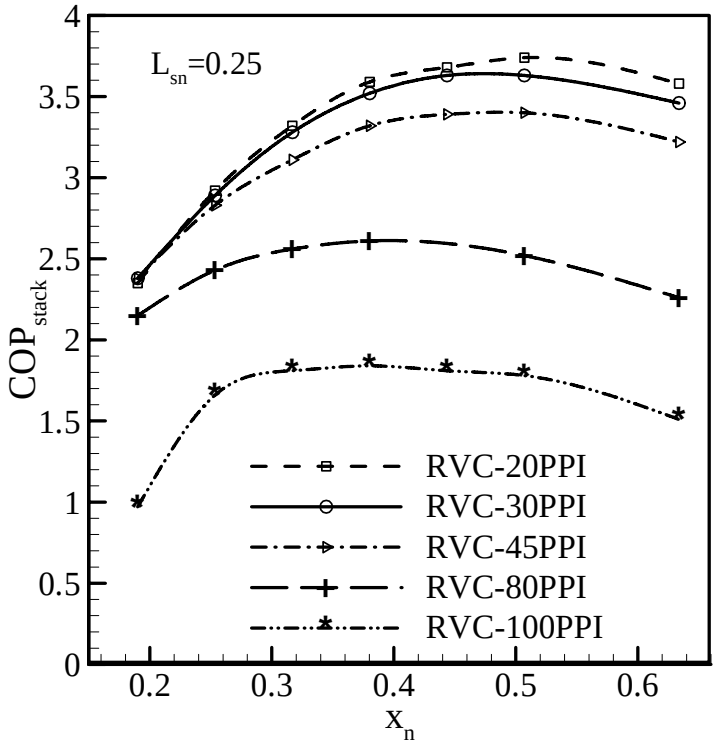

Figure 7.22: COP of the heat pump stack versus non-dimensional stack center position from the pressure anti-node as a function of stack porosity. The lines are visual guide.

The COPR shows a parabolic behavior in Fig. 7.23 with a maximum for all stacks, but the magnitude and the position of the peak changes as the stack porosity changes. 45 PPI grade shows the best performance when the stack center is located 3 ($\approx \lambda/30$) cm from the pressure anti-node. Therefore, for random porous structure such as RVC stacks, the maximum performance is not observed at a location $\approx \lambda/20$ from the pressure anti-node, rather the distance is $\approx \lambda/30$. At this maximum location, COP is roughly 20% of Carnot's COP, which is much less than Corning ceramic stack. Figure 7.24 presents the COPR of the heat pump stack versus non-dimensional stack center position from the pressure anti-node as a function of stack porosity at a constant stack length of 2 cm. Three different pore sizes are shown from 45 to 100 PPI as the remaining other two pore sizes (20 and 30 PPI) produce very small temperature difference and hence are not suitable for considering as stacks in thermoacoustic heat pumps. In order to organize the data other stack lengths of 1, 1.5, and 2.5 cm are not presented in Fig. 7.24. Comparison of Fig. 7.23 and 7.24 shows that as the stack length decreases from 4 cm to 2 cm, the

COPR increases. One reason is due to the decrease in COPC as the temperature difference increases for 2 cm long stack. Another reason is due to the decrease in absorbed acoustic power for 2 cm long stack which increases the COP. In Fig. 7.24, comparing COPR of all the RVC stacks; 80 PPI grade shows the best performance with a maximum value at a stack position which is 2 cm from the pressure anti-node. At this maximum location, COP is roughly 40% of Carnot's COP, which is less than Corning ceramic stack (60%). Note that at this position maximum temperature difference is also observed for 80 PPI grade. Therefore, to obtain maximum temperature difference across the stack ends at steady state 80 PPI RVC stack of 2 cm length should be used. This stack produces the maximum temperature difference of 48°C at a hot side temperature of 63°C while heat pump is driven at a frequency of 350 Hz and as drive ratio of 0.03%. To obtain the highest COPR, Ceramic stack with a length 2.5 cm and a pore size of 1.27 mm should be used.

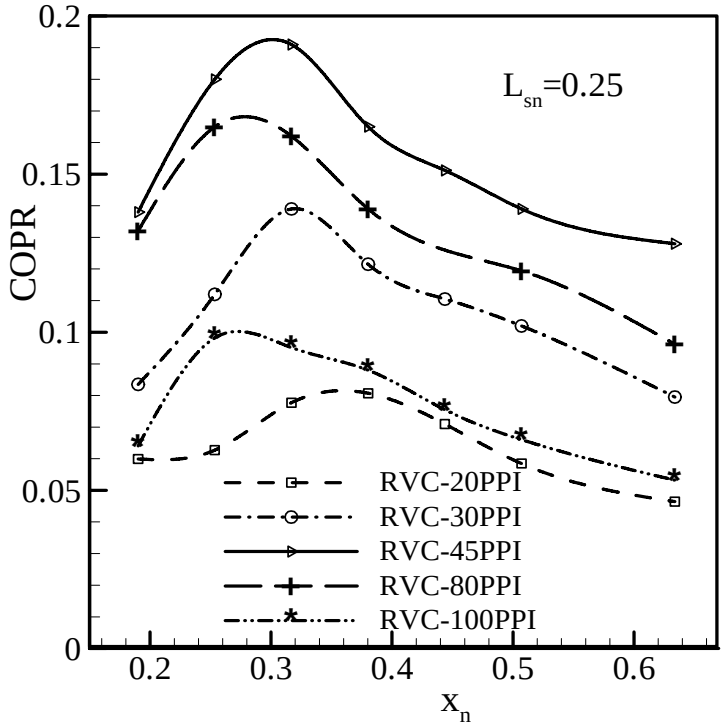

Figure 7.23: COPR of the heat pump stack versus non-dimensional stack center position from the pressure anti-node as a function of stack porosity. The lines are visual guide.

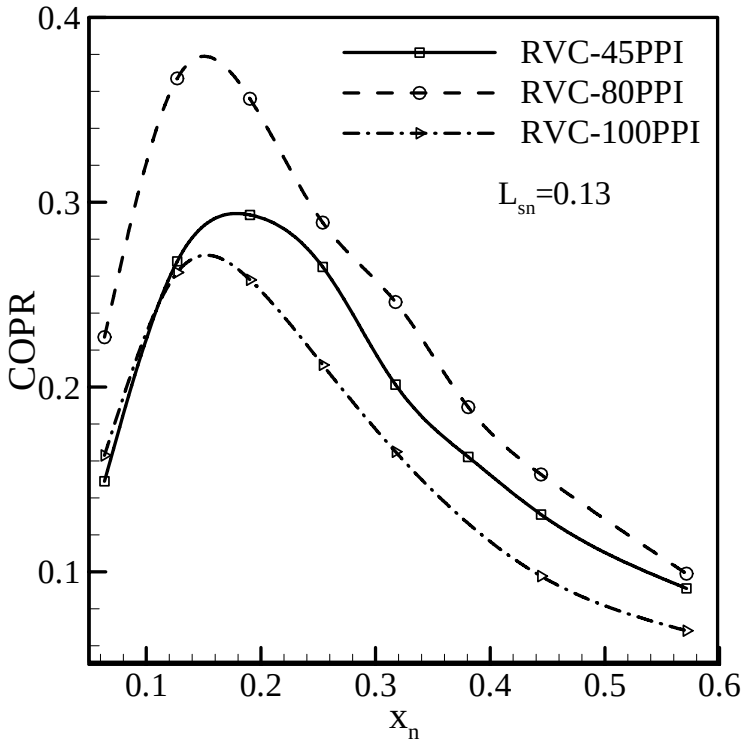

Figure 7.24: COPR of the heat pump stack versus non-dimensional stack center position from the pressure anti-node as a function of stack porosity at a constant stack length of 2 cm. The lines are visual guide.

7. 8 Conclusions

The influence of the geometry, material, dimension, and position of the stack on the behavior of the heat pump is studied systematically. The performance of the thermoacoustic heat pump, using stacks of different materials (Celcor ceramic, RVC, and Kapton plastic), geometries (square cross section, open foam, and circular), lengths (1 cm to 6.5 cm for Celcor ceramic stack, and 1 cm to 4 cm for RVC stacks), and positions (0.5 cm to 8 cm) is measured. The thermoacoustic heat pump has been able to highlight the general features of the thermoacoustic effect. The only limitation of the present experiment is that the DR is low (0.03%). Due to the limited resources available regarding the loudspeaker and the amplifier, the operating DR could not be increased. Based on the results presented in this study, one may make the following observations regarding the performance of stacks:

- There is no qualitative difference in temperature gradient developed along the stack length vs. stack center position regarding to stack length, geometry, and material. But the time evolution of temperature profiles for regular stack geometry is quite different than the random porous geometry. For the regular stack geometry cooling effect is observed for the half of the stack whereas heating effect is observed for the other half. There is no such distinct region for a random porous geometry. The reason might be the diffusion heat transfer from the hot to the cold end and also the viscous dissipation of acoustic work. Thermoacoustic effect starts earlier for random porous geometry compared to the regular stack geometry.

- The present study shows that temperature difference across the stack ends, maximum temperature at the hot end of the stack, and COPR depend on the stack geometry, dimension, material, and position of the stack. 2 cm long (0.02λ) 80 PPI RVC stack produces the maximum temperature difference (48°C) across the stack ends and also the maximum temperature (63°C) at the hot end of the stack when the stack center is located 2 cm from the nearest pressure anti-node. Therefore, RVC stacks (especially 80 PPI) are suitable for operation of small scale thermoacoustic heat pumps.

- For RVC stacks, power density depends on pore size and stack length. Power density increases linearly as the pore density increases from 20 PPI to 80 PPI, but decreases if the pore density continues to increase. Power density also increases linearly as the stack length increases. But the effect of stack length on power density is more pronounced in RVC stack than the Corning Celcor stack. Highest cooling power is observed for the 4 cm long 80 PPI RVC stack.

- Acoustic work absorbed by the RVC stack increases linearly from 20 PPI to 45 PPI grades as a function of stack position. Whereas for 80 PPI and 100 PPI grades, acoustic work absorbed by the stack increases exponentially as a

function of stack position. Acoustic work also increases as the RVC stack length increases.

- For Corning Celcor stack, the power density at the hot side of the stack is almost independent to the stack length.

- The acoustic power absorbed by the Celcor stack increases linearly as the stack length increases with a steep slope for larger stack length. Acoustic power also increases linearly as the center of the Corning Celcor stack from the pressure anti-node increases.

- The optimum performance is obtained when 2.5 cm (0.025λ) long Corning Celcor stack is located 4.25 cm $(\approx \lambda/20)$ from the pressure antinode which is in agreement with the existing literature. Therefore, when thermoacoustic devices are used as heat pumps, a compromise has to be made between the COPR and the maximum temperature at the hot side or the maximum temperature difference between the extremities of the stack ends.

- At low DR, temperature gradient generated across the stack ends agrees with the linear theory predictions.

In conclusion, the performance measurements show that the maximum values of temperature gradient, the thermoacoustic heat flow and the coefficient of performance compared to Carnot coefficient of performance of thermoacoustic refrigerators depend on the geometry, dimension, material, and position of the stack. Maximum COPR is obtained at a distance of $(\approx \lambda/20)$ from the pressure antinode when 2.5 cm (0.025λ) Corning Celcor stack is used. For RVC stacks maximum temperature difference and maximum COPR is obtained at a distance of $(\approx \lambda/50)$ from the pressure antinode.

The present study also examines the temperature fields at different locations of the stack plate surface and the surrounding working fluid. Based on the results presented in this study, one may make the following observations regarding the thermal interactions between the porous stack and the working fluid:

- First temperatures along the stack and the nearby gas show linear behavior for the operating conditions considered. Temperature measurements along the stack reveal a linear behavior along the stack and the corresponding gas residing near the stacks.

- Second temperature gradient along the stack plate is less than that of along the working fluid. Therefore, accurate measurement of temperature difference along the stack using linear theory should be modified to take into account this difference of temperature gradient through the stack plate and the working fluid along with the physical processes considered by Lotton et al. [2009].

Chapter 8

Experimental Results on Heterogeneous Porous Media as Stacks

8.1 Introduction

One of the ways to improve the power density of thermoacoustic devices is to improve the power density of the stack element. To improve the power density of a stack, several authors have examined stacks of different geometries such as using pin array stacks by Swift and Keolian [1993], RVC stacks by Adeff et al. [1998], and Jung et al. [2010]. Another approach to enhance the performance of the stack is to replace the typical parallel plate stacks that are much longer than the acoustic displacement amplitude, by parallel plate segments which are only a fraction of the displacement amplitude long and randomly oriented to each other (Bösel et al. [1993]). This simplified stack arrangement was expected to benefit from improved heat transfer characteristics and an anisotropic thermal conductivity (Bösel et al. [1993]).

The present study introduces the novel concept of “alternative conducting and insulating materials” as stack arrangement, in order to achieve high power density and to reduce the inherent irreversibilities inside stacks of thermoacoustic devices. Therefore, the present study replaces the RVC stack that is much longer than the acoustic displacement amplitude used in Chapter 7, by RVC and aluminum foams which are only a fraction of the displacement amplitude long and alternately oriented to each other. This stack arrangement is expected to benefit from anisotropic thermal conductivity, thereby reducing one of the limiting mechanisms the diffusion heat transfer from the hot stack end to the cold end. The range of thermal conductivity of RVC foams are 0.033 - 0.055 W/m K for the selected pore sizes (20 to 100 PPI) that are available by the manufacturer (ERG [2009]). Aluminum foams of 20 PPI and 40 PPI grades have thermal conductivity of 9.78 W/m K (ERG [2009]). Also the present study examines combinations of Ceramic

(thermal conductivity of 1.46 W/m K) and different porosities RVC and aluminum foams as heterogeneous stacks. This alternative conducting and insulating materials may also be used in regular parallel plate stacks by replacing the longer parallel plate by smaller plates of high and low thermal conductivities which are only a fraction of the acoustic displacement amplitude long and alternately oriented to each other.

8.2 Experimental Results on Temperature Difference across the Stack Ends

Three different RVC and two different aluminum foam samples manufactured by ERG. (ERG [2009]) are studied here. The aluminum foams are identified by the manufacturer according to pore density with values of 20 pores per inch, 20 PPI and 40 PPI. The bulk density of all aluminum foam samples is 216 kg/m^3. The pore sizes for the 20 PPI and 40 PPI aluminum foams are 1.27 mm and 0.64 mm, respectively. The three RVC foam samples are identified by the manufacturer as 45 PPI, 80 PPI, and 100 PPI. The RVC foam samples have pore sizes of 0.56, 0.32, and 0.25 mm, respectively. The bulk density of all RVC foam samples is 49.5 kg/m^3 (ERG [2009]).

Four different combinations of RVC and aluminum foam samples, two different combinations of Ceramic and RVC foams, and two different combinations of Ceramic and aluminum foams are utilized in this section. Therefore, in total eight different combinations of heterogeneous stack geometries are considered in the present study in order to test the suitability of using the heterogeneous stack configuration in thermoacoustic devices. The total length of the sample in these eight combinations is 2 cm. Since in Chapter 7, 2 cm long 80 PPI RVC stack shows the maximum temperature difference across the stack ends and maximum hot end temperature. Table 8.1 shows combination 1 and 2. In combination 1, 1 cm long 45 PPI RVC foam is sandwiched between two 0.5 cm long 40 PPI aluminum foam. In combination 2, 1 cm long 80 PPI RVC foam is sandwiched between two 0.5 cm long 40 PPI aluminum foam. Table 8.2 shows combination 3 and 4. In combination 3, 0.5 cm long 40 PPI aluminum foam and 0.5 cm long 45 PPI RVC foam are placed alternately to each other. In combination 4, 0.5 cm long 40 PPI aluminum foam and 80 PPI RVC foam placed alternately to each other.

Table 8.3 shows combinations 5-8, by considering 20 and 40 PPI aluminum foam samples together with 1 cm long Corning Celcor stack, and by 80 and 100 PPI RVC foams with Celcor stack. For each combination temperatures are measured at eight different positions of the stack from the pressure anti-node. The eight different combinations are shown in Figs. 8.1(a) - (h).

(a) Combination 1 (40PPI AL+45PPI RVC+40PPI AL)

(b) Combination 2 (40PPI AL+80PPI RVC+40PPI AL)

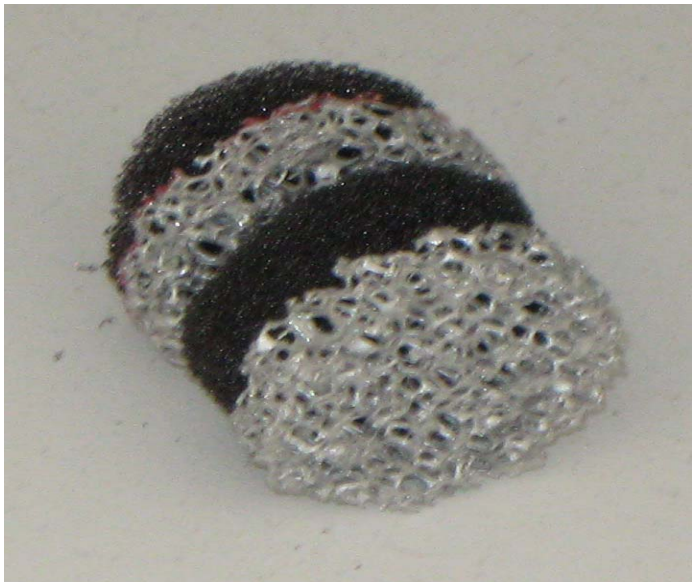

(c) Combination 3 (40PPI AL+80PPI RVC+40PPI AL+80 PPI RVC)

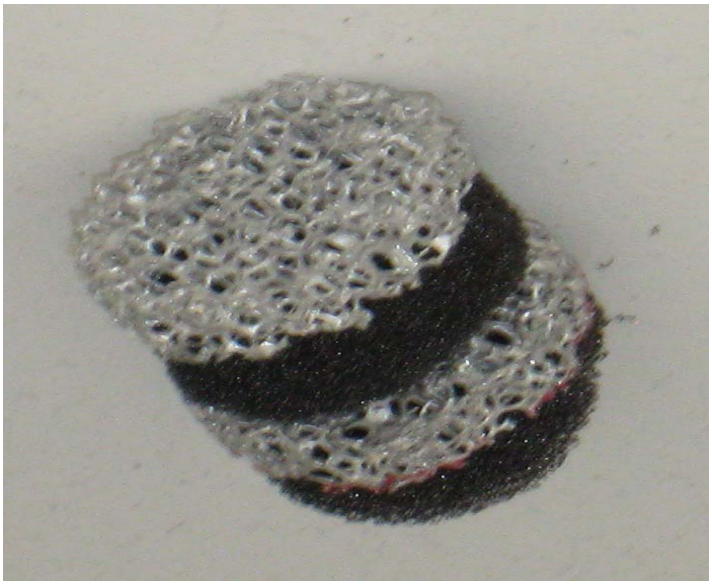

(d) Combination 4 (80PPI RVC+40PPI AL+80PPI RVC+40PPI AL)

(e) Combination 5 (20PPI AL+1 cm Celcor+20PPI AL)

(f) Combination 6 (40PPI AL+ 1 cm Celcor+40PPI AL)

(g) Combination 7 (80PPI RVC+1 cm Celcor+80PPI RVC)

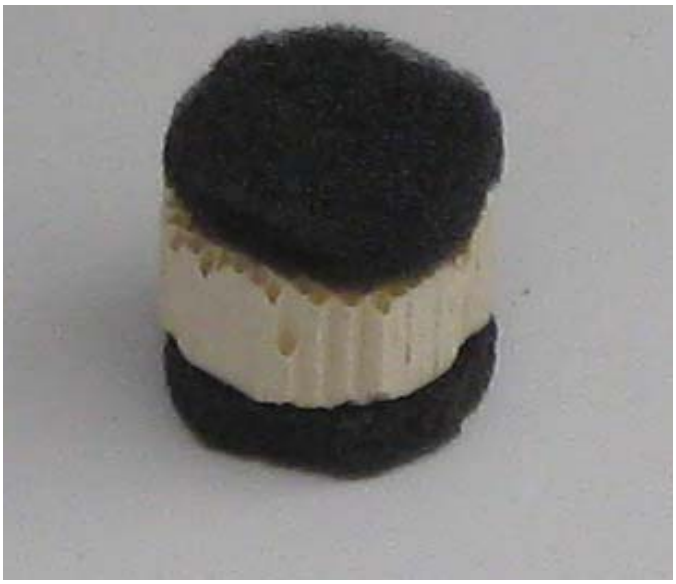

(h) Combination 8 (100PPI RVC+1 cm Celcor+100PPI RVC)

Figure 8.1: Eight combinations of heterogeneous stack structure are shown in (a) to (h).

Table 8.1: Combination 1 and 2

Combination	Material 1	Material 2	Material 1
Combination 1	40 PPI AL, 0.5 cm long	45 PPI RVC, 1 cm long	40 PPI AL, 0.5 cm long
Combination 2	40 PPI AL, 0.5 cm long	80 PPI RVC, 1 cm long	40 PPI AL, 0.5 cm long

Table 8.2: Combination 3 and 4

Combination	Material 1	Material 2	Material 1	Material 2
Combination 3	40 PPI AL, 0.5 cm long	80 PPI RVC, 0.5 cm long	40 PPI AL, 0.5 cm long	80 PPI RVC, 0.5 cm long
Combination 4	80 PPI RVC, 0.5 cm long	40 PPI AL, 0.5 cm long	80 PPI RVC, 0.5 cm long	40 PPI AL, 0.5 cm long

Table 8.3: Combination 5-8

Combination	Material 1	Material 2	Material 1
Combination 5	20 PPI AL, 0.5 cm long	Celcor, 1 cm long	20 PPI AL, 0.5 cm long
Combination 6	40 PPI AL, 0.5 cm long	Celcor, 1 cm long	40 PPI AL, 0.5 cm long
Combination 7	80 PPI RVC, 0.5 cm long	Celcor, 1 cm long	80 PPI RVC, 0.5 cm long
Combination 8	100 PPI RVC, 0.5 cm long	Celcor, 1 cm long	100 PPI RVC, 0.5 cm long

Therefore, a total of 64 cases have been examined for the heterogeneous case. The reason for considering combinations 1 and 5 is that for both combinations, both materials have almost similar pore sizes, therefore the acoustic flow will not be disturbed while entering from one porous medium to another. Combination 2 is considered to observe the effect of flow disturbance on thermal field as different porosities foams are placed together. Combination 3 and 4 illustrate the difference between high and low thermal conductivity stack materials at the stack ends. Combinations 6-8 give a picture of the thermal field of regular Celcor stack with random porous structures of different thermal conductivities and porosities.

Figure 8.2 shows the temperature difference vs. non-dimensional stack center position form the pressure anti-node as a function of stack combination 1, 2, 3, and 4. For all these

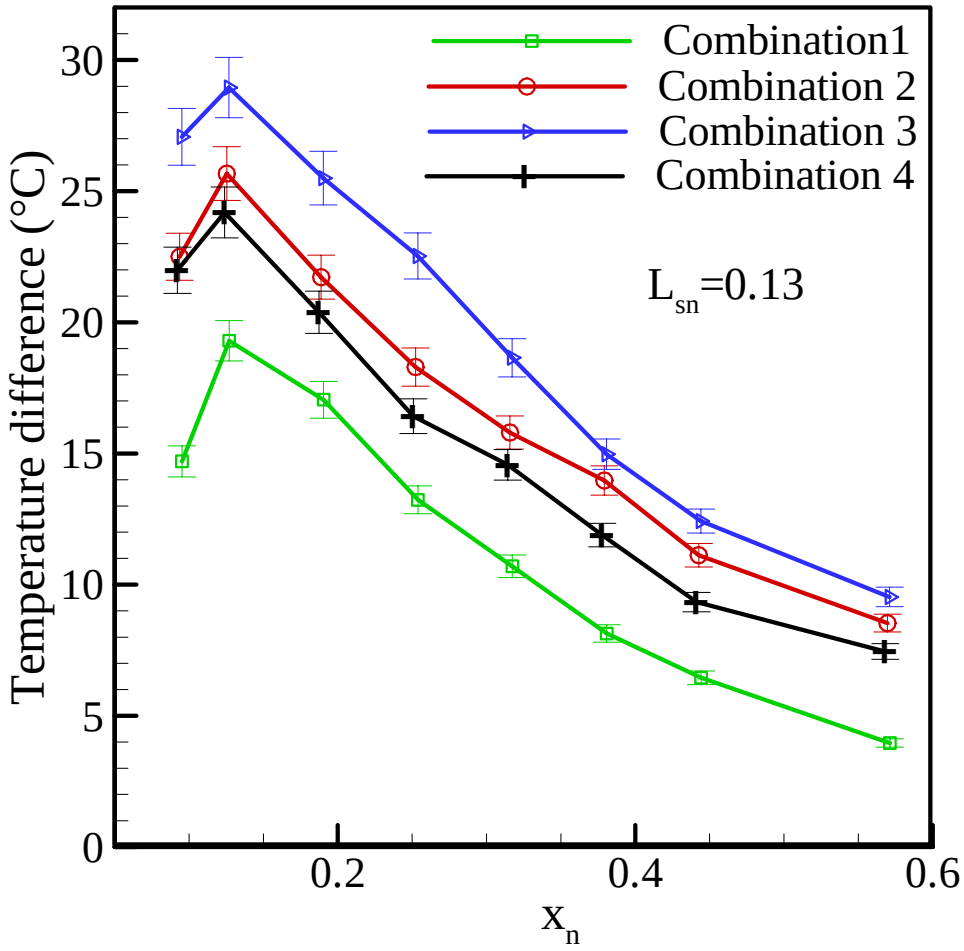

Figure 8.2: Temperature difference vs. non-dimensional stack center position form the pressure anti-node for different stack material composition.

four combinations maximum temperature difference is obtained when the stack center is located 2 cm from the nearest pressure anti-node also shown in Fig. 7.3 in Chapter 7 for the homogeneous stack. The maximum temperature difference is changed as the combination is changed with a maximum (29°C) for combination 3. But the maximum temperature difference obtained from combination 3 is less than homogeneous 80 PPI RVC stack (48°C) as shown in Chapter 7. Therefore, temperature difference is not increased while the homogenous RVC stack is replaced by a heterogeneous structure i.e., a combination of RVC and aluminum foams. The reason might be the lengths of RVC

and aluminum foams that are used in this study are far larger than the acoustic displacement amplitude. The range of acoustic displacement amplitude ($2u_1/\omega$) that depends on the position of the stack in the standing wave is 0.08 mm- 0.6 mm. The length of 80 PPI RVC foam is 1 cm and it is sandwiched between two 0.5 cm long 40 PPI aluminum foams in combination 3. The reason for not using the lengths of foam samples as equal or less than the acoustic displacement amplitude is due to the difficulty of cutting the RVC foam samples in such small pieces which are very brittle. Figure 8.3 shows the comparison of performance of homogeneous and heterogeneous stack structure that presents the maximum temperature difference across the stack ends. In Fig. 8.3, the

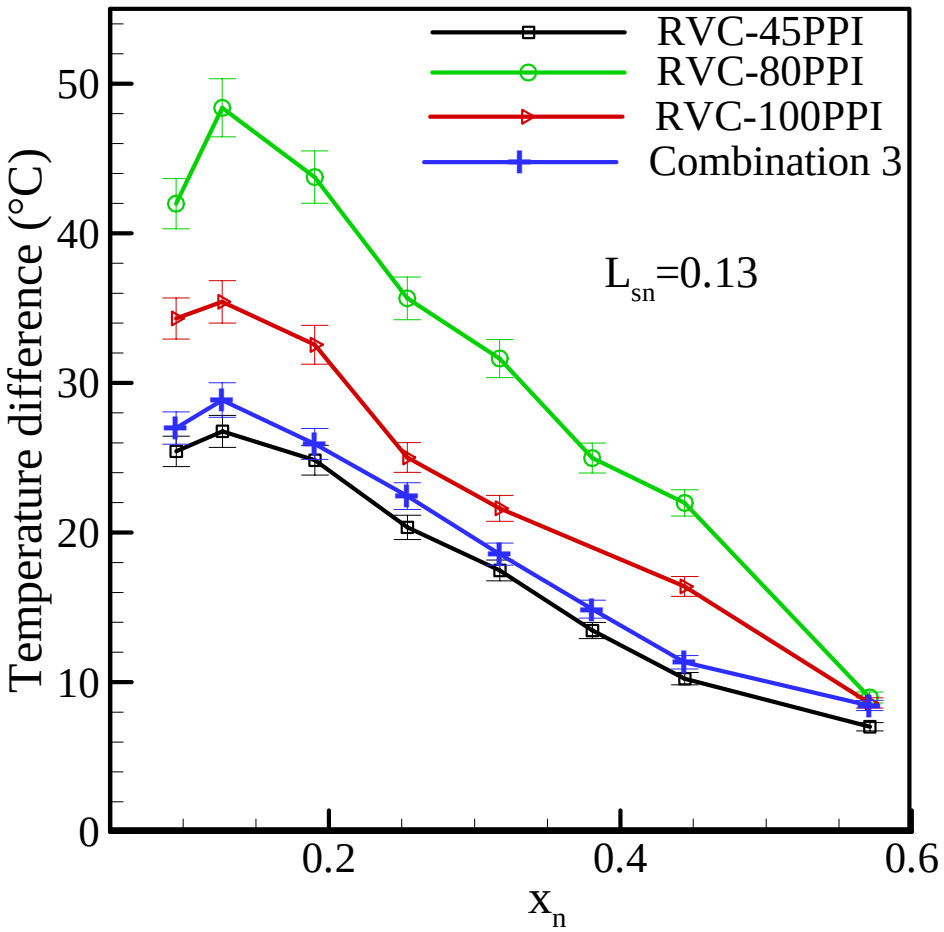

Figure 8.3: Temperature difference vs. non-dimensional stack center position form the pressure anti-node for homogeneous and heterogeneous stack material composition.

length of the stack is 2 cm. Combination 3 performs better than 45 PPI RVC stack. But 80 and 100 PPI grades perform better than combination 3.

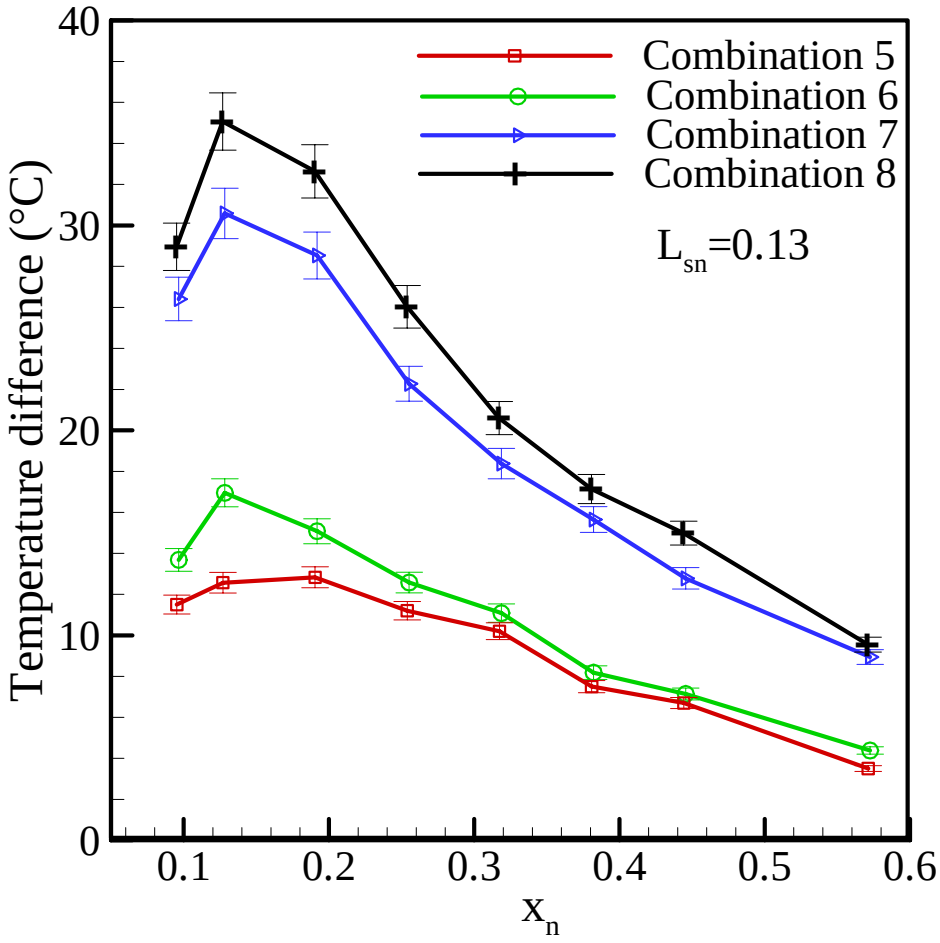

Figure 8.4: Temperature difference vs. non-dimensional stack center position form the pressure anti-node for different stack material composition.

Figure 8.4 shows the temperature difference vs. non-dimensional stack center position form the pressure anti-node as a function of stack combination 5, 6, 7, and 8. Combinations 7 and 8 show better performance than combinations 5 and 6. Among all the eight combinations, combination 8 shows the best performance by producing maximum temperature difference at the stack ends. Maximum temperature difference of 35°C is observed while using combination 8. As shown is Table 8.3, in combination 8, the length of the Ceramic stack is 1 cm and it is sandwiched between two 0.5 cm long 100 PPI RVC foams. Even though the pore sizes are different along the length of the heterogeneous stack arrangement (combination 8), it produces maximum temperature

difference at the stack ends. This performance is comparable to homogeneous 100 PPI RVC stack and better than homogeneous Ceramic stack length of 2 cm. While using homogeneous Ceramic stack in Chapter 7, 4 cm long stack shows the best performance regarding the temperature difference across the stack ends. The performance of combination 8 is comparable to homogeneous Ceramic stack length of 4 cm. Figure

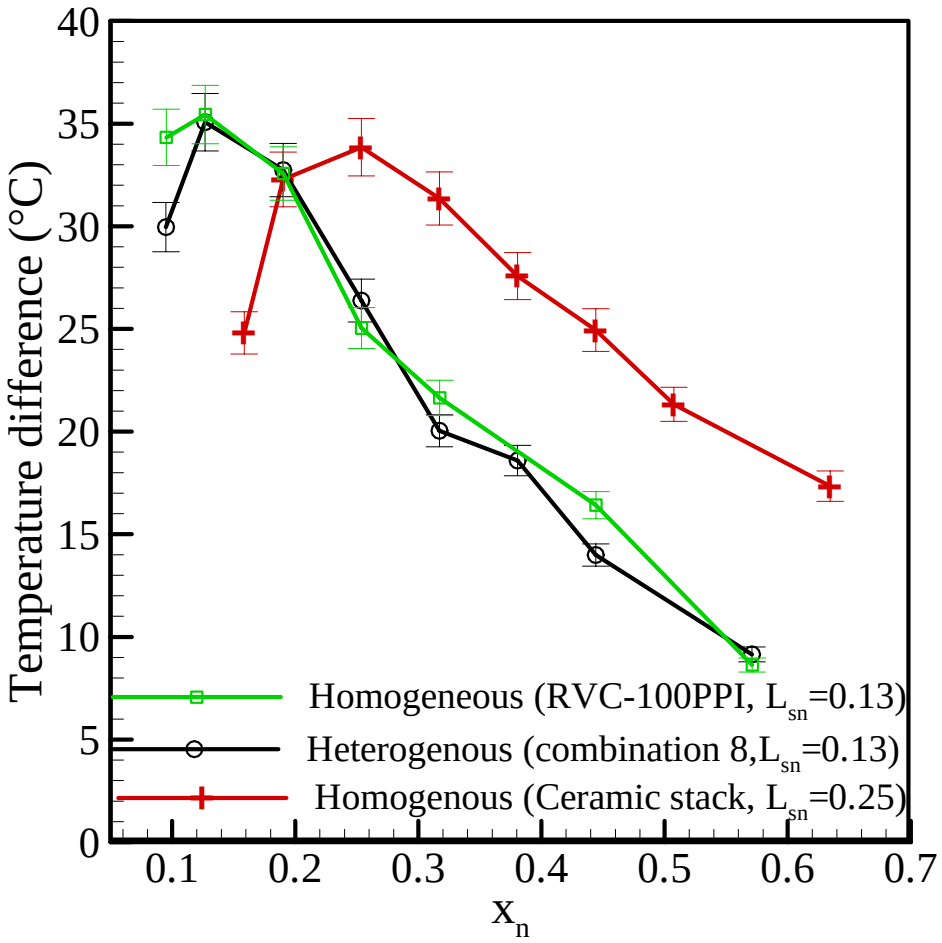

Figure 8.5: Temperature difference vs. non-dimensional stack center position form the pressure anti-node for different stack material composition.

8.5 shows the temperature difference vs. non-dimensional stack center position form the pressure anti-node for these three different stack configurations. Form Fig. 8.5, it is clear that 100 PPI RVC stack and combination 8 shows the similar performance. 4 cm long Ceramic stack also shows similar performance, only for this case the curve has shifted to the right because of different length than the two previous cases. One interesting feature

obtains form these experiments is that combination 7 produces the minimum temperature at the cold end which is 10.93°C≈11°C This minimum temperature result considers all the experiments in Chapter 7 and Chapter 8. Therefore, heterogeneous stack arrangement using Ceramic and 80 PPI RVC stack can be used in thermoacoustic refrigeration to achieve low temperature cooling. Combination 7 and 8 are preferable to use in small scale thermoacoustic devices because of their almost identical performance to that of ceramic stack which is 4 cm long. Combination 7 and 8 might also be used in small scale thermoacoustic devices as an alternate to 100 PPI RVC foam because of the larger acoustic power absorbed by RVC foam. It is anticipated that combination 7 or 8 might absorb less acoustic power than the 100 PPI RVC foam because of their configuration.

To understand the effect of return diffusive heat transfer, Figs. 8.6 (a) to (c) show the time evolution of temperature profiles at two extreme ends of the stack for (a) combination 2, (b) combination 7, and (c) combination 8. The temperatures at the two extreme ends of the stack for combination 2 increase with time. This might be due to the effect of return diffusive heat transfer or viscous dissipation while these effects are not visible for combinations 7 and 8. Combinations 1 to 4 follow the similar temperature

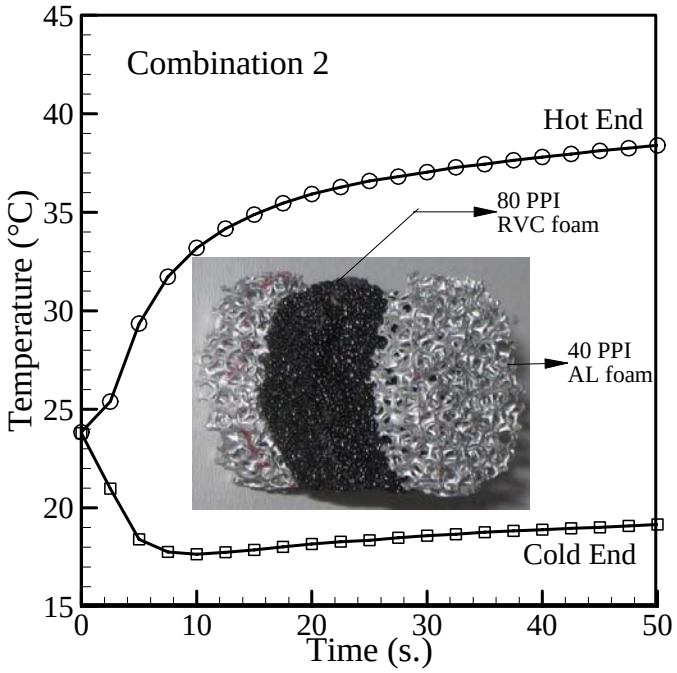

(a)

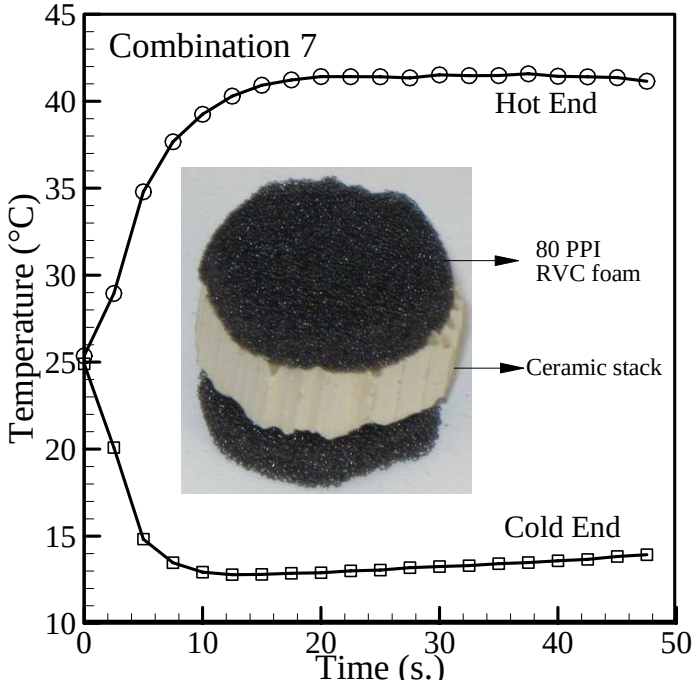

(b)

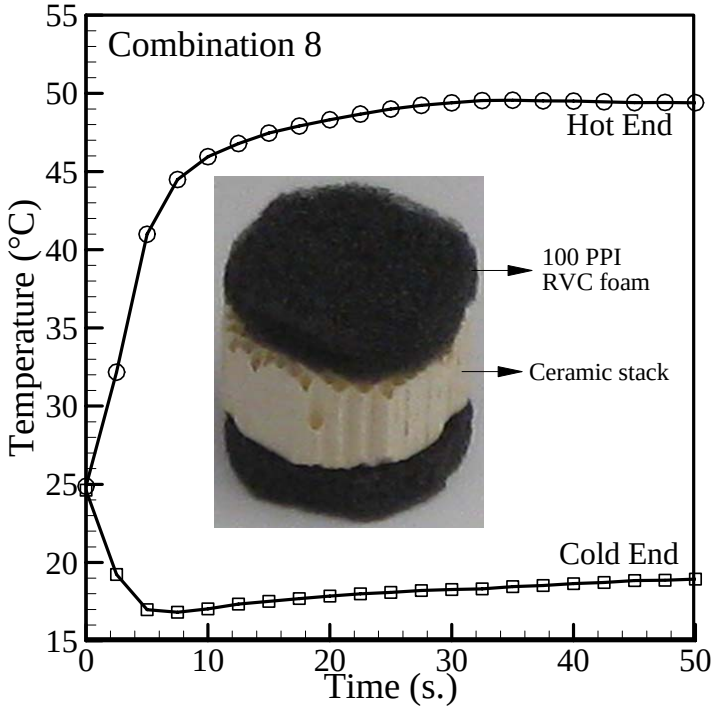

(c)

Figure 8.6: Time evolution of temperature profiles at two extreme ends of the stack for (a) combination 2, (b) combination 7, and (c) combination 8.

profiles with time to that of Fig. 8.6 (a) (not shown in Fig. 8.6). This is a very preliminary study. Much work needs to be done in order to understand the heat transfer in the vertical and horizontal directions along the stack. To accomplish this, numerical simulations must be performed. Also, heterogeneous stacks using regular parallel plate stacks should be tested and compared with the existing results.

8.3 Conclusions

The present study has introduced a novel concept of “alternative conducting and insulating materials” as stack arrangement, in order to achieve high power density and to reduce the inherent irreversibilities inside stacks of thermoacoustic devices. Eight different combinations of stack configurations have been considered for the present work. From the experiments it is observed that combination 8 performs better than all other combinations using 1 cm long Ceramic stack sandwiched between two 0.5 cm long 100 PPI RVC foams. Combination 8 performs similar to homogeneous 100 PPI RVC stack and better than 2 cm Ceramic stack. One interesting feature obtains form these experiments is that combination 7 produces the minimum temperature at the cold end which is 11°C. Therefore, heterogeneous stack arrangement using Ceramic and 80 PPI RVC stack can be used in thermoacoustic refrigeration to achieve low temperature cooling rather than homogeneous Ceramic or RVC stacks. Again, since combination 8 and 4 cm long Ceramic stack shows similar performance, combination 8 is preferred for compact thermoacoustic engines since it requires smaller stack length.

Chapter 9

Numerical Solutions to Nonlinear Thermoacoustics

9.1 Introduction

In Chapter 4 and Chapter 5, analytical approach was applied to solve the thermoacoustic governing equations in the linear regime. Because of the linear approximations the effects of nonlinearities could not be understood on the thermoacoustic parameters. One possible option is to use a higher order perturbation expansion. A closed form of solution to the higher order approximate equations is a real challenge. Some limited work on the higher order results are available in the literature [Hamilton et al. [2002a], Hamilton et al. [2002b], Hamilton et al. [2003], Waxler [2001]]. A second option is to solve the complete governing equations numerically. Therefore, the primary objective of this chapter is to identify the non-linear effects in different components of a thermoacoustic device numerically. Since non-linear effects are present in different components of a thermoacoustic device and thus influence its performance. This chapter is devoted to present the numerical work-done in this research, starting from the simplest possible case, this work proceeds towards the complicated problem of thermoacoustics. Computer simulations are truly an important research tool to understand phenomena from experiments and to support the theory of thermoacoustics. The objectives of thermoacoustic modeling in this chapter are therefore:

- To simulate certain thermoacoustic phenomena (energy flux density and work flux).
- To help in interpreting and understanding observed thermoacoustic phenomena.
- Provide results of sufficient detail to substitute for difficult experiments.

9.1.1 Chapter Outline

To start,

- A simple problem of viscous oscillation of an ideal gas in front of a loudspeaker is considered in order to test the suitability of using a commercial CFD package STAR-CD (the name STAR stands for Simulation of Turbulent flow in Arbitrary Regions) produced by Computational Dynamics Ltd. ([2007]) to simulate transient sound waves for various operating conditions. Conditions are chosen to cover typical operating conditions of existing thermoacoustic engines;

- Then, this simple problem is modified by introducing an array of thin plates in the simulation domain to simulate thermoacoustic effects. In each case, the most effort is directed to present the velocity, temperature, and pressure amplitudes and as well as energy streamline and energy flux density vectors. As a verification of the modeling, comparisons of numerical model results to previous numerical results (Cao et al. [1996]) are performed;

- After verification of the modeling to simulate thermoacoustic effects, the present study examines the influence of drive ratio, mean pressure, and Prandtl number on the power density, coefficient of performance, and entropy generation rate within the stack region. As there is evidence (Swift [1988], Tijani [2002]) that increasing the drive ratio, mean pressure, and lowering the Prandtl number might enhance the power density and coefficient of performance of a thermoacoustic device. Also increasing the drive ratio and mean pressure introduces nonlinearities within the stack region. Therefore the effects of nonlinearities on the thermoacoustic parameters can also be analyzed;

- Then this thin plate is modified by introducing an array of thick plates in the simulation domain to simulate the practical thermoacoustic effects;

- Next, flow and thermal fields in a resonant channel are considered to observe the energy field, nonlinear, and entropy generation phenomena within the resonator. The flow field result has verified with existing analytical solutions. The outcome of this research has application for developing miniature thermoacoustic devices.

9.2 Prandtl number, Drive ratio, Stack Spacing, Mean pressure, and Stack Performance

The first two and the last two bullet point topics are presented in Appendix C with detailed discussion of formulation and numerical method, stopping criteria, and errors in numerical simulations used in commercial code STAR-CD [2007]. Also simple oscillation of a viscous ideal gas is simulated and verified followed by the simulation of thermoacoustic effect in an array of thin plates. Once the thermoacoustic effects produced by STAR-CD are verified with existing works, the current section analyzes the effects of variation of Prandtl number and geometric and operating conditions on the stack performance.

One approach to increase the power density of a thermoacoustic device is to increase the drive ratio. The goal of building powerful and efficient thermoacoustic devices has generated interest in high amplitude studies. Experimental investigations on devices driven at high amplitudes reveal the importance of understanding the non-linear effects (Poese and Garrett [2000]). Another approach to increase the performance of a thermoacoustic device is to decrease the Prandtl number. Viscous friction has a negative effect on the performance of thermoacoustic devices (Swift [1988], Tijani [2001]). Lower values of Prandtl number can be obtained by using gas mixtures of heavy and light monatomic gases. Tijani [2001] showed experimentally that decreasing the Prandtl number to 0.2 leads to a coefficient of performance relative to Carnot which is 70% higher than with pure helium. Prandtl number of 0.2 is obtained with a mixture of 30% xenon and 70% helium. Also increasing the mean working pressure might increase the cooling power of the device. Tijani [2001] did not examine the effect of p_m, DR, and stack spacing on the performance of a thermoacoustic device that uses low Prandtl number fluids. The present study thus examines the influence of DR, mean pressure, stack spacing, and Prandtl number on the non-linearity, power density, acoustic work, COP, and entropy generation rate within the stack. The entropy generation distribution is obtained by post processing the velocity and temperature distribution data (at different operating conditions using different Prandtl number fluids) from the numerical

simulations. The results can be used to determine which geometric, operating conditions, and working fluid has the highest thermal efficiency.

9.2.1 Geometric and Operating Conditions

Table 9.1 shows the thermal and physical properties of fluid and Table 9.2 shows the geometric and operating conditions considered in the present investigation. Working fluids of two different Prandtl numbers are employed. Helium and a mixture of 90% helium and 10% xenon are used that gives Prandtl number of 0.7 and 0.28, respectively. In Table 9.2, particle displacement amplitude, $\zeta = 2u_A/\omega$. For all of the test cases considered stack length is constant at 226.13 (0.024λ) mm. For helium as the working fluid, 100 Hz operating frequency is considered. The wavelength is kept constant and the frequency is allowed to vary as the sound velocity varies with the change of gas for helium and xenon mixture. For a mixture of helium and xenon, a frequency of 48.89 Hz is considered. Table 9.3 shows the total enthalpy flow due to the heat pumping effect, entropy generation, acoustic power absorbed by the refrigerator, and COP data for all the test cases considered in the present investigation. The acoustic power absorbed by the refrigerator is obtained by integrating the time averaged acoustic energy flux over the stack channel cross section at boundary 23 (Fig. C.8(b))

$$W_{xm} = \int_{y=0}^{y=y_0} \overline{p_1(x,y)u_1(x,y)}\, dy\,. \tag{9.1}$$

In Eq. (9.1), the over bar indicates the time averaged quantity.

The total mean enthalpy carried along the stack plate, E_y, is

$$E_y = \int_{\text{near end}} \overline{E}_y\, dx\,, \tag{9.2}$$

where the integration is performed over the particle displacement amplitude distance from the stack end (Fig. C.8(b)). E_y (Right hand side of Eq. (9.2)) is obtained from Eq.

(C.18). The quantity E_y is a measure of the energy transported by thermoacoustic heat pumping along the stack plate. COP is obtained by dividing Eq. (9.2) by Eq. (9.1).

By applying the second law of thermodynamics to an infinitesimal Cartesian control volume in a 2-D flow field, following expression can be developed for the rate of entropy production per unit volume, for the fluid which is in local thermal equilibrium (Bejan [1996]):

$$S_{gen} = \frac{1}{T}\nabla \cdot q - \frac{1}{T^2} q \cdot \nabla T + \rho \frac{Ds}{Dt}, \tag{9.3}$$

where S_{gen} is the volumetric rate of entropy generation, q is the heat flux vector, T is the local fluid temperature (which is assumed equal to the mean temperature for the present problem), s is the specific entropy, and ρ is the local fluid density. Using the conservation of mass, energy, and Gibb's equation, we obtain the volumetric entropy generation rate as follows:

$$S_{gen} = -\frac{1}{T^2} q \cdot \nabla T + \frac{\mu}{T}\Phi, \tag{9.4}$$

where Φ is the dissipation function given by the following expression:

$$\Phi = \left\{ -\frac{2}{3}\left(\frac{\partial u}{\partial x} + \frac{\partial v}{\partial y}\right)^2 + 2\left(\frac{\partial u}{\partial x}\right)^2 + 2\left(\frac{\partial v}{\partial y}\right)^2 + \left(\frac{\partial v}{\partial x} + \frac{\partial u}{\partial y}\right)^2 \right\}, \tag{9.5}$$

for a 2-D Cartesian frame of reference. Furthermore, substituting $q = -k \nabla T$ into Eq. (9.4) yields

$$S_{gen} = \frac{k}{T^2}\left[\left(\frac{\partial T}{\partial x}\right)^2 + \left(\frac{\partial T}{\partial y}\right)^2\right] + \frac{\mu}{T}\left\{2\left(\frac{\partial u}{\partial x} + \frac{\partial v}{\partial y}\right)^2 + \left(\frac{\partial v}{\partial x} + \frac{\partial u}{\partial y}\right)^2\right\}. \tag{9.6}$$

The detailed derivation of Eq. (9.6) is available on Mahmud [2005]. The two terms on the right hand side of Eq. (9.6) represent the heat transfer and fluid friction losses terms in

the make up of S_{gen}. The right hand side of Eq. (9.6) is a sum of square terms and always positive. Fluid friction irreversibility ratio is calculated to understand the importance of fluid friction effect over total entropy generation rate.

$$\text{Fluid friction irreversibility ratio} = \frac{S_{gen}(\text{fluid friction})}{S_{gen}(\text{fluid friction}) + S_{gen}(\text{heat transfer})}. \tag{9.7}$$

Table 9.1: Properties of working fluids at a p_m of 10 bar and a temperature of 300K (Tijani [2001]).

Fluid variables	90% helium and 10% xenon	helium
C_p (specific heat, J/kg·K)	1200	5200
μ (dynamic viscosity, Pa·s)	1.95×10^{-5}	2.0185×10^{-5}
k (thermal conductivity, W/m·K)	0.0765	0.1498
M (molecular weight, g/mol)	16.73	4.0
δ_k (mm)	0.248	0.239
ρ (kg/m^3)	6.71	1.6
a (m/s)	500	1020

Table 9.2: Operating Conditions

Run No.	**Fluid**	y_0 **(mm)**	**DR %**	p_m **(kPa)**	δ_k **(mm)**	ζ **(mm)**	Re_δ
1	He	$3.33\,\delta_k$	1.7	10	2.39	33.1	23.38
2	He	$3.33\,\delta_k$	1.7	100	0.756	33.1	73.94
3	He	$3.33\,\delta_k$	1.7	1000	0.239	33.1	233.81
4	He	$3.33\,\delta_k$	5	10	2.39	97.28	68.77
5	He	$3.33\,\delta_k$	5	100	0.756	97.28	217.46

6	He	$3.33\,\delta_k$	5	1000	0.239	97.28	687.67
7	He	$3.33\,\delta_k$	8.5	10	2.39	165.38	116.9
8	He	$3.33\,\delta_k$	8.5	100	0.756	165.38	369.7
9	He	$3.33\,\delta_k$	8.5	1000	0.239	165.38	1169
10	He	$3.33\,\delta_k$	10	10	2.39	194.56	137.5
11	He	$3.33\,\delta_k$	10	100	0.756	194.56	434
12	He	$3.33\,\delta_k$	10	1000	0.239	194.56	1375
13	He	$2.0\,\delta_k$	5	100	2.39	97.28	217.5
14	He	$2.0\,\delta_k$	5	1000	0.756	97.28	687.7
15	He	$2.0\,\delta_k$	8.5	100	0.756	165.38	369.68
16	He	$2.0\,\delta_k$	8.5	1000	0.756	165.38	369.68
17	He	$1.0\,\delta_k$	1.7	10	2.39	33.1	23.38
18	He	$1.0\,\delta_k$	1.7	100	0.756	33.1	73.9
19	He	$1.0\,\delta_k$	1.7	1000	0.239	33.1	233.81
20	He	$1.0\,\delta_k$	5	10	2.39	97.28	68.77
21	He	$1.0\,\delta_k$	5	100	0.756	97.28	217.46
22	He	$1.0\,\delta_k$	5	1000	0.239	97.28	687.67
23	He	$1.0\,\delta_k$	8.5	10	2.39	165.38	116.9
24	He	$1.0\,\delta_k$	8.5	100	0.756	165.38	369.7
25	He	$1.0\,\delta_k$	8.5	1000	0.239	165.38	1169
26	He	$1.0\,\delta_k$	10	10	2.39	194.56	137.5
27	He	$1.0\,\delta_k$	10	10	0.756	194.56	434
28	He	$1.0\,\delta_k$	10	10	0.239	194.56	1375
29	He-Xe	$3.33\,\delta_k$	1.7	100	0.786	33.1	107.7
30	He-Xe	$3.33\,\delta_k$	1.7	1000	0.249	33.1	340.6
31	He-Xe	$3.33\,\delta_k$	5	100	0.786	97	316.8
32	He-Xe	$3.33\,\delta_k$	5	1000	0.249	97	1001.9

33	He-Xe	$3.33\,\delta_k$	10	100	0.786	194.65	633.7
34	He-Xe	$3.33\,\delta_k$	10	1000	0.249	194.65	2003.8
35	He-Xe	$1.0\,\delta_k$	1.7	100	0.786	33.1	107.7
36	He-Xe	$1.0\,\delta_k$	1.7	1000	0.249	33.1	340.6
37	He-Xe	$1.0\,\delta_k$	5	100	0.786	97	316.8
38	He-Xe	$1.0\,\delta_k$	5	1000	0.249	97	1001.9
39	He-Xe	$1.0\,\delta_k$	10	100	0.786	194.65	633.7
40	He-Xe	$1.0\,\delta_k$	10	1000	0.249	194.65	2003.8
41	He	$3.33\,\delta_k$	1.7	10	2.39	33.1	23.38
42	He	$3.33\,\delta_k$	1.7	100	0.756	33.4	73.9
43	He	$3.33\,\delta_k$	5	100	0.756	97.28	217.46

Table 9.3: Energy Flux Density, Acoustic Work, COP, and Entropy Generation Data

Run No.	L_s (mm)	E_y (kW)	S_{gen} (mm)	W_{xm} (W)	COP
1	$6.84\,\zeta$	-0.045	0.0452	-10.158	4.5
2	$6.84\,\zeta$	-0.244	0.455	-100.22	1.64
3	$6.84\,\zeta$	-1.41	4.55	-1002.2	1.0
4	$2.32\,\zeta$	-0.278	0.389	-106.41	2.4
5	$2.32\,\zeta$	-1.1516	3.89	-851.463	1.33
6	$2.32\,\zeta$	-3.639	30.86	-8551.37	0.43
7	$1.38\,\zeta$	-0.8196	1.108	-245.58	3.34
8	$1.38\,\zeta$	-2.57	11.17	-2454.41	1.05
9	$1.38\,\zeta$	-8.1	110.705	-24560.6	0.33
10	$1.17\,\zeta$	-1.07	1.52	-336.558	3.18
11	$1.17\,\zeta$	-3.349	15.4	-3365.22	1
12	$1.17\,\zeta$	-10.53	153	-33646.4	0.33

13	2.32 ζ	-1.17	6.73	-1144.05	1.02
14	2.32 ζ	-3.71	67.51	-11421.5	0.33
15	1.17 ζ	-2.58	36.74	-3222.14	0.80
16	1.17 ζ	-6.35	367.35	-32221.4	0.22
17	6.84 ζ	-9.78E-03	0.196	-1.9671	0.57
18	6.84 ζ	-0.229	1.96	-172.081	1.33
19	6.84 ζ	-0.735	19.54	-1722.64	0.43
20	2.32 ζ	-0.314	1.63	-141.03	2.23
21	2.32 ζ	-0.988	16.37	-1413.31	0.7
22	2.32 ζ	-3.12	163.93	-14116.1	0.22
23	1.38 ζ	-0.671	4.63	-382.882	1.76
24	1.38 ζ	-2.095	46.54	-3843.71	0.55
25	1.38 ζ	-6.612	466.15	-38447.2	0.17
26	1.17 ζ	-0.849	6.38	-513.94	1.66
27	1.17 ζ	-2.66	64.1	-5163.5	0.52
28	1.17 ζ	-8.396	639.92	-51637	0.16
29	6.84 ζ	-0.128	0.184	-41.6512	3.1
30	6.84 ζ	-1.00	1.85	-659.43	1.53
31	2.32 ζ	-0.605	1.62	-363.065	1.67
32	2.32 ζ	-1.91	16.24	-3505.36	0.55
33	1.17 ζ	-1.74	6.1	-1343.87	1.29
34	1.17 ζ	-5.5	60.7	-13532.5	0.41
35	6.84 ζ	-0.121	0.653	-105.195	1.15
36	6.84 ζ	-0.382	6.46	-937.914	0.41
37	2.32 ζ	-0.527	5.61	-806.357	0.65
38	2.32 ζ	-1.67	56.16	-8064.07	0.21
39	1.17 ζ	-1.44	20.69	-2857.23	0.50
40	1.17 ζ	-4.55	206.98	-28568.2	0.16
41	3.1 ζ	-2.37E-02	0.0799	-13.2541	1.79
42	3.1 ζ	-0.13	0.0589	-132.93	0.98

43	1.0 ζ	-0.584	6.875	-1088.53	0.54

9.2.2 Boundary Conditions of the Computational Domain

The boundary conditions specified in **Section** C.4.1 are considered in the present computation, only the left vertical boundary, boundary 41 in Fig. C.8(b) is replaced by a closed end. The right vertical boundary, boundary 23 in Fig. C.8(b) is unchanged and an incoming acoustic wave is introduced into the computational domain through this boundary. The incident wave travels through the domain, reflects by the resonator end wall, travels back, and exits through the boundary 23 in Fig. C.8(b). The superposition of the incident and reflected waves creates a standing wave in the domain. The method used by Cao et al. [1996] to create a standing wave by replacing the closed end (boundary 41 in Fig. 9.8(b)) by an incoming acoustic wave is not used in this section. Because this method requires choosing the correct phasing between the two traveling waves to get correct energy flows. The solution procedures remain the same to that indicated in **Section** C.3.

Once the solutions have converged, an energy balance of the domain is checked in order to test the validity of the converged solutions. At steady state, the time averaged *x*-component of energy flux at boundary 23 (E_{x23}) should be equal to the time averaged heat flux at the plate (q_{56}). Any differences between these two quantities can be considered to be an error. An error is defined as follows

$$E_{x23} + q_{56} = q_{error}\,. \tag{9.8}$$

This error is caused from numerical and convergence errors. A simulation is considered to have converged when the errors are of the order of 1%. The convergence test results are presented in Appendix C.

9.3 Results

9.3.1 Effect of DR

Figure 9.1(a) to (j) compare the selected time averaged velocity contours, temperature

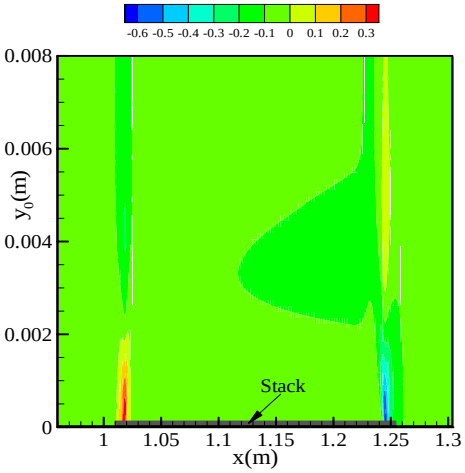

(a) *x*-component of velocity,12x magnification factor

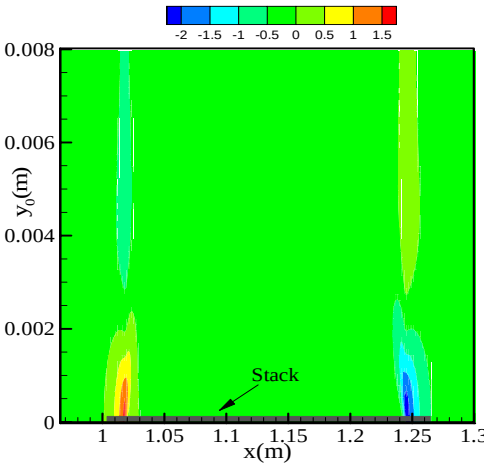

(b) *x*-component of velocity,12x magnification factor

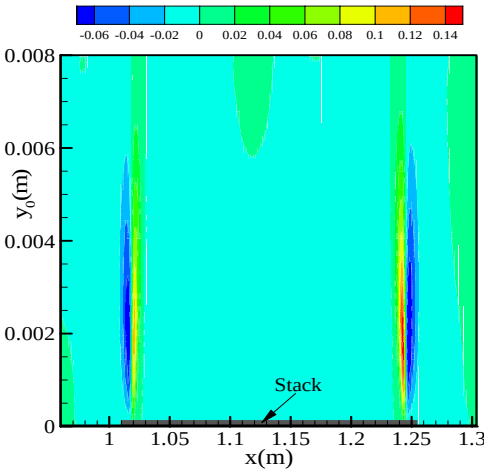

(c) *y*-component of velocity,12x magnification factor

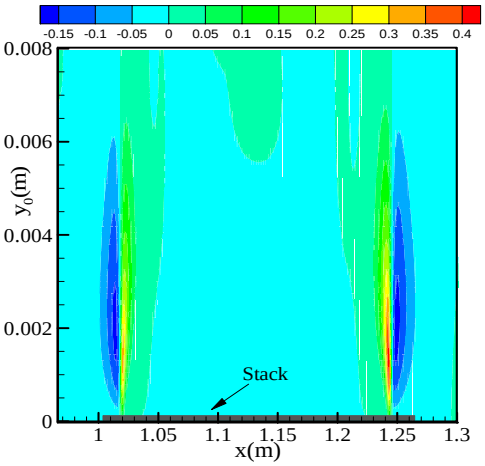

(d) *y*-component of velocity,12x magnification factor

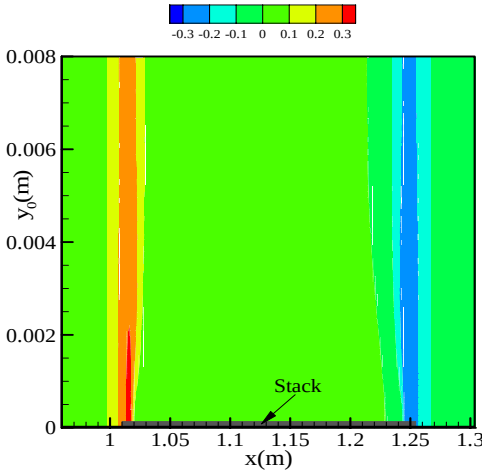

(e) Temperature, 12x magnification factor

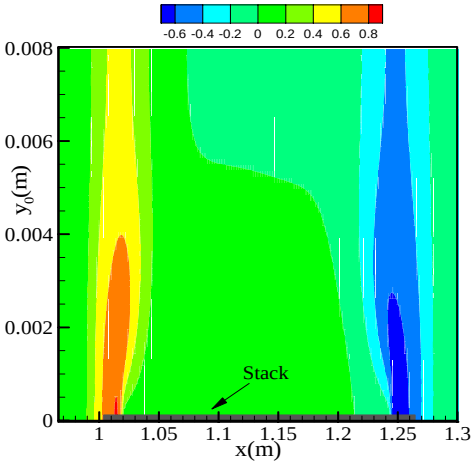

(f) Temperature,12x magnification factor

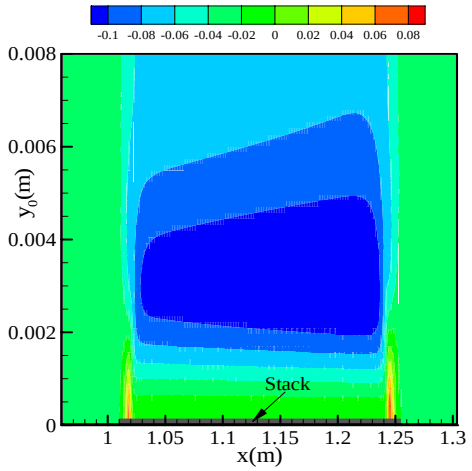

(g) E_x, 12x magnification factor

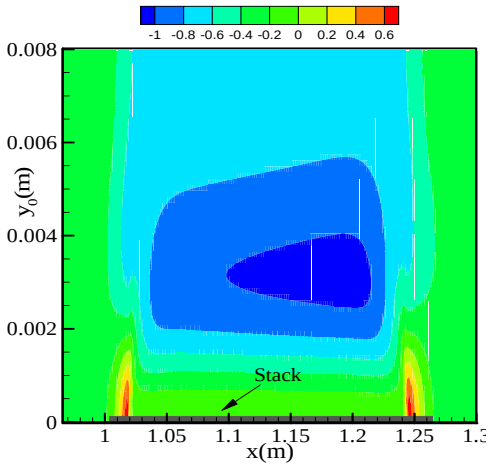

(h) E_x ,12x magnification factor

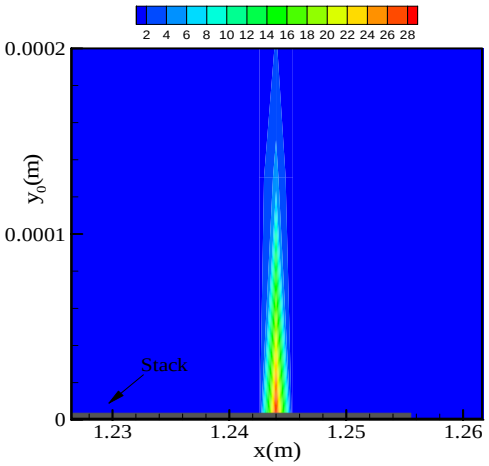

(i) Total volumetric entropy generation rate,130x magnification factor

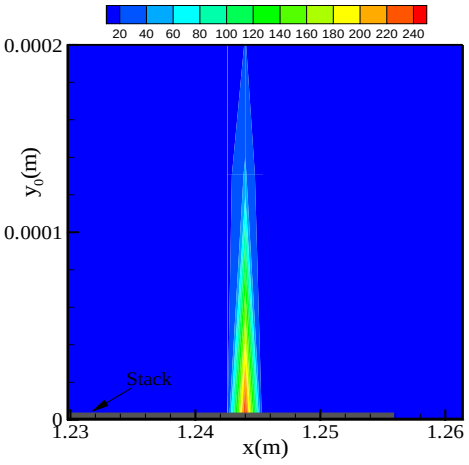

(j) Total volumetric entropy generation rate, 130x magnification factor

Figure 9.1: Time averaged contours (a) and (b) *x*-component of velocity, (c) and (d) *y*-component of velocity, (e) and (f) temperature, (g) and (h) *x*-component of energy flux density, (i) and (j) total volumetric entropy generation rate in the computational domain.

contours, energy flux density contours in the *x*-direction, and total volumetric entropy generation rate in the computational domain for the DR of 1.7% and 5%, respectively (Run No. 1 and 4). Figure 9.1 thus compare two different operating conditions while helium is used as a working fluid, with $p_m = 10$ kPa, $f = 100$ Hz, $y_0 = 3.33\delta_k$, $\delta_k = 2.39$ mm, and stack lengths are 6.84 and 2.32 times particle displacement amplitude.

The *x*-component of time averaged velocity contours show circulations at the stack edges that are at opposite directions. Circulations are also observed along the vertical centre of the channel at the stack edges. The *y*-component of time averaged velocity contours show counter rotating circulations at the stack edges. The strength of counter rotating circulations at the stack edges are increased as the DR is increased from 1.7% to 5% in Fig. 9.1 (a) to (d). The magnitude of circulations at the right end of the stack is larger than the left end, since the left end is near the velocity node of the standing wave in Fig. 9.1 (a) and (b). Time averaged temperature contours show positive and negative fluctuations near the left and right ends of the stack, with increased magnitude of fluctuations at higher DR. These results are expected, since as the DR is increased keeping the p_m constant, the amplitude of fluctuations increases within the computational domain, and thereby increasing the time averaged velocity and temperature contours. Time averaged velocity contours in the *x*- direction (Fig. 9.1 (a) and (b)) is not symmetric with respect to the vertical stack center, as the magnitudes of flow circulations are higher near the right stack end. Since the right end of the stack is near the velocity anti-node, thereby showing increased magnitude of flow circulation at that location compared to the left end.

Time averaged *x*-component of energy flux density in Fig. 9.1(g) and (h) show negative values which indicate energy transport from the right end to that of the left end. The maximum energy transport occurs at a distance of thermal penetration depth from the plate surface, which is also predicted by Swift [1988] and observed in Chapter 7. Less energy flows near the stack plate surface because of the viscous effect and almost isothermal thermal condition near the stack plate surface except at the edges. At lower DR, the extent of maximum *x*-component of energy flux density values is almost twice the thermal penetration depth, but for higher DR, the maximum extent is lowered to 1.7 times the thermal penetration depth. Therefore, at higher DR, stack plate spacing should be lower than the lower DR regarding energy transport along the stack.

Time averaged *x*-component of velocity gradients in the *y*-direction show peak values near the stack edges, with larger magnitudes for higher DR (as shown in Fig. C.18(a) and

(b) in Appendix C). Time averaged *y*-component of velocity gradients in the *y*-direction also shows peak values near the stack edges in Fig. C.18(c) and (d) (in Appendix C) that extent vertically up to the thermal penetration depth. By postprocessing the velocity and temperature data, the frictional entropy generation rates compared to the total entropy generation rates (Eq. (9.7)) are calculated in the computational domain. To calculate the volume averaged entropy generation, Eq. (9.6) is evaluated at each cell, multiplied by the cell volume, and then summed over the entire domain. The sum is then divided by the whole domain volume. Figure C.18 (e) and (f) (in Appendix C) show fluid friction irreversibility ratios (Eq. (9.7)) with peak values near the stack edges. This ratio varies between 0 and 1, 0 is the limit where heat transfer irreversibility dominates, and 1 is the limit where fluid friction irreversibility dominates. Irreversibility ratios are higher near the stack edges, and also for the high DR cases in the space between the stack plates, especially near the stack plate surface. For higher DR, the stack edges and space between the stack plates are dominated by fluid friction irreversibility.

Time averaged temperature gradients in the *y*-direction show peak values near the stack edges, with larger magnitudes for higher DR in Figs. C.18(g) and (h) (in Appendix C). For higher DR, temperature gradients are observed almost up to the thermal penetration depth from the stack plate surface. Only right i.e., cold stack end is shown with negative temperature gradients near the edge. Although velocity and temperature gradients are observed at the stack edges, fluid friction irreversibility dominates near the stack edges and within the stack region because of higher velocity gradients near the stack surface. Figures 9.1(i) and (j) show the total volumetric entropy generation rate in the computational domain with peak values near the stack edges. Only the right stack edge is shown in the figure. Entropy is generated up to the thermal penetration depth from the stack plate surface. The larger entropy generation rate is due to the increased velocity and temperature gradients at higher DR. This result also supports the finding (Fig. 4.17(a)) in Chapter 4.

Temporal Variation of Flow and Thermal Fields to Understand the Nonlinear Behavior

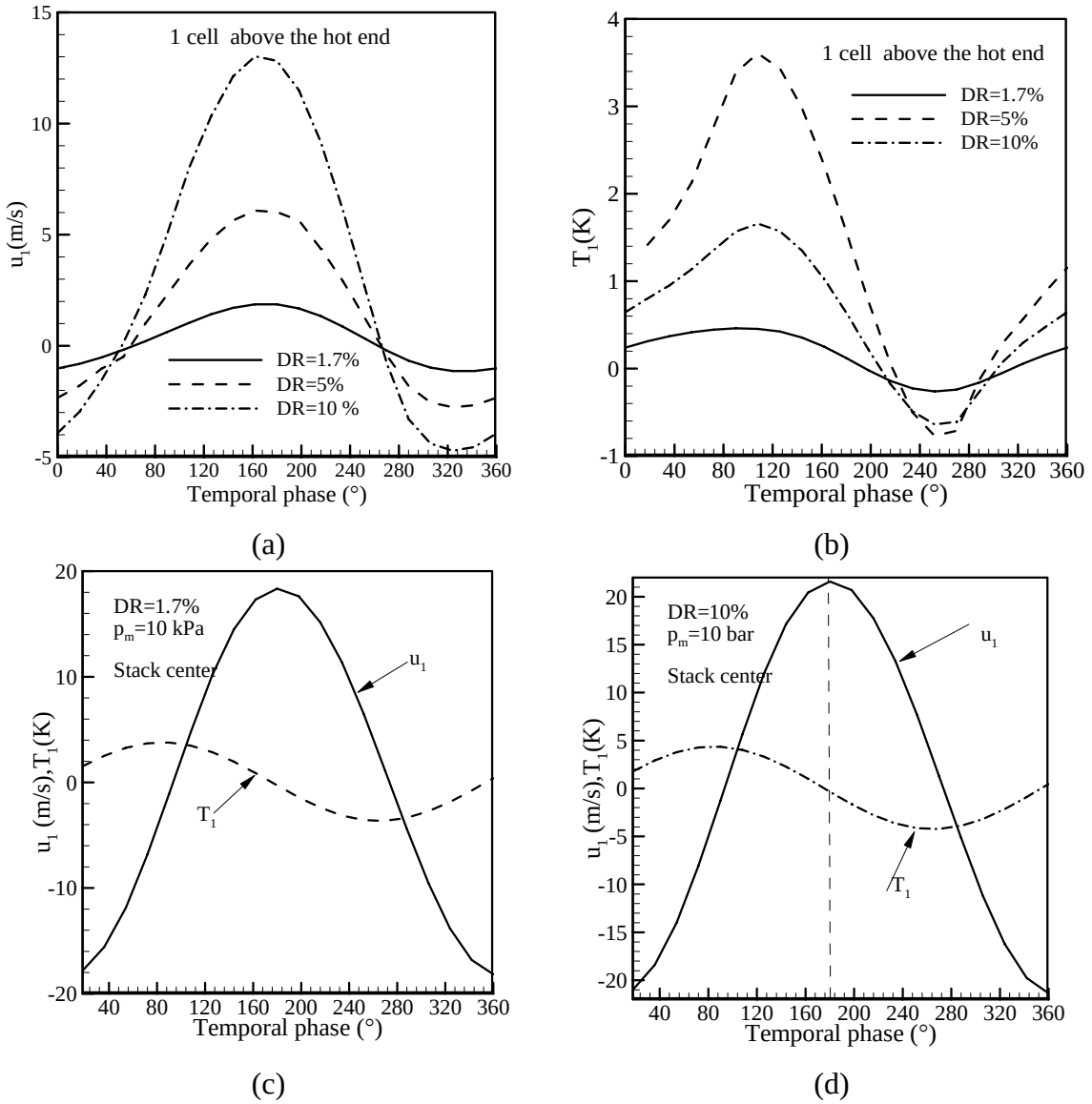

Figure 9.2: Time variation of (a) *x*-component of velocity and (b) temperature at different DR, and *x*-component of velocity and temperature at (c) DR=1.7%, p_m=10 kPa and (d) DR=10%, p_m=1000 kPa.

Figure 9.2 shows the temporal variations of flow and thermal fields at the stack edge (one cell above the stack hot end point "5" in Fig. C.8(b)) in Figs. 9.2(a) and (b) and at the stack center (point "S" in Fig. C.8(b)) in Figs. 9.2(c) and (d). Temperature and velocity oscillations at the edges of the stack plate are highly nonlinear for all the DR considered in the present study. This nonlinear behavior is due to the transition from an adiabatic

behavior outside the stack to an isothermal behavior on the stack plate surface. This behavior is also observed analytically by Gusev et al. [2001] and numerically by Marx and Blanc Benon [2004], and confirms that there is indeed temperature harmonic generation at the edges of the stack plate. Temperature and velocity oscillations (Figs. 9.2(c) and (d)) show linear behavior at the stack center for all the conditions considered in the present study.

The summary of Figs. 9.1 (a) to (j) and Figs. 9.2(a) to (d) or increasing the DR from 1.7% to 10% is as follows:

- Convection heat transfer dominates near the stack edges compared to the conduction and *y*-component of velocity exists only near the stack edges.
- Temperature and velocity oscillations at the stack edge are nonlinear and linear at the stack plate center for all the DR considered in the present study.
- The amplitudes of velocity and temperature oscillations increase with DR up to DR=5%, after that as the DR increases, the amplitudes of velocity fluctuations increase but not the temperature.
- Energy flux density in the *x*-direction is less near the stack plate surface, increases as one moves away vertically up from the surface, and becomes maximum around δ_k from the stack plate surface.
- Energy flux density in the *y*-direction increases as the DR increases.
- The larger entropy generation rate is observed at higher DR due to the increased velocity and temperature gradients.
- As the DR increases at constant p_m, the acoustic power absorbed and the heat pumping power of the stack increase, thereby showing (in Table 9.3) lower COP for all the stack spacing considered in the present study.

9.3.2 Effect of Prandtl Number (Pr)

Figure 9.3(a) to (j) show the effect of Pr on the flow, thermal, energy fields, and irreversibility distributions within the stack region. Working fluids of two different Pr are

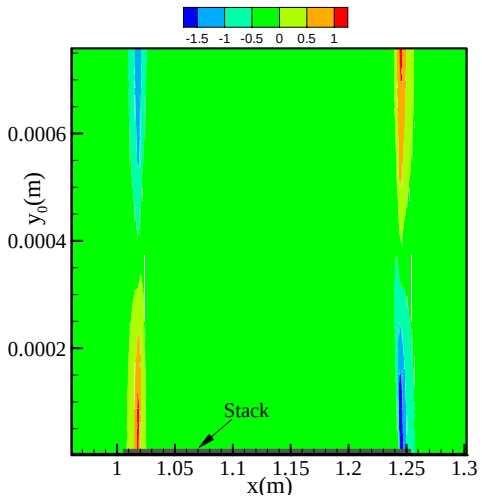

(a) *x*- components of velocity contours, 12x magnification factor

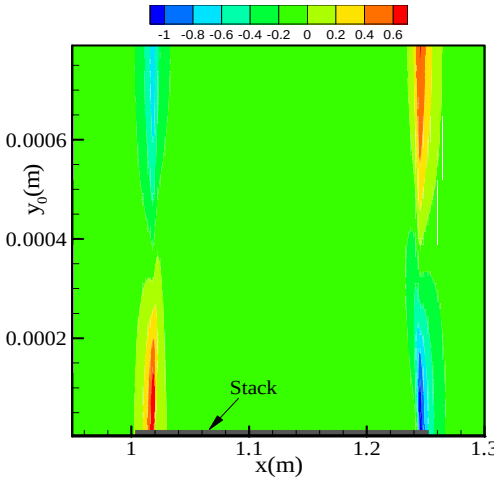

(b) *x*- components of velocity contours,12x magnification factor

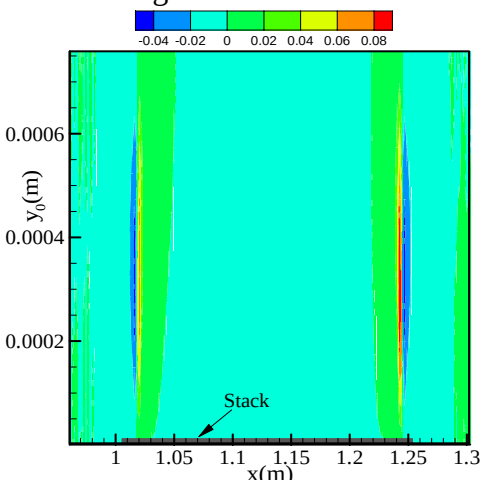

(c) *y*- components of velocity contours,12x magnification factor

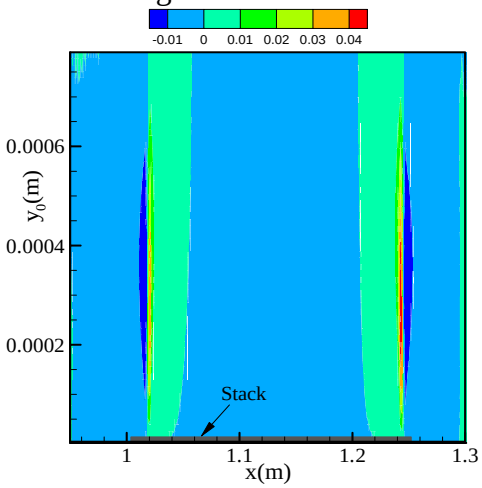

(d) *y*- components of velocity contours,12x magnification factor

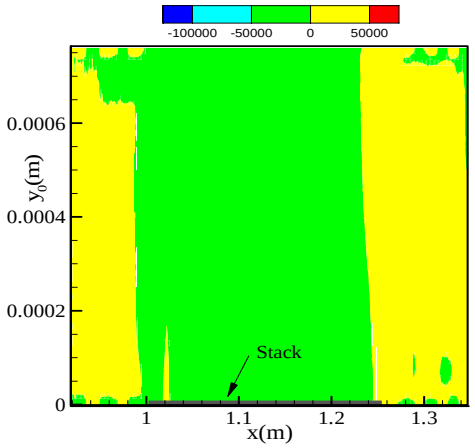

(e) *x* -component of velocity gradient in the *y* direction, 12x magnification factor

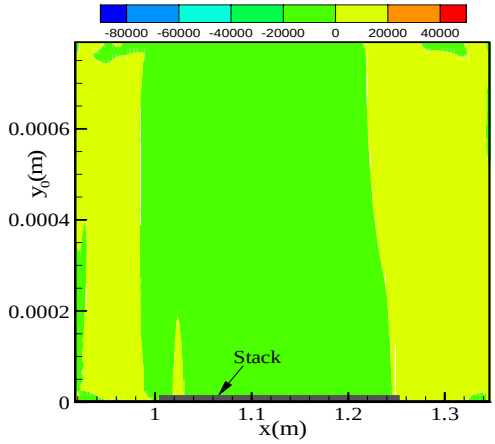

(f) *x*- component of velocity gradient in the *y* direction, 12x magnification factor

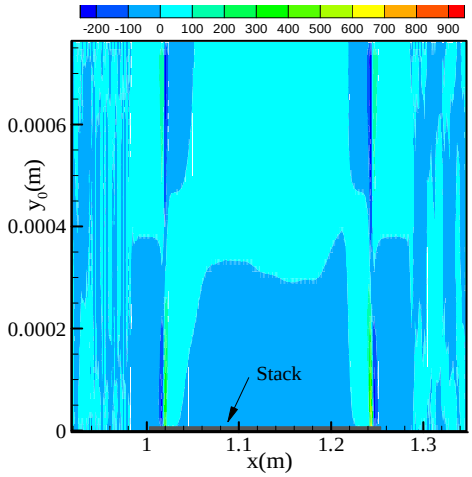

(g) *y*-component of velocity gradient in the *y* direction 12x magnification factor

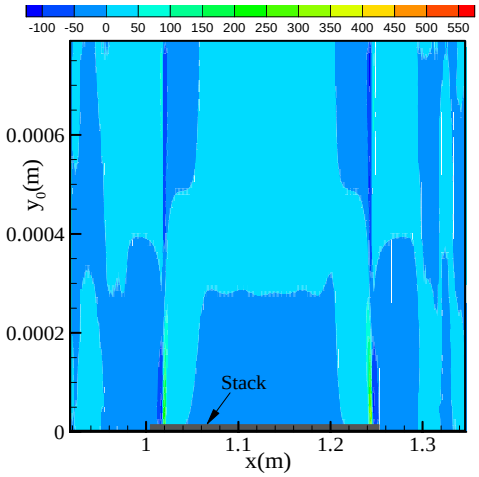

(h) *y*-component of velocity gradient in the *y* direction 12x magnification factor

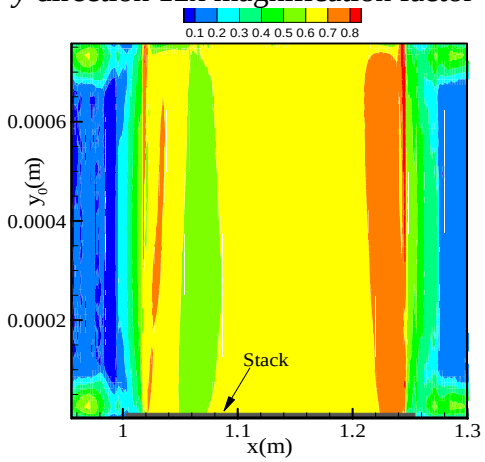

(i) fluid friction irreversibility ratio contours, 12x magnification factor

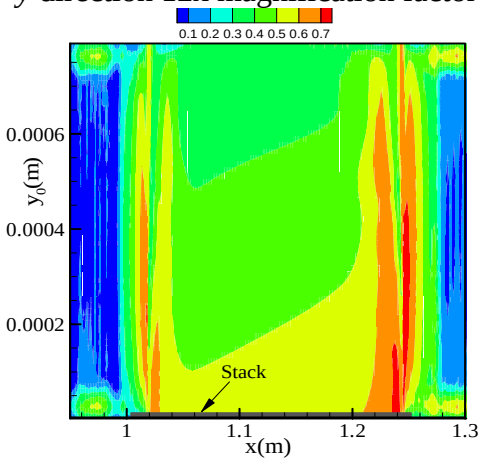

(j) fluid friction irreversibility ratio contours, 12x magnification factor

Figure 9.3: Time averaged *x* and *y* components of velocity contours (a) and (c) for helium, (b) and (d) for a mixture of helium and xenon. *x* and *y* components of velocity gradients in the y direction (e) and (g) for helium, and (f) and (h) for a mixture of helium and xenon, fluid friction irreversibility ratio contours (i) for helium, (j) for a mixture of helium and xenon. The operating conditions are $y_0 = \delta_k$, $p_m = 1$ bar, and $DR = 1.7\%$.

employed in this study as mentioned in **Section** 9.2. These two are 0.7 and 0.28, respectively. No other study in the existing literature examines the influence of Pr except Tijani [2001] who investigated the influence of Pr on the COP and COPR of a thermoacoustic device using experiment and linear theory predictions. The present study examines the effect of Pr on flow, thermal, energy fields, and irreversibility distributions within the stack region for the first time. Two different cases Run No. 19 ($\mathrm{Pr} = 0.7$,

DR=1.7%, $p_m = 10$ bar) and 36 ($\mathrm{Pr} = 0.28$, DR=1.7%, $p_m = 10$ bar) are considered in this section. It is observed in Fig. 9.3(a) and (b) that for the *x*-component of velocity contours, the strength of flow circulation is higher for the large Pr fluid. The *y*-component of velocity contours show counter rotating circulations near the stack edges, with increased intensity for large Pr fluid. *X* and *y* components of velocity gradients in the *y* direction contours show higher values for high Pr fluid. The stack plate acts as a strong producer of fluid friction irreversibility while high Pr working fluid is used. The highest rate of entropy generation occurs in the regions with highest shear stresses, i.e., close to the stack plate surface near the edges. Higher flow circulation magnifies the velocity gradients and

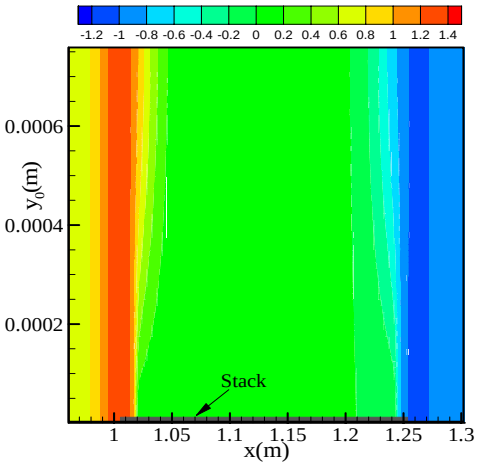

(a) Temperature contours, 12x magnification factor

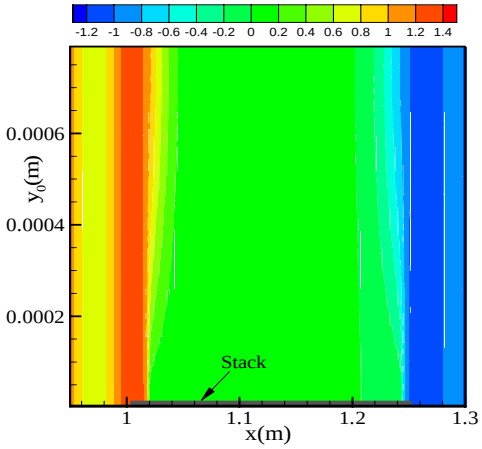

(b) Temperature contours, 12x magnification factor

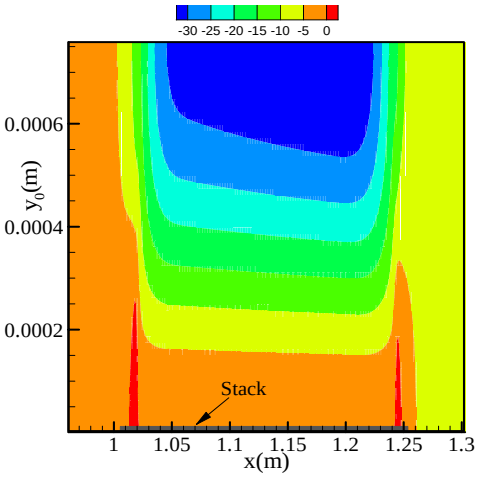

(c) E_x, 12x magnification factor

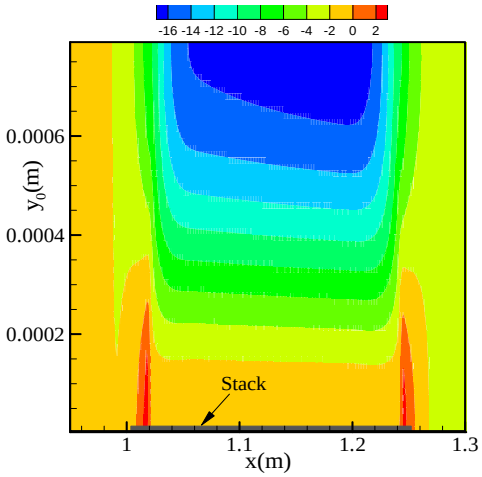

(d) E_x, 12x magnification factor

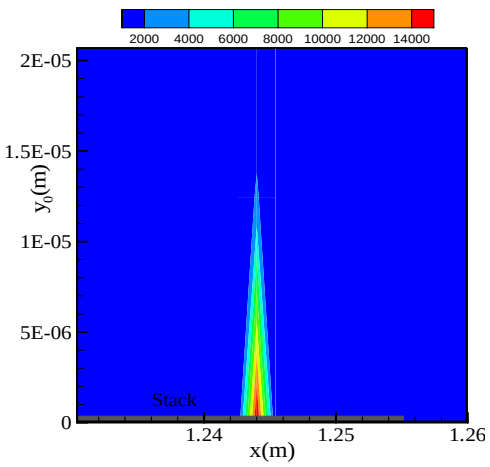

(e) Total entropy generation rate, 130x magnification factor

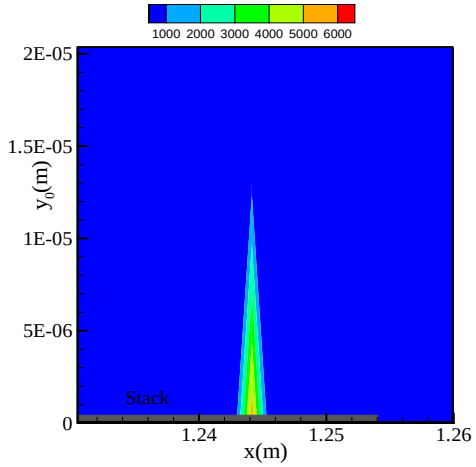

(f) Total entropy generation rate, 130x magnification factor

Figure 9.4: Time averaged temperature contours (a) for helium and (b) for a mixture of helium and xenon. *x* component of energy flux density (c) for helium, and (d) for a mixture of helium and xenon. Total entropy generation rate (e) for helium, and (f) for a mixture of helium and xenon. The operating conditions are $y_0 = \delta_k$, $p_m = 1$ bar, and $DR = 1.7\%$.

hence increases the entropy generation rates. Therefore, entropy generation due to frictional effects are higher for large Pr fluid that produces higher flow circulations near the stack ends. For helium, fluid friction irreversibility exists within the entire stack plate region due to higher viscosity of helium compared to the gas mixture. For the gas mixture fluid friction irreversibility peaks near the stack edges, and exists within the stack region near the edges only. Therefore, fluid friction irreversibility dominates for smaller stack plate spacing with high Pr fluid. Time averaged temperature contours in the computational domain are shown in Figs. 9.4(a) and (b) for helium and a mixture of helium and xenon for the identical operating conditions as stated above. It is shown that temperature variations are obtained at the stack edges. The space between the stack plates shows a very small change of temperature. Both Figs. 9.4(a) and (b) show identical values of temperature fluctuations.

Time averaged temperature gradients in the *y* direction show negligible effect of Pr (not shown here). Time averaged *x*-component of energy flux density values in Figs. 9.4(c) and (d) show maximum values at a distance of thermal penetration depth from the stack

surface, with higher values for helium. This result is expected since *x*-component of energy flux density values are dominated by the enthalpy term (as shown in the second term of Eq. (C.18)) and enthalpy terms are higher for helium.

Total volumetric entropy generation rate in Fig. 9.4(e) and (f) show peak values near the stack edges, with higher values for helium gas. Since total entropy generation rate as indicated in Eq. (9.6) is a function of velocity and temperature gradients, and these gradients are higher for helium gas, therefore showing higher irreversibility for helium gas.

For the similar DR and p_{m} the COP is higher for lower Pr fluid at $y_0 = 3.33\delta_k$. Since for the lower Pr fluid, acoustic power absorbed by the stack decreases compared to the higher Pr fluid. Although, the heat pumping power of the stack decreases for the lower Pr fluid. At $y_0 = 1.0\delta_k$, the COP is lower for low Pr fluid. Even though, the acoustic power absorbed by the stack decreases at this stack plate spacing, the heat pumping power of the stack decreases too, thereby decreasing the COP compared to helium gas.

The summary of the effect of changing the Pr of the working fluid is as follows:

- COP is higher for lower Pr fluid at $y_0 = 3.33\delta_k$.
- At $y_0 = 1.0\delta_k$, the COP is lower for low Pr fluid.

9.3.3 Effect of p_m

Run No. 1, 2, and 3 are considered to examine the effect of p_m on thermoacoustic effect and entropy generation rate. As the p_m is increased for a constant DR from 10 kPa to 1000 kPa, the stack plate spacing is reduced. Therefore, accommodating more gas within the stack region and enhancing energy flux density in the *x* and *y* directions. Time averaged temperature and velocity contours show higher amplitudes with higher p_m (up to $p_m = 100\,\mathrm{kPa}$). After that the velocity amplitudes increase with pressure but not temperature. *X* and *y* components of velocity gradient contours in the *y* direction show

higher values at higher p_m. Temperature gradient in the *y* direction show higher values at higher p_m. The increase in *x* component of velocity gradient in the *y* direction and temperature gradient in the *y* direction are significant compared to *y* component of velocity gradients in the *y* direction. Therefore, higher entropy generation rate is observed with higher p_m. An order of magnitude increase in entropy generation rate is observed with the p_m. This result also supports the finding (Fig. 4.17(b)) in Chapter 4.

9.3.4 Effect of Stack Plate Length

Run No. 2, 5, and 8 are considered to examine the effect of stack plate length on thermoacoustic effect and entropy generation rate. In these runs the length of the stack varies from 6.84 to 1.38 times the particle displacement amplitude. The stack plate length compared to particle displacement amplitude is varied in these cases by increasing the DR (from 1.7 to 10 %). Therefore, as the stack plate length decreases compared to particle displacement amplitude, the temperature and velocity fluctuations at the stack edges increase. *X* and *y* components of velocity gradients contours in the *y* direction show higher values for smaller stack length compared to particle displacement amplitude (not shown here). Temperature gradient in the *y* direction show higher values too. The increase in *x* component of velocity gradient in the *y* direction and temperature gradient in the *y* direction are significant compared to *y* component of velocity gradients in the *y* direction. Therefore, higher energy flux density and entropy generation rate are observed with larger DR or when the stack plate length decreases compared to particle displacement amplitude. Therefore, the present study shows that thermoacoustic effect is observed even when the stack plate is equal to the particle displacement amplitude long.

9.3.5 Effect of Stack Plate Spacing (y_0)

For all the stack spacing considered in the present investigation, a circulation is observed in between the stack plate region while velocity vectors are observed and are shown in **Section** 9.4.2. As the stack plate spacing decreases from $3.33\delta_k$ to $1.0\delta_k$, heat pumping power decreases which is also observed by Tijani [2001]. Once the spacing becomes

smaller than about $2.0\delta_k$, the thermoacoustic effect is reduced, which decreases the cooling power. As the stack plate spacing decreases, the fluctuating velocity inside the stack increases, also the whole gas layer between the plates contributes to the viscous shear, thereby increasing the viscous dissipation within the stack. These results in increase in absorbed acoustic power and hence decrease in COP. As the stack plate spacing decreases from $3.33\delta_k$ to $2.0\delta_k$, heat pumping power remains almost unchanged. For $y_0 > 2.0\delta_k$, the boundary layer assumption holds (as shown in Fig. 4.6(b)) and the cooling power is proportional to the product of the total perimeter of the stack plate (Π) and the thermal penetration depth (δ_k) (Eq. (76) of Swift [1988]). An increase in the stack spacing means a decrease of the number of plates and hence a decrease of perimeter (Tijani [2001]). This results in a decrease in cooling power. But the acoustic power absorbed by a stack increases as y_0 decreases from $3.33\delta_k$ to $2.0\delta_k$, thereby decreasing the COP for stack plate spacing lower than $3.33\delta_k$. Therefore, for all the cases considered, maximum cooling power is observed at $y_0 = 2.0\delta_k$ and maximum COP is obtained at $y_0 = 3.33\delta_k$. These findings are supported by Tijani [2001]. Similar behavior is also observed for helium and xenon mixture.

9.3.6 Results on Cooling Power, Acoustic Work, COP, and Entropy Generation

Figure 9.5(a) and (b) show the *y*-component of Energy flux density (E_y) versus Reynolds number ($\mathrm{Re}_\delta = \frac{\sqrt{2\rho}\,u_A}{\sqrt{\mu\omega}}$) as a function of stack plate spacing for both of the working fluids. For larger stack plate spacing (between $y_0 = 3.33\delta_k$ and $1.0\delta_k$), larger E_y is observed with higher slope for both of the working fluids. Helium shows higher E_y values compared to the gas mixture. This is also observed by Tijani [2001]. The symbols are numerical results and the lines are linear fit through the data points. As

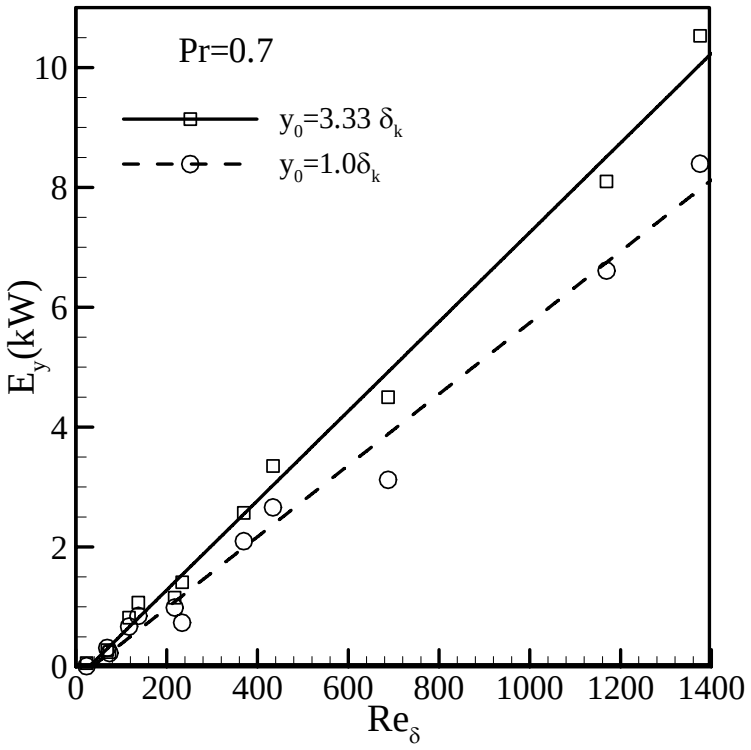

(a)

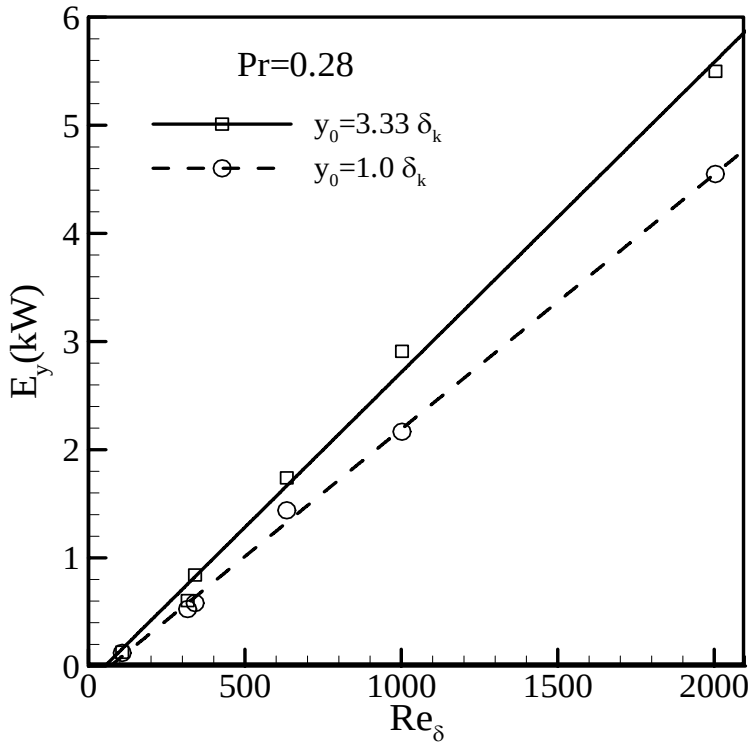

(b)

Figure 9.5: E_y versus Re_δ as a function of stack plate spacing for (a) helium, and (b) a mixture of helium and xenon.

shown by Eq. (66) (Swift [1988]), cooling power is inversely proportional to the product of $\rho_m a$, where a is the adiabatic speed of sound and ρ_m is the mean density of fluid. The product of $\rho_m a$ increases while the gas mixture is used thereby reduces the cooling power of a thermoacoustic device. Equation (66) of Swift [1988] is presented below where H_2 and V are the cooling power and the volume of the device.

$$\frac{H_2}{V} \approx \frac{f}{2}\frac{T_m \beta}{1+\varepsilon_s}\frac{P_0^2}{\rho_m a^2}. \tag{9.9}$$

Figure 9.6(a) shows E_y versus p_m as a function of DR for both of the stack spacing. The lines are visual guide. A linear increase of E_y is observed with p_m up to 100 kPa with higher slope for larger DR, after that E_y increases, but with a lower slope compared to that of the lower p_m. The reason might be explained in the following way. E_y is

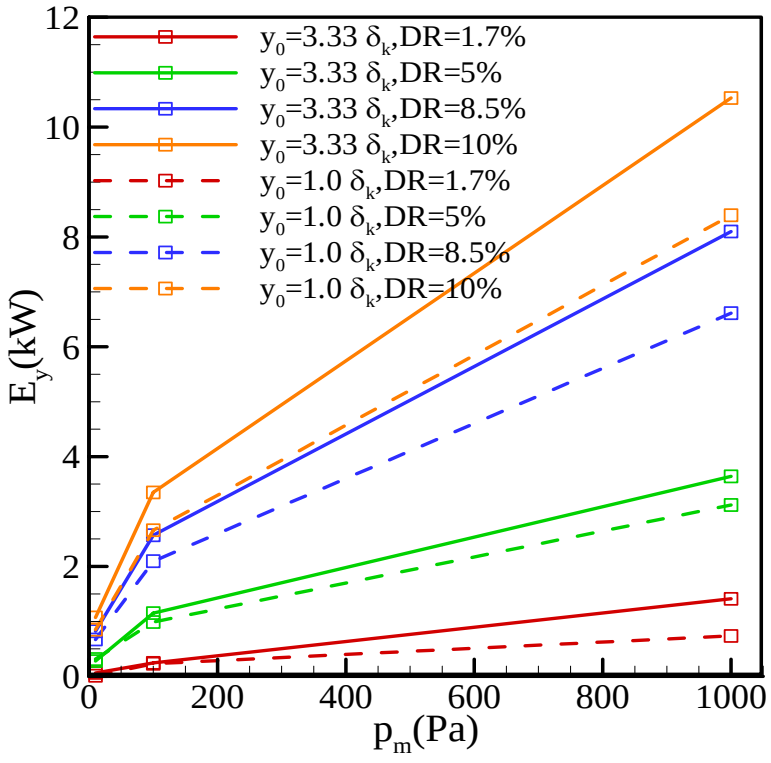

(a)

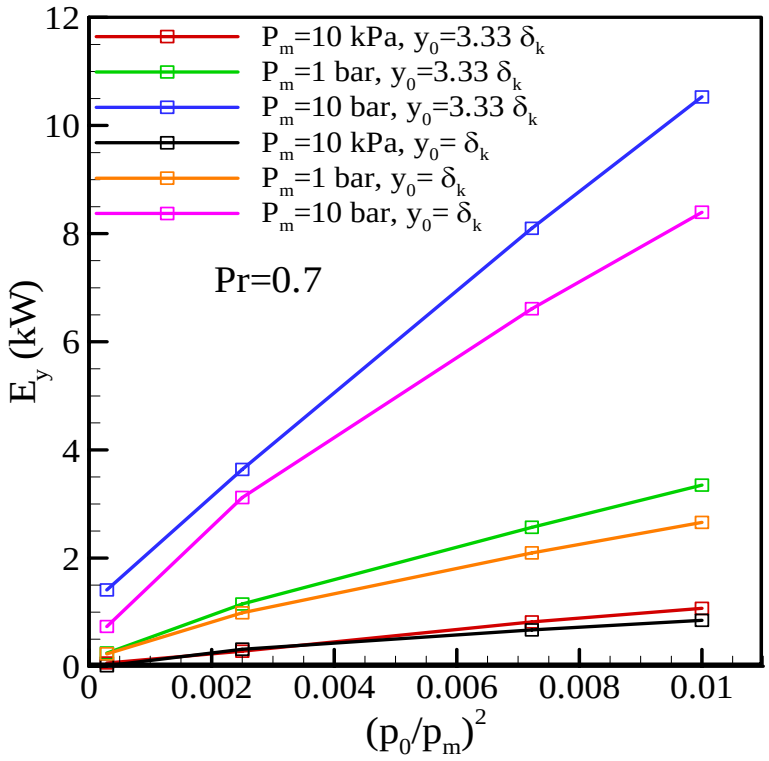

(b)

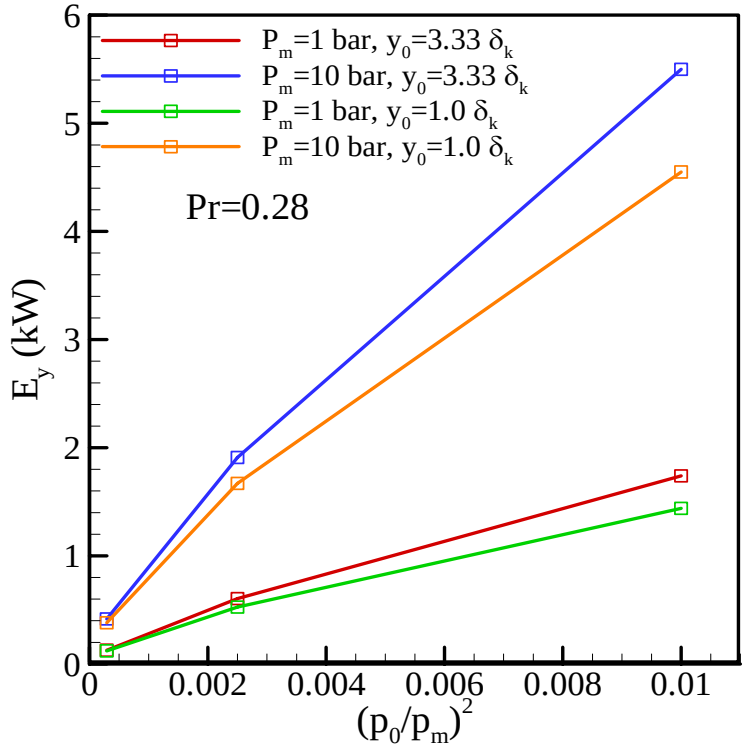

(c)

Figure 9.6: (a) E_y versus p_m as a function of DR. E_y versus $(p_0/p_m)^2$ as a function of stack plate spacing for (b) helium, and (c) a mixture of helium and xenon.

proportional to the time and spatial averaged product of $(u_1 T_1)$. As the p_m and DR increase beyond 100 kPa and 5%, the amplitude of temperature fluctuation saturates, but the velocity keeps increasing. This temperature saturation is the reason for the change of behavior at higher p_m and DR. Figures 9.6(b) and (c) show E_y versus $(p_0/p_m)^2$ as a function of stack plate spacing for both of the working fluids. Figure 9.6(b) and (c) are for DR=1.7% to 10% and for helium and a mixture of helium and xenon. For both figures a linear profile is also observed with increased slope for higher p_m and larger spacing. Figures 9.6(b) and (c) show that E_y is linearly proportional to the amplitude square up to DR=5%, after that the slope decreases slightly compared to that of the lower *DR*. Swift[1988] using linear theory showed a linear behavior (in Eq. (A 30)) between E_y and amplitude square. Swift [1992] also showed experimentally the linear variation of E_y versus $(p_0/p_m)^2$ up to DR=10%. Figure 9.7(a) shows the effect of p_m and DR on the performance of a thermoacoustic device at $y_0 = 3.3\delta_k$. The symbols are numerical results and lines are visual guide. Cooling power and acoustic power increase with the increase of DR and p_m. Since as the DR increases or as the p_m increases at a constant DR, amplitudes of acoustic fluctuations increase, thereby increasing the acoustic power and cooling power. At higher p_m; at $p_m = 10$ bar, the increase in acoustic power is significant compared to the cooling power, and hence a decrease in COP is observed. As p_m increases, u_1 and p_1 increase, thereby increasing the acoustic power (Eq. (9.1)). E_y is proportional to time and spatial averaged product of $(u_1 T_1)$, and since T_1 saturates after $p_m = 100$ kPa, therefore the increase in E_y is less than acoustic power and hence a decrease in COP is observed. Maximum COP is obtained at $DR = 1.7\%$, $p_m = 10$ kPa, and $y_0 = 3.3\delta_k$. For each of the DR and stack spacing considered, maximum COP is observed at $p_m = 10$ kPa and COP decreases as the stack spacing decreases from $3.33\,\delta_k$ to $1.0\,\delta_k$. COP also gradually decreases as the p_m and DR increase from 10 kPa

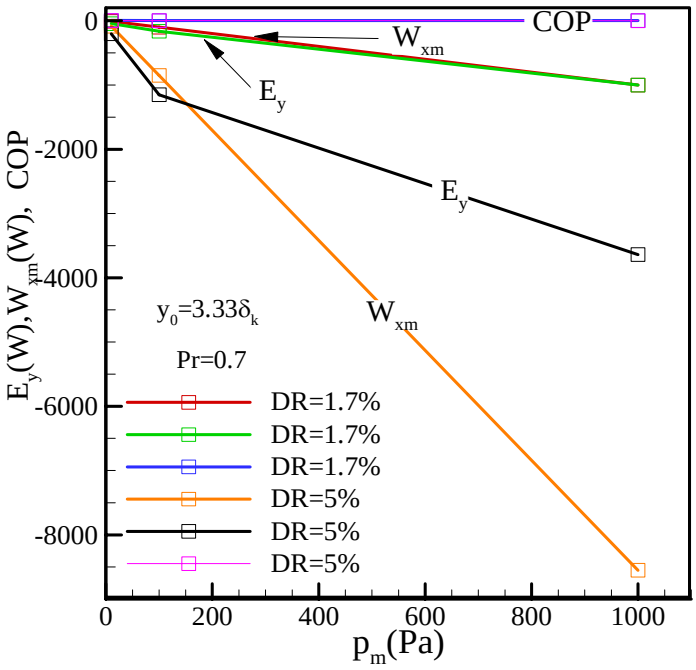

(a)

Figure 9.7: (a) E_y, W_{xm}, and COP versus p_m as a function of DR at $\mathrm{Pr} = 0.7$ and $y_0 = 3.33\delta_k$.

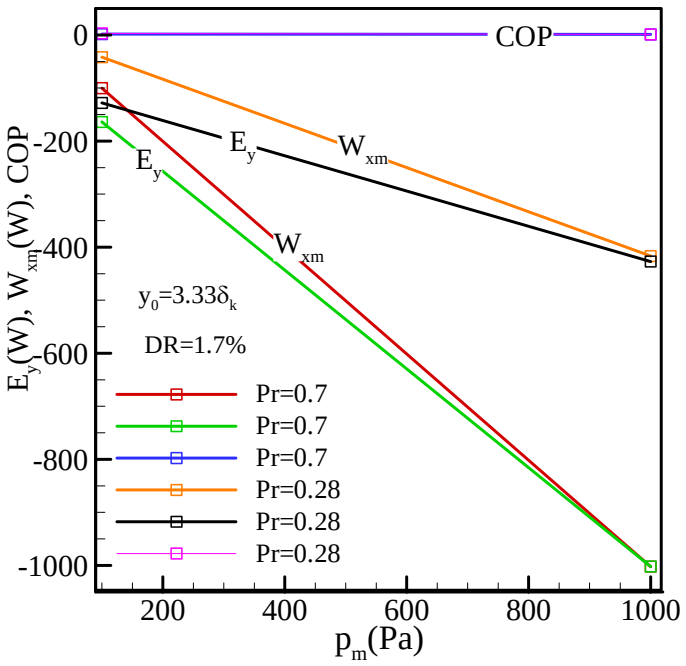

(b)

Figure 9.7: (b) E_y, W_{xm}, and COP versus p_m as a function of Pr at $y_0 = 3.33\delta_k$ and DR=1.7%.

to 10 bar, and 1.7% to 10%, respectively. The effect of p_m is more pronounced at higher DR. An important finding of this study is that cooling power and acoustic power absorbed by a thermoacoustic refrigerator increase as the p_m and DR increase, but the increase of acoustic power is more significant than the cooling power at higher DR and p_m. Therefore, COP decreases at higher DR and p_m.

Now, Fig. 9.7(b) shows the effect of Pr and p_m on the performance of a thermoacoustic device at $y_0 = 3.33\delta_k$ and $DR = 1.7\%$. The symbols are numerical results and lines are visual guide. Cooling power decreases as Pr decreases from 0.7 to 0.28, but the decrease is more prominent at higher p_m. Acoustic power absorbed by a refrigerator decreases as the Pr decreases, but the decrease is significant at lower p_m. An average 22% decrease in cooling power and a 58% decrease in acoustic power are observed (at $y_0 = 3.33\delta_k$) as Pr changes from 0.7 to 0.28. A 53% increase in COP is observed at $DR = 1.7\%$, $p_m = 1000$ kPa, and $y_0 = 3.33\delta_k$. Thus decreasing the Pr at $y_0 = 3.33\delta_k$ is favorable for enhancing the device's performance. For the similar experimental conditions, Tijani [2001] found a 31% increase in COP when Pr is changed from 0.7 to 0.28. However, Tijani [2001]'s experimental work considered a stack plate spacing of $y_0 = 2.78\delta_k$, $DR = 1.4\%$, a frequency of 141 Hz, and a temperature difference of almost 60°C across the stack ends. Tijani [2001] calculated the cooling power and the acoustic work using Eq. (76) and (80) of Swift [1988]. The present numerical modeling result is for an isothermal stack plate of spacing $y_0 = 3.33\delta_k$, a frequency of 48.99 Hz, and $DR = 1.7\%$. A 53% increase in COP is observed compared to Tijani [2001]'s 31%. Tijani [2001]'s experimental work did not indicate any uncertainty in results. Therefore, the agreement if quite good even though the present study overestimates the increase in COP value. It is expected, since the present numerical modeling is for an idealized condition, does not have any temperature gradient along the stack plate, no heat exchangers, and no fluctuations of temperature along the stack plate surface. In the present work, acoustic work and cooling power are evaluated directly from the numerical results using Eq. (9.1) and (9.2). Tijani [2001] did

not consider any variation in p_m in their experiments. COP increases 78% for reducing the Pr from 0.7 to 0.28 at $y_0 = 3.33\delta_k$, at atmospheric pressure and at DR=1.7% compared to 53% at $p_m = 1000$ kPa. Therefore, lowering the Pr at atmospheric pressure gives better performance regarding to COP and total irreversibility. The increase in COP is due to the lower acoustic work absorption and low irreversibility. At $y_0 = 1.0\delta_k$, the decrease in Pr from 0.7 to 0.28 decreases the COP values. Therefore, decreasing the Pr for lower stack plate spacing does not improve the performance of a thermoacoustic device. Tijani [2001] did not consider the effect of stack plate spacing in their experiments. Similar to $\mathrm{Pr} = 0.7$, as the DR increases for each of the p_m considered; the COP also decreases at $\mathrm{Pr} = 0.28$. Since the increase in cooling power with DR and p_m are lower than the acoustic work.

A comparison of total entropy generation (S_{gen}) versus DR is plotted in Fig. 9.8 at a p_m of 10 kPa and compared to the results of Ishikawa and Mee [2002]. A very good

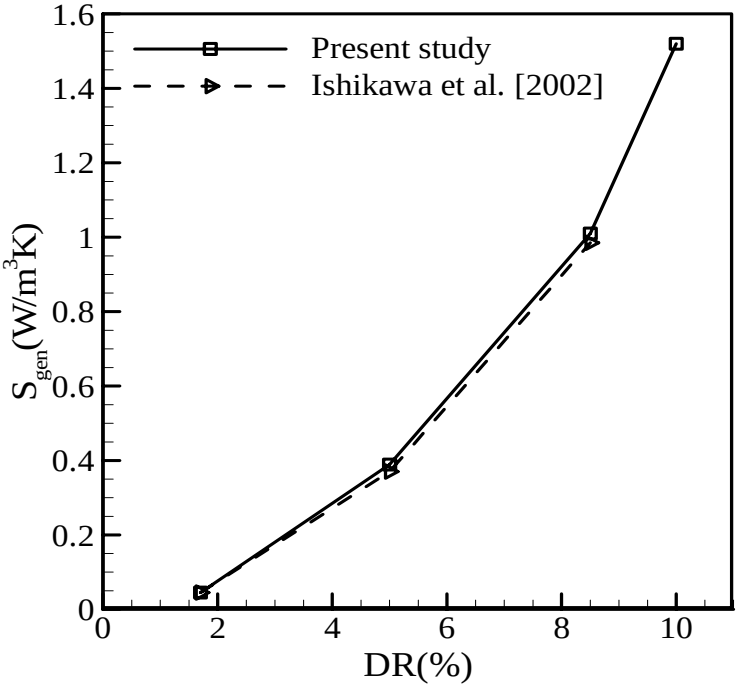

Figure 9.8: Comparison of S_{gen} versus DR with existing literature.

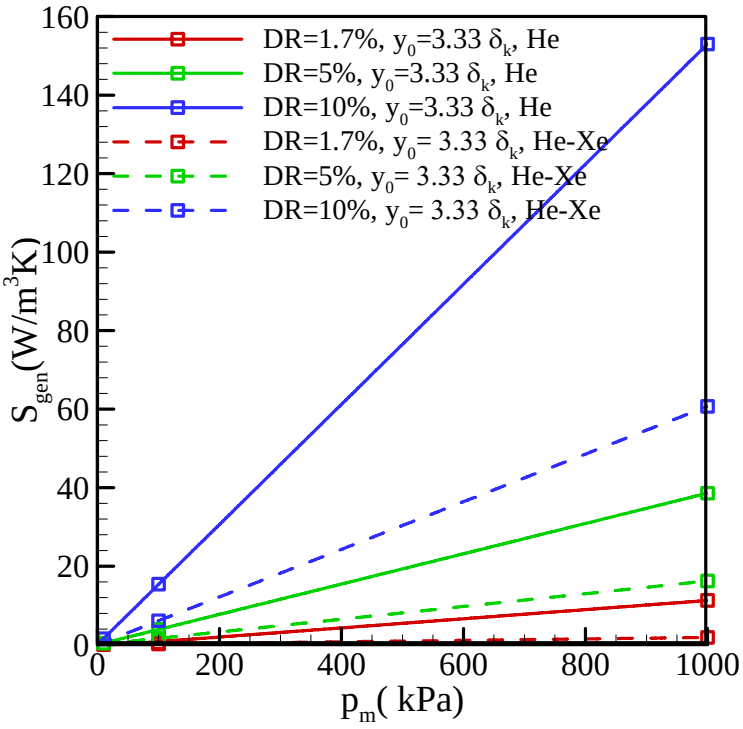

(a)

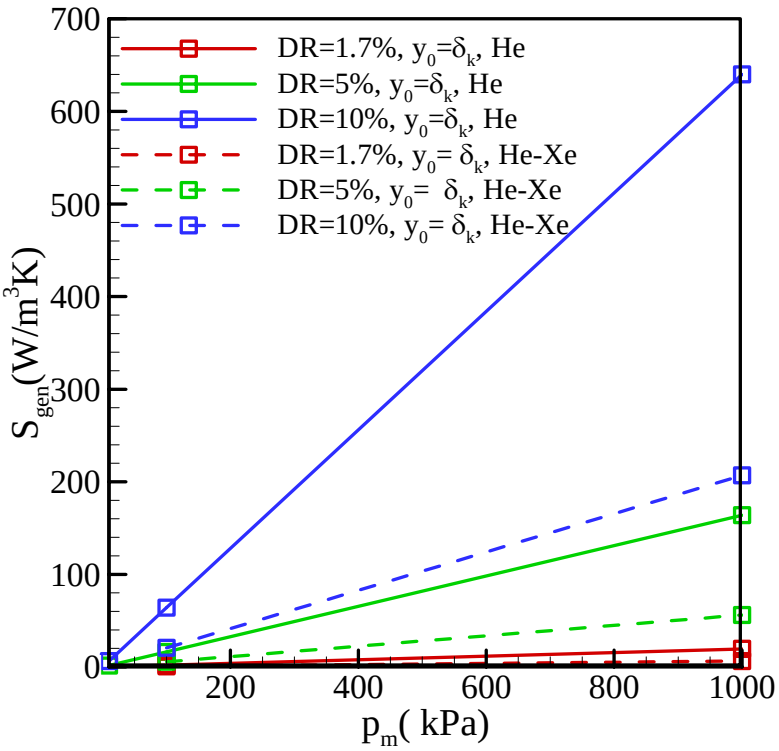

(b)

Figure 9.9: S_{gen} versus p_m as a function of DR at a stack spacing of (a) 3.33 δ_k and (b) 1.0 δ_k for both Pr fluids.

agreement is obtained between the two numerical results. This comparison gives us confidence that the entropy generation calculated in the present investigation is free from errors.

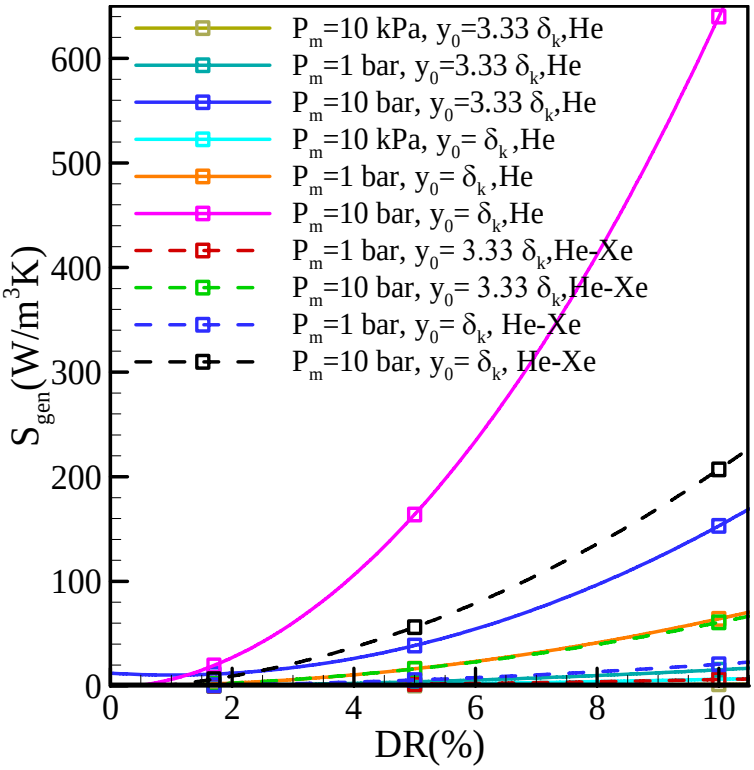

Figure 9.10: S_{gen} versus DR as a function of p_m, stack spacing, and working fluid.

Figure 9.9(a) and (b) show total entropy generation, S_{gen} versus p_m as a function of DR at a stack spacing of 3.33 δ_k and 1.0 δ_k for both Prandtl number fluids. A linear increase of S_{gen} is observed with p_m, with higher slope for smaller spacing, which is expected. Figure 9.10 shows S_{gen} versus DR as a function of p_m, stack spacing, and working fluid. The quadratic dependence is expected from the fact that the dominant terms in Eq. (9.6) vary with the square of velocity and temperature gradients.

9.4 Conclusions

The effects of Pr, DR, p_m, stack spacing, and stack length on flow, thermal, energy flux density, cooling power, acoustic power, COP, and entropy generation rate are examined numerically for thin stack plate limit. Entropy generation is used as an indicator to quantify the significance of irreversibilities. Entropy production characterizes the extent of the dissipation of mechanical energy into internal energy and includes both thermal and frictional irreversibilities. The conclusions are summarizes as follows:

- Regarding the flow field, circulations are observed at the stack plate edges and at the center of the stack channel when stack spacing is equal to the thermal penetration depth for all DR and p_m considered. The intensity of flow circulations increases as the DR, p_m, Pr, and stack plate spacing increase.

- *Y*- component of energy flux density (E_y) is observed when the stack length is almost equal to the particle displacement amplitude which is also supported by the existing literature (Ishikawa and Mee [2002]). E_y is maximum at the stack edges which is also supported by the experimental results in Chapter 7. The numerical results show that E_y increases linearly with Re_δ. E_y also increases linearly with square of DR for both of the working fluids at low p_m. As the p_m increases the slope of the linear profile decreases compared to the lower p_m. Maximum E_y is observed at $y_0 = 2.0\,\delta_k$ and maximum COP is obtained at $y_0 = 3.33\,\delta_k$. Therefore, it is concluded that a plate spacing of $y_0 = 3.33\,\delta_k$ should be optimal for thermoacoustic refrigeration.

- An important finding of this study is that cooling power and acoustic power absorbed by a thermoacoustic refrigerator increase as the p_m and DR increase, but the increase of acoustic power is more significant than the cooling power at higher DR and p_m. Therefore, COP decreases at higher DR and p_m.

- To reduce the viscous loss by reducing the working fluid's Pr is not a good option for all the stack plate spacing. COP increases 78% by reducing the Pr from 0.7 to 0.28 at $y_0 = 3.33\delta_k$, at atmospheric pressure and at DR=1.7% compared to 53% at $p_m = 1000\,\text{kPa}$. Therefore, lowering the Pr at atmospheric pressure gives better performance regarding to COP and total irreversibility. But COP decreases as reducing the Pr from 0.7 to 0.28 at $y_0 = 1.0\delta_k$ and for all the p_m and DR considered. Therefore, for optimum stack performance atmospheric pressure along with $y_0 = 3.33\delta_k$ and low Pr working fluid should be considered.

- The numerical results show that fluid friction irreversibility dominates heat transfer irreversibility within the stack region for all of the cases considered, because of the high shear stress near the stack edges and high stack surface shear effects. Therefore, fluid friction irreversibility and thus total entropy generation increase for smaller stack spacing, higher DR, higher p_m, and high Pr fluid. S_{gen} varies linearly with the p_m and quadratically with the DR. The numerical results show that cooling power and irreversibility have similar trends of variation with Pr. Therefore, lower Pr fluid at stack plate spacing of $y_0 = 3.33\delta_k$, low p_m (100 kPa) and DR (1.7%) are favorable for less irreversibility and higher COP.

Chapter 10

Conclusions and Recommendations

10.1 Contributions to Thermoacoustic Research

Significant contributions of the present research to the thermoacoustic literature are summarized as follows (see **Section** 10.2 for details):

- Analytical porous media *models* are developed using the linear Darcy Law and the non-linear Brinkman-Forchheimer extended Darcy Law for random porous stacks that provide a theoretical understanding and design methodology of random stack environment that are required to understand and increase the efficiency of thermoacoustic devices.

- *Random* stack performance is evaluated as a function of geometry, material, dimension, and position in the presence of a standing wave. The outcome of this research has application to the search for efficient stack configuration for particular applications (especially for use in small scale thermoacoustic devices).

- *Heterogeneous* stack performance is examined for different configurations and compared to homogeneous stacks. This research's contribution is to examine and propose a new stack geometry that has the ability to reduce the irreversibility present in the typical homogeneous stacks.

- The literature on thermoacoustic working fluid *mixtures* is extended numerically to examine the performance effects of working fluid, geometry, and operating conditions. This research has application to determine which geometric, operating conditions, and working fluid has the highest thermal performance.

The information obtained from the present study are useful not only in thermoacoustic devices but for other devices such as those that have components subject to oscillatory flows.

10.2 Conclusions

A promising candidate for refrigeration and electricity generation is a thermoacoustic engine. The development of more compact thermoacoustic energy conversion devices will enable implementation of a variety of small scale systems, such as micro-electro-mechanical systems (MEMS), sensor networks, and unmanned vehicles. Thermoacoustic systems can also be used for waste heat recovery and conversion. The complicated thermal interactions between the stack plate and the gas, between the stack and heat exchangers, energy flow mechanisms within the stack and between the stack and heat exchangers, and inherent irreversibilities inside a thermoacoustic device present a real challenge for thermo-fluid modeling and understanding. In order to tackle these thermoacoustics modeling and understanding challenges, this thesis work takes a step forward by conducting research into four major areas with a focus on thermoacoustic device stack and resonator. The four major areas of research are as follows:

- Mathematical modeling for random porous medium using linear Darcy flow model.
- Mathematical modeling for random porous medium using non-linear Brinkman Forchheimer extended Darcy flow model.
- Experimental works with homogeneous and heterogeneous stacks.
- Numerical work to capture the effects of working fluids, nonlinearities, geometric, and operating conditions on the performance of stacks and resonators.

The major areas of research and their outcomes are elaborated in the next paragraphs.

A relatively novel approach to increase the power density of a thermoacoustic device is to incorporate porous foams in between the channel walls. The idea of filling the space

between the channel walls with a porous medium is to increase the heat exchange surface area between the gas and the porous medium and thereby increasing the power density. To understand the oscillatory gas thermodynamics and energy transfer in porous stacks that is embedded in between the channel walls:

- Mathematical models are developed for momentum equation using Darcy flow model (Bejan (1984)) and by considering local thermal equilibrium assumption between the porous matrix and trapped fluid in the void space for the energy equation. Analytical expressions for fluctuating velocity, temperature, pressure, Nusselt number, energy flow, and acoustic power are obtained after simplifying and solving the governing differential equations with reasonable approximations. The expressions developed are compared with existing literatures and good agreements are observed. Numerical calculations show that better refrigeration performance is achievable using RVC foam ($\phi = 0.92$, $K = 2.09 \times 10^{-8}\,\mathrm{m}^2$) or aluminum foam ($\phi = 0.9$, $K = 3.36 \times 10^{-8}\,\mathrm{m}^2$) as porous media instead of bare parallel plates. Non-dimensional global energy flux (E_2/E_0) values indicate that using porous medium in between the parallel plates show significantly better performance while $Lc_k \le 2$. It is found that the expression of Nusselt number for steady flow cannot be used in oscillatory random porous medium because of the phase difference between the temperature gradient at the wall and the temperature difference between the wall and the space averaged temperature.

- In order to examine the inherent irreversibilities, entropy generation inside channel walls filled with a porous medium has been examined by applying second law analysis. The expressions of fluctuating velocity, and temperature distributions discussed in the previous paragraph are used in subsequent entropy generation analysis. One important item revealed in this study is that entropy generation inside the porous medium completely follows the trend of imaginary part of $\tilde{f}_k$ profile. Another major contribution of this research is to identify the location of maximum $S_{gen,1}$ which is identical to the location of maximum

thermoacoustic heat and work transport. Therefore, a compromise has to be made to design a thermoacoustic device considering maximum entropy generation and heat or work transport. Blockage ratio (B) and the temperature gradient ratio (Γ) greatly influence the total non-dimensional entropy generation (N_s) of the stack. The minimum values of N_s are observed when B and Γ are close to 1. This implies that a zero thickness stack having temperature gradient equal to the critical temperature gradient provides minimum irreversibility in the stack where copper foam, air as the working fluid, and stack center position close to the pressure anti-node are used. The minimum amount of entropy generation determines the optimum design parameters of stacks leading to highest heat removal rate in a thermoacoustic refrigerator and highest conversion of heat energy to acoustic energy in a thermoacoustic heat engine.

A second approach for porous media modeling considers the Brinkman Forchheimer extended Darcy model (Vafai and Kim [1989]) for the modeling of momentum equation. Brinkman Forchheimer extended Darcy model is considered to account for the presence of high porosity and high velocity fluid flow bounded by impermeable walls. To understand the oscillatory gas thermodynamics and energy transfer in such porous stacks

- Mathematical models are developed for momentum equation using Brinkman-Forchheimer-extended Darcy model and energy equation using local thermal equilibrium assumption between the porous matrix and trapped fluid in the void space. The addition of Forchheimer term includes nonlinearity in the momentum equation which makes it impossible to obtain a closed form of analytical solution for the velocity. Taylor series expansion technique is utilized to transform this non-linear term to a linear form. By using the linear perturbation analysis (Swift [1988])), the governing momentum and energy equations are linearized and solved in order to obtain the fluctuating velocity, temperature, and energy flux inside the porous medium. To verify the present study, the temperature difference obtained across the stack ends is compared with the experimental results. A very good agreement is obtained between the modeling and the experimental results.

The expression of temperature difference across the stack ends obtained in the present study is also compared with the existing thermoacoustic literature (Swift [1988]). The proposed expression surpasses the existing expression.

Experimentally, the present study has designed and built a thermoacoustically-driven thermoacoustic refrigerator (TADTAR) and compared the performance of a TADTAR to that of a typical thermoacoustic heat pump (TAR). The summary of the conclusions is as follows:

- The position of the prime mover stack has no control on the cooling power of the heat pump.

- To optimize the performance of a TADTAR, the prime mover and the heat pump stack should be located $\approx \lambda/20$ from the pressure anti-node.

- A comparison between a typical thermoacoustic heat pump (TAR) and a TADTAR for the identical operating conditions shows better heat flow from the hot side of the stack, low acoustic work absorption, higher COP and COPR for the TAR.

To search for efficient stack geometries for particular applications:

- In the current research, the influence of the geometry, material, dimension, and position of the stack on the performance of a thermoacoustic heat pump is examined. Different prototype thermoacoustic devices have been designed, built, and tested in this thesis to perform different experimental measurements. The performance is measured in terms of temperature difference across the stack ends, the hot end temperature, and the COPR of the stack. Stacks of different materials (Celcor ceramic, RVC, and Mylar plastic), geometries (square cross section, open foam, and circular), lengths (1 cm to 6.5 cm for Celcor ceramic and 1 cm to 4 cm for RVC foam), and positions (0.5 cm to 8 cm) is measured.

The thermoacoustic heat pump designed and built has been able to highlight the general features of the thermoacoustic effect. The major conclusion drawn from this research is that the temperature difference across the stack ends and the maximum temperature at the hot end of the stack and COPR depend on the stack geometry, dimension, material, and position of the stack in the standing wave. In order to obtain maximum temperature difference across the stack ends and maximum temperature at the hot end of the stack, 2 cm long (0.02λ) 80 PPI RVC stack should be used and placed at a distance of 2 cm $(\approx \lambda/50)$ from the pressure anti-node. Therefore, RVC stacks (especially 80 PPI) are suitable for operation of small scale thermoacoustic devices. The operating condition is constant for this study with a frequency limit of 350 Hz in air, 100kPa atmospheric pressure, and $DR = 0.03\%$. For these operating conditions, maximum COPR is obtained when 2.5 cm (0.025λ) long Corning Celcor stack is located 4.25 cm $(\approx \lambda/20)$ from the pressure antinode. Therefore, when thermoacoustic devices are used as heat pumps, a compromise has to be made between the COPR and the maximum temperature at the hot side or the maximum temperature difference between the extremities of the stack ends.

To understand the complicated thermal interactions between the stack plate and the gas, the present study also experimentally examines the temperature fields at different locations of the stack plate surface and the surrounding working fluid. One may make the following observations regarding the thermal field within the porous stack:

- Temperature measurements along the stack reveal a linear behavior along the stack and the corresponding gas residing near the stacks for the tested operating conditions. Temperature gradient along the stack plate is less than that of along the working fluid. Therefore, accurate measurement of temperature difference along the stack using linear theory should be modified to take into account this difference of temperature gradient through the stack plate and the working fluid.

To reduce the inherent irreversibilities inside a thermoacoustic device and to increase the power density of a thermoacoustic device, the present study has introduced a second and a novel concept of "alternative conducting and insulating materials" as stack arrangement.

- Eight different combinations of stack configurations have been considered in the present research using different combinations of stack materials, geometries and dimensions. While the heterogeneous stack arrangement does not produce better performance in terms of temperature difference across the stack ends compared to the homogeneous stack, but minimum temperature (of 11°C) is obtained for a heterogeneous stack arrangement. Therefore, heterogeneous stack arrangement using Ceramic and 80 PPI RVC stack (of combined length 2 cm) can be used in thermoacoustic refrigeration to achieve low temperature cooling rather than homogeneous Ceramic or RVC stacks. Heterogeneous stack arrangement (Ceramic stack length of 1 cm sandwiched between two 0.5 cm long 100 PPI RVC foams) is preferred for compact thermoacoustic engines since it requires smaller stack length than 4 cm long Ceramic stack for the similar performance.

To understand the effects of working fluid, geometric, and operating conditions an array of thin and thick stack plates have been modeled numerically using the full Navier Stokes, mass, energy equation, and equation of state using helium as the working fluid. First the thermoacoustic couple plate is maintained at a constant temperature (i.e., thin plate limit); DR is varied from 1.7 to 10%, Pr varied between 0.7 and 0.28, stack plate spacing is varied from $3.33\,\delta_k$ to $1.0\,\delta_k$, and mean pressure is varied from 10 kPa to 1000 kPa. For all of the test cases considered stack length is constant at 226.13 mm (0.022λ). Because of constant stack length, while the DR is changed, stack length becomes long and short compared to the particle displacement amplitude. Therefore, the present study also considers the effect of stack length. Results are presented in terms of velocity, temperature, velocity gradients, temperature gradients, energy flux density, irreversibility distribution ratio, Bejan number, and entropy generation contours. Summary of the conclusion of the results is:

- An important finding of this study is that cooling power and acoustic power absorbed by a thermoacoustic refrigerator increase as the p_m and DR increase, but the increase of acoustic power is more significant than the cooling power at higher DR and p_m. Therefore, COP decreases at higher DR and p_m. To reduce the viscous loss by reducing the Pr is not a good option for all the stack plate spacing. COP increases 78% by reducing the Pr from 0.7 to 0.28 at $y_0 = 3.33\delta_k$, at atmospheric pressure and at DR=1.7% compared to 53% at $p_m = 1000\,\text{kPa}$. Therefore, lowering the Prandtl number at atmospheric pressure gives better performance regarding to COP and total irreversibility. But COP decreases as reducing the Pr from 0.7 to 0.28 at $y_0 = 1.0\delta_k$ and for all the mean pressure and DR considered. Fluid friction irreversibility dominates heat transfer irreversibility within the stack region for all of the cases considered; because of the high shear stress near the stack edges and high stack surface shear effects. Therefore, fluid friction irreversibility and thus total entropy generation increases for smaller stack spacing, higher DR, higher mean pressure, and high Pr. Entropy generation varies linearly with the mean pressure and quadratically with DR. The numerical results show that cooling power and irreversibility have similar trends of variation with Pr.

10.3 Recommendations for Future Research

Several suggestions for future research include:

- Porous media modeling offers the possibility for the development of additional models for foams with higher thermal conductivity such as aluminum and copper foams. These high thermal conductivity foams can be used in heat exchangers to enhance the gas side heat transfer.

- Numerical solutions of heterogeneous stack arrangement to understand the flow, thermal, and energy fields within such a stack arrangement.

- Design and Development of small scale thermoacoustic engines for electricity production or as alternatives to low-energy-density batteries.

- Employing traveling wave configurations to improve the efficiency of a thermoacoustic engine.

References

Adeff J.A. and Hofler T.J. Design and construction of a solar powered, thermoacoustically driven, thermoacoustic refrigerator. The Journal of the Acoustical Society of America, 107(6) (2000) L37-L42.

Adeff J.A. and Hofler T.J. Performance improvements for the solar powered, thermoacoustically driven, thermoacoustic refrigerator. The Journal of the Acoustical Society of America, 108 (No. 5, Pt. 2) (2000).

Adeff J.A., Hofler T.J., Atchley A.A., and Moss W.C. Measurements with reticulated vitreous carbon stacks in thermoacoustic prime movers and refrigerators. The Journal of the Acoustical Society of America, 104 (1998) 32-38.

Akhavanbazaz M., Siddiqui K., and Bhat R. B. The impact of gas blockage on the performance of a thermoacoustic refrigerator. Experimental Thermal Fluid and Science, 32 (2007) 231-239.

Arnott W. Pat, Bass H. E., and Raspet R. General formulation of thermoacoustics for stacks having arbitrarily shaped pore cross sections. The Journal of the Acoustical Society of America, 90 (1991) 3228–3237.

Arpaci V.S., Selamet A., and Kao S.H. Introduction to Heat Transfer. Prentice Hall, New York, 2000.

Atchley A.A., Hofler T.J., Muzzerall M.L., Kite M.D., and Ao C. Acoustically generated temperature gradients in short plates. The Journal of the Acoustical Society of America, 88 (1990) 251– 263.

Babei H., Siddiqui K., and Christy WA. Sustainable thermoacoustic refrigeration system for gas turbine power plants. In 17th symposium of industrial application of gas turbines (IGAT); Banff, Canada; 2007.

Babei H. and Siddiqui K. Design and optimization of thermoacoustic devices. Energy Conversion and Management, 46 (2008) 3585-3589.

Babaei H. and Siddiqui K. Modified theoretical model for thermoacoustic couples. International Journal of Thermal Science, 50 (2011) 206-213.

Bailliet H., Lotton P, Bruneau M, Gusev V, Valiere JC, Gazenbel B. Acoustic power flow measurement in a thermoacoustic resonator by means of laser Doppler anemometry (LDA) and microphone measurement. Applied acoustics, 1 (2000) 1-11.

Barrett R., Berry M, Chan T.F., Demmel J., Donato J.M., Dongarra J., Eijkhout V., Pozo R., Romine C., and Vorst H.K. Templates for the solution of linear systems: Building blocks for iterative methods, http://www.siam.org/books

Bejan A. Convection Heat Transfer, Wiley, New York, 1984.

Bejan A. Entropy Generation Minimization, CRC Press, New York, 1996.

Bejan A. Advanced Engineering Thermodynamics, Wiley, New York, 2006.

Bejan A. Fundamental of exergy analysis, entropy generation minimization, and the generation of flow architecture. International Journal of Energy Research 26 (2002)545–565.

Besnoin E. Numerical study of thermoacoustic heat exchangers, Ph. D. Dissertation, Dept. of Mechanical Engineering, The Johns Hopkins University, Baltimore, USA, 2001.

Berson A., Michard M., Blanc-Benon P. Measurement of acoustic velocity in the stack of a thermoacoustic refrigerator using particle image velocimetry. Heat and Mass Transfer, 44 (2008) 1120-1135.

Biwa T, Ueda Y, Yazaki T, Mizutani U. Work flow measurements in a thermoacoustic engine. Cryogenics, 41 (2001) 305-310.

Blanc-Benon P., Besnoin E., and Knio O. Experimental and computational visualization of the flow field in a thermoacoustic stack. Comptes Rendus Mecanique, 331(2003)17-24.

Bösel J., Trepp Ch., and Fourie J.G. An alternative stack arrangement for thermoacoustic heat pumps and refrigerators. The Journal of the Acoustical Society of America, 106 (1999)707–715.

Brewster J. R., Raspet R., Bass H. E. Temperature discontinuities between elements of thermoacoustic devices. The Journal of the Acoustical Society of America, 102(6) (1997) 3355–3360.

Brinkman H.C. Calculation of the viscous force extended by a flowing fluid on a dense swarm of particles. Applied Scientific Resources, A1 (1947) 27-34.

Burmeister L.C. Convective Heat Transfer, Wiley, New York, 1992.

Cao N., Olson J.R., Swift G.W., and Chen S. Energy flux density in a thermoacoustic couple. Journal of the Acoustical Society of America, 99 (1996) 3456–3464.

Çengel Y.A. Introduction to Thermodynamics and Heat Transfer, Second Edition, 2008, McGraw-Hill, New York, NY 10020, USA.

Ceperley P.H. Resonant travelling wave heat engine, US Patent 4,355,517 (1982).

Chang Y.J. and Wang C.C. A Generalized Heat Transfer Correlation for Louver Fin Geometry. International Journal of Heat and Mass Transfer, 40 (3) (1997) 533–544.

DeltaEC. Version-6.0, (www.lanl.gov/thermoacoustics), 2007.

Emmanuel C. N., Celik S., and Wang X. Experimental study on the heat transfer at the heat exchanger of the thermoacoustic refrigerating system. Applied Thermal Engineering, 27 (2007) 2435-2442.

ERG Materials and aerospace corporation, 900 Stanford Avenue, Oakland, CA 94608, USA, 2009 (www.ergaerospace.com).

Feldman K.T. and Carter R.L. A study of heat driven pressure oscillations in a gas. Journal of Heat Transfer, 92(1970) 536-541.

Fu H.L., Fu Leong K.C., Huang X.Y., and Liu C.Y. An experimental study of heat transfer of a porous channel subjected to oscillating flow. Journal of Heat Transfer, 123 (2001)162–170.

Garrett S.L. and Hofler T.J. Thermoacoustic refrigeration. ASHARE Journal, 34(1992) 28–36.

Garrett S.L., Adeff J.A., and Hofler T.J. Thermoacoustic refrigerator for space applications, Journal of Thermophysics and Heat Transfer, 7 (1993) 595–599.

Garrett S. L., Perkins D.K., Gopinath A. Thermoacoustic refrigerator heat exchangers: design, analysis and fabrication, in: G.F. Hewitt (Ed.), Proceedings of the Tenth International Heat Transfer Conference, Brighton, UK, 375-380, 1994.

Garrett S.L. High power thermoacoustic refrigerator. U.S. Patent No.5, 647, 216 (1997).

Garrett S.L. Resource letter: TA-1: Thermoacoustic engines and refrigerators. American Journal of Physics, 72(2004)11–17.

Garrity P.T., Klausner J.F., and Mei R. Performance of Aluminum and Carbon Foams for Air Side Heat Transfer Augmentation. Journal of Heat Transfer, 132 (2010) 121901-9.

Gifford W.E. and Longsworth R.C. Surface heat pumping. Advanced Cryogenics Engineering, 11(1966) 171-190.

Gochman S., Ronen R., Anati I., Berkovits A., Kurts T. A., Naveh A., Saeed A.Z., Sperber, and Valentine R.C. The Intel Pentium M processor: microarchitecture and performance.Intel Technology Journal, 7 (2003) 21–36.

Guoqiang L. and Ping C. Friction factor and Nusselt number for thermoacoustic transport phenomena in a tube. Journal of Thermophysics and Heat Transfer, 14 (2000) 566–573.

Gusev V., Lotton P., Bailliet H., Job S., and Bruneau M. Thermal wave harmonics generation in the hydrodynamic heat transport in thermoacoustics. The Journal of the Acoustical Society of America, 109 (2001) 84–90.

Gusev V. Asymptotic theory of nonlinear acoustic waves in a thermoacoustic prime-mover. Acoustica, 86 (2000) 25–38.

Haji-Sheikh A., Nield D.A., and Hooman K., Heat transfer in the thermal entrance region for flow through rectangular porous passages. International Journal of Heat and Mass Transfer, 49 (2006) 3004–3015.

Hamilton M.F., Ilinskii Y.A., and Zabolotskaya E.A. Nonlinear two-dimensional model for thermoacoustic engines. The Journal of the Acoustical Society of America, 111 (2002a) 2076–2086.

Hamilton M.F., Ilinskii Y.A., and Zabolotskaya E.A. Effect of thermal conductivity on acoustic streaming in a narrow channel. The Journal of the Acoustical Society of America, 111 (2002b) 2076–2086.

Hamilton M.F., Ilinskii Y.A., and Zabolotskaya E.A. Thermal effects on acoustic streaming in standing waves. The Journal of the Acoustical Society of America, 114 (2003) 3092–3101.

Hofler T.J. Thermoacoustic refrigeration design and performance. Ph.D. dissertation, University of California, San Diego, USA, 1986.

Holmberg D.G., Chen G.S., and Lin H.T. Thermal modeling and performance analysis of a thermoacoustic refrigerator. The Journal of the Acoustical Society of America, 114 (2003) 782–792.

http://www.lanl.gov/thermoacoustics/press.html, Hot is cool in hell, Qdrive News, June 18, 2010.

http://www.lanl.gov/thermoacoustics/press.html, Sound makes electricity for space: Technology Research News October 6/13, 2004.

http://www.corning.com/environmentaltechnologies/products_services/corning_celcor_substrates_stationary_applications.aspx, Corning 2010.

Ishikawa H. Investigation of optimum design of heat exchangers of thermoacoustic engines. Ph.D. dissertation, The University of Queensland, 1999.

Ishikawa H., and Mee D.J. Numerical investigation of flow and energy fields near a thermoacoustic couple. Journal of the Acoustical Society of America, 111(2002) 831–839.

Ishikawa H. and Hobson P.A. Optimization of heat exchanger design in a thermoacoustic engine using a second law analysis. International Communications in Heat and Mass Transfer, 23(1996) 325–334.

Jensen C., and Raspet R., Thermoacoustic properties of fibrous materials. The Journal of the Acoustical Society of America, 127 (2010) 3470– 3484.

Jeromen A. A simplified thermoacoustic engine demonstration. American Journal of Physics, 71 (2003) 496-498.

Jin T., Chen G.B., Wang B.R., and Zhang S.Y. Application of thermoacoustic effect to refrigeration. Review of Scientific Instruments, 74 (1) (2003) 677–679.

Junj S. and Matveev K. I. Study of a small-scale standing-wave thermoacoustic engine. Journal of Mechanical Engineering Science, 224 (1) (2010)133-141.

Kaviany M. Principles of Heat Transfer in Porous Media, Springer-Verlag, New York, 1995.

Khaligi B., Sumanatran V., Kevin S. and Fischer S. Environmental impact study of alternative automotive refrigerants. The earth technologies forum, the conference on climate change and ozone protection, Sept. 27-29, 2000.

Kimura S., Bejan A. The heatline visualization of convective heat transfer, Journal of Heat Transfer 105 (1983) 916–919.

Kinsler L. W., Frey A. R., Coppens A. B. and Sanders J. V. Fundamental of Acoustic, Wiley, New York, 2000.

Kim Y.T., Suh S.J., Kim M.G. Linear resonant duct thermoacoustic refrigerator having regenerator stacks. In: Proceedings of the 16th International Congress on Acoustics, June (1998) 821-825.

Landau L.D. and Lifshitz E.M. Fluid Mechanics. Pergamon Press, New York, 1982.

Leong K.C. and Jin L.W. An experimental study of heat transfer in oscillating flow through a channel filled with an aluminum foam. International Journal of Heat and Mass Transfer, 48 (2005) 243–253.

Leong K.C. and Jin L.W. Heat transfer of oscillating and steady flows in a channel filled with porous media. International Communications in Heat and Mass Transfer, 31(2004) 63–72.

Leschziner M.A. Modeling turbulent reacting flows by finite-volume-methods-current status and future predictions. International Journal of Heat and Fluid Flow, 10 (1989) 186-196.

Liu J. and Garrett S.L. Characterization of a small moving-magnet electrodynamic linear motor. The Journal of the Acoustical Society of America, 118(4) (2005) 2289–2295.

Liu J. and Garrett S. L. Relationship between Nusselt number and the thermoviscous (Rott) functions. The Journal of the Acoustical Society of America, 119, 3(2006) 1457–1462.

Lotton P., Blanc-Benon Ph., Bruneau M., Gusev V., Duffourd S., Mironov M., and Poignand G. Transient temperature profile inside thermoacoustic refrigerators. International Journal of Heat and Mass Transfer, 52 (2009) 4986-4996.

Mahmud S. MHD and porous media thermoacoustic stacks optimization, Ph.D. thesis, Department of Mechanical Engineering, University of Waterloo, Waterloo, ON, Canada, 2005.

Mahmud S. and Fraser R.A. The thermagoustic irreversibility for a single-plate thermoacoustic system. International Journal of Heat and Mass Transfer, 49 (2006) 3448-3461.

Mahmud S. and Fraser R.A. Mixed convection-radiation interaction in a vertical porous channel: Entropy generation. Energy, 28 (15) (2003) 1557-1577.

Mahmud S. and Fraser R.A. Single-plate thermoacoustic system: Conjugate problem with inviscid flow. International Journal of Exergy, 2 (2005a) 69–89.

Mahmud S. and Fraser R.A. Therporaoustic convection: modeling and analysis of flow, thermal, and energy fields. Journal of Heat Transfer, 13 (10) (2009)101011-1-12.

Mahmud S. and Fraser R. A. An analytical solution and computer simulation for a multi-plate thermoacoustic system, International Journal of Exergy, 2 (2005b) 207–230.

Mahmud S. and Fraser R.A. Therporaoustic convection: Modeling and analysis of flow, thermal, and energy fields. Journal of Heat Transfer, 131(2009)111-123.

Marx D. and Blanc-Benon P. Numerical simulation of stack-heat exchangers coupling in a thermoacoustic refrigerator. AIAA Journal, 42(7) (2004) 1338-1347.

Mahmud S. and Fraser R.A. Visualizing energy flow through energy streamlines and pathlines. International Journal of Heat and Mass Transfer, 50 (2007) 3990–4002.

Marx D. and Blanc-Benon Ph. Numerical calculations of the temperature difference between the extremities of a thermoacoustic stack plate. Cryogenics, 45 (2005) 163-172.

Matveev K.I. Thermoacoustic energy analysis of transverse-pin and tortuous stacks at large acoustic displacements. International Journal of Thermal Sciences, 49 (2010) 1019-1025.

Matveev K.I. and Jung S. Miniature thermoacoustic engine. Presented in 159th Acoustical Society of America Meeting, Baltimore, MD, USA, April 22, 2010.

Merkli P. and Thomann H. Thermoacoustic effects in a resonance tube. Journal of Fluid Mechanics, 70 (1975) 161–177.

Moreau S., Bailliet H., and Valiere Jean-C. Effect of a stack on Rayleigh streaming cells investigated by laser Doppler velocimetry for application to thermoacoustic devices, The Journal of the Acoustical Society of America, 125(6) (2009) 3514–3517.

Mozurkewich G. Heat transfer from transverse tubes adjacent to a thermoacoustic stack. The Journal of the Acoustical Society of America, 110 (2001) 841–847.

Nabavi M., Siddiqui K. and Dargahi J. Simultaneous measurement of acoustic and streaming velocities using synchronized PIV technique. Measurement Science and Technology, 18 (2007) 1811-1817.

Nabavi M., Siddiqui K. and Dargahi J. Experimental investigation of the formation of acoustic streaming in a rectangular enclosure using a synchronized PIV technique. Measurement Science and Technology, 19 (2008 (a)) 065405-065414.

Nabavi M., Siddiqui K. and Dargahi J. Influence of differentially heated horizontal walls on the streaming shape and velocity in a standing wave resonator. International Communications in Heat and Mass Transfer, 35 (2008 (b)) 1061-1064.

Nabavi M., Siddiqui K. and Dargahi J. Effects of transverse temperature gradient on acoustic and streaming velocity fields in a resonator cavity, Applied Physics Letters, 93 (2008 (c)) 051902.

Nield, D. A., and Bejan, A., Convection in Porous Media. 3rd ed., *Springer-Verlag*, Berlin, 2006.

NATIONAL INSTRUMENTS. 2009, Operating Instructions and Specifications NI 9211 4-Channel Thermocouple Input Module.http://www.ni.com/pdf/manuals/373466d.pdf.

NATIONAL INSTRUMENTS. 2010, http://www.ni.com/labview/.

OMEGA ENGINEERING INC., Color Codes for Thermocouples, Wire and Connectors, tolerances, special limits of error, reference guide, accessed 20- April, 2009,http://www.omega.com/ppt/pptsc.asp/ref=XC_K_TC_WIRE&Nav=temh06

OMEGA ENGINEERING INC., 2009b,
http://www.omega.com/prodinfo/ThermocoupleSensor.html

Paek J, Braun JE, Mongeau L. Characterizing heat transfer coefficients for heat exchangers in standing wave thermoacoustic coolers. The Journal of the Acoustical Society of America, 118 (2005) 2271–2280.

Patankar S. V. and Spalding D. B. A calculation procedure for heat, mass, and momentum transfer in three- dimensional parabolic flow. International Journal of Heat and Mass Transfer, 15 (1972) 1787–1806.

Petculescu G. and Wilen L. A. High –amplitude thermoacoustic effects in a single pore. The Journal of the Acoustical Society of America, 109 (2001) 942–949.

Piccolo A. and Pistone G. Estimation of heat transfer coefficient in oscillating flows: The thermoacoustic case. International Journal of Heat and Mass Transfer, 49 (2006) 1631-1642.

Piccolo A. and Cannistraro G. Convective heat transport along a thermoacoustic couple in the transient regime. International Journal Thermal Sciences, 41 (2002) 1067-1075.

Poese M.E. and Garrett S.L. Performance measurement on a thermoacoustic refrigerator driven at high amplitude. The Journal of the Acoustical Society of America, 107(2000) 2480–2486.

Poignand G., Blanc-Benon Ph., Jondeau E., Gaviot E., Camberlein L., Penelet G., and Lotton P. Characterization of heat flux through the heat exchangers of a thermoacoustic cooler. The Journal of the Acoustical Society of America, 127(2010) 1984–1984.

Poignand G., Lihoreau B., Lotton, P., Gaviot, E., Bruneau, M., Gusev, V. Optimal acoustic fields in compact thermoacoustic refrigerators, Applied Acoustics, 68 (2007) 642-659.

Qdrive, 2010, (http://www.qdrive.com/UI/default.aspx).

Rayleigh L. The theory of sound. Dover, New York, 1945.

Reid R.S. and Swift G.W. Experiments with a flow through thermoacoustic refrigerator. The Journal of the Acoustical Society of America, 108(6) (2000) 2835-2842.

Richardson E. G., and Tyler, E. The transverse velocity gradient near the mouths of pipes in which an alternating or continuous flow of air is established, Proceedings of Royal Society of London, A 42 (1929) 1–15.

Roh H., Raspet R., and Bass H. E. Parallel capillary-tube-based extension of thermoacoustic theory for random porous media. The Journal of the Acoustical Society of America, 121(3) (2007)1443-1421.

Rott N. The influence on heat conduction on acoustic streaming. Zeitschrift fur Angewandte Mathematic und Physik, 25 (1974a) 417–421.

Rott N. The heating effect connected with non-linear oscillations in a resonance tube. Zeitschrift fur Angewandte Mathematic und Physik, 25 (1974b) 619–634.

Rott N. Thermoacoustics. Advances in Applied Mechanics, 20 (1980)135–175.

Smith R.W.M., Keolian R.M., and Garrett S.L. High efficiency 2-kW thermoacoustic driver. The Journal of the Acoustical Society of America, 105(1999)1072-1078.

Sondhauss C. Ueber die schallschwingungen der luft in erhitzten glasröhren und in gedeckten pfeifen von ungleicher weite. Annual Physics, 79(1850)1-8.

Spalding D.B. The PHOENICS Beginner's Guide TR 100. CHAM, Bakery House, 40 High Street, Wimbledon Village, London SW 19 5AU, UK.

Star CD. Version-3.22, CD-Adapco Group, USA, (www.cd-adapco.com), 2007.

Swift G.W. and Keolian R.M. Thermoacoustic in pin-array stacks. The Journal of the Acoustical Society of America, 94 (1993) 941–943.

Swift G.W. Analysis and performance of a large thermoacoustic engine. The Journal of the Acoustical Society of America, 92 (1992)1551–1563.

Swift G.W. Thermoacoustic engines. The Journal of the Acoustical Society of America, 84 (1988) 1145–1180.

Swift G.W. Thermoacoustics: A unifying perspective for some engines and refrigerators. Condensed Matter and Thermal Physics Group, Los Alamos National Laboratory, LA-UR 99-895, 2002.

Tasnim S.H., Mahmud S., and Fraser R.A. Thermal measurements and performance calculations of a thermoacoustic heat pump. Accepted for publication in Journal of Heat and Mass Transfer in August (Submission Ref. No. HMT-10-0394, 2010).

Tasnim S.H. and Fraser R.A. Modeling and analysis of flow, thermal, and energy fields within stacks of thermoacoustic engines filled with porous media: A conjugate problem. Journal of Thermal Science and Engineering Applications, 1 (2009) 041006-1-12.

Temkin S. Elements of Acoustics, Wiley, New York, 1981

Thompson M.W. and Atchley A. A. Simultaneous measurement of acoustic and streaming velocities in a standing wave using laser Doppler anemometry. The Journal of The Acoustical Society of America, 117(4) (2005)1828–1838.

Tijani M.E.H. Loudspeaker-driven thermo-acoustic refrigeration, Ph.D. thesis, Eindhoven University of Technology, Netherlands, 2001.

Tnag K, Lei T., Jin T., Lin X.G., and Xu Z.Z. A standing-wave thermoacoustic engine with gas-liquid coupling oscillation, Applied Physics Letters, 94 (2009) 254101-254103.

Vafai K. Handbook of Porous Media, Marcel Dekker, New York, 2000.

Vafai K. and Kim C.L. Forced convection in a channel filled with a porous medium: An exact solution. Journal of Heat Transfer, 111(1989) 1103-1106.

Vafai K. and Tien C.L. Boundary and inertia effects on flow and heat transfer in porous media. International Journal of Heat and Mass Transfer, 24(1981)195–203.

Versteeg H.K. and Malalasekera W. An introduction to computational fluid dynamics: The finite volume method, Prentice Hall, England, 1995.

Wakeland R. S. and Keolian R. M. Thermoacoustics with idealized heat exchangers and no stack. The Journal of the Acoustical Society of America, 111 (2002) 2654–2664.

Wakeland R. S. Use of electrodynamic drivers in thermoacoustic refrigerators. The Journal of the Acoustical Society of America, 107(2) (2000) 827–832.

Waxler R. Stationary velocity and pressure gradients in a thermoacoustic stack. The Journal of The Acoustical Society of America, 109 (2001) 2739–2750.

Wetzel M. and C. Hermann. Experimental study of thermoacoustic effects on a single plate part ii: Heat transfer. Heat and Mass Transfer, 35 (1999) 433-441.

Wetzel M. and C. Hermann. Experimental study of thermoacoustic effects on a single plate part i: Temperature fields. Heat and Mass Transfer, 36 (2000) 7-20.

Wheatley J., Swift G.W., and Migliori A. The natural heat engine. Los Alamos Science, (1986)2–29.

Wheatley J., Hofler T., Swift G.W., and Migliori A. An intrinsically irreversible thermoacoustic heat engine. The Journal of the Acoustical Society of America, 74 (1983)153–170.

Wheeler J.A. and Ganji R.A. Introduction to Engineering Experimentation, 3rd ed., Prentice Hall, 2010.

Wilen L.A. Dynamic pressure measurements of the thermal dissipation function of reticulated vitreous carbon. The Journal of the Acoustical Society of America, 109 (2001) 179-184.

Wollan J.J., Swift G. W., Backhaus S., and Gardner D.L. Development of a thermoacoustic natural gas liquefier. Proceedings of AIChE Meeting, New Orleans LA, March 11-14, 2002

Worlikar A.S. and Knio O.M. Numerical study of oscillatory flow and heat transfer in a loaded thermoacoustic stack. Numerical Heat Transfer (Part A), 35 (1999) 49 –65.

Worlikar A.S., Knio O.M. and Klein R. Numerical simulation of a thermoacoustic refrigerator: Stratified flow around the stack. Journal of Computational Physics, 144 (1998) 299–324.

www.nrcan.gc.ca, 2011

Yazaki T., Tominaga A., and Narahara Y. Experiments on thermally driven acoustic oscillations of gaseous helium. Journal of Low Temperature Physics, 41(1980) 45-50.

Zoontjens L., Howard C.Q., Zander A.C., and Cazzolato B.S. Numerical study of flow and energy fields in thermoacoustic couples of non-zero thickness. International Journal of Thermal Sciences, 48 (2009) 733-746.

Zouzoulas G. Heat transfer from tubes in cross flow. Advances in Heat Transfer, 8 (1972) 93-105.

Appendix A

A.1 General Theory of Thermoacoustics

The general thermoacoustic theory is first developed by Rott [1980] and later reviewed by Swift [1988]. Starting with the linearization of the continuity, Navier-Stokes, and energy equations, the authors developed the thermoacoustic equations. The thermoacoustic equations are three fold: the first equation consists of Rott's wave equation, which is the wave equation for the pressure in the presence of a temperature gradient along the stack; the energy equation, which describes the energy flow in thermoacoustic systems; and the third equation that is an expression for the acoustic power absorbed (refrigerator) or produced (prime mover) in the stack. No attempt is made in this section to derive theses equations, as in Chapter 4, detailed derivations of these equations are discussed. Also detailed derivations of the equations are available in Mahmud [2005] and Tijani [2001]. However, approximations in order to derive the thermoacoustic equations are discussed, and also are utilized in Chapter 4 and 5. The notation used by Swift [1988] and Tijani [2001] are followed.

The geometry used to derive the thermoacoustic equations is a stack of parallel plates are illustrated in Figs. (A.1) and (A.2). The stack is placed in a gas- filled resonator. The

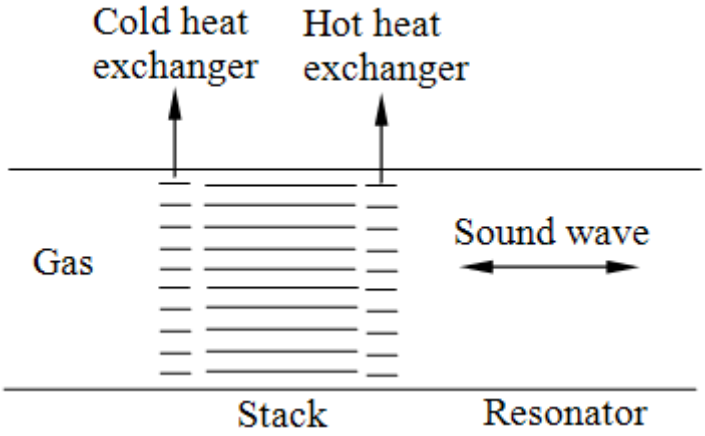

Figure A.1: Overall view of the geometry used for the derivation of thermoacoustic expressions.

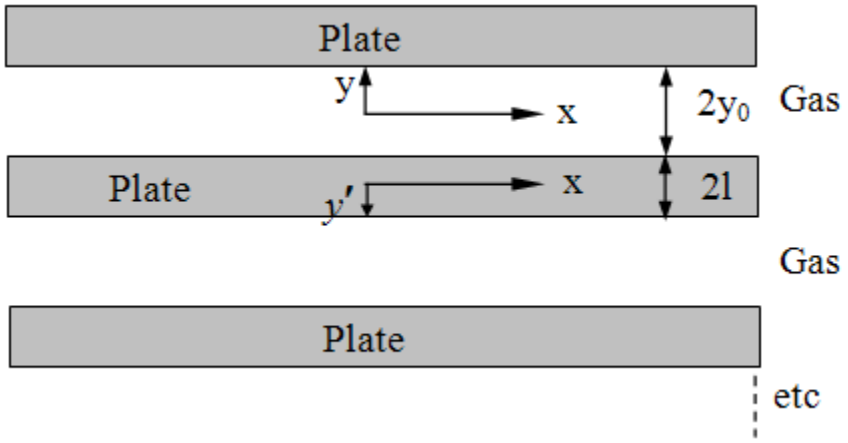

Figure A.2: Expanded view of the stack section. Each plate has thickness $2l$ and each gas layer has thickness $2y_0$.

stack plates have a thickness $2l$ and gas spacing $2y_0$. The x-axis represents the longitudinal direction (also the direction of fluid oscillation), and the y axis perpendicular to the planes of the parallel plates. The location $y = 0$ is chosen to be the midpoint between the two adjacent plates and $y = y_0$ at the gas-solid boundary. An y' axis is considered for the plates, with $y' = 0$ in the center of the plate and $y' = l$ at the boundary. So there are two opposite coordinate systems as indicated in Fig. (A.2).

First summarize the assumptions which are used in deriving the general equations of thermoacoustics:

- The plates are perfectly rigid and stationary.
- The theory is linear except the energy transport; nonlinear effects (such as streaming, vortex formation, turbulence etc.) are neglected.
- The temperature spanned along the stack is much smaller than the absolute temperature.
- The wave length is much larger than the thermal penetration depth.
- Oscillating variables have harmonic time dependence at a single angular frequency ω.
- The mean porous medium temperature ($T_m(x)$) to be independent of y and to be the same as that of the plate.

Now decompose all the physical quantities into time average quantities and time varying quantities as Rott [1980]

$$p = p_m + p_1(x)e^{i\omega t}, \tag{A.1}$$

$$T = T_m(x) + T_1(x,y)e^{i\omega t} \tag{A.2}$$

$$u = u_1(x)e^{i\omega t}, v = v_1(y)e^{i\omega t} \tag{A.3}$$

$$T_s = T_m(x) + T_{s1}(x,y)e^{i\omega t}, \tag{A.4}$$

$$\rho = \rho_m(x) + \rho_1(x,y)e^{i\omega t}, \tag{A.5}$$

where p, T, u, v, T_s, and ρ are pressure, temperature, velocity in the x and y directions, temperature in the solid, and density, respectively. The terms with the subscript "*m*" is the mean and with the subscript "1"is the fluctuating part (always a complex expression) of the individual variables. ω represents the angular frequency which equals 2π f, where f is the ordinary frequency. Equations (A.1) to (A.5) are obtained by applying the linearized thermoacoustic approximation (Rott [1980]) which assumes that all terms that are higher than the first order are neglected compared to the mean term, except for the energy flux, heat flux, and the work flux.

The fundamental physics concerned with thermoacoustics is described by continuity, Navier- Stokes, and energy equations (Landau and Lifshitz [1982])

$$\frac{\partial \rho}{\partial t} + \nabla.(\rho v) = 0, \tag{A.6}$$

$$\rho\left[\frac{\partial v}{\partial t} + (v.\nabla)v\right] = -\nabla p + \nabla.\sigma', \tag{A.7}$$

$$\frac{\partial}{\partial t}\left(\rho e + \frac{1}{2}\rho|v|^2\right) = -\nabla.\left[\left(\rho h + \frac{1}{2}\rho|v|^2\right)\right]v - k_f\nabla T - \nabla.\sigma'. \tag{A.8}$$

Where e, h, and σ' are the internal energy per unit mass, enthalpy per unit mass, and the nine-component viscous stress tensor, respectively. Two of its components are

$$\sigma'_{xx} = \mu\left(2\frac{\partial u}{\partial x} - \frac{2}{3}\nabla.v\right) + \zeta\nabla.v\,, \tag{A.9}$$

$$\sigma'_{xy} = \mu\left(\frac{\partial u}{\partial y} + \frac{\partial v}{\partial x}\right), \tag{A.10}$$

where μ is the dynamic (shear) viscosity and ζ is the bulk viscosity. The other seven components of σ' can be obtained from Eqs. (A.9) and (A.10) by switching among *x*, *y*, and *z*, and *u*, *v*, and *w*, in the obvious way.

After using all the approximations as discussed above and the required boundary conditions, the expressions of fluctuating velocity, temperature, and pressure are

$$u_1 = \left(\frac{i}{\omega\rho_m}\frac{\partial p_1}{\partial x}\right)\left\{1 - \frac{\cosh\left[(1+i)y/\delta_\nu\right]}{\cosh\left[(1+i)y_0/\delta_\nu\right]}\right\}\,, \tag{A.11}$$

$$\begin{aligned} T_1 = {} & \frac{T_m\beta\, p_1}{\rho_m\, C_p} - \frac{1}{\rho_m\omega^2}\frac{dT_m}{dx}\frac{dp_1}{dx}\left[1 - \frac{\mathrm{Pr}}{(\mathrm{Pr}-1)}\frac{\cosh\left\{\frac{(1+i)}{\delta_\nu}y\right\}}{\cosh\left\{\frac{(1+i)}{\delta_\nu}y_0\right\}}\right] \\ & - \left[\frac{T_m\beta\, p_1}{\rho_m\, C_p} + \frac{1}{\rho_m\omega^2}\frac{\left(1+\frac{\varepsilon_s f_\nu}{f_k}\right)}{(\mathrm{Pr}-1)}\frac{dT_m}{dx}\frac{dp_1}{dx}\right]\frac{1}{(1+\varepsilon_s)}\frac{\cosh\left\{\frac{(1+i)}{\delta_k}y\right\}}{\cosh\left\{\frac{(1+i)}{\delta_k}y_0\right\}}\,, \end{aligned} \tag{A.12}$$

$$\left[1 + \frac{(\gamma\text{-}1)}{(1+\varepsilon_s)}f_k\right]\mathrm{p}_1 + \frac{\rho_m \mathrm{a}^2}{\omega^2}\frac{\mathrm{d}}{\mathrm{dx}}\left[\frac{1-f_\nu}{\rho_m}\frac{dp_1}{dx}\right] - \beta\frac{\mathrm{a}^2}{\omega^2}\frac{f_k - f_\nu}{(1-\mathrm{Pr})(1+\varepsilon_s)}\frac{dT_m}{dx}\frac{dp_1}{dx} = 0\,. \tag{A.13}$$

In Eq. (A.12), ε_s is the heat capacity ratio between the stack plate and the gas and is defined as

$$\varepsilon_s = \frac{\rho_m C_p \delta_k}{\rho_c C_c \delta_s} \frac{\tanh\left[(1+i)y_0/\delta_k\right]}{\tanh\left[(1+i)l_0/\delta_s\right]} \quad . \tag{A.14}$$

Here, ρ_c and C_c are the density, and specific heat capacity of the stack material, and δ_s is the thermal penetration depth in the solid. It is the lateral distance through which heat can diffuse within a solid in a time $2/\omega$.

$$\delta_s = \sqrt{\frac{2k_c}{\omega \rho_c C_c}} \quad , \tag{A.15}$$

where k_c is the thermal conductivity of the solid stack material.

Now, the expression for acoustic power (produced by the stack in the case of a prime mover and absorbed by the stack in the case of a refrigerator) per unit length of the stack is

$$\begin{aligned} \frac{dW_2}{dx} = &-\frac{1}{2A}\omega\left[\frac{\rho_m \Im(-f_v)}{|1-f_v|^2}|\tilde{U}_1|^2 + \frac{(\gamma-1)\Im(-f_k)}{\rho_m a^2(1+\varepsilon_s)}|p_1|^2\right] \\ &+\frac{1}{2}\omega\left[\frac{\beta}{\omega(1-\mathrm{Pr})(1+\varepsilon_s)}\frac{dT_m}{dx}\Re\left\{\frac{\tilde{f}_k - \tilde{f}_v}{(1-\tilde{f}_v)}p_1\tilde{U}_1\right\}\right] \end{aligned}, \tag{A.16}$$

where $\Re[\ ]$, and $\Im[\ ]$ signify the real and imaginary parts, tilde (~) denotes the complex conjugation, U_1 is the volumetric velocity, and A is the cross-sectional area of the gas. The subscript 2 is used to indicate that the acoustic power is a second-order quantity; the product of two first-order quantities, p_1 and u_1. Equation (A.16) supports Eq. (2.12), which shows that work flux is quadratic in the acoustic amplitude p_1 or u_1. Comparing Eq. (2.12) and Eq. (A.16) shows how viscosity changes the work flux equation.

The expression for total energy flow (or energy flux density) along the stack is

$$E_2 = \frac{1}{2}\Re\left[p_1\widetilde{U}_1\left(1-\frac{T_m\beta\left(f_k-\widetilde{f}_v\right)}{\left(1+\mathrm{Pr}\right)\left(1+\varepsilon_s\right)\left(1-\widetilde{f}_v\right)} \right)\right] + \frac{\rho_m C_p\left|U_1\right|^2}{2A\omega\left(1-\mathrm{Pr}\right)\left|1-f_v\right|^2}\frac{dT_m}{dx}\Im\left[\widetilde{f}_v+\frac{\left(f_k-\widetilde{f}_v\right)\left(1+\varepsilon_s f_v/f_k\right)}{\left(1+\mathrm{Pr}\right)\left(1+\varepsilon_s\right)}\right]-\left(Ak_f+A_c k_c\right)\frac{dT_m}{dx} \quad . \tag{A.17}$$

In Eq. (A.17), A_c is the cross-sectional area of the stack material. Through out this thesis Eq. (A.16) and (A.17) are utilized to evaluate the acoustic work absorbed or produced by the stack, and the total energy flow or cooling load from the cold heat exchanger. The Coefficient of performance of a heat pump is calculated using the following expression given below:

$$COP = \frac{E_2}{W_2} \, . \tag{A.18}$$

A.2 Uncertainty Analysis

A.2.1 Introduction

Every measurement is subject to some uncertainty. A measurement result is only complete if it is accompanied by a statement of the uncertainty in the measurement. Measurement uncertainties can come from the measuring instrument, from the item being measured, from the environment, from the operator, and from other sources. Such uncertainties can be estimated using statistical analysis of a set of measurements, and using other kinds of information about the measurement process. The uncertainty of a measurement is defined as the difference between the measured value and the true value of the measurand. Errors in experiment generally fall into two categories: bias errors (systematic errors) and precision errors (random errors). Precision errors are detected by a lack of repeatability in the measurement output and can be reduced by generating multiple data and averaging them. Bias errors are often not obvious to the experimenter and very difficult to reduce. Major sources of the bias errors are calibration error, accuracy of the instrument etc. The uncertainty of a measurement system is an estimate of the limits of errors in the measurements. In a typical measurement system, there are a large number of error sources known as elemental error sources and each can generate either a bias or precision error.

The objective of the experimental program in this thesis is to measure temperatures at different locations of the stack and also in the gas. An uncertainty analysis of the apparatus and data is performed in the following sections. Following assessment of the accuracy of the instruments and sensors used in the experiment, the impact of these uncertainties on the reported value of temperature difference is presented.

A.3 Measurement of Uncertainties

When estimating the uncertainty in measured and calculated quantities, both systematic and random uncertainties need to be considered. These elemental uncertainties are combined to give an overall uncertainty in a measured quantity using the root-sum-squares method (Wheeler and Ganji [2010]). This method is expressed mathematically

$$W_x = \left(B_x^2 + P_x^2\right)^{0.5}, \tag{A.19}$$

where W_x represents the total uncertainty in the measured quantity x. B_x represents the systematic uncertainty based on the uncertainty of the instruments, while P_x represents the random uncertainty of x based on statistical analysis of the data.

A.3.1 Random Uncertainty

Random uncertainties are calculated based on statistical analysis of the data assuming a 95% confidence interval. To estimate the random uncertainty of a measurement, multiple readings are taken, typically on the order of 10, the sample standard deviation is calculated using Eq. A.20, and multiplied by the appropriate Student t factor.

$$S_x = \left(\sum_{i=1}^{n} \frac{\left(x_i - \bar{x}\right)^2}{\left(n-1\right)} \right)^{1/2}. \tag{A.20}$$

For the degrees of freedom $\left(n-1\right)$, and a 95% confidence interval $\left(\alpha/2 = 0.025\right)$, in all cases the value of t is taken to be 2.262, which corresponds to 10 independent measurements (n). Thus the random uncertainty in the mean of x is determined from

$$P_x = \pm t \frac{S_x}{\sqrt{n}}. \tag{A.21}$$

A.3.2 Bias Uncertainty

A bias or systematic uncertainty does not vary during repeated readings and is independent on the sample size. The confidence level in the uncertainty, w, is the same as the confidence level for B and P. The systematic uncertainty is combined using root-sum-squares method (RSS):

$$B_x = \left[\sum_{i=1}^{k} B_i^2 \right]^{1/2}. \tag{A.22}$$

In Eq. (A.22), there are *k* elemental systematic uncertainties pertaining to the measured variable *x*. The following section describes the uncertainty associated with the instrumentations used in the measurement (systematic) and the random uncertainties.

A.3.3 Bias Uncertainties for Additive Functions

When the result (R) has an additive from, R will be expressed as

$$R = a_1 x_1 + a_2 x_2 + \cdots\cdots + a_n x_n = \sum a_i x_i \,, \tag{A.23}$$

the uncertainty in the result may then be expressed as

$$W_R = \left[\sum \left(a_i W_{xi}\right)^2\right]^{\frac{1}{2}}. \tag{A.24}$$

A.4 Uncertainty in Measured Values

Sample calculation of uncertainty in measured value is presented for the following configuration of experiment.

Stack Information

L_s (cm)	x_c (cm)	Material
4	3	Ceramic

Experimental Data

T_C (°C)	T_H (°C)	T_m (°C)	Pressure (pa)
14.65	45.14	25.52	100

All temperature measurements are performed using K-type thermocouples and a NI USB-9211A data acquisition system. In 10 measurements in the above test of the thermocouple's repeatability, average value of 44.18°C and 15.2°C for the hot and cold

end temperatures are determined. The standard deviation of 0.52 °C for the hot and cold end temperatures is obtained.

For measuring the position of the stack center form the pressure anti-node, a tape measure is used with a calibration uncertainty of 0.1%. In this case, 0.1 percent of 3 cm is 0.03 mm. The divisions on the tape are millimeters. Reading to the nearest division gives an error of no more than ±0.5 mm. We can take this to be a uniformly distributed uncertainty (the true readings could lie variously anywhere in the 1 mm interval - i.e. ±0.5 mm). To find the uncertainty, W, we divide the half-width (0.5 mm) by √3, giving W = 0.3 mm approximately (Wheeler et al. [2010]). Measuring the temperature data at close proximities of the stack ends give us confidence that in this case, a length uncertainty of ±0.3 mm would give rise a ±0.5°C in temperature uncertainty. The systematic and random elemental uncertainties are identified in the following table, with an assumed confidence level of 95% for the systematic uncertainties:

Table A1: The systematic (B) and random elemental uncertainties (S stands for standard deviation) for the temperature measurement

Elemental Error	B (°C)	S (°C)
Calibration (thermocouple)	0.1	-
Typical thermocouple error (NI [2009])	1.2	-
Calibration (tape measure)	0.5	-
Repeatability	-	0.52 (9 degrees of freedom)

The random uncertainty determined from repeatability using Eq. (A.21) is

$$P_x = \pm t\frac{S_x}{\sqrt{n}} = \pm 2.262\frac{0.52}{\sqrt{10}} = 0.37\ ^\circ C\,.$$

The systematic uncertainty in the hot end temperature measurement is (using Eq. (A.22))

$$B_x = \left(0.1^2 + 1.2^2 + 0.5^2\right)^{1/2} = 1.3^\circ C\,.$$

The total uncertainty in the measurements can be calculated from Eq. (A.19) as:

$$W_x = \left(B_x^2 + P_x^2\right)^{0.5} = \left((1.3)^2 + (0.37)^2\right)^{0.5} = 1.35°\text{C}$$

which is 3.0% of the mean measured value at the hot end of the stack and 8.8% of the mean temperature at the cold end of the stack.

A.4.1 Uncertainty in Temperature Difference

The temperature difference across the stack end is calculated as

$$\Delta T = T_2 - T_1 = T_2 + (-1)T_1 . \tag{A.25}$$

The uncertainty associated with ΔT can be calculated using Eq. (A.24)

$$W_{\Delta T} = \left[\left(-1 \times W_{T1}\right)^2 + \left(W_{T2}\right)^2\right]^{\frac{1}{2}} . \tag{A.26}$$

From calculation in **Section** A.3, total uncertainty of T_1 and T_2 i.e., cold and hot end temperature is 1.35°C. Therefore, the total uncertainty in ΔT (using Eq. (A.26) is

$$W_{\Delta T} = \left[\left(-1 \times 1.35\right)^2 + \left(1.35\right)^2\right]^{\frac{1}{2}} = 1.92 \ °\text{C}$$

which is 6.6% of the mean temperature difference across the stack end when the stack is located 3 cm from the pressure anti-node. On average the standard deviation at the hot and cold ends of the stack is 0.55°C. This standard deviation at the hot and cold ends of the stack give total uncertainty in ΔT as 1.92 °C (using Eq. (A.26)), which is 4% of the maximum ΔT (48 °C) in the measurements. Therefore, an uncertainty of 4% is used in plotting graphs in Chapter 6, 7, and 8 for ΔT and an uncertainty of 1.36 °C is used in plotting graphs in Chapter 7 for temperature measurements at different locations on the stack plate surface.

Appendix B

B.1 Transformation of Energy Equation (in Chapter 4)

This part of the appendix will now elaborate on the transformation of energy equation (in Chapter 4) from Eq. (4.3) to Eq. (4.5) and show through scale analysis that the ignored terms can reasonably be ignored. Because of the improvement in understanding that would be conveyed to the reader from providing some detail on the linearization and scale analysis this attempt has been made to incorporate them into appendix B.

We are neglecting all terms that are higher than the first order fluctuation term, in order to linearize the governing equations, and to adopt the linearized thermoacoustic theory proposed by Rott [1980].

According to Bejan [1984], the energy equation inside the porous medium is

$$\rho_f C_{pf}\left[\sigma\frac{\partial T}{\partial t}+u\frac{\partial T}{\partial x}+v\frac{\partial T}{\partial y}\right]=k\left[\frac{\partial^2 T}{\partial x^2}+\frac{\partial^2 T}{\partial y^2}\right]+\beta T\left[\phi\frac{\partial p}{\partial t}+u\frac{\partial p}{\partial x}+v\frac{\partial p}{\partial y}\right]. \qquad \text{(B.1)}$$

The first term on the left hand side of Eq. (B.1) is the transient term; second and third terms are energy transfer by a moving fluid. The first and second terms on the right hand side are energy transfer due to contribution of conduction and the rest of the terms are work of compression (or expansion) due to the change of gas volume. The viscous dissipation term is neglected in Eq. (B.1). Also the contribution from radiation is small at moderate temperatures (Schlichting [1968]), and we will neglect it completely. This differential equation (Eq. (B.1)) will be expanded and linearized using Eqs. (A.1) to (A.5) of Appendix A.1. The first term in the square bracket on the left hand side of Eq. (B.1) is:

$$\sigma\frac{\partial T}{\partial t}=\sigma\frac{\partial}{\partial t}\left(T_m+T_1\,e^{i\omega t}\right)=\sigma\, i\omega T_1 e^{i\omega t}, \qquad \text{(B.2)}$$

$\frac{dT_m}{dt}=0$, since T_m is not a function of time in Eq. (A.2) of Appendix A.1.

The second term in the square bracket on the left hand side of Eq. (B.1) is:

$$u\frac{\partial T}{\partial x}=u_1 e^{i\omega t}\frac{\partial}{\partial x}\left(T_m+T_1\,e^{i\omega t}\right)=u_1 e^{i\omega t}\frac{dT_m}{dx}+u_1 e^{2i\omega t}\frac{\partial T_1}{\partial x}\approx e^{i\omega t}u_1\frac{dT_m}{dx}. \qquad \text{(B.3)}$$

where the approximation results from linearization, that is, it is recognized that the $u_1 \frac{\partial T_1}{\partial x}$ term is a quadratic (second-order) term and can be removed. Similarly, the $v \frac{\partial T}{\partial y}$ term can also be eliminated in forming the linearized energy equation.

The first term in the first square bracket on the right hand side of Eq. (B.1) is:

$$\frac{\partial^2 T}{\partial x^2} = \frac{\partial^2}{\partial x^2}(T_m + T_1 e^{i\omega t}) = e^{i\omega t} \frac{\partial^2 T_1}{\partial x^2}, \tag{B.4}$$

In a typical thermoacoustic problem, T_m is considered a linear function of x only (according to Swift [1988]), therefore, $\frac{d^2 T_m}{dx^2} = 0$.

The second term in the first square bracket on the right hand side of Eq. (B.1) is:

$$\frac{\partial^2 T}{\partial y^2} = \frac{\partial^2}{\partial y^2}(T_m + T_1 e^{i\omega t}) = e^{i\omega t} \frac{\partial^2 T_1}{\partial y^2}, \tag{B.5}$$

but since T_m is a function of x only (Swift [1988])), $\frac{d^2 T_m}{dy^2} = 0$.

The first term in the second square bracket on the right hand side of Eq. (B.1) is:

$$\frac{\partial p}{\partial t} = \frac{\partial}{\partial t}\left(p_m + p_1 e^{i\omega t}\right) = i\omega p_1 e^{i\omega t}, \tag{B.6}$$

since p_m is not a function of t (Swift [1988]).

The second term in the second square bracket on the right hand side of Eq. (B.1) is:

$$u \frac{\partial p}{\partial x} = u_1 e^{i\omega t} \frac{\partial}{\partial x}\left(p_m + p_1 e^{i\omega t}\right) = u_1 e^{i\omega t} \frac{dp_m}{dx} + u_1 e^{2i\omega t} \frac{dp_1}{dx} = e^{2i\omega t} u_1 \frac{dp_1}{dx} \approx 0, \tag{B.7}$$

since p_m is not a function of x (Swift [1988]), $\frac{dp_m}{dx} = 0$. The $u_1 \frac{\partial p_1}{\partial x}$ term is a quadratic (second-order) term. For these reasons, this term is eliminated from the linearized energy

equation. The $u\frac{\partial p}{\partial x}$ term is negligible compared to the $\frac{\partial p}{\partial t}$ term as will be shown later by scale analysis. Also, the $v\frac{\partial p}{\partial y}$ term is eliminated, since *p* in Eq. (A.1) is not a function of *y*.

Adding all remaining terms, the energy equation becomes,

$$\rho_f C_{pf}\left[\sigma i\omega T_1 e^{i\omega t} + e^{i\omega t}u_1\frac{dT_m}{dx}\right] = k\left[\frac{\partial^2 T_1}{\partial x^2}+\frac{\partial^2 T_1}{\partial y^2}\right]e^{i\omega t} + i\omega\beta T_m p_1 e^{i\omega t}, \tag{B.8}$$

which can be simplified to

$$k\frac{\partial^2 T_1}{\partial y^2} - \sigma i\omega\rho_f C_{pf}T_1 = -\rho_f C_{pf}\frac{K}{\mu}\frac{dT_m}{dx}\frac{dp_1}{dx} - i\omega\beta T_m p_1. \tag{B.9}$$

Scaling analysis is now used to neglect the $\frac{\partial^2 T_1}{\partial x^2}$ term relative to the $\frac{\partial^2 T_1}{\partial y^2}$ term. At any axial location, the following scales can be considered for the present study: $x \sim \overline{\lambda}$, and $y \sim \delta_k$, where $\overline{\lambda} = \lambda/2\pi$, λ is the acoustic wavelength, δ_k is the thermal penetration depth, and $\overline{\lambda} >> \delta_k$.

Therefore, conduction in the *x*- direction can be scaled as: $\frac{\partial^2 T_1}{\partial x^2} \sim \frac{T_1}{\overline{\lambda}^2}$,

and conduction in the *y*- direction can be scaled as: $\frac{\partial^2 T_1}{\partial y^2} \sim \frac{T_1}{\delta_k{}^2}$.

We can produce a quantitative justification for the elimination of the $\frac{\partial^2 T_1}{\partial x^2}$ term by taking the ratio of this term to the $\frac{\partial^2 T_1}{\partial y^2}$ term.

$$\frac{\frac{\partial^2 T_1}{\partial x^2}}{\frac{\partial^2 T_1}{\partial y^2}} \sim \frac{\frac{T_1}{\bar{\lambda}^2}}{\frac{T_1}{{\delta_k}^2}} \sim \left(\frac{\delta_k}{\bar{\lambda}}\right)^2.$$

For the present problem, the wavelength of sound wave propagating through helium at 500 *Hz* frequency, 255 K temperature, and 10 bar pressure is 1.88 m and δ_k is 0.12 mm (using Table 1 of Swift [1988]). Therefore, for the present problem, the ratio of $\left(\frac{\delta_k}{\bar{\lambda}}\right)^2 \sim$ 1.61e-7. In thermoacoustics, the working gases are typically air, helium, or any other inert gas, the frequency range is 100 to 500 Hz, mean pressure range is 100-1000 kPa, and the temperature is around 300 K. Therefore, the ratio of $\left(\frac{\delta_k}{\bar{\lambda}}\right)^2$, range from 1.17e-6 to 4.42e-9 for air as the working fluid, and 4.63e-6 to 1.85e-8 for helium. In thermoacoustics, as long as $\lambda >> \delta_k$, then $\frac{\partial^2 T_1}{\partial x^2}$ term in Eq. (B.8) is negligible compared to the $\frac{\partial^2 T_1}{\partial y^2}$ term. This term is neglected by Swift [1988] (Eq. 16), and Liu and Garrett [2006] (Eq. 19).

Now, the $u\frac{\partial p}{\partial x}$ term is small compared to the $\frac{\partial p}{\partial t}$ term. We can produce a quantitative justification for the elimination of the $u\frac{\partial p}{\partial x}$ term by taking the ratio of this term to the $\frac{\partial p}{\partial t}$ term.

Time, t, can be scaled with 1/ω, where ω (1/s) is the angular frequency of oscillation.
And u can be scaled as: u_1

Therefore, $\frac{\partial p}{\partial t}$ can be scaled as: ωp,

and $u\frac{\partial p}{\partial x}$ can be scaled as: $u_1 \frac{p}{\bar{\lambda}} \sim u_1 k_w p$, where k_w is the wave vector $= \frac{2\pi}{\lambda}$

$\frac{u\frac{\partial p}{\partial x}}{\frac{\partial p}{\partial t}} \sim \frac{u_1 k_w p}{\omega p} \sim \frac{u_1}{a} << 1$, since a is the adiabatic sound speed, and u_1 is the velocity in the x-direction. For the present problem, the ratio of $\frac{u_1}{a}$ = Mach number $= 0.018$

B.2 Alternate Pressure Equation

A simplified pressure equation can be derived combining the linearized continuity and the Darcy momentum equations after subsequent integration and simplification. The derived pressure equation is not similar to a standing wave pressure fluctuation. As shown in the equation below:

$$p_1 = \frac{1}{2}\left[\frac{i\omega\rho_1}{\phi\rho_m}\frac{\mu}{K}\right]\left(x^2 - L_1^2\right) + \frac{p_{L1} - p_{L2}}{L_1 - L_2}\left(x - L_1\right) + \frac{1}{2}\left[\frac{i\omega\rho_1}{\phi\rho_m}\frac{\mu}{K}\right]\left(L_1 + L_2\right)\left(L_1 - x\right) + p_{L1}, \qquad \text{(B.10)}$$

where L_1 and L_2 are the distances of the two stack ends from a reference location where $x = 0$. However, for such a formulation, it can be assumed that the pressure fluctuation outside the porous stack is similar to the standing wave. Therefore, p_{L1} and p_{L2} are two known pressures at two stack ends. Equation (B.10) is plotted along with the standing wave pressure equation (Eq. (4.38)) in Fig. B.1. It can be observed from Fig. B.1 that two equations show negligible difference along the stack.

The particular expression of the fluctuating velocity (Eq. (B.11)) is obtained after substituting the expression of p_1 from Eq. (B.10) into the general velocity expression given in Eq. (4.2). This particular expression (Eq. (B.11)) guarantees the mass

conservation. The fluctuating velocity given in Eq. (4.39) does not conserve the mass quantity because it is obtained after substituting the standing wave pressure expression given in Eq. (4.38).

$$u_1 = -\left[\frac{i\omega\rho_1}{\phi\rho_m}\right]x - \frac{K}{\mu}\frac{1}{(L_1 - L_2)}\left[(p_{L1} - p_{L2}) - \frac{1}{2}\left(\frac{i\omega\rho_1}{\phi\rho_m}\frac{\mu}{K}\right)(L_1^2 - L_2^2)\right] \tag{B.11}$$

As the difference between the two expressions of pressure is negligible (evident from Fig. B.1), therefore, the difference between the two expressions of velocity should be negligible. Note that, in Chapter 4, the new pressure (Eq. (B.10)) and velocity (Eq. (B.11)) expressions are used for subsequent calculation in the Results and Discussion Section.

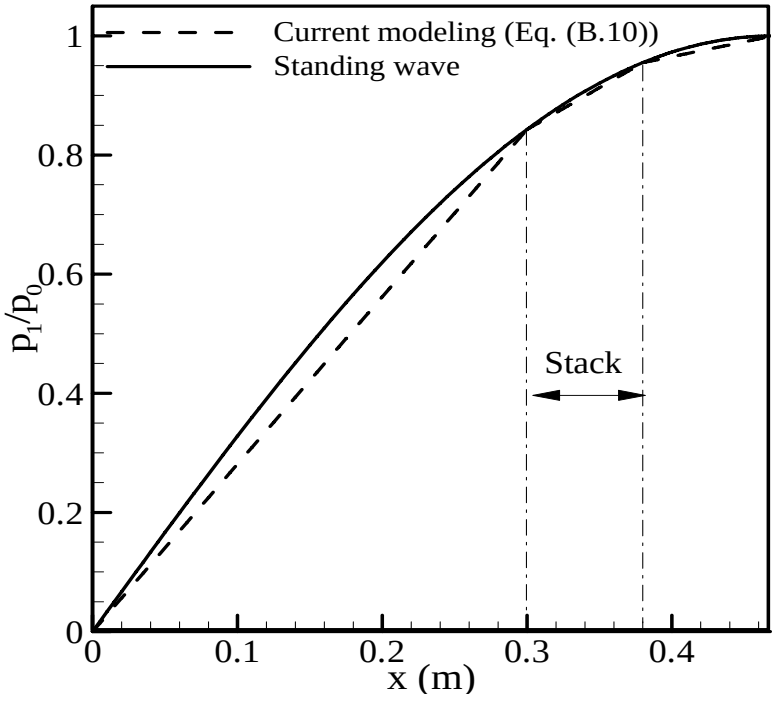

Figure B.1: Comparison of non-dimensional fluctuation pressure using current modeling and the standing wave. Table 1 of Swift [1988] is used as the data regarding the plot. The values of ϕ and K are chosen to that of Fu et al. [2001] using 45 PPI Reticulated Vitreous Carbon (RVC) foam.

The modified energy flux density (E_2) instead of Eq. (4.32) can be written as follows:

$$E_2 = -\frac{\Pi}{2}\Re\left(\frac{\phi p_1}{\sigma} - \frac{\rho_m C_p u_1}{i\omega\sigma}\frac{dT_m}{dx}\right) y_0\left[\left(1-\frac{f_k}{1+\varepsilon_s\sqrt{\sigma}}\right)\left\{\frac{K}{\mu}\frac{p_{L1}-p_{L2}}{L_1-L_2} + \frac{i\omega\rho_1}{\rho_m}\left(\frac{L_1+L_2}{2}-x\right)\right\}\right], \quad \text{(B.12)}$$
$$-\left(y_0\Pi\, k\ + l\,\Pi\, k_c\right)\frac{dT_m}{dx}$$

In deriving Eq. (B.12), it is assumed that the working fluid is an ideal gas and therefore, $T_m\beta$ =1. Equations (4.53) and (4.54) for the work flux will remain unchanged.

Appendix C

Verification of Viscous Oscillating Flow and Thermoacoustic Effects

C.1 Introduction

None of the study in the existing literature consider a code STAR-CD [2007] that uses the finite volume technique to discretize the governing equations and thus to simulate thermoacoustic effects. In general, equation discretization using the finite volume technique is more straight forward and is still the most popular method (Leschziner [1989]). Detailed about the method of simulation is discussed in **Section** C.2. In the present study, for handling thermoacoustic cases two subroutines have been added to the code: stack.f and partmb.f. Subroutine stack. f prepares the grid, places the appropriate boundary conditions and several control parameters for STAR-CD from user defined fluid, flow, and geometric parameters. Subroutine partmb.f performs time-averaging of different parameters; velocity, temperature, entropy generation, etc. It calculates local and global energy flux densities, acoustic work, local and global entropy generation rates, and prepares input file for energy streamfunction calculation.

C.2 Formulation and Numerical Method

The governing equations to be solved for simulating the flow, thermal, and energy fields in a two dimensional Cartesian co-ordinates are the continuity, momentum, and energy equations. In vector form, these equations are expressed as (Versteeg and Malalasekera [1995])

$$\frac{\partial U}{\partial t}+\frac{\partial}{\partial x}F+\frac{\partial}{\partial y}G=\frac{\partial F_v}{\partial x}+\frac{\partial G_v}{\partial y}. \qquad \text{(C.1)}$$

The vectors are:

$$U = \begin{bmatrix} \rho \\ \rho u \\ \rho v \\ E \end{bmatrix},\ F = \begin{bmatrix} \rho u \\ \rho u^2 + p \\ \rho uv \\ (E+p)u \end{bmatrix},\ G = \begin{bmatrix} \rho v \\ \rho uv \\ \rho v^2 + p \\ (E+p)v \end{bmatrix} \tag{C.2}$$

$$F_v = \begin{bmatrix} 0 \\ \tau_{xx} \\ \tau_{xy} \\ u\tau_{xx} + v\tau_{xy} - q_x \end{bmatrix},\ G_v = \begin{bmatrix} 0 \\ \tau_{xy} \\ \tau_{yy} \\ u\tau_{xy} + v\tau_{yy} - q_y \end{bmatrix}, \tag{C.3}$$

shear stress, total energy, and heat flux terms are

$$\tau_{xx} = \frac{4}{3}\mu\frac{\partial u}{\partial x} - \frac{2}{3}\mu\frac{\partial v}{\partial y},\ \tau_{yy} = \frac{4}{3}\mu\frac{\partial v}{\partial y} - \frac{2}{3}\mu\frac{\partial u}{\partial x},\ \tau_{xy} = \mu\left(\frac{\partial u}{\partial y} + \frac{\partial v}{\partial x}\right), \tag{C.4}$$

$$E = \frac{p}{\gamma - 1} + \frac{1}{2}\rho\left(u^2 + v^2\right),\quad q_x = -k\frac{\partial T}{\partial x}, \text{ and } \quad q_y = -k\frac{\partial T}{\partial y}. \tag{C.5}$$

In Eqs. (C.1) to (C.5), u, v, p, T, ρ, C_p, β, k, and μ are the axial velocity, transverse velocity, pressure, temperature, fluid density, fluid specific heat, thermal expansion coefficient, thermal conductivity, and dynamic viscosity, respectively. The viscosity μ and thermal conductivity k are temperature dependent (Swift [2002]), with

$$\mu = \mu_m\left(\frac{T}{T_m}\right)^{b_\mu}, \tag{C.6a}$$

and

$$k = k_m\left(\frac{T}{T_m}\right)^{b_k}, \tag{C.6b}$$

with subscript "m" representing values at temperature T_m. The values for exponent are chosen from Swift [2002].

Helium/air is assumed to be an ideal gas, so that the state equation is

$$p = \rho RT, \tag{C.7}$$

where R is the gas constant per unit mass.

The above equations are solved numerically to compute dynamical physical quantities. The commercial code STAR-CD (which solves the governing equations using a finite volume method (Versteeg and Malalasekera [1995]) is used for the current simulations. The governing differential equations (Eqs. (C.1) to (C.5)) are integrated over the finite volume of a computational cell and over a finite time. A second-order central difference scheme (Versteeg and Malalasekera [1995]) is used for the discretisation of the convective and diffusive terms and a first-order fully implicit scheme for time. After selecting the discretisation schemes, Eqs. (C.1) to (C.5) are rearranged to a set of the finite volume equations generally having the form,

$$a_p \Omega_p = a_N \Omega_N + a_S \Omega_S + a_E \Omega_E + a_W \Omega_W + b, \tag{C.8}$$

where a_p, a_N, etc. are coefficients expressing convection and diffusion, b presents the source approximate to any variable for the cell. A two-dimensional control volume diagram is shown in Fig. C.1, where a typical control volume has a central node P and

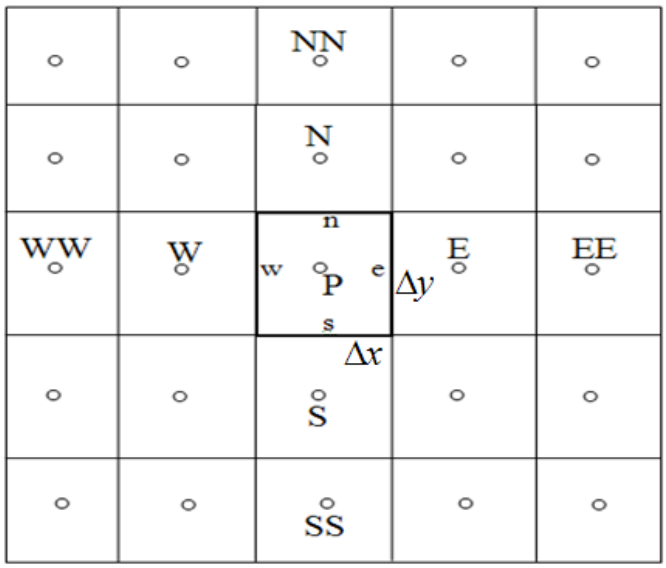

Figure C.1: Cell arrangements

four faces denoted by e, w, n, and s. Lower case characters at the cell faces indicate where velocities are stored. A staggered grid arrangement is used for velocities. The solution procedures are the TDMA (Tri-diagonal matrix algorithm) line-by-line solver of the algebraic equations and the SIMPLE (Semi-Implicit Method for Pressure Linked Equations) (Patankar and Spalding, [1972]) algorithm to ensure correct linkage between pressure and velocity. The basic idea of the SIMPLE algorithm is that first the pressure field is guessed, then the corresponding velocity fields are computed using the momentum equation and the resulting errors in the continuity equation are computed. Based on these errors, corrections that are needed to be made to pressure and velocities are computed. This process is iterated until the imbalances in the conservation equations at each cell are within the convergence criteria set by the user.

C.2.1 Stopping Criteria

STAR-CD has three levels of iteration in order to solve systems of linear equations. The first level is the linear equation solver, the second level is the SIMPLE algorithm, and last the sweep. The first iteration level solves the N_x (the total number of cell in x direction) by N_y (the total number of cell in y direction) system of equations for a variable Ω using a choice of linear equation solvers at each slab, where a slab is an x-y array of cells at each z. At the second iteration level, the SIMPLE algorithm is used. Usually one iteration suffices if the problem is elliptic since the slab is going to be visited many times. At the third iteration level, the solution algorithm proceeds slab by slab sweeping across all z cells (for a 3-D problem). The iteration stops when the sum of the absolute values of the differences in the finite volume equation after each sweep fall below a user specified reference value. In STAR-CD, the user specifies the residual criteria for all levels of iterations. A firm residual criteria means that the simulation requires longer time to complete.

C.2.2 Errors in Numerical Simulations

C.2.2.1 General Errors

Numerical errors are caused mainly from

- discretization of the governing equations,
- convergence error,
- approximation of boundary conditions, and
- round off errors.

Discretization errors can be estimated from the numerical scheme selected and grid dependency tests. While using commercial software, the user has limited control over this type of error, except refining the grid. Errors introduced by boundary conditions depend on how closely the physical boundary conditions can be represented in the model and how boundary conditions are discretized. Round off errors are introduced by the limited arithmetic precision of the computer, and usually are much smaller than the others mentioned. Convergence error is the difference between the solution at the current iteration and the exact solution. The magnitude of this error depends on the residual criteria selected. Barrett et al. [1994] suggested that a good stopping criterion should

- Identify when the error (the difference between the analytical and numerical solutions) is small enough to stop.
- Stop if the error is no longer decreasing or is decreasing too slowly, and
- Limit the maximum amount of time spent iterating.

A more general method for estimating convergence error is described in **Section** C.6.

C.3 Simple Oscillation of a Viscous Ideal Gas

Consider an acoustic driver/energy source (e.g. loudspeaker) is placed near one of the ends of an open-closed tube as shown in Fig. C.2(a). A part of the acoustic energy produced by such a source enters into the tube in the form of a traveling acoustic wave. This wave travels through the tube, reaches the other end, and reflects back into the tube again in the form of a traveling acoustic wave. So, (as shown in Fig. C.2(a)), in the presence of an acoustic energy source, the acoustic wave that reflects from the closed end

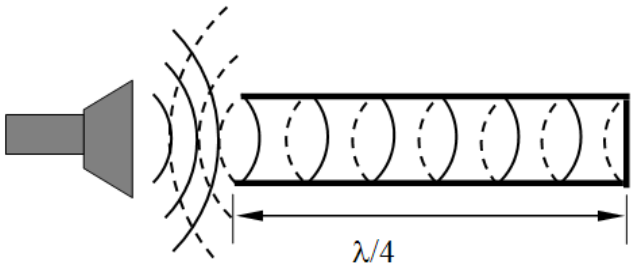

(a)

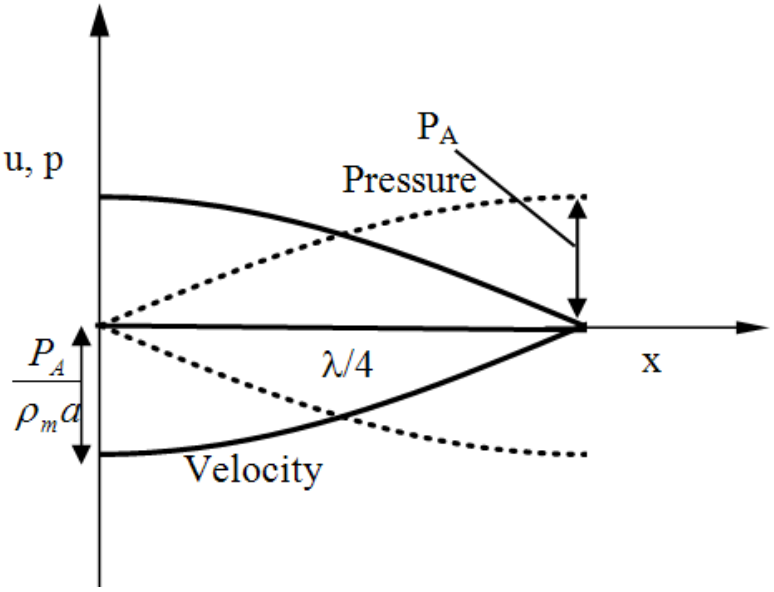

(b)

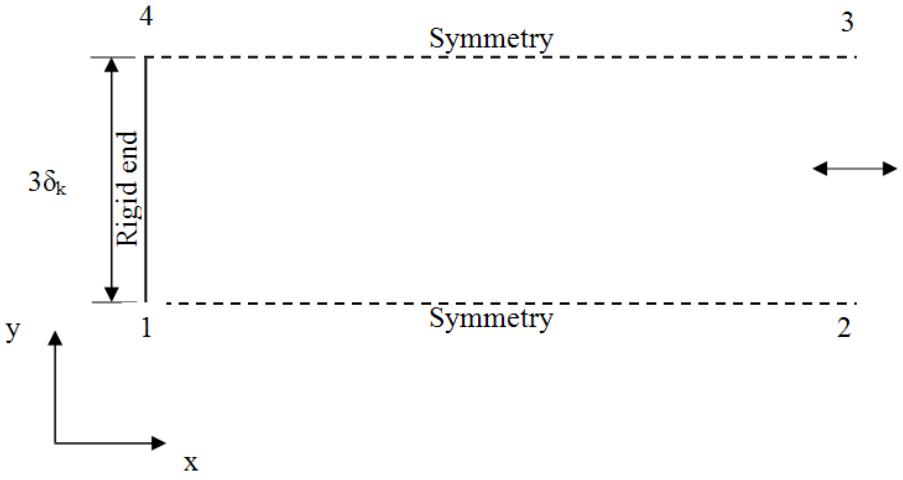

(c)

Figure C.2: Schematic diagram of (a) formation of standing wave, (b) pressure and velocity distributions, and (c) computational domain and boundary conditions.

interacts with the oncoming traveling wave to produce what is termed as a standing wave or a stationary wave (Fig. C.2(b)). Now, using the numerical scheme described in **Section** C.2, the numerical results (velocity, pressure and temperature amplitudes) for a 2-D standing wave simulation can be compared to the standard first order analytical solution for a 1-D standing wave as given in Eqs. (C.13), (C.14), and (C.15) for pressure, velocity and temperature, and also with the numerical results of Ishikawa [1999]. A schematic of the system being modeled is shown in Fig. C.2(c). The standing wave can be simulated using the boundary conditions described below:

The pressure, velocity, and temperature at the open end (boundary side 23 in Fig. C.2(c)) are expressed as in terms of a mean component and a first order fluctuating component (Rott [1980]) as follows:

$$p = p_m + \Re\left\{ p_1 e^{i\omega t} \right\}, \tag{C.9}$$

$$u = \Re\left\{ u_1 e^{i\omega t} \right\}, \tag{C.10}$$

$$T = T_m + \Re\left\{ T_1 e^{i\omega t} \right\}, \tag{C.11}$$

where p_m and T_m are mean pressure and temperature respectively, $\Re\{\ \}$ signifies the real part, and $p_1, u_1,$ and T_1 are the pressure, the velocity, and the temperature oscillations of the standing wave. The time dependency of a particular variable is represented by $\exp(i\omega t)$ where ω represents the angular frequency that equals $2\pi f$, and f is the ordinary frequency. $p_1, u_1,$ and T_1 for an ideal standing wave are:

$$p_1 = p_0 \cos(k_1 x), \qquad u_1 = -i\frac{p_0}{\rho_m a}\sin(k_1 x), \quad \text{and} \quad T_1 = \frac{p_0 \cos(k_1 x)}{\rho_m C_p}, \tag{C.12}$$

where p_0 is the pressure amplitude at the pressure antinode of the wave, a is the adiabatic sound speed, $k_1 = \left(\frac{2\pi}{\lambda}\right)$ is the wave number, ρ_m is the mean density, and C_p is the

specific heat of the gas at a constant pressure. The expression for oscillating velocity (u_1) in Eq. (C.12) is obtained from linearized first order, inviscid momentum equation, using the expression of oscillating pressure (p_1) (from Eq. (C.12)). The relation between oscillating temperature (T_1) and oscillating pressure (p_1) in Eq. (C.12) is discussed in Chapter 2 (Eq. (2.5)). Using Eq. (C.12), the final expressions for Eqs. (C.9), (C.10), and (C.11) are

$$p = p_m + p_0 \cos(k_1 x)\cos(\omega t), \tag{C.13}$$

$$u = \frac{p_0}{\rho_m a}\sin(k_1 x)\sin(\omega t), \tag{C.14}$$

$$T = T_m + \frac{p_0}{\rho_m C_p}\cos(k_1 x)\cos(\omega t), \tag{C.15}$$

The boundary conditions at side 14 (left wall, closed end, in Fig. C.2(c)) are

$$\begin{aligned} u &= 0 \\ v &= 0 \\ \frac{dT}{dx} &= 0, \end{aligned} \tag{C.16}$$

and symmetry boundary conditions at boundary sides 12 and 34 (horizontal sides, in Fig. C.2(c)).

In order to make comparisons, mean pressure of 1000 kPa, mean temperature of 300 K, frequency of 100 Hz and 500 Hz, and a DR of 1.0 and 5.0 % are chosen. These DRs' correspond to Mach numbers of 5.99E-03 and 2.99E-02 respectively. The Mach number (u_1 / a) is calculated based on the velocity amplitude at the velocity antinode and the speed of sound (a) based on the mean temperature, following Cao et al. [1996]. The conditions listed in Table C.1 are chosen to cover typical operating conditions of thermoacoustic engines. Tests are carried out for selected cases to investigate the dependence of the numerical results on the grid size, time step size, and other variables such as frequency, DR, domain length, and working fluids. The dependence of the results

on the DR can be checked by comparing the simulation results for cases 1 and 2, the dependence on the frequency by cases 1 and 3, and the dependence on the domain length and working fluid by cases 1 and 4. The domain length in the *x*-direction is 1/16 of the acoustic wave length for cases 1 to 3, and for case 4, 1/4 of the acoustic wave length. For all the cases considered, domain height in the *y*-direction is three times the thermal penetration depth (since symmetry boundary condition is applied at the horizontal boundaries of the computational domain, the domain length in the *y*-direction is insignificant).

Table C.1: Operating conditions for the standing wave simulations, $p_m=1.0\times10^6$ *Pa*, T_m =300 K, domain height $y_0=3\delta_k$.

Case	Working fluid	Frequency (Hz)	Drive ratio (%)	Wave Length (m)	Domain Length (m)	δ_k (mm)
1	helium	100	1	10.191	$\lambda/16$	0.239
2	helium	100	5	10.191	$\lambda/16$	0.239
3	helium	500	5	2.038	$\lambda/16$	0.107
4	air	100	1	3.461	$\lambda/4$	0.266

The numerical results of Table C.1 for velocity, pressure and temperature amplitudes and their comparisons to the standard first order analytical solutions (Eqs. (C.13), (C.14), and (C.15)) along with the numerical results of Ishikawa [1999] for some of the cases are presented below. When cases 1 and 2 are considered, the only difference is the increased DR (case 2), which increases the pressure, velocity, temperature, and particle displacement amplitudes (for case 2). Therefore for case 2, less control volumes are required in the *x*-direction to capture the flow and thermal fields and consequently less time to obtain converged solution than case 1. For case 3, operating frequency is 5 times higher compared to that of case 2, therefore refining the time step size compared to case 2 gives better accuracy. For all of the cases as mentioned in Table C.2, steady state is achieved in between 8 to 12 cycles. The maximum deviation between the computations and the analytical results is 0.8%.

C.3.1 Results

C.3.2 Spatial Grid Dependency Tests and Tests on Time Step of a Standing Wave

In a standing wave, the gas oscillates in the x-direction throughout the simulation domain. The present simulation is nominally 1-D and the domain does not include any of the tube walls except at the rigid end. In order to test the dependence of the simulation results on grid resolution in the x-direction, the grid size Δx is varied for case 1 using

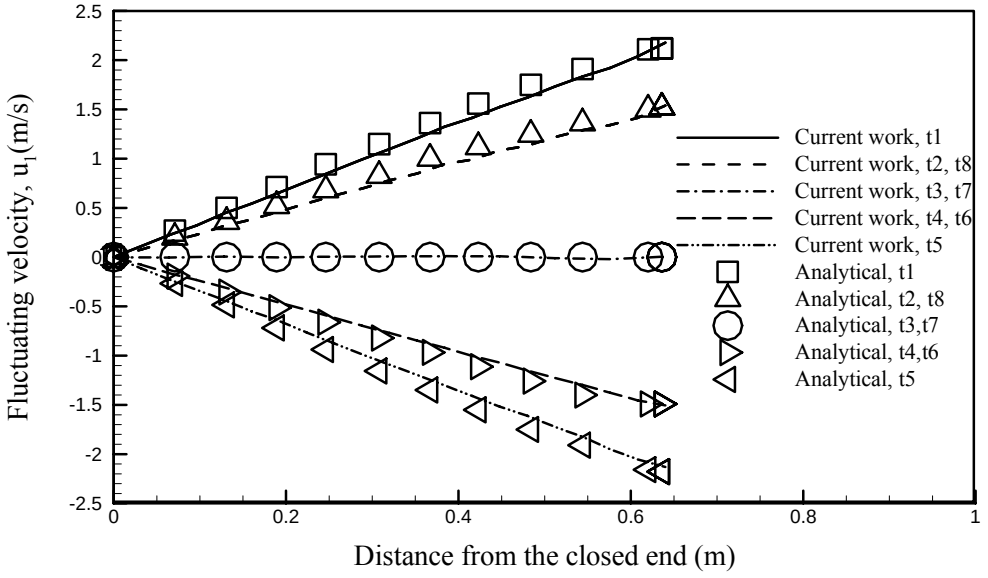

(a)

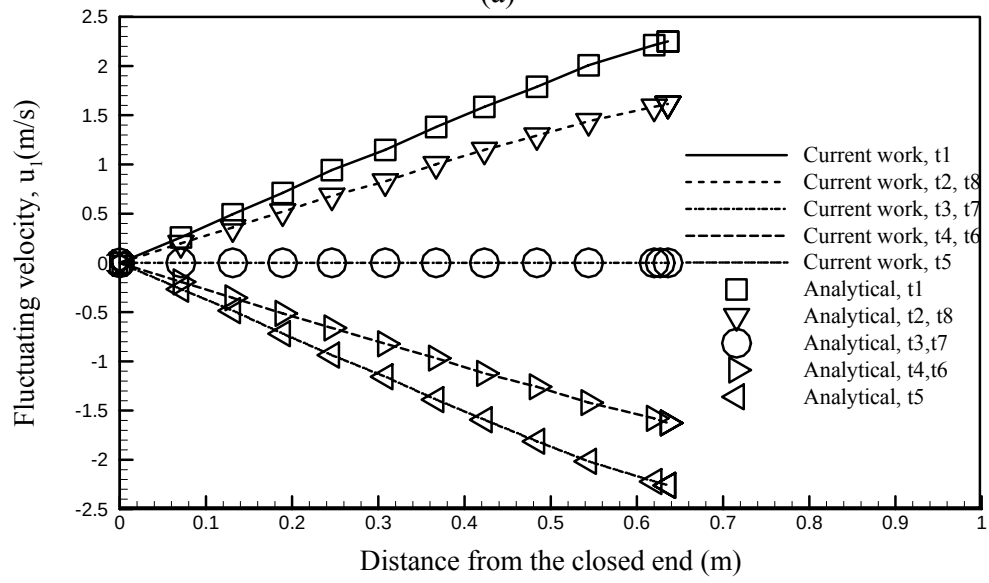

(b)

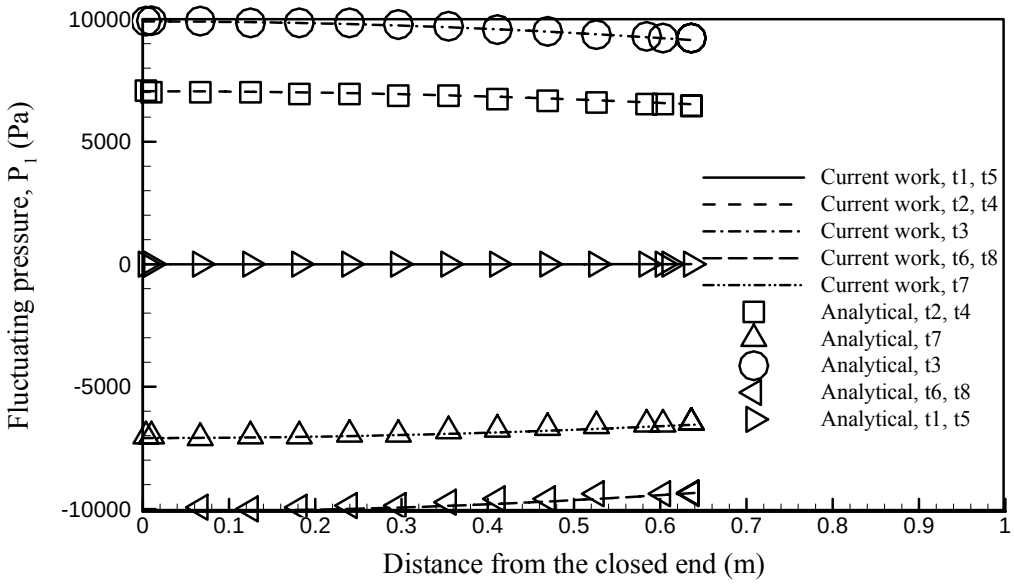

(c)

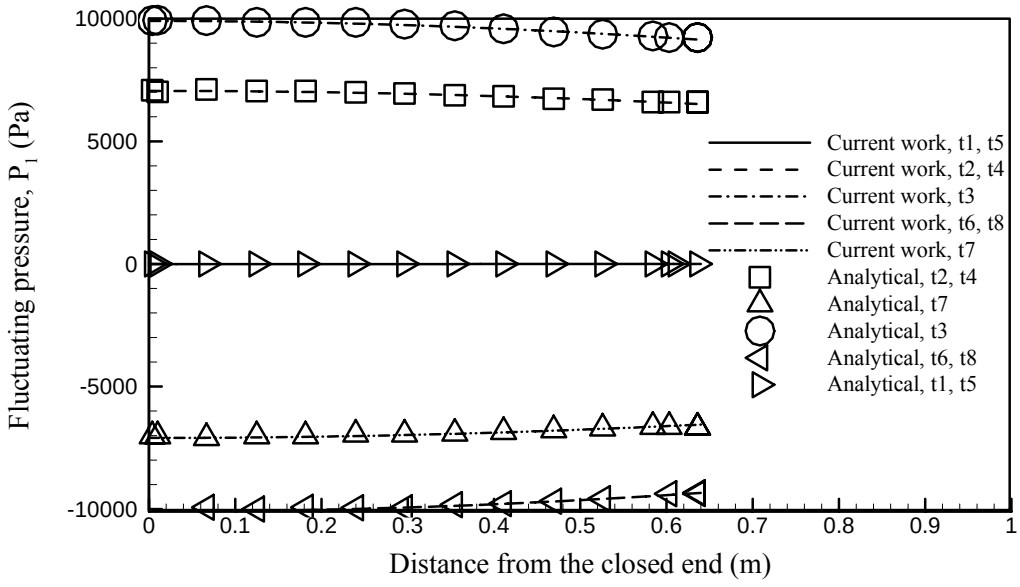

(d)

$\Delta x/\lambda = 9.6\times10^{-4}$, 3.2×10^{-4}, and 2.09×10^{-4}. For all the cases the time step size is 0.5% of the duration of cycle (also used by Ishikawa [1999]). The numerical simulation results for $\Delta x/\lambda = 3.2\times10^{-4}$ and 2.09×10^{-4} and the analytical solutions for pressure, velocity, and temperature (Eqs. (C.13, C.14, and C.15)) as a function of the *x*-coordinate at time steps every 1/8 of a cycle are shown in Figs.C.3(a) to (f). In Figs. C.3(a) to (f), $t1 = T/8,\ t2 = 2T/8 \cdots t8 = T.\ T$ is the duration of a cycle. Steady state is achieved after 8 cycles. The simulation agreed with the analytical solutions to within 0.3% for

$\Delta x/\lambda = 2.09\times10^{-4}$ and 0.5% for $\Delta x/\lambda = 3.2\times10^{-4}$. Also comparisons with Ishikawa's [1999] results are presented in Figs. C.4(a) to (c), for velocity, pressure, and temperature

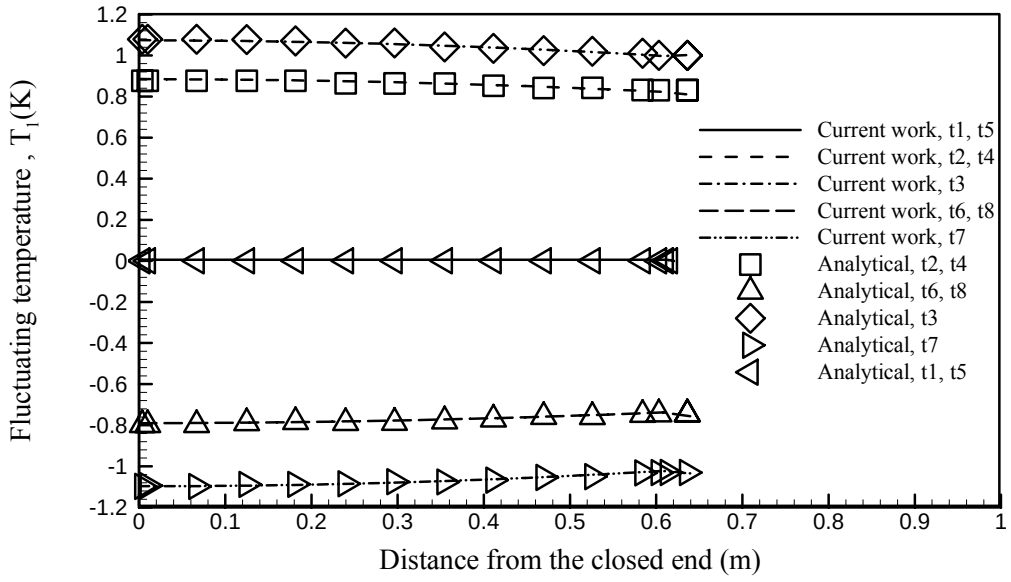

(e)

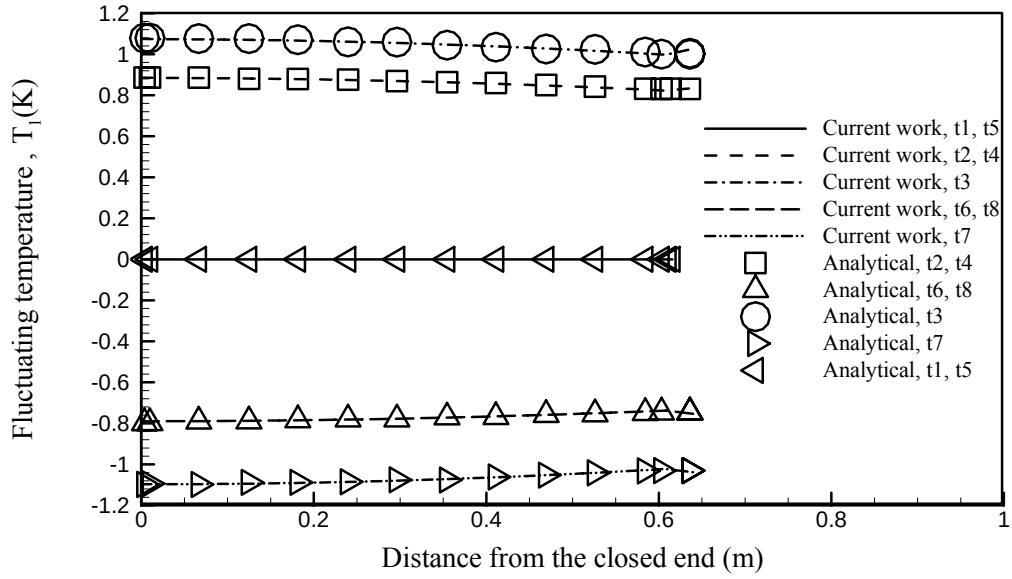

(f)

Figure C.3: Velocity fluctuations for (a) $\Delta x/\lambda = 3.2e-4$, (b) $\Delta x/\lambda = 2.09e-4$ .Pressure fluctuations for (c) $\Delta x/\lambda = 3.2e-4$, (d) $\Delta x/\lambda = 2.09e-4$. Temperature fluctuations for (e) $\Delta x/\lambda = 3.2e-4$ and (f) $\Delta x/\lambda = 2.09e-4$.

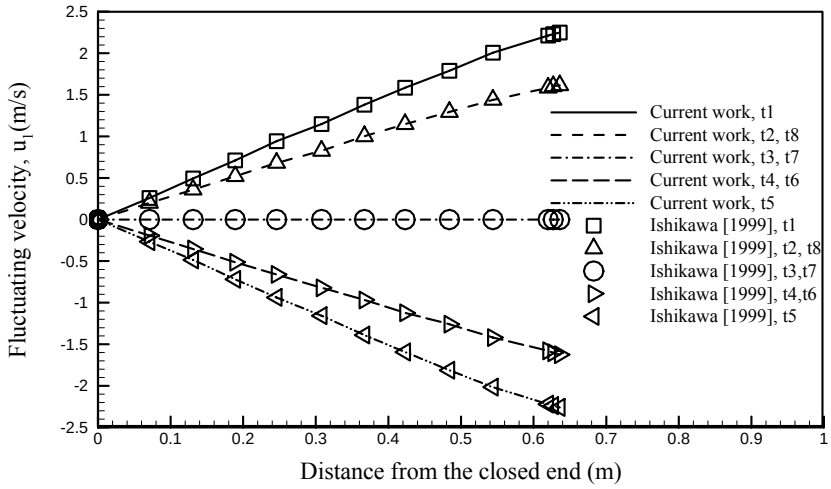

(a)

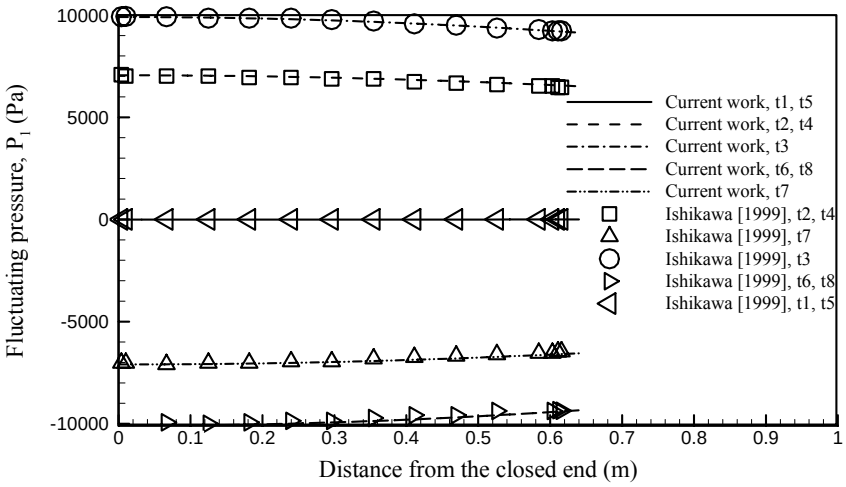

(b)

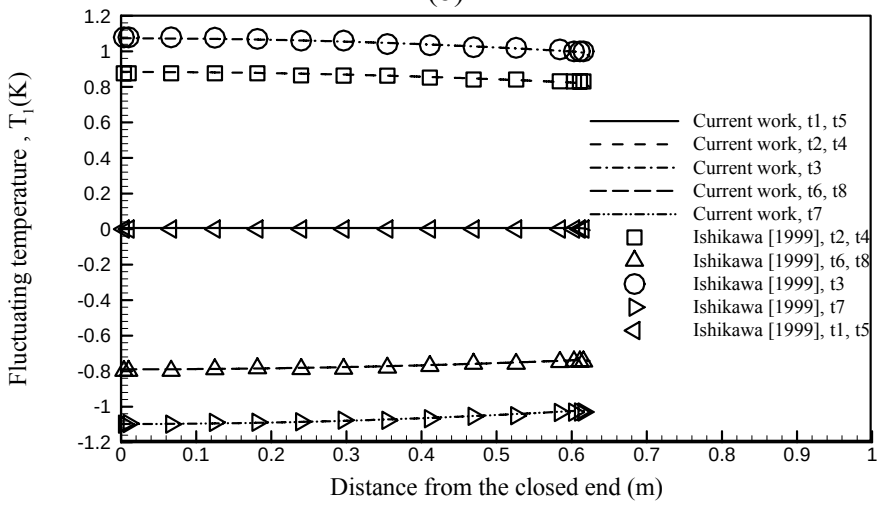

(c)

Figure C.4: Comparisons of present (a) velocity, (b) pressure, and (c) temperature fluctuations with Ishikawa [1999].

profiles for $\Delta x/\lambda = 2.09\times10^{-4}$ and Δt=0.5% of the duration of cycle. Ishikawa's data are read from his thesis (Ishikawa [1999]), and will contain read off error. Good agreement (0.8%) is obtained between the present results and Ishikawa's work [1999], which can be considered to be within the limitation of the accuracies of the simulations, moreover the numerical code used by Ishikawa is written in single precision as opposed to the current numerical code which is written in double precision. Codes written in single precision are proven to be sufficient for most problems (Spalding [1991]). However, codes written in single precision generally cannot meet as strict a residual criterion, even after many iteration, as can those written in double precision. Uniformly spaced grids are used for all the simulations presented in Table C.1. Ishikawa [1999] showed that it is not necessary to have a fine grid even at the rigid end (Fig. C.2(c)) where the acoustic wave is reflected.

The sensitivity of the solutions to the time step size is tested for case 1 presented in Table C.1. The time step sizes tested are 0.625, 0.5, and 0.3125 % of the duration of cycle. For the entire time step sizes tested, the simulations agreed with the analytical solutions to within 0.3%. Therefore, for case 1, simulation results are independent on the above mentioned time step sizes. The effect of time step size on fluctuating velocity, pressure, and temperature for cases 2 (*DR*=5%) and 3 (frequency 500 Hz and *DR*= 5%) are presented in Figs. C.5(a) to (f) and Figs. C.6(a) to (f).

C.3.3 Dependence on Other Variables

C.3.3.1 Dependence on DR

The simulation for the higher DR condition, case 2 ($DR = 5\%$) in Table C.1, is tested with two different grid sizes $\Delta x/\lambda = 3.47\times10^{-4}$ and 3.12×10^{-4} in the *x*-direction. For both of the cases Δ*t*=0.5 % of the duration of cycle. It is observed that simulation results are independent on the grid size. Further investigation is performed to observe the

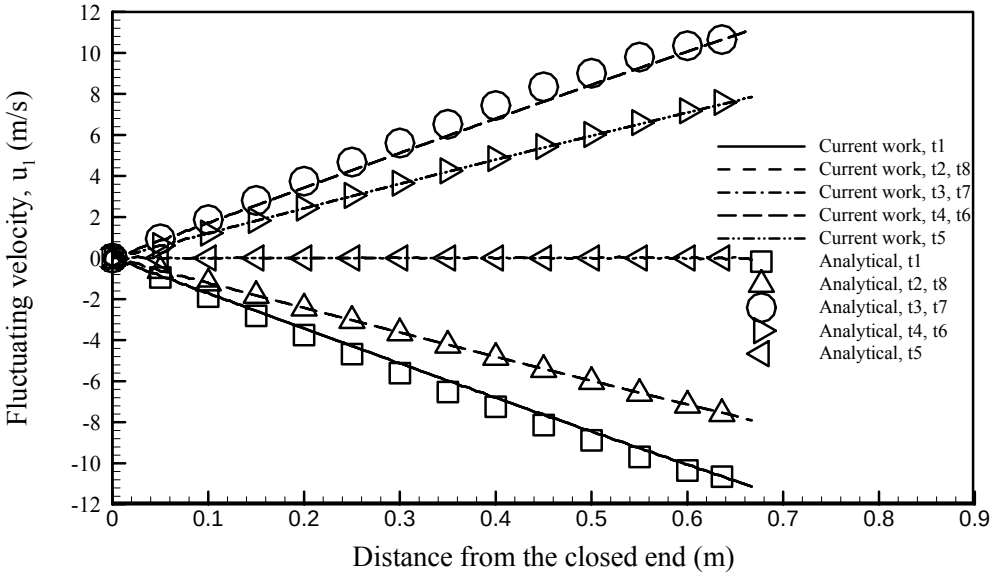
Fluctuating velocity, u_1 (m/s)
Distance from the closed end (m)
Current work, t1
Current work, t2, t8
Current work, t3, t7
Current work, t4, t6
Current work, t5
Analytical, t1
Analytical, t2, t8
Analytical, t3, t7
Analytical, t4, t6
Analytical, t5

(a)

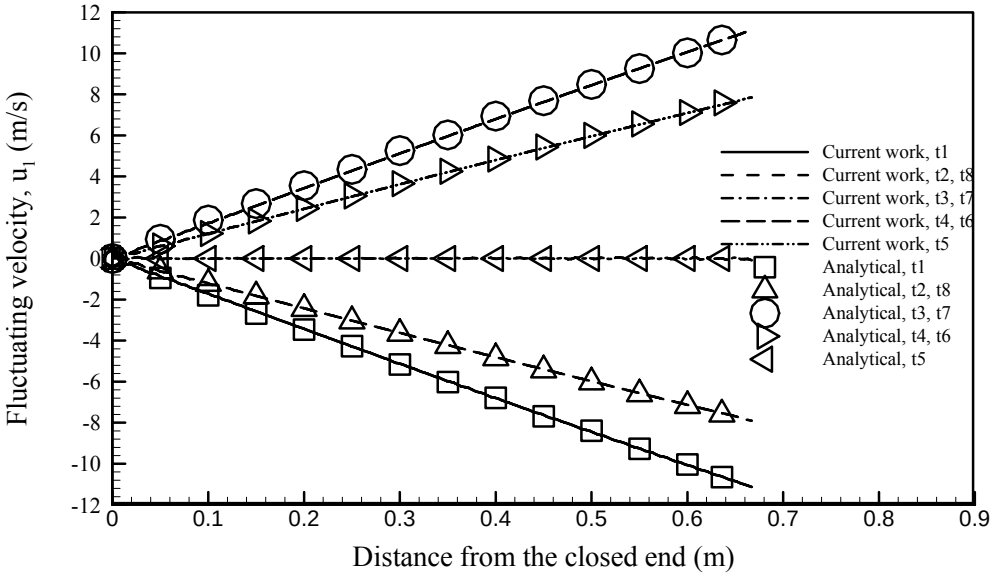
Fluctuating velocity, u_1 (m/s)
Distance from the closed end (m)
Current work, t1
Current work, t2, t8
Current work, t3, t7
Current work, t4, t6
Current work, t5
Analytical, t1
Analytical, t2, t8
Analytical, t3, t7
Analytical, t4, t6
Analytical, t5

(b)

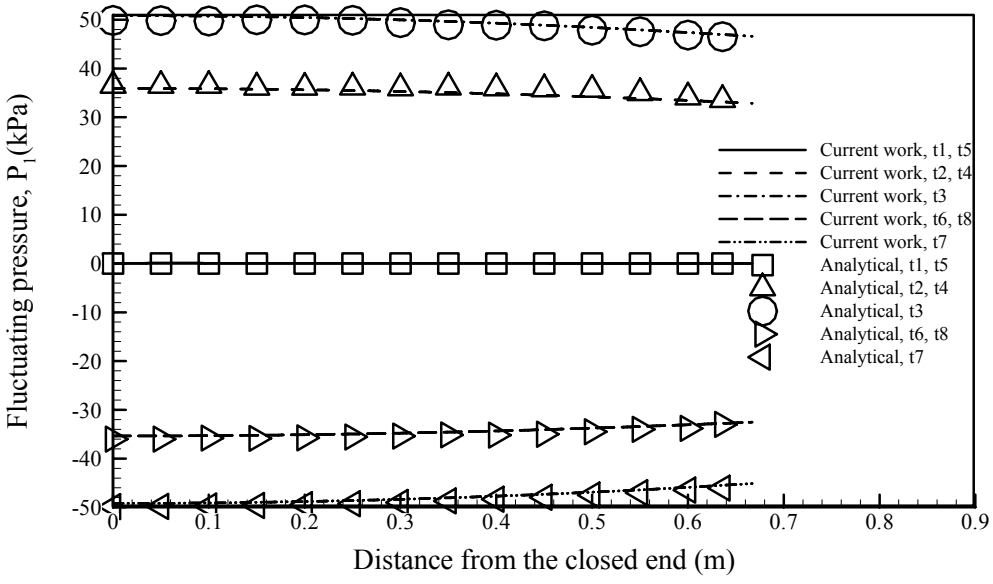
Fluctuating pressure, P_1(kPa)
Distance from the closed end (m)
Current work, t1, t5
Current work, t2, t4
Current work, t3
Current work, t6, t8
Current work, t7
Analytical, t1, t5
Analytical, t2, t4
Analytical, t3
Analytical, t6, t8
Analytical, t7

(c)

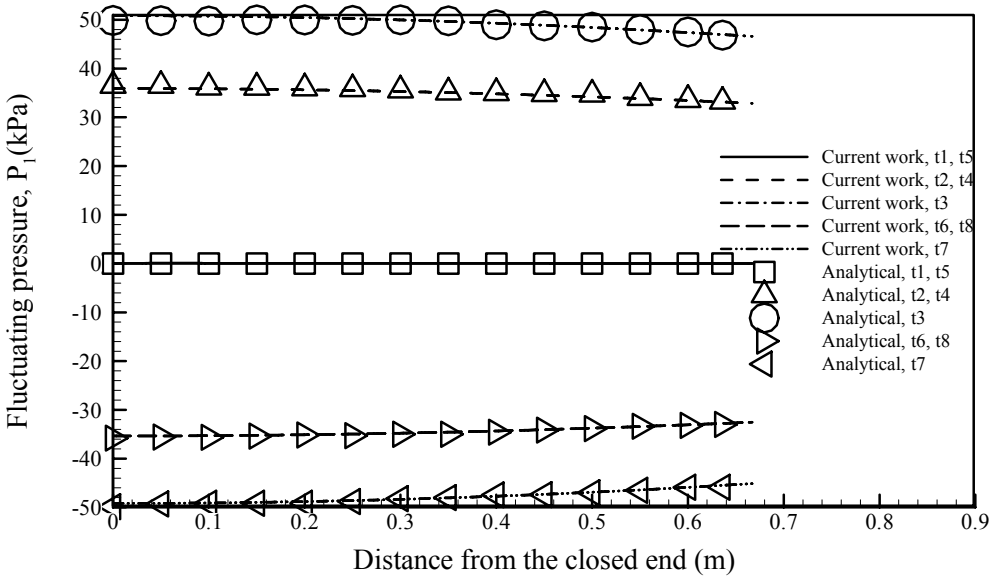
Fluctuating pressure, P_1(kPa)
Distance from the closed end (m)
Current work, t1, t5
Current work, t2, t4
Current work, t3
Current work, t6, t8
Current work, t7
Analytical, t1, t5
Analytical, t2, t4
Analytical, t3
Analytical, t6, t8
Analytical, t7

(d)

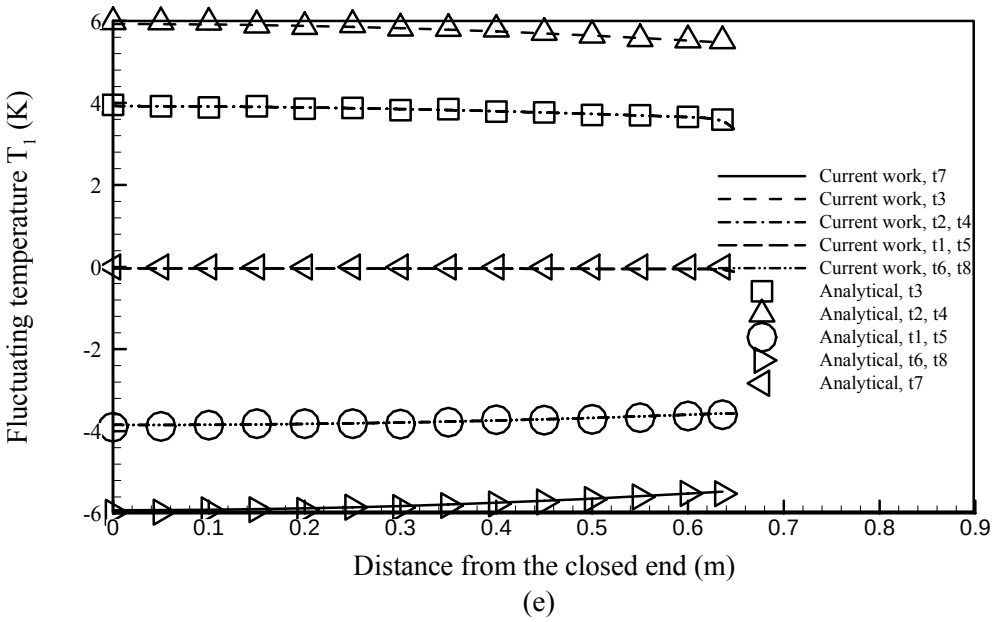

(e)

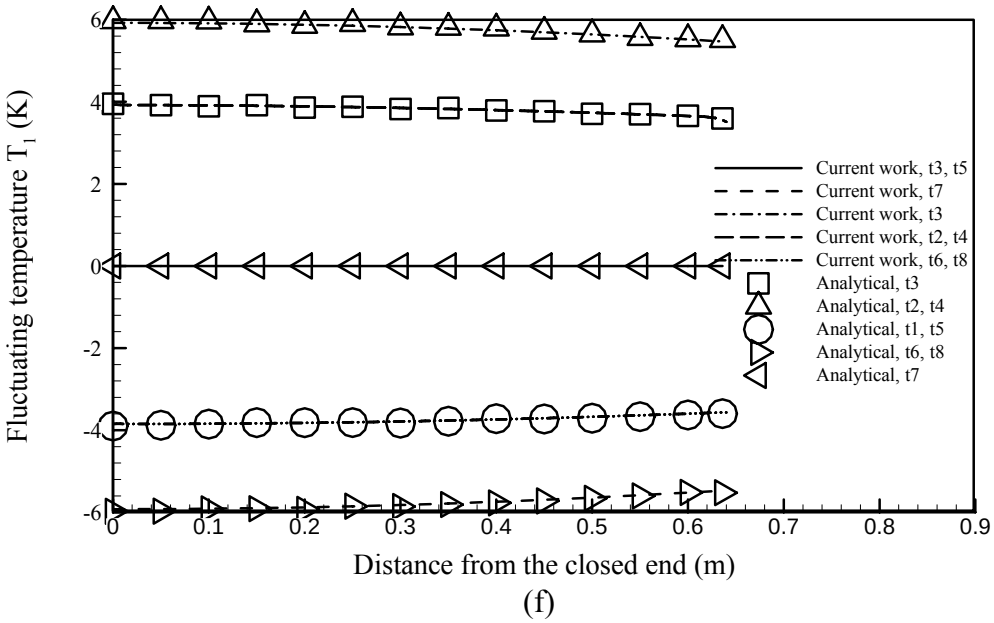

(f)

Figure C.5: Velocity fluctuations for (a) Δt = 5.0e-5 s, (b) Δt=2.5e-5 s. Pressure fluctuations for (c) Δt = 5.0e-5 s, (d) Δt=2.5e-5 s. Temperature fluctuations for (e) Δt = 5.0e-5 s, (f) Δt=2.5e-5 s.

dependence of the simulation results on the time step size by considering Δt =0.5 and 0.25 % (=5.0×10^{-5} sec. and 2.50×10^{-5} sec.) of the duration of cycle. Simulation results improve with the decrease of the time step size. The numerical simulation results for Δt=0.5 and 0. 25 % of the duration of cycle is compared with the analytical solutions for pressure, velocity, and temperature (Eqs. (C.13, C.14, and C.15)) as a function of the *x*-

coordinate at time steps every 1/8 of a cycle are shown in Figs.C.5(a) to (f). Steady state is achieved after 11 cycles. The simulation agreed with the analytical solutions to within 0.8% for Δt=0.25% of the duration of cycle. Therefore, simulation results are independent on the DR for the cases considered.

C.3.3.2 Dependence on Frequency

The simulation for the higher frequency condition, case 3 (frequency=500 Hz, and *DR*=5%) in Table C.1, is tested with three different time step sizes: 0.625, 0.5, and 0.3125% of the duration of cycle. Although the time step sizes expressed as a percentage of the duration of a cycle are the same as those for case 1, the actual time step size is only 20% of that for the lower frequency cases as the duration of the cycle is shorter when the frequency is higher. The grid size Δx is varied using $\Delta x/\lambda = 3.2\times10^{-4}$ and 2.09×10^{-4}. It is observed that simulation results are independent on the grid size. Further investigation is performed to observe the dependence of the simulation results on the time step size by considering Δt=0.625, 0.5 and 0.3125% of the duration of the cycle. Simulation results improve with the decrease of the time step size. The numerical simulation results for Δt=0.5 and 0.3125% (=2.5×10^{-6} sec. and 6.25×10^{-6} sec.) of the duration of cycle and the analytical solutions for pressure, velocity, and temperature as a function of the *x*-coordinate at time steps every 1/8 of a cycle are shown in Figs. C.6(a) to (f). Steady state

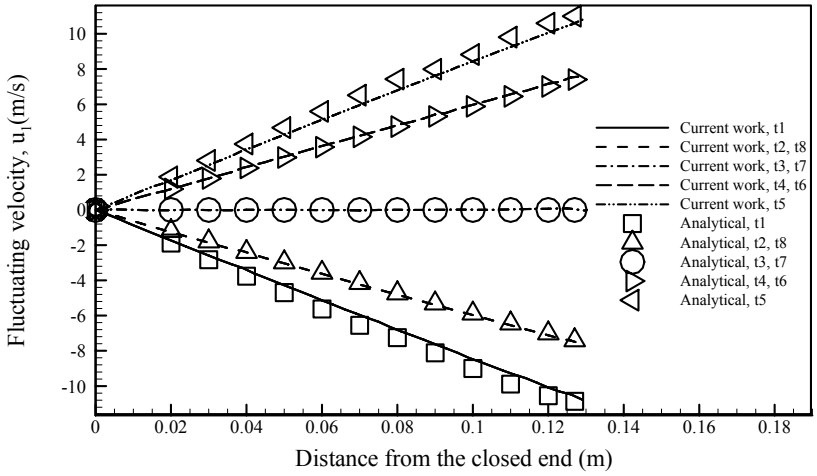

(a)

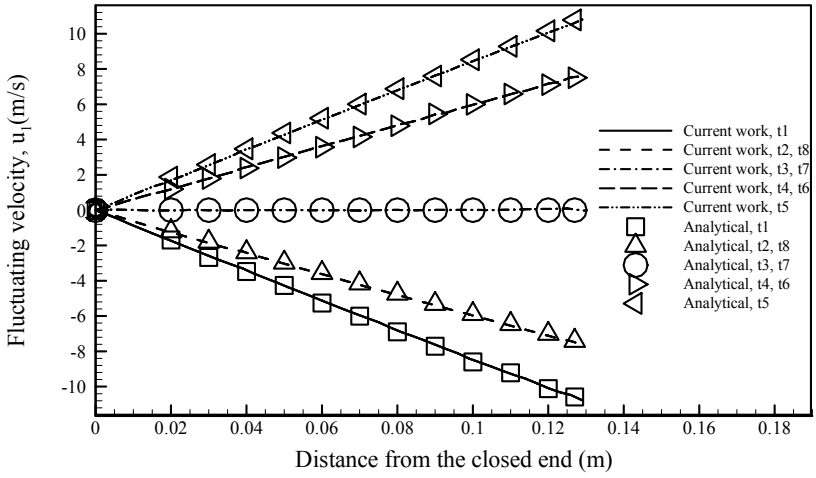
Fluctuating velocity, u_1(m/s)
Distance from the closed end (m)
Current work, t1
Current work, t2, t8
Current work, t3, t7
Current work, t4, t6
Current work, t5
Analytical, t1
Analytical, t2, t8
Analytical, t3, t7
Analytical, t4, t6
Analytical, t5

(b)

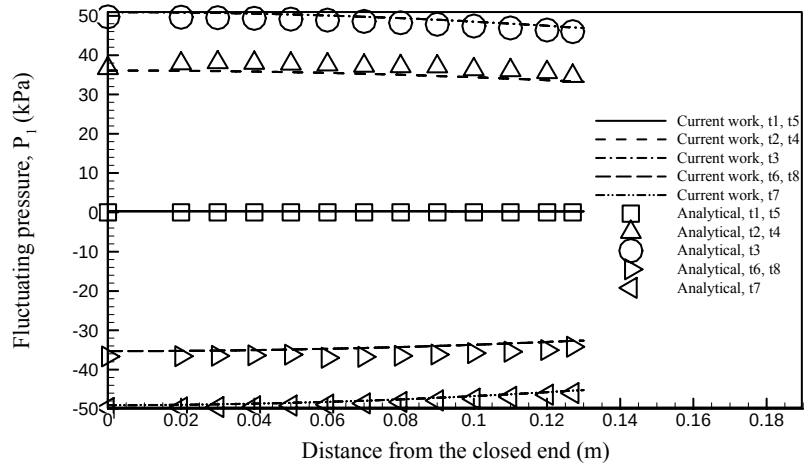
Fluctuating pressure, P_1 (kPa)
Distance from the closed end (m)
Current work, t1, t5
Current work, t2, t4
Current work, t3
Current work, t6, t8
Current work, t7
Analytical, t1, t5
Analytical, t2, t4
Analytical, t3
Analytical, t6, t8
Analytical, t7

(c)

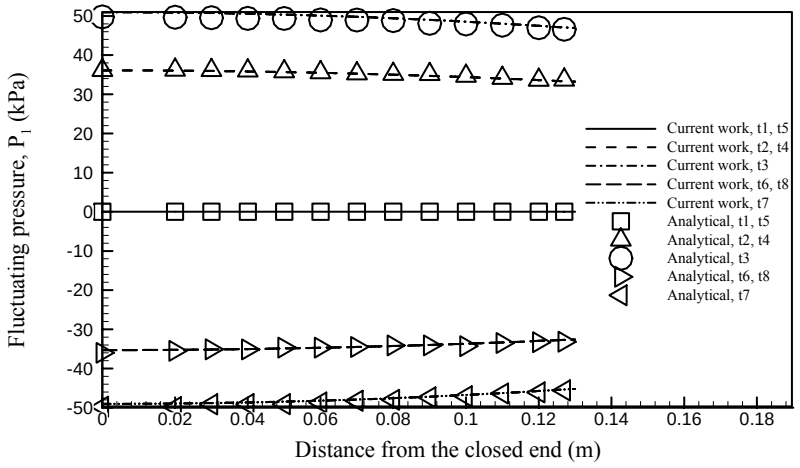
Fluctuating pressure, P_1 (kPa)
Distance from the closed end (m)
Current work, t1, t5
Current work, t2, t4
Current work, t3
Current work, t6, t8
Current work, t7
Analytical, t1, t5
Analytical, t2, t4
Analytical, t3
Analytical, t6, t8
Analytical, t7

(d)

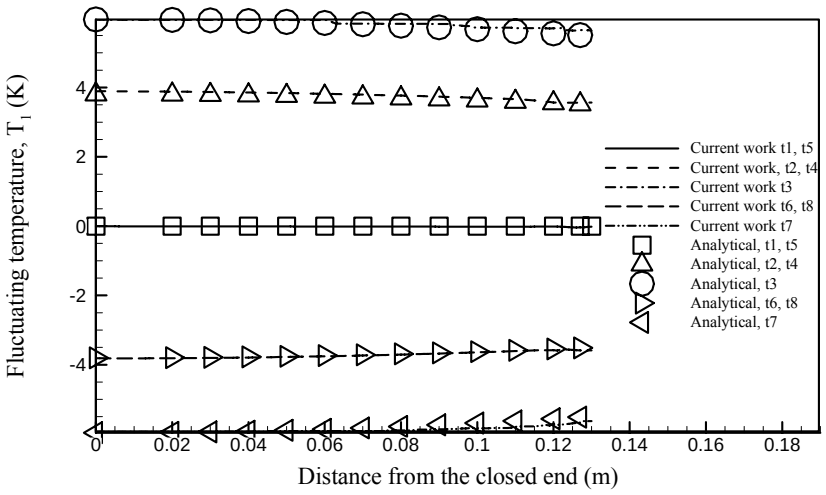

(e)

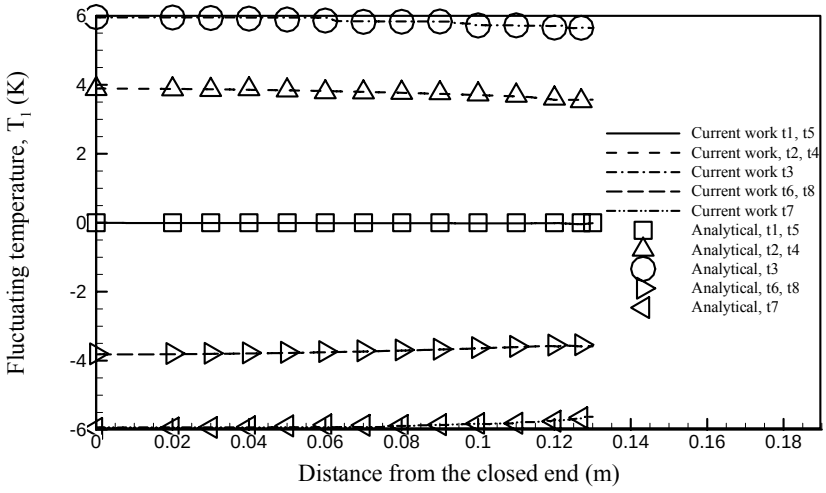

(f)

Figure C.6: Velocity fluctuations for (a) Δt = 2.5e-5 s. (b) Δt = 6.25e-6 s. Pressure fluctuations for (c) Δt = 2.5e-5 s., (d) Δt = 6.25e-6 s. Temperature fluctuations for (e) Δt = 2.5e-5 s., and (f) Δt = 6.25e-6 s.

is achieved after 12 cycles. The simulations agreed with the analytical solutions to within 0.32% for Δt= 0.3125% and 0.8% for Δt= 0.5% of the duration of cycle. Therefore, simulation results are independent on frequency for the cases considered.

C.3.3.3 Dependence on the Working Fluid and Domain Length

Dependence of the computed solutions on the domain length and of the working fluid is tested using case 4 (air is chosen as the working fluid and domain length is considered to

be quarter of a wave length) of Table C.1. Three different grid sizes $\Delta x/\lambda = 9.99\times10^{-4}$, 8.928×10^{-4}, and 8.33×10^{-4} are considered in the *x*-direction. For all of these cases Δt=0.5% of the duration of cycle is used. Refining the time step size does not improve the results. Figures C.7(a) to (f) show the simulation results for $\Delta x/\lambda = 9.99\times10^{-4}$ and 8.33×10^{-4} compared with the analytical solutions for pressure, velocity, and temperature as a function of the *x*-coordinate at time steps every 1/8 of a cycle. The simulation agreed with the analytical solution to within 0.5% for $\Delta x/\lambda = 9.99\times10^{-4}$ and to approximately

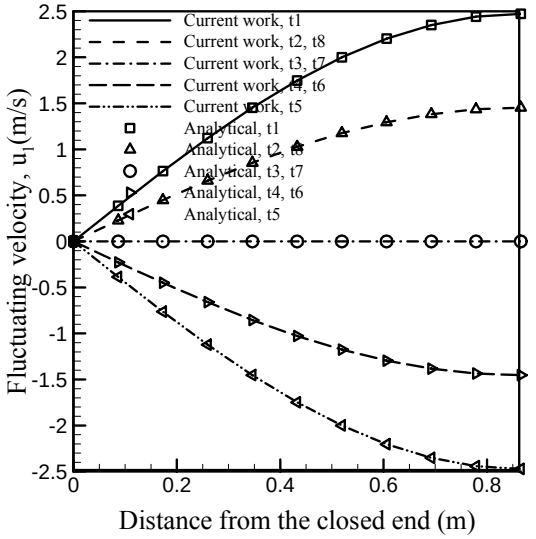

(a)

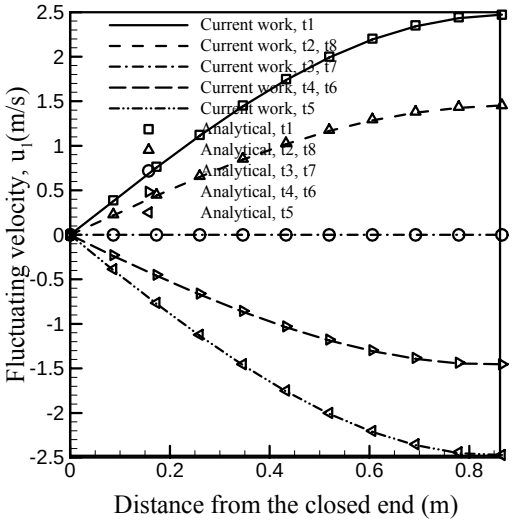

(b)

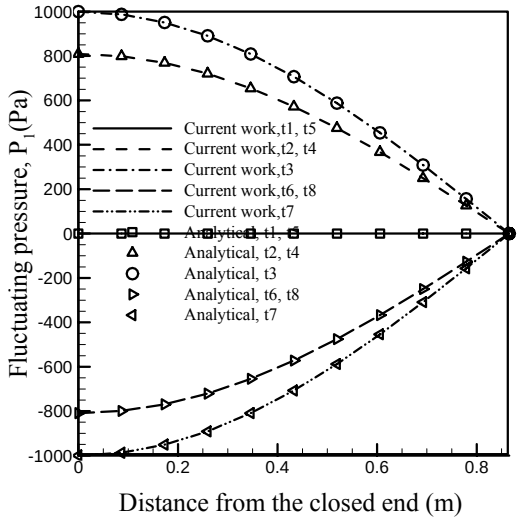

(c)

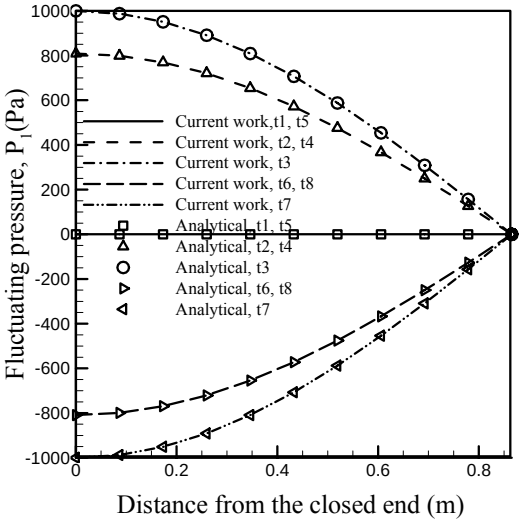

(d)

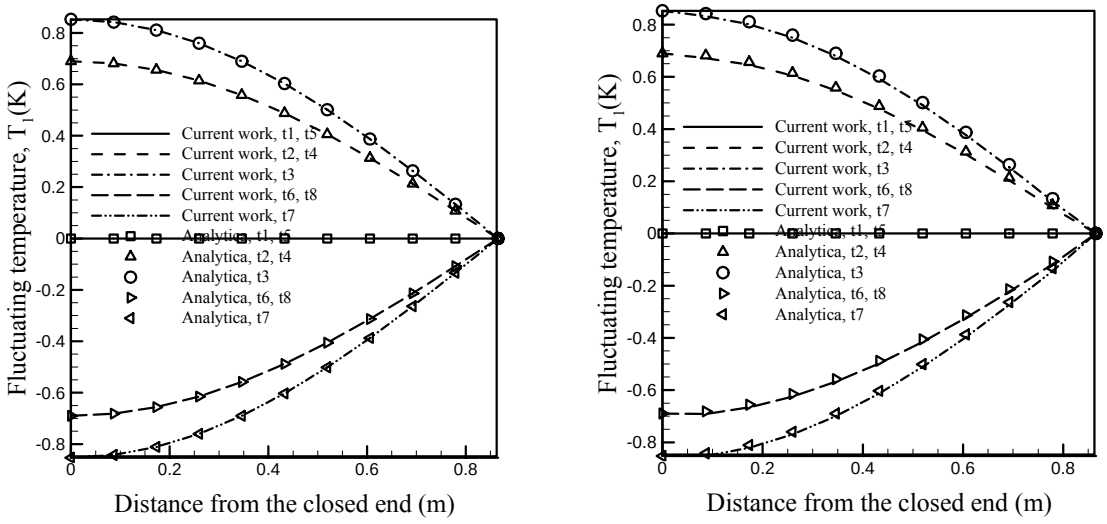

Figure C.7: Velocity fluctuations for (a) $\Delta x / \lambda = 9.99e-4$, (b) $\Delta x / \lambda = 8.33e-4$.
Pressure fluctuations for (c) $\Delta x / \lambda = 9.99e-4$, (d) $\Delta x / \lambda = 8.33e-4$.
Temperature fluctuations (e) $\Delta x / \lambda = 9.99e-4$, and (f) $\Delta x / \lambda = 8.33e-4$.

0.3% for 8.33×10^{-4}. Therefore, simulation results are independent on the domain length and of the working fluid considered in case 4.

C.4 Simulation of Thermoacoustic Effects in an Array of Thin Plates

The purpose of this section is to test the suitability of using STAR-CD to simulate thermoacoustic effects. In order to check if the thermoacoustic effect is simulated correctly, the results (energy flux density) from the simulations are compared with the results of numerical simulations (Run No. 2 and 5) performed by Cao et al. [1996]. The reason that the results of Cao et al. [1996] are chosen is that the investigation of Cao et al. [1996] is one of only a few numerical studies of thermoacoustic stacks that solve the full, two-dimensional Navier Stokes equation along with the energy equation.

Arrays of thin plates that are maintained at a constant temperature are included in the simulation domain. By applying the same oscillatory boundary conditions at the right and left ends of the simulation domain as those used in the standing wave simulations (**Section** C.3), a thermoacoustic couple can be simulated. The way Cao et al. chose the

extent of the simulation domain in order to reduce its size and the way the boundary conditions are specified are exactly followed in the current simulation to replicate the test cases of Cao et al. [1996]. From a physical point of view, an isothermal stack plate boundary condition is not very realistic because there is typically a temperature gradient along the stack plate due to thermoacoustic effects. However, this condition allows us to obtain thermoacoustic effect. It also allows a mean temperature gradient to develop in the fluid. From a computational point of view, an isothermal stack plate is attractive because a shorter time is required to reach a steady state within the stack region. Only 20 iterations are required to reach a steady state. Moreover, this simple problem allows the study of important phenomena, such as the effect of working fluid, geometric, and operating conditions on the stack performance.

C.4.1 Geometry and Boundary Conditions

A schematic of the system being modeled is shown in Fig. C.8(a). The thermoacoustic

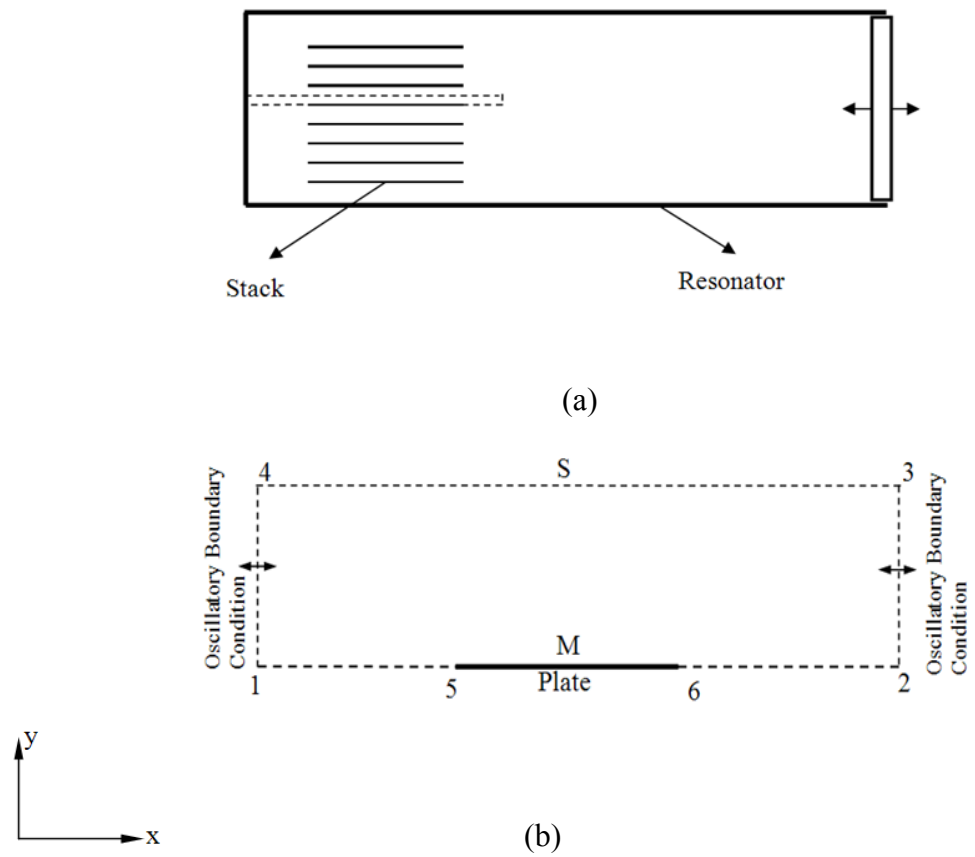

Figure C.8: (a) Computational domain and (b) boundary conditions.

couple is a stack of a few short plates which have thickness usually small compared to the other two dimensions. The problem can be regarded as two-dimensional in the case of small aspect ratio of the gap between the plates to the width of the plates. Since a stack is composed of a large number of identical plates, the problem can be further simplified by considering the domain in Fig. C.8(b). Table C.2 lists the parameters used by Cao et al, where L_s is the length of the stack, L_c is the length of the computational domain, and x_E is the starting position of the stack. The domain contains one surface of an isothermal single plate in a helium filled resonator. The plate thickness is not modeled. y_0 is the plate half-spacing. The above mentioned operating conditions are chosen in the current simulation

Table C.2: Parameters used in Cao et al. [1996]

Run No.	Pr	δ_k / y_0	x_E / λ	M	L_s	L_c	Mean Press. (kPa)	Mean Temp. (K)	Frequency (Hz)
2	0.68	0.3	0.1	0.01	0.024λ	0.041λ	10	300	100
5	0.68	0.3	0.1	0.03	0.024λ	0.041λ	10	300	100

to replicate the test cases of Cao et al. [1996]. Tables C.3 to C.5 list the magnitudes of the input variables, fluid, flow, and geometric properties for run 2. The selected boundary conditions in the current simulation are similar to the standing wave simulations (**Section** C.3) except the left boundary (boundary side 14, in Fig. C.8(b)) is replaced by oscillating velocity and temperature as in the right boundary 23 in Fig. C.8(b). The boundary conditions on the plate (5 to 6) in Fig. C.8(b) are

$$\begin{aligned} u &= 0, \\ v &= 0, \text{and} \\ T &= T_m \end{aligned} \tag{C.17a}$$

The distance of the vertical boundaries from the plate is 0.02λ. The boundary conditions on the horizontal surfaces (boundary side 43, 15 and 62) are

$$\begin{aligned} v &= 0, \\ \frac{dT}{dy} &= 0 \end{aligned} \tag{C.17b}$$

Table C.3: Input Variables

Mean pressure of the fluid (kPa)	10
Mean temperature of the fluid (K)	300
Frequency (Hz)	100
DR (Drive ratio)	1.7%

Table C.4: Flow Variables

Mean sound speed (m/sec.)	1019.143
Amplitude of the fluct. pressure (Pa)	170
Amplitude of the fluct. velocity (m/sec.)	10.395
Amplitude of the fluct. temperature (K.)	2.037

Table C.5: Other Variables

Wavelength (mm)	10191.43
Thermal penetration depth (mm)	2.390
Viscous penetration depth (mm)	2.000
Vertical distance of the domain (mm)	7.966
Length of the stack (mm)	244.549
Length of the domain (mm)	426.453
Particle displacement length (mm)	16.538

C.4.2 Preliminary Tests

Before simulating the test cases, some of the grid dependency tests are carried out in the current work by varying the grid sizes around those used by Cao et al. [1996].

C.4.2.1 Grid Dependency Tests

Run 2 of Cao et al. [1996] have used as the datum condition for grid dependency tests. The grid spacing (Δx_1=3.0575mm, Δy_1 =0.207 mm) used by Cao et al. [1996] in the x and y directions is uniform. Since the computational domain in the x direction contains only a small portion of the stack region, and the spacing between the stack plates in the y

direction is of the order of the viscous penetration depth, uniform grid spacing in the x and y directions are justified. Three different cases considered for the grid dependency and convergence tests are presented in Table C.6.

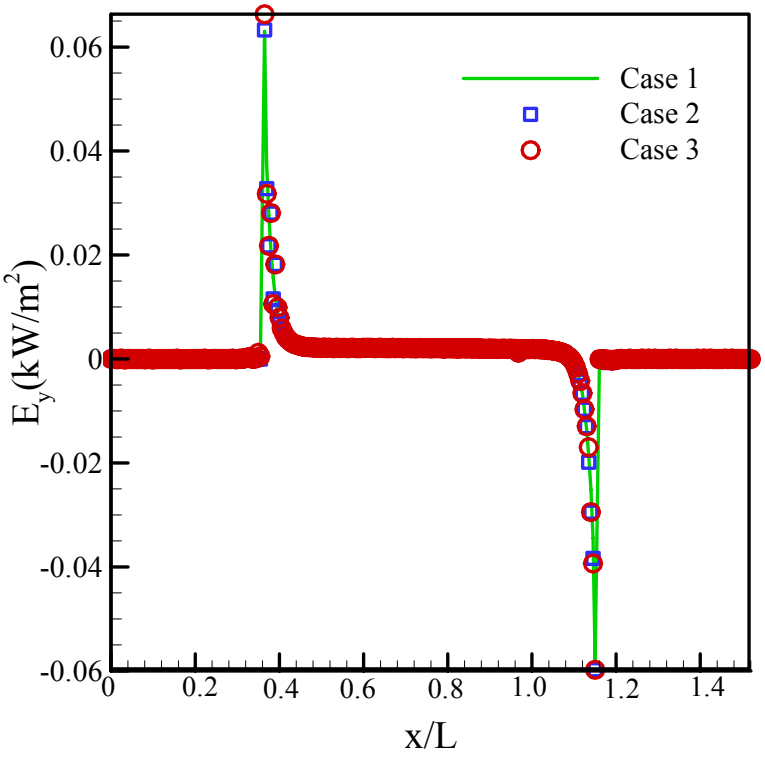

Figure C.9: Time averaged energy flux density in the y-direction at the surface of the plate for all the three different cases.

Figure C.9 shows all of the cases that have been considered for the vertical component of time-averaged energy flux density E_y (kW/m^2) vs. x/L at the plate surface. Energy flux density is discussed in **Section** C.4.3.1. The shapes of the curves are almost identical for all of the cases considered but the differences are largest near the left edge of the plate. The differences in the heights of the peaks at each end of the plate are more dependent on the size of Δx than on those of Δy and Δt. This is because the x-coordinates of the cell center in some simulations are slightly offset due to the differences in grid sizes and when the peak is very sharp, the offset will result in a peak height.

Table C.6: Cases considered for the grid dependency and convergence tests

Case	Δx	Δy	Δt
1	$0.7\Delta x_1$	$0.7\Delta y_1$	0.25% of the duration of cycle
2	$0.7\Delta x_1$	$0.7\Delta y_1$	0.5% of the duration of cycle
3	$0.8\Delta x_1$	$0.7\Delta y_1$	0.25% of the duration of cycle

C.4.2.2 Convergence Tests

When an array of thin plates are introduced into the simulation domain, other criteria to stop the iterations are also considered based on the important quantity in the thermoacoustic effect. Therefore, time averaged y-component of energy flux density (Eq. (C.18)) at the stack plate surface or the time averaged heat flux are considered. Monitoring the convergence rate of either quantity is appropriate as the *y*-component of energy flux at the stack surface should be equal to the heat flux in to the plate. Heat flux is calculated using Fourier's Law of heat conduction with the temperature gradient being based on the temperature of the stack plate and that of the gas at Δy cell away from the surface. In the current work, a simulation is considered to have converged when the relative change in the time averaged heat and energy fluxes are of the order of 0.1% for two consecutive cycles. At steady state, any energy dissipated within the simulation domain should leave through the isothermal stack plate and the same amount of energy should enter the domain through boundary 23. At boundaries 23 and 14, the amplitudes of $p_1, u_1,$ and T_1 are prescribed, not their gradients, therefore the boundaries can compensate for any energy dissipation in the domain. Results of convergence tests are provided in Appendix C.6.

C.4.3 Comparisons of the Results

C.4.3.1 Energy Flux Density

Cao et al. [1996] have used an expression for energy flux density vector given in Eq. (C.18), the concept of which was introduced by Landau and Lifshitz [1982]. Detailed of the energy flux density equation is discussed in Chapter 4.

$$\dot{\mathbf{E}} = \rho \mathbf{V}\left(\frac{1}{2}|\mathbf{V}|^2 + h\right) - \mathbf{V}.\boldsymbol{\sigma} - k\,\mathbf{grad}(T) \qquad \text{(C.18)}$$

Cao et al. [1996] calculate $\dot{\mathbf{E}}$ (W/m^2) near a thermoacoustic couple and present their results quantitatively using energy flux density. Comparison of the current numerical result with the result of Cao et al. [1996] for the vertical component of time-averaged energy flux density E_y (kW/m^2) vs. x/L at the plate surface is presented in Fig. C.10. The

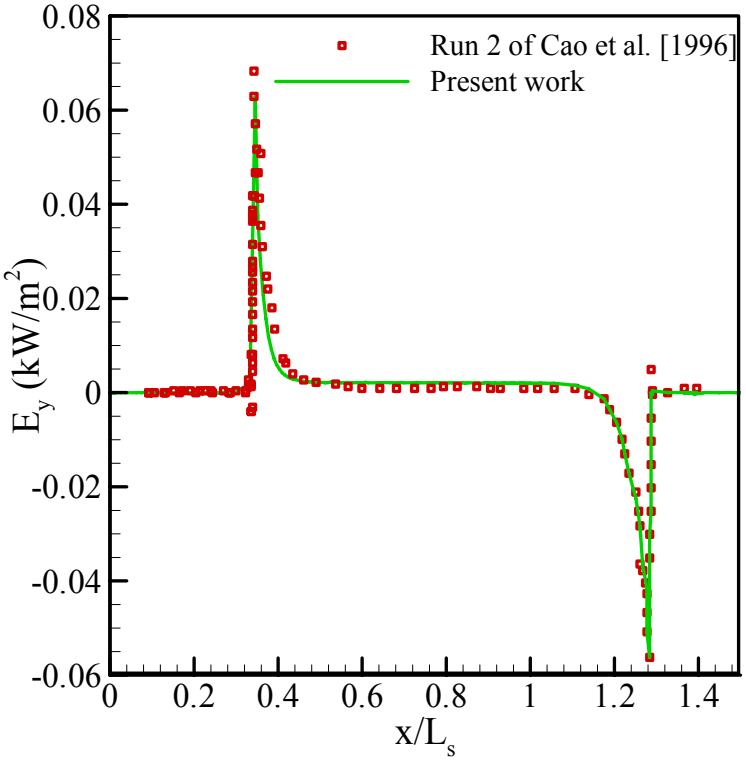

Figure C.10: Energy flux density at the plate surface for run 2 of Cao et al. [1996] and the current work.

grid sizes are $\Delta x = 1.423$ mm and $\Delta y = 0.131$ mm, and the time step size is chosen to be 0.25% of the duration of cycle, i.e., case 2 of Table C.6 has been considered. The data of Cao's work are read from their paper (Cao et al. [1996]) and will contain a read off error. Overall the agreement is sound (within 1%) with the result of Cao et al. [1996], except at the left edge of the plate where the results differ by approximately 6%. However, this is not considered significant as the peak is very narrow and sharp and its height depends on the grid resolution as discussed in **Section** C.4.2.1. The time averaged energy flux at the

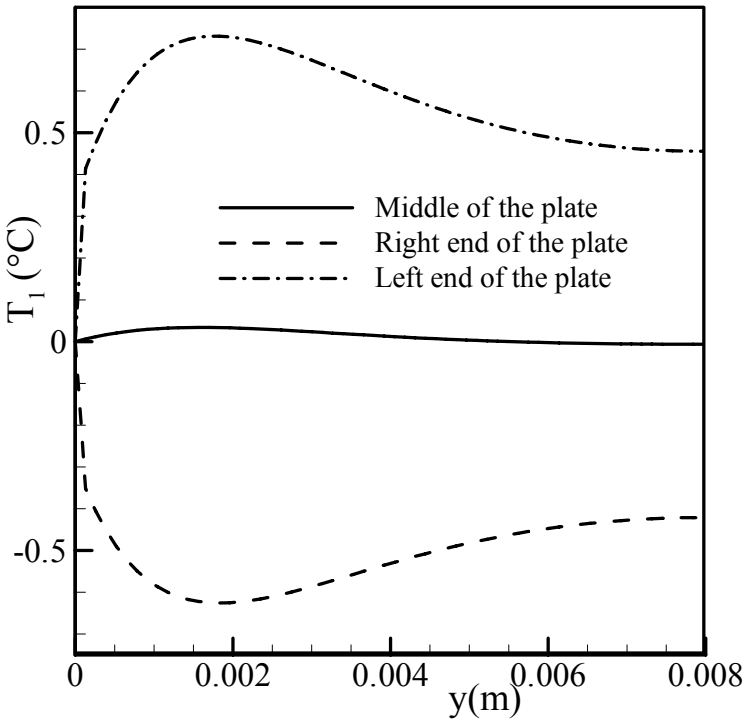

Figure C.11: Time averaged temperature fluctuations vs. y.

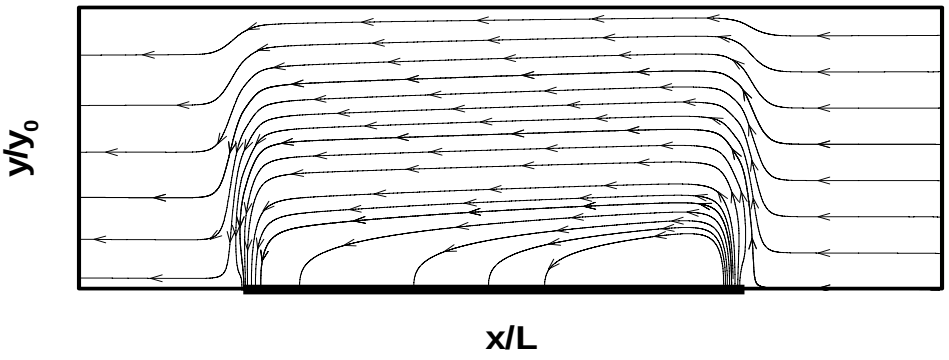

Figure C.12: Energy streamline pattern at the plate surface. The whole computational domain is displayed: $0 \le y/y_0 \le 1;\ 0.8 \le x/L \le 1.7$.

wall surface is negative for a heat flux entering the gas from the wall and positive for it leaving the gas through the wall. Recall that, at the lower boundary (boundary 56) in Fig. C.8(b), where velocity is zero, the strong energy flux density at the edges of the plate is due to heat conduction term. In the middle of the plate, the negligible energy flux density values are due to the small conduction terms (as shown by the temperature profiles in Fig. C.11). In Cao's results, the small spikes (which are numerical errors as they do not reflect the physical situation) appear just outside of both edges of the stack plate which do not appear in the current simulation.

For temporally periodic problems like thermoacoustic engines, the time-averaged total energy flow is a conserved quantity (like mass flow in an incompressible fluid); so that it can be displayed using streamlines (Cao et al. [1996], Mahmud and Fraser [2007]). Mahmud and Fraser [2007] proposed "energy streamlines" as a visualization tool for total energy flow in 2-D problems. "Total energy" includes all relevant forms of energy; for example thermal, potential, kinetic, magnetic, electrical, and chemical. Kimura and Bejan [1983] proposed ''heatline" as a powerful alternative way to visualize thermal energy flow. Heatlines simultaneously consider both conducted and convected thermal energies (will be discussed in **Section** C.8.3). One of the essential requirements before calculating the energy stream functions is to formulate the energy flux density vector ($\dot{\mathbf{E}}$) for a particular problem. At any particular location (for example, $P(x, y)$) inside the channels, $\dot{\mathbf{E}}$ of that location is tangent to the energy streamline passing through the point $P(x, y)$. In 2-D problems, the energy stream function can be calculated by solving a Poisson equation of type (Mahmud and Fraser [2007])

$$\frac{\partial^2 \Phi}{\partial x^2} + \frac{\partial^2 \Phi}{\partial y^2} = -(\nabla \times \dot{\mathbf{E}}).\hat{\mathrm{k}} = \frac{\partial E_x}{\partial y} - \frac{\partial E_y}{\partial x}, \tag{C.19}$$

where Φ, $\dot{\mathbf{E}}$, and $\hat{\mathrm{k}}$ are the energy stream function, energy flux density vector, and unit vector to the z direction, respectively. The required boundary condition for Eq. (C.19) is

$$\Phi_{\mathrm{P,\,b}} = \Phi_{\mathrm{ref,\,b}} + \int_{\mathrm{ref,\,b}}^{\mathrm{P,\,b}} \dot{\mathbf{E}}.\hat{\mathbf{n}}\, ds_{\mathrm{b}}, \tag{C.20}$$

where subscripts 'b', 'ref', and 'P' represent value at the boundary, reference value, and a particular point in the boundary, respectively. ds_b is a small boundary segment whose surface normal is represented by $\hat{\mathbf{n}}$.

A typical energy streamline pattern of $\dot{\mathbf{E}}$ from the current simulation is presented in Fig. C.12. The density and direction of the energy streamlines (in Fig. C.12) indicate the magnitude and direction of the energy flux density. A magnification factor 50 is used in the y-direction for a clear visualization of the streamline pattern. The streamlines terminating on solid boundaries (in Fig. C.12) indicate energy flux due to conduction of heat since the velocity dependent terms in Eq. (C.18) are zero on solid boundary;

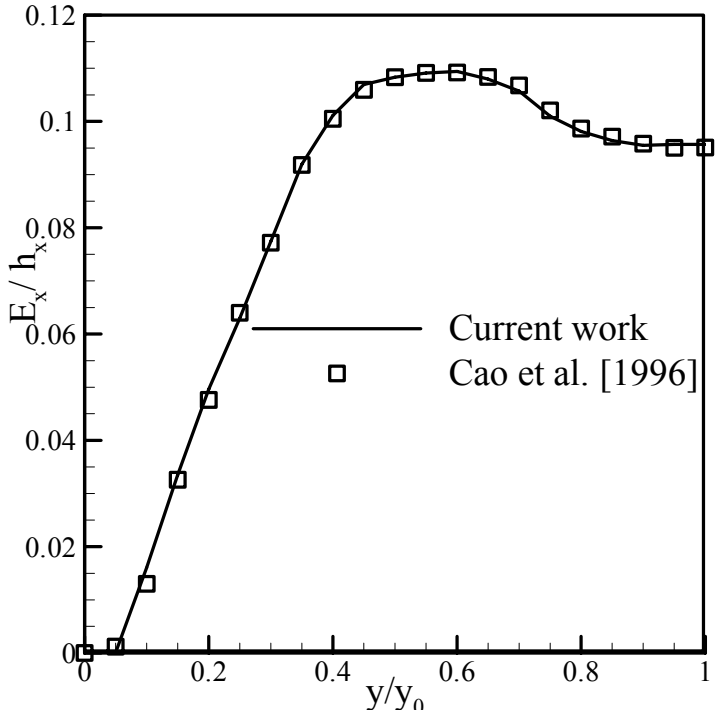

Figure C.13: Normalized energy flux in the *x* direction at the middle of the stack vs. y/y_0.

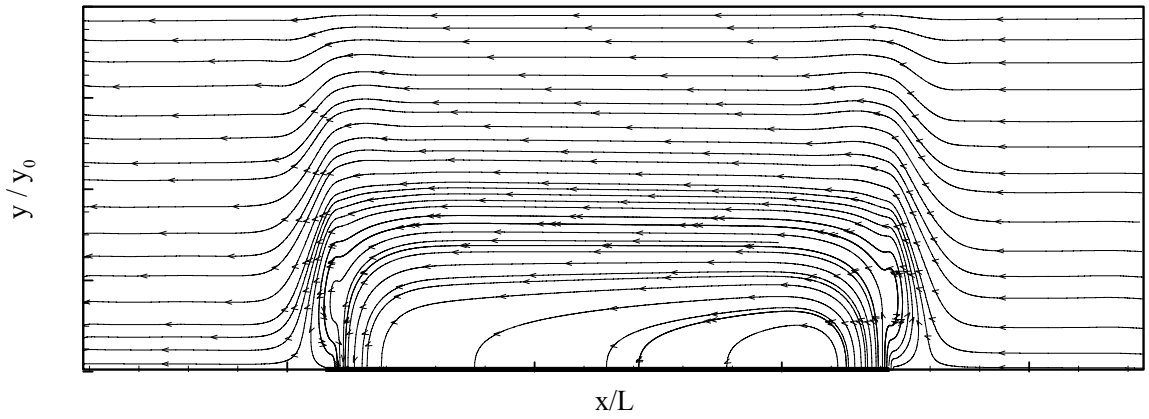

(a)

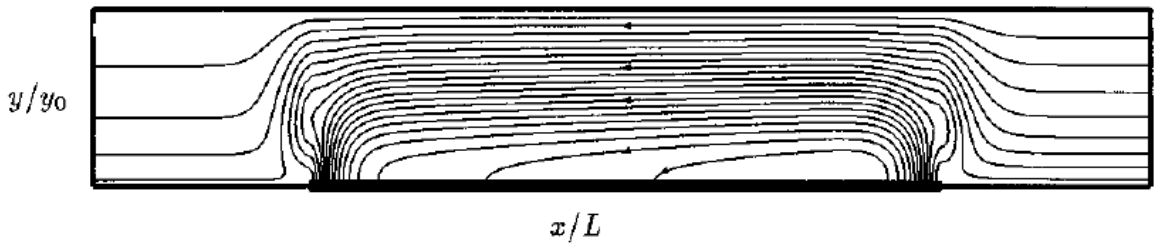

(b)

Figure C.14: (a) Energy streamline, the whole computational domain is displayed: $0 \le y / y_0 \le 1;\ 0.8 \le x / L \le 1.7$. (b) Energy streamline pattern of Cao et al. [1996] for case 1, $0 \le y / y_0 \le 1;\ 0 \le x / L \le 1.7$.

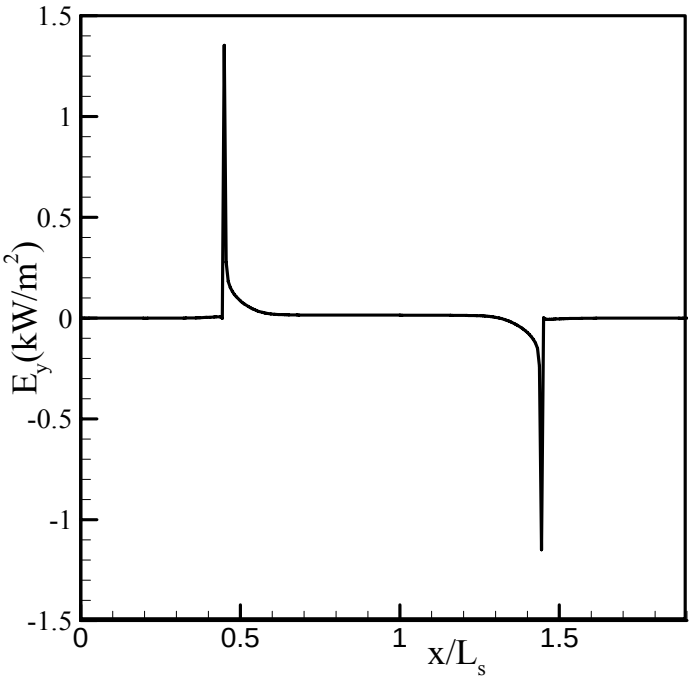

Figure C.15: Present result of energy flux in the *y* direction at the plate surface for run 5 of Cao et al. [1996].

elsewhere, they also include the velocity-dependent terms in Eq. (C.18). Energy flows almost horizontally from a source at the right end to a sink at the left end of the plate. Near the middle of the plate, the plate does not exchange appreciable net energy with the fluid (also shown in Chapter 7).

Now, Run No. 5 of Cao et al. [1996] is used to compare with the results of the current work. Cao et al. [1996] have provided the *x*-component of energy flux density data in the middle of the thermoacoustic stack, vs. y/y_0, at the center of the plate for Run No. 5. The only input parameter that has changed in Run No. 5 is the Mach number. Now Mach number has changed from 0.01 in run 2 to 0.03 in Run No. 5 which corresponds to a *DR*=5%. The time averaged *x*-component of energy flux density values is normalized by Cao et al. [1996] using the expression below:

$$h_x = \rho_m C_p \overline{T_1 u_1}, \tag{C.21}$$

where T_1 and u_1 are the temperature and velocity at point *S* in Fig. C.8(b). Thus Cao et al. [1996] have only used the second term of Eq. (C.18) in Eq. (C.21). This term is assumed to be dominant at point *S* in Fig. C.8(b), because at the center of the plate, the

temperature gradients in both the x and y directions and the y –component of velocity are very small. Figure C.13 presents the normalized energy flux in the x direction at the middle of the stack vs. y/y_0. The results of Cao et al. [1996] and the present work are in good agreement. Figures C.14(a) and (b) and Fig. C.15 present the energy streamline pattern for the current simulation, as well as Cao et al. [1996] for run 1, and the energy flux in the y direction for the current simulation, respectively. In Fig. C.14 (a), the vertical scale is stretched 50 times to show the details. The energy flux in the y direction is increased when Mach number is increased from 0.01 (in Fig. C.10) to 0.03 (in Fig. C.15), since energy flux density is proportional to the squared of Mach number (Eq. (66) of Swift [1988]).

C.4.3.2 Flow and Thermal Fields

In order to investigate the flow field, the instantaneous velocity fields are shown for Run No. 2. Figures C.16(a) to (h) show instantaneous velocity vectors at 1/8, 2/8 to 8/8 of a cycle respectively. Overall, sudden changes in the velocity profile are observed only at both edges of the plate at most time steps. Instantaneous velocity vectors at time step

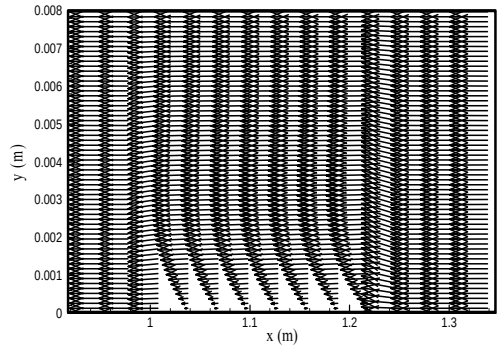

(a) $t1 = \tau / 8$

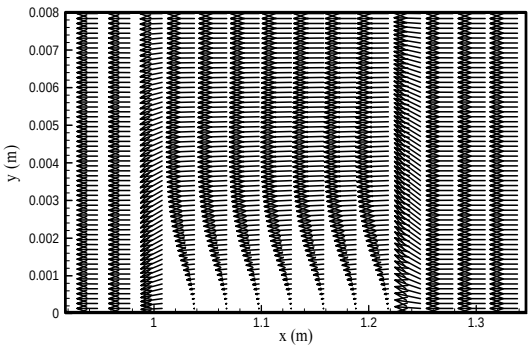

(b) $t2 = 2\tau / 8$

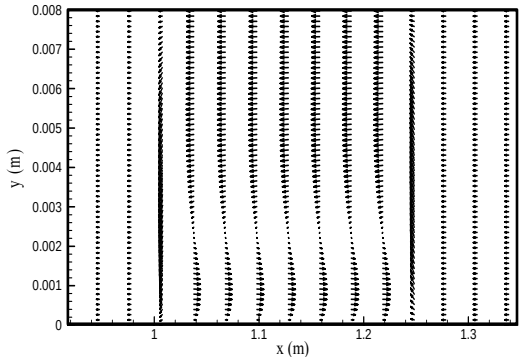

(c) $t3 = 3\tau / 8$

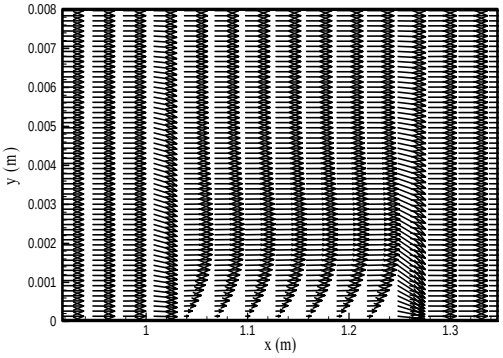

(d) $t4 = 4\tau / 8$

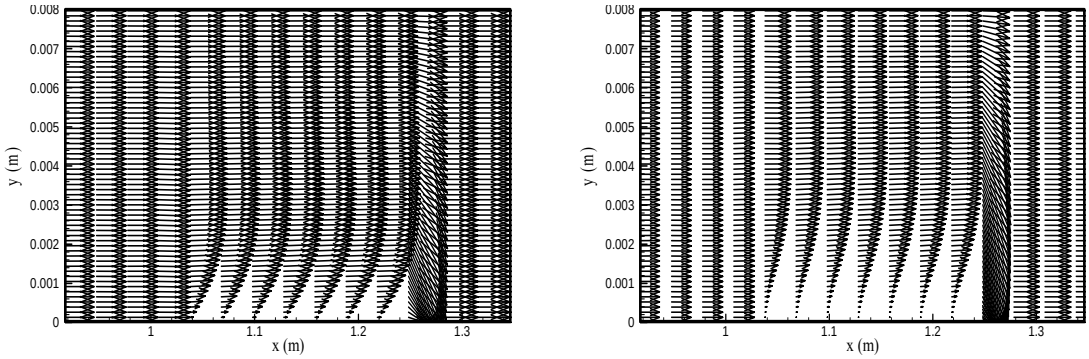

(e) $t5 = 5\tau / 8$ (f) $t6 = 6\tau / 8$

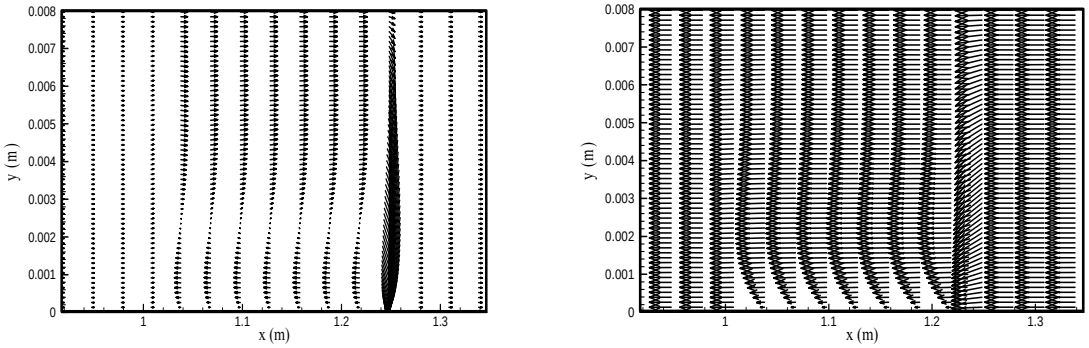

(g) $t7 = 7\tau / 8$ (h) $t8 = 8\tau / 8$

Figure C.16: Instantaneous flow fields, only every fifteenth vector is shown in the *x*- direction and every vector in the *y*-direction.

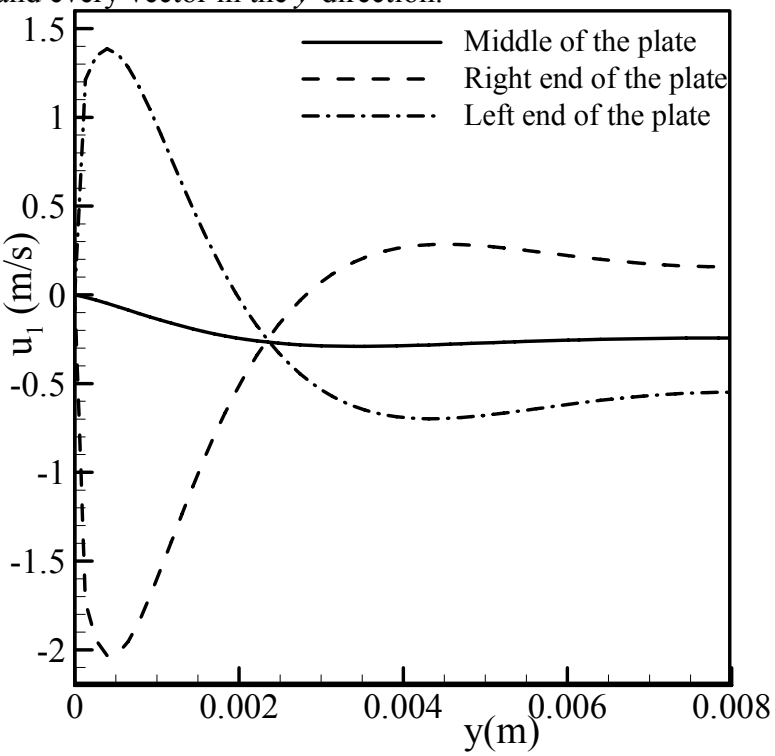

Figure C.17: Time averaged u_1 vs. y.

$t = 3\tau/8$ (when the flow changes direction), show a pattern which is characteristic of a vortical motion over the plate. At this time step, the flow near the plate ends and the flow near the center of the passage are in opposite directions. Figure C.17 presents time averaged u_1 as a function of y at three different locations on a stack plate. The time averaged velocity profile show circulations near the stack edges and a uniform profile at the middle of the plate. Therefore flow near the stack edges is non-linear at $DR = 1.7\%$, and the magnitude of flow circulation is higher near the right stack end, since this end is near the velocity anti-node.

Therefore, the numerical simulations performed in **Section** C.4.3 show that STAR-CD has been able to simulate thermoacoustic effect produced by the interaction between the oscillating fluid and the stack plate surface. A very good agreement is observed between the present simulation and the results in the existing literature (Cao et al. [1996]). An increase in fluid temperature near the pressure anti-node and a decrease near the velocity anti-node is observed which is typical for a thermoacoustic refrigerator. Flow circulations are observed near the stack edges with increased magnitude near the velocity anti-node of the standing wave.

The next section presents some of the results of the influence of Pr and DR on flow and thermal fields.

C.5 Some Results of Variation of Pr and Operating Conditions on Flow and Thermal Fields

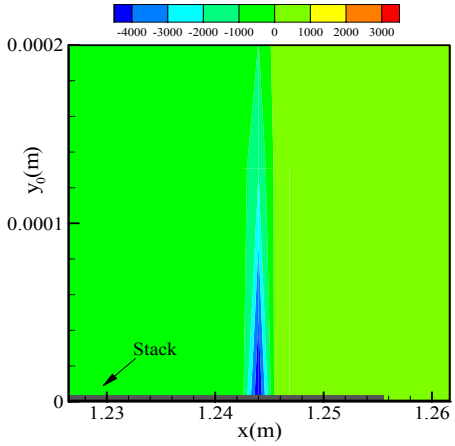

(a) x-component of velocity gradients in the y-direction, 130x magnification factor

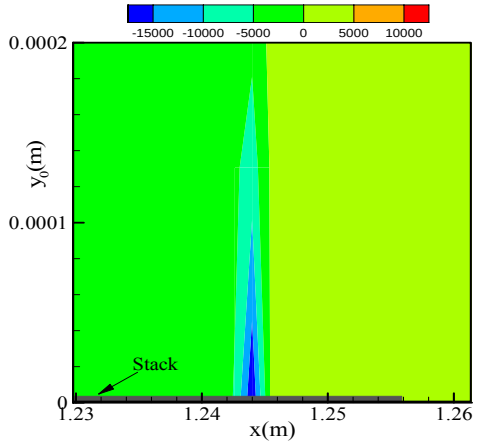

(b) x-component of velocity gradients in the y-direction,130x magnification factor

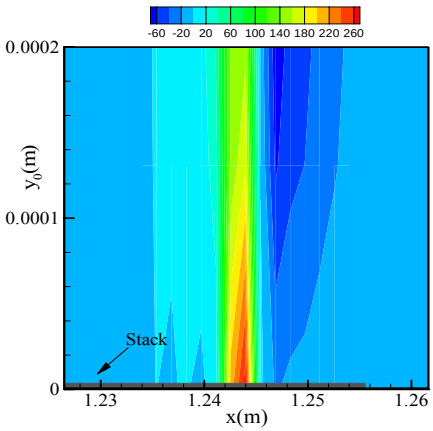

(c) *y*-component of velocity gradients in the *y*-direction, 130x magnification factor

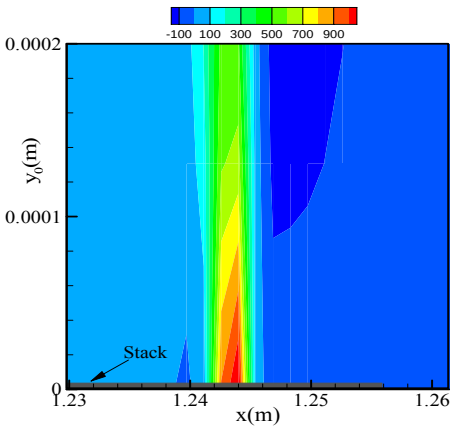

(d) *y*-component of velocity gradients in the *y*-direction, 130x magnification factor

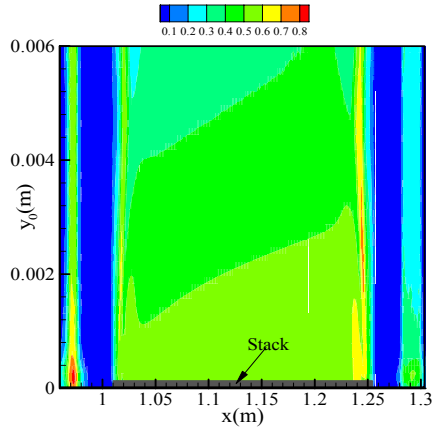

(e) fluid friction irreversibility ratio,12x magnification factor

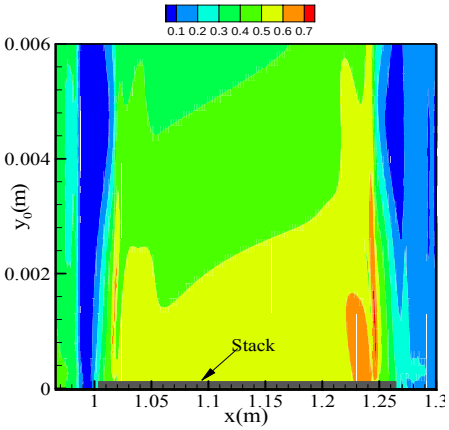

(f) fluid friction irreversibility ratio,12x magnification factor

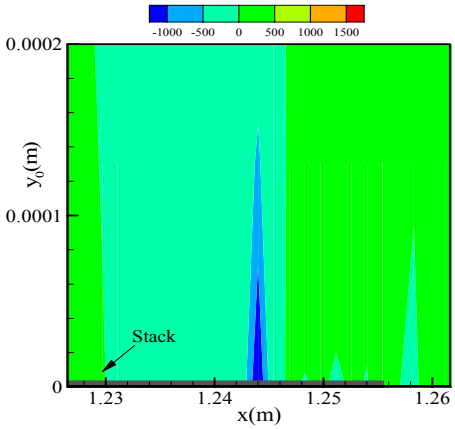

(g) temperature gradients in the *y*-direction, 130x magnification factor

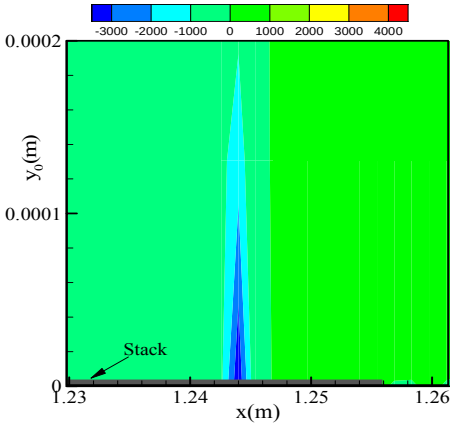

(h) temperature gradients in the *y*-direction, 130x magnification factor

Figure C.18: (a) and (b) *x*-component of velocity gradients in the *y*-direction, (c) and (d) *y*-component of velocity gradients in the *y*-direction, (e) and (f) fluid friction irreversibility ratios, (g) and (h) temperature gradients in the *y*-direction.

Figure C.18(a) to (h) show some of the results for Run No. 1 and 4 (in Table 9.1) that is for the DR of 1.7% and 5%, respectively. Figure 9.18(a) to (h) thus compare two different operating conditions while helium is used as a working fluid, with $p_m = 10$ kPa, $f = 100$ Hz, $y_0 = 3.33\delta_k$, $\delta_k = 2.39$ mm, and stack lengths are 6.84 and 2.32 times particle displacement amplitude.

C.6 Convergence Monitoring of the Thermoacoustic Couple Model of Section C.4

When an array of thin plates is introduced into the simulation domain, it takes longer to reach a steady state than the standing wave simulations. The difference between the two cases is that for a standing wave simulation the computational domain is adiabatic, whereas for the thin plate's simulations, there is an isothermal region.

Time averaged heat flux or *y*-component of energy flux density at the plate surface is an important thermoacoustic effect. In the current work, a simulation is considered to have converged when the relative change in the time averaged heat and energy fluxes are of the order of 0.1% for two consecutive cycles. In order to test whether a solution has been converged or not, time averaged *y*-component of energy flux density at the plate surface are plotted in Fig. C .19 for Run 2 of Cao et al. [1996] for three cycles. For the last two consecutive cycles E_y values almost coincide with each other as shown in Fig. C.19. Figure C.20 shows the time averaged heat flux (Q_y) at the stack plate surface for the similar case to that of Fig. C.19. Time averaged heat flux at the stack plate surface should be equal to the time averaged *y*-component of energy flux density because of the zero velocities at the stack plate surface. Outside the stack plate surface, time averaged heat flux is zero because of the zero temperature gradient in the *y*-direction. The difference between the integration of heat flux (Fig.C.19) and *y*-component of energy flux density (Fig.C.20) over the stack plate surface are within 0.05% for run no. 2 and 5 of Cao et al. [1996] that have been replicated in the present study in **Section** C.4, and therefore have achieved steady state solutions.

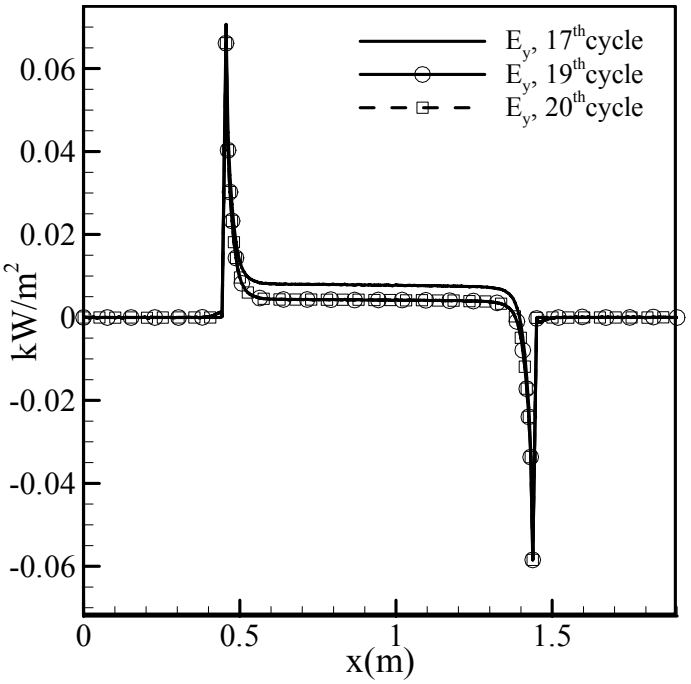

Figure C.19: Time averaged *y*-component of energy flux density at the stack plate surface for run 2 of Cao et al. [1996], for three cycles.

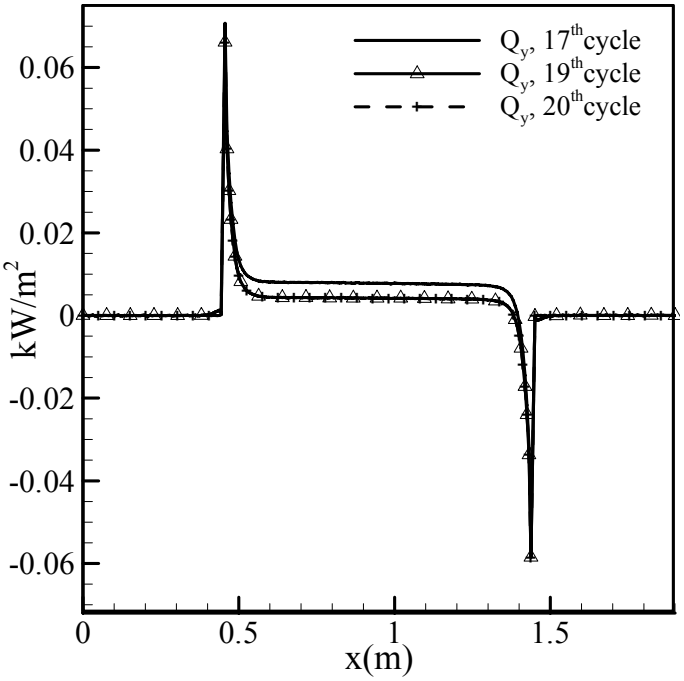

Figure C.20: Time averaged heat flux at the stack plate surface for run 2 of Cao et al. [1996], for three cycles.

C.7 Convergence Monitoring of the Thermoacoustic Couple Model of Section 9.2

Table C.7 shows the convergence results for all the cases considered in Section C.4. The negative E_{x23} means that energy flows from the boundary 23(in Fig. C.8(b)) in to the computational domain. E_y is negative when energy enters the domain through the isothermal plate and positive when it is going out of the domain.

Table C.7: Convergence results for all cases

Run. no	Fluid	y_0 (mm)	DR %	E_{x23} (kW)	q_{56} (kW)	E_y (kW)	q_{error} (%)
1	He	$3.33\,\delta_k$	1.7	-0.04	0.045	0.045	0.5
2	He	$3.33\,\delta_k$	1.7	-0.234	0.244	0.244	1
3	He	$3.33\,\delta_k$	1.7	-1.4	1.41	1.41	1
4	He	$3.33\,\delta_k$	5	-0.277	0.278	0.278	0.1
5	He	$3.33\,\delta_k$	5	-1.15	1.15	1.15	0.16
6	He	$3.33\,\delta_k$	5	-3.63	3.64	3.64	0.9
7	He	$3.33\,\delta_k$	8.5	-0.8186	0.82	0.82	0.1
8	He	$3.33\,\delta_k$	8.5	-2.56	2.57	2.57	1
9	He	$3.33\,\delta_k$	8.5	-8.09	8.1	8.1	1
10	He	$3.33\,\delta_k$	10	-1.065	1.07	1.07	0.5
11	He	$3.33\,\delta_k$	10	-3.34	3.35	3.35	0.9
12	He	$3.33\,\delta_k$	10	-10.52	10.53	10.53	1
13	He	$2.0\,\delta_k$	5	-1.16	1.17	1.17	1
14	He	$2.0\,\delta_k$	5	-3.7	3.71	3.71	1
15	He	$2.0\,\delta_k$	8.5	-2.57	2.58	2.58	1
16	He	$2.0\,\delta_k$	8.5	-6.34	6.35	6.35	1
17	He	$1.0\,\delta_k$	1.7	-0.00932	0.00978	0.00978	0.046

18	He	$1.0\,\delta_k$	1.7	-0.219	0.229	0.229	1
19	He	$1.0\,\delta_k$	1.7	-0.726	0.735	0.735	0.9
20	He	$1.0\,\delta_k$	5	-0.311	0.314	0.314	0.3
21	He	$1.0\,\delta_k$	5	-0.984	0.988	0.988	0.4
22	He	$1.0\,\delta_k$	5	-3.11	3.12	3.12	1
23	He	$1.0\,\delta_k$	8.5	-0.667	0.671	0.671	0.4
24	He	$1.0\,\delta_k$	8.5	-2.089	2.095	2.095	0.6
25	He	$1.0\,\delta_k$	8.5	-6.61	6.612	6.612	0.2
26	He	$1.0\,\delta_k$	10	-0.842	0.849	0.849	0.7
27	He	$1.0\,\delta_k$	10	-2.65	2.66	2.66	1
28	He	$1.0\,\delta_k$	10	-8.393	8.396	8.396	0.3
29	He-Xe	$3.33\,\delta_k$	1.7	-0.124	0.128	0.128	0.4
30	He-Xe	$3.33\,\delta_k$	1.7	-0.409	0.417	0.417	0.8
31	He-Xe	$3.33\,\delta_k$	5	-0.603	0.605	0.605	0.2
32	He-Xe	$3.33\,\delta_k$	5	-1.9	1.91	1.91	1
33	He-Xe	$3.33\,\delta_k$	10	-1.73	1.74	1.74	1
34	He-Xe	$3.33\,\delta_k$	10	-5.49	5.5	5.5	1
35	He-Xe	$1.0\,\delta_k$	1.7	-0.119	0.121	0.121	0.2
36	He-Xe	$1.0\,\delta_k$	1.7	-0.376	0.382	0.382	0.6
37	He-Xe	$1.0\,\delta_k$	5	-0.516	0.527	0.527	1.1
38	He-Xe	$1.0\,\delta_k$	5	-1.66	1.67	1.67	1
39	He-Xe	$1.0\,\delta_k$	10	-1.43	1.44	1.44	1
40	He-Xe	$1.0\,\delta_k$	10	-4.54	4.55	4.55	1
41	He	$3.33\,\delta_k$	1.7	-0.0226	0.0237	0.0237	0.11
42	He	$3.33\,\delta_k$	1.7	-0.12	0.13	0.13	1
43	He	$3.33\,\delta_k$	5	-0.579	0.584	0.584	0.5

C.8 Simulation of 2-D Stack

The flow, thermal, and energy fields near and within 2-D stack plates are simulated by numerical solution of the unsteady compressible Navier–Stokes, continuity, energy equations, and the equation of state (for air as the working fluid) in this section. The stack is assumed to be consisting of flat plates of equal thickness. The temperature of the stack is governed by the energy equation; therefore the entire problem is treated as a conjugate heat transfer problem.

C.8.1 Geometry and Boundary Conditions

A schematic of the system (2-D rectangular geometry), position of the stack in the acoustic field, and boundary conditions being modeled are shown in Fig. C.21(a), (b) and

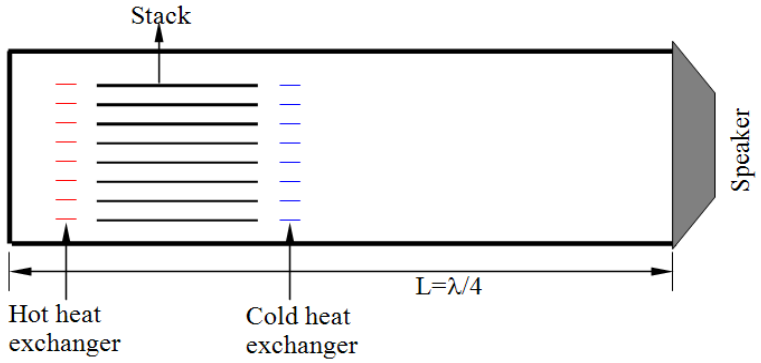

(a)

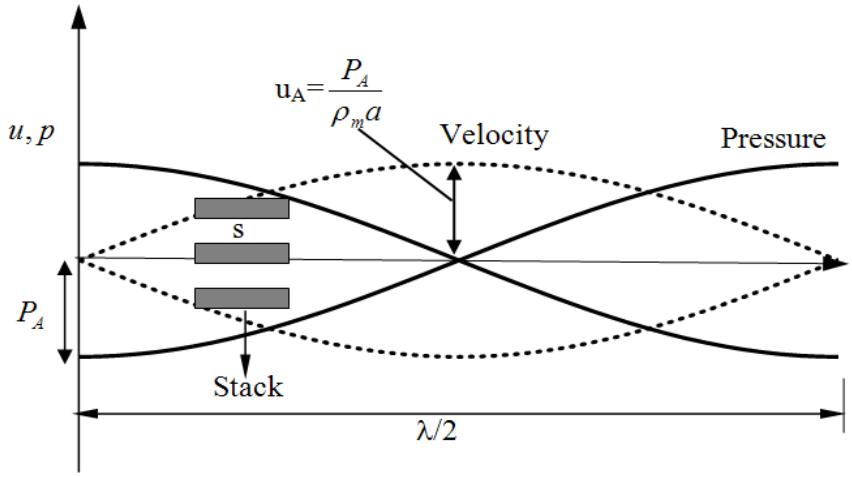

(b)

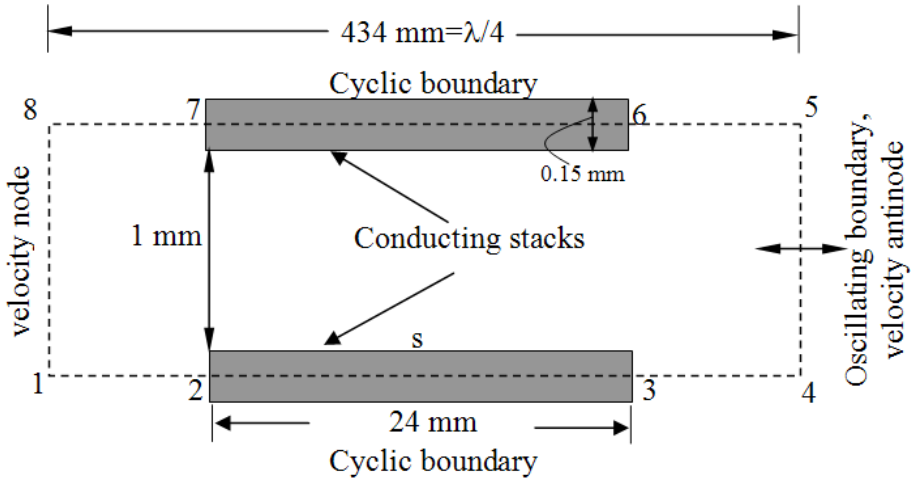

(c)

Figure C.21: (a) Thermoacoustic refrigerator, (b) location of the stack in the sound field, and (c) computational domain and boundary conditions.

(c), respectively. The computational domain includes the resonator end and finite thickness stack plates of length 24 mm (Blanc-Benon et al. [2003]), which is 1.4% of the acoustic wavelength. The computational domain in Fig. C.21(c) extends from the velocity node from the left to the velocity antinode to the right. The center of the stack plate (s) is assumed to be located midway between the velocity anti-node and the velocity node. The stack plates are made of glass and are modeled using a thermal conductivity $k_s = 1.0 W/mK$. The resonance tube is filled with air at a mean pressure $p_m = 100$ kPa and a mean temperature $T_m = 300K$. A drive ratio (is the ratio between pressure amplitude at the pressure anti-node (p_0) and the mean pressure (p_m)) of 0.7% is chosen. The resonance frequency of the tube is 200 Hz.

The boundary conditions on the vertical boundaries (boundary14 and boundary 23) are identical to **Section** C.4.1. The boundary conditions on the plate (gray area) are

$$u = 0, v = 0, \tag{C.22}$$

whereas cyclic boundary conditions are applied at horizontal boundaries sides 14 and 58 (horizontal sides, in Fig. C.21(c)) by imposing

$$T_{12} = T_{87}, T_{23} = T_{76}, T_{34} = T_{65}, \tag{C.23}$$

and

$$u_{12} = u_{87}, v_{12} = v_{87}, u_{34} = u_{65}, v_{34} = v_{65},$$

and the temperature of the stack is governed by the energy equation

$$\frac{\partial(\rho_s e_s)}{\partial t} = \frac{\partial}{\partial x_j}(k_s \frac{\partial T_s}{\partial x_j}), \tag{C.24}$$

in which $e_s = c_v T_s$ is the specific internal energy of the solid, ρ_s and k_s are the density and thermal conductivity of the solid material, and j=1, 2. The temperature dependence of all solid properties is ignored.

Turbulence is neglected for the present simulations because the critical Reynolds number, $\mathrm{Re}_\delta = \frac{\sqrt{2}u_A}{\sqrt{\nu\omega}} =$ 24.5 as defined by Merkli and Thomann [1975] is below 400. The domain length in the *x*-direction is equal to the 1/4 of the acoustic wave length and in the *y*-direction 6.7 times the gas viscous penetration depth evaluated at the mean temperature, respectively. In the present study, N_x=360, N_y=100, evenly spaced rectangular grids, where N_x and N_y are the number of control volumes in the *x* and *y* directions respectively. Further increase in N_x and N_y provide negligible improvement. The time step sizes tested are 0.25% and 0.5% of the duration of the cycle. To obtain better results, a time step size of 0.25% of the duration of the cycle is used for the present study.

C.8.2 Flow and Thermal Fields

Table C.8 and C.9 show the geometric and flow parameters that are considered for the present simulation. Figures C.22(a) to (c) show the pressure, velocity, and temperature fluctuations at 10 time steps in a cycle along the surface of the stack plate for pressure and temperature, and 6 cells away from the stack plate for velocity. The bump in the velocity profile indicates the presence of the stack. For providing a pictorial representation

Table C.8: Geometric parameters

Thickness of the stack (l)	0.15 mm
Stack spacing (y_0)	1 mm
Stack length(L_s)	24 mm
Blockage ratio ($B = y_0/(y_0 + l)$)	0.87

Table C.9: Flow parameters

Drive ratio (%)	0.7
Particle displacement amplitude=$2u_A/\omega$	2.76 mm
Reynolds number($\mathrm{Re}_\delta = \sqrt{2}\,u_A/\sqrt{\omega\nu}$)	24.5
Viscous penetration depth ($\delta_\upsilon = \sqrt{2\nu/\omega}$)	0.16 mm
y_0/δ_υ	6.7

of the flow, velocity streamlines are presented in Figs. C.23(a) to (j) at 1/10, 2/10 to 10/10 of a cycle respectively. A velocity streamline is defined as a continuous line within the fluid of which the tangent at any point is in the direction of the velocity at that point. Evolution of the streamline distribution during an acoustic cycle is summarized as follows. Figure C.23(a) is generated at the time at which the acoustic velocity reaches its first peak at the right oscillating boundary (side 45). For the first three time steps (Figs. C.23(a) to (c)), the fluid is approaching from right to left and the streamline

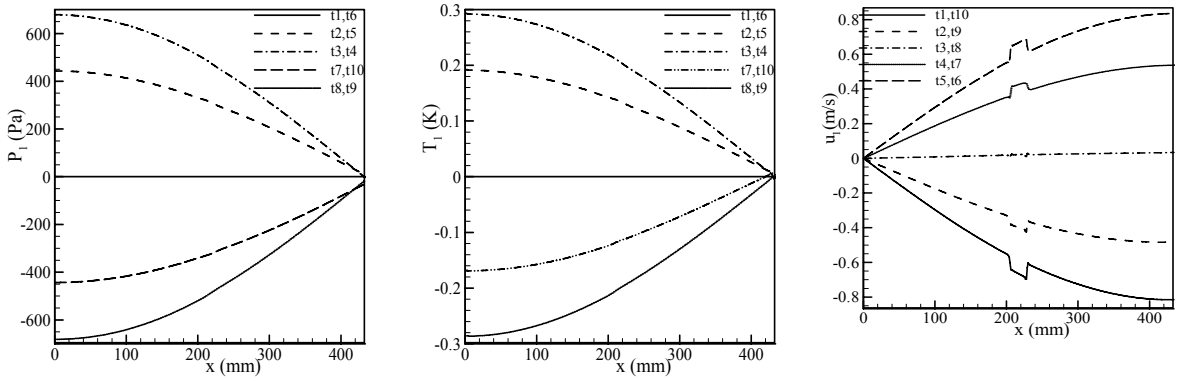

(a) (b) (c)

Figure C.22: Fluctuations of variables along the horizontal axis at the surface of the plate, t_1=T/10, t_2=2T/10, ……,t_{10}=T, (a) pressure, (b) temperature, and (c) velocity.

distribution is uniform everywhere. The flow decelerates as time progresses (Figs. C.23(b) to (c)). At the beginning of the 4th step (Fig. C.23(d)), the flow reverses and the streamlines show the presence of a pair of concentrated eddies located close to the plates. The concentrated eddies close to the plates are washed away as the flow accelerates at 5th step (Fig. C.23(e)). The acoustic velocity reaches its second peak in Fig. C.23(f) and starts to decelerate in Figs. C.23(g) to (h), reverses it direction in Fig. C.23(i), and gradually increases in Fig. 9.30(j). That is how an acoustic cycle is completed and a new

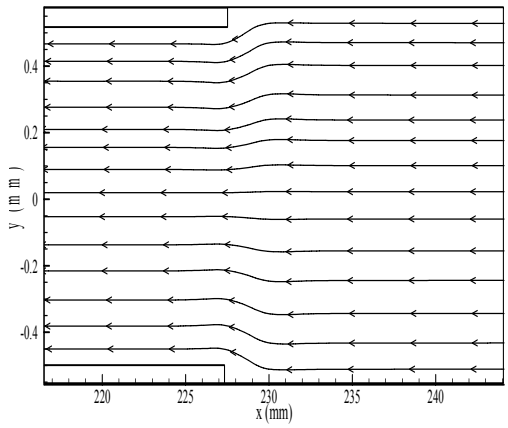

(a) t_1=T/10

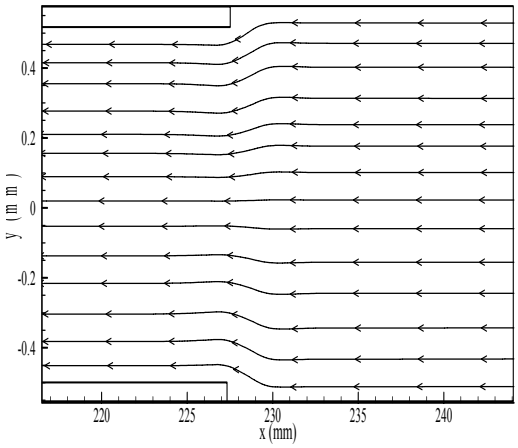

(b) t_2=2T/10

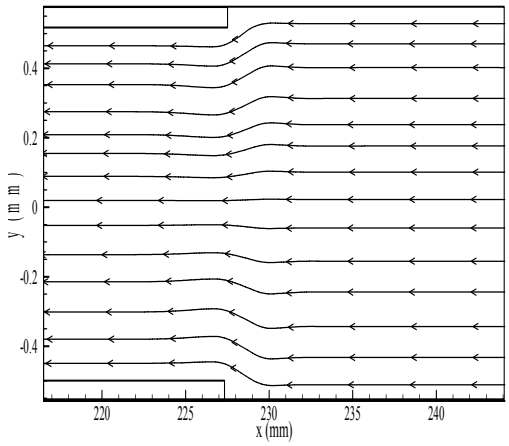

(c) t_3=3T/10

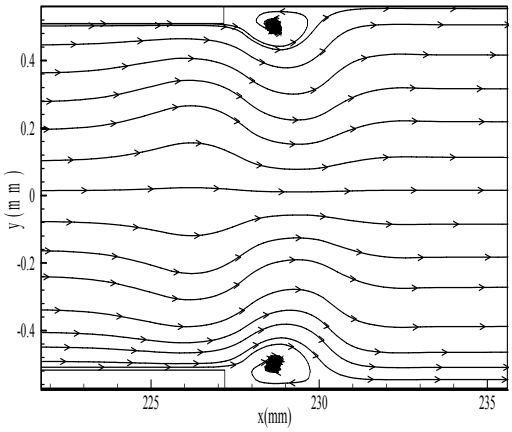

(d) t_4=T4/10

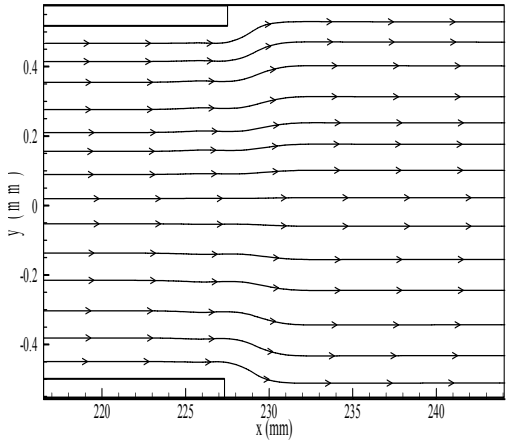

(e) t_5=5T/10

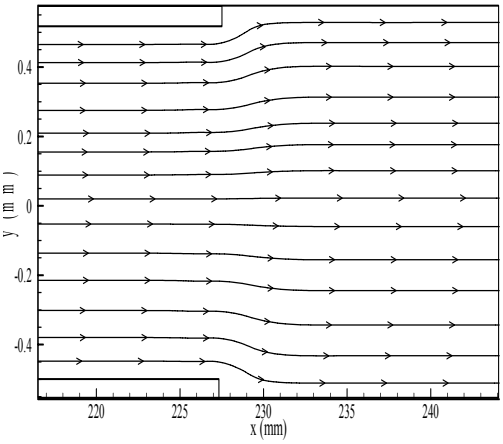

(f) t_6=6T/10

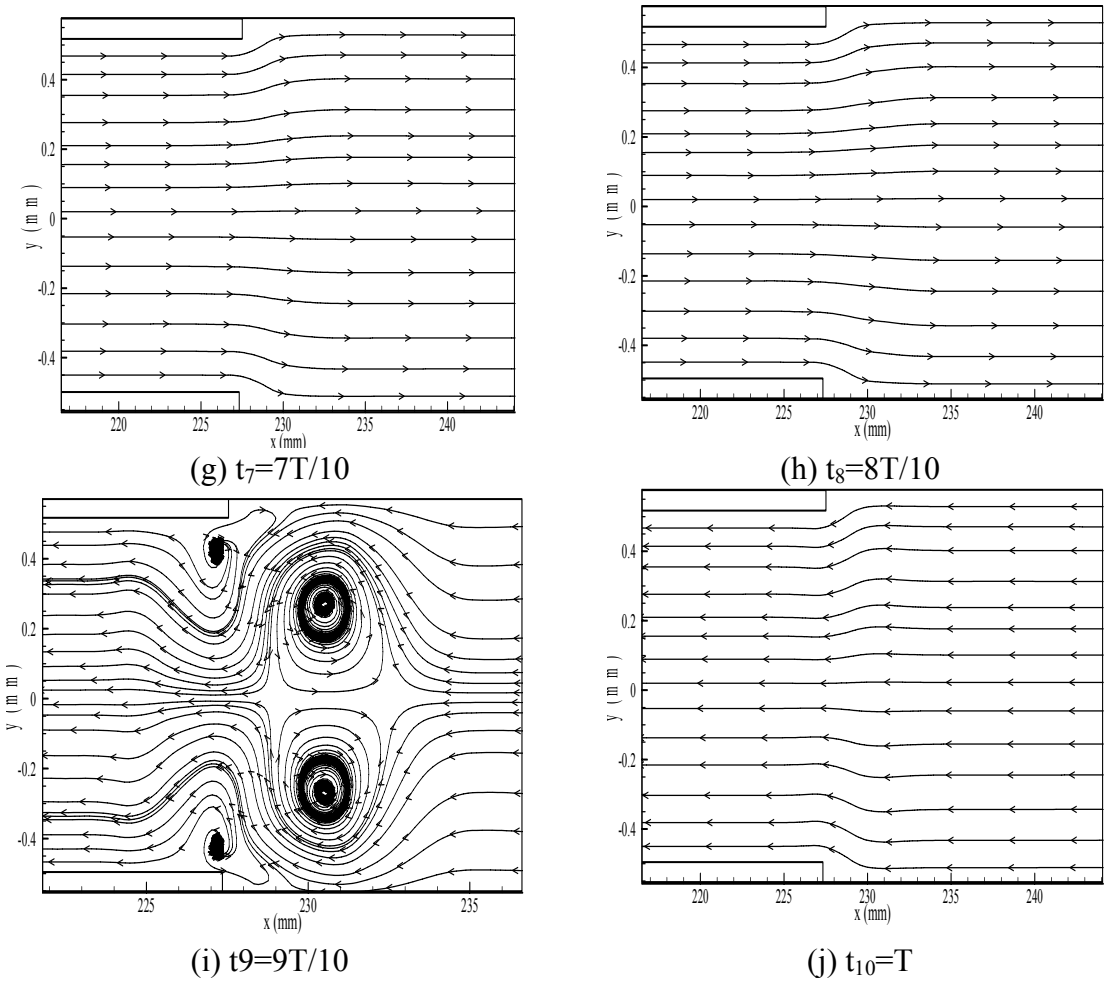

Figure C.23: Instantaneous oscillating velocity streamlines at 10 time step in a cycle. 15 x magnification factor is used.

cycle will begin again. Figures 9.30(a) and (f) are separated by one-half cycle; each is generated at a time when the acoustic velocity reaches its peak at the right oscillating boundary (side 45). The corresponding acoustic accelerations peak has opposite directions. Comparison of Figs. C.23(a) and (f) shows that the streamline distributions at these two stages are not mirror images with respect to the horizontal mid plane. The results of this visualization are in good qualitative agreement with the experimental results of Wetzel and Hermann [2000] and the numerical results of Worlikar and Knio [1999] and Worlikar et al. [1998], and Blanc-Benon et al. [2003]. It is observed that if the DR is increased from 0.7 to 2%, the strength of vortices at the stack edges increases. Also the thickness of the stack plate changes the streamline pattern near the stack region.

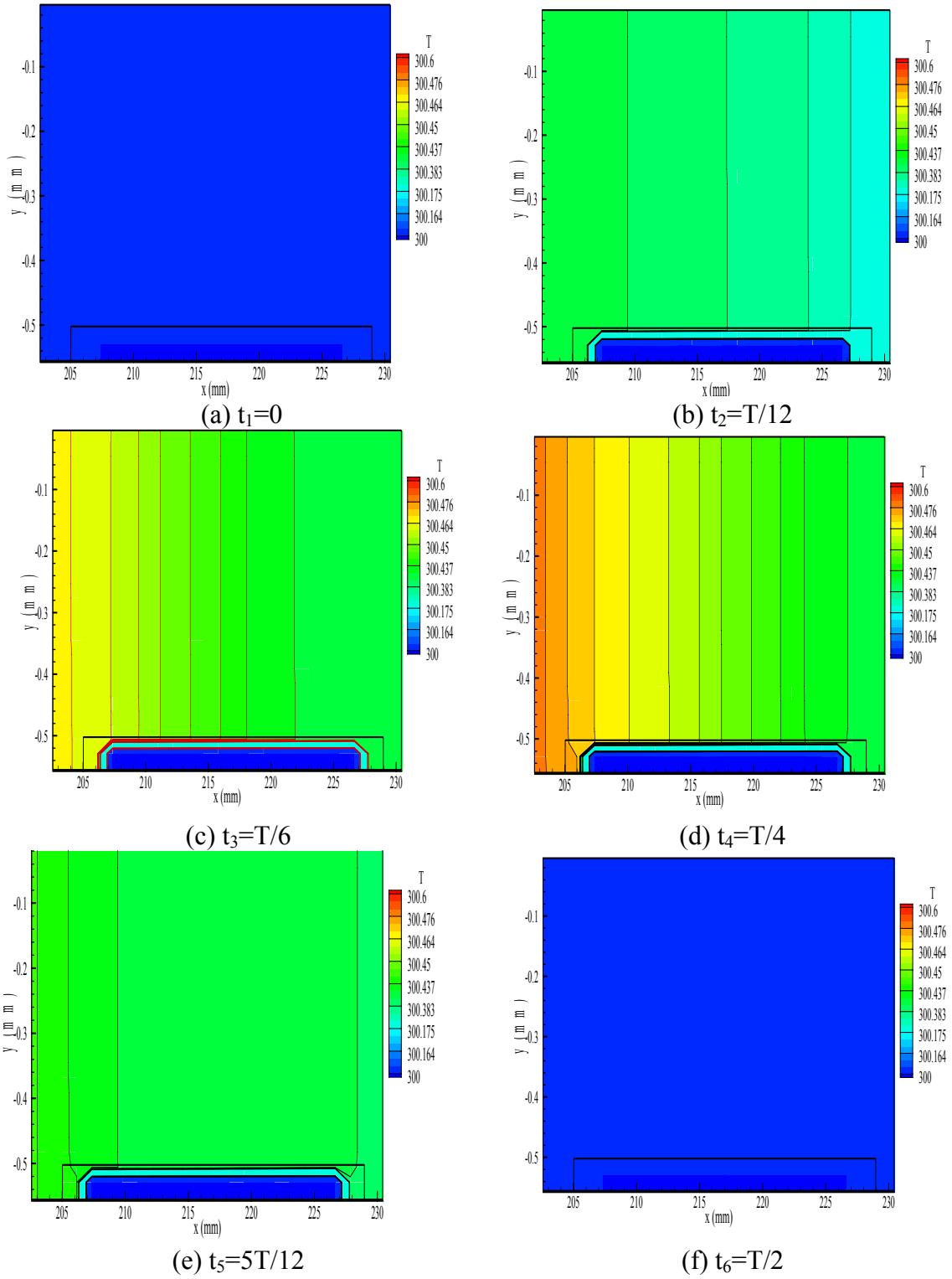

(a) $t_1=0$ (b) $t_2=T/12$

(c) $t_3=T/6$ (d) $t_4=T/4$

(e) $t_5=5T/12$ (f) $t_6=T/2$

Figure C.24: Time dependent temperature fields in the lower half at six time instants, $t_1=0$; $t_2=T/12$; $t_3=T/6$; $t_4=T/4$; $t_5=5T/12$; $t_6=T/2$, respectively of one half of a cycle. 12 x magnification factor is used. Temperature scale is in Kelvin.

The time dependent temperature distributions in the lower half of the channel are shown in Figs. C.24(a) to (f). The upper half of the temperature fields mirrors the distributions displayed in Fig. C.24. Evolution of the temperature contours during one half of an acoustic cycle is summarized as follows. Figure C.24(a) is generated at the time at which the temperature reaches 300 K, which is the reference temperature at the right oscillating boundary (side 45). Everywhere thermal equilibrium is maintained at the beginning of an acoustic cycle (in Fig. C.24(a)). As time progresses (starting from Fig. C.24(b)), the temperatures of the computational domain and of the stack near the edges start to change. The left end of the stack edge which is near the pressure anti-node becomes warmer than the right end. Vertically, temperature is changing from the solid fluid interface to the inside of the stack up to a distance of 0.016 mm, which is very small compared to the thermal penetration depth (0.18 mm). From a heat transfer point of view the most interesting finding of this study is the temperature gradient developed along the stack during half of an acoustic cycle, within a distance of the particle displacement distance (2.76 mm) away from the edges of the stack plate. Temperature at the middle of the stack is equal (300 K) every where or very little temperature difference exists. This indicates that temperature within the stacks has not reached steady state yet. At steady state condition, a moderate temperature gradient will be developed along the stack plate, high temperature in the left edge, and gradually decreasing toward the right. The working fluid is fully compressed in Fig. C.24(d) showing maximum temperature near the pressure anti-node in the working fluid and in the stack end. As time progresses, as illustrated in Fig. C.24(e), the working fluid gradually expands and cools down, and in Fig. C.24(f); the working fluid is fully expanded. During the second half of the acoustic cycle the working fluid is subjected to compression, and the temperature distribution goes through the phases displayed in Fig. C.24 in reversed order. Figure C.25(a) shows the time averaged temperature fluctuations for two different locations; along the stack plate and one cell above of it. The left end of Fig. C.25(a) along the stack plate surface shows higher temperature fluctuation than the right end and near the middle of the plate temperature fluctuations are zero. Therefore, Fig. C.25(a) supports the findings of Fig. C.24 and thermoacoustic effect can be observed even within 0.1 second of the start of the

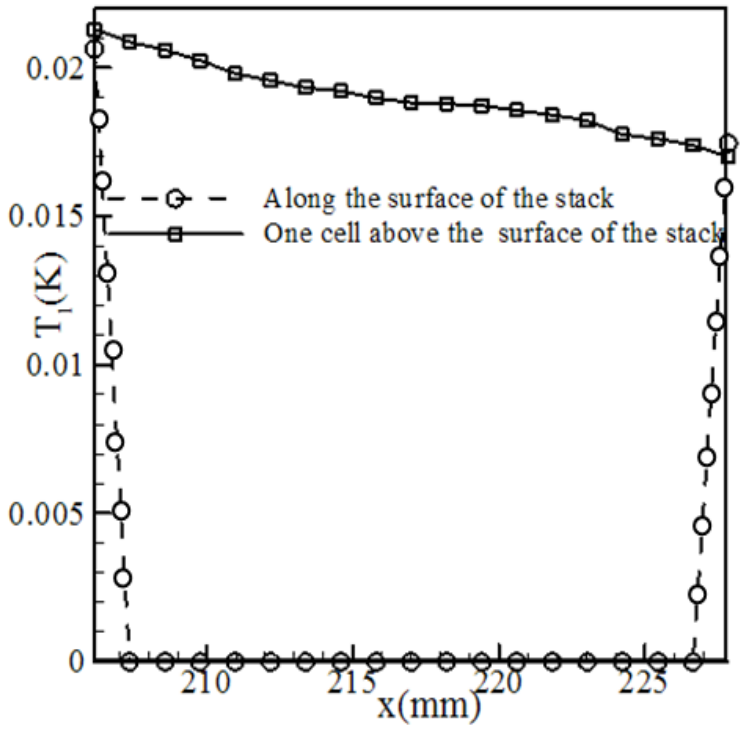

Figure C.25: (a) Time averaged temperature distribution vs. x.

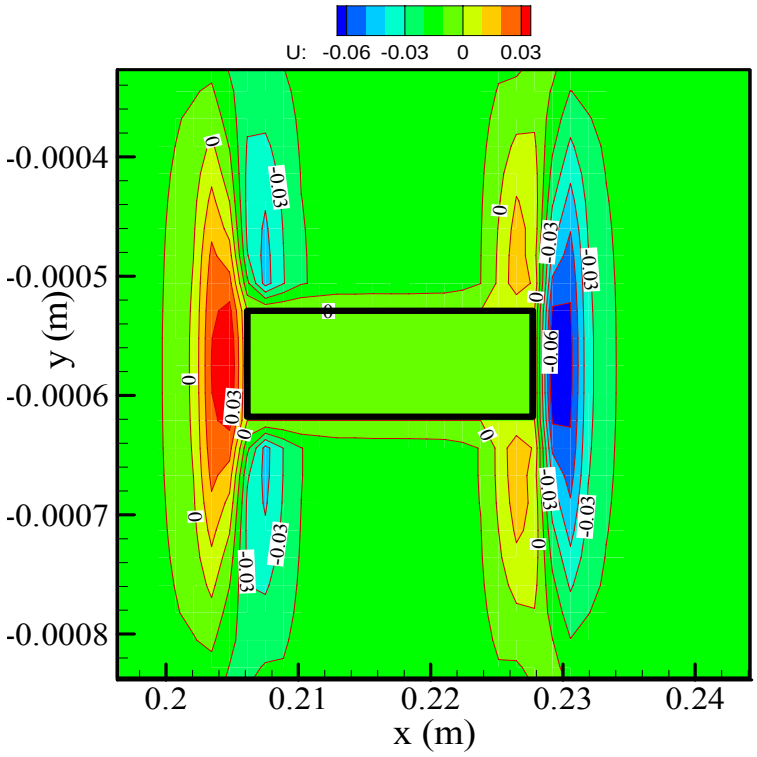

Figure C.25: (b) Time averaged x-component of velocity contours, 9x magnification factor is used. The unit of *u* is in m/s.

simulation or applying the acoustic wave in the resonator for the operating condition that has been considered in the present study. The fluid temperature distribution one cell above of the stack plate surface in Fig. C.25(a) depicts almost a linear distribution. There is a small difference in fluid and stack plate temperature at the left and right ends of the stack plate; at the right end the fluid temperature is lower than the stack plate temperature and at the left end, the fluid temperature is higher than that of the stack end. These fluctuating temperature distributions would correspond to the thermoacoustic cycle described by the movement of a gas parcel in Swift [1988]. Figure C.25(b) shows time averaged *x*- component of velocity contours. Concentrated vortices are observed near the edges, in between the stack plates (not shown in Fig. C.25(b)), and in the open region. The generation of vortices in between the stack plates is not surprising, since the ratio of stack spacing to viscous penetration depth is large.

As previously mentioned, a non-isothermal stack plate simulation is costly because a temperature gradient develops in the stack plate, which requires considerable amount of time. The temperature contours within the stack plate shows that temperature has not been reached steady state yet. Since, in steady state solution, a constant temperature gradient develops along the stack plate. Therefore, the present results are for the transient regime. Steady state results could not be produced since during running the cyclic simulations the "restart facility" in STAR-CD could not be used. The restart facility allows the user to take the results of one simulation as initial conditions for another simulation. It was originally seemed a suitable option for the present simulation to reach steady state. The flow and thermal fields of the last time step of one cycle were the initial conditions for the first time step of the next cycle. However, it was noticed that the restart facility in STAR-CD did not transfer all the results from the generated file since every time a new cycle was simulated using the restart facility, there was a glitch in plots of pressure, velocity, and temperature versus time. This appeared at the first time step of every new run.

C.8.3 Energy Fields

The energy interaction between a solid stack plate and the acoustically driven working fluid is investigated by visualizing energy streamline pattern in the neighborhood of the

solid stack plate. For unsteady, periodic problems like thermoacoustics, energy stream functions are calculated from the time averaged velocity, temperature, and other relevant properties (density, viscosity, specific heat, and thermal conductivity of the working fluid and also the thermal conductivity of the solid stack material). The display of the energy streamline is more useful for understanding the physics of the flow for thermoacoustic problems.

Kimura and Bejan [1983] proposed heat line as a visualization tool for thermal energy flow in convection heat transfer problem. The heat line is derived from a heat function that satisfies the steady state energy equation. Kimura and Bejan define the heat function φ_H for an incompressible inviscid 2-D flow,

$$\frac{\partial \varphi_H}{\partial y} = \rho C_p u T - k \frac{\partial T}{\partial x}, \tag{C.25}$$

$$-\frac{\partial \varphi_H}{\partial x} = \rho C_p v T - k \frac{\partial T}{\partial y}, \tag{C.26}$$

where ρ, C_p, u ,v, T, $\frac{\partial T}{\partial x}$, and $\frac{\partial T}{\partial y}$ are the density, the specific heat at constant pressure, x, and y component velocity, temperature and temperature gradient in the x, and y direction respectively. By combining Eq. (C.25) and (C.26) with the energy equation for incompressible inviscid 2-D flow, the heat line can be obtained numerically. It is not possible to derive a heat function analytically for two dimensional viscous compressible flow.

The variables of interest in thermoacoustic problems are time average heat flux and work flux. Since the energy streamline pattern and energy flux density display the total energy (heat flux and work flux), therefore visualizing energy streamline and evaluating energy flux density may be more useful. Figure C.26(a) and (b) show the energy flux density contours in the x and y directions, respectively. In Fig. C.26 energy flows horizontally from the cold end of the stack to that of the hot end. Energy flows in the air and within the stack because of the temperature gradient along the stack. No such energy streamline

pattern is available in the existing literature. The present work shows the energy streamline pattern in the fluid and in the stack plate regions for the first time. Vertical

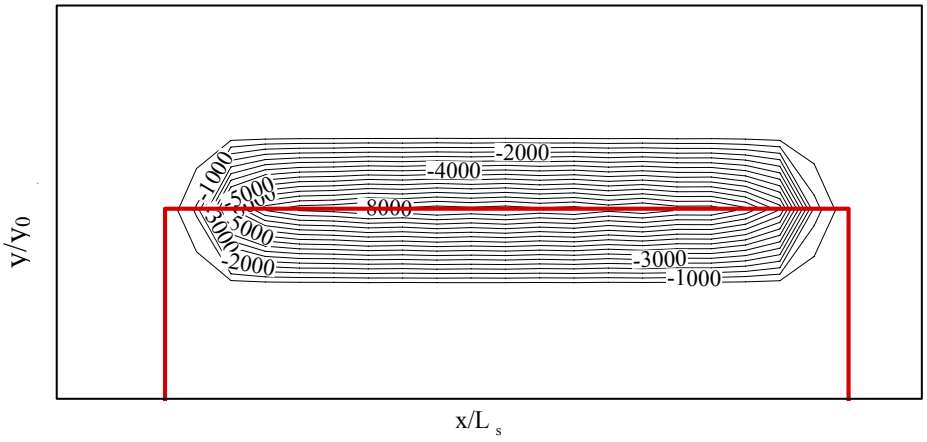

(a) E_x

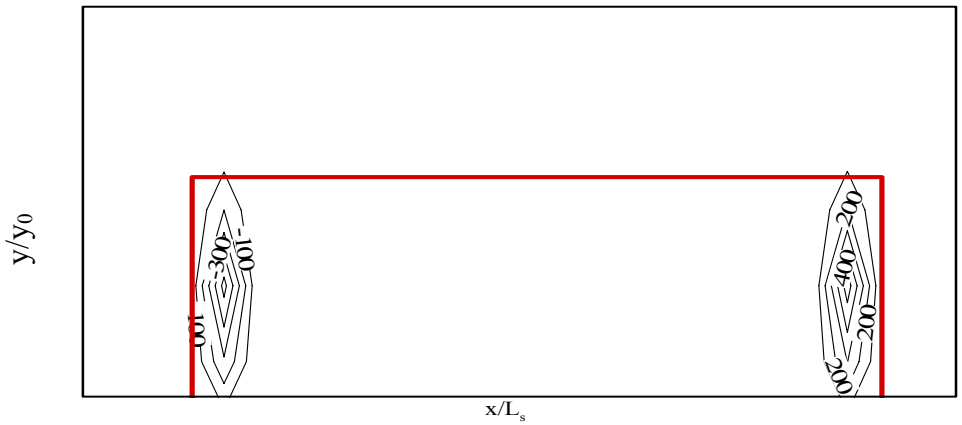

(b) E_y

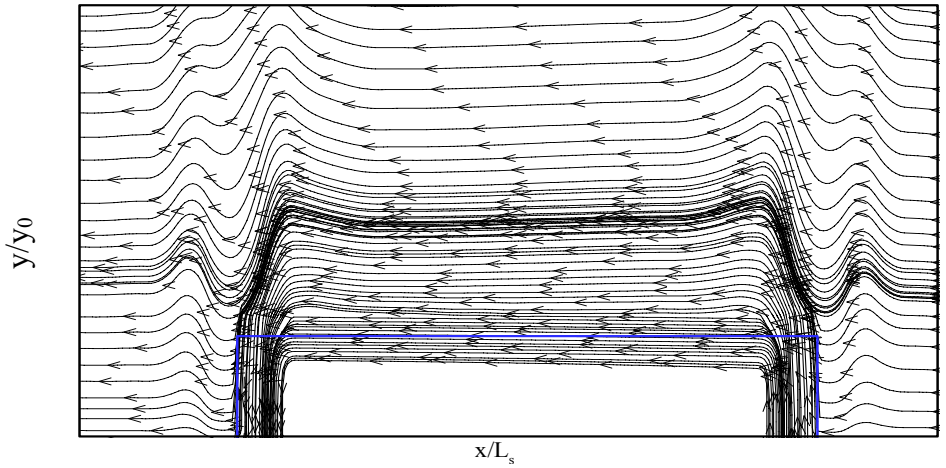

(c) Energy streamlines

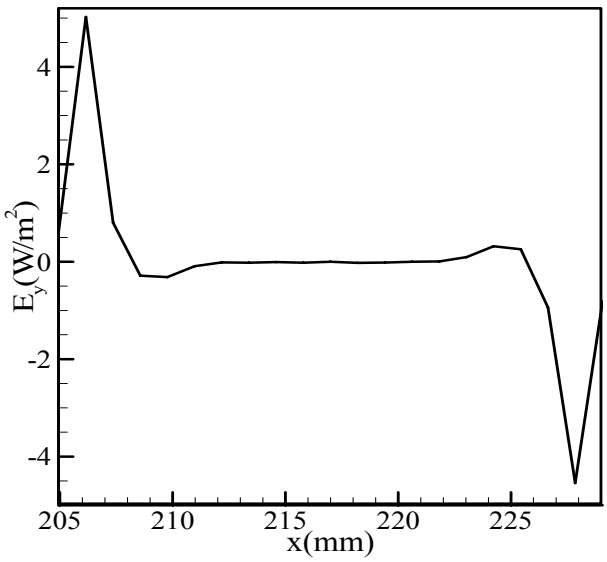

(d)

Figure C.26: Contours of energy flux density for $14 \le x/L_s \le 17$ and $0 \le y/y_0 \le 0.5$ (a) along the x direction, (b) along the y direction, (c) energy streamlines, and (d) y-component of energy flux density along x. 20 x magnification factor is used in (a) and (b), and 18 x in (c). The unit of energy flux density in (a) and (b) is W/m^2.

energy flux density in Fig. C.26(b) is concentrated near the stack ends. Energy stream lines pattern in Fig. C.26(c) support the findings of Fig. C.26(a) and (b). Figure C.26(d) shows y-component of energy flux density in the x-direction. Figure C.26(d) follows the similar behavior to that Fig. C.10 for the thin plate limit.

C.9 Conclusions

Section C.8 considers an array of thick stack plate in the computational domain by solving energy equation inside the stack plates. Counter rotating flow circulations are observed at the stack edges and also in the outer region of the stack, because of the finite thickness of the stack plate. The difference between the thin and thick stack plate simulation in the flow field is that the outer circulations due to finite thickness of the stack plate are absent in the thin plate limit. For the thick plate, to develop a temperature gradient within the solid stack needs much longer time. A linear temperature distribution is obtained within the fluid near the stack plate that supports the experimental results of Chapter 7. Y-component of energy flux density shows identical behavior to that of thin

plate results, but the x-component of energy flux density shows different behavior because of the different boundary condition at the stack plate. Energy flows horizontally within the stack plate and the fluid because of the temperature gradient within the stack plate and both temperature and velocity gradients within the fluid.

C.10 Energy Fields in a Resonant Channel

Now energy fields in a resonant channel are simulated and results are presented in terms of energy streamline and energy flux density values. Comparisons of the current numerical work with analytical solutions (Hamilton et al. [2003]) for velocity field are performed. No previous results for energy streamline and energy flux density values near and within a resonator are reported in the literature. This work presents the first attempt to calculate energy flux density values and energy streamline patterns in a resonant channel. The energy streamline patterns and energy flux values agree qualitatively with the experimental work of Merkhli and Thomann [1975].

The hydro- and thermodynamic processes near and within a two-dimensional resonant channel are simulated by numerical solution of the compressible Navier-Stokes, continuity, energy equations, and the equation of state (for air as the working fluid). The resonator walls are maintained at a constant temperature and the effects of gas viscosity, resonator wall spacing, and heat conduction of the gas are investigated concentrating on the time averaged velocity, temperature, energy streamlines and energy flux density in the gas. Energy streamline contours and energy flux density plots qualitatively agree with Merkhli and Thomanns' observations [1975]. It is observed that energy transfer inside the channel consisted of two factors for the cases considered: one due to conduction term and the other due to enthalpy term. The results are applicable to thermoacoustic devices.

C.10.1 Computational Domain and Boundary Conditions

Numerical solution to the equations of motion presented in this investigation considers a description that accounts for the combined effects of nonlinearity, viscosity, heat conduction, and multidimensional flow. The greatest impediment to direct numerical simulation has been the computation time required for adequate resolution of the acoustic field throughout the resonator. The difficulty results from the widely different length scales encountered in thermoacoustic engines. The large dimension is the length of the resonator, which is comparable to the acoustic wavelength at the fundamental natural frequency. The small dimension is the diameter of the channel (a few viscous penetration depths); these two lengths can differ by several orders of magnitude. For adequate

resolution of the field structure within the channel small time steps compared to the period of acoustic oscillation and fine mesh structure (see **Section** C.10.2.1) are chosen.

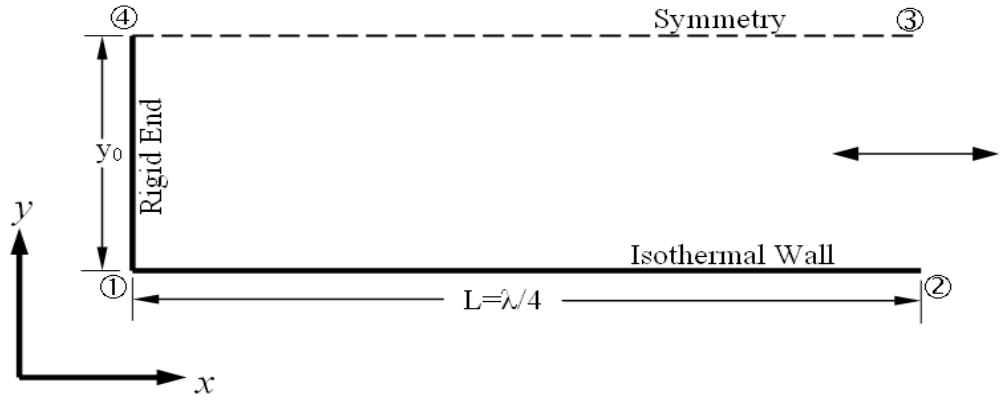

Figure C.27: Computational domain and boundary conditions.

A schematic of the system (2-D rectangular geometry) being modeled is shown in Fig. C.27, because of the symmetric condition with respect to the horizontal center of the channel, only half of the channel (from the bottom wall to the center) is considered. No-slip and isothermal boundary conditions are applied at boundary side 12 (bottom horizontal wall in Fig. C.27), assuming that the wall is made of a solid with infinite thermal conductivity and heat capacity and symmetry boundary condition at boundary side 34 (top horizontal wall in Fig. C.27). The left wall (boundary side 14 in Fig. C.27) is a rigid adiabatic wall. The pressure, the velocity, and the temperature at the open end (boundary side 23 in Fig. C.27) are expressed as in terms of Eqs. (C.13), (C.14), and (C.15) in order to represent the action of a standing wave.

In the present simulation air at a mean pressure of 100 kPa, mean temperature of 298.15 K, frequency of 92.245 Hz and a DR of 1.0% is chosen. The DR corresponds to Mach number of 7.143E-03. The Mach number (u_1 / a) is calculated based on the velocity amplitude at the velocity antinode and the speed of sound (a) based on the mean temperature, following Cao et al. [1996]. Turbulence is neglected for the present simulations because the critical Reynolds number, $\mathrm{Re}_\delta = \sqrt{2}u_A / \sqrt{(\nu\omega)} = 36.444$ as

defined by Merkhli and Thomann [1975] is below 400. In defining the critical Reynolds number viscous penetration depth, δ_v is used as the characteristic length.

The domain length in the *x*-direction is equal to the 1/4 of the acoustic wave length and in the *y*-direction 3, 4, and 10 times the gas viscous penetration depth evaluated at the mean temperature, respectively. The overbar is used to denote the time average of any variable *z*, over an integer number of periods,

$$\bar{z} = \frac{\omega}{2\pi} \int_0^{2\pi/\omega} z \, dt. \tag{C.27}$$

The time average is calculated over a time domain of several periods excluding the initial transient stage of the solution which usually takes several periods.

To visualize the direction of heat flux, temperature contours generally are sufficient for steady heat transfer problems but they are not suitable when convection is involved. When convection is involved, energy flux density (Eq. (C.18)) is useful for visualizing energy transfer. The energy flux density is calculated within the resonant channel and the results are presented qualitatively (through energy streamlines, Figs. C.37- C.38) and quantitatively in Figs. C.32- C.33, and C.39-C.40.

C.10.2 Results and Discussion

C.10.2.1 Comparison

Figure C.28 shows the variation of the *x* component of streaming velocity along the channel at *x/L*=0.5 for the width of the channel 10 times the viscous penetration depth. In this figure, the vertical axis is the *x* component of the dimensionless time averaged streaming velocity (u_{st}/u_R), u_{st} and u_R are the time average streaming velocity and the reference velocity given by $u_R = 3u_1^2/16a$, where u_1 is the maximum oscillatory velocity at the velocity antinode. This reference velocity value represents the maximum streaming velocity in case of a perfect sinusoidal wave form in wide channels obtained by Rayleigh [1945]. Results from Hamilton et al. [2003] are also included in the same figure (dashed

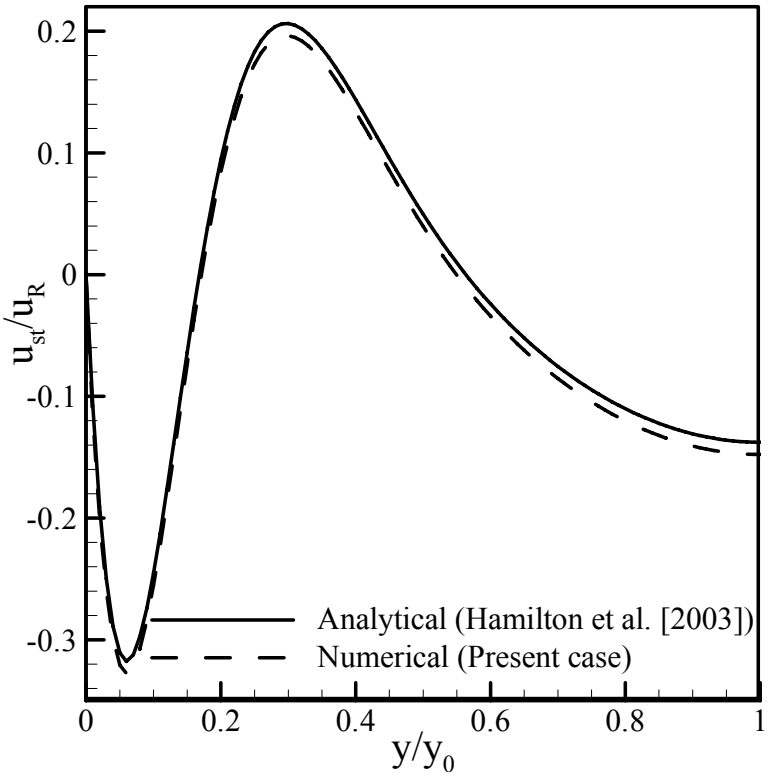

Figure C.28: Time averaged *x*-component of streaming velocity along the tube for $y_0=10\delta_\mu$ at $x/x_0=0.5$.

line). The interaction between the acoustic waves in viscous fluids and solid boundaries is responsible for a secondary, steady circulatory flow, namely acoustic streaming, which is superimposed on the dominating first order acoustic velocity. This second order, steady flow is evaluated based on the average mass transport velocity:

$$u_{st} = \frac{\overline{\rho u}}{\overline{\rho}}. \tag{C.28}$$

In Eq. (C.28), the instantaneous density and *x*-component of velocity are time averaged over a time domain of several periods. The predictions of the current study compare well with the results from Hamilton et al. [2003]. The maximum difference between the predictions of the current study and Hamilton et al's solution [2003] is approximately 4.8%. The results given in the reference solution are for a resonator in which the sound field is assumed to be formed by shaking the system with a harmonic excitation. Since the present study considers a resonator with an applied standing wave boundary, the resulting velocity field slightly differs. Results from the present simulations are presented

as solid lines with $\Delta x/\lambda = 8.33e-4$, and $\Delta y/\lambda = 4.285e-6$, evenly spaced in Fig. C.28. Further reducing Δx and Δy provides negligible improvement. We consider the quantitative agreement in Fig. C.35 sufficient for our purposes here and use $\Delta x/\lambda = 8.33e-4$, and $\Delta y/\lambda = 4.285e-6$, and time step size 0.5 % for the rest of the calculation with channel width 10 times the viscous penetration depth. With channel widths 4 and 3 times the viscous penetration depth (comparisons not shown here), $\Delta x/\lambda = 8.33e-4$, and $\Delta y/\lambda = 2.078e-6$, and time step size 0.5 %, and $\Delta x/\lambda = 8.33e-4$, and $\Delta y/\lambda = 1.87e-6$, and time step size 0.5 % are used for the rest of the calculations.

C.10.2.2 Flow and Energy Fields

The fundamental natural frequency of the resonator in the presence of viscosity and heat conduction is chosen to be one that maximizes Eq. (40) (*x*-component of velocity) of Hamilton et al. [2003] at the velocity antinode of the resonator i.e., at $x=L$, and $y=y_0$ (in Fig. C.27). Figure C.29(a), (b), and (c) show the axial distributions of pressure, velocity, and temperature fluctuations at 8 time steps in a cycle with width of the channel 10 times the viscous penetration depth, at $y/y_0 = 0.5$. Axial distribution of time averaged temperature amplitudes at $y/y_0 = 0.5$ along the channel are presented for width of the channel 10 and 4 times the viscous penetration depth in Figs. C.30-C.31. The time averaged temperature profiles in Figs. C.30 and C.31 show heating at the closed end

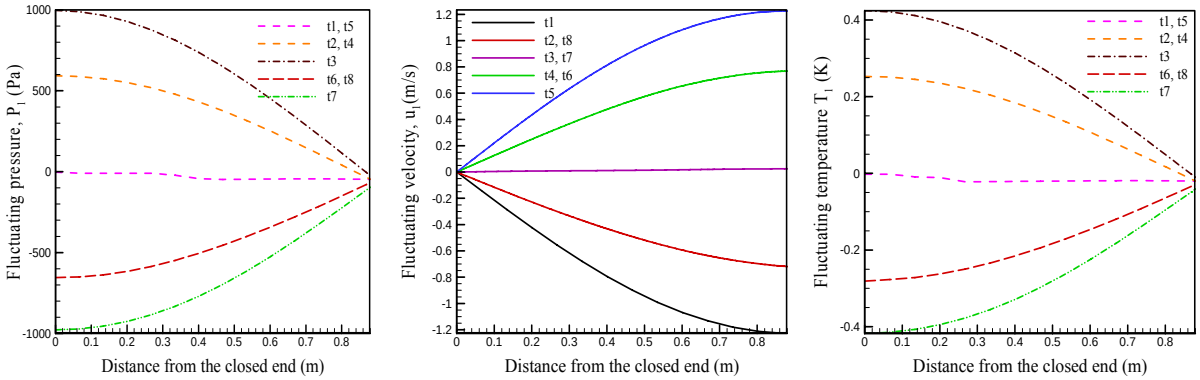

(a) (b) (c)

Figure C.29: (a) Fluctuating pressure, (b) velocity, and (c) temperature along the tube axis, $t1=T/8$, $t2=2T/8$……. $t8=T$.

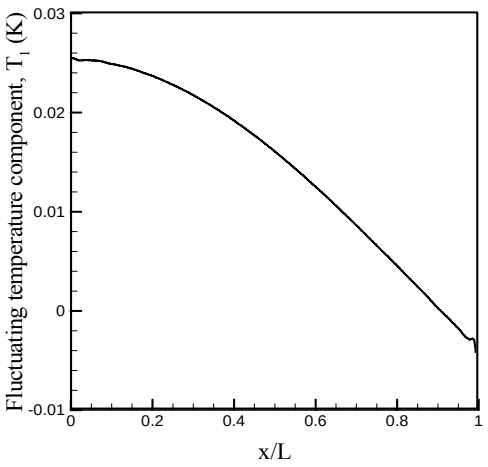

Figure C.30: Time averaged temperature, y_0=10 δ_μ, $y/y_0 = 0.5$.

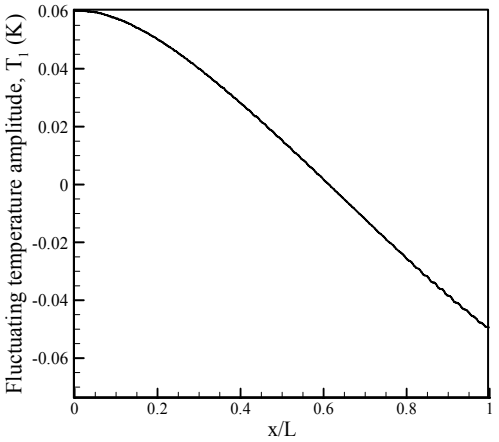

Figure C.31: Time averaged temperature, y_0=4 δ_μ, $y/y_0 = 0.5$.

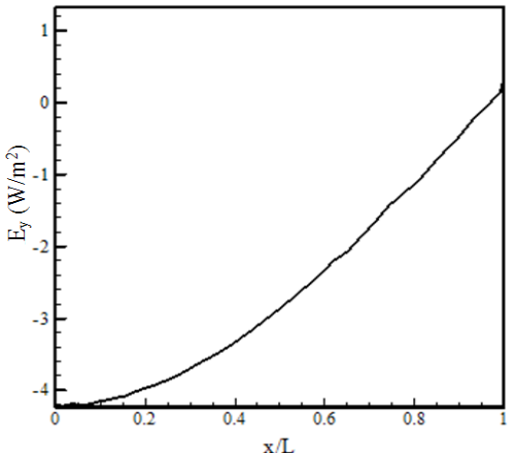

Figure C.32: Time averaged y- component of energy flux density with y_0=10 δ_μ along the wall.

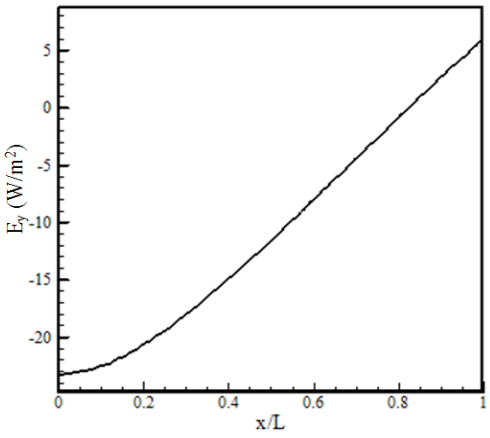

Figure C.33:Time averaged y-component of energy flux density with y_0=4 δ_μ along the wall.

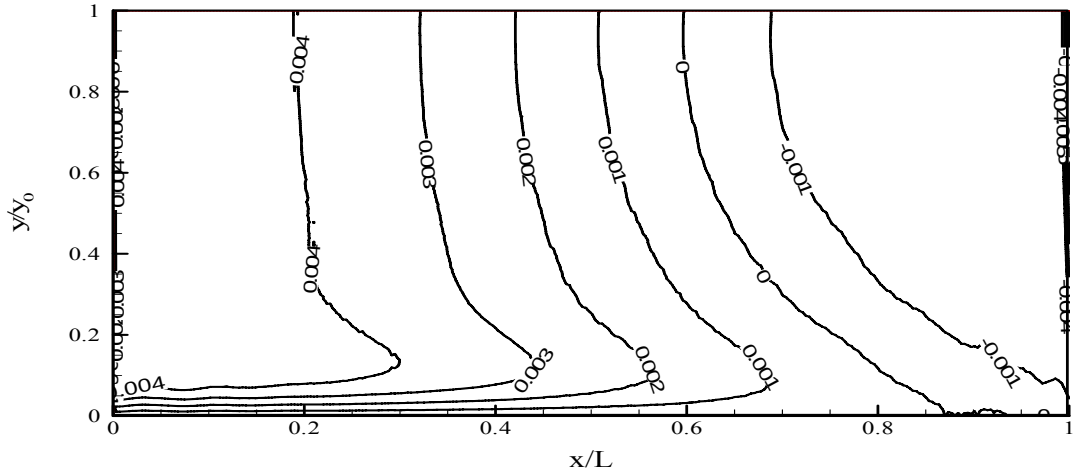

Figure C.34: Time averaged fluctuating temperature contours (in °C) with y_0=10δ_μ.

(pressure antinode) and cooling at the open end (velocity antinode of the standing wave). Merkhli and Thomann [1975] observed similar behavior at their experiments. Higher heating and cooling effects are observed for lower width of the resonator in Fig. C.31. The y – component of energy flux density (E_y) plots in Figs. C.32 and C.33 are along the wall of the channel, where the enthalpy term is zero because of the zero-velocity boundary condition at the wall. The vertical energy flux at the wall is due to the heat conduction term. The time averaged energy flux at the wall surface is positive for a heat flux entering the gas from the wall and negative for it leaving the gas through the wall. Higher E_y is observed in Fig. C.33 due to higher velocity and temperature gradients at lower width of the resonator. Figures C.34 and C.35 show the time averaged oscillating amplitude of temperature contours (in °C) for width of the channel 10 and 4 times the viscous penetration depth. The positive temperature contours (in Figs. C.34 and C.35) show heating of the fluid near the closed end (pressure antinode), and the negative contours show cooling near the driver end (velocity antinode). The dense temperature contours within the thermal penetration depth near the closed end (in Figs. C.34 and C.35) show higher energy transfer at that location which is also supported by the y – component of energy flux density plots (Figs. C.32 and C.33). Time averaged x-component of velocity contours in Fig. C.36 show opposite counter rotating circulations between the channel walls due to the interaction of the sound field with the channel wall boundaries. This type of flow is observed among others by Hamilton et al. [2003] analytically, Thompson et al. [2005], Nabavi et al. [2007, 2008 (a), 2008 (b), 2008(c)] experimentally in a resonator, Moreau et al. [2009] experimentally in a resonator with a stack, and Marx and Blanc-Benon [2004] numerically within an array of stack plates. But the appearance of counter rotating vortices diminishes as the width of the channel becomes smaller than 4 times the viscous penetration depth.

Typical energy streamline patterns presented in Figs. C.37 and C.38 for widths of the channel 10 and 4 times the viscous penetration depth, show net heat pumping effect from a source at the right to a sink at the left. No such heat pumping effect is observed for width of the channel about 3 times the fluid's viscous penetration depth (not shown here).

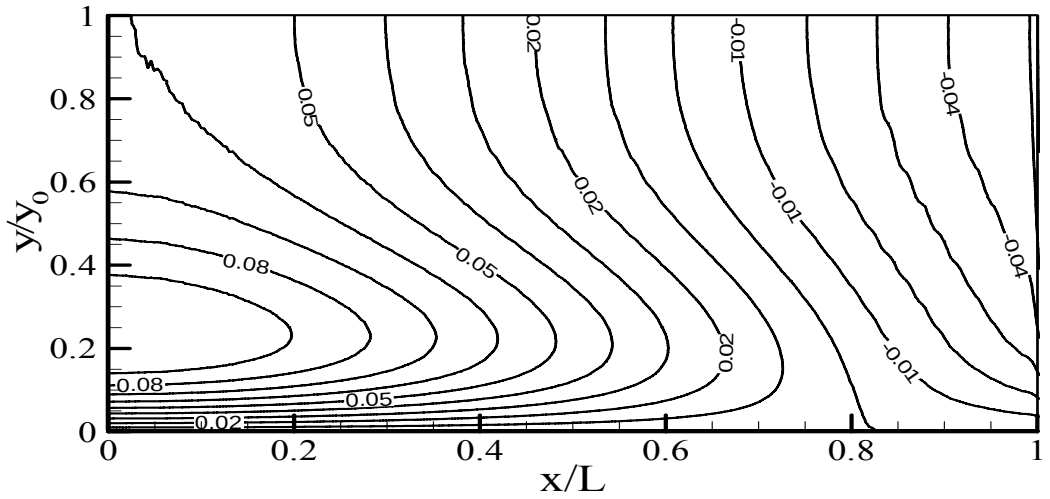

Figure C.35: Time averaged fluctuating temperature contours (in °C) with y_0=4 δ_μ.

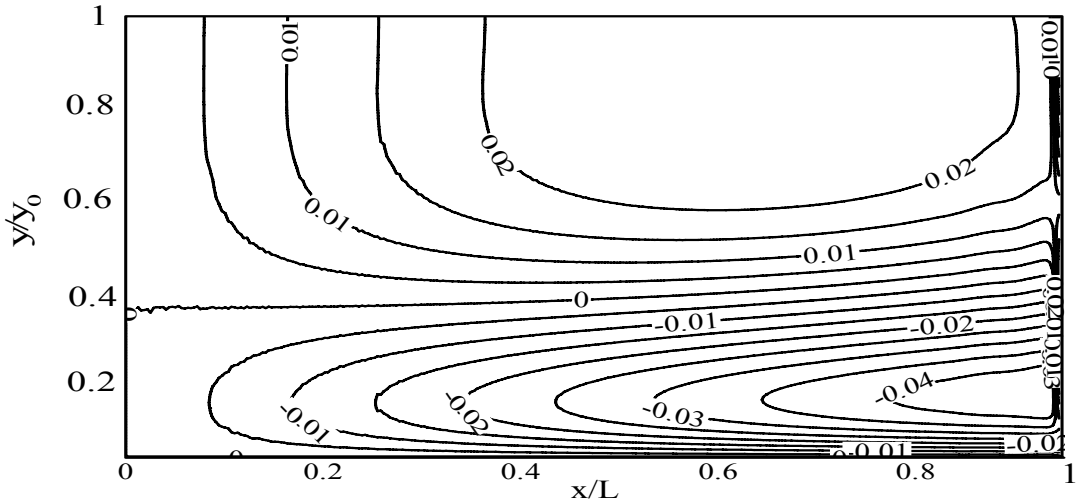

Figure C.36: Time averaged velocity contours (in m/s) with y_0=4 δ_μ.

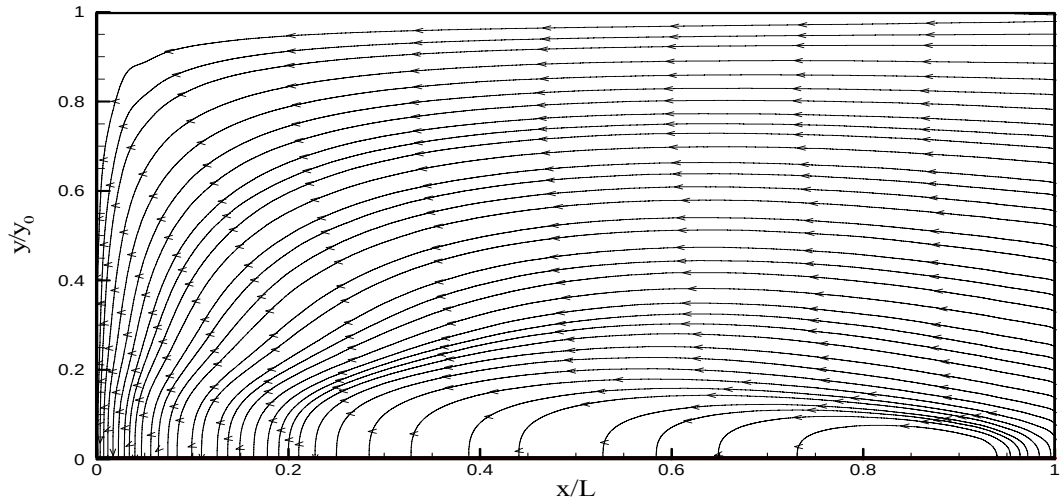

Figure C.37: Energy streamlines with y_0=10δ_μ.

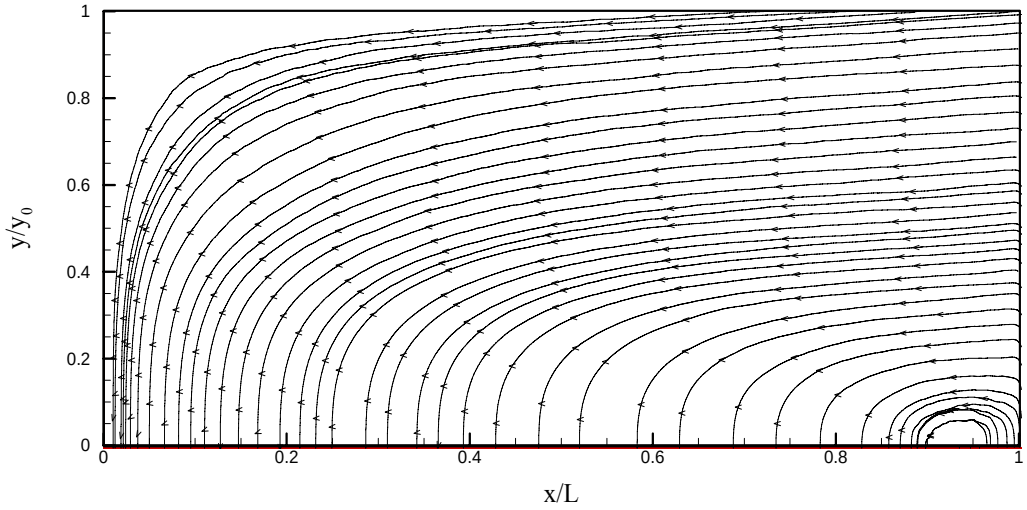

Figure C.38: Energy streamlines with $y_0=4\delta_\mu$.

The high density of the energy streamlines (Figs. C.37 and C.38) near the closed end supports the vertical energy flux density profiles (Figs. C.32 and C.33) that show high values near close end of the resonator and less values near the open end. Figures C.32, C.33, C.37, and C.38 qualitatively support Merkhli and Thomanns' results [1975]. Merkhli and Thomanns' [1975] observed experimentally that the wave motion is attended by time-averaged net heat flows. The longitudinal heat flux is transported from the velocity antinode to the adjacent pressure antinodes (Figs. C.37 and C.38); and the transverse heat flux is rejected to the environment in a region near the pressure antinode (Figs. C.32 and C.33) or is absorbed from the environment in a region near the velocity antinode.

Figures C.39 and C.40 show the time averaged oscillating amplitudes of temperature in the transverse direction at the middle of the channel for width of the channel 10 and 4 times the viscous penetration depth. There is temperature overshoot (Fig. C.39, for width of the channel 10 times the viscous penetration depth) near the wall and a plug flow near the center line. There is no variation of pressure along the transverse direction at the middle of the channel (not shown here). The axial energy flux density is presented at the axial center of the channel in the transverse direction in Figs. C.41-C.42 for width of the channel 10 and 4 times the viscous penetration depth. The horizontal energy flux (Eq.

(C.18)) is zero at the wall because of the zero- velocity and isothermal boundary conditions at the wall. The strong energy flux near the wall is possibly due to the conduction and the enthalpy term. Energy flux density disappears for the width of the channel three times the viscous penetration depth.

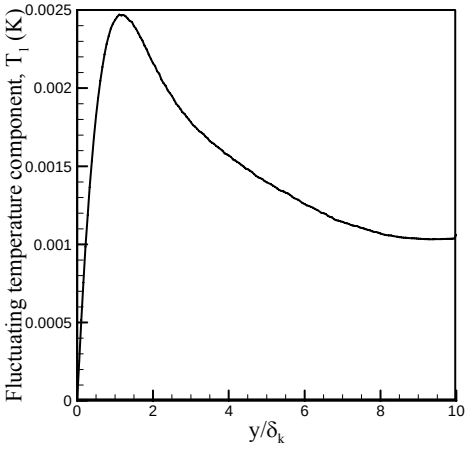

Figure C.39: Time averaged temperature, y_0=10 δ_μ, *x/L*=0.5.

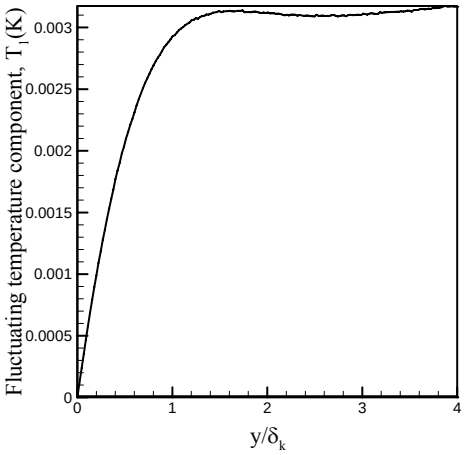

Figure C.40: Time averaged temperature, y_0=4 δ_μ, *x/L*=0.5.

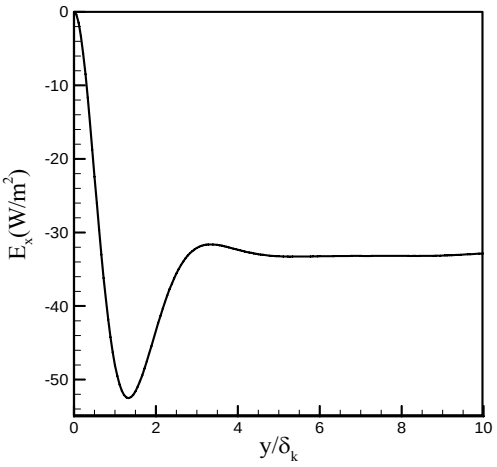

Figure C.41: Time averaged *x*- component of energy flux density with y_0=10 δ_μ, *x/L*=0.5.

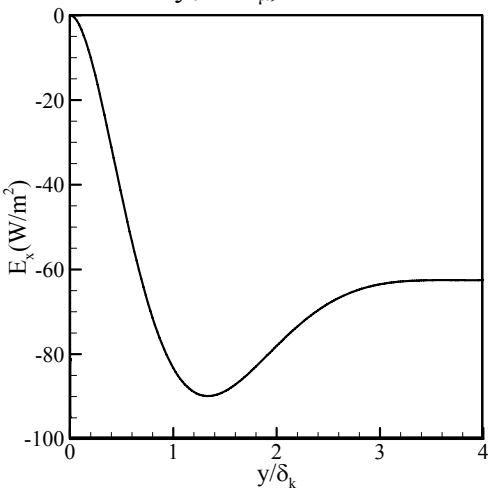

Figure C.42: Time averaged *x*- component of energy flux density with y_0=4 δ_μ, *x/L*=0.5.

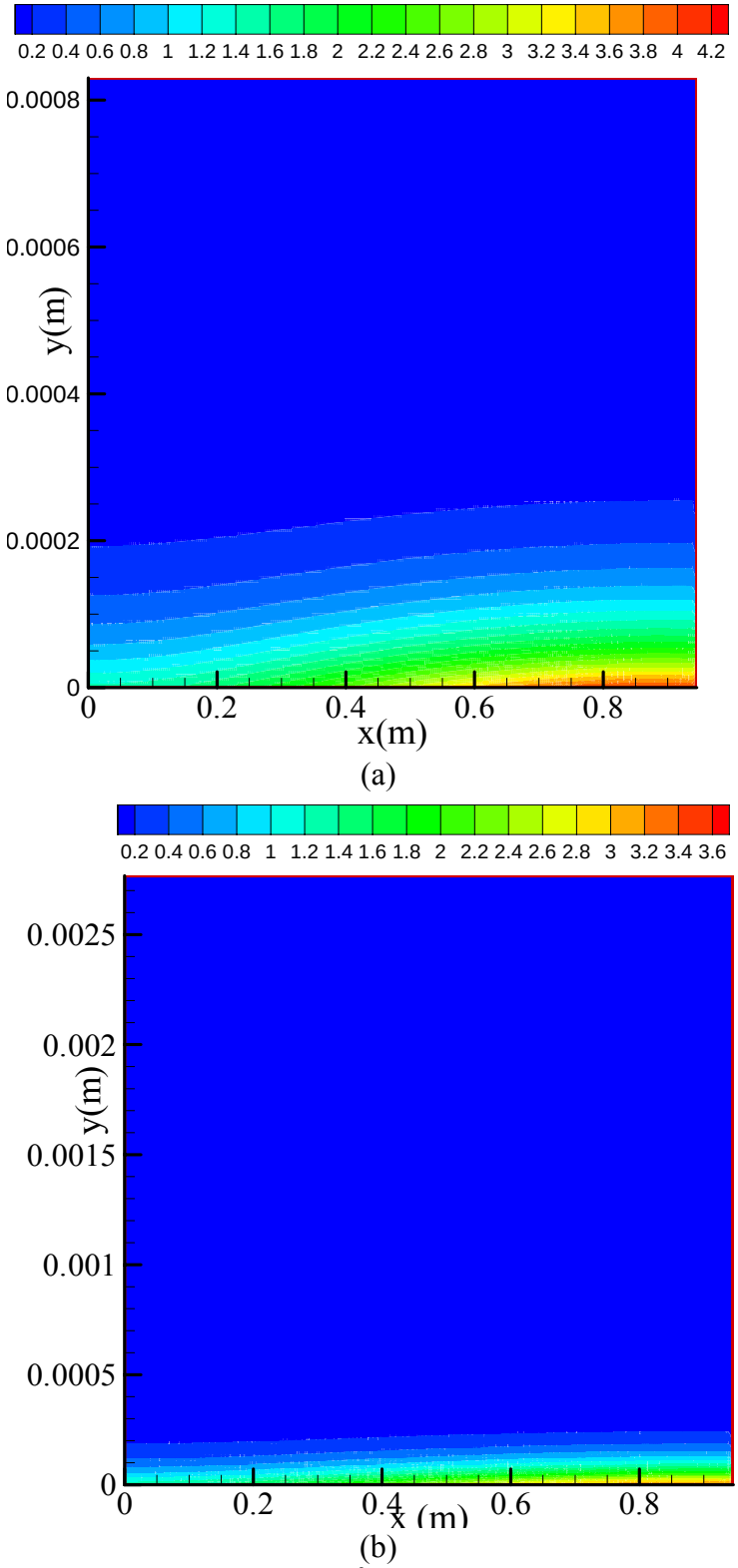

Figure C.43: Entropy generation rate (W/m^{3}K) inside resonator when (a) $y_0 = 4\delta_k$, and (b) $y_0 = 10\delta_k$.

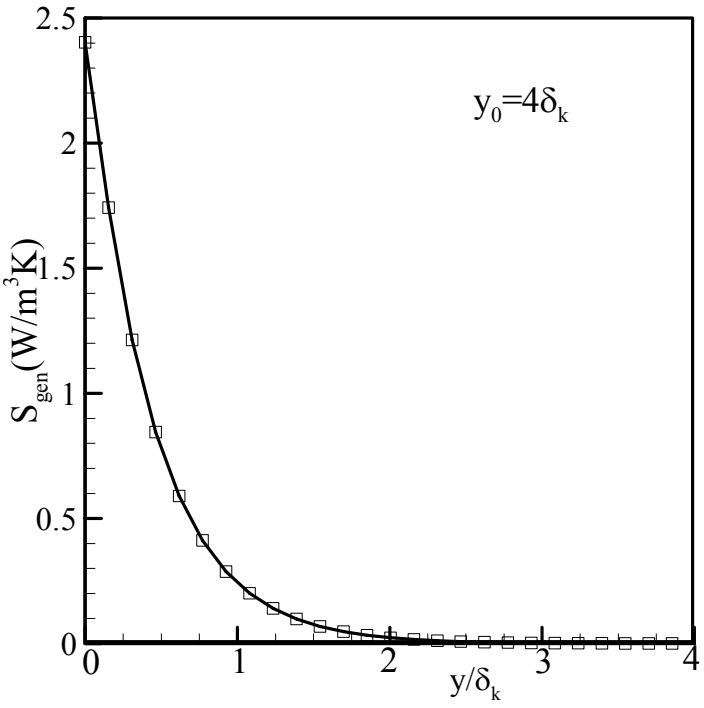

(a)

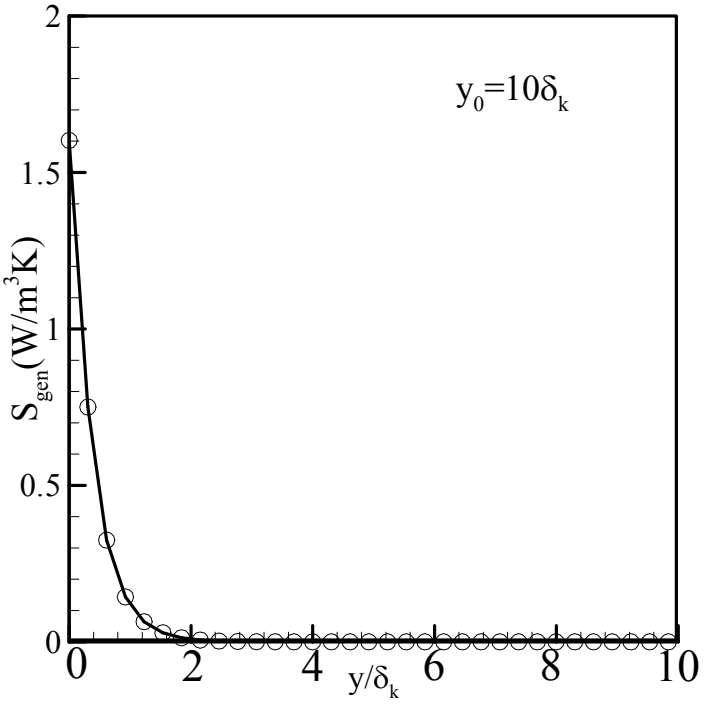

(b)

Figure C.44: Entropy generation rate (W/m^3K) along the vertical center line of the resonator when (a) $y_0 = 4\delta_k$, and (b) $y_0 = 10\delta_k$.

Figure C.43 shows entropy generation contours when (a) $y_0 = 4\delta_k$, and (b) $y_0 = 10\delta_k$. For both of the resonator widths, entropy generation is concentrated near the resonator wall and especially near the velocity anti-node, because of high shear stress. Entropy generation inside the resonator for both of the widths is dominated by fluid friction irreversibility. Total entropy generation rate is 1.11 W/m^{3}K at $y_0 = 4\delta_k$ compared to 0.53 W/m^{3}K at $y_0 = 10\delta_k$. Entropy generation rate is higher for lower resonator spacing because of higher shear stress experienced by the working fluid. Figure C.44 shows the entropy generation rate (W/m^{3}K) along the vertical center line of the resonator when (a) $y_0 = 4\delta_k$, and (b) $y_0 = 10\delta_k$. For $y_0 = 4\delta_k$, entropy is generated almost half of the resonator height, whereas for $y_0 = 10\delta_k$, entropy is generated up to $2\delta_k$ from the resonator horizontal wall. Maximum entropy is generated near the wall, which is expected because of high shear stress near the wall. It then gradually decreases away from the wall because of less shear stress. Therefore, in order to develop miniature thermoacoustic devices this entropy generation due to enhance viscous loss should be considered. Using lower Pr fluid might reduce the viscous loss within the resonator.

C.11 Conclusions

In **Section** C.10, the oscillating gas motion in a resonant channel is studied numerically. The channel walls are assumed as isothermal while the width of the channel wall is varied to observe the main effects influencing gas motion in a resonant channel, i.e., nonlinearity of resonance flow, together with viscous and thermal gas interactions with the wall.

- A net heat pumping effect is observed from the right end of the channel to the left end with the channel width about 10 and 4 times the viscous penetration depth. No such effect is observed with the channel width about 3 times the thermal penetration depth.

- A pair of counter rotating vortices is observed in between the channel walls for width of the channel about 10 and 4 times the viscous penetration depth. Whereas a single circulation is observed while the channel width is about 3 times the

thermal penetration depth or lower (also observed by Marx and Blanc Benon [2004] in between a pair of stack plates).

- Energy streamline contours and energy flux density plots qualitatively agree with Merkhli and Thomanns' observations [1975]. It is observed that energy transfer inside the channel consisted of two factors for the cases considered: one due to the conduction term and the other due to the enthalpy term.

- The entropy generation inside the resonator shows that fluid friction irreversibility dominates heat transfer irreversibility. Total entropy generation rate is higher for smaller resonator wall spacing compared to the larger one because of the higher shear stress for lower spacing. Therefore, in order to develop miniature thermoacoustic devices this entropy generation due to enhance viscous loss should be considered.